Applied Condition Monitoring 4

Fakher Chaari
Radoslaw Zimroz
Walter Bartelmus
Mohamed Haddar *Editors*

Advances in Condition Monitoring of Machinery in Non-Stationary Operations

Proceedings of the Fourth International Conference on Condition Monitoring of Machinery in Non-Stationary Operations, CMMNO'2014, Lyon, France December 15–17

Springer

Applied Condition Monitoring

Volume 4

About this Series

The book series Applied Condition Monitoring publishes the latest research and developments in the field of condition monitoring, with a special focus on industrial applications. It covers both theoretical and experimental approaches, as well as a range of monitoring conditioning techniques and new trends and challenges in the field. Topics of interest include, but are not limited to: vibration measurement and analysis; infrared thermography; oil analysis and tribology; acoustic emissions and ultrasonics; and motor current analysis. Books published in the series deal with root cause analysis, failure and degradation scenarios, proactive and predictive techniques, and many other aspects related to condition monitoring. Applications concern different industrial sectors: automotive engineering, power engineering, civil engineering, geoengineering, bioengineering, etc. The series publishes monographs, edited books, and selected conference proceedings, as well as textbooks for advanced students.

More information about this series at http://www.springer.com/series/13418

Fakher Chaari · Radoslaw Zimroz
Walter Bartelmus · Mohamed Haddar
Editors

Advances in Condition Monitoring of Machinery in Non-Stationary Operations

Proceedings of the Fourth International Conference on Condition Monitoring of Machinery in Non-Stationary Operations, CMMNO'2014, Lyon, France December 15–17

Springer

Editors
Fakher Chaari
National School of Engineers of Sfax
Sfax
Tunisia

Radoslaw Zimroz
Diagnostics and Vibro-Acoustics Science Laboratory, Institute of Mining Engineering
Wrocław University of Technology
Wroclaw
Poland

Walter Bartelmus
Diagnostics and Vibro-Acoustics Science Laboratory, Institute of Mining Engineering
Wrocław University of Technology
Wroclaw
Poland

Mohamed Haddar
Mechanical Engineering Department
National School of Engineers of Sfax
Sfax
Tunisia

ISSN 2363-698X ISSN 2363-6998 (electronic)
Applied Condition Monitoring
ISBN 978-3-319-20462-8 ISBN 978-3-319-20463-5 (eBook)
DOI 10.1007/978-3-319-20463-5

Library of Congress Control Number: 2015943058

Springer Cham Heidelberg New York Dordrecht London

Printed on acid-free paper

Springer International Publishing AG Switzerland is part of Springer Science+Business Media (www.springer.com)

Preface

This book presents the proceedings of the 4th edition of the conference on Condition Monitoring of Machinery in Non-stationary Operations CMMNO'2014 held in Lyon-France from 15 to 17 December 2014. This conference series follows three other successful conferences which took place in Ferrara (Italy) in 2013, Hammamet (Tunisia) in 2012 and Wroclaw (Poland) in 2011. This edition of the conference attracted about 70 participants who had the opportunity to discuss a number of important topics in the field condition monitoring of machinery in non-stationary operations.

To simplify problem of condition monitoring of machines, many researches a priori assumes several critical conditions: test rig with simple design (one stage gearbox), single damage artificially introduced in the system and constant loading conditions (or even no load is applied in the system). Such assumption might be good to clearly present new signal processing technique etc, however, to validate new findings in industrial applications probably more complex signals should be considered. Last decade brought many papers proving that this rough assumptions are no longer valid since in reality machines are subjected to complex condition such us variable loads, speed, multiple faults, severe operations, etc.

The objectives of CMMNO'2014 conference is to offer a forum for researchers to present and discuss their latest advances with theoretical and applied development of methods and techniques related to the condition monitoring of machinery in such complex conditions.

The papers presented in this book are classified into 3 mains topics that were discussed during CMMNO'2014: Condition monitoring techniques (in general) and two special sections focused on key steps in Condition monitoring, namely Signal processing for condition monitoring and Data mining for condition monitoring.

In Part I (Signal Processing) several topics are discussed. In modern condition monitoring there is an active group of researchers focused on electrical signals analysis for fault detection. In the book, among others, authors combine two directions, electrical signals and angular speed approach. Recently, Instantaneous Angular Speed Measurement is very promising direction for condition monitoring of rotating machines.

In this part also identification of vibration signals, especially for complex systems (bearings damage in gearbox, bearings in presence of non-Gaussian noise) is discussed. It was noticed by researchers, that automatic processing and robustness of techniques is very important for industrial applications. Often techniques should not require extra information that requires being blind, adaptive or data-driven as EMD. For complex system a decision might be based on multidimensional data analysis.

Also tracking issue of non-stationary signal's components is noticed by using time frequency method. All these mentioned issues are discussed in Part I—signal processing for condition monitoring.

Due to intensive data acquisition systems development, one might say that it is relatively easy to acquire data from industrial systems nowadays. Unfortunately, problem of data analysis from such systems still exists and even maybe it is more critical (due to number of available data) then before. Part II in the book contains methodologies of how to deal with such problems. It might be related directly to SCADA data analysis, as well as fundamental issues for condition monitoring as for example an optimal threshold or decision boundaries selection.

Very often to classify/recognize data there is a need to use advanced tools based on artificial intelligence including neural network, genetic algorithm etc. However, industrial application would be interested in whole systems rather than single procedures, so example of expert system shell for mining industry is also presented.

Part III of this book will be dedicated to latest advances in techniques used for condition monitoring of machinery in non-stationary operations including model-based approaches. Several case studies concerning methods and techniques for detection of defects in machinery were presented. Papers on bearing fault diagnosis in wind turbines generators, planetary gearbox will show implementation of amplitude and phase demodulation techniques, acoustic emission and adaptive vibration diagnostic techniques for complicated machinery. Fatigue life estimation of bearings running under non-stationary conditions will also discussed. Other interesting case studies will be presented concerning crack identification in structures, influence of sensors mounting on condition monitoring of aircraft engine rotor. Two other papers will be interested to conveyor belts behavior, maintenance and safety. Three papers will be interested to dynamic models of transmission running under non-stationary operating conditions. They will discuss gear systems and elevators.

The chapters presented in this book were peer reviewed. The editors would like to thank all the members of the organizing committee, the scientific committee and the referees, for their efforts in keeping high scientific level for CMMNO conference. The editors are also grateful to Springer for continuous support to this conference.

Fakher Chaari
Radoslaw Zimroz
Walter Bartelmus
Mohamed Haddar

Contents

Part I Signal Processing

Method of Analysing Non-stationary Electrical Signals 3
Georgia Cablea, Pierre Granjon and Christophe Bérenguer

Electrical Modeling for Faults Detection Based on Motor Current Signal Analysis and Angular Approach 15
Aroua Fourati, Nabih Feki, Adeline Bourdon, Didier Rémond, Fakher Chaari and Mohamed Haddar

Electrical Induction Motor Higher Harmonics Analysis Based on Instantaneous Angular Speed Measurement 27
Marco Spagnol, Luigi Bregant and Alessandro Boscarol

Evaluation and Improvement of Accuracy in the Instantaneous Angular Speed (IAS) and Torsional Vibration Measurement Using Zebra Tapes 43
Antonio Palermo, Karl Janssens and Laurent Britte

Vibration Analysis of Copper Ore Crushers Used in Mineral Processing Plant—Problem of Bearings Damage Detection in Presence of Heavy Impulsive Noise 57
Radoslaw Zimroz, Jakub Obuchowski and Agnieszka Wyłomańska

Analysis and Signal Processing of a Gearbox Vibration Signal with a Defective Rolling Element Bearing 71
Nader Sawalhi and Suri Ganeriwala

Monitoring Based on Time-Frequency Tracking of Estimated Harmonic Series and Modulation Sidebands 87
Timothée Gerber, Nadine Martin and Corinne Mailhes

Blind Extraction of Instantaneous Frequency for Order Tracking in Rotating Machines Under Non-stationary Operating Conditions 99
O. Cardona-Morales, E.F. Sierra-Alonso and G. Castellanos-Dominguez

New Criteria for Adaptive Blind Deconvolution of Vibration Signals from Planetary Gearbox 111
Jakub Obuchowski, Agnieszka Wylomanska and Radoslaw Zimroz

Automatic and Full-Band Demodulation for Fault Detection—Validation on a Wind Turbine Test Rig 127
Marcin Firla, Zhong-Yang Li, Nadine Martin and Tomasz Barszcz

Robust Information Indices for Diagnosing Mechanical Drives Under Non-stationary Operating Conditions 139
Boštjan Dolenc, Pavle Boškoski and Đani Juričić

Empirical Mode Decomposition Combined with Empirical Wavelets for Extracting Bearing Frequencies in a Noisy Environment and Early Detection of Defects 151
Mourad Kedadouche, Marc Thomas and Antoine Tahan

Knife Diagnostics with Empirical Mode Decomposition 167
Michele Cotogno, Marco Cocconcelli and Riccardo Rubini

Detection of Gear Faults in Variable Rotating Speed Using EEMD Decomposition and Instantaneous Frequency 177
Hafida Mahgoun, Ahmed Felkaoui, Semchedine Fedala and Fakher Chaari

Multidimensional Signal Analysis for Technical Condition, Operation and Performance Understanding of Heavy Duty Mining Machines 197
Pawel K. Stefaniak, Radoslaw Zimroz, Pawel Sliwinski, Marek Andrzejewski and Agnieszka Wyłomanska

Part II Data Mining

Analyzing State Dynamics of Wind Turbines Through SCADA Data Mining 213
Francesco Castellani, Davide Astolfi and Ludovico Terzi

Using SCADA Data for Fault Detection in Wind Turbines: Local Internal Model Versus Distance to a Wind Farm Reference 225
Alexis Lebranchu, Sylvie Charbonnier, Christophe Berenguer and Frédéric Prevost

On Optimal Threshold Selection for Condition Monitoring 237
Đani Juričić, Nada Kocare and Pavle Boškoski

Diagnostic Features Modeling for Decision Boundaries Calculation for Maintenance of Gearboxes Used in Belt Conveyor System 251
Paweł K. Stefaniak, Agnieszka Wyłomańska, Radoslaw Zimroz, Walter Bartelmus and Monika Hardygóra

Vertical Axis Wind Turbine States Classification by an ART-2 Neural Network with a Stereographic Projection as a Signal Normalization 265
Tomasz Barszcz, Andrzej Bielecki, Marzena Bielecka, Mateusz Wójcik and Mirosław Włuka

Electric Motor Bearing Diagnosis Based on Vibration Signal Analysis and Artificial Neural Networks Optimized by the Genetic Algorithm 277
Fenineche Hocine and Felkaoui Ahmed

Gear Fault Diagnosis Based on Angular Measurements and Support Vector Machines in Normal and Nonstationary Conditions 291
Semchedine Fedala, Didier Rémond, Rabah Zegadi and Ahmed Felkaoui

Diversity Measures in Classifier Ensembles Used for Rotating Machinery Fault Diagnosis 309
Wojciech Jamrozik

Diagnostics of Slow Rotating Bearings Using a Novel DAI Based on Acoustic Emission 321
Sylvester A. Aye, P. Stephan Heyns and Coenie J.H. Thiart

Development of Expert System Shell for Coal Mining Industry 335
Piotr Przystałka, Wojciech Moczulski, Anna Timofiejczuk, Mateusz Kalisch and Marek Sikora

Part III Condition Monitoring Techniques

Analysis of a Planetary Gearbox Under Non-stationary Operating Conditions: Numerical and Experimental Results 351
Cristián Molina Vicuña and Fakher Chaari

Model-Based Estimation of Elevator Rail Friction Forces 363
Ekaitz Esteban, Oscar Salgado, Aitzol Iturrospe and Inge Isasa

Modelling and Simulation of Gear Systems Dynamics for Supporting Condition Monitoring Using Mathematica 375
Walter Bartelmus and Juliusz Grabski

Wind Turbine Generator Bearing Fault Diagnosis Using Amplitude and Phase Demodulation Techniques for Small Speed Variations. 385
Ehsan Mollasalehi, Qiao Sun and David Wood

Diagnostics of a Defective Bearing Within a Planetary Gearbox with Vibration and Acoustic Emission 399
Faris Elasha, Matthew Greaves and David Mba

Methodology for the Estimation of the Fatigue Life of Rolling Element Bearings in Non-stationary Conditions 413
Urko Leturiondo, Oscar Salgado, Diego Galar and Madhav Mishra

Adaptive Vibration Diagnostic Technique for Bearings Condition Monitoring of Complicated Machines 425
Alexey Mironov, Pavel Doronkin and Alexander Priklonsky

Study on Rotating Machine Vibration Behavior Using Measured Vibro-Acoustic Signals. 439
Akilu Yunusa-Kaltungo, Jyoti K. Sinha and Adrian D. Nembhard

A Probabilistic Approach to the Crack Identification in a Beam-like Structure Using Monitored Mode Shapes and Their Curvature Data with Uncertainty. 447
Sergey Shevtsov, Igor Zhilyaev, Paul Oganesyan and Vladimir Akopyan

Condition Monitoring of Aircraft Engine Rotor System with Stiffness Anisotropy of Rotor Supports. Comparative Analysis of Accelerometers Mounting Schemes 463
S.V. Semenov, M.Sh. Nikhamkin, N.A. Sazhenkov and I.V. Semenova

Operational Safety of Steel-Cord Conveyor Belts Under Non-stationary Loadings 473
Ryszard Blazej, Leszek Jurdziak and Witold Kawalec

Condition Monitoring of Conveyor Belts as a Tool for Proper Selection of Their Replacement Time 483
Ryszard Błażej, Leszek Jurdziak and Witold Kawalec

Part I
Signal Processing

Method of Analysing Non-stationary Electrical Signals

Georgia Cablea, Pierre Granjon and Christophe Bérenguer

Abstract Considering the non-stationary operating conditions of wind turbines, electrical signals measured at the stator of their generators will also present variations around their fundamental frequency. This paper presents a method able to efficiently analyse electric quantities measured at the generator stator. The obtained outputs consist in electrical features that fully describe the electrical information contained in the measured three-phase quantities. These features can be directly used or further analysed to obtain efficient fault indicators. The proposed method relies on using the instantaneous symmetrical components to describe the quantities and complex-valued filtering to select the content around the fundamental frequency. The obtained sample per sample algorithm can be implemented on-line, and is able to process stationary or non-stationary quantities in order to extract the useful information around the fundamental frequency. The performance of the proposed method, as well as its capability to detect mechanical faults, is illustrated using experimental data.

Keywords Condition monitoring · Wind turbine · Tree-phase electrical signals · Non-stationary signals · Electrical signature analysis

Contents

1 Introduction 4
2 Method for Electrical Signature Analysis 5
2.1 Model and Features of Three-Phase Signals 5

G. Cablea (✉) · P. Granjon · C. Bérenguer
Gipsa-Lab, Grenoble University, Grenoble, France
e-mail: georgia.cablea@gipsa-lab.grenoble-inp.fr

P. Granjon
e-mail: pierre.granjon@gipsa-lab.grenoble-inp.fr

C. Bérenguer
e-mail: christophe.berenguer@gipsa-lab.grenoble-inp.fr

F. Chaari et al. (eds.), *Advances in Condition Monitoring of Machinery in Non-Stationary Operations*, Applied Condition Monitoring 4,
DOI 10.1007/978-3-319-20463-5_1

2.2 Estimation Algorithm 7
3 Experimental Results 8
3.1 Electrical Indicators Behaviour 9
3.2 Mechanical Fault Detection Capabilities 11
4 Conclusions 13
References 13

1 Introduction

In terms of renewable energy, wind farms provide a promising mean to extract energy from the wind. Wind turbines, whether they are onshore or offshore, are still a developing technology [1]. Though their reliability has improved in time, it can be further increased by implementing efficient condition monitoring systems and predictive maintenance strategies. Currently, vibration analysis seems to be the most popular condition monitoring technique [2] for such systems. Nonetheless, while vibration analysis focuses on mechanical faults, it has been shown [1] that the electrical sub-assemblies (generator, converter, etc.) are also critical components in wind turbines. In terms of monitoring the electrical sub-assemblies, using the signals measured at the output of the generator represents the obvious solution. The main challenge in monitoring wind turbines is that they often run under non-stationary operating conditions because of wind speed fluctuations. This drastically limits the amount of stationary data generally used by classical condition monitoring systems. An efficient CMS must then be able to manage and analyse such non-stationary data in order to generate efficient fault indicators. Electrical signals measured at the stator of a wind turbine generator contain most information around the electrical fundamental frequency. Considering the non-stationary operating conditions of the turbine, electrical signals will also present variations around their fundamental frequency. Nonetheless, these variations are smaller than, for example, variations in the vibrations signals.

In this paper, the proposed method relies on using the instantaneous symmetrical components [3] to describe the quantities and complex-valued filtering [4] to select the content around the fundamental frequency. The method of symmetrical components decompositions is a widely used method in the fields of power network calculations [3] (network modelling and control, power quality monitoring, fault detection, etc.) and monitoring of three-phase electrical machines [5]. More recently, an increased interest is shown towards monitoring mechanical faults in the drive trains using electrical quantities measured at the stator of three-phase electrical motors [6, 7] and generators [8, 9].

Section 2 presents the considered signals model and the method for estimating the electrical quantities. A brief overview of the whole algorithm is then provided in Sect. 2.2. The performance of the proposed method and its ability to be used in

mechanical fault detection applications is presented in Sect. 3 using experimental signals obtained from a test-bench for a wind turbine.

2 Method for Electrical Signature Analysis

2.1 Model and Features of Three-Phase Signals

The three-phase electrical signals (currents and voltages) are generically denoted by x in what follows. Such signals mainly consist in a fundamental component of frequency f_0, with possible amplitude and frequency modulations, some harmonics and additive noise. Therefore they are usually analysed around their fundamental frequency. Equation (1) gives a simple analytical signal model of three-phase signals around f_0. The relation between the real signal and the analytical one is given by $x(t) = \Re\{\underline{x}(t)\}$.

$$\begin{bmatrix} \underline{x}_1(t) \\ \underline{x}_2(t) \\ \underline{x}_3(t) \end{bmatrix} = \begin{bmatrix} X_1(t) \\ X_2(t)e^{-j\left(\frac{2\pi}{3}+\rho_1(t)\right)} \\ X_3(t)e^{-j\left(\frac{4\pi}{3}+\rho_2(t)\right)} \end{bmatrix} e^{j2\pi\int_0^t f_0(u)\,\mathrm{d}u} + \begin{bmatrix} n_1(t) \\ n_2(t) \\ n_3(t) \end{bmatrix} \tag{1}$$

In Eq. (1) the signal on phase 1 is considered the reference signal and the quantities described around f_0 are:

- $\underline{x}_1(t)$, $\underline{x}_2(t)$ and $\underline{x}_3(t)$ representing the three-phase signals;
- $X_1(t)$, $X_2(t)$ and $X_3(t)$ representing the instantaneous magnitudes of the signals and containing possible amplitude modulations;
- $\rho_1(t)$ and $\rho_2(t)$ representing the small errors in phase shifts between phases;
- $f_0(t)$ representing the instantaneous frequency of the components and containing eventual frequency modulations;
- $n_1(t)$, $n_2(t)$ and $n_3(t)$ representing additive noise.

The magnitude and frequency modulations may be due to changes in the operating point of the system or to fault occurrence (i.e. mechanical faults in rotating machines [7], broken rotor bar [10], bearing faults [5], etc.).

Perfectly balanced three-phase quantities would have the same amplitude on all phases and a phase shift of $\frac{2\pi}{3}$ between each of the phases. This corresponds to $X_1(t) = X_2(t) = X_3(t)$ and $\rho_i(t) = 0$. However, real systems are never perfectly balanced. The electrical unbalance is generally due to faults in the three-phase systems (i.e. winding stator faults in rotating machines [11]). One way to separate any three-phase unbalanced system into balanced components is to apply the Lyon transform [3, 12, 13].

$$\begin{bmatrix} \underline{x}_+(t) \\ \underline{x}_-(t) \\ \underline{x}_0(t) \end{bmatrix} = \frac{2}{3} \begin{bmatrix} 1 & a & a^2 \\ 1 & a^2 & a \\ 1 & 1 & 1 \end{bmatrix} \begin{bmatrix} \underline{x}_1(t) \\ \underline{x}_2(t) \\ \underline{x}_3(t) \end{bmatrix} \tag{2}$$

where:

- $a = e^{j\frac{2\pi}{3}}$, called the Fortescue [14] operator, represents a phase shift of $\frac{2\pi}{3}$;
- $\underline{x}_+(t)$, $\underline{x}_-(t)$ and $\underline{x}_0(t)$ are generically called instantaneous symmetrical components and are the positive-, negative- and zero-sequence components respectively.

Considering Eq. (1), which describes the content of the measured signal around f_0, and applying the transformation from Eq. (2) to split the signal into its balanced and unbalanced parts, the instantaneous symmetrical components of the system around $+f_0$ are obtained. At each frequency, the instantaneous positive-sequence component describes the balanced quantities in the system, whereas the instantaneous negative- and zero-sequence ones quantify the amount of unbalance in the system for the respective frequencies [6]. While depending on the system configuration $x_0(t)$ may not always be related to a fault (i.e. in four wire connections $i_0(t)$ is related to the neutral current), in what follows the more generic scenario in which the zero-sequence component quantifies faults to ground is considered.

The linear transformation of Eq. (2) applied to the mono-component signals of Eq. (1) leads to the mono-component signals of $\underline{x}_+(t)$, $\underline{x}_-(t)$ and $\underline{x}_0(t)$, neglecting the noise. Using the instantaneous symmetrical components one can demodulate the amplitude and frequency [13, 15] as:

$$X_+(t) = |\underline{x}_+(t)| \quad X_-(t) = |\underline{x}_-(t)| \quad X_0(t) = |\underline{x}_0(t)| \tag{3}$$

$$f_{x_+}(t) = \frac{1}{2\pi}\frac{d\theta_+(t)}{dt}, \quad \text{with: } \theta_+(t) = \angle \underline{x}_+(t) \tag{4}$$

In order to quantify the amount of electrical unbalance in a system, one can use the advantage provided by the use of symmetrical components, that is the separation into balanced and unbalanced quantities. Using the magnitudes of such components, an electrical unbalance indicator can be defined as in (5). Regarding the indicator presented in Eq. (5), it should be further emphasised that it only characterises the electrical unbalance around the fundamental frequency f_0 [13].

$$u_{\underline{x}}(t) = \sqrt{\frac{|\underline{x}_-(t)|^2 + |\underline{x}_0(t)|^2}{|\underline{x}_+(t)|^2 + |\underline{x}_-(t)|^2 + |\underline{x}_0(t)|^2}} \tag{5}$$

If both currents and voltages are available, instantaneous three-phase electrical powers can also be estimated using the instantaneous positive-sequence components of the voltages and currents as:

$$\text{Complex power: } \underline{p}_{+}(t) = \frac{3}{2}\underline{v}_{+}(t)\underline{i}_{+}^{*}(t) \tag{6}$$

$$\text{Active power: } \underline{P}_{+}(t) = \Re\left\{\underline{p}_{+}(t)\right\} \tag{7}$$

$$\text{Reactive power: } \underline{Q}_{+}(t) = \Im\left\{\underline{p}_{+}(t)\right\} \tag{8}$$

$$\text{Apparent power: } \underline{S}_{+}(t) = \left|\underline{p}_{+}(t)\right| \tag{9}$$

$$\text{Power factor: } \cos(\varphi_0), \text{ where} \varphi_0 = \angle \underline{p}_{+}(t) \tag{10}$$

2.2 Estimation Algorithm

In order to summarize the steps needed to implement this method, the estimation algorithm has been graphically represented in Fig. 1a for the computed quantities for the voltages and currents independently and in Fig. 1b for computing the electrical power related quantities using the positive sequence components. In this section the algorithm is briefly described, while more details are provided in [13].

In Fig. 1a, at the input of the algorithm there are the electrical three-phase quantities. The first step of the algorithm is a down-sampling step. Considering that the fundamental frequency of electrical signals is not a high frequency and in order to save computation time this step may be implemented if needed, depending on the sampling frequency used by the acquisition system. In order to select the frequency content around the fundamental, a complex-valued bandpass filter [4] is used. The

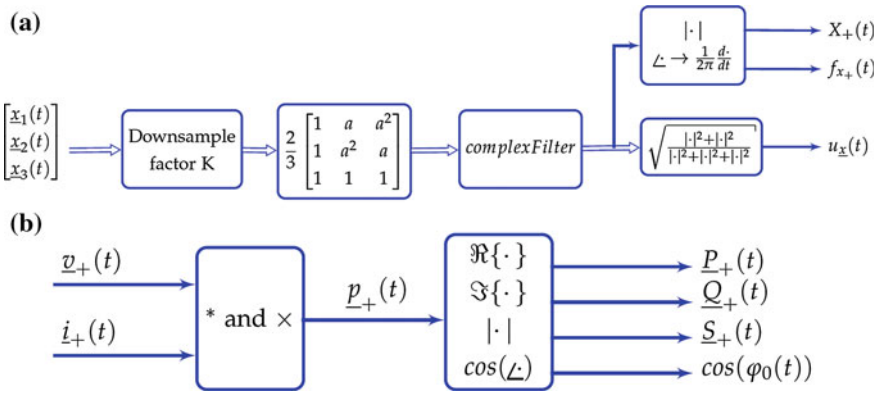

Fig. 1 Estimation algorithm. **a** Algorithm estimating the electrical three-phase quantities. **b** Algorithm estimating the electrical powers features

filter is implemented as a finite impulse response filter with complex-valued coefficients. Because of the linear time-invariant characteristic of the filter and of the symmetrical components transformation, these operations can and have been switched in the implementation of the algorithm. In the end, the instantaneous symmetrical components are used to compute the electrical unbalance indicator. The positive sequence component is also used for the amplitude and frequency demodulation step, thus obtaining the instantaneous magnitude and frequency of the positive sequence component around the fundamental frequency.

Figure 1b graphically depicts the algorithm for the estimation of the electrical powers related features computed using the positive sequence components of the voltages and currents. As emphasised by the figure, the operations used for these estimations are simple and thus low time-consuming making this algorithm appropriate for embedded implementations.

Considering that a filter is used to select the bandwidth around the fundamental frequency of the electrical signals, if the frequency varies too much it may get out of the assigned bandwidth. In most real wind turbine systems however, the generator output would be connected to the main grid, which will impose a constant fundamental frequency. The output signals frequency would not be allowed to vary too much, if at all. Another possible way to overcome this limitation could also be to use an adaptive filtering approach for the complex bandpass filter.

3 Experimental Results

An experimental test-bench has been developed in the CETIM laboratory in Senlis, France. This bench emulates the structure and behaviour of a wind turbine. The structure is presented in Fig. 2a. The operating conditions are determined by controlling the speed of the low speed shaft, which is considered to be the system input. For this paper, the electrical signals are acquired at the output of the generator. An experiment was conducted for ≈200 h during which an accelerated deterioration of the main bearing was induced by applying axial and radial forces on

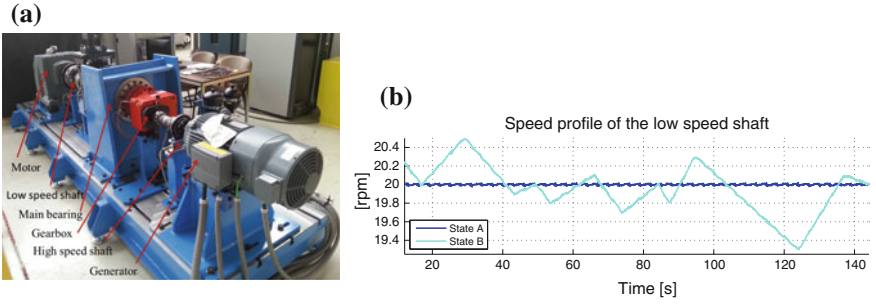

Fig. 2 Experimental set-up. **a** Experimental test bench. **b** Speed profile of the low speed shaft

the main bearing. Throughout the experiment several operating conditions were alternated. In this paper, two of the operating states are considered. Presented in Fig. 2b, State A denotes the stationary conditions while State B uses non-stationary input signals. All other operating parameters for the system are the same for both states. At the end of the experiment, an inner race fault was observed in the main bearing.

3.1 Electrical Indicators Behaviour

In what follows, the signals used have been recorded at ≈19 h into the experiment for a duration of ≈145 s for state A and state B, consequently. The goal of this section is to present the capability of the computed indicators to estimate and track the evolution of the electrical quantities and to compare their behaviour in stationary and non-stationary conditions. For this purpose, the chosen measurements are the voltages. Nonetheless, similar results have been obtained also by using the currents and the estimated electrical powers.

For the non-stationary signal the time-frequency representation (spectrogram) of the voltage positive sequence component is presented in Fig. 3. The evolution of the fundamental frequency of the voltages can be observed in the figure. The profile of the fundamental frequency of this estimated quantity bears a close resemblance to the speed profile of the low speed shaft presented in Fig. 2b. The variations of the instantaneous amplitude and frequency of the fundamental component contain information related to changes in the operating conditions as well as to mechanical phenomena occurring in the system, hence the need for demodulations.

Figure 4a depicts the estimation of the instantaneous fundamental frequency of the electrical signals, computed using the voltage positive sequence component. While for state A the value of the estimation is almost constant, for state B the time evolution of the frequency bears a close resemblance to the speed variations of the low speed shaft (see Fig. 2b), as expected. Figure 4b depicts the instantaneous magnitude estimated for the voltage positive sequence components computed

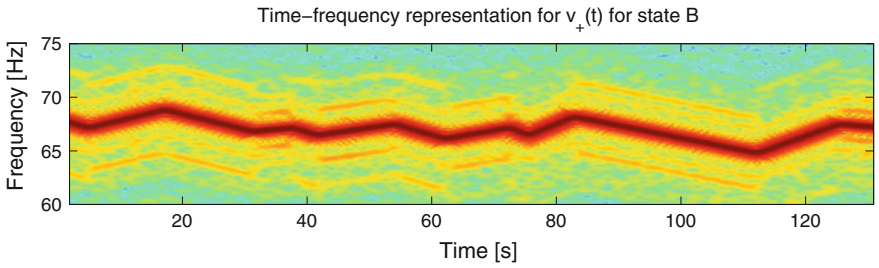

Fig. 3 Time-frequency representation around the fundamental frequency of the voltage positive sequence component for non-stationary conditions

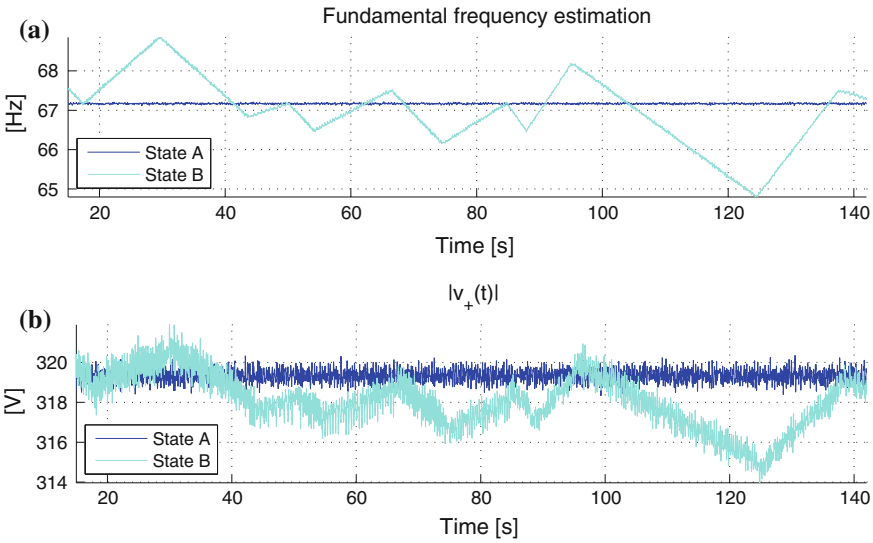

Fig. 4 Frequency and amplitude modulations of the positive sequence component of the voltages. **a** Estimation of the fundamental frequency of $v_+(t)$. **b** Amplitude of the voltages positive sequence component

around the fundamental frequency f_0. While for the stationary case in state A this magnitude remains almost constant, for the non-stationary case of state B the magnitude is obviously influenced by the variation of the rotating speed imposed at the input of the system.

Figure 5 depicts the results obtained for the unbalance indicator computed for the voltages. While there was no electrical unbalance present in the system throughout the whole experiment, the goal of presenting this result is to show that this indicator is not influenced by the non-stationary conditions in state B. While theoretically the value of this indicator should be 0 in case of electrically balanced systems, in practice real systems are not perfectly balanced. This explains the small value greater than null that this indicator presents.

In this section, the performance of the proposed indicators was illustrated using the experimental results obtained using the voltages measurements. The presented

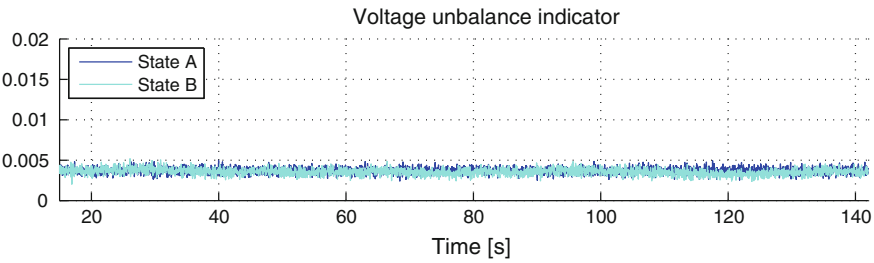

Fig. 5 Voltage unbalance indicator computed around f_0

results show good performance in terms of estimating and tracking electrical features. Moreover, it has been shown that the unbalance indicator is not affected by the non-stationary operating conditions. Similar results have been obtained also for the currents and electrical power estimations.

3.2 *Mechanical Fault Detection Capabilities*

The goal of the performed experiment was to induce accelerated deterioration of the main bearing and to study the fault signature on various measured signals. At the end of the test, an inner race bearing fault occurred in the main bearing. This fault was confirmed by physical inspection after the experiment was finished. The fault frequency is known to be $f_f = 3.4506$ Hz and the start of its evolution was determined by using vibration signals acquired by accelerometers placed on the respective bearing. For this section, three sets of signals will be considered before the fault and three sets after the fault occurred, for both stationary and non-stationary conditions.

Figure 6a, b present the power spectral densities (PSDs) (using Welch's method [16]) computed for the magnitude of the positive sequence component of the voltages. Figure 6a depicts these PSDs computed under the stationary conditions in

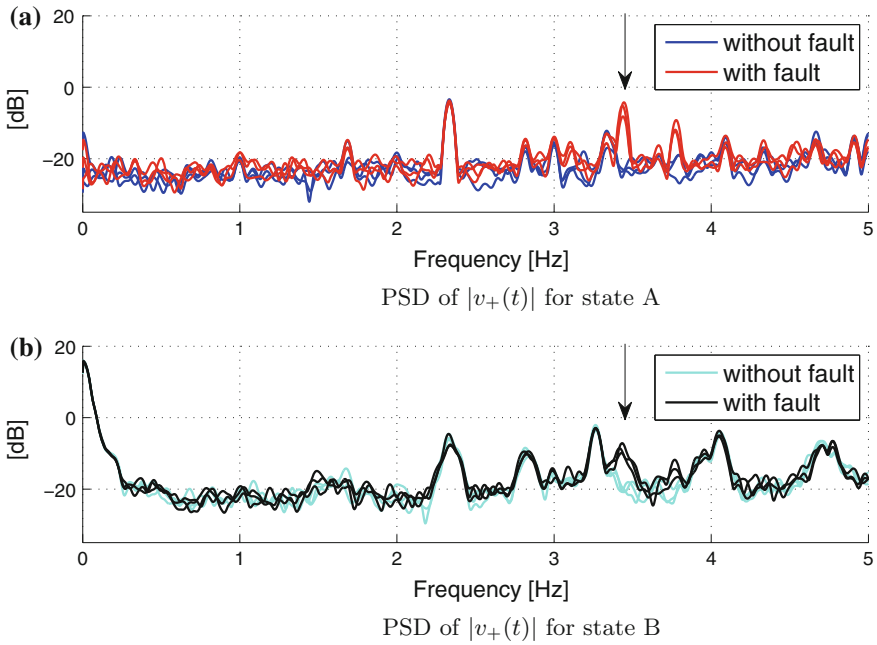

Fig. 6 PSD of $|v_+(t)|$ for **a** stationary and **b** non-stationary operating conditions

state A. The blue curves show the results of the sets before the fault occurred while the red profiles show the resulting PSDs after the inner race bearing fault occurred. As it can be seen in the figure, after the fault a new peak appears at the fault frequency f_f. This fault frequency is also modulated by the rotating frequency of the low speed shaft, thus two smaller peaks can be observed at $f_f + f_{\text{rot}}$ and $f_f - f_{\text{rot}}$. The other peaks present in the PSD of the magnitude of the voltage positive sequence component in Fig. 6a are accounted for by mechanical phenomena. For example, the peak located at 2.33 Hz corresponds to the epicyclic gear train frequency computed for a rotating speed of the low speed shaft of 20 rpm.

Figure 6b presents the same results computed for state B. By comparing to Fig. 6a, one can observe that mainly the same peaks are present. However, in the non-stationary case the peaks in the PSD are not as high and they are wider. It is worth emphasising that this approach of analysing the spectral content of the signals may not be the optimum in terms of estimation performance, but it can be observed that for small variations in the signals, it can be used as a rough estimator. Due to the fact that the rotating frequency is varying, the modulations induced by the fault are not as clear as in the stationary case, but they are visible nonetheless. Furthermore, constraints regarding the use of the complex valued band-pass filter have to be considered when using this approach for non-stationary conditions with higher speed variations.

Figures 7a, b depict the PSDs computed for the estimated fundamental frequency of the positive sequence component of the voltages. As for the magnitude indicator,

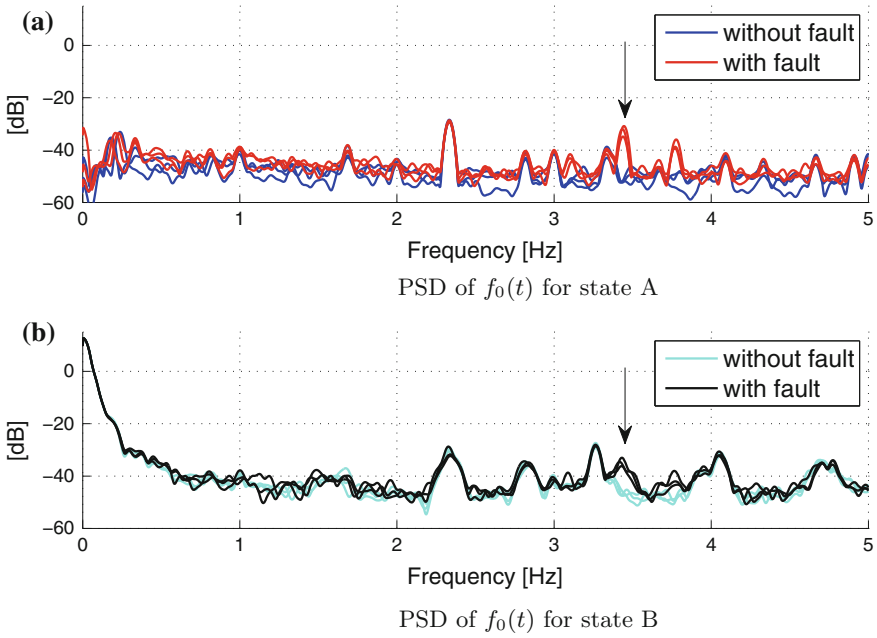

Fig. 7 PSD of the instantaneous fundamental frequency for **a** stationary and **b** non-stationary operating conditions

the frequency indicator also shows a peak at the fault frequency after the fault has occurred in both stationary and non-stationary scenarios.

The choice to search for mechanical faults signatures in the voltage signals and not in the currents is due to the fact that the system from which these signals are measured is a voltage generator. In that case, its output voltages are obviously influenced by the generator condition and the mechanical phenomena occurring on its shaft. On the other hand, the load influence is not negligible in the currents and may complicate fault detection.

4 Conclusions

In the first part of the paper, the theoretical tools used to describe electrical three-phase quantities have been presented, as well a proposed set of electrical features that are to be computed. The proposed approach can easily be implemented as a sample-per-sample algorithm, thus making it suitable also for non-stationary signals and on-line monitoring of systems. In the second half of the paper, it has been shown that the proposed method of analysing electrical three-phase signals presents good performance in terms of estimation and tracking of the evolution of the quantities in both stationary and non-stationary conditions. This was achieved by applying the method on electrical three-phase signals measured at the output of the generator, in a complete system simulating a wind turbine. The proposed electrical unbalance indicator has also been shown not to be affected by the non-stationary operating conditions. Moreover, it has been shown that using these estimated features, at least one type of mechanical fault (inner race bearing fault) can be detected.

As future work, this method could be extended to automatically detect more electrical and mechanical faults by further developing the definitions of specific fault indicators. Moreover, by using an adaptive filtering approach for the complex valued filter, the method can be extended for use in an even wider area of applications on electrical three-phase systems operating under non-stationary conditions.

Acknowledgements This research has been partly supported by KIC InnoEnergy, a company supported by the European Institute of Innovation and Technology (EIT), through KAStrion European project.

The authors would like to thank CETIM (Centre Technique des Industries Mécaniques) for providing the test-bench and experimental data.

References

1. Tavner PJ (2012) Offshore wind turbines reliability, availability and maintenance. Institution of Engineering and Technology, London

2. García Márquez FP, Tobias AM, Pinar Pérez JM, Papaelias M (2012) Condition monitoring of wind turbines: techniques and methods. Renew Energy 46:169–178
3. Paap G (2000) Symmetrical components in the time domain and their application to power network calculations. IEEE Trans Power Syst 15:522–528
4. Reilly A, Frazer G, Boashash B (1994) Analytic signal generation-tips and traps. IEEE Trans Signal Process 42:3241–3245
5. Choqueuse V, Benbouzid MEH, Amirat Y, Turri S (2012) Diagnosis of three-phase electrical machines using multidimensional demodulation techniques. IEEE Trans Ind Electron 59:2014–2023
6. Granjon P (2011) Condition monitoring of motor-operated valves in nuclear power plants. In: 8th international conference on condition monitoring and machinery failure prevention technologies, vol 1. , Cardiff, UK, pp 109–119
7. Blodt M, Granjon P, Raison B, Régnier J (2010) Mechanical fault detection in induction motor drives through stator current monitoring theory and application examples. In: Zhang W (ed) Fault detection. In-Tech, Vukovar
8. Al Ahmar E, Choqueuse V, Benbouzid MEH, Amirat Y, El Assad J, Karam R, Farah S (2010) Advanced signal processing techniques for fault detection and diagnosis in a wind turbine induction generator drive train: a comparative study. In: Energy conversion congress and exposition (ECCE), IEEE, Atlanta, GA, pp 3576–3581
9. Zhang P, Neti P (2013) Detection of gearbox bearing defects using electrical signature analysis for Doubly-fed wind generators. In: Energy conversion congress and exposition (ECCE), IEEE, Denver, CO, pp 4438–4444
10. Stefani A, Bellini A, Filippetti F (2009) Diagnosis of induction machines' rotor faults in time-varying conditions. IEEE Trans Ind Electron 56:4548–4556
11. Bouzid MBK, Champenois G (2013) New expressions of symmetrical components of the induction motor under stator faults. IEEE Trans Ind Electron 60:4093–4102
12. Lyon WV (1954) Transient analysis of alternating current machinery—an application of the method of symmetrical components. The Technology Press of MIT and Wiley, New York
13. Cablea G, Granjon P, Bérenguer C (2014) Method for computing efficient electrical indicators for offshore wind turbine monitoring. Insight Nondestr Test Condition Monit 56:443–448
14. Fortescue CL (1918) Method of symmetrical co-ordinates applied to the solution of polyphase networks. Trans Am Inst Electr Eng XXXVII:1027–1140
15. Boashash B (1992) Estimating and interpreting the instantaneous frequency of a signal—Part I: Fundamentals. Proc IEEE 80:520–538
16. Welch P (1967) The use of fast Fourier transform for the estimation of power spectra: A method based on time averaging over short, modified periodograms. IEEE Trans Audio Electroacoust 15:70–73

Electrical Modeling for Faults Detection Based on Motor Current Signal Analysis and Angular Approach

Aroua Fourati, Nabih Feki, Adeline Bourdon, Didier Rémond, Fakher Chaari and Mohamed Haddar

Abstract Recently, Motor Current Signal Analysis (MCSA) appears as an effective tool for fault diagnosis in rotating machinery and proved to be sufficient for detecting localized mechanical faults in electromechanical systems operating in stationary conditions. In the case of non-stationary conditions, speed variations must be distinguished from angular velocity perturbation caused by the presence of a defect. In the framework of diagnosis of rotating machinery, angular approaches are well suited to make monitoring resistive to speed disturbances. This paper proposes a reformulation of the MCSA associated with angular approach in modeling multiphysic behavior. The resulting model described in this paper can be used to investigate of the influence of the Instantaneous Angular Speed (IAS) variations on the electrical responses of the whole rotating system.

Keywords Motor current signal analysis condition monitoring · Non-stationary conditions · Rotating machines · Angular approach

A. Fourati (✉) · A. Bourdon · D. Rémond
LaMCoS UMR5259, CNRS, INSA-Lyon, University of Lyon, Lyon, France
e-mail: aroua.fourati@insa-lyon.fr; arwafourati@gmail.com

A. Bourdon
e-mail: adeline.bourdon@insa-lyon.fr

D. Rémond
e-mail: didier.remond@insa-lyon.fr

A. Fourati · N. Feki · F. Chaari · M. Haddar
La2MP, National School of Engineers of Sfax, Sfax BP 1173-3038, Tunisia
e-mail: fekinabih@gmail.com

F. Chaari
e-mail: fakher.chaari@gmail.com

M. Haddar
e-mail: mohamed.haddar@enis.rnu.tn

F. Chaari et al. (eds.), *Advances in Condition Monitoring of Machinery in Non-Stationary Operations*, Applied Condition Monitoring 4,
DOI 10.1007/978-3-319-20463-5_2

Contents

1 Introduction 16
2 Asynchronous Motor Model Formulation 17
3 Introducing Instantaneous Angular Speed Disturbances 20
4 Results and Discussions 21
5 Conclusion and Perspectives 24
References 25

1 Introduction

Induction motors connected to mechanical systems are widely used in industrial applications due to their robustness, their compactness, low cost and high degree of reliability. Condition monitoring and diagnosis of these systems by detecting small variations of their dynamic behavior are among challenges to improve their availability. The use of stator current signals constitutes a non-intrusive method to acquire information necessary to diagnosing electromechanical systems and thus to ensure effective monitoring. Many researches focused on this framework and proved the capacity of this method to explicit mechanical defect localized on the electromechanical system related to the motor [1, 2]. In a previous work, [3] an analytical model of an asynchronous motor has been proposed and proved the possibility to detect pitting in a geared system operating under stationary conditions. The classical theory of these motors is based on the assumption that the current produced by their stator winding is sinusoidally distributed in time. This assumption is limited to systems operating under stationary conditions. However, in real cases, current components related to faults are confused to those resulting from dynamic variations, and thus, are very difficult to extract without a dedicated signal processing. Moreover, some recent results in rotating machine monitoring have proven that the shaft rotation speed contains dynamic responses of faulted components in now well-known Instantaneous Angular Speed (IAS) signal [4].

To overcome these difficulties of non-stationary operating conditions, for example, velocity variations that can hide the appearance of defects on the current signal, angular approaches seems to be well suited. In [5], a new way of writing differential equations in rotating machines by translation into the angular domain was proposed and proved the interest of angular sampling in rotating machines [6]. When addressing the case of rotating machines operating under non-stationary conditions, every time their rotating element passes through a disturbance, a perturbation takes place. These perturbations are managed by the rotation periodicity of the machine whatever the overall rotational speed. This leads to the new assumption that the stator current is periodically distributed in reference with the angular position of the shaft of rotating machines.

In this paper, the authors' purpose is to develop a new approach to investigate the MCSA method on electromechanical systems operating under non-stationary conditions in order to analyze in a more efficient way the information given by stator currents for the detection of defects. Firstly, stator's current and torque responses of a healthy motor are presented under this new formalism. In a second step, the proposed study is extended to present the responses under two different excitations mechanisms which are varying IAS due to the presence of bearing faults.

2 Asynchronous Motor Model Formulation

For the framework of detecting faults in electromechanical systems, the common assumption is based on the fact that a magnetic disturbance is created in the air gap of the induction machine whenever the system passes through a mechanical fault (like bearing spall for example). For this purpose, a permeance network model is used Fig. 1. The interest in this model is motivated by its capacity to detect very small magnetic disturbances and to offer a detailed representation of the machine magnetic state which is sensitive to faults.

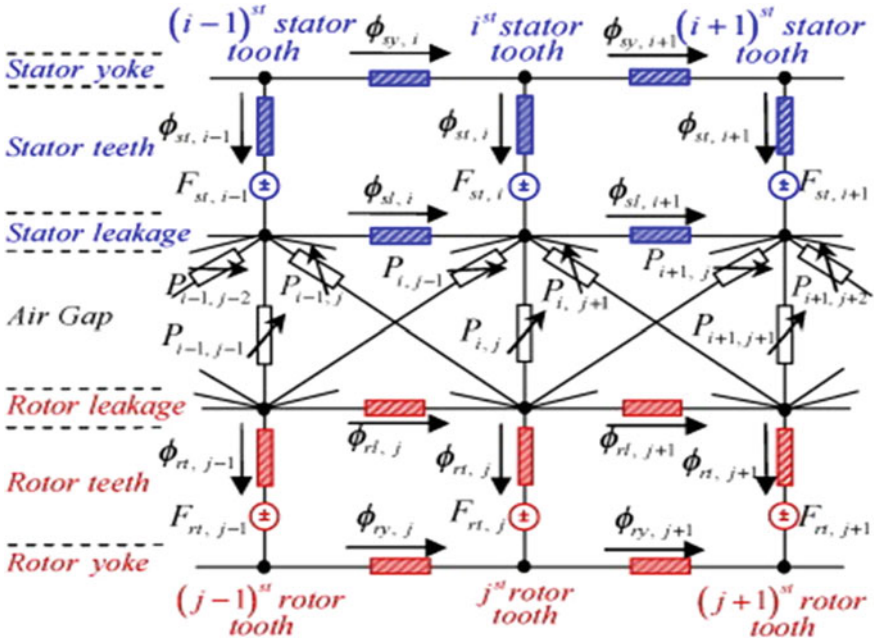

Fig. 1 A part of the permeance network model [7]

In order to simulate its magnetical behavior, the induction machine is discretized on a finite number of nodes. In The overall network, N_n nodes are uniformly distributed. Between each two node there is a branch representing flux circulation. Each flux tube is characterized by its permeance. Permeances in the stator and the rotor are supposed to be constants whereas permeances of the air-gap are varying. In the complete permeance network model, there are N_b branches and N_{bent} branches in the gap, these numbers are relative to the stator teeth and the rotor numbers n_s and n_r, where $N_{bent} = n_s \cdot n_r$ and $N_b = 3n_s + 3n_r + N_{bent}$.

Where $\phi_{sy,i}$, $\phi_{st,i}$, $\phi_{sl,i}$, $\phi_{ry,j}$, $\phi_{rt,j}$ and $\phi_{rl,j}$ are stator yoke, stator teeth, stator leakage, rotor leakage, rotor teeth and rotor yoke flux. $F_{st,i}$ and $F_{rt,j}$ are stator teeth and rotor teeth magnetomotive forces. $P_{i,j}$ is the air-gap permeance which connect the ith stator tooth and the jth rotor tooth.

In the temporal domain, an induction machine is modeled using a unique differential equation combining its electrical and magnetical behavior as following [7]:

$$\left[[L_t]_{(n_{ph}+n_r,n_{ph}+n_r)}+[G(t)]_{(n_{ph}+n_r,n_{ph}+n_r)}\right]\frac{d\{I(t)\}_{(n_{ph}+n_r,1)}}{dt} + \left[[R_t]_{(n_{ph}+n_r,n_{ph}+n_r)}+\frac{d[G(t)]_{(n_{ph}+n_r,n_{ph}+n_r)}}{dt}\right]\{I(t)\}_{(n_{ph}+n_r,1)}=\{V(t)\}_{(n_{ph}+n_r,1)} \quad (1)$$

where $\{I(t)\}$ is the generalized stator and rotor current vector, $\{V(t)\}$ is the stator and rotor voltage supply vector, $[L_t]$ and $[R_t]$ are respectively matrix of inductances and resistances of the rotor and the stator, n_{ph} and n_r are respectively the number of stator phases and the number of rotor teeth and $[G(t)]$ is the matrix describing the electro-magnetical behavior of the induction machine.

These parameters will be involved to calculate the $[G(t)]$ matrix. In this model we consider stator and rotor permeances as constant whereas permeances on the air-gap depend dynamically from the angular displacement between the stator and the rotor as shown in Fig. 2. This consideration induces the angular-depending character of the induction machine.

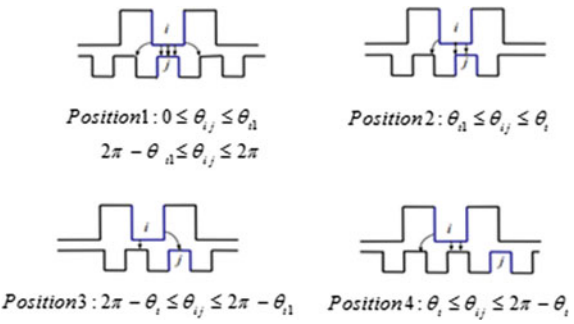

Fig. 2 Evolution of the angular position between a couple of stator and rotor teeth

For each couple of teeth; *i*th stator tooth and *j*th rotor tooth, the value of the permeance is updated for every rotor position relatively to the following expression [8]:

$$P(\theta_{ij}) = \begin{cases} P_{\max} & \text{if } 0 \le \theta_{ij} \le \theta_{t1} \text{ and } 2\pi - \theta_{t1} \le \theta_{ij} \le 2\pi \\ P_{\max} \frac{1+\cos \pi \frac{\theta - \theta_{t1}}{\theta_t - \theta_{t1}}}{2} & \text{if } \theta_{t1} \le \theta_{ij} \le \theta_t \\ P_{\max} \frac{1+\cos \pi \frac{\theta - 2\pi + \theta_{t1}}{\theta_t - \theta_{t1}}}{2} & \text{if } 2\pi - \theta_t \le \theta_{ij} \le 2\pi - \theta_{t1} \\ 0 & \text{if } \theta_t \le \theta_{ij} \le 2\pi - \theta_t \end{cases} \quad (2)$$

where θ is the rotor angular displacement relatively to the stator, θ_{ij} the *j*th rotor tooth rotational displacement referring to *i*th stator tooth, θ_t and θ_{t1} are limit angles representing the angular variation of the permeance and $P_{\max}$ is the maximal value of the permeance of any couple of teeth.

The expression of $P_{\max}$ depends on geometrical characteristics of the motor. It is defined as:

$$P_{\max} = \frac{\mu_0 L_m L_{dr}}{e} \quad (3)$$

where μ_0 is the air-gap permeability, L_{m} is the machine length, L_{dr} is the rotor tooth width and e is the air-gap thickness.

The starting point of the classical temporal approach for modeling the motor is based on the fact that the temporal variable is linearly coupled to the angular variable through a constant rotating speed as provided by Eq. (4), and then modeling will be limited to a stationary operating conditions system.

$$\theta = \omega t \quad (4)$$

To overcome these limitations, we proceeded by an angular sampling. This approach was well defined in [4]. Let θ be the angular position of the rotor. For non-stationary rotating machines, the relation which links temporal to angular variables is provided by means of the IAS function $\tilde{\omega}$ as following:

$$\frac{\mathrm{d}t}{\mathrm{d}\theta} = \frac{1}{\tilde{\omega}(\theta)} \quad (5)$$

Then, a reformulation of the permeance network model used to calculate variations of current signals in the case of an asynchronous motor in an angular domain is proposed as following:

$$\begin{cases} \left[[L_\theta]_{(n_{ph}+n_r,n_{ph}+n_r)}+[G(\theta)]_{(n_{ph}+n_r,n_{ph}+n_r)}\right]\dfrac{d\{I(\theta)\}_{(n_{ph}+n_r,1)}}{d\theta}\tilde{\omega}(\theta) \\ \left[+[R_\theta]_{(n_{ph}+n_r,n_{ph}+n_r)}+\dfrac{d[G(\theta)]_{(n_{ph}+n_r,n_{ph}+n_r)}}{d\theta}\tilde{\omega}(\theta)\right]\{I(\theta)\}_{(n_{ph}+n_r,1)}=\{V(t)\}_{(n_{ph}+n_r,1)} \\ \dfrac{dt}{d\theta}=\dfrac{1}{\tilde{\omega}(\theta)} \end{cases} \tag{6}$$

In order to minimize the number of equations and the dependence on the angular variable, a basis change is defined. If we consider a relative frame whose axes are rotating in accordance with the rotor angular displacement, resulting projected currents are obtained according to the relation:

$$\begin{Bmatrix} I_d(\theta) \\ I_q(\theta) \end{Bmatrix} = \sqrt{\frac{2}{3}}\begin{bmatrix} \cos(\omega_s t) & \cos\left(\omega_s t-\frac{2\pi}{3}\right) & \cos\left(\omega_s t+\frac{2\pi}{3}\right) \\ -\sin(\omega_s t) & -\sin\left(\omega_s t-\frac{2\pi}{3}\right) & -\sin\left(\omega_s t+\frac{2\pi}{3}\right) \end{bmatrix}\cdot\begin{Bmatrix} I_1(\theta) \\ I_2(\theta) \\ I_3(\theta) \end{Bmatrix} \tag{7}$$

Coupling the electrical model of the induction machine to a mechanical model of a defective system, the magnetic torque is expressed as:

$$C_{em}(\theta)=\frac{1}{2}\sum_i^{n_s}\sum_j^{n_r}\frac{dP_{ij}}{d\theta}\varepsilon_{ij}^2 \tag{8}$$

where n_s and n_r are respectively stator and rotor tooth number, P_{ij} and ε_{ij} are respectively the permeance and the magnetic potential difference in the air-gap which connects the ith stator tooth and the jth rotor tooth; Then it must be noticed that differential equations expressed in the angular domain are nonlinear but with parameters which can be explicitly calculated, therefore decreasing calculation time.

3 Introducing Instantaneous Angular Speed Disturbances

Comparing to temporal domain, in the differential Eq. (6) the rotational speed appears explicitly written in the angular domain. This allows integrating a disturbance of the IAS in the model, this dynamic behavior being proven to be induced by typical bearing faults. The form of the disturbance is inspired from the model developed in [9] as a function of the angular position of the shaft. The expression proposed to characterize the disturbance is defined as a periodic function; each occurrence is divided into 3 areas as shown in Fig. 3:

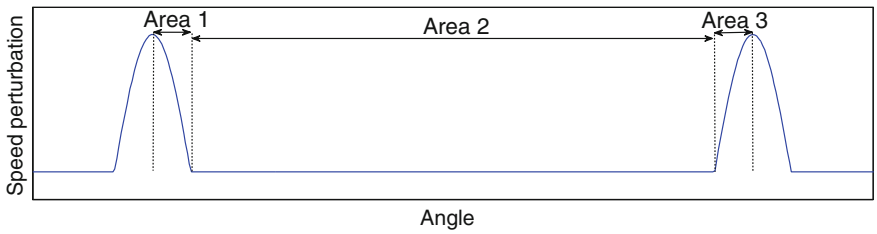

Fig. 3 Angular variation of the disturbance function

$$\begin{aligned} &\text{Area1: } \Delta\omega(\theta) = \omega_p \sin\left(\frac{\pi}{L_p}\left(\theta - \theta_1 + \frac{L}{2}\right)\right) \\ &\text{Area2: } \Delta\omega(\theta) = 0 \\ &\text{Area3: } \Delta\omega(\theta) = \omega_p \sin\left(\frac{\pi}{L_p}(\theta - \theta_3)\right) \end{aligned} \tag{9}$$

where ω_p and L_p are respectively the amplitude and angular length of the perturbation.

4 Results and Discussions

In order to show results of the motor current signal analysis (MCSA) method coupled to the angular approach, current signal of a machine has been simulated without and with IAS perturbations. The considered model is a 50 kW, 50 Hz, 400 V, 2 poles, 24 stator slots, 30 rotor slots, star connected, standard squirrel cage induction motor rotating at a stationary speed $\omega = 300$ rad/s.

Figure 4 shows a sinusoidal stationary variation of the stator first phase current. When projected onto d-axis, the combination of the three phase currents oscillates stationary Fig. 5. Theses oscillations appear due to discontinuities of the magnetic flux passing through the stator and rotor slots. Although the motor is currently working in stationary conditions, we can, also notice some perturbations in the torque curve Fig. 6. These perturbations are about 8 % of the torque value and depend of geometrical parameters of the motor.

After adding the perturbation function to the constant rotational speed as recalled in Fig. 7, the stator first phase current variations Fig. 8, the projection of stator currents Fig. 9 and the torque Fig. 10 versus angular position of the rotor are presented.

Through these figures, it was shown that a perturbation may not appear in either the stator per phase current or the torque curve. On the contrary, it appears clearly as a periodic perturbation in the d-axis projected signal. This perturbation appears each time a speed perturbation takes a place. It was proven through this graph that a

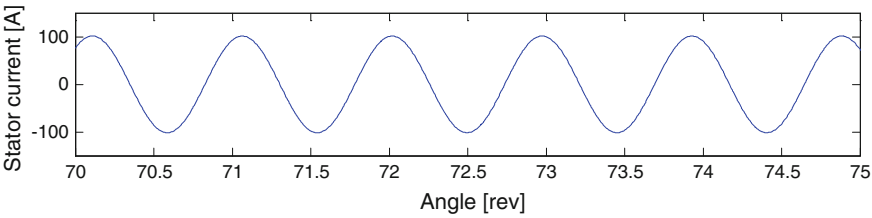

Fig. 4 Stator current versus angle of rotation for a constant rotational speed $\omega = 300$ rad/s

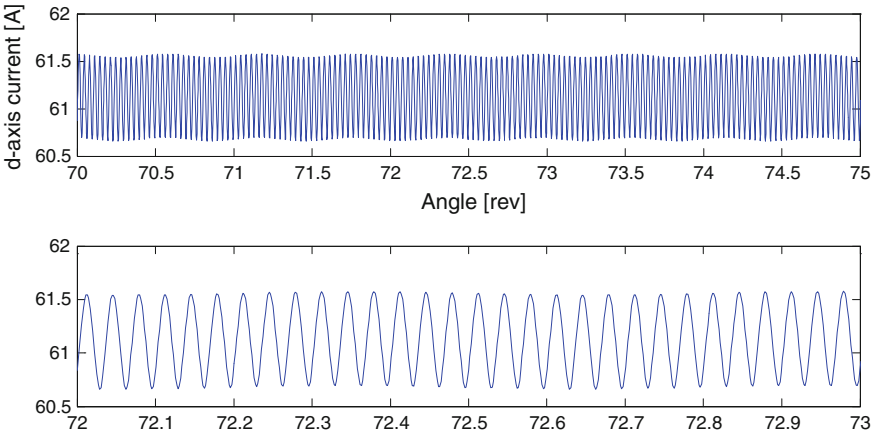

Fig. 5 d-axis current and zoom of the d-axis current for a constant rotational speed $\omega = 300$ rad/s

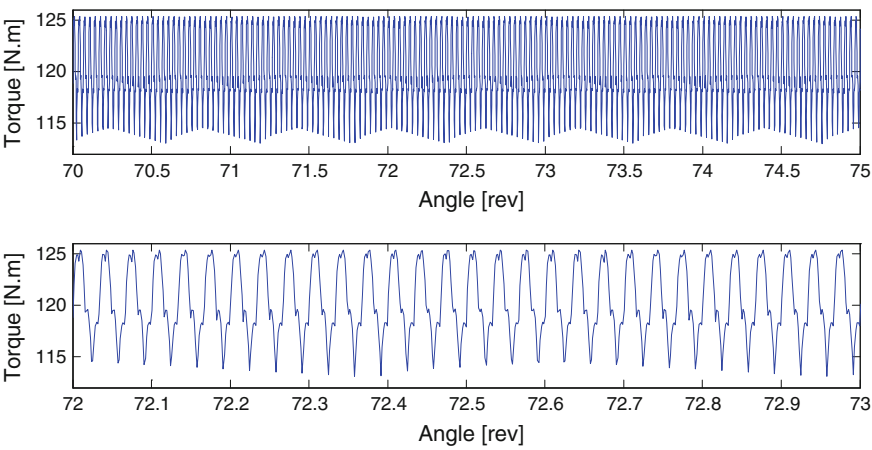

Fig. 6 Torque and zoom of the torque for a constant rotational speed $\omega = 300$ rad/s

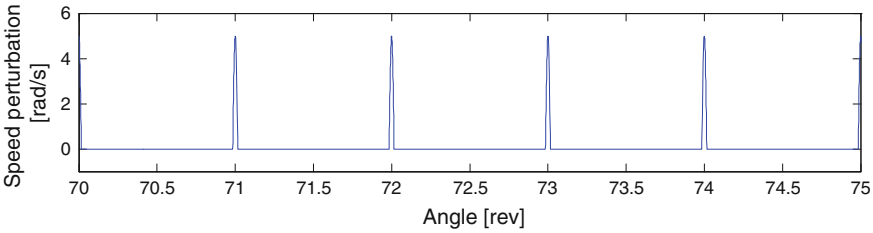

Fig. 7 Stator current versus angle of rotation for a disturbed rotational speed

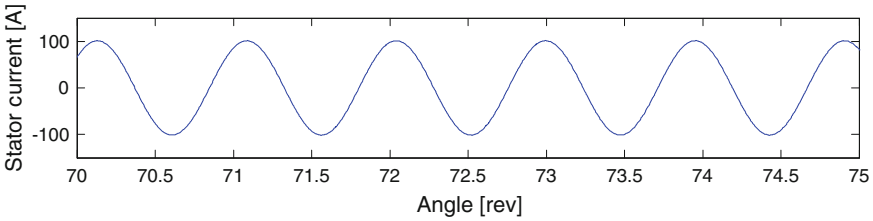

Fig. 8 Stator current versus angle of rotation for a disturbed rotational speed

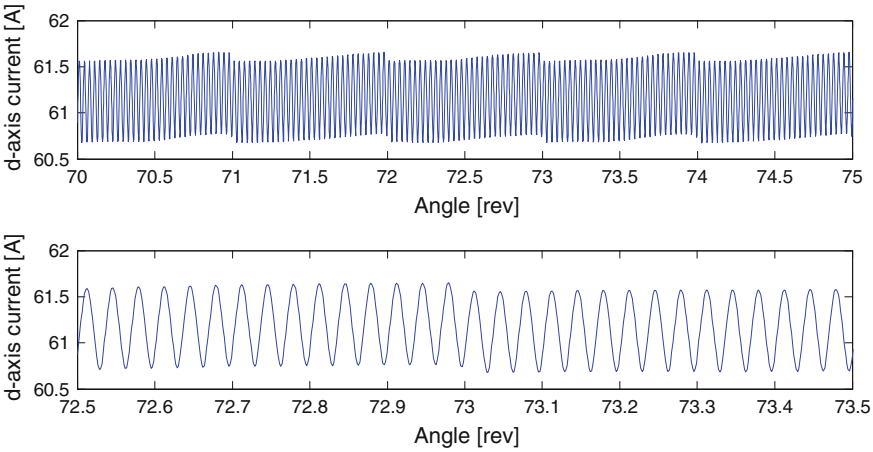

Fig. 9 *d*-axis current and zoom of the *d*-axis current for a disturbed rotational speed

very small perturbation in the rotation speed can be distinguished in the projected signal, proving the capacity of this method to small faults detection. It remains to address the sensitivity of the method to the perturbation amplitude.

The simulation demonstrates also the importance of considering angular domain for modeling the motor in term of computation time. A comparison between model

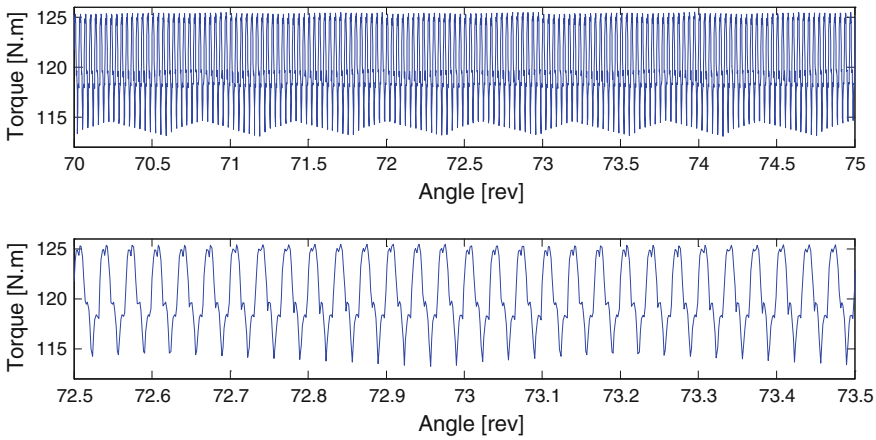

Fig. 10 Torque and zoom of the torque for a disturbed rotational speed

runs in time and angular domains was performed for 1 s of a stationary motor rotation. Through this comparison is noticed that using angular domain reduce 70 % of the simulating time. This is justified by the fact that a large part of the numerical calculation was performed analytically. In fact, angular modeling allows determining the instantaneous angular variation of each coefficient of the $[G(\theta)]$ matrix and its derivate with respect to angle. Regarding these coefficients, it is noticed that they are depending on angularly periodic functions independently of the rotation speed. This ascertainment strengthens our angular approach to modeling.

5 Conclusion and Perspectives

The work presented in this paper is an extension of a previous one aimed to formulate an analytical modeling of the MCSA for systems operating under stationary conditions. By introducing angular approach in classical models, an original reformulation of the method is presented to make it available for rotating systems operating under non-stationary conditions. The validation of this new methodology improves the use of MCSA. It also emphasizes the potential of the angular approach to solve non-stationary problems and extend its application on electrical machines. Results for constant and disturbed angular speed of the motor shows the importance of dealing with non-stationary conditions to get effective monitoring.

From a modeling viewpoint, coupling the electrical model with a mechanical one seems to be a natural extension of the present work in order to simulate perturbations induced by the presence of a fault on stator current signals.

Acknowledgements Authors gratefully acknowledge Rhone-Alpes Council support via mobility grant “Acceuil Doc” 13722.

References

1. Blodt M, Granjon P, Raison B, Rostaing G (2008) Models for bearing damage detection in induction motors using stator current monitoring. IEEE Trans Ind Electron 5(4)
2. Rajagopalan S, Habetler TG, Harley RG, Sebastian T, Lequesne B (2006) Current/voltage-based detection of faults in gears coupled to electric motors. IEEE Trans Ind Appl 42(6)
3. Feki N, Clerc G, Velex Ph (2013) Gear and motor fault modeling and detection based on motor current signal analysis. Electr Power Syst Res 95:28–37
4. Renaudin L, Bonnardot F, Musy O, Doray JB, Rémond D (2010) Natural roller bearing fault detection by angular measurement of true instantaneous angular speed. Mech Syst Signal Process 24(7):1998–2011
5. Bourdon A, André H, Rémond D (2010) A new way of writing motion equations in rotating machines by translation into the angular domain. In: Proceedings of the 8th IFToMM international conference on rotor dynamics, KIST, Seoul, Korea, 12–15 September 2010
6. Rémond D, Antoni J, Randall RB (2014) Editorial for the issue on instantaneous angular speed (IAS) processing and angular applications. Mech Syst Signal Process 44:1–4
7. Feki N (2012) Modélisation électro-mécanique de transmissions par engrenages- Applications à la détection et au suivi des avaries, N° 2012 ISAL 0041 INSA of Lyon
8. Ostovic V (1989) Dynamics of saturated electric machines. Springer, New York
9. Bourdon A, André H, Rémond D (2014) Introducing angularly periodic disturbances in dynamic models of rotating systems under non-stationary conditions. Mech Syst Signal Process 44:60–71

Electrical Induction Motor Higher Harmonics Analysis Based on Instantaneous Angular Speed Measurement

Marco Spagnol, Luigi Bregant and Alessandro Boscarol

Abstract This paper proposes the measurement of Instantaneous Angular Speed (IAS) as a condition monitoring tool for Induction Motors (IMs). The main advantages with respect to vibration and Motor Current Signature Analysis (MCSA) are the high resolution of the result obtained combined with small data storage. The hi-quality information shows many hi-order harmonics that are not easy to interpret and correlate with the machine construction. In this paper a review of the analytic characteristics frequencies due to electromagnetic effects is reported and, furthermore, theoretical results and experiments are compared. From the comparison obtained, the authors conclude that IAS has the potential of extract information due to the rotor's skewness.

Keywords Instantaneous angular speed · Induction motor · Electromagnetic noise · Frequency analysis · Condition monitoring

Contents

1 Introduction 28
1.1 Fault Diagnosis Techniques 29
1.2 Mechanical-Electrical Interaction 30
2 Experimental Setup 30
3 Characteristic Frequencies 31
3.1 Magneto-Motive Force (MMF) Space Harmonics in IAS Spectrum 31
3.2 Time Harmonics and Other Frequencies 33

M. Spagnol (✉) · L. Bregant
Universitá degli Studi di Trieste, Trieste, Italy
e-mail: marco.spagnol@phd.units.it

L. Bregant
e-mail: bregant@units.it

A. Boscarol
Nidec ASI S.p.A, Monfalcone, Italy

F. Chaari et al. (eds.), *Advances in Condition Monitoring of Machinery in Non-Stationary Operations*, Applied Condition Monitoring 4,
DOI 10.1007/978-3-319-20463-5_3

3.3 Slip Effect 36
3.4 Rotor Influence 36
4 Conclusions 39
References 39

1 Introduction

Induction motors (IMs) are frequently used in industries and can be one of the most important components of a system. The maintenance of this equipment is very important from a business and a safety point of view, so the electrical machine reliability has been an hot topic in industry for decades. Three mayor surveys were done in order to classify the major damages:

- 1983 by the Electric Power Research Institute (EPRI), project performed by General Electric (GE)
- 1985 by the Institute of Electrical and Electronics Engineers, Inc. (IEEE)
- 1995 by the Institute of Electrical and Electronics Engineers, Inc. (IEEE)

These surveys are published in [1]. Other recent studies confirm the results of former surveys, such as [2–4]. Bearings and stators are the components where improvement of maintenance and redesign programs may most significantly increase motor reliability. Note that the most frequently failing components are ground insulation (18.5 %) and sleeve bearings (9.7 %), followed by ball bearings (4.9 %) [5] (Table 1).

The previous studies showed that inadequate maintenance and poor installation/testing are significant causes of failures. On-line condition monitoring technologies and Precision Maintenance [6, 7] are proved to improve the motor reliability. For instance, motor bearing failures would be significantly reduced if the driven equipment is properly aligned through the operative life regardless of the loading conditions.

Thanks to the collaboration between Nidec ASI S.p.A and Universitá degli Studi di Trieste, a confirmation of this failure distribution was obtained.

Table 1 Main faults in electrical machines

Failure	Percentage (%)
Bearings damaged (lubrication, misalignment, unbalance)	41
Stator faults	37
Rotor faults	10
Other faults	12

1.1 Fault Diagnosis Techniques

This section introduces recent developments in fault diagnostics of IMs, by providing theoretical guidelines and practical considerations. Reference [8] reports a complete bibliography on IMs Faults Detection and Diagnosis up to December 1999. Measurement techniques for fault detection are based on different measurement approaches: stator current measurement, vibration measurements (acceleration, velocity, displacement) as well as the method proposed in this work, the Instantaneous Angular Speed (IAS) Analysis.

MCSA—Motor Current Signature Analysis the stator current is used as diagnostic signal; "stator current is the most used diagnostic signal in the industrial applications" [9], since it enables for non invasive diagnostic and does not require the use of additional probes. A related problem during field measurements is the exposure to live parts. This may result in exposing the persons involved in the test set-up to electrical shock or arc-flash hazards [10]. A review of MCSA diagnostic techniques is reported in [11, 12]. MCSA is not always reliable for bearing fault detection [13], since the amplitude of fault signatures in the current signal is very low, except in some dedicated operating conditions. In [9] the most common algorithms applied to MCSA are reported. There is an inverse relationship between the fault detection ease and the importance to the user of that fault detection. In fact, there are dozens of papers published on broken rotor bars and only two or three on the use of MCSA for bearing faults detection, in spite of several studies that show bearing faults to account for almost 50 % of IM failures as opposed to around 10 % for rotor cage problems [12].

Vibrations Many faults can be detected using acceleration, velocity or displacement sensors. Many books explain how to implement a condition monitoring system [14, 15]. Angular Resampling, Envelope Analysis and Cyclostationarity are the common techniques used in order to remove the speed fluctuations, emphasize the presence of a fault and find a signal that vary cyclically with time. Sometimes the main problem is the transfer path of the vibration signal through the machine walls.

IAS—Instantaneous Angular Speed Some work has been done recently in order to show the capability of IAS to detect bearing faults [16, 17] and broken rotor bars [18–20]. The IAS measurements is very informative for low speed and high radial load situations, but can also be applied for higher speed motors with a counter with high counting frequencies [21]. A common method used to acquire the IAS is through an incremental optical encoder and a counter board in order to measure the time elapsed between rising edge of the encoder's signal. In this way, the angular information is directly acquired. In a previous research, acceleration and IAS were compared [22] and the slip effect due to IM behaviour was detected. In this work, the behaviour of the electrical motor is explained from the IAS point of view. The aim is to perform condition monitoring tasks using only the encoder connected to the rotor.

1.2 Mechanical-Electrical Interaction

In an electric motor, noise and vibration are related to the excitation forces produced by the electromagnetic field present in the stator and rotor of the motor. The behaviour of a motor can be affected by the variation of these fields due, for example, to the presence of an inverter (e.g. the switching frequency can be seen in the vibration spectrum), by a grid variation [23, 24] or by the motor's design. Thus, the healthy IM also has a specific spectrum signature when there are no faults [25, 26]. In bibliography [27–31], different analytical formulas of the electromagnetic forces are reported. In the next section these main frequencies are summarized. These can be found in the current, vibration and IAS spectra.

2 Experimental Setup

The motor adopted for the test is an ELETTRONICA SANTERNO MJ 90 LA 4 B3 02/07, 1.5 kW 4 poles electric IM, driven by a 380 V, 50 Hz line current, Fig. 1. The motor's specifications are reported in Table 2. The encoder installed (Not Driving End NDE) is a TEKEL TSW80P with 1024 pulses per revolution (ppr) and its shaft is rigidly connected to the rotor, while the encoder's case is fixed at the stator through a joint, Fig. 2. The motor is provided of a fan with 7 blades made in fiber reinforced plastic. In this setup there are also installed: a torquemeter, a magnetic brake and a fly-wheel. The data acquisition system is based on National Instruments hardware, using the internal 80 MHz counter and purposely developed MATLAB software.

The IAS measurement uses the elapsed time counting method. The key feature of this approach is the implicit angular sampling that, combined with an FFT processing, generates an order spectrum. Quantities related to speed variation, such as bearing faults, become fixed in the order spectrum.

The results presented in this paper show that IAS is very sensitive and not filtered by structural resonance.

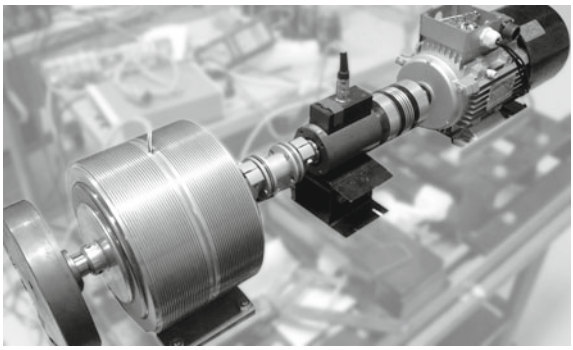

Fig. 1 Experimental test rig

Table 2 Motor MJ90LA4B3 specifications

P_n (kW)	N_n (rpm)	T_n (Nm)	I_n 400 V (A)	$\cos\phi$	μ (%)	J (kg m^2)	m (kg)	S	R
1.5	1390	10.3	3.52	0.78	78.6	0.0035	14	24	22

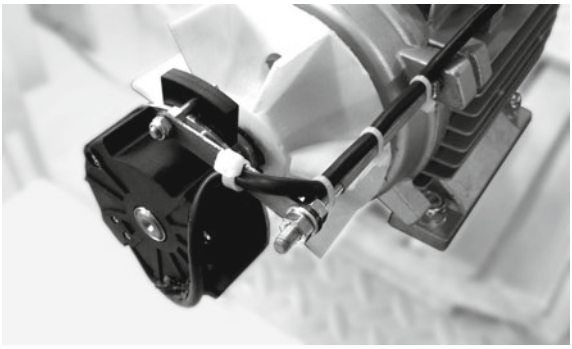

Fig. 2 TEKEL TSW80P encoder

3 Characteristic Frequencies

Rotor and stator excite magnetic flux density waves in the air gap. The slots, the distribution of windings in slot, the input current waveform distribution, the air gap permeance fluctuation, the rotor eccentricity and the phase unbalance give rise to mechanical deformations and vibrations. Magnetomotive force (MMF) space harmonics, time harmonics, slot harmonics, eccentricity harmonics and saturation harmonics, produce parasitic higher harmonic forces and torques. In order to explain peaks found in IAS spectrum, a review of the analytical formulas of electromagnetic fields generation in IM is done. In this paper only MMF space harmonics in IAS spectrum are reported. In Table 3 the main parameters for an IM are reported.

3.1 Magneto-Motive Force (MMF) Space Harmonics in IAS Spectrum

The current flowing into the stator of an IM generates an electromagnetic excitation which consists in an infinite number of harmonic MMFs changing in time according to $\cos(\omega t)$ and in space according to $\cos(vp\theta_s)$. A three-phase ($m = 3$) ideal motor with balanced sinusoidal currents is considered. Three windings are shifted in space by $2\pi/3$ electrical degrees. Three input currents are injected into the

Table 3 Induction machine main parameters

f	Fundamental frequency	s	Slip
p	Pole pair number	m	Number of phases
k, g	Ordinal numbers	v	Harmonic order
v_+	Harmonic order (forward)	v_-	Harmonic order (backward)
R	Rotor slot (bars)	S	Stator slot
F_{mv}	MMF Amplitude	θ_s	Angle (stator ref)
o_v	Order in IAS spectrum	f_r	Frequency in current spectrum
sk	Skewness		
$P = 2p$	Poles		
$\omega = 2\pi f$	Angular frequency		
$n_s = f/p$	Synchronous speed		
$n_{s_v} = \mp f/(vp)$	Synchronous speed for vth harmonic		
$n_m = (1 - s)n_s$	Mechanical speed		
$\tau_s = 1/n_s$	Synchronous speed period		
$\tau_m = 1/n_m$	Mechanical speed period		
$n_{sl} = n_s - n_m$	Slip speed		
$s = n_{sl}/n_s$	Slip definition		
$sf = psn_s$	Slip frequency		
$s_v = 1 - v(1 - s)$	Slip for vth harmonic		
$fs_v = f[1 - v(1 - s)]$	Slip frequency for vth harmonic		
$v = 2mg + 1$	The order of the space harmonics		
$\mu = \frac{gS_2}{p} + 1$	The order of the rotor space harmonics		

stator with theoretically the same amplitude and the same phase shift equal to $2\pi/3$ electrical degrees. This generates a total MMF of:

$$F_1(\theta_s, t) = \sum_v^{\infty} F_{mv} \cos[(2\pi f)t \mp (vp)\theta_s] = \sum_v^{\infty} F_{mv} \cos[(vp)\theta_s \mp (2\pi f)t] \quad (1)$$

with:

$$v_+ = 2km + 1 \quad v_- = 2km - 1 \quad v = 2\,km \pm 1 \quad (2)$$

or using another notation [25],

$$v = 2gm + 1 \quad g = 0, \pm 1, \pm 2, \ldots \quad v = 1, -5, 7, -11, 13, \ldots \quad (3)$$

$$F_1(\theta_s, t) = \sum_v^{\infty} F_{mv} \cos[(2\pi f)t - (vp)\theta_s] = \sum_v^{\infty} F_{mv} \cos[(vp)\theta_s - (2\pi f)t] \quad (4)$$

In this specific case (three-phase stator winding), the harmonics present in the spectrum $v = mk$ with $k = 1, 3, 5, \ldots$ do not exist. The forward-rotating harmonics

$v_+ = 1, 7, 13, 19, \ldots$ are the arithmetic sum of waves in all three phases, while the backward-rotating harmonics $v_- = 5, 11, 17, 23, \ldots$ are zero, [29]. $v = 5, 7$ are a consequence of trapezoidal phase MMF shape [25]. IM are characterized by the presence of the slip s. This parameter is correlated to the load/speed of the machine. At the motor's startup the slip is 1, at no load is 0, with load $0 < s < 1$. Other slip-dependent parameters are defined in Table 3. The magnetic flux in the rotor and in the stator are running with the same synchronous speed n_s, since $n_s = n_s(1 - s) + sn_s$. Considering a constant fundamental frequency (the grid supply frequency varies approximately between 49 and 51 Hz), the current in the stator completes a revolution in θ_s, while the rotor does it in θ_m (with $\tau_s \neq \tau_m$) owing to the slip. The encoder senses this latter speed. The Eq. 4 describes the MMF with a periodicity w_v of

$$w_v = 0, 12, 12, 24, 24, 36, 36, \ldots \tag{5}$$

for

$$v = 1, -5, 7, -11, 13, -17, 19, \ldots \tag{6}$$

while in the IAS spectrum these orders can be found at o_v, Eq. 7. w_v can be seen in Fig. 3. This equation does not take into account the fundamental frequency because it does not have an influence on the generated periodicity.

$$o_v = \frac{p}{1 - s}\ (v - 1) \tag{7}$$

In Fig. 4 the harmonics generated in IAS spectrum by the MMF space harmonics are reported ($v = -20, -1, \ldots, 1, 20$ in order to consider a not ideal machine). Note that $v = -5, 7$ have the same absolute value $o_v = 12.425$, $v = 3, 9, 15, \ldots$ can be correlated to stator eccentricity, while even space harmonics are due to mechanical unbalance. These harmonics exactly excite the frequencies found calculating stator and rotor combinations [30]

$$o_v = 0, 4.142, 8.283, 12.425, 16.566, 20.708, 24.849, 28.991, 33.132, \ldots \tag{8}$$

3.2 Time Harmonics and Other Frequencies

In the bibliography, it is suggested to analyze the second time harmonic in the frequency spectrum. This allows to detect current supply unbalance as suggested in [15, 22, 29, 32] (Table 4):

$$f_r = 2f \tag{9}$$

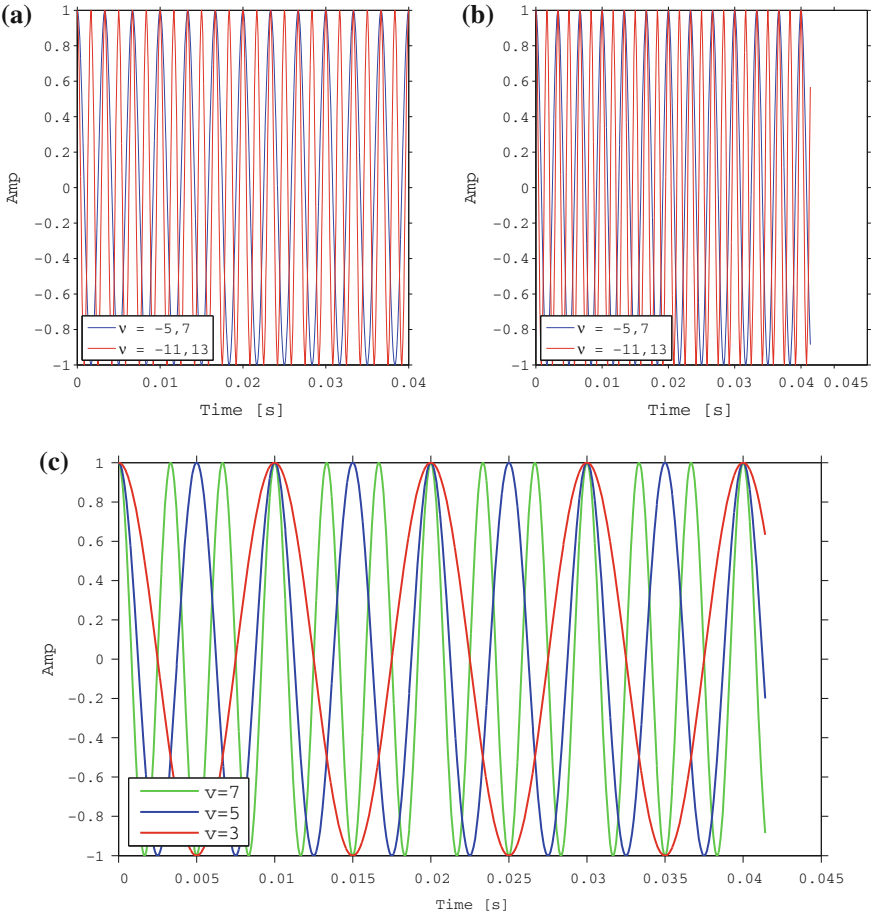

Fig. 3 MMF periodicity w_ν: **a** considering a period τ_s; **b** considering a period τ_m; **c** considering a period τ_m and showing $\nu = 3, 5, 7$

Fig. 4 Rotor skewness

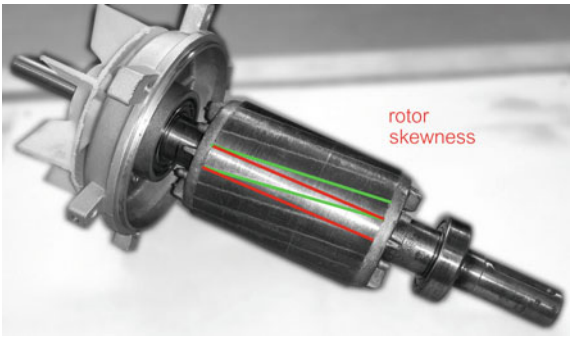

Table 4 Current harmonic frequencies, ($p = 2$, $s = 0.03417$)

v	1	2	3	4	5
o_v	0	2.0708	4.1415	6.2123	8.2830
v	6	7	8	9	10
o_v	10.3538	12.4245	14.4953	16.5661	18.6368
v	11	12	13	14	15
o_v	20.7076	22.7783	24.8491	26.9199	28.9906
v	16	17	18	19	20
o_v	31.0614	33.1321	35.2029	37.2736	39.3444
v	−1	−2	−3	−4	−5
o_v	−4.1415	−6.2123	−8.2830	−10.3538	−12.4245
v	−6	−7	−8	−9	−10
o_v	−14.4953	−16.5661	−18.6368	−20.7076	−22.7783
v	−11	−12	−13	−14	−15
o_v	−24.8490	−26.9199	−28.9906	−31.0614	−33.1321
v	−16	−17	−18	−19	−20
o_v	−35.2029	−37.2736	−39.3444	−41.4152	−43.4859

that, for a 50 Hz supply frequency, is:

$$f_r = 2 \cdot 50 = 100 \text{ Hz} \tag{10}$$

the existence of this frequency component could also be due to by the presence of the MMF space harmonic $v = 3$:

$$f_r = 2f = o_3 \, n_m \tag{11}$$

with, Eq. 7:

$$o_3 = \frac{p}{1-s}(3-1) = \frac{2p}{1-s} \tag{12}$$

and:

$$f_r = 2f = o_3 \quad n_m = \frac{2p}{1-s} \, \frac{1-s}{p} \, f = 2f \tag{13}$$

The consequence is that, in the IAS spectrum, the 100 Hz in frequency spectrum seen in MCSA corresponds to the IAS' order 4.1415 for a four-pole motor with a 50 Hz supply frequency and slip $s = 0.03417$. Instead, the time harmonic $f_r = 3f$ (seen in MCSA) is related to the motor's saturation and other causes [27].

3.3 Slip Effect

Figure 5 shows the IAS measurement of the same motor in two different experimental configurations:

- TR motor only (no load)
  - 0.00 Nm RMS − $s = 0.00088$
- EL torquemeter, magnetic brake (three loads) [21, 22]
  - 0.00 Nm RMS (2.17 A RMS) − $s = 0.00175$
  - 2.60 Nm RMS (2.27 A RMS) − $s = 0.01466$
  - 6.16 Nm RMS (2.75 A RMS) − $s = 0.03417$

In the *EL* case, there is a strong component owing to unbalanced currents or stator eccentricity. In this specific case it is probably related to the eccentricity because a new experimental setup, with the same motor and a stiffer coupling that fixed the rotor in a better position, shows a lower amplitude of the MMF space harmonic $v = 3$. Order 3 keeps the same amplitude through the various measurements, so it is an indicator of the measurement quality. Sidebands are present around these orders at $2ps$. The IAS spectrum of the IM can be divided into two zones:

- orders 0–16: current space and time harmonics effect
- orders 16–40: rotor/stator slotting, skewness effect, saturation

In Table 5, the calculation of o_v (Eq. 7) is extended to the four different configurations of slip ($s = 0.00088, 0.00175, 0.01466, 0.03417$). In Fig. 6 these orders are highlighted.

3.4 Rotor Influence

The conductors (bars) are often skewed slightly along the length of the rotor to reduce noise and smooth out torque fluctuations that might result at some speeds due to interactions with the pole pieces of the stator, Fig. 4. In Fig. 7, a phenomenon correlated to the rotor skewness is present.

This effect can be seen in those orders integer order + $2ps$ with sidebands. The latter can be calculated with Eq. 14. In Table 6 these sidebands are calculated for two different motors. The first involved in the experiment has a skew of 1 bar. The value of o_v is very close to the experimental value 0.282. Considering geometric tollerances, the value 1.033 can be assigned to the skewness parameter sk. Sidebands are present also in the second motor, but further investigation is necessary because it has $R = 32$ and $\mathrm{sk} = 1.5$, so the result is $o_{\mathrm{sk}} = 0.2813$, Table 6.

The physical explanation of these sidebands is very simple: at every integer order, the rotor feels the electromagnetic pull (main order correlated with $2ps$) and

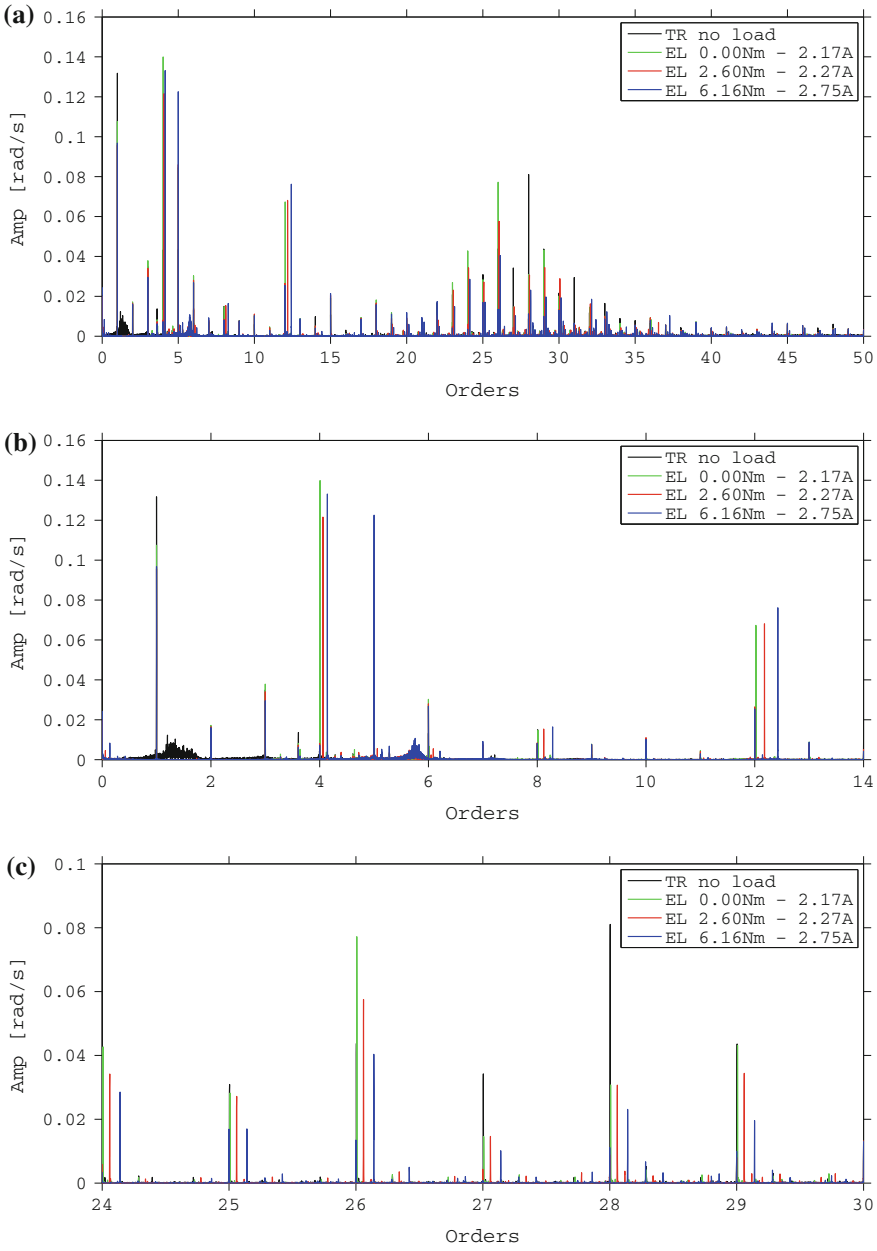

Fig. 5 Harmonics in IAS spectrum, TR (only motor) and EL configuration ($s_1 = 0.00088$, $s_2 = 0.00175$, $s_3 = 0.01466$, $s_4 = 0.03417$)

Table 5 IAS current harmonic frequencies o_v, ($p = 2$)

s	0.00088	0.00175	0.01466	0.03417
v = 11, −9	±20.0176	±20.0351	±20.2976	±20.7076

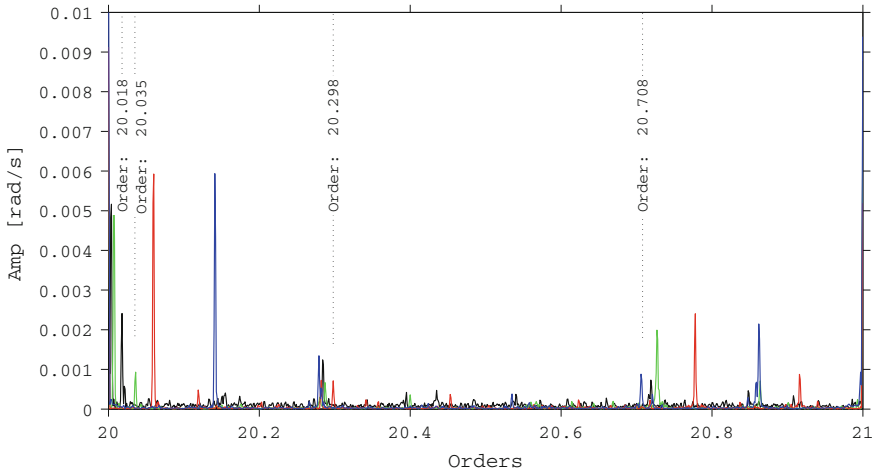

Fig. 6 MMF Harmonics in IAS spectrum, TR (only motor) and EL configuration ($s_1 = 0.00088$, $s_2 = 0.00175$, $s_3 = 0.01466$, $s_4 = 0.03417$)

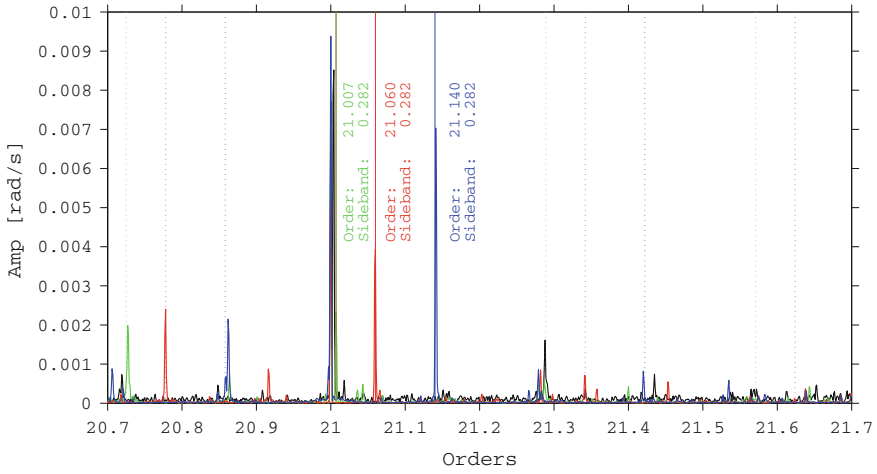

Fig. 7 Skew Harmonics in IAS spectrum, TR (only motor) and EL configuration ($s_1 = 0.00088$, $s_2 = 0.00175$, $s_3 = 0.01466$, $s_4 = 0.03417$)

Table 6 Sidebands in the IAS spectrum due to the rotor skewness ($p = 2$, $m = 3$)

R	22	22	32
sk	1	1.033	1.5
O_{sk}	0.2727	0.2817	0.2813

owing to the presence of skewness, the number of pole pairs, the number of phases and the number of rotor bars, a modulation around the main order appears. If confirmed, it may be a very interesting result because this effect probably cannot be seen in MCSA due to the smearing of the peaks. The IAS spectrum, being fixed with the rotor, allows this kind of information extraction.

$$o_{sk} = \frac{p\, m\, \mathrm{sk}}{R} \tag{14}$$

4 Conclusions

This research shows the influence of current supply effect in the IAS measurement. Motor noise and vibrations can be predicted using analytical formulas found in bibliography. Nevertheless, further work must be done in order to identify all the harmonics and sidebands present in the spectrum. From the experiments it is clear that the saturation harmonics are very strong in induction machines. Sidebands were found probably correlated to the rotor skewness.

Acknowledgements This research is supported by Universitá degli Studi di Trieste, Nidec ASI S. p.A. and "Programma Operativo del Fondo Sociale Europeo 2007/2013 della Regione Autonoma Friuli Venezia Giulia".

References

1. IEEE Standards (2012) Historical reliability data for IEEE 3006 standards: power systems reliability
2. Penrose HW, Large electric motor reliability: what did the studies really say?, Dreisilker Electric Motors http://www.mt-online.com/feb2012/large-electric-motor-reliability-what-did-the-studies-really-say
3. Bonnett AH (2010) Root cause failure analysis for AC induction motors in the petroleum and chemical industry. In: 2010 record of conference papers industry applications society 57th annual Petroleum and Chemical Industry conference (PCIC)
4. Bonnett AH, Soukup GC (1992) Cause and analysis of stator and rotor failures in three-phase squirrel-cage induction motors. IEEE Trans Ind Appl 28(4):921–937
5. Albrecht PF, Appiarius JC, McCoy RM, Owen EL, Sharma DK (1986) Assessment of the reliability of motors in utility applications—updated. IEEE Trans Energy Convers EC-1 (1):39–46

6. SKF, Precision maintenance PrM fundamentals (in Italian), http://www.skf.com/it/services/customer-training/corsi-di-formazione-skf-italia/manutenzione/fondamenti-di-precision-maintenance-prm/index.html
7. Sondalini M, Summary report on using and introducing precision maintenance, lifetime reliability solutions http://www.lifetime-reliability.com/free-articles/precision-maintenance/Using_and_Introducing_Precision_Maintenance.pdf
8. Benbouzid MEH (1999) Bibliography on induction motors faults detection and diagnosis. IEEE Trans Energy Convers 14(4):1065–1074
9. Giri F (2013) AC electric motors control: advanced design techniques and applications. Chapter 14 fault detection in induction motors. Wiley, New York
10. Durocher DB, Feldmeier GR (2004) Predictive versus preventive maintenance. IEEE Ind Appl Mag 10(5):12–21
11. Nandi S, Toliyat HA, Li X (2005) Condition monitoring and fault diagnosis of electrical motors-a review. IEEE Transa Energy Convers 20(4):719–729
12. Benbouzid MEH (2000) A review of induction motors signature analysis as a medium for faults detection. IEEE Trans Industr Electron 47(5):984–993
13. Bellini A, Immovilli F, Rubini R, Tassoni C (2008) Diagnosis of bearing faults of induction machines by vibration or current signals: a critical comparison. In: 2008. IAS '08 industry applications society annual meeting, IEEE
14. Randall RB (2011) Vibration-based condition monitoring: industrial, aerospace and automotive applications. Wiley, New York
15. Scheffer C, Girdhar P (2004) Practical machinery vibration analysis and predictive maintenance. Elsevier Science, London
16. Renaudin L, Bonnardot F, Musy O, Doray JB, Rémond D (2010) Natural roller bearing fault detection by angular measurement of true instantaneous angular speed. In: Proceedings of ISMA 2010, Leuven
17. Bourdon A, Chesné S, André H, Rémond D (2014) Estimation of the size of a spall defect on a rolling bearing outer ring using Instantaneous angular speed measurements. In: Proceedings of ISMA 2014, Leuven
18. Ben Sasi AY, Gu F, Li Y, Ball AD (2006) A validated model for the prediction of rotor bar failure in squirrel-cage motors using instantaneous angular speed. Mech Syst Sig Process 20 (7):1572–1589
19. Alwodai A, Gu F, Ball AD (2012) A comparison of different techniques for induction motor rotor fault diagnosis. J Phys Conf Ser 364(1):012066
20. Pennacchi P (2008) Computational model for calculating the dynamical behaviour of generators caused by unbalanced magnetic pull and experimental validation. J Sound Vib 312 (1-2):332–353
21. Spagnol M, Bregant L (2014) Instantaneous angular speed analysis, measurement errors and signal filtering. In: Proceedings of 9th IFToMM international conference on rotor dynamics IFToMM ICORD 2014, Milan
22. Spagnol M, Bregant L (2013) Instantaneous angular speed: encoder-counter estimation compared with vibration data. Diagnostyka 14(3):
23. De Bauw K, Petit F, Matthys K, Doucement S (2014) Investigating grid-induced turbo-generator vibrations: a multidisciplinary challenge. In: Proceedings of 9th IFToMM international conference on rotor dynamics IFToMM ICORD 2014, Milan
24. Mair M, Weilharter B, Ellermann K (2014) Rotor vibrations in electrical machines due to electromagnetic forces. In: Proceedings of 9th IFToMM international conference on rotor dynamics IFToMM ICORD 2014, Milan
25. Joksimovic GM, Riger J, Wolbank TM, Peric N, Vasak M (2013) Stator-current spectrum signature of healthy cage rotor induction machines. IEEE Trans Ind Electron 60(9):4025–4033
26. Gyftakis KN, Kappatou JC (2013) The impact of the rotor slot number on the behaviour of the induction motor. Adv Power Electron ID 837010
27. Toliyat HA, Nandi S, Choi S, Meshgin-Kelk H (2012) Electric machines: modeling, condition monitoring, and fault diagnosis. Taylor & Francis, Boca Raton

28. Tavner P, Ran L, Penman J (2008) Condition monitoring of rotating electrical machines. Institution of Engineering and Technology, London
29. Gieras JF, Wang C, Lai JC (2005) Noise of polyphase electric motors. Taylor & Francis, Boca Raton
30. Timár PL (1989) Noise and vibration of electrical machines., Studies in electrical and electronic engineeringElsevier, New York
31. Heller B, Hamata V (1977) Harmonic field effects in induction machines. Elsevier Scientific Pub. Co., Amsterdam
32. Ben Sasi AY, Gu F, Payne B, Ball AD (2004) Instantaneous angular speed monitoring of electric motors. J Qual Maint Eng 10(2):123–135

Evaluation and Improvement of Accuracy in the Instantaneous Angular Speed (IAS) and Torsional Vibration Measurement Using Zebra Tapes

Antonio Palermo, Karl Janssens and Laurent Britte

Abstract This paper analyses from an experimental standpoint the measurement error in the Instantaneous Angular Speed (IAS) and Torsional Vibration (TV) measurement by means of zebra tapes. A precision gear test rig is exploited to compare against calibrated high accuracy analog encoders and low-cost digital encoders taken as angular references, after performing a measurement error analysis. It is shown analytically and experimentally how compensation of systematic errors leads to a substantially increased measurement accuracy. The benefits introduced by such compensation are demonstrated, leading to the conclusion that zebra tapes show high potential for extremely accurate measurement of Torsional Vibrations, both in terms of angular position and IAS.

Keywords Zebra tapes · Torsional vibration · IAS · Accuracy · Calibration

Contents

1 Introduction 44
2 Experimental Setup 45
2.1 Design Features and Instrumentation 45
2.2 Encoders Measurement Error 47

A. Palermo (✉) · K. Janssens · L. Britte
Siemens Industry Software NV, Leuven, Belgium
e-mail: antonio.palermo@siemens.com

K. Janssens
e-mail: karl.janssens@siemens.com

L. Britte
e-mail: laurent.britte@siemens.com

A. Palermo
Department of Mechanical Energy and Management Engineering (DIMEG), University of Calabria, Rende, Italy

A. Palermo
Department of Mechanical Engineering, KU Leuven, Leuven, Belgium

F. Chaari et al. (eds.), *Advances in Condition Monitoring of Machinery in Non-Stationary Operations*, Applied Condition Monitoring 4,
DOI 10.1007/978-3-319-20463-5_4

3 Measurement Error of Zebra Tapes 48
3.1 Analytical Considerations 48
3.2 Experimental Measurement 50
4 Conclusions 54
References 55

1 Introduction

Instantaneous Angular Speed (IAS) and, more in general, Torsional Vibrations (TV) carry a considerable amount of information on the health and usage status of rotating machinery, e.g. in vehicle [1], power generation [2], oil and gas [3], aviation [4] and marine sectors [5]. It has been shown that IAS performs very well as a sensitive and robust indicator for early detection of faults [6]. However, accurate IAS and TV measurement poses several intrinsic challenges related to acquiring signals from rotating mechanical components, often at high speed and in environments difficult to access and to instrument. Traditional instrumentation for TV and IAS analysis includes encoders, laser vibrometers or paired accelerometers which pose significant limitations to practical implementation [7]. In an effort towards overcoming such difficulties and aiming towards a simplification of the instrumentation phase, a few measurement techniques have been introduced to use angular coders[1] which allow minimal modifications of the components to be tested. A relatively new technique in this group uses so-called zebra tapes (*sensor*[2]), which are constituted by a sequence of black and white stripes, directly glued or engraved on the component of interest. Therefore the angular position can be coded detecting the stripes passage by means of an optical probe (*measuring transducer*). Recent investigations highlight *accuracy* limitations for this technique, aside its great versatility and practical instrumentation. Accuracy limitations of coder-based techniques can be due to the combination of the sensor and measuring transducer or due to the acquisition and processing of the angular position [8]. *Measurement errors* related to the formers can be due to mechanical mounting or due to the non-uniform distribution of angular subdivisions [9, 10]. Provided that the measurement is free of aliasing, errors related to the acquisition of the signal are mainly due to digital quantization of time [11], while errors related to processing are mainly due to angular position reconstruction starting from discrete samples [12, 13]. In this paper, the total measurement error of zebra tapes is measured against a *calibrated* angular reference. A reliable measurement is reached by exploiting a precision gear test rig for which a special positioning system has been designed, in order to install on the same shaft a high-accuracy analog encoder and a low-cost digital encoder.

[1]The term "coder" is used here to denote a measurement instrument which subdivides and enumerates one rotation in a discrete number of angular positions.

[2]Terms in *italic* are used according to the definition provided by the International Vocabulary of Metrology (VIM) [15].

2 Experimental Setup

2.1 Design Features and Instrumentation

The main aim of the adopted test rig, shown in Fig. 1, is to allow the heavy instrumentation of a test gear pair which can be subject to tightly controlled operating conditions and which has well-characterised boundary conditions. Manufacturing tolerances were specified and verified using a coordinate measuring machine and using Geometric Dimensioning and Tolerancing (GD&T) for each mechanical component as well as for the assembly. As a general figure, tolerance bands were kept at a component level within a few micron, with an assembly level stack-up below 20 micron. These design features lend themselves well to performing also accurate torsional vibration measurements. More detailed discussion on the design as well as on the instrumentation of the test rig can be found in [14], while the main specifications of the rig are reported in Table 1.

A relevant aspect for the purposes of the present paper is that both test shaft ends are accessible. Each shaft end is instrumented with one high-accuracy analog encoder and one low-cost digital encoder. However, only one shaft will be used for the present study. Encoder specifications are reported in Table 2.

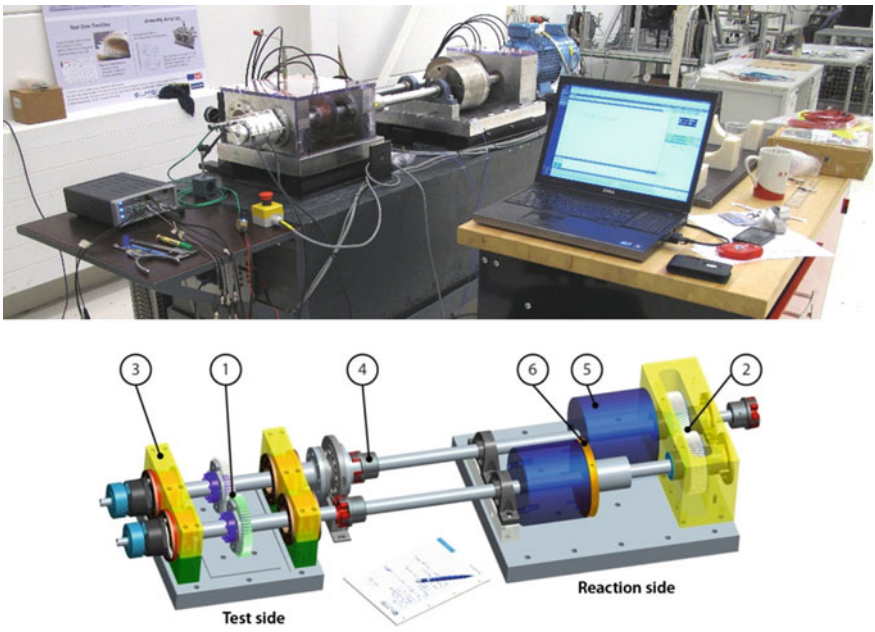

Fig. 1 *Top* Physical installation. *Bottom* Three-dimensional representation of the test rig: *1* Test gears; *2* reaction gears; *3* bearings support plates; *4* flexible couplings; *5* flywheels; *6* clutch flange for preload

Table 1 Possible operating conditions for the test gear pair

Parameter	Range	Uncertainty
Speed	0–4500 rpm (0–75 Hz)	Measured
Torque	0–500 Nm	±0.05 %
Angular misalignments	0–2 mrad	0.1 mrad
Parallel misalignments	0–0.3 mm	0.020 mm

The high-accuracy encoders have a measurement error described by *calibration diagrams* individually provided by the manufacturer, given that the encoders are mounted according to the specified tolerances. Centering and alignment tolerances are particularly important for these encoders, because the rotor and the stator allow limited relative displacements. The low-cost encoders on the other hand do not have a description for the distribution of their measurement error, therefore if successfully mounted on the same shaft they can be calibrated against the high-resolution encoders. Positioning tolerances for these encoders are not critical, because the only motion allowed between rotor and stator is relative rotation, thanks to an integrated high-precision double-row ball bearing. Since the stator of the low-cost encoder does not move with respect to the shaft, it can be taken (after coordinate machine measurement) as reference to correctly center and align the stator of the high-accuracy encoder. An encoders positioner has been manufactured to fulfil this requirement, shown in Fig. 2 together with inner and outer positioning surfaces for both the encoders. In this way, the high-accuracy encoder is not sensitive to the misalignment which in future studies will be imposed to the shaft.

Finally, zebra tapes are installed on different shaft diameters (more details in Sect. 3). Zebra tapes have been scanned using a round spot probe with 1 mm diameter, mounted at a distance of circa 1 mm, and an Optel-Thevon 152 M sensor, which is able to generate a TTL signal up to a bandwidth of about 1×10^6 pulses per second and has also an analog output.

All signals are acquired using a Siemens LMS SCADAS Mobile acquisition system equipped with voltage input channels for the analog encoder and the zebra

Table 2 Encoder specifications

Encoder model	Number of divisions	Signal type	One-revolution accuracy	Spacing accuracy	Recommended measuring step
Heidenhain RON 285C	18000	Analog Sine	1.38×10^{-3} deg (±5 arcsec)	±1 %	1.00×10^{-4} deg (0.36 arcsec)
Heidenhain ERN 120	5000	Digital TTL	5.55×10^{-3} deg (±20 arcsec)	–	–

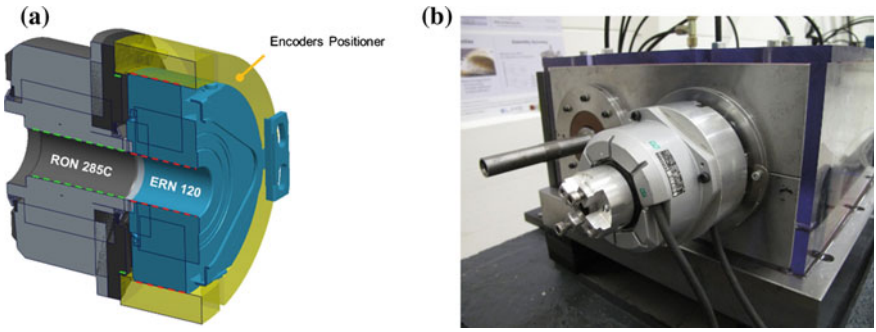

Fig. 2 **a** Encoders positioner and positioning surfaces (indicated by *dashed lines*); **b** encoders installation

tapes (24 bit ADC sampling at 204.8 kHz) and an RV4 module for rotational vibration providing digital encoder channels (input pulse rate up to 204.8 kHz synchronised with an 820 MHz clock).

2.2 Encoders Measurement Error

Since encoder assembly tolerances were taken into account when designing the test rig and the encoders positioner, it is assumed according to specifications that assembly errors do not play a significant role in the overall measurement error. Given that the acquisition system has a timer clock of 820 MHz yielding a time resolution of 1.2 ns, also the time quantization error is negligible [16]. Furthermore, measurements have been performed at low speed ($\sim$20 rpm) for two reason. Firstly, as explained in Sect. 3.1 and Eq. 7, the non-uniform spacing of gratings can be characterized with respect to the angular position, which is independent of speed. Secondly, the high-accuracy encoders saturate very quickly the sampling frequency of 204 kHz. Figure 3 reports the measurement error for the high-accuracy encoders, according to the calibration diagrams provided by the manufacturer, and for the low-cost encoders, measured against the high-accuracy encoders using the mounting system described in the previous paragraph.

It is evident from the graph that the overall peak to peak error magnitude for the high-accuracy encoders (2.65×10^{-4} deg) is about one order of magnitude lower than the one of the low-cost encoder (3.27×10^{-3} deg). However, a single magnitude value provides only limited information about the measurement error: it is useful, especially when processing data in the angle domain, to analyze the angular frequency (order) distribution of the measurement error. By performing a Fourier Transform of the errors in angle domain, it can be seen that the measurement error is limited to the first few orders and that, above this band, both the high-accuracy and the low-cost encoders have a measurement error well below 1×10^{-4} deg (Fig. 4).

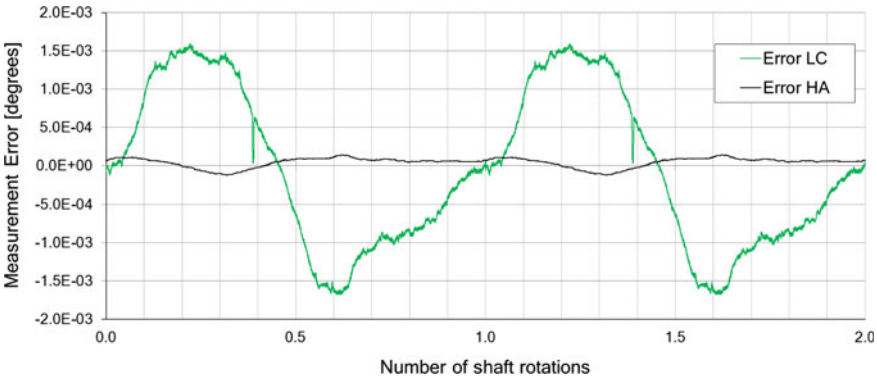

Fig. 3 Measurement error of the high-accuracy (*HA*) and the low-cost (*LC*) encoders

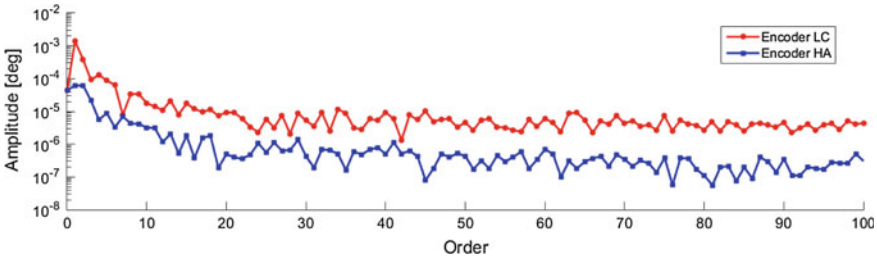

Fig. 4 Order distribution for the measurement error of the HA and the LC encoders

3 Measurement Error of Zebra Tapes

3.1 Analytical Considerations

Zebra tapes are currently used to generate a voltage square waveform which is periodic with the passage of a stripe pair. The rising or the falling edge of the square wave can be used as a trigger to detect a discrete angular position increment given in degrees by:

$$\Delta\theta_e = \frac{360}{N} \tag{1}$$

where $\Delta\theta_e$ is the estimated or nominal angle increment, and N is the number of stripe pairs of the zebra tape. In reality, the angle increments are affected by a measurement error. In this paper this error is assumed to be due to the non-uniform distribution of angular subdivisions, given the discussion in Sect. 2.1. This assumption is basically taking the measurement error as *systematic* and will be

validated on the next paragraph. Under this assumption the total angular position can be written as:

$$\theta_e(i) = \theta_t(i) + e_c[\theta_t(i)], \quad i = 1, \ldots, N \tag{2}$$

where $\theta_e(i)$ is again an estimated angle and is also a discrete variable, as the index i takes natural values which cycle over the total number of stripe pairs N. $\theta_t(i)$ has the same characteristics, but represents *true* angular position. e_c is the cumulative measurement on the angular position and is a function of the true angular position, since this error varies from stripe pair to stripe pair. While these variables are periodic in the angle domain, they also have an associated time stamp which tracks their occurrence in time.

It is useful to add one additional definition of error, the spacing error e_s:

$$e_s[\theta_t(i)] = e_c[\theta_t(i+1)] - e_c[\theta_t(i)] \tag{3}$$

The true angle can be retrieved by subtracting the cumulative measurement error:

$$\theta_t(i) = \theta_e(i) - e_c[\theta_t(i)] \tag{4}$$

This description of the angular position is sufficient for the purposes of this paper. Besides the angular position, the IAS is defined as the time derivative:

$$\Omega_e(t) = \frac{d\theta_e(i)}{dt} \tag{5}$$

The subscript indicates again that this value is estimated. Even if the periodic index has been replaced by time t, this time variable is still discrete so that the IAS value is an average estimation between two subsequent angular increments and the two related time stamps. To let the measurement error appear explicitly in the definition of the IAS, Eq. 2 can be substituted in Eq. 5. In this way, the true value of the IAS can also be calculated. Considering that $\Omega_t(t) = \frac{d\theta_t(i)}{dt}$ and that e_c is a composite function of θ_t, Eq. 5 becomes:

$$\Omega_e(t) = \Omega_t(t) + \frac{de_c[\theta_t(i)]}{d\theta_t(i)} \cdot \frac{d\theta_t(i)}{dt} = \Omega_t(t)\left(1 + \frac{de_c[\theta_t(i)]}{d\theta_t(i)}\right) \tag{6}$$

From Eq. 6 it is clear that to have an accurate IAS measurement, the derivative of the cumulative error in angle domain should be minimized. Since it is an additive term to the ideal factor of 1 between Ω_t and Ω_e, this derivative can be interpreted as a normalized percentage stray fluctuation of the estimated IAS. It should also be pointed out that this error on the IAS does not vary with speed in angle domain (the derivative is with respect to the function θ_t). In time domain, instead, this error increases linearly with the true angular velocity.

Among other methods, finite differencing on the discrete functions can be used to compute the derivative of the cumulative error:

$$\Omega_e(t) = \Omega_t(t)\left(1 + \frac{e_c[\theta_t(i+1)] - e_c[\theta_t(i)]}{\theta_t(i+1) - \theta_t(i)}\right) = \Omega_t(t)\left(1 + \frac{e_s[\theta_t(i)]}{\Delta\theta_t(i)}\right) \quad (7)$$

The ratio between the spacing error and the angle increment is what drives the accuracy of the IAS measurement. Namely, a higher number of stripe pairs is not beneficial to accuracy if the spacing error does not also reduce. And this is typically the case: the spacing error e_s is a property of the tape printing process and is independent on the number of stripe pairs. An optimal accuracy trade-off should therefore be thought for IAS measurement: more stripe pairs are beneficial for bandwidth but increase the importance of keeping low the spacing error as the angle increments $\Delta\theta_t$ become smaller. Equivalently, given a rotor diameter to be instrumented, accuracy is improved if its circumference is instrumented with fewer stripe pairs of larger size.

3.2 Experimental Measurement

Zebra tape measurement error has been assessed at two different shaft diameters. Two types of tape have been used: a 1 mm Optel-Thevon tape and a laser-printed tape (1200 dpi resolution on 100 g/m^2 copier paper) where stripes have a chosen stripe width. The Optel-Thevon tape is supported by a tough and oil-resistant plastic layer. However the laser-printed tape, although only suitable for clean environments, has been used to choose the stripe size to obtain a specific and integer number of angular divisions over the full shaft circumference. This number can be chosen as a multiple of the order of interest, e.g. to minimize leakage and avoid windowing the signal. The analyzed cases are listed in Table 3 and shown in Fig. 5.

For the printed tape, it is useful to consider tape dimensions up to micron level, as the total tape length comes from a stack-up. Moreover, the zebra tape is drawn using vector graphics (and not by pixelated rasters) to improve accuracy and resolution. The stripes are in fact defined by analytically exact geometric entities before being sent to the printer.

Table 3 Main characteristics of the analyzed zebra tape cases

Case name	Shaft diameter (mm)	Type of tape	Number of stripe pairs	Stripe pair width (mm)
OT-40	40	Optel-Thevon	63	2.000
P-40	40	Paper	57	2.204
P-66	66	Paper	104	2.004

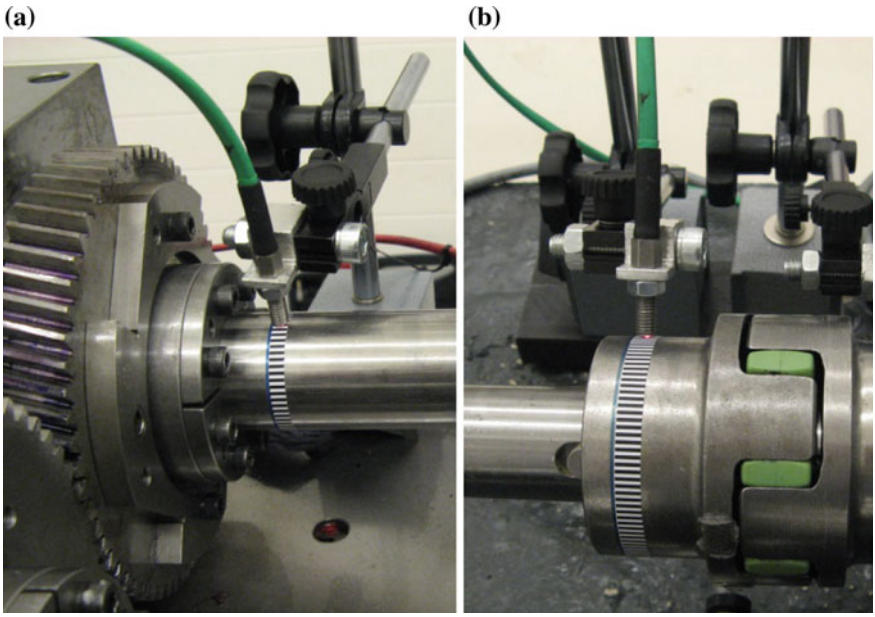

Fig. 5 Zebra tape instrumentation: **a** Ø40 mm shaft; **b** Ø66 mm shaft

True angles for obtaining the measurement error of the zebra tapes have been measured using the low-cost encoders. Error magnitudes were found to be, in fact, more than two orders of magnitude higher.

The measured cumulative error e_c and the spacing error e_s are reported in Fig. 6, and metrics of their variability along a full rotation are reported in Table 4. Excluding from consideration the error due to the butt joint[3] [17], it is possible to compare the Optel-Thevon and the printed tape on the same shaft diameter. The former performs substantially better than the latter.

All the tapes, at each location, show an extremely repeatable measurement error, validating the assumption of systematic error: three full rotations are in fact plotted in Fig. 6a and are very well overlapping. The trend for the error in the OT-40 case is linear because the butt joint error is 1.7 deg larger, circa $\sim$30 %, with respect to the nominal size, is distributed over the remaining stripes [17]. For the P-40 and P-66 cases, such trend is not visible because the butt joint effect is considerably more limited.

It is interesting to look at the order distribution of the error (Fig. 7), which drops with increasing order number, but remains at least three orders of magnitude higher with respect to the encoder case (Fig. 3).

[3]The butt joint occurs at the junction between the two ends of the tape folded around the full rotor circumference.

Table 4 Variability metrics for Optel-Thevon and printed zebra tapes, excluding the butt joint effect

Case name	e_s P-P	e_s StD	Stripe pair width error StD
OT-40	0.159 deg	±0.036 deg	±0.013 mm
P-40	0.310 deg (+95 %)	±0.058 deg (+61 %)	±0.020 mm (+54 %)
P-66	0.177 deg	±0.033 deg	±0.019 mm

StD Standard Deviation, *P-P* peak to peak

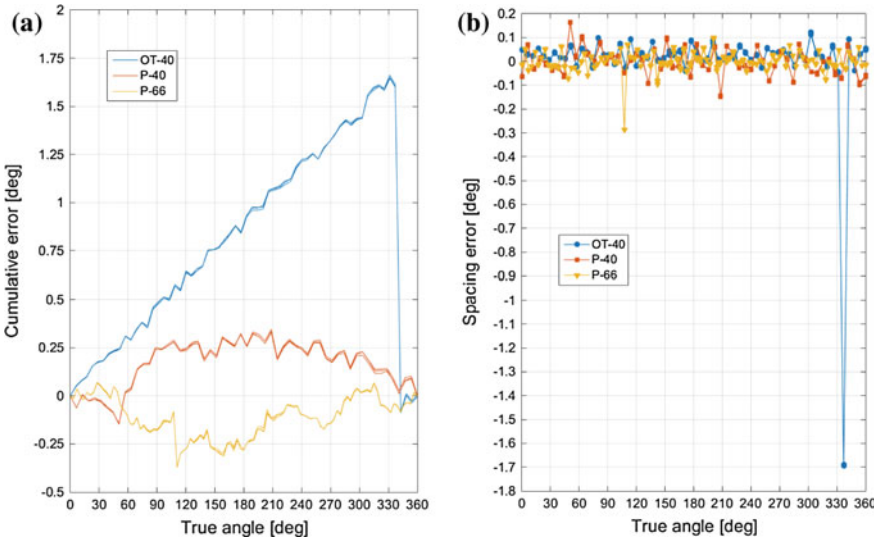

Fig. 6 Zebra tapes measurement error: **a** cumulative (e_c), **b** spacing (e_s)

The systematic error can be compensated in the attempt of improving the measurement accuracy of the zebra tapes. Calibration diagrams can be generated by taking the average of the cumulative error e_c (Fig. 6a) and can be used in Eq. 4 to obtain the true value of the angular position. The result of this operation is shown in Fig. 8.

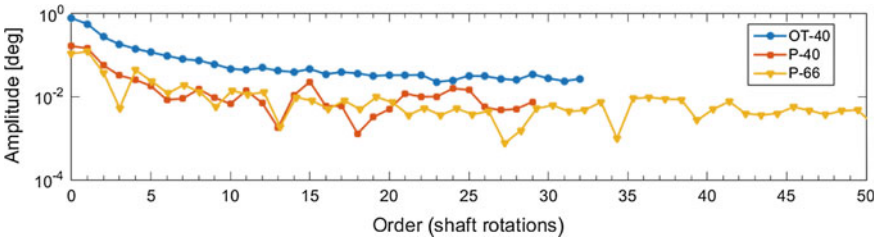

Fig. 7 Order distribution of the cumulative measurement error

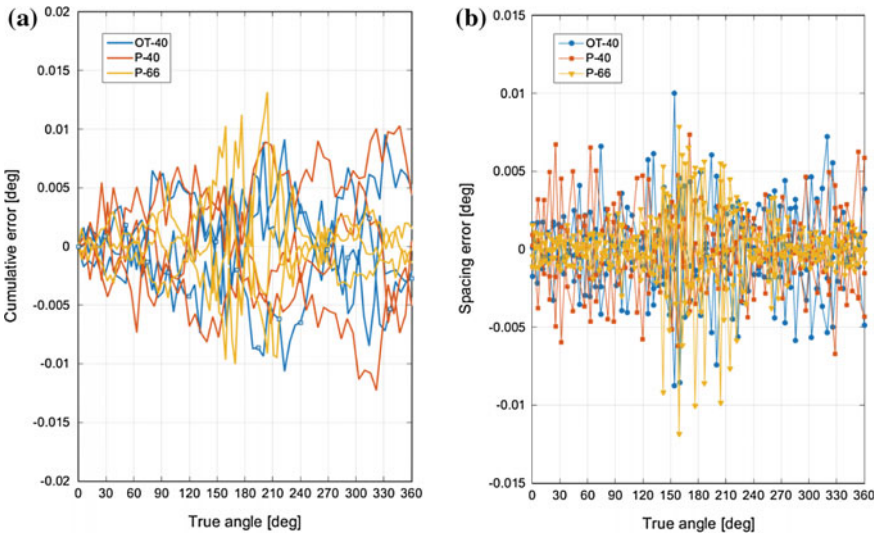

Fig. 8 Calibrated zebra tapes measurement error: **a** cumulative (e_c), **b** Spacing (e_s)

The systematic error compensation reduces the error to a band of about one order of magnitude, going from ±0.1 to ±0.01 deg. Furthermore, the trend of the remaining measurement error is no longer repeatable and periodic. Thus, once the systematic error component has been removed, the residual error can be further attenuated by synchronous averaging on subsequent turns. The results of this procedure are shown in Fig. 9 for the P-66 case: synchronous averaging allows

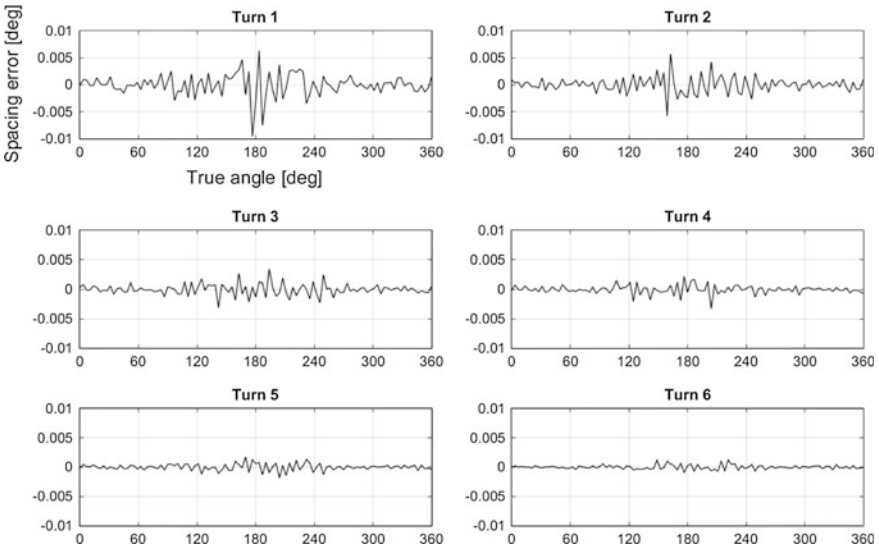

Fig. 9 Synchronous averaging of measurement error for subsequent number of turns

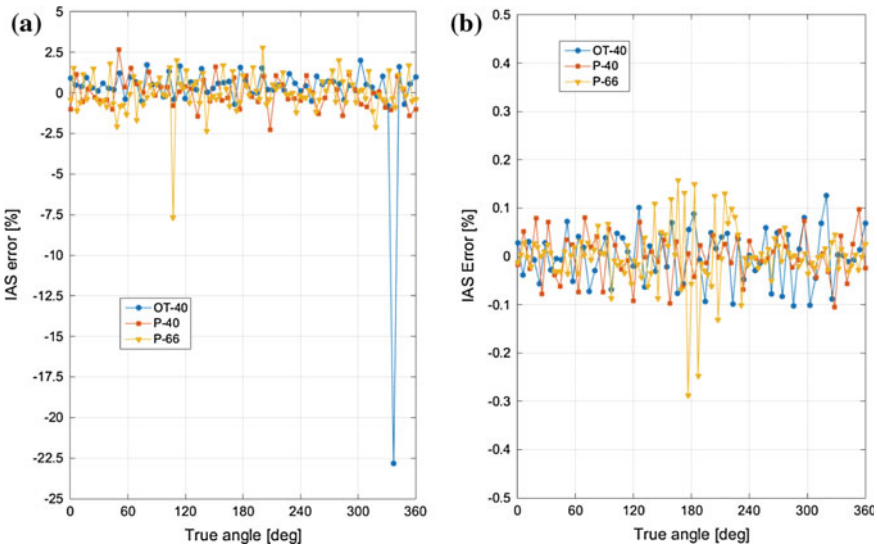

Fig. 10 IAS percentage measurement error for zebra tapes **a** not calibrated, **b** calibrated

reducing progressively the residual error and entering the measurement accuracy range of the optical encoders (circa ±0.001 deg).

Similar considerations can be performed for the IAS measurement. In particular, the error term described in Eq. 7 has been calculated and plotted in Fig. 10a. The error is dominated by the butt joint effect and it can be brought to around ±2 % using the correction algorithm proposed in [17]. Calibration of the zebra tape dramatically improves the measurement error, reducing it to about ±0.2 % (Fig. 10b).

4 Conclusions

Measurement error for zebra tapes has been investigated exploiting accurate angular references and a precision gear test rig. Different shaft locations have been analyzed, with high-quality and laser-printed zebra tapes. An analytical description of the errors in terms of angular position and of IAS has been provided. In particular, the spacing error is found to be an important parameter to describe the measurement error. This parameter is periodic in angle domain and, be isolated in an error term which is independent of angular velocity and can be interpreted as a normalized error percentage. On the experimental side, for the analyzed case, it is found that the dominant component of the error on the angular position is systematic and in the order of ±0.1 deg. Calibration reduces this error of one order of magnitude to about ±0.01 deg. Synchronous averaging of the residual error brings the accuracy in the

range of ±0.001 deg. Similarly happens for the IAS, where the error is reduced from about 2 % to about 0.2 % by tape calibration. These improvement can be substantially beneficial when high accuracy is required, e.g. in the case of early detection of faults, gear transmission error measurement or angle of twist measurement.

Zebra tapes show high potential to allow an extremely accurate measurement of Torsional Vibrations, both in terms of angular position and IAS. Calibration and synchronous averaging allow entering in the measurement error range of optical encoders with minimal instrumentation complexity.

Acknowledgements The results described in this paper have been obtained through research activities funded by the People Programme (Marie Curie Actions) of the 7th Framework Programme of the European Union FP7/2007-2013, under the contract with the Research Executive Agency (REA) n. 324336 and the related research project DEMETRA—"Design of Mechanical Transmissions: Efficiency, Noise and Durability Optimization" (www.fp7demetra.eu).

References

1. Leclère Q, Pruvost L, Parizet E (2010) Angular and temporal determinism of rotating machine signals: the diesel engine case. Mech Syst Signal Process 24:2012–2020
2. Borghesani P, Pennacchi P, Chatterton S, Ricci R (2014) The velocity synchronous discrete Fourier transform for order tracking in the field of rotating machinery. Mech Syst Signal Process 44:118–133
3. Rossi V, Naldi L, Depau V (2009) Torsional vibrations in rotordynamic systems: smart investigation methods. ASME Turbo Expo 2009:607–616
4. Zhang X, Yu SD (2009) Torsional vibration of crankshaft in an engine–propeller nonlinear dynamical system. J Sound Vib 319:491–514
5. Cardona-Morales O, Avendaño LD, Castellanos-Domínguez G (2014) Nonlinear model for condition monitoring of non-stationary vibration signals in ship driveline application. Mech Syst Signal Process 44:134–148
6. Renaudin L, Bonnardot F, Musy O, Doray JB, Rémond D (2010) Natural roller bearing fault detection by angular measurement of true instantaneous angular speed. Mech Syst Signal Process 24:1998–2011
7. Janssens K, Britte L (2014) Comparison of torsional vibration measurement techniques. Advances in condition monitoring of machinery in non-stationary operations. Springer, Berlin, pp 453–463
8. Li Y, Gu F, Harris G, Ball A, Bennett N, Travis K (2005) The measurement of instantaneous angular speed. Mech Syst Signal Process 19:786–805
9. Resor BR, Trethewey MW, Maynard KP (2005) Compensation for encoder geometry and shaft speed variation in time interval torsional vibration measurement. J Sound Vib 286:897–920
10. Rivola A, Troncossi M (2014) Zebra tape identification for the instantaneous angular speed computation and angular resampling of motorbike valve train measurements. Mech Syst Signal Process 44:5–13
11. André H, Girardin F, Bourdon A, Antoni J, Rémond D (2014) Precision of the IAS monitoring system based on the elapsed time method in the spectral domain. Mech Syst Signal Process 44:14–30
12. LMS International, a Siemens Business, Academy—Technology information, Torsional vibration measurement and analysis white paper, http://www.lmsintl.com/torsional-vibration

13. Remond D (1998) Practical performances of high-speed measurement of gear transmission error or torsional vibrations with optical encoders. Meas Sci Technol 9:347
14. Palermo A, Anthonis J, Mundo D, Desmet W (2013) A novel gear test rig with adjustable shaft compliance and misalignments, Part I: design and part II: instrumentation. In: Proceedings of the CMMNO Conference 2013, University of Ferrara
15. ISO/IEC Guide 99:2007—International vocabulary of metrology—Basic and general concepts and associated terms (VIM)
16. Palermo A, Britte L, Janssens K, Mundo D, Desmet W (2013) Gear transmission error measurement accuracy using low-cost digital encoders. In: RASD Conference 2013, Pisa, Italy
17. Janssens K, Van Vlierberghe P, Claes W, Peeters B, Martens T, D'Hondt P (2010) Zebra tape butt joint detection and correction algorithm for rotating shafts with torsional vibrations. In: Proceedings of the ISMA, pp 20–22

Vibration Analysis of Copper Ore Crushers Used in Mineral Processing Plant—Problem of Bearings Damage Detection in Presence of Heavy Impulsive Noise

Radoslaw Zimroz, Jakub Obuchowski and Agnieszka Wyłomańska

Abstract Vibration analysis of rolling element bearings (REB) used in copper ore crushers is discussed in the paper. The purpose of the analysis is to detect localized damage in REB. The problem of damage detection in REB is widely described in literature, in general. However, known techniques might be not successful in case of crushers due to presence of heavy non-Gaussian, impulsive noise. Impulsiveness of the signal from bearings is commonly used as an indicator of damage as well as a filter optimization criterion in order to enhance raw observation (to extract informative part—signal of interest (SOI)). A crusher is a kind of machine which use a metal surface to crumble materials into small fractional pieces. During this process, as well as during entering material stream into the crusher, a lot of impacts/shocks appear. They are present in vibration signal acquired from bearing's housing. These non-periodic, strong impulses are non-informative from diagnostic point of view and should be removed from the raw signal before further processing, because they mask completely informative, cyclic impulses related to damaged part of REB. Unfortunately, impulsiveness cannot be basis for signal extraction anymore. So, commonly used kurtosis-based optimization of pre-filtering (kurtogram, spectral kurtosis) cannot be used here. Promising approach is to search for cyclic/periodic nature of impulses (envelope analysis, spectral correlation density, protrugram, etc.). However, as mentioned, even before enveloping there is also a need to pre-filter the signal. In the paper we will introduce the problem including

R. Zimroz · J. Obuchowski (✉)
Diagnostics and Vibro-Acoustics Science Laboratory, Wroclaw University of Technology, Na Grobli 15, 50-421 Wroclaw, Poland
e-mail: jakub.obuchowski@pwr.edu.pl

R. Zimroz
e-mail: radoslaw.zimroz@pwr.edu.pl; rzimroz@cuprum.wroc.pl

R. Zimroz
KGHM CUPRUM Ltd, CBR Sikorskiego 2-8, 53-659 Wrocław, Poland

A. Wyłomańska
Hugo Steinhaus Center, Wroclaw University of Technology, Janiszewskiego 14a, 50-370 Wroclaw, Poland
e-mail: agnieszka.wylomanska@pwr.edu.pl

F. Chaari et al. (eds.), *Advances in Condition Monitoring of Machinery in Non-Stationary Operations*, Applied Condition Monitoring 4,
DOI 10.1007/978-3-319-20463-5_5

description of the machine, investigation on structure of vibration and we will present preliminary results of vibration processing using protrugram approach. At the end, we will propose an enhancement of protrugram in order to identify cyclo-stationary signal in presence of randomly spaced impulses and narrowband amplitude modulation of discrete components.

Keywords Crusher bearing diagnostics · Amplitude modulation · Rolling element bearing · Non-Gaussian noise · Protrugam

Contents

1 Introduction 58
2 Motivation 60
2.1 Experiment Description 60
2.2 Preliminary Real Data Analysis 61
3 Model of the Signal and Simulated Data Analysis 63
3.1 Simulation of Vibration Signal 63
3.2 Analysis of Simulated Signal 64
4 Adaptation of Protrugram 67
5 Conclusion 69
References 69

1 Introduction

One of the key steps in condition monitoring of machines is to extract information about damage. A special class of damage detection problems is recognition of local damage in rotating machines. When a vibration signal is used, extraction of the information about damage often comes down to searching an informative signal, its extraction and, finally, description of the informative signal using some parameter (s) called diagnostic feature(s). The problem is widely investigated in the literature [1–4]. For instance, one can find the informative signal using time-domain detectors, among which some of the most known are based on kurtosis [3, 5–12]. A key feature of the signal used as a basis for detection is its impulsiveness. However, for damage detection at early stages, when signal to noise ratio is poor/informative signal is weak [3, 13–15], in presence of high energy deterministic components, damage detection becomes difficult and requires advanced signal processing including averaging, model based filtering, decomposition or adaptive filtering [9, 16–20]. Mentioned above kurtosis is also used for pre-processing of the raw signal in order to improve its signal-to-noise ratio (SNR). In this approach, detection (and also diagnosis of the damage) is performed via envelope and envelope spectrum analysis. In this method, damage detection is based on periodicity of the

informative signal (more precisely, periodicity of the envelope of the signal). In our case, the machine (copper ore crusher) produces randomly spaced in time heavy impulsive disturbances related to normal operation of the machine, similarly as reported in [7, 8, 11–13, 21]. It makes impossible detection of damage in time domain, moreover due to very poor signal to noise ratio, even envelope spectrum analysis is not able to detect damage based directly on the raw vibration. Unfortunately, impulsiveness cannot be basis for signal extraction anymore. So, the commonly used kurtosis-based optimization of pre-filtering (kurtogram, spectral kurtosis) cannot be applied here. Due to serious influence of randomly spaced impacts to statistical measures of the process, proposed recently by Obuchowski et al. [11, 12] set of statistics did not provide good results, neither. Promising approach is to search for cyclic/periodic nature of impulses. As mentioned, an envelope analysis without pre-filtering do not provide acceptable results. Last decades brought deep knowledge on cyclo-stationary approach [1, 2, 13, 22–28]. Preliminary results of application of spectral coherence density map to crusher vibration were presented in [21]. Although, the problem is still challenging since the SCDM is a computationally expansive tool. Moreover, it gives 2D map as results that is not easy to interpret in industrial reality.

Jablonski and Barszcz proposed a method that incorporates periodicity of the impacts related to damage, called protrugram [7]. It exploits kurtosis applied to amplitude spectrum of envelope instead of time series. In this paper, we will analyze performance of protrugam in context of our data. It will be shown that, the protrugram is also encumbered with disadvantages, namely it is sensitive to narrowband (sinusoidal) amplitude modulation of the discrete carrier. In the paper we investigate possibility of using the protrugram and propose a kind of enhancement to overcome the mentioned problem of narrowband amplitude modulation. Proposed novel method is based on simple observation, that for local damage one might see family of equally spaced components in the envelope spectrum that might be considered as periodicity in the spectrum. In case of narrowband modulation, envelope spectrum will have one component, definitely no periodicity can be assumed. We will focus on simulation to present the idea of the proposed solution. The paper is structured as follows: Sect. 2 contains a description of the investigated machine and provides preliminary analysis of the vibration signal form the crusher. In Sect. 3 we present analysis of a simulated signal with characteristics that closely follow the real signal. The novel methodology designed to indicate the cyclic impulsive signal in presence of non-impulsive amplitude modulated components is described in Sect. 4. The last section contains conclusion.

2 Motivation

2.1 Experiment Description

The machine discussed here is a heavy duty crusher used in a mineral processing plant. The crusher is a kind of a machine which uses a metal surface to crumble materials into small fractional pieces (Fig. 1). During this process, as well as during entering material stream into the crusher, a lot of impacts/shocks appear. They are present in vibration signal acquired from the bearing's housing. Several crushers were investigated in different conditions. Vibration from bearings housing in horizontal and vertical direction and tacho signal have been measured using Endevco accelerometers BruelKjaer Laser probe, NI DAQ card and Labview Signal Express. Signals were acquired for idle mode as well as for different values of load (volume and granulation of material stream) with approx 120 s duration each, however, for further investigation shorter signals were selected. Sampling frequency was set to 25 kHz.

Apart from expected cyclic impulsive signal related to damage and non-informative intense impulsive noise, several discrete components might appear from rotating shafts of engine located nearby. Belt transmission is used to pass torque from the electric motor to crusher. A 23264 SKF bearings are used in the crusher. Assuming more or less stationary speed expected bearings fault frequencies are presented in Table 1. In [21] it is reported that the signal we analyze contains cyclic impulsive modulation and several harmonics of 30 Hz occur. Due to Table 1, the damage reveals in the inner race.

Fig. 1 A crusher—general view (note bearings with *yellow* housing)

Table 1 Bearing frequencies: 23264 CCK/W33

No.	Description	Value/unit
1.	ni—Rotational speed of the inner ring	180 r/min
2.	ne—Rotational speed of the outer ring	0 r/min
3.	Fi—Rotational frequency of the inner ring	3 Hz
4.	Fe—Rotational frequency of the outer ring	0 Hz
5.	Fc—Rotational frequency of the rolling element and cage assembly	1.3 Hz
6.	Fr—Rotational frequency of a rolling element about its own axis	10.6 Hz
7.	Fip—Over-rolling frequency of one point on the inner ring	30.7 Hz
8.	Fep—Over-rolling frequency of one point on the outer ring	23.3 Hz
9.	Frp—Over-rolling frequency of one point on a rolling element	21.1 Hz

2.2 *Preliminary Real Data Analysis*

Figures 2 and 3 present the time series and spectrogram of the raw vibration signal acquired on the rolling element bearing using an accelerometer located on the housing in vertical direction. Length of the signal is 10 s and frequency sampling equals to 25 kHz. One can see a lot of impulses of different amplitudes in the time series (Figs. 2a and 3a), but it is difficult to assess whether they are cyclic or not.

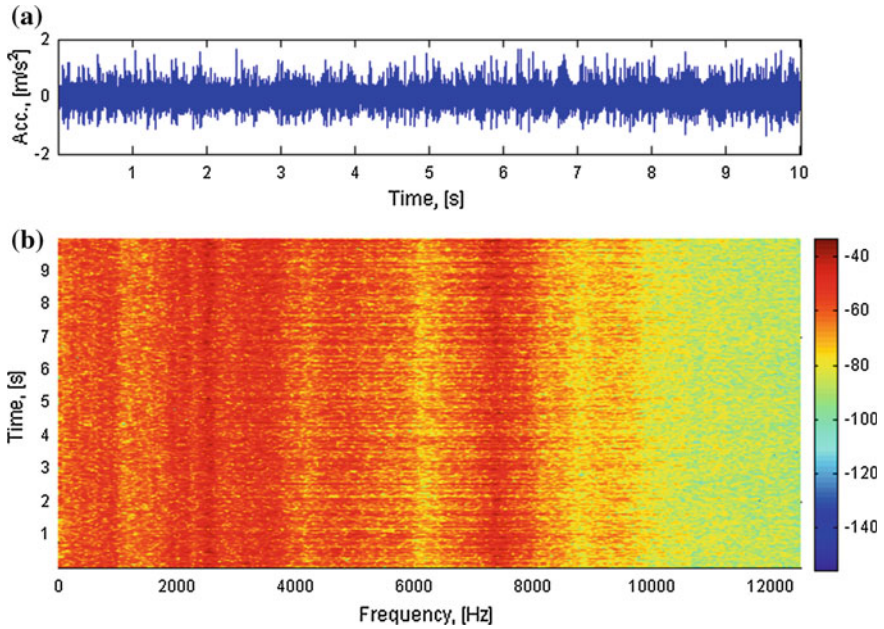

Fig. 2 Time series (**a**) and spectrogram (**b**) of the raw vibration signal from the bearing operating in a crusher

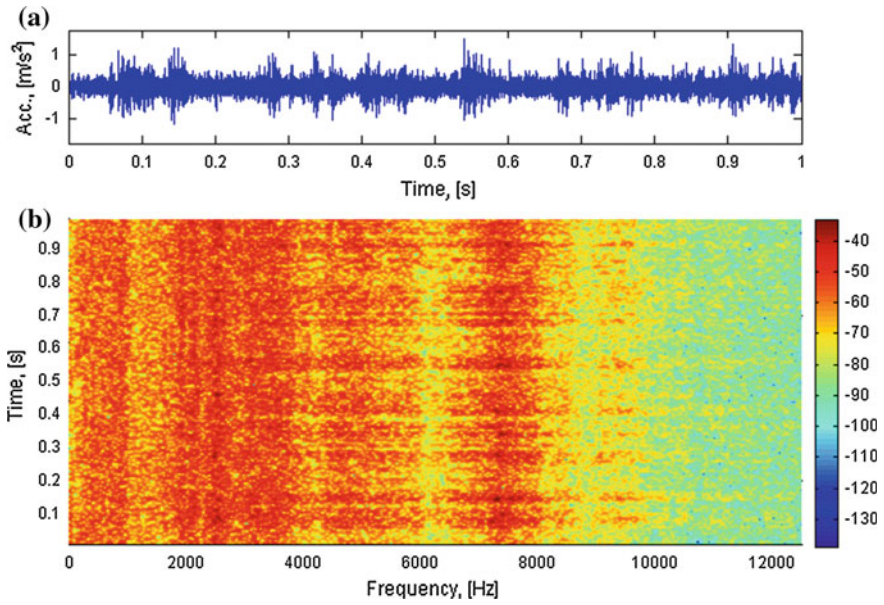

Fig. 3 Time series (**a**) and spectrogram (**b**) of the raw vibration signal from the bearing operating in a crusher (first second only)

The spectrogram demonstrates that there are a few resonances of the system, e.g. 2000–000 Hz and around 7500 Hz (Figs. 2b and 3b). Most of the energy is contained below 10,000 Hz. Impulses present in the time series cover almost whole spectrum. Envelope spectrum of this signal is presented in Fig. 4a. As it can be noticed, none of the 30 Hz harmonics are indicated.

The largest amplitude among low frequencies is at the frequency of 3.4 Hz and there is only one harmonic related to this frequency. It suggests that there are amplitude modulated components and the modulating function is close to a sine

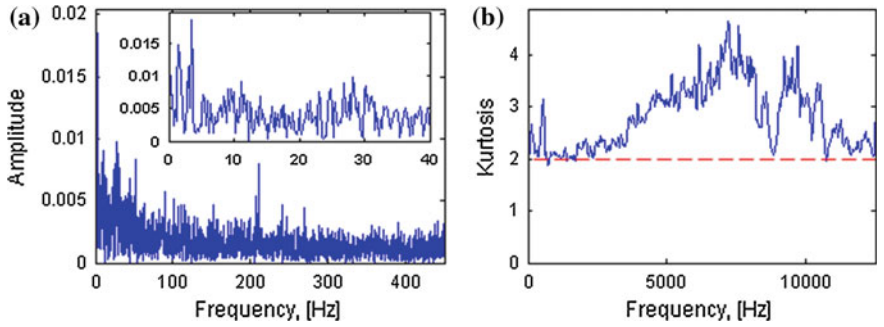

Fig. 4 Envelope spectrum (**a**) and spectral kurtosis (**b**) of the raw vibration signal from the bearing operating in a crusher

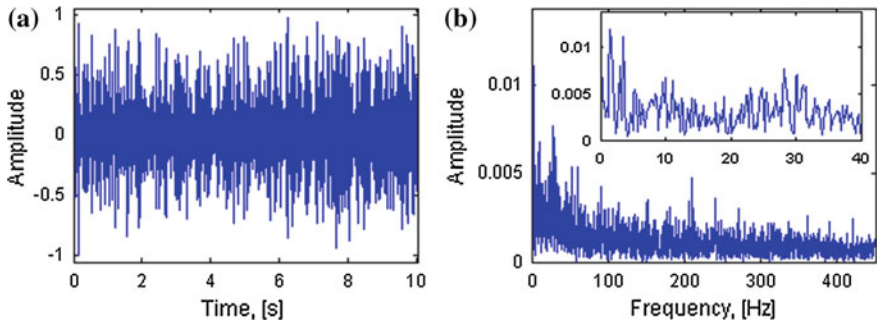

Fig. 5 Time series (**a**) and its envelope spectrum (**b**) of the raw vibration signal filtered using the SK-based filter

wave. Figure 4b presents the spectral kurtosis of the raw vibration signal calculated from the time-frequency map in Fig. 2b. We calculate the spectral kurtosis from a spectrogram, i.e. each value in Fig. 3b is a normalized fourth order moment of absolute value of the short-time Fourier transform. For comprehensive definition of the spectral kurtosis we refer to [6]. Parameters of the short-time Fourier transform are: 500-sample length Kaiser window with parameter 5470 overlapping samples (94 % overlap), FFT is calculated in 1024 points. As it can be seen, there are two peaks in the spectral kurtosis at low frequencies and SK significantly exceeds 2 at the whole frequency band above 3000 Hz except about 9000 Hz. The signal filtered using the SK and its envelope spectrum (Fig. 5) do not reveal the fault frequency (multiplies of 30 Hz).

3 Model of the Signal and Simulated Data Analysis

3.1 Simulation of Vibration Signal

Since the real vibration signal is very complex and the carrier frequencies of the signal of interest (SOI) are unknown we propose to analyze a simulated signal. It is designed to possess properties noticed during analysis of the real signal.

The simulated signal is a mixture of amplitude modulated sinusoidal components with modulation frequency equal to 4 Hz and a sine wave as the modulation function, cyclic impacts with cyclic frequency of 30 Hz and carrier frequencies 2500–3500 Hz as well as non-cyclic impulses with center frequency 5000 Hz, different bandwidths. The SOI impulse was simulated using Matlab function gauspuls with center frequency Fc = 3000 Hz and fractional bandwidth Bw that is uniformly distributed on [0.2, 0.3] interval. Next, single impulse was repeated at equally spaced intervals to get cyclic SOI signal. Noncyclic impulse was also simulated with using Matlab function gauspuls but with center frequency

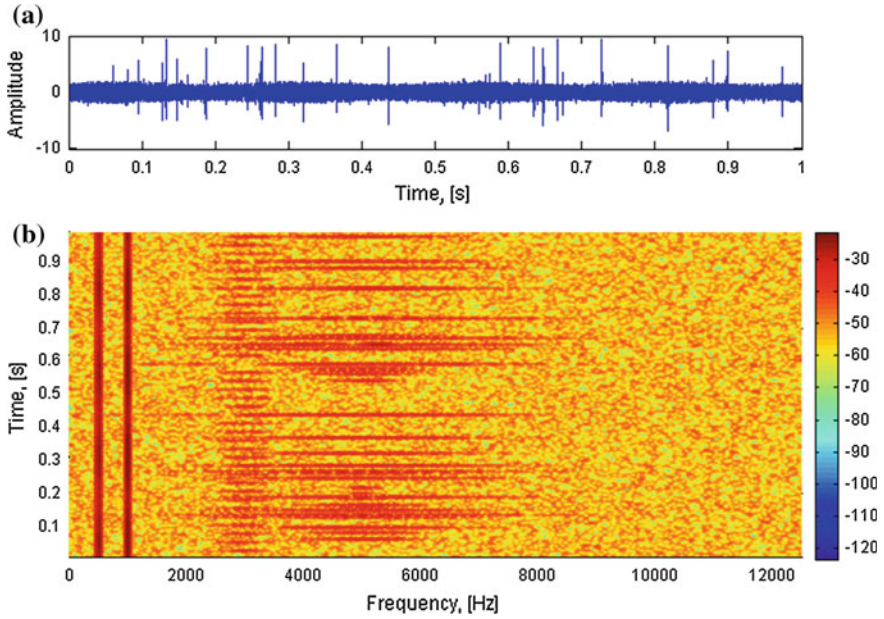

Fig. 6 Time series (**a**) and spectrogram (**b**) of the simulated vibration signal

Fc = 5000 Hz and fractional bandwidth Bw with a uniform distribution on [0, 1] interval. Locations of the non-cyclic impulses are randomly distributed on the time axis and follow the uniform distribution. At the end we have added the amplitude modulated sinusoidal components for frequencies 500 and 1000 Hz with modulation frequency equal to 4 Hz.

The time series and spectrogram are presented in Fig. 6. Length of the signal is 1 s and frequency sampling equals to 25,000 Hz. Parameters of short-time Fourier transform are the same as in the real signal case, i.e. 500-sample length Kaiser window, 470 overlapping samples and 1024 FFT points.

3.2 Analysis of Simulated Signal

In order to be consistent with real data analysis, first we present the spectral kurtosis of the simulated signal, see Fig. 7. As we observe, the classical method of damage detection does not properly indicate the informative frequency band (2500–3500 Hz). The highest values of kurtosis we observe for frequency band 3500–7500 Hz where the non-cyclic impulses appear.

Because for the simulated signal the method based on the spectral kurtosis fails, we propose here to use methods which are based not on the impulsiveness of the examined signal but rather on its cyclic behavior. Since the simulated signal is

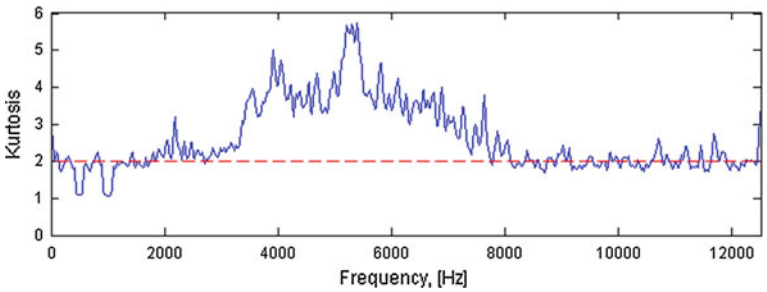

Fig. 7 Spectral kurtosis of the simulated signal

consisted of 3 components (AM discrete components at 500 and 1000 Hz, SOI at around 3000 Hz and non-cyclic impulses at about 3500–7500 Hz), we perform analysis of 3 signals obtained using band-pass filters. The first signal (cut-off frequencies 250–1250 Hz) contains AM discrete components with carrier frequencies 500 and 1000 Hz modulated by a 4 Hz sine wave. The second signal (2500–3500 Hz) is consisted of cyclic impulses that simulate the SOI. The last signal (5500–6500 Hz) contains non-cyclic impulses with random amplitudes.

In Fig. 8 we present the time series and envelope spectra of the simulated signal filtered using band-pass filters for three mentioned pairs of cut-off frequencies. As we observe, there is a huge difference in behavior of envelope spectra of time series corresponding to analyzed frequency bands, namely for the first time series corresponding to frequency band 250–1250 Hz (Fig. 8a) on the envelope spectrum (Fig. 8b) we can observe the modulation frequency equal to 4 Hz, for the second time series (Fig. 8c) the cyclic impulses are observable on the envelope spectrum (Fig. 8d), while in Fig. 8e we observe impulses which are non-cyclic, thus the corresponding envelope spectrum (Fig. 8f) does not indicate any specific frequency.

Since in the literature one can find a cyclicity indicator called the protrugram, we follow this concept and calculate kurtosis of the envelope spectra. We recall that the protrugram is defined as kurtosis of envelope spectrum of signals obtained using a bank of band-pass filters. The set of central frequencies of the band-pass filters is consisted of equally spaced points on the frequency axis (e.g. 200 points). Bandwidth of the band-pass filters is chosen subjectively, e.g. 500 Hz. For comprehensive description of the protrugram and instruction on appropriate choose of parameters (i.e. bandwidth and center frequencies) we refer to [7].

For the envelope spectrum presented in Fig. 8b the kurtosis is equal to 2593.27. This huge value is strongly related to the two amplitude modulated discrete components in the frequency band 250–1250 Hz. For the envelope spectrum presented in Fig. 8d the kurtosis is equal to 198.84 and the large value of this statistic is related to the cyclic impulses in the time series. For the envelope spectrum presented in Fig. 8f the kurtosis has the smallest value comparing to others.

In Fig. 9 we present the protrugram with bandwidth equal to 500 Hz for simulated signal presented in Fig. 6. It is worth mentioning that the bandwidth of the

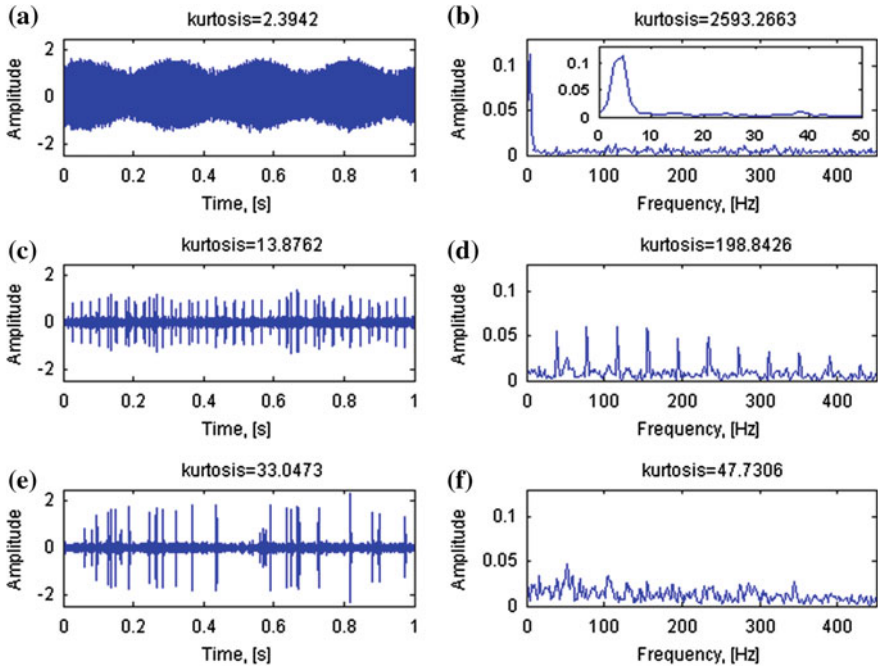

Fig. 8 Time series (*left panels*) and envelope spectra (*right panels*) of the simulated signal filtered using band-pass filters with cut-off frequencies: 250–1250 Hz (**a**–**b**), 2500–3500 Hz (**c**–**d**) and 5500–6500 Hz (**e**–**f**)

protrugram is narrower (500 Hz) than the bandwidth of bandpass filters involved in signals presented in Fig. 8 (1000 Hz), thus values of kurtosis in the protrugram (Fig. 9) does not follow values of kurtosis in Fig. 8b, d. Although, kurtosis of envelope spectra of AM discrete components is still higher than for cyclic impulses and the lowest kurtosis of those 3 components is reported by non-cyclic impulses. As we observe the protrugram indicates two informative frequency bands, the first one related to the amplitude modulation of discrete components (i.e. for frequency band 250–1250 Hz) and the second one for frequency band 2500–3500 Hz for which the cyclic impulses were simulated. This result indicates that for analyzed

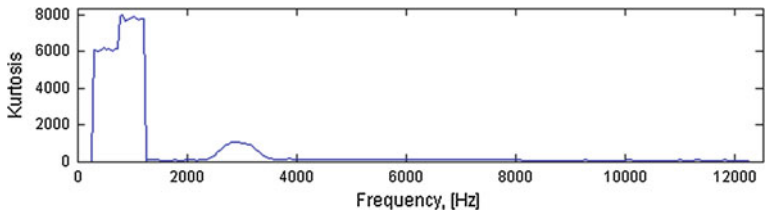

Fig. 9 Protrugram of the simulated signal. Bandwidth equal to 500 Hz

signals corresponding to crusher's vibration time series there is a need to extend the methodology of bearings damage detection based on the protrugram. One of the possible extensions is presented in the next section.

4 Adaptation of Protrugram

In this section we discuss a solution to the problem revealed in Sect. 3. We propose to incorporate the fact that in the case of locally damaged bearing, the envelope spectrum of the informative signal is consisted of at least several equally spaced spectral components—harmonics of the fault frequency. The peaks are equally distributed in the envelope spectrum, thus it is reasonable to consider testing of its periodicity for example by using amplitude spectrum alternatively to kurtosis. If the sub-signal (related to a given center frequency and bandwidth) is a cyclic pulse train, then its envelope spectrum is consisted of a family of spikes at multiplies of the fault frequency. Since amplitudes of these harmonics decrease with increasing frequency, it is reasonable to calculate amplitude spectrum from a limited range of the envelope spectrum. The upper bound of the range might be set as e.g. 15 times the largest fault frequency among characteristic frequencies for a given machine. Thus, upper bound might be easily set using information about the considered machine. The lower bound is not necessary if the envelope spectrum is normalized by subtracting its arithmetic mean. Finally, we propose to calculate a measure of impulsiveness of the amplitude spectrum of the mean-normalized envelope spectrum, e.g. kurtosis.

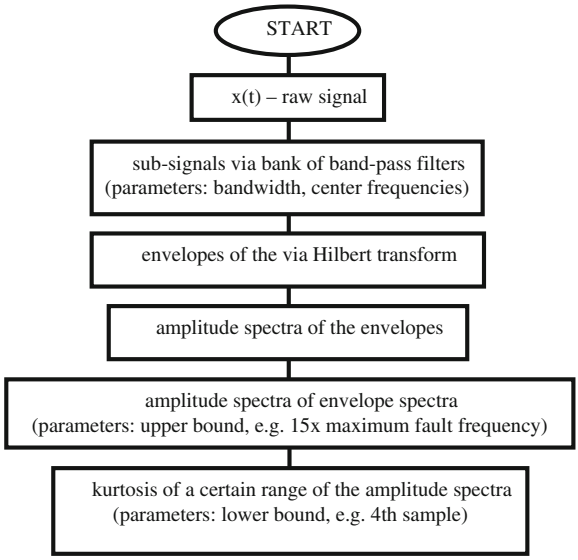

Fig. 10 Block diagram of the algorithm proposed in Sect. 4

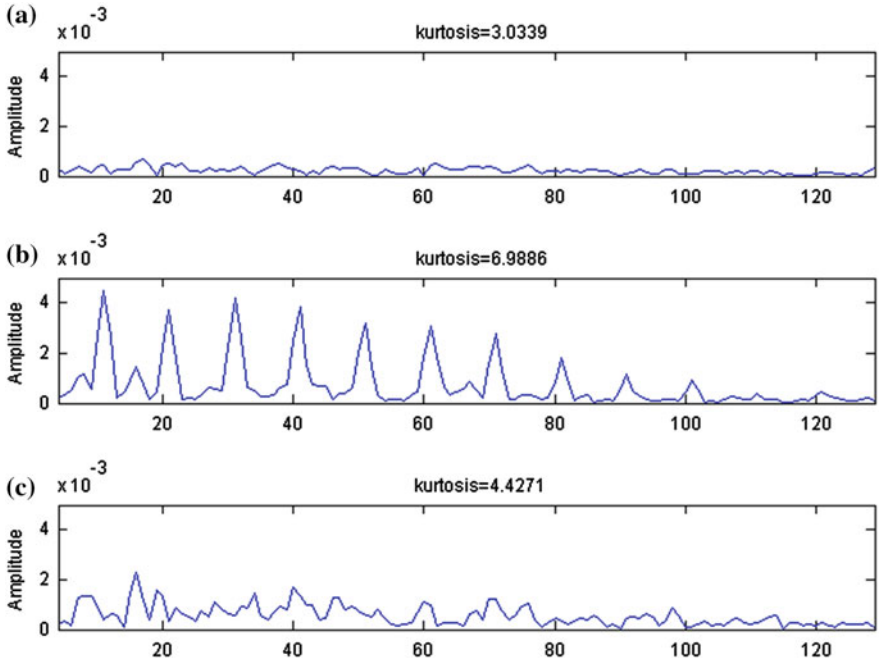

Fig. 11 Amplitude spectra of envelope spectra of the simulated signal filtered using band-pass filters with cut-off frequencies: 250–1250 Hz (**a**), 2500–3500 Hz (**b**) and 5500–6500 Hz (**c**)

Since amplitude spectrum of the mean-normalized envelope spectrum might contain large values at a few first points of frequency axis, we recommend to calculate kurtosis of the whole amplitude spectrum except a few first values. Such large values are related to slow variations of temporary mean of any envelope spectrum. Figure 10 presents a block diagram with algorithm for calculating the proposed indicator of a cyclic pulse train.

If the modulation function of a sub-signal is a sine wave, then its envelope spectrum is dominated by a single harmonic related to the frequency of the modulation function (in Sect. 2 it is 3.4 Hz, in Sect. 3—4 Hz). Then, kurtosis of such envelope spectrum is large and protrugram might indicate the related frequency band as informative. On the other hand, amplitude spectrum of such envelope spectrum dominated by the single-spike does not indicate any cyclic events, thus such frequency band is not indicated as informative. If the considered sub-signal is consisted of non-cyclic impulses or just a white Gaussian noise, then its envelope spectrum does not contain any cyclic phenomena. Thus, amplitude spectrum of such envelope spectrum does not contain any harmonics with amplitudes significantly larger than others. To distinguish between informative and non-informative amplitude spectra of envelope spectra one can calculate kurtosis of them, as it is presented in Fig. 11. Here, kurtosis is calculated from the whole amplitude spectrum except three first values and amplitude spectrum is calculated from 300 first

amplitudes of envelope spectrum (it covers frequencies between 0 Hz and about 450 Hz). The reason of such bounding has been already mentioned—a few first values often dominate the amplitude spectrum of envelope spectrum. One can see, that both shape and kurtosis of the amplitude spectra in Fig. 11a, c are quite similar and both of them are significantly different from those presented in Fig. 11b.

5 Conclusion

In the paper a problem of impulsive cyclic signal (SOI) detection for bearings diagnostics is discussed. Contrary to "classical" bearings signals, our vibration signal is mixture of several deterministic components, SOI and—what is critical issue for detection- impulsive noise. Commonly used kurtosis based detectors or preprocessors cannot help in this case because they are more sensitive to high energy non-informative, impulsive noise than for cyclic impulsive SOI. In this paper we present results of application of protrugram, a relatively novel tool developed by Jablonski and Barszcz for similar problem, however, some modification of the protrugram has been done to overcome drawback of the method that appeared during processing of vibration from the crusher.

To make the paper more clear, we decided to limit illustration of the method to reality-inspired simulation signal. However, the final result is very good and we believe that it will also work for real vibration signal from the crusher.

Acknowledgements This work is partially supported by the statutory grant No. B40044 (Jakub Obuchowski).

References

1. Antoni J, Bonnardot F, Raad A, El Badaoui M (2004) Cyclostationary modeling of rotating machine vibration signals. Mech Syst Signal Process 18(6):1285–1314
2. Antoni J (2009) Cyclostationarity by examples. Mech Syst Signal Process 23(4):987–1036
3. Randall RB, Antoni J (2011) Rolling element bearing diagnostics-A tutorial. Mech Syst Signal Process 25(2):485–520
4. Obuchowski J, Wylomanska A, Zimroz R (2014) Recent developments in vibration based diagnostics of gear and bearings used in belt conveyors. Appl Mech Mater 683:171–176
5. Antoni J (2007) Fast computation of the kurtogram for the detection of transient faults. Mech Syst Signal Process 21:108–124
6. Antoni J, Randall R (2006) The spectral kurtosis: application to the vibratory surveillance and diagnostics of rotating machines. Mech Syst Signal Process 20:308–331
7. Barszcz T, Jabłoński A (2011) A novel method for the optimal band selection for vibration signal demodulation and comparison with the kurtogram. Mech Syst Signal Process 25 (1):431–451
8. Barszcz T, Jabłoński A (2009) Analysis of kurtogram performance in case of high level non-Gaussian noise. In: Proceedings of ICSV, Kraków, Poland

9. Dybała J, Zimroz R (2014) Rolling bearing diagnosing method based on empirical mode decomposition of machine vibration signal. Appl Acoust 77:195–203
10. Lin J, Zuo M (2003) Gearbox fault diagnosis using adaptive wavelet filter. Mech Syst Signal Process 17(6):1259–1269
11. Obuchowski J, Wyłomańska A, Zimroz R (2014) Selection of informative frequency band in local damage detection in rotating machinery. Mech Syst Signal Process 48(1–2):138–152
12. Obuchowski J, Wylomanska A, Zimroz R (2013) Stochastic modeling of time series with application to local damage detection in rotating machinery. Key Eng Mater 569–570:441–448
13. Barszcz T, Zimroz R, Urbanek J, Jabłoński A, Bartelmus W (2013) Bearings fault detection in gas compressor in presence of high level of non-Gaussian impulsive noise. Key Eng Mater 569–570:473–480
14. Urbanek J, Barszcz T, Zimroz R, Antoni J (2012) Application of averaged instantaneous power spectrum for diagnostics of machinery operating under non-stationary operational conditions. Measure: J Int Measure Confederation 45(7):1782–1791
15. Zimroz R, Bartelmus W (2012) Application of adaptive filtering for weak impulsive signal recovery for bearings local damage detection in complex mining mechanical systems working under condition of varying load. Solid State Phenom 180:250–257
16. Makowski RA, Zimroz R (2011) Adaptive bearings vibration modeling for diagnosis. Lecture notes in computer science (including subseries lecture notes in artificial intelligence and lecture notes in bioinformatics) 6943 LNAI, pp 248–259
17. Makowski RA, Zimroz R (2013) A procedure for weighted summation of the derivatives of reflection coefficients in adaptive Schur filter with application to fault detection in rolling element bearings. Mech Syst Signal Process 38(1):65–77
18. Makowski RA, Zimroz R (2014) New techniques of local damage detection in machinery based on stochastic modeling using adaptive Schur filter. Appl Acoust 77:130–137
19. Obuchowski J, Wyłomańska A, Zimroz R (2014) The local maxima method for enhancement of time-frequency map and its application to local damage detection in rotating machines. Mech Syst Signal Process 46(2):389–405
20. Wyłomańska A, Obuchowski J, Zimroz R, Hurd H (2014) Periodic autoregressive modeling of vibration time series from planetary gearbox used in bucket wheel excavator. In: Fakher C et al (eds) Cyclostationarity: theory and methods lecture notes in mechanical engineering, pp 171–186
21. Zimroz R, Obuchowski J, Wyłomańska A (2014) Bearings damage detection in presence of heavy non-Gaussian noise via cyclo-stationary analysis. Vibroengineering PROCEDIA 3:88–92
22. Bloomfield P, Hurd HL, Lund RB (1994) Periodic correlation in stratospheric ozone data. J Time Ser Anal 15(2):127–150
23. Broszkiewicz-Suwaj E, Makagon A, Weron R, Wylomanska A (2004) On detecting and modeling periodic correlation in financial data. Phys A 336:196–205
24. Gladyshev EG (1961) Periodically correlated random sequences. Soviet Math 2:385–388
25. Hurd HL, Miamee A (2007) Periodically correlated random sequences. Spectral theory and practice. Wiley, New Jersey
26. Randall R, Antoni J, Chobsaard S (2001) The relationship between spectral correlation and envelope analysis for cyclostationary machine signals. Appl Ball Bearing Diagn Mech Syst Syst Process 15(5):945–962
27. Vecchia AV (1985) Periodic autoregressive-moving average (PARMA) modeling with applications to water resources. JAWRA J Am Water Resour Assoc 21(5):721–730
28. Zimroz R, Bartelmus W (2009) Gearbox condition estimation using cyclo-stationary properties of vibration signal. Key Eng Mater 413–414:471–478

Analysis and Signal Processing of a Gearbox Vibration Signal with a Defective Rolling Element Bearing

Nader Sawalhi and Suri Ganeriwala

Abstract This paper provides a systematic signal processing of a vibration signal measured from a gearbox driven by a three phase motor, which is controlled by a variable frequency drive (VFD). The vibration signal being processed was obtained from a test rig with a defective bearing, thus the signal represents a rich content of different types of signals. Power spectrum density (PSD) and time-frequency analysis (using Morlet wavelets) were used after a visual inspection of the signal in the time domain. The sidebands in the vicinity of the VFD carrier frequencies were used to verify the speeds of each shaft in the gearbox and to provide information about the amount of slippage between the VFD frequency and the shaft speed. As no information was provided at the time of analysis about the number of teeth of each gear, order tracking and harmonic/sideband cursors were used to deduce this information and to later obtain a synchronous average for each shaft and a residual signal for the diagnosis of the bearing fault. Finally, Bearing diagnosis was performed on the residual signal obtained earlier using a semi automated bearing diagnosis tool which includes whitening the signal, removing the transfer path effect using minimum entropy deconvolution (MED) and finding the best band for envelope analysis using spectral kurtosis (SK).

Keywords Gearbox · Rolling element bearings · Variable frequency drive · Order tracking · Envelope analysis

N. Sawalhi (✉)
Prince Mohammad Bin Fahd University, Khobar, Saudi Arabia
e-mail: nsawalhi@pmu.edu.sa

S. Ganeriwala
SpectraQuest, Inc., Richmond, USA
e-mail: suri@spectraquest.com

F. Chaari et al. (eds.), *Advances in Condition Monitoring of Machinery in Non-Stationary Operations*, Applied Condition Monitoring 4,
DOI 10.1007/978-3-319-20463-5_6

Contents

1 Introduction 72
2 Experimental Test Rig and Vibration Acquisition 73
3 Vibration and Tachometer Signal Processing 73
3.1 Time Domain Overlaid with Tachometer 73
3.2 Frequency Content and the Power Spectrum Density (PSD) 74
3.3 Time-Frequency Analysis 74
3.4 Order Tracking and Signal Separation 75
4 Bearing Fault Diagnosis 80
5 Summary and Conclusions 84
References 85

1 Introduction

Vibration signals acquired from gearboxes contain rich information about the health of gears and bearings. The analysis of acquired signals requires the knowledge of the number of gear stages, the number of teeth on each gear and the input or output angular velocities. A tachometer signal (speed reference) is usually acquired along with the vibration signal. The presence of the tachometer signal provides the means to estimate speed variations and to remove speed fluctuations from the vibration signal using angular re-sampling (also known as order tracking) [1]. In the absence of a tachometer signal, the vibration signal itself can be used to extract this information [2, 3], which can be then used for order tracking [4, 5]. If no information is available about the number of teeth in each gear, the order tracked signal can be used to mine this information by setting families of harmonic and sideband cursors and fine tuning these families to estimate the number of teeth for each pinion/gear [6]. The use of time-frequency presentations has been discussed in a number of publications and can be utilized very efficiently for the gear signals, e.g. [1, 7, 8]. Bearing fault diagnosis in gearboxes has been discussed in a number of publications, e.g. [9–11].

In this paper, the processing of a vibration signal from a gearbox with a defective bearing is discussed. The paper serves the purpose of providing a systematic means of handling and processing vibration signals from VFD driven gearboxes. The paper is organized as follows: after this introductory section, the gearbox test rig from which the vibration signal was acquired is presented in Sect. 2. Section 3 discusses the different stages of processing to provide an understanding of the different features and frequencies presented. This includes inspecting the time domain signal, the frequency domain (using power spectrum density), the time-frequency joint presentation, the order tracked signal and shaft synchronous averages. The bearing fault diagnosis is discussed in Sect. 4 utilizing the semi-automated approach presented in Ref. [12]. Section 5 provides summary and conclusions. Finally acknowledgment and references are given.

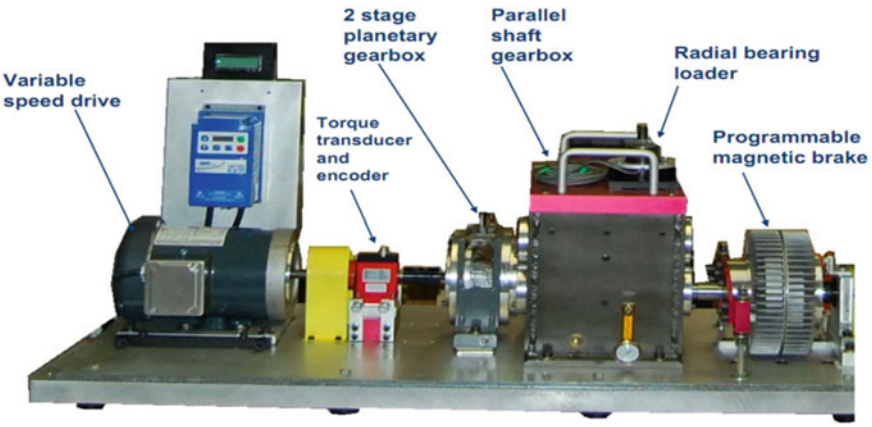

Fig. 1 Gearbox dynamic simulation test rig

2 Experimental Test Rig and Vibration Acquisition

Figure 1 shows a picture of the gearbox dynamic simulation test rig. The gearbox has two parallel stages of helical gears. A notch fault was introduced into the inner race of the bearing supporting the intermediate shaft. The load was applied through the radial bearing loader. Both vibration and tachometer signals were collected at a high sampling frequency of 102,400 Hz. The VFD frequency (input frequency) was set to 18 Hz.

3 Vibration and Tachometer Signal Processing

3.1 Time Domain Overlaid with Tachometer

Figure 2 presents a first look into the vibration time domain signal overlaid with the tachometer. Although it could be argued that no much information could be gained from inspecting the time domain, it is however a fundamental practice to examine the signal prior to any further analysis to ensure validity and gain some insight into the nature of the signal. The four periods presented in Fig. 2 show the meshing pattern as well as a number of impacts (impulse responses), associated with the bearing fault.

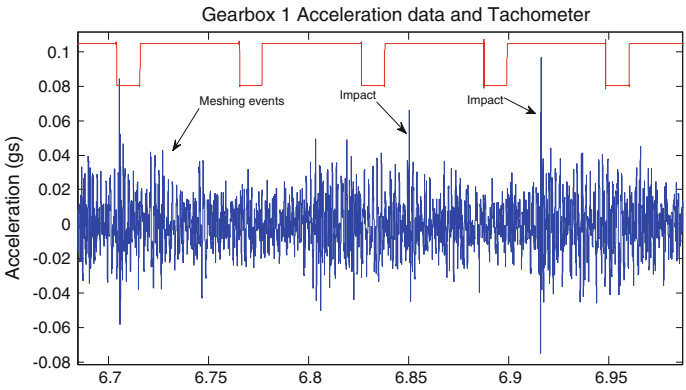

Fig. 2 Vibration time domain signal overlaid with the tachometer signal

3.2 Frequency Content and the Power Spectrum Density (PSD)

The power spectrum density (PSD) of the vibration signal is presented in Fig. 3. A first examination is provided in Fig. 3a using a low resolution of 12.5 Hz/line. This enables the examining of structural resonances and frequencies dominating the signal. For instance if an envelope analysis is to be carried out, a band between 20 and 22 kHz or any band between 25 and 35 kHz would be appropriate. A simple band pass envelope analysis between 20 and 22 kHz was attempted and the result is shown in Fig. 4. The envelope spectrum of Fig. 4 shows the presence of the Ball Pass Frequency, inner race (BPFI) thus indicating the presence of an inner race fault in the intermediate shaft bearing (BPFI = 52.2 Hz). A high resolution version of the PSD (0.098 Hz/line) as shown in Fig. 3b highlights a family of harmonics spaced at 6 kHz (VFD carrier frequency). A zoom in around one of the VFD carrier frequencies and inspecting the sidebands (using sidebands cursors) gives very helpful information about mechanical and electrical modulation as can be seen from Figs. 5 and 6. The sidebands of Fig. 5 show the VFD frequency (18 Hz) while Fig. 6a shows the intermediate shaft speed (approximately 9.48 Hz). The family of sidebands of the high speed shaft frequency (input speed) of 16.39 Hz at is shown in Fig. 6b. Further details about the low shaft speed, the gear mesh frequencies and the frequency content of the signal are discussed in the next two sections.

3.3 Time-Frequency Analysis

Morlet Wavelet analysis [13] was selected to provide a sense about the time-frequency content for the vibration signal. It is not an aim of this paper to

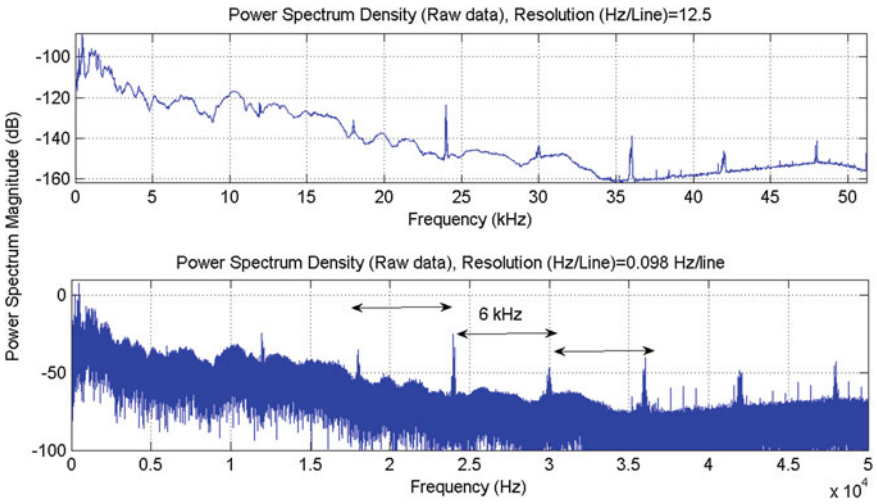

Fig. 3 Power spectrum density (PSD) **a** coarse resolution of 12.5 Hz/line **b** fine resolution of 0.098 Hz/Line

compare between the different time-frequency presentations, but rather to show a sample of what can be gained from such analysis. Time-frequency analysis normally provides information about speed fluctuations, transient events, verification of information obtained from time and frequency domain data, extra observation such distinguishing between electrical and mechanical faults, signal modulation and more. The major two intense regions in the time-frequency plot (Fig. 7a, b) are noticed around the 450 Hz and the 250 Hz. These are thought of as the 1st and 2nd gear mesh frequencies respectively. At around 450 Hz (Fig. 7a) approximately 10 events in one second are observed. This corresponds to a modulation of approximately 10 Hz and corresponds to the intermediate shaft frequency. This was observed as sidebands at 9.47 Hz (see Fig. 6a) around the VFD carrier. At around 250 Hz (Fig. 7b) four major events in one second can be seen. This corresponds to a modulation of approximately 4 Hz which is recognized as the low speed shaft.

3.4 Order Tracking and Signal Separation

Order tracking (angular re-sampling) was performed on the signal and the procedure described in [6] was used to estimate the number of teeth on each shaft. The order tracked spectrum showing the 1st and 2nd gear mesh frequencies is presented in Fig. 8. Note the use of scaling in Hz (virtual scale) rather than orders to show the range of frequency of the first and second gear mesh frequencies. Figure 9 shows the harmonics (order scaling).

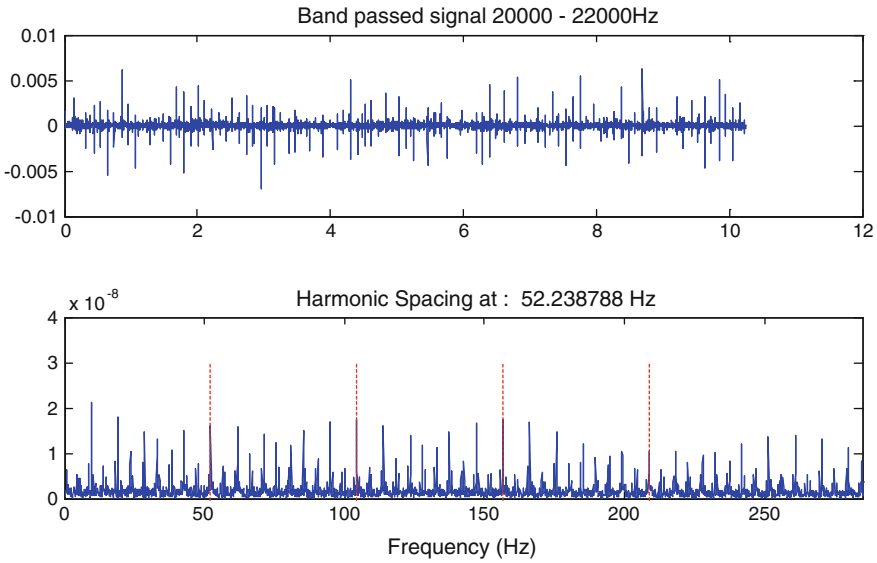

Fig. 4 *Top* Band passed signal between 20 and 22 kHz. *Bottom* Squared envelope spectrum of the top signal

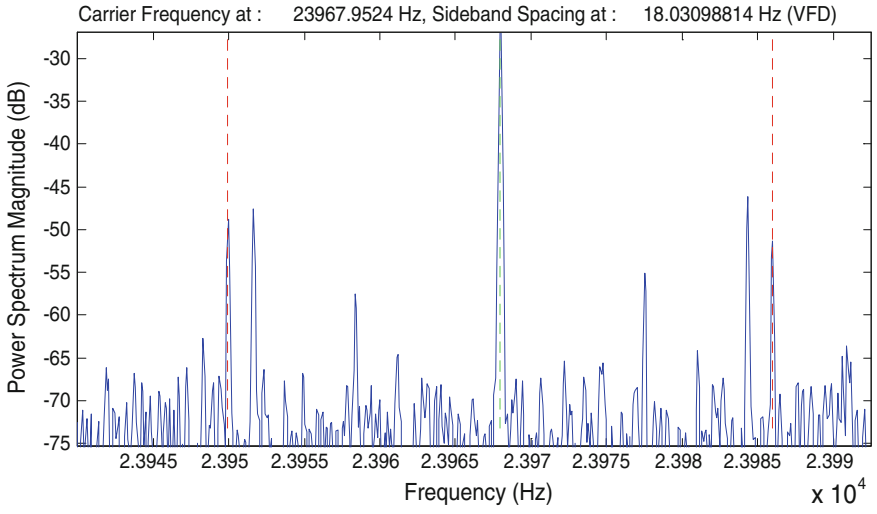

Fig. 5 Sideband cursors in the vicinity of the VFD carrier frequency at the VFD frequency of 18 Hz

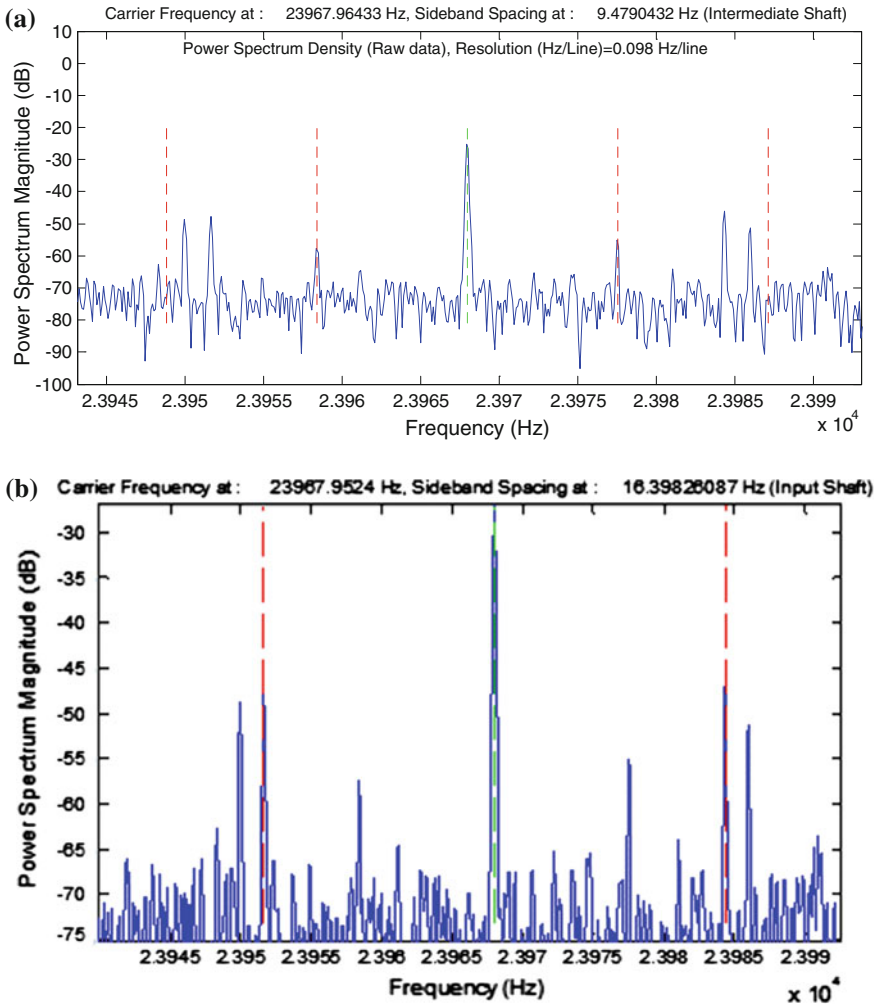

Fig. 6 Sideband cursors in the vicinity of the VFD carrier **a** sidebands at the intermediate shaft frequency **b** sidebands d at the high shaft frequency

Figure 9 shows the finely tuned harmonics of the intermediate shaft over the order tracked spectrum (two stages of tracking with respect to the intermediate shaft). The gear mesh frequencies are matched at harmonics number 25 (second gear mesh) and harmonic number 47 (1st gear mesh). This indicates that the number of teeth of the pinion in the second stage is 25 while the gear of the first stage is 47. Figure 10 shows the quality of the harmonic cursor of matching the gear mesh frequency and its sidebands.

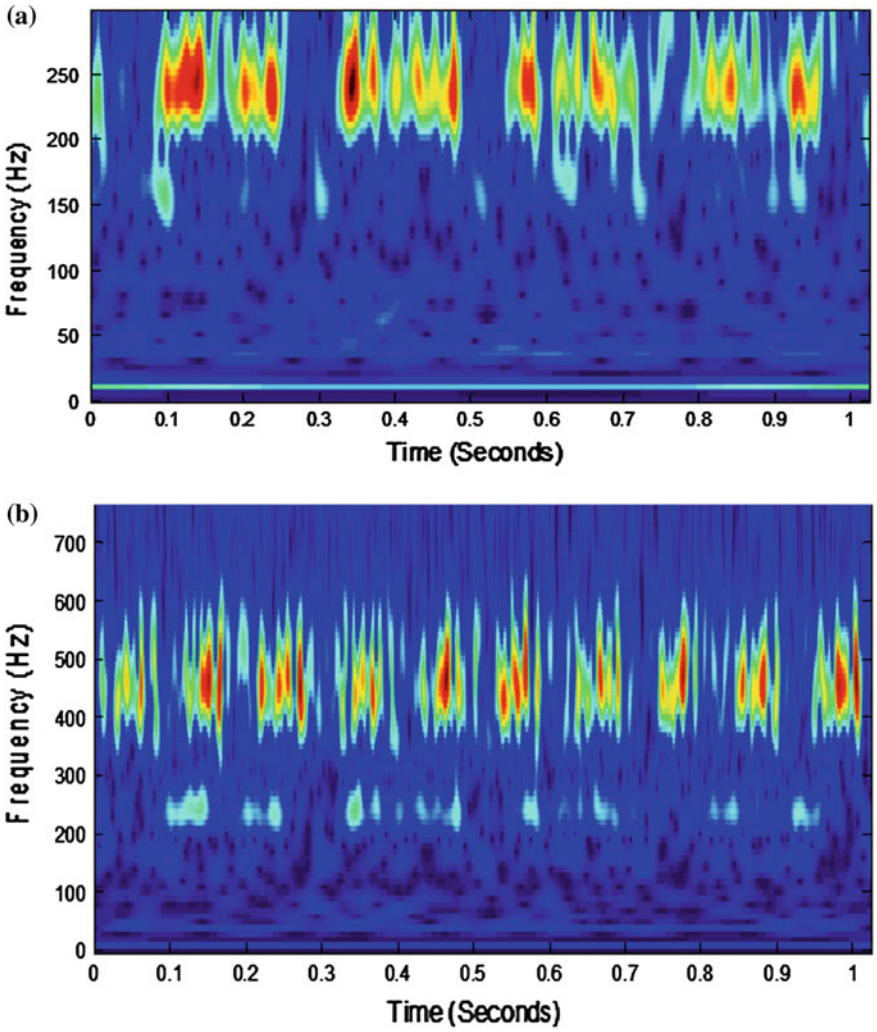

Fig. 7 Time-frequency analysis using Morlet wavelets. **a** A zoom in analysis between 0 and 250 Hz. **b** A zoom in analysis between 0 and 700 Hz

Figure 11 shows the determination of the number of teeth of the second stage gear. This is found to be 56 by using the harmonic cursor tracking of the low speed shaft. The last, but perhaps the least accurate is the pinion of the first stage. The harmonics of the high speed shaft for the order tracked signal are shown in Fig. 12. Analysis indicates that the number of teeth are 27 and the harmonic cursor align with some frequencies, but these are not very clear as was the case for the intermediate and low speed shafts.

This stage of analysis included also the extraction of a synchronous average for each shaft as seen in Fig. 13 and a residual signal (Fig. 14) after subtracting the synchronous averages from the raw signal

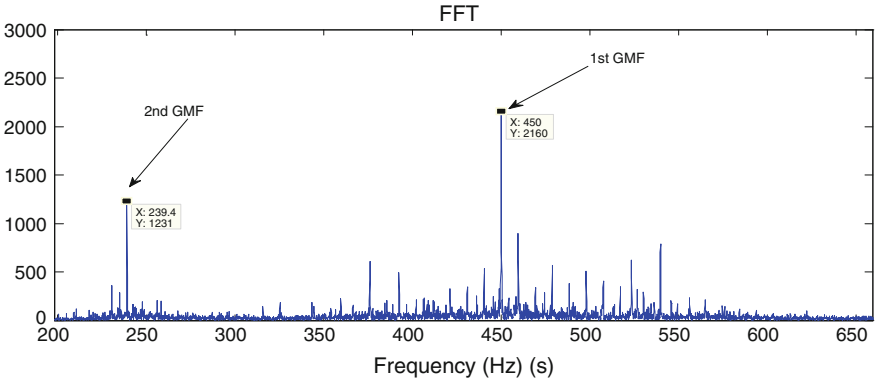

Fig. 8 Order tracked signal's spectrum with respect to the input shaft

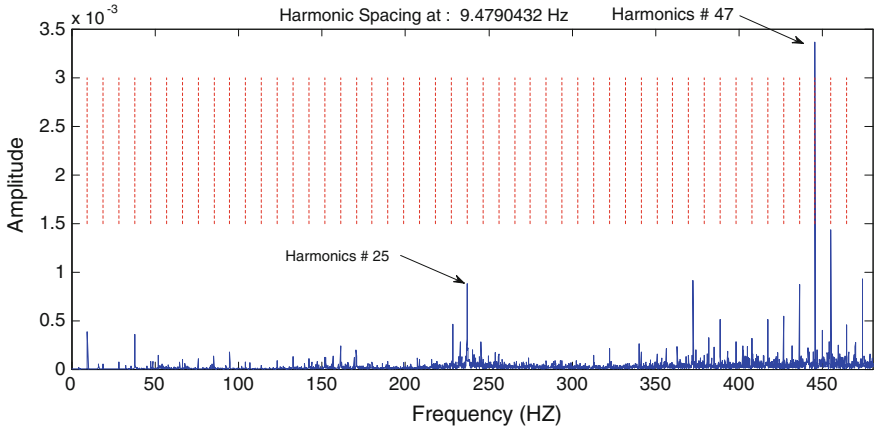

Fig. 9 Harmonics of the intermediate shaft frequency

4 Bearing Fault Diagnosis

The bearing fault processing stages are summarized in Fig. 15 [12]. The first stage is to remove the discrete components of the shafts and gears and the discrete components from the VFD. In this processing, discrete random separation (DRS) [14] was use. This utilizes the signal itself by generating a linear transfer function (using FFT methods) between the signal and a delayed version. The second stage involves whitening the signal and removing the effect of the transfer path [12]. The results of stages 1 and 2 of the processing are shown in Fig. 16, where a clear visualization of the bearing impact impulses can be seen [minimum

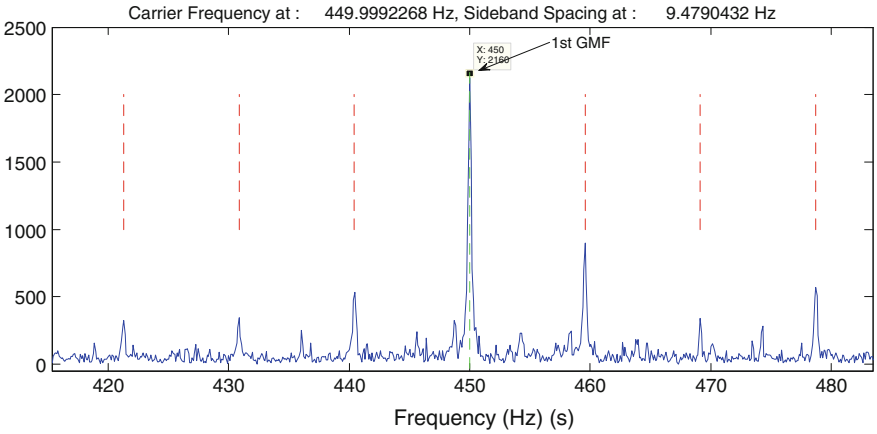

Fig. 10 Zoom in around the 1st gear mesh frequency showing the harmonics/sidebands of the intermediate shaft frequency

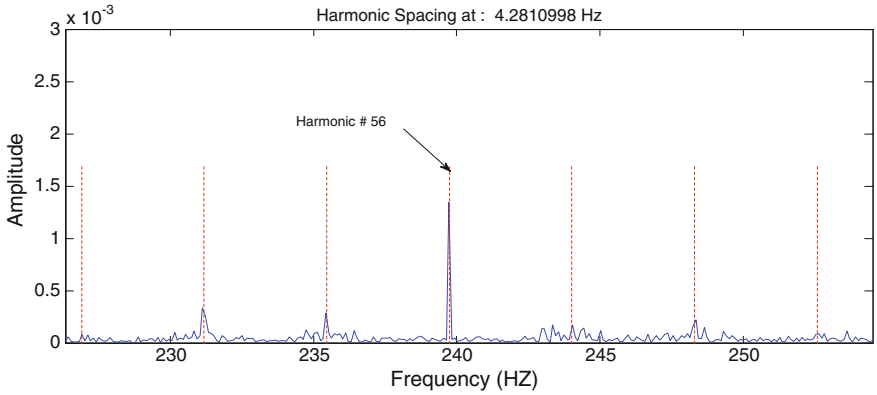

Fig. 11 Harmonics of the low speed shaft (after order tracking with respect to the low speed shaft) showing the 2nd gear mesh matches perfectly harmonic number 56

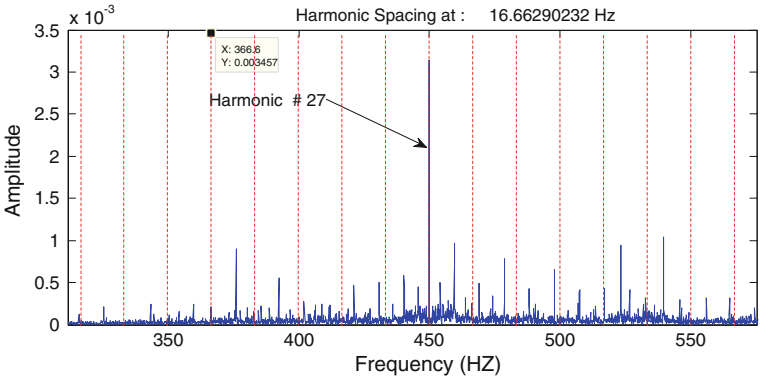

Fig. 12 Harmonics of the high speed shaft and the determination of the number of teeth for the 1st stage pinion

entropy deconvolution (MED) filter length of 4096 and an error tolerance of 0.001 were used]. The third and fourth stages of processing include using the wavelet *kurtogram* [13] and envelope analysis to diagnose the fault. The *kurtogram* helps in identifying the best band for envelope analysis and the result shown in Fig. 17

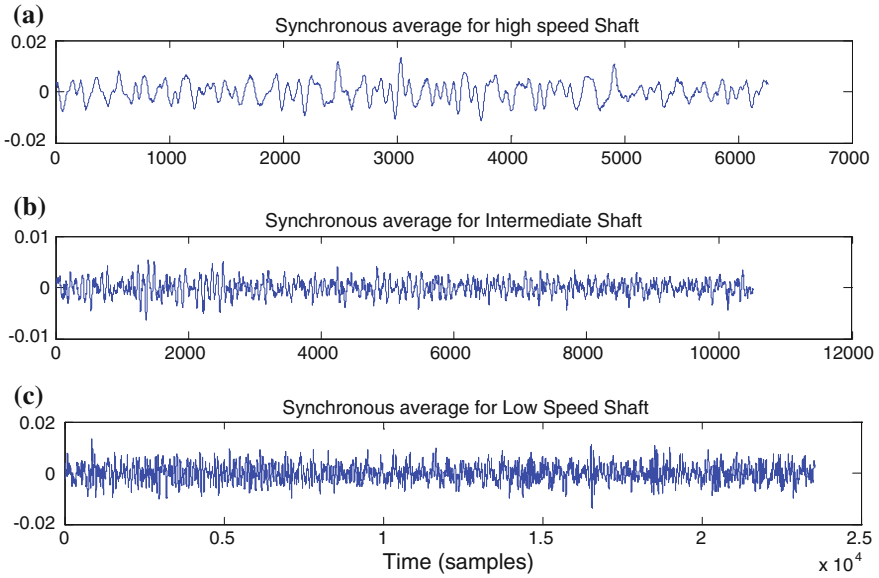

Fig. 13 **a** Synchronous average of high speed shaft. **b** Synchronous average for the intermediate shaft. **c** Synchronous average of the low speed shaft

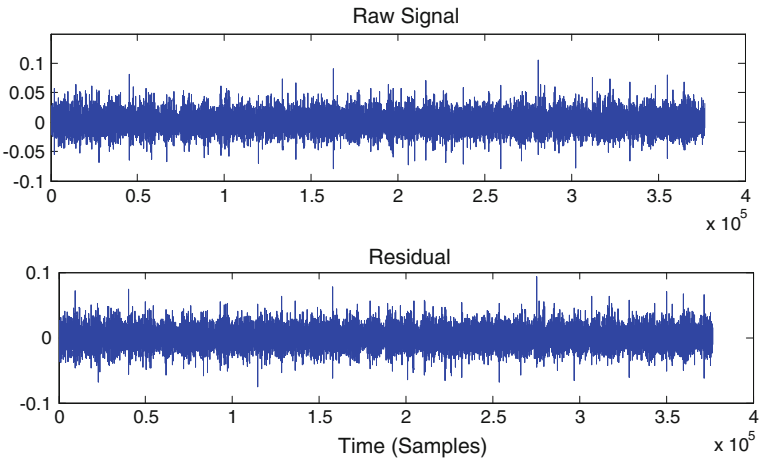

Fig. 14 *Top* Raw signal. *Bottom* Residual signal

indicates that bands between 20 and 30 kHz are suitable. The envelope analysis based on the auto band selection (Fig. 18) shows clearly the ball pass frequency and its harmonics, with strong sidebands (modulation) at the intermediate shaft speed as well as harmonics of the intermediate shaft frequency.

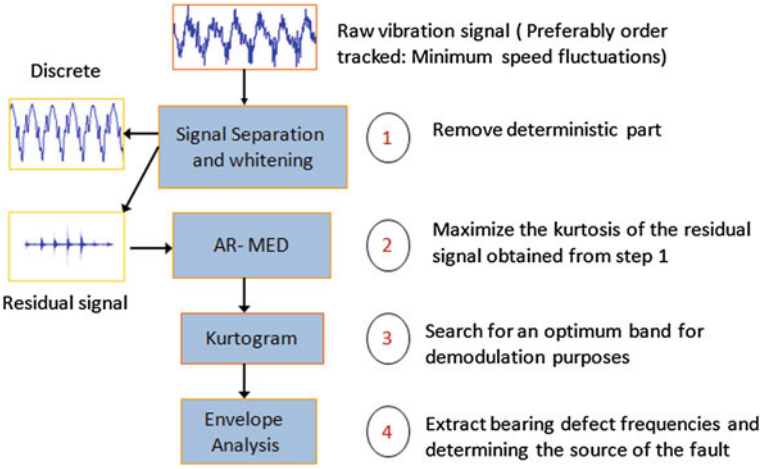

Fig. 15 Bearing fault diagnosis processing stages

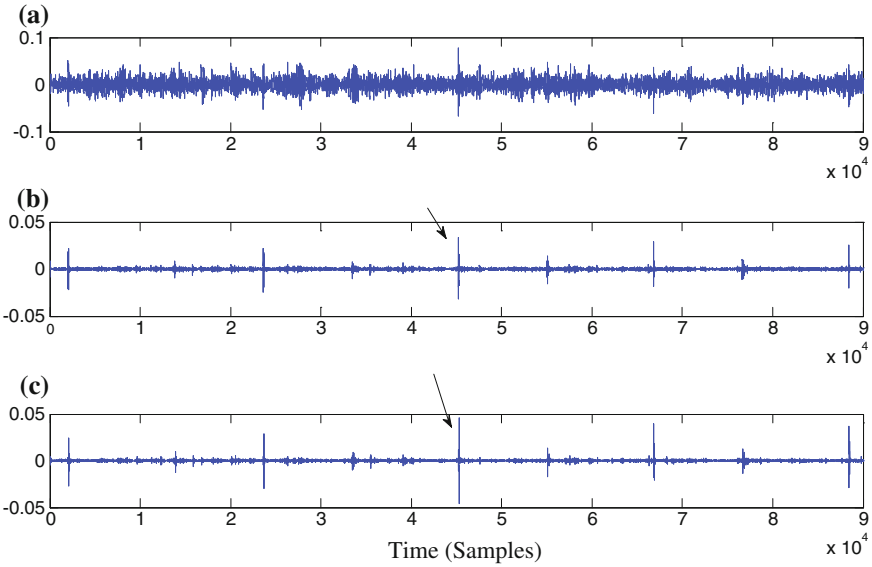

Fig. 16 *Top* DRS residual. *Middle* autoregressive whitening (AR). *Bottom* Minimum entropy deconvolution filtered signal

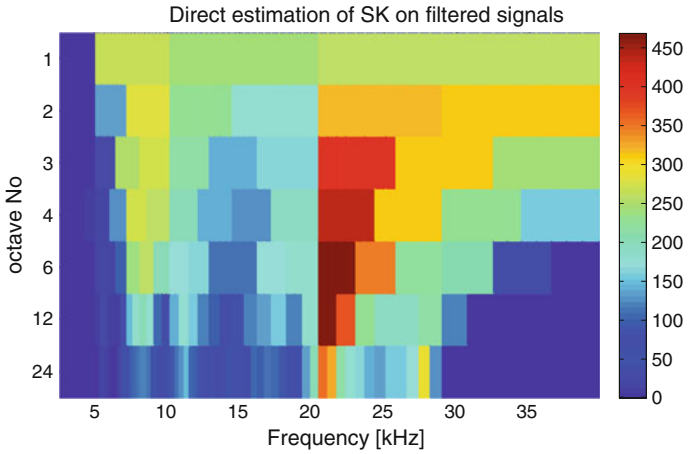

Fig. 17 Wavelet kurtogram of the bottom signal of Fig. 16

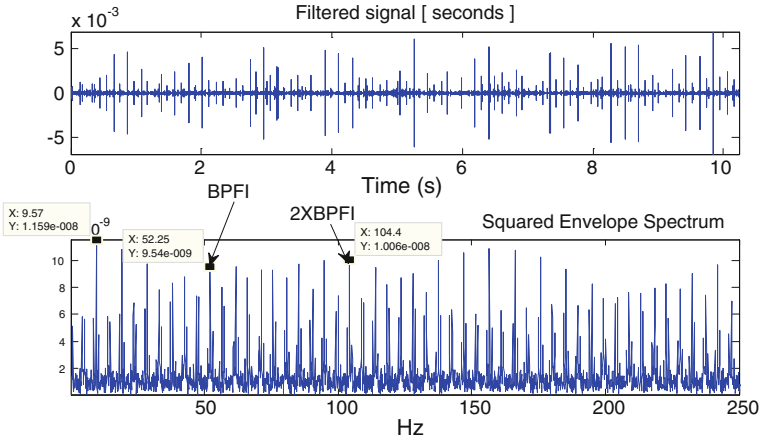

Fig. 18 *Top* Filtered signal based on wavelet kurtogram maximum kurtosis. *Bottom* Squared envelope spectrum

5 Summary and Conclusions

This paper has presented a systematic analysis and handling for a vibration signal of a two stage gearbox, driven by a variable frequency drive (VFD) and with a notch fault introduced to the inner race of the intermediate shaft bearing. The processing included the examination of the time domain signal, the frequency domain (for content and modulation) and the time-frequency domain for transients and modulations. Modulations of VFD carrier frequency were used to identify shaft speeds and slippage. This was clearly seen through using sideband cursors. An attempt to identify the number of teeth on each gear was carried out by using order tracking and finely tuned harmonic cursors. The number of teeth on the second stage and the gear of the first stage were identified with confidence. The pinion of the first stage couldn't be firmly confirmed. The inner race fault in the intermediate stage has been clearly identified. This was initially found by simple envelope analysis (guided by inspecting the spectrum in dB scale) and later by a semi-automated analysis which included signal separation and a number of enhancements.

Acknowledgments The authors would like to thank Mr. Jun Yang from SpectraQuest® China for providing the data used for analysis. The first author is thankful for SpectraQuest® for their financial and technical support to complete this work.

References

1. Forrester BD (1991) Time-frequency domain analysis of helicopter transmission vibration. Department of Defence, Aeronautical Research Laboratory, propulsion report 180
2. Coats MD, Sawalhi N, Randall RB (2009) Extraction of tacho information from a vibration signal for improved synchronous averaging. Paper presented at ACOUSTICS 2009, Australian Acoustical Society, Adelaide, 23–25 Nov 2009
3. Combet F, Zimroz R (2009) A new method for the estimation of the instantaneous speed relative fluctuation in a vibration signal based on the short time scale transform. Mech Syst Signal Process 23(4):1382–1397
4. Combet F, Gelman L (2007) An automated methodology for performing time synchronous averaging of a gearbox signal without speed sensor. Mech Syst Signal Process 21(6):2590–2606
5. Bonnardot F, El Badaoui M, Randall RB, Danière J, Guillet F (2005) Use of the acceleration signal of a gearbox in order to perform angular resampling (with limited speed fluctuation). Mech Syst Signal Process 19:766–785
6. Sawalhi N, Randall RB (2014) Gear parameter identification in wind turbines using diagnostic analysis of gearbox vibration signals. Mech Syst Signal Process 42(1–2):368–376
7. Wang X, Makis V, Yang M (2010) A wavelet approach to fault diagnosis of a gearbox under varying load conditions. J Sound Vib 329(9):1570–1585
8. Fan XF, Zuo ML (2006) Gearbox fault detection using Hilbert and wavelet packet transform. Mech Syst Signal Process 20(4):966–982
9. Antoni J, Randall RB (2002) Differential diagnosis of gear and bearing faults. J Vib Acoust 124:165–171
10. Sawalhi N, Randall RB (2008) Localised fault diagnosis in rolling element bearings in gearboxes. Paper presented at the fifth international conference on condition monitoring and machinery failure prevention technologies, Edinburgh, pp 15–18
11. Sawalhi N (2009) Vibrations of spalled rolling element bearings, diagnostics, prognostics and dynamic simulations. VDM Verlag, 29 May 2009. ISBN 3639152417
12. Sawalhi N, Randall RB, Endo H (2007) The enhancement of fault detection and diagnosis in rolling element bearings using minimum entropy deconvolution combined with spectral kurtosis. Mech Syst Signal Process 21(6):2616–2633
13. Sawalhi N, Randall RB (2005) Spectral Kurtosis optimization for rolling element bearings. ISSPA conference, Sydney, Australia
14. Antoni J, Randall RB (2004) Unsupervised noise cancellation for vibration signals: Part II–a novel frequency domain algorithm. Mech Syst Signal Process 18:103–117

Monitoring Based on Time-Frequency Tracking of Estimated Harmonic Series and Modulation Sidebands

Timothée Gerber, Nadine Martin and Corinne Mailhes

Abstract A condition monitoring system (CMS) is a key element in a predictive maintenance strategy allowing to reduce the operating costs of the monitored system. However, the system-driven generation of health indicators requires the knowledge of the system kinematics and the configuration of thresholds which may induce lots of false alarms. In this paper, we propose a generic and data-driven method to automatically generate system health indicators without any a priori knowledge on the monitored system or the acquired signals. The proposed method is based on the automatic detection of spectral content characterising every acquired signal. Within these successive spectral contents, peaks, harmonics series and modulation sidebands are then tracked over time and grouped in time trajectories which will be used to generate the system health indicators.

Keywords Condition monitoring · Tracking · Surveillance · Fault diagnosis · Harmonics · Sidebands · Signal processing · Wind turbines

Contents

1 Introduction 88
2 Identification of Spectral Peaks and Spectral Structures 89

T. Gerber (✉) · N. Martin
Univ. Grenoble Alpes, GIPSA-Lab, F-38000 Grenoble, France
e-mail: timothee.gerber@gipsa-lab.grenoble-inp.fr

N. Martin
e-mail: nadine.martin@gipsa-lab.grenoble-inp.fr

T. Gerber · N. Martin
CNRS, GIPSA-lab, F-38000 Grenoble, France

C. Mailhes
IRIT/ENSEEIHT/TéSA, University of Toulouse, Toulouse, France
e-mail: corinne.mailhes@enseeiht.fr

F. Chaari et al. (eds.), *Advances in Condition Monitoring of Machinery in Non-Stationary Operations*, Applied Condition Monitoring 4,
DOI 10.1007/978-3-319-20463-5_7

3 Time-Frequency Tracking of Peaks and Structures 90
3.1 Tracking of Spectral Peaks 91
3.2 Tracking of Harmonic Series 92
3.3 Tracking of Modulation Sidebands 92
3.4 Generation of the System Health Indicators 93
4 Experiments 93
4.1 Description of the Wind Turbine Test Rig 93
4.2 Medium Degradation of the Main Bearing 94
4.3 Full Degradation of the Main Bearing 95
5 Conclusions 97
References 98

1 Introduction

The installation of a Condition Monitoring System (CMS) on a mechanical machine (e.g., on a wind turbine) aims to reduce the operating costs by applying a predictive maintenance strategy [1]. The CMS is composed of sensors acquiring signals from which system health indicators are computed and monitored. System-driven computation of these indicators requires the monitored system kinematics and is done by averaging large or narrow spectral bands. The averaging and the need for predefined thresholds for fault detection may induce lots of false alarms while reducing the ability to detect a fault early.

To get precise health indicators whatever the system is, we propose a generic and data-driven monitoring strategy without any a priori knowledge on the system or the measured signals. The first step consists in analyzing and extracting the spectral content of each successive signal acquired by the CMS. This content is composed of single spectral peaks, or peaks grouped in more complex structures like harmonic series or modulation sidebands. Each spectral structure is characterized by several parameters, including for example the number of peaks, the characteristic frequencies and the energy [2].

The second step is a time-frequency tracking of the spectral structures through all available signals. It results in the creation of spectral structure trajectories from which the system health indicators will be derived. This approach has the particularity to create meaningful indicators, each one describing a part of the system. This assertion is particulary true in the mechanical domain where the spectral frequencies allow to identify precisely the mechanical parts of the system [3]. In comparison, the approach in [4] uses anonymous indicators, which are not easily linkable to the system parts. Moreover, the decision in [4] about the system state is made for each new signal, without taking the previous state into account. On the contrary, the tracking used in this paper keeps record of the evolution of the indicators, and thus of the system health.

The time-frequency tracking method proposed in this paper is based on the McAulay and Quatieri method [5] which has been originally designed for a single

peak tracking in speech signals. We have adapted [5] in order to account not only for single spectral peak evolution but also for the evolution of more complex structures such as harmonic series or modulation sidebands. Moreover, the proposed method is made robust against the possible non-detection of spectral structures for some isolated signals among all the acquisitions thanks to a sleep state adapted from [6]. Finally, in every trajectory the temporal evolution of each spectral structure parameter can be monitored and used as precise system health indicators.

The paper is organised as follows. The identification of spectral peaks, harmonics series and modulation sidebands is presented in Sect. 2. Section 3 details the proposed time-frequency tracking method. In Sect. 4, the proposed method is validated on real-world signals acquired on a wind turbine test rig. Conclusions and perspectives are given in Sect. 5.

2 Identification of Spectral Peaks and Spectral Structures

Different kinds of signals are recorded by a CMS: vibration, acoustic or electrical signals. In order to analyse a signal whatever its modality, we propose a generic and data-driven method to automatically identify, inside the estimated spectrum, the spectral peaks and the spectral structures. By "spectral structure", we mean a set of peaks linked by a mathematical relation. The two types of spectral structures considered in this paper are (1) the harmonic series, where the peaks have a frequency which is a multiple of a fundamental frequency, and (2) the modulation sidebands, in which peaks are equally spaced around a carrier frequency. The different steps of the method illustrated in Fig. 1 are fully automatic and do not need any a priori knowledge or settings.

Let us consider a sensor acquiring signals s^n at time instants t^n, where n denotes the signal index and t^n is the time elapsed in operating hours since the beginning of the surveillance. This time instant t^n is also the beginning of the acquisition of the signal s^n for a given duration. Each signal is analysed independently by the following process. A preanalysis verifies that the signal has been correctly acquired. For example, the preanalysis verifies that there is no saturation in the time signal or that an anti-aliasing filter has been correctly used during the acquisition. Moreover, the preanalysis extracts fundamental information about the signal s^n [7], as an

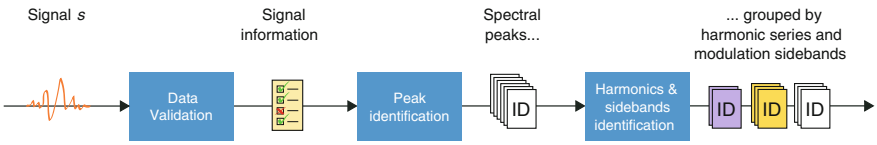

Fig. 1 The different steps of spectral content extraction: the data validation step assesses some global properties of the signal in order to ease the identification of spectral peaks which are finally grouped in harmonic series or modulation sidebands

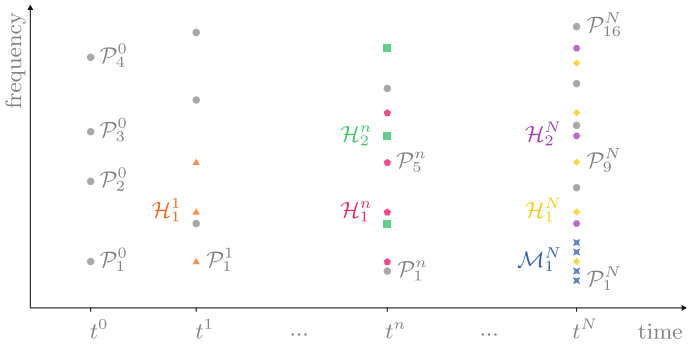

Fig. 2 A discrete time-frequency map illustrating the identification of peaks and structures for every signal acquired. Peaks which belong to the same structure share the same *shape* and *colour*. *Grey circles* represent the peaks which are not in a structure

estimation of its signal-to-noise ratio or its non-stationarity rate. Then, a "multi-cycle" spectral analysis strategy [8] detects the peaks present in the spectrum, by merging the peak detected in several spectrum estimations. The list of detected peaks $\mathcal{P}_i^n$ is sorted in ascending order of frequency, with $i \in \{1, \ldots, N_{\mathcal{P}}^n\}$ being the index of the peak and $N_{\mathcal{P}}^n$ being the total number of peaks.

Finally, the list of peaks is parsed to identify the harmonic series $\mathcal{H}_j^n$ and the modulation sidebands $\mathcal{M}_k^n$ present in the spectrum [2], where j and k are the index of the harmonic series and the modulation sideband respectively. These spectral structures are characterised by several parameters, including for example the number of peaks and the energy of the structure.

The identification of spectral peaks and structures in a sequence of signals s^n is summarized in Fig. 2 by the discrete time-frequency map. Each detected peak is represented by a color and shape combination. Peaks with the same color and shape belong to the same spectral structure while the grey circles represent the peaks which does not belong to any structure. Further readings at [2, 8] for a detailed presentation of this steps.

3 Time-Frequency Tracking of Peaks and Structures

Time-frequency tracking is a problematic already present in the literature. Several methods are based on McAulay and Quatieri one [5] which is efficient but designed for peak tracking only. In [9], the tracking algorithm is based on a hidden Markov model and thus has a high computation complexity. Meanwhile, others methods [10, 11] are able to track spectral structures like harmonic series. However, the number of structure tracked should be low or given a priori.

In our CMS context, the tracking method should be: (1) able to track both peaks and structures, (2) generic, thus necessitating no a priori information, and (3) able to

deal with a large amount of signals, with thousands of peaks and hundreds of spectral structures. To our knowledge, none of the methods verifies all the criteria. Therefore, we propose to derive a method from the one of McAulay and Quatieri which is the one with the lowest complexity. We adapted their method to track not only peaks but also spectral structures.

However, the CMS context is quite different from the audio signal one. The CMS acquires signals on a irregular temporal basis meaning that the state of the system could be completely different between two acquisitions. This is troublesome for tracking operations. Therefore, the main hypothesis to use our proposed tracking method is that the signals are all acquired in a "constant machine state", where the operational parameters are constant during the acquisition and are the same for every acquisition. Angular resampling [12] may be performed as a pre-process to assess that the constant machine state hypothesis is verified.

3.1 Tracking of Spectral Peaks

The peak tracking is done sequentially and peak by peak, starting from the lowest frequencies. Suppose that the tracking is done up to time t^n and up to peak $\mathcal{P}_{i-1}^n$. The trajectory $\mathcal{T}^{\mathcal{P}}$ of the next peak $\mathcal{P}_i^n$ will now be linked to a peak at time t^{n+1} by the following 2-step process.

Step 1: A search for candidate is made in the research interval Δf around the frequency f_i^n. If there is no candidate, the trajectory of the peak $\mathcal{P}_i^n$ dies. In the case of multiple candidates, the one with the nearest frequency to f_i^n is elected as the best candidate.
Step 2: The best candidate from step 1 has to verify the backward compatibility condition. In other words, the frequency of the best candidate has to be closer to f_i^n than to any other peak at time t^n. When the backward condition is met, the best candidate is added in the peak $\mathcal{P}_i^n$ trajectory. If there is no other candidate in the search interval, the trajectory of the peak $\mathcal{P}_i^n$ dies. Else, the association is made with the second best candidate in the search interval.

To sum up, the peak trajectories are constructed sequentially with

$$\mathcal{P}_j^{n+1} \in \mathcal{T}^{\mathcal{P}_i^n} \quad \underbrace{\text{if } f_i^n - \frac{\Delta f}{2} \leq f_j^{n+1} \leq f_i^n - \frac{\Delta f}{2}}_{\text{search interval}}$$
$$\underbrace{\text{with } f_j^{n+1} = \underset{l=1,\ldots,N_{\mathcal{P}}^n}{\arg\min} \left| f_i^n - f_l^{n+1} \right|}_{\text{best candidate}} \quad \text{and} \quad \underbrace{\left| f_i^n - f_j^{n+1} \right| < \left| f_{i+1}^n - f_j^{n+1} \right|}_{\text{backward compatibility condition}}. \tag{1}$$

In the original method, every peak is part of a trajectory, even if it is alone in its trajectory. We propose to start new trajectories only if at least two successive peaks

will be included in it. Moreover, the original method is not robust against the possible non-detection of peaks, as the trajectory directly dies. We propose to introduce a *sleep state* as proposed in [6] to solve this problem. As a consequence, a trajectory can fall asleep and wake up. If the trajectory sleeps for a too long time (2 successive signals in our algorithm), the trajectory finally dies.

In order to be as generic as possible, the search interval Δf is chosen as a multiple of the spectral resolution (10 times in our algorithm). This resolution only depends on the signal length and is computed during the spectral peak identification (see Sect. 2).

3.2 Tracking of Harmonic Series

The tracking of harmonic series is done by applying the strategy explained in Sect. 3.1 to the set of fundamental frequencies f_j^n of all harmonic series $\mathcal{H}_j^n$. When two harmonic series are associated, the peaks inside the series are automatically tracked according to their harmonic rank. This structural approach is more robust than tracking each peak independently as the tracking is efficient even if some peaks are missing in the harmonic series. One of the missing peak can even be the peak representing the fundamental frequency.

3.3 Tracking of Modulation Sidebands

The modulation sidebands $\mathcal{M}_k^n$ are characterized by two parameters to track; the carrier frequency f_k^n and the modulation frequency Δf_k^n. However, in the proposed method only the peaks belonging to at least one harmonic series could be considered as a potential carrier frequency. Therefore, the carrier frequency has already been tracked during the tracking of harmonic series (see Sect. 3.2).

It becomes then possible to track the modulation sidebands thanks to the strategy explained in Sect. 3.1 applied on the set of modulation frequencies Δf_k^n present around each carrier frequency trajectory.

As for harmonic series, when modulation sidebands are tracked, the peaks inside the modulation are automatically tracked thanks to their modulation frequency. As a consequence, to track all the spectral content without redundancy, the tracking operations are done in the following order: (1) identification of the harmonic series trajectories $\mathcal{T}^{\mathcal{H}}$, (2) identification of the modulation sideband trajectories $\mathcal{T}^{\mathcal{M}}$, and (3) the identification of remaining peak trajectories $\mathcal{T}^{\mathcal{P}}$. The remaining peaks are the peaks which are not yet in any trajectory after harmonic and modulation tracking.

3.4 Generation of the System Health Indicators

The system health indicators are generated from the time evolution of a set of parameters [2] characterising the spectral structure in the trajectories previously computed. In a healthy system, the temporal behaviour of any parameter characterizing the system should not evolve drastically, while a default should result in a noticeable variation of some of them.

Thus, we have associated to each peak trajectory some classical parameters as its frequency f_i, associated with its frequency uncertainty Δf_i and its related amplitude A_i, while harmonic series and modulation sideband trajectories are associated with more elaborated indicators: the fundamental/modulation frequency, the number of peaks within the harmonic or modulation series, the energy, the density D_j, the harmonic distortion THD_j and the richness R_j. The three last parameters are detailed in (2),

$$D_j = \frac{\text{card}(\mathcal{H}_j)}{r_j^{\max}}, \quad THD_j = \frac{\sum_{i=2}^{N_j^{\max}} A_i^2}{A_1^2}, \quad R_j = \frac{r_j^{\max}}{N_j^{\max}}, \tag{2}$$

with $\mathcal{H}_j$ denoting the harmonic/modulation series, $r_j^{\max}$ the rank of the last harmonic in the series, $N_j^{\max}$ being the maximum possible size of the series considering the fundamental frequency and the highest frequency in the spectrum. Note that for modulation sidebands these equations are adapted and computed both on the left and the right side of the carrier frequency. Moreover, an optional demodulation step [12] can be applied on each modulation sideband to have extra indicators like the amplitude and frequency modulation indexes.

In the next section, experiments highlighting the interest of such indicators are presented. However, in these detailed experiments not all the above indicators are shown or used. At the present stage of our work, the idea is to characterize as finely as possible the system evolution in order to be able to feed a classification tool which will constitute the future system diagnosis automatic tool.

4 Experiments

4.1 Description of the Wind Turbine Test Rig

A test rig developed by the CETIM within the frame of the KAStrion project (http://www.gipsa-lab.fr/projet/KASTRION/) has been designed according to a wind turbine kinematics. Instead of the blades, a geared-motor of 10 kW generates the rotation of the main shaft (around 20 RPM). A multiplier with a ratio of 100:1 increases the rotational speed, allowing the generator to operate around 2000 RPM.

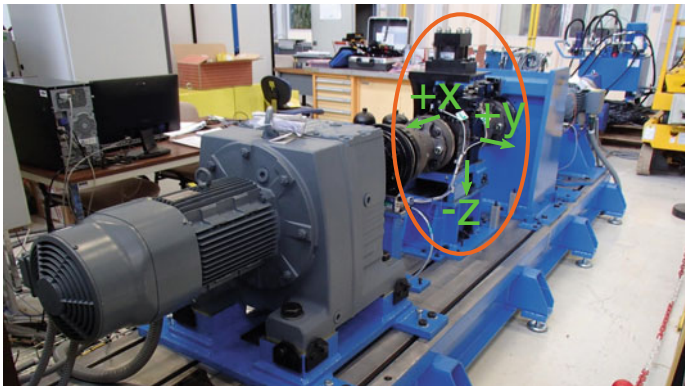

Fig. 3 A picture of the wind turbine test rig. The 3 accelerometers are represented by *green arrows*. The main bearing and its loading unit is circled in *orange*

Among the several sensors installed on the test rig (accelerometers, thermocouples, torquemeters, tachometers, voltage and current probes), we will focus on the 3 accelerometers which take place on the main bearing and which are illustrated in Fig. 3. The $+x$ accelerometer is in the axial direction while the $+y$ and $-z$ are in radial directions.

The vibration acquisition is done while the test rig works under stationary conditions which remain the same for every acquisition. Therefore, the hypothesis of constant machine state is met. Each vibration signal lasts 150 s and is sampled at 39,062.5 Hz.

One of the rig tasks consists in damaging the main bearing thanks to a loading unit and non-stationary working conditions which have been programmed to simulate real wind speed profiles. The results of the proposed method on the degradation of two different main bearings is presented in Sects. 4.2 and 4.3.

4.2 Medium Degradation of the Main Bearing

For each accelerometer, 12 vibration signals were recorded during the main bearing medium degradation. In each signal, an average of 19,400 peaks were detected and grouped in 750 harmonic series and 21,500 modulation sidebands. If these numbers seem large, one has to remember that the identification methods operate over all the signal frequency band without any a priori.

Let us first consider the $-z$ accelerometer. After the tracking operations, 1084 harmonic series trajectories and 564 modulation sideband trajectories are identified. Among the remaining peaks, 9327 trajectories are created.

One of the trajectory is particularly interesting. It is a harmonic series trajectory which energy suddenly and rapidly increases from approximatively 0.011 to

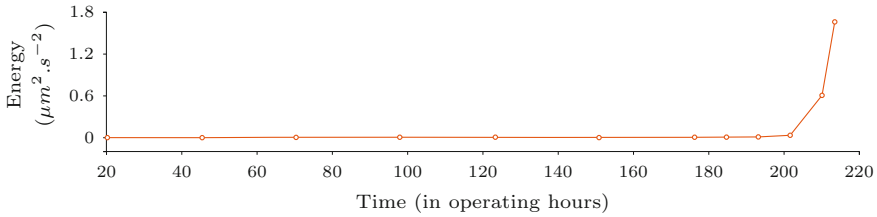

Fig. 4 Medium degradation of the main bearing. The energy in the inner ring harmonic series starts increasing around 200 operating hours. After 214 h, the test is stopped and the bearing is dismantled for inspection

1.6 $\mu m^2\ s^{-2}$ after 203 operating hours (see Fig. 4). The fundamental frequency of this harmonic series is 2.72 Hz and corresponds to the Ball Pass Frequency of the Outer ring (BPFO) of the main bearing.

The wear test is stopped after 214 operating hours although the rig is still able to operate. The main bearing is dismantled for visual inspection; 3 small flaking were present on the outer ring. This confirms the relevancy of the automatically generated indicator.

The results of the other accelerometers ($+x$, $+y$) will not be presented here as they show high similarity to the result of accelerometer $-z$.

4.3 Full Degradation of the Main Bearing

For this second wear test, another kind of main bearing is used with a different kinematics. Let us consider the $+y$ accelerometer. 17 vibration signals were recorded, containing an average of 9000 peaks, 600 harmonic series and 12,000 modulation sidebands. After the tracking operations, we get 828 harmonic series trajectories and 9373 modulation sideband trajectories. 12,406 peak trajectories are created among the remaining peaks.

Figure 5 shows one harmonic series trajectory deserving a special attention. On the top of the figure, peaks are symbolised by small grey circles on the discrete time-frequency map. The time localization of the peaks correspond to the signal acquisition timestamp. The zoom in the top left corner shows the high peak density. Among these detected peaks, a particular peak at 3.45 Hz is tracked from 44 to 189 operating hours and is represented by bigger and blue circles. About 129 h, this peak trajectory evolves to become a harmonic series trajectory with more and more peaks (see the increasing number of blue circles). Also, the energy of this trajectory increases and is represented by the orange plot in the middle of Fig. 5. The last plot in the bottom of Fig. 5 shows that the frequency of the trajectory is slightly decreasing.

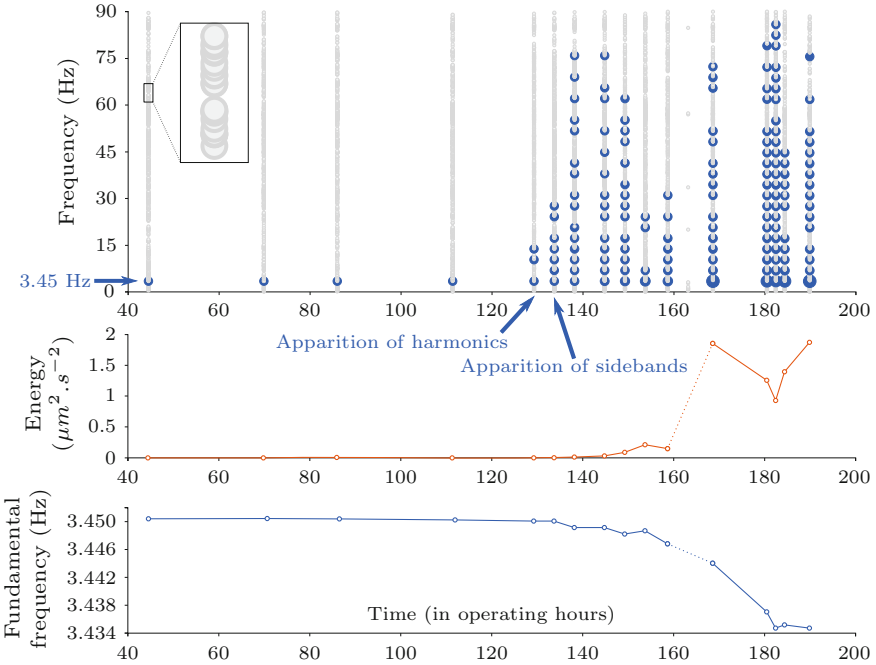

Fig. 5 Evolution of the main bearing fault, at the $+y$ accelerometer. Detected peaks are represented by small *grey circles* on the time-frequency map (*top*). *Blue* and *bigger circles* belongs to the same harmonic series trajectory linked to the inner ring fault. Below, two trends of the harmonic series

Moreover, a 0.33 Hz modulation sidebands started to appear after 134 operating hours around the 3.45 Hz carrier frequency. As shown in Fig. 6, the number of sidebands increases accordingly to the severity of the fault.

The 3.45 Hz corresponds to the Ball Pass Frequency of the Inner ring (BPFI). The apparition of harmonics and sidebands at 129 and 134 operating hours respectively are early warnings of a fault birth. The fault severity is then characterized by the increase in both energy and number of sidebands. The slightly decreasing frequency is explained by the fact that the inner ring wear generates slipping.

A second harmonic series trajectory also deserves some attention. Its fundamental frequency of 2.54 Hz corresponds to the BPFO. As shown in Fig. 7, its

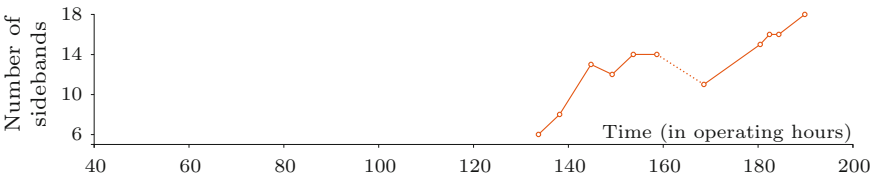

Fig. 6 Evolution of the number of modulation sidebands around the slowly evolving carrier frequency starting at 3.45 Hz. The modulation frequency is equal to 0.333 Hz

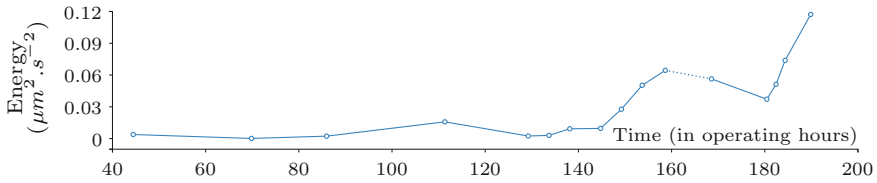

Fig. 7 Propagation of the fault: the energy of the outer ring harmonic series is also increasing after 145 operating hours

energy starts increasing from 144 operating hours, that is 15 operating hours after the early warning of the BPFI fault. It means that the fault is spreading in the main bearing and its severity is increasing.

On the top of Fig. 5, it is possible to see on the time-frequency map that around 163 h few peaks were detected in the signal. The spectral analysis was not able to identify the peaks and structures for this particular signal. Indeed, other tests [7] were applied and concluded on the fact that this signal was highly non-stationary due to a high impulse in the vibration signal. Nevertheless, the tracking of harmonic series and modulation sidebands was not stopped as it is shown in Figs. 5, 6 and 7. In fact, the sleep state allowed the tracking to continue. The sleep state is represented by a dotted line on the different curves.

The combination of the four automatically generated indicators (the energy and the frequency of the harmonic series at 3.45 Hz, the number of sidebands around the carrier frequency 3.45 Hz and the energy of the harmonic series at 2.54 Hz) mirrors out the failure and confirms the value of the proposed data-driven method. These four indicators are part of a long list of automatically generated indicators.

In order to deal with this long list of indicators, related work [12] focused on using a posteriori the kinematic information (if available) to identify and to label the trajectories linked to the kinematic of the monitored system. As a consequence, the number of labelled trajectories is much smaller than the total number of trajectories and several redundant modulation trajectories are then grouped under the same label. This optional step of adding information is not mandatory for the proposed method, although it allows to reduce the number of indicators to look at.

Moreover, the indicators of a healthy system will not vary much, while the indicators of a faulty system will evolve drastically. Therefore, to make a full automatic system health diagnosis, further work will focus on identifying automatically the evolving indicators which are the most interesting ones.

5 Conclusions

We proposed in this paper a complete generic and data-driven method to automatically generate system health indicators. The two steps of the proposed method are (1) the identification of the spectral structures present in each signal spectrum,

and (2) the tracking of these spectral structures through all the available signals. The trajectories constructed during the tracking operations are finally used to derive the system health indicators from the structure parameters.

The proposed approach is validated on real-world signals, recorded on a wind turbine test rig. Two different main bearings have been damaged. In both cases, the system health indicators automatically generated could detect the fault in its early stage. The severity of the faults is characterised by the time evolution of the health indicators.

The number of system health indicators generated is large. Therefore, future work will focus on sorting and classifying these indicators to make a fully automatic tool for system diagnosis.

Acknowledgments The KAStrion project has been supported by KIC InnoEnergy, a company supported by the European Institute of Innovation and Technology, and has the mission of delivering commercial products and services, new businesses and innovators in the field of sustainable energy through the integration of higher education, research, entrepreneurs and business companies.

We would also like to thank the CETIM, partner of the project, for providing the signals coming from the wind turbine test rig.

References

1. Márquez PFG, Tobias AM, Pérez MJP, Papaelias M (2012) Condition monitoring of wind turbines: techniques and methods. Renew Energy 46:169–178
2. Gerber T, Martin N, Mailhes C (2013) Identification of harmonics and sidebands in a finite set of spectral components. In CM & MFPT 2013, Kraków
3. Randall RB (2011) Vibration-based condition monitoring. Wiley, New York
4. Hang J, Zhang J, Cheng M (2013) Fault diagnosis of wind turbine based on multi-sensors information fusion technology. IET Renew Power Gener 8(August):289–298
5. McAulay R, Quatieri T (1986) Speech analysis/synthesis based on a sinusoidal representation. IEEE Trans Acoust Speech Signal Process 34:744–754
6. Serra X (1997) Musical sound modeling with sinusoids plus noise. Musical Signal Process 1–25
7. Martin N, Mailhes C (2009) A non-stationary index resulting from time and frequency domains. In: CM & MFTP 2009
8. Mailhes C, Martin N, Sahli K, Lejeune G (2006) Condition monitoring using automatic spectral analysis. In: Structural health monitoring, Spain
9. Depalle P, Garcia G, Rodet X (1993) Tracking of partials for additive sound synthesis using hidden Markov models. In: Acoustics speech and signal processing
10. Maher RC, Beauchamp JW (1994) Fundamental frequency estimation of musical signals using a two-way mismatch procedure. J Acoust Soc Am 95(April):2254–2263
11. Duan Z, Han J, Pardo B (2014) Multi-pitch streaming of harmonic sound mixtures. IEEE/ACM Trans Audio Speech Lang Process 22:138–150
12. Firla M, Li Z-Y, Martin N, Barszcz T (2014) Full-band demodulation in automatic application for fault detection—a wind turbine test rig case study. In: Condition monitoring of machinery in non-stationary operations

Blind Extraction of Instantaneous Frequency for Order Tracking in Rotating Machines Under Non-stationary Operating Conditions

O. Cardona-Morales, E.F. Sierra-Alonso and G. Castellanos-Dominguez

Abstract Order tracking (OT) is a technique for vibration analysis under non-stationary operating conditions, which considers the speed or load is time-varying in order to obtain machine health indicators. Nonetheless, information about the rotational speed implies a priori knowledge about the machine. Therefore, in this paper is proposed a blind instantaneous rotational speed extraction methodology that extracts a set of instantaneous frequencies (IF), from a filter bank applied to the original signal, using the Hilbert transform. The signal is transformed into order domain using velocity synchronous discrete Fourier transform (VSDFT), taking each estimated IF as a possible reference shaft speed. Then, the kurtosis is used as a non-stationarity criterion aiming to select a suitable instantaneous reference shaft speed. The methodology is tested in a simulated signal and a test rig which exhibit non-stationary behavior. As a result the closest component to the rotational speed is extracted without priori knowledge of the machine.

Keywords Order tracking · Instantaneous frequency · Non-stationary vibration signal

O. Cardona-Morales (✉) · E.F. Sierra-Alonso · G. Castellanos-Dominguez
Signal Processing and Recognition Group, Universidad Nacional de Colombia, Manizales, Colombia
e-mail: ocardonam@unal.edu.co

E.F. Sierra-Alonso
e-mail: efsierraa@unal.edu.co

G. Castellanos-Dominguez
e-mail: cgcastellanosd@unal.edu.co

F. Chaari et al. (eds.), *Advances in Condition Monitoring of Machinery in Non-Stationary Operations*, Applied Condition Monitoring 4,
DOI 10.1007/978-3-319-20463-5_8

Contents

1 Introduction 100
2 Theoretical Background 101
2.1 Instantaneous Frequency Extraction 101
2.2 Order and Angular Domain Transform 101
2.3 On the Angle-Order Map Stationarity 102
3 Experimental Set-up 103
3.1 Probabilistic Identification of Instantaneous Rotational Speed 104
3.2 Numerical Experiment 104
3.3 Test Rig Experiment 107
4 Conclusion 109
References 110

1 Introduction

Vibration analysis under non-stationary conditions has become important inasmuch as the first signs of damage can be identified in the machine transient state. Non-stationarity is mainly caused by machine operation conditions such as variable speed and load [1]. In that sense, one of the most used methods for vibration analysis under non-stationary regime is order tracking (OT), particularly, traditional methodologies such as Kalman-OT [2] and Computed-OT [3]. However, these approaches require the rotational speed measurement that, in practice, its availability could be expensive or even impossible. As an alternative, rotational speed can be extracted from the vibration signal using time-frequency representations, nonetheless, either under low speed fluctuations [4] or large speed fluctuations [5, 6], a priori knowledge about the machine is required. Therefore, a blind identification of instantaneous rotational speed, from the vibration signal, reduces the necessity of a priori knowledge. In that sense, there are mainly two limitations: (i) a lack of information about the multiplicity factor of the orders, due to generally the state-of-the-art approaches use the rotational speed, i.e. the fundamental order is known, and the extracted component is associated with the highest energy component; and (ii) how to ensure that the extracted instantaneous frequency (IF) is indeed related to the rotational speed. The proposed methodology solves the aforementioned problems using a normalized version of the angle-order map obtained by the velocity synchronous discrete Fourier transform (VSDFT), aiming to remove the need of a priori knowledge about the multiplicity factor of the spectral orders. In order to ensure that the extracted IF is highly related to rotational speed, it is assumed that the extracted IF most correlated to reference rotational speed produces the most stationary angle-order map. Therefore, two stationarity measures are proposed: kurtosis coefficient of variation (Kurtosis-CV) and correlation of angle instants based on principal component analysis (PCA index). The methodology is carried out using a simulated signal and a vibration signal from a

test rig under non-stationary operating conditions, where the proposed approach selects successfully the IF more related to rotational speed.

2 Theoretical Background

2.1 Instantaneous Frequency Extraction

Let $S(t,f)$ the spectrogram of a signal $x(t) \in \Re$, where (t,f) denotes time and frequency domains, respectively. The instantaneous frequency $f_{\max}(t)$, expressed in Hz, can be extracted by an algorithm of maxima tracking [5] defined as follows:

$$\begin{aligned} f_{\max}(t) &= \arg\max_{f}(S(t,f)) : \forall f \in \Delta f_n \\ \Delta f_n &= [f_{\max}(t-\delta_t)-\delta, f_{\max}(t-\delta_t)+\delta] \end{aligned} \tag{1}$$

where δ is a constant that controls the width of search interval, Δf_n. In order to avoid drawbacks with vibration signals that have closed orders two steps are needed: (i) the algorithm should be initialized in the global maximum of the time-frequency map, and (ii) a forward-backward search is made from that maximum. For the sake of simplicity in the rest of the paper the variable is introduced denoting the instantaneous frequency expressed in radians.

2.2 Order and Angular Domain Transform

Velocity Synchronous Discrete Fourier transform (VSDFT) is a parametric method that allows mapping a signal $x(t)$, into its order domain $\{\Omega\}$, using the instantaneous shaft speed $\omega(t)$ as a reference parameter, and it is defined as follows:

$$\Im(\Omega) = \int_{-\infty}^{\infty} x(t)\omega(t)\mathrm{e}^{-j\Omega\theta(t)}\mathrm{d}t \tag{2}$$

where $\theta(t) = \int \omega(t)\mathrm{d}t$, is the angular displacement, and the signal in angular domain $x(\alpha)$ is obtained by the computation of inverse discrete Fourier transform (IDFT) from $\Im(\Omega)$. Detailed explanation about the VSDFT and its analysis in discrete time can be found in [7].

Since the VSDFT performance depends on the accuracy of the extracted $\omega(t)$, the instantaneous frequency $\hat{\omega}(t) = \beta\omega(t)$ is used as reference speed, obtaining a scaled version such that $\arg\max_t(\hat{\omega}(t)) = 1$, where the order and angular axis are scaled by β and β^{-1} respectively. This scaled version of $\omega(t)$ allows mapping $x(t)$

to a "pseudo-angular domain", providing the advantage that any order could be used instead of basic rotational speed.

2.3 On the Angle-Order Map Stationarity

An angle-order map $A(\alpha, \Omega)$ is computed by means the spectrogram of $x(\alpha)$ with respect to Ω, and it is assumed that this map is highly stationary, for which the probability distribution does not present considerable changes through the angle domain. Thereby, it is possible to introduce two different measures of stationarity: the kurtosis coefficient of variation (CV) and eigenvalue analysis so called PCA. It is worth noting that the map is highly stationary only if the waveform of extracted instantaneous frequency is close to the actual rotational speed.

2.3.1 Kurtosis Coefficient of Variation

The kurtosis is computed per angle instant, $K = \{\kappa(\alpha_0), \kappa(\alpha_1), \ldots, \kappa(\alpha_{M-1})\}$, where $\kappa(\alpha_i)$ is the kurtosis for the α_ith angular instant, i.e. the kurtosis of $A(\alpha_i, \Omega)$ for all Ω in the order domain. Having that the energy into the angle-order map should be distributed in the orders, it is expected that $\kappa(\alpha_i)$ presents low variation at α_j, for all $i \neq j$. Therefore, the kurtosis based-index that quantifies the stationarity of the map is the CV of K defined as:

$$c_v(K|A(\alpha, \Omega)) = \sigma(\mathrm{K})/\mu(\mathrm{K}) \tag{3}$$

where $\sigma(\cdot)$ and $\mu(\cdot)$ stand the standard deviation and mean operators, respectively. It is important to notice that different scales per angular instants could affect the kurtosis, for which a statistically normalization per α_i is performed before kurtosis computation.

2.3.2 Correlation of Angle Instants

In practice the angle-order map $A(\alpha, \Omega)$, could be associated with a matrix in $\Re^{\Omega_b \times M}$ where Ω_b and M are the order bins and the amount of angular instants, respectively. In that sense, a PCA problem is understood in terms of the correlation between angular instants, being $X \in \Re^{M \times M}$ the correlation matrix associated to $A(\alpha, \Omega)$ and λ_i the ith eigenvalue of X. Thereby, λ_i represents the variability of α_ith angular instant, and in consequence, a stationarity index can be defined as:

$$\psi(A(\alpha,\Omega)) = \sum_{i=0}^{M-1} \lambda_i, \tag{4}$$

where a map is highly stationary if it presents low values of λ_i.

3 Experimental Set-up

In this work, blind instantaneous rotational speed estimation algorithm is introduced (Algorithm 1). Usually, the vibration signal presents a high broadband, therefore, it is necessary to define a narrow band of frequencies that comprise a reasonable amount of orders. Afterwards, an iterative search by partitions over frequency bands is included, where a set of extracted and scaled IF per partition is built, and the relationship between estimated IF and rotational speed is measured over its corresponding angle-order map. Lastly, the IF most related to rotational speed (i.e. the most accurate) is selected when the obtained angle-order map presents maximum stationarity.

Algorithm 1
Probabilistic identification of instantaneous rotational speed

Inputs: the vibration signal $x(t)$, and the work interval $[a, b]$

1. Compute the spectrogram of $x(t)$, noted as $S(t,f)$
2. Define an initial uniform partition for $i = 0$, $P_i = \{j\Delta p + a | j = 0, \ldots, J-1\}$ such that $J = 3$, where $\Delta p = (b-a)/(J-1)$ and J is the partition size.
3. Constrain the frequency domain of $S(t,f)$ to $[0, k\Delta p + a]$; for each j, resulting $\bar{S}_{i,j}(t,f)$.
4. Extract an IF per $\bar{S}_{i,j}(t,f)$ and scale it to the unity, obtaining $\hat{\omega}_{i,j}(t)$.
5. Compute $\Im_{i,j}(\Omega)$ which is the VSDFT using each $\hat{\omega}_{i,j}(t)$ as reference shaft speed.
6. Compute IDFT per $\Im_{i,j}(\Omega)$ obtaining the vibration signal in "pseudo-angular domain", noted as $x_{i,j}(\alpha)$.
7. Obtain the pseudo-angle-order map $\mathrm{A}_{i,j}(\alpha,\Omega)$ per $x_{i,j}(\alpha)$.
8. Compute the proposed stationarity measures, $c_v(\mathrm{K}|A_{i,j}(\alpha,\Omega))$ or $\psi(\mathrm{A}_{i,j}(\alpha,\Omega))$ per j.
9. Select the extracted IF $\hat{\omega}(t)$ with the minimum variability value noted ρ_i, as the most closed to the rotational speed.
10. Stop when $J = f_{b[a,b]}$, where $f_{b[a,b]}$ is the amount of frequency bins in $[a, b]$.

11. Construct a finer partition (i.e. $P_i \subseteq P_{i+1}$), $P_{i+1} = \{j\Delta p + a | j = 0, \ldots, J-1\}$, making $J = 2J^- - 1$, where J^- is the previous value of J. Increase $i = i + 1$, and then repeat step three.

Output: $\hat{\omega}(t)$

3.1 Probabilistic Identification of Instantaneous Rotational Speed

Proposed stationarity measures of $A(\alpha, \Omega)$, in Sect. 2.3, are related to estimation error between the estimated reference and the theoretical shaft speeds. This fact will be evidenced in numerical experiment, in Sect. 3.2. In practice, the algorithm converges for an iteration N_p when the size of the partition P_{N_p} is greater than the amount of frequency bins in the interval $[a, b]$, because all $\rho_i|_{i > N_p}$ are equal to ρ_{N_p}. In order to avoid unnecessary iterations, a stop criterion can be defined as $|\rho_{m_s} - \rho_{m_s+1}| < \varepsilon$ for $N_p > m_s > N_s$, where N_s is a fixed value and ε is small enough. The stop criterion allows an error estimation, in the sense that it does not assure that output $\hat{\omega}(t)$ is the best extracted from $S(t,f)$, but it reduces the partition size achieving a solution.

3.2 Numerical Experiment

A simulated vibration signal $x(t)$ is built as a superposition of orders {1, 2, 3, 7, 11.2}, with a theoretical shaft speed $\omega(t) = t^6 e(-4t)$ and a sampling frequency of 2.5 kHz. The signal is contaminated with additive white Gaussian noise (AWGN) with signal to noise ratio of 3 dB. Simulated signal and its corresponding rotational speed are shown in Fig. 1. The methodology includes a preprocessing stage, where the signal is low-pass filtered at 300 Hz with a 9th order Chebyshev filter and down-sampled to 625 Hz, because the rotational speed is associated to low spectral range. The work interval $[a, b]$ for the Algorithm 1, is [35, 300]Hz, because the maximum of the reference rotational speed is 30 Hz. Thereby, the selected interval ensures enough orders for the extraction task. The width of the search interval δ is fixed to 1 Hz and the STFT parameters are a Hanning window of 256 points and 1024 frequency bins. The working interval and window are fixed considering the minimum expected frequency in the signal, and the algorithm stops when the partition size is greater than the amount of frequency bins inside the considered interval.

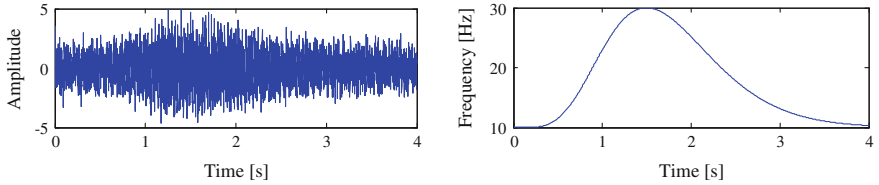

Fig. 1 Simulated vibration signal (*left*) and its shaft reference speed (*right*)

The experiment is carried out with the kurtosis and PCA approaches explained in Sect. 2.3, determining the measure that selects the best extracted IF, and afterwards, these measures are compared with the relative error between all the extracted rotational speed $\hat{\omega}_{i,j}(t)$, and the theoretical $\omega(t)$ by the following expression:

$$\xi = 100\left\|\hat{\omega}_{i,j}(t) - \omega(t)\right\|_2 \Big/ \|\omega(t)\|_2 \tag{5}$$

where the relative error is ξ and $\|\cdot\|_2$ stands for the norm 2.

3.2.1 Kurtosis Approach

In Fig. 2 (left) is shown minimum value ρ_i and relative error ξ per *i*th partition, and Fig. 2 (right) shows the CV $c_v(K|A_{8,j}(\alpha, \Omega))$ and the relative error ξ for all the cut frequencies for the 8th partition. The relative error shows that the best $\hat{\omega}(t)$ is estimated at first iteration; therefore the stop criterion, mentioned in Sect. 3.1, reduces significantly the amount of iterations. Nonetheless, the relationship between the relative error and the Kurtosis-CV for the finer partition Fig. 2 (right) is not

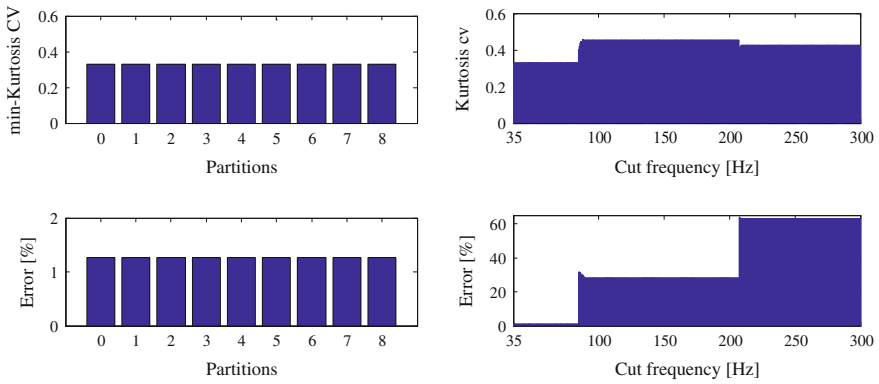

Fig. 2 Kurtosis-CV minimum (ρ_i) and relative error per partition (*left*), and the corresponding Kurtosis-CV and relative error for all the cut frequencies in the 8th partition (*right*)

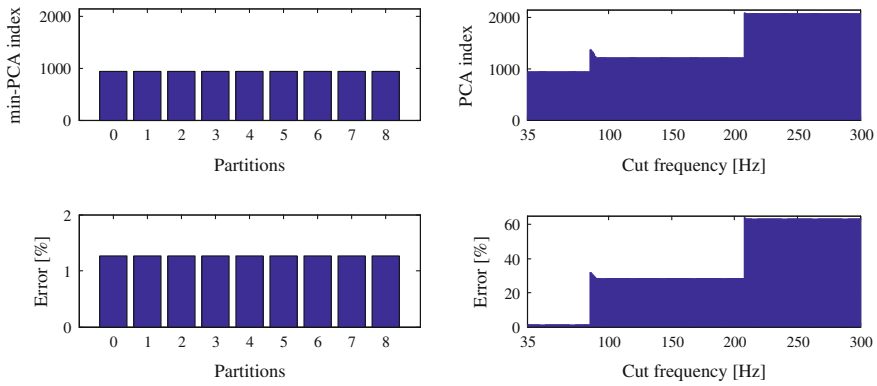

Fig. 3 Stationarity measure PCA based and relative error per partition (*left*), PCA based stationarity measure and relative error of the 8th partition for all the cut frequencies defined by that partition (*right*)

direct (i.e. the Kurtosis-CV does not have the same shape or is not highly correlated with the relative error).

3.2.2 PCA Approach

Aiming to compare with the kurtosis approach, the same experiment was performed using the stationarity measure PCA based. Figure 3 (left) shows the best value ρ_i and relative error per partition, and Fig. 3 (right) shows $\psi(A_{8,j}(\alpha, \omega))$ and relative error for all cut frequencies defined by the finer partition. As well as Kurtosis-CV, the best solution is achieved from the first iteration with a partition size of $J = 3$, taking into account that there are only 3 orders in the working interval. In consequence, the initial partition captures the best extracted IF from the spectrogram of the vibration signal.

In this case the PCA based stationarity measure and relative error are highly correlated, and hence, it captures the behavior of the relative error for all possible extracted IF from the vibration signal. As both measures select the same IF, $\hat{\omega}(t)$, the angle order-map is the same. As a result, the best IF, $\beta\hat{\omega}(t)$, extracted with Algorithm 1, is shown in Fig. 4 (left) as a white line inside of STFT, and Fig. 4 (right) shows the VSDFT and the angle-order map of the original signal using $\hat{\omega}(t)$ as reference shaft speed. In VSDFT is possible to observe the orders components 1, 2, 3 and 7, while the order 11.2 is not shown because it is outside of the working interval [35, 300]Hz. Since the angular domain transformation is done with $\hat{\omega}(t)$ where the maximum is the unity, the map is not exactly an angle-order map, inasmuch as the axis are scaled by the constant $\beta = 30$, as mentioned in Sect. 2.1. However, the desired effect of unfold the map by a transformation is hold.

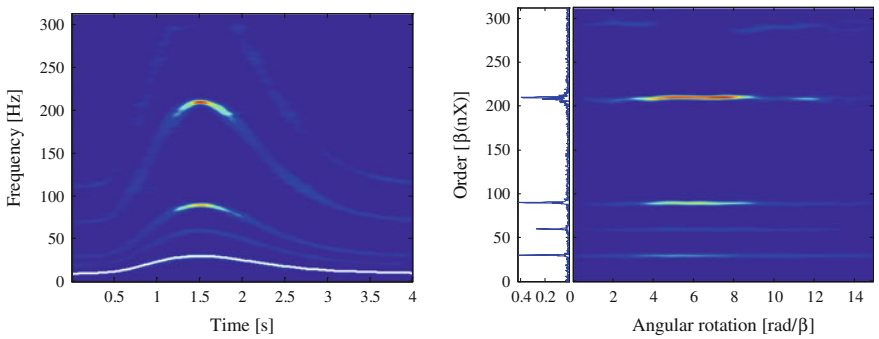

Fig. 4 Extracted rotational speed (*white line*) and the STFT of the vibration signal (*left*), the VSDFT and the angle-order map with the extracted IF as reference (*right*)

3.3 Test Rig Experiment

The laboratory experiment was carried out in a test rig composed by a DC electromotor of 2HP (with a maximum speed of 1800 rpm), two drilling wheels for emulating the shaft unbalance and rigid coupling for misalignment. It also has two bearing housings where the sensor can be located. The sensor is a standard accelerometer and it is located perpendicularly to shaft in horizontal direction. The measuring dynamic range was from 0 to 1800 rpm during 4 s, starting in steady state and reaching maximum operating condition, with a sampling frequency of 20 kHz. Vibration signal is preprocessed by means of a 9th order low-pass Chebyshev filter with cut frequency at 1.2 kHz, and down-sampled to 2.5 kHz. Considering that run-up test goes until 1800 rpm or 30 Hz. Inasmuch as the maximum speed is similar to the simulated signal case, the work interval used is [35, 300]Hz, and the signal is once again low-pass filtered to 300 Hz and down-sampled to 625 Hz. The STFT has 1024 frequency bins and a Hanning window of 256 points, and the parameter $\delta = 1$ Hz. The Fig. 5 shows the pre-processed vibration signal (left) and the test rig scheme (right). In this experiment the reference shaft speed was not measured; therefore, the IF extraction performance is defined using the two proposed

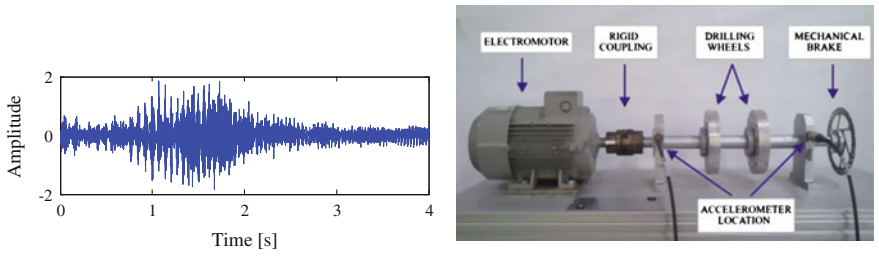

Fig. 5 Run-up pre-processed vibration signal (*left*) and test rig scheme [8] (*right*)

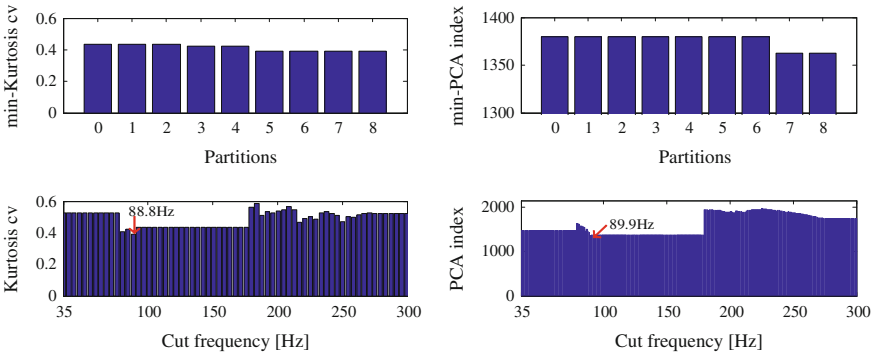

Fig. 6 Stationarity measures kurtosis-CV (*left*) and PCA index (*right*) per iteration and for the fifth and seventh partition respectively

angle-order map stationarity measures. A visual validation is performed in the obtained angle-order map by extracted IF.

3.3.1 Kurtosis and PCA Approaches

Figure 6 shows the minimum ρ_i for each partition P_i and all variability values obtained at 5th and 7th partition using Kurtosis-CV (left) and PCA index (right) respectively. Kurtosis-CV achieves the best extracted IF constraining the frequency with the low pass filter at a cutfrequency of 88.8 Hz, whereas PCA index uses 89.8 Hz, which means that both approaches provide a similar solution. Nevertheless, Kurtosis-CV converges faster than PCA index because those use five and seven partitions to achieve the optimal IF, respectively. In practical terms, Kurtosis-CV requires a partition size $J = 65$ and PCA index $J = 257$, which implies a high computational cost when PCA index is used. Moreover, it is possible find an optimal IF taking into account at least 10 orders in the work interval, which implies that the stop criterion can be applied after the fourth iteration i.e. $N_s = 3$, where the partition size is $J = 17$.

In order to compare the selected IFs for Kurtosis-CV and PCA index, Fig. 7 shows in (a) spectrogram of the original signal with the selected $\beta\hat{\omega}(\mathrm{t})|\beta = 30$, for Kurtosis-CV and PCA index, green and blue dash-dot lines respectively; and (b) a zoom in spectral range [5, 32]Hz, allowing to observe a light difference between optimal IF obtained with each approach, where the extracted IF using PCA index reaches a maximum frequency of 30 Hz, whereas by means Kurtosis-CV it does not happens. This result has a remarkable difference in angle-order map (shown in Fig. 8) because using PCA index (Fig. 8) is possible seeing a better definition of spectral orders such as 2 and 3. Nonetheless, the angle-order map obtained is similar using both approaches, for practical purposes i.e. difference energy between order components, and hence, PCA index based stationarity measure is a better

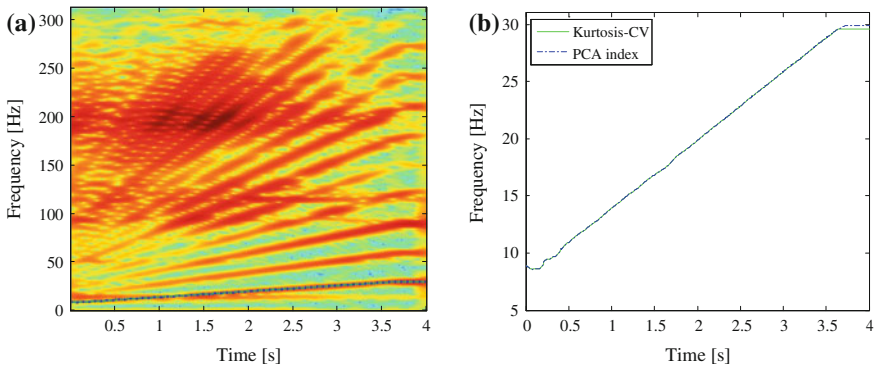

Fig. 7 Optimal estimated IF from non-stationary vibration signal using Kurtosis-CV (*green line*) and PCA index (*blue line*): **a** inside of spectrogram and **b** [5, 32]Hz

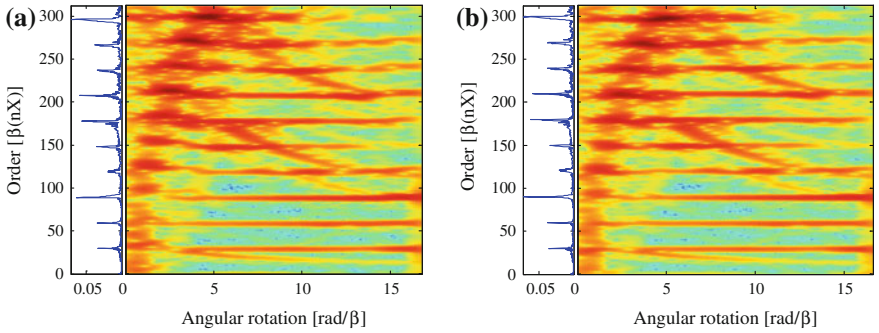

Fig. 8 Angle-order map obtained using the optimal estimated IF by **a** Kurtosis-CV, and **b** PCA index

indicator of the extracted IF quality than Kurtosis-CV because it is closer to relative error. This fact is evidenced in the numerical experiment. Yet, PCA index requires the computation of a correlation matrix which relates angular instants, and uses more iterations to reach the best IF, therefore, it implies high computational cost in comparison with Kurtosis-CV.

4 Conclusion

A blind instantaneous rotational speed extraction algorithm is proposed, which iteratively constructs a set of possible instantaneous rotational speeds, and selects the one that produces the most stationary angle-order map as the best. In order to measure the stationarity of the angle-order map, two approaches were proposed

(PCA index and Kurtosis-CV) and tested in a numerical and a real test rig experiments. Both measures achieve high accuracy in terms of the selected IF, but Kurtosis-CV employs a lower dimension, due to it does not require a computation as large as a correlation matrix. Since IF estimation could be limited by trade-off in time and frequency resolution of the spectrogram, as future work, the proposed algorithm will be tested under different parametric or non-parametric time-frequency representations, and more complex mechanical systems like wind turbines.

Acknowledgments The authors acknowledge to Universidad Nacional de Colombia for financial support by research project "Sistema de monitoreo de condición en turbinas de generación eléctrica", with HERMES code 23079.

References

1. Ge Z, Kruger U, Lamont L, Xie L, Song Z (2010) Fault detection in non-Gaussian vibration systems using dynamic statistical-based approaches. Mech Syst Sign Proc 24:2972–2984
2. Wang KS, Heyns SP (2011) Application of computed order tracking, Vold-Kalman filtering and EMD in rotating machine vibration. Mech Syst Sign Proc 25:416–430
3. Villa LF, Reñones A, Peran J-R, de Miguel LJ (2011) Angular resampling for vibration analysis in wind turbines under non-linear speed fluctuation. Mech Syst Sign Proc 25:2157–2168
4. Combet F, Zimroz R (2009) A new method for the estimation of the instantaneous speed relative fluctuation in a vibration signal based on the short time scale transform. Mech Syst Sign Proc 23:1382–1397
5. Zhao X, Kong Q, Guo Q (2008) Study of time-frequency order tracking of vibration signals of rotating machinery in changing state. IEEE Computer Society
6. Urbanek J, Barszcz T, Antoni j (2013) A two-step procedure for estimation of instantaneous rotational speed with large fluctuations. Mech Syst Sign Proc 38:96–102
7. Borghesani P, Pennacchi P, Chatterton S, Ricci R (2014) The velocity synchronous discrete fourier transform for order tracking in the field of rotating machinery. Mech Syst Sign Proc 44:118–133
8. Cardona-Morales O, Avendano LD, Castellanos-Dominguez G (2014) Nonlinear model for condition monitoring of non-stationary vibration signals in ship driveline application. Mech Syst Sign Proc 44:134–148

New Criteria for Adaptive Blind Deconvolution of Vibration Signals from Planetary Gearbox

Jakub Obuchowski, Agnieszka Wylomanska and Radoslaw Zimroz

Abstract In the paper performance of the adaptive blind deconvolution algorithm in application to a vibration signal with time-varying informative frequency band (IFB) is analyzed. The time-varying nature of the IFB might be caused by e.g. time-varying load or speed, time-varying signal-to-noise ratio (SNR), presence of other damages with distributed nature or time-varying transmission path, especially for source signals that propagate through a rolling element bearing or a planetary gearbox. Linear time-invariant filters cannot follow such phenomena, i.e. they might indicate too wide or too narrow frequency band as informative. Thus, the filtered signal contains too much noise or does not contain the whole information about the damage, respectively. Adaptive blind deconvolution is a time-varying filter which in each step tends to a filter that minimizes or maximizes given criterion of the deconvolved signal. In the classical version it maximizes kurtosis of the deconvolved signal, since high kurtosis (impulsiveness) is expected in the case of local damage. There exist also alternative measures that might provide equivalent results, or sometimes better in specific cases. Such combination of impulsiveness detection and ability of adaptation due to non-stationary operational conditions seems to be very promising. The methodology is illustrated by analysis of real data representing vibration acceleration of a heavy-duty rotating machinery (planetary gearbox used in

J. Obuchowski (✉) · R. Zimroz
Diagnostics and Vibro-Acoustics Science Laboratory, Wroclaw University of Technology, Na Grobli 15, 50-421 Wroclaw, Poland
e-mail: jakub.obuchowski@pwr.edu.pl

R. Zimroz
e-mail: radoslaw.zimroz@pwr.edu.pl; rzimroz@cuprum.wroc.pl

A. Wylomanska
Hugo Steinhaus Center, Institute of Mathematics and Computer Science, Wroclaw University of Technology, Janiszewskiego 14a, Wroclaw, Poland
e-mail: agnieszka.wylomanska@pwr.edu.pl

R. Zimroz
KGHM CUPRUM Ltd CBR, Sikorskiego 2-8, 53-659 Wroclaw, Poland

F. Chaari et al. (eds.), *Advances in Condition Monitoring of Machinery in Non-Stationary Operations*, Applied Condition Monitoring 4,
DOI 10.1007/978-3-319-20463-5_9

bucket wheel excavator) operating in industrial conditions of an open-pit mine. The analyzed signal reveals strong dependency between time-varying load applied to the gearbox and properties of cyclic impulses related to damage.

Keywords Planetary gearbox · Non-stationary operations · Local damage · Time-varying damage signature · Adaptive blind deconvolution

Contents

1 Introduction 112
2 Methodology 114
2.1 Adaptive Filter for Kurtosis Maximization 114
2.2 Generalization 116
3 Application of Adaptive Blind Deconvolution 117
4 Conclusion 123
References 123

1 Introduction

Vibration analysis is one of the most common technique used in the field of damage diagnostics in rotating machines. Diagnostics of machines operating in stationary conditions is a well-known problem and methods described in [1, 2] are sufficient. In the literature a lot of signal processing algorithms (e.g. filters) that help to extract information about the damage might be found. If the considered algorithm is a filter, then the information might be contained in both filter's coefficients or in the output of the filter, called a residual signal. For instance, AR gram represents variability of amplitude response of an autoregressive (AR) model fitted to subsequent short-time windows of the considered signal [3]. Another example of application of an AR model (extended to ARMA—AR moving average) to non-stationary signals is called TARMA (time-varying autoregressive moving average). In this method the coefficients of the ARMA model vary in time, for instance they might vary in a stochastic way (SP-TARMA) or deterministic (FS-TARMA) [4]. The way in which the coefficients vary provide an information about changes of the system. Another example where the information is contained in time-varying coefficients of a filter is an adaptive Schur algorithm [5–7]. In [6] authors proved that weighted summation of the derivatives of reflection coefficients in the adaptive Schur algorithm might provide an excellent indication of a damage in rolling element bearings. In this paper we also focus on an adaptive filter, but here the coefficients are calculated using different criterion than the mean square error (MSE). The choice of such filter is motivated by a possibility that the filter with time-varying coefficients might track time-varying structure of a vibration signal which occurs during non-stationary operations. Moreover, even under stationary operational regime in the case of local

damage the structure of the signal varies, i.e. a cyclic wide-band spectral excitation occurs. The use of an optimization criterion that incorporate the idea of impulsiveness, sparsity or non-Gaussianity detection might provide better noise cancellation. The term "noise" refers to both signal in frequency bands outside the informative band related to each impact and signal between impacts. In recent years, such kind of filters have found many applications in processing of non-stationary signals. For instance, adaptive filters driven by a maximum-kurtosis or maximum-skewness criterion were used for speech signal dereverberation [8–12] and ultra-wideband (UWB) signals processing [13].

Algorithm that incorporates a time-invariant filter with coefficients optimized using maximum-kurtosis criterion is called "minimum entropy deconvolution" (MED) and was originally developed for processing of seismic signals [14]. There are also similar algorithms based on non-Gaussianity, sparsity or impulsiveness detection and their applications [15–17]. In [15] a review on several different measures might be found. Since the problems and needs in seismic signals processing, speech signals dereverberation and vibration signals processing for damage detection are somewhat similar, such kind of a blind deconvolution has been also applied to machine diagnostics [18–24]. In this paper we investigate an adaptive blind deconvolution driven by criteria different than kurtosis. Problems in damage detection under non-stationary operations are often related with time-varying informative frequency band (IFB). It might vary from short to wide bandwidth or the IFB might even completely change during a sufficiently long measurement. Such variations of IFB might be caused by e.g. time-varying rotational speed or load. Even under constant speed and load regime the use of an adaptive filter might be beneficial. For instance, in a case of rolling element local damage the amplitude of the pulse train is time-varying [1] which might result in time-varying IFB. Moreover, the vibration signal might be contaminated by vibrations from another machines in the system. Frequency structure of such vibrations can also vary in time, thus cancellation of such contamination constitutes another problem that might be solved using an adaptive filter. If these problems are solved by the adaptive filter driven by the maximum-kurtosis criterion or another measure of sparsity, non-Gaussianity or impulsiveness then it would make it possible to establish an on-line condition monitoring system, since such algorithms often operate in real-time. In the paper we recall the adaptive algorithm with several criteria for update of coefficients and provide some interesting results related to the mentioned properties of the algorithm. Since there are a lot of variants of such adaptive filter and many ways to determine its parameters, we do not provide a meaningful comparison with many existing methods. Nevertheless, we compare the results with those obtained by certain existing methods and explain the differences.

The paper is structured as follows: In Sect. 2 the classical version of the adaptive filter driven by maximum-kurtosis criterion is recalled and its generalization is provided, as well as a discussion concerning the meaning of parameters and alternative versions of the algorithm. Section 3 contains results of application of the adaptive filter to real vibration signals from machines that operate in non-stationary operational conditions. The last section contains conclusions.

2 Methodology

2.1 Adaptive Filter for Kurtosis Maximization

In this section we recall the basic algorithm for calculation of coefficients of adaptive filter that maximizes kurtosis of residuals. The idea is presented in [8, 25, 26] and is based on a gradient-descent algorithm that maximizes the normalized fourth-order moment of linear prediction (LP) residuals. Originally, there are two versions of obtaining the output of the algorithm. The first one is to get the LP residual signal, use it to calculate coefficients of the adaptive filter upon the given gradient and obtain the final signal by applying the inverse LP filter. Alternative way of obtaining the final signal is to run two-filters instead of using the inverse LP filter, i.e. calculate the adaptive filter coefficients on the basis of LP residuals, copy the coefficients and apply the filter directly to the measured signal. On the other hand, in the literature related to damage diagnostics the step of impulsiveness enhancement is often preceded by LP-residuals step (called pre-whitening [27, 28]), but the inverse LP filter is not applied after impulsiveness enhancement. In this paper we follow this concept, i.e. we calculate coefficients of the adaptive filter that maximizes kurtosis (or other function) on the basis of LP residuals and the final signal is obtained just by application of the adaptive filter to the LP residuals.

Let x_n, $n = 1, \ldots, N$ and $\tilde{x}_n$, $n = 1, \ldots, N$ be the raw vibration signal obtained during data acquisition and the LP-residual signal, respectively. $\mathbf{h}(n) = [h_1(n), \ldots, h_L(n)]$ denotes the L-tap adaptive filter coefficients at time n. The final adaptive filter residuals $\mathbf{y}(n)$ at time n are calculated as follows [8, 25]:

$$y(n) = \mathbf{h}(n)^{\mathrm{T}} \tilde{\mathbf{x}}(n), \tag{1}$$

where $\tilde{\mathbf{x}}(n) = [\tilde{x}(n), \ldots, \tilde{x}(n - L + 1)]$. $\mathbf{h}(n)$ depends on the objective function $J(n)$ (called also the cost function [29]) which in the classical case is the normalized fourth-order moment, i.e. $J(n) = \frac{\mathbb{E}\{y^4(n)\}}{\mathbb{E}^2\{y^2(n)\}} - 3$ [8]. General equation for filter's coefficients update is:

$$\mathbf{h}(n + 1) = \mathbf{h}(n) + \mu f(n) \tilde{\mathbf{x}}(n), \tag{2}$$

where $\mu \in (0, 1)$ is the step-size and $f(n)$ is the feedback function. μ controls speed of the adaptation and $f(n)$ depends on the gradient of the objective function $J(n)$. The gradient is given by

$$\frac{\partial J}{\partial \mathbf{h}} = \frac{4(\mathbb{E}\{y^2\}\mathbb{E}\{y^3\mathbf{x}\} - \mathbb{E}\{y^4\}\mathbb{E}\{y\tilde{\mathbf{x}}\})}{\mathbb{E}^3\{y^2\}}. \tag{3}$$

Using the stochastic approximation technique we obtain [8, 29, 30]

$$\frac{\partial J}{\partial \mathbf{h}} \approx \frac{4(\mathbb{E}\{y^2\}y^3 - \mathbb{E}\{y^4\}y)}{\mathbb{E}^3\{y^2\}}\tilde{\mathbf{x}}. \tag{4}$$

Thus,

$$f(n) = \frac{4(\mathbb{E}\{y^2(n)\}y^3(n) - \mathbb{E}\{y^4(n)\}y(n))}{\mathbb{E}^3\{y^2(n)\}}, \tag{5}$$

where

$$\mathbb{E}\{y^k(n)\} = \beta\mathbb{E}\{y^k(n-1)\} + (1-\beta)y^k(n), \quad k = 2, 4. \tag{6}$$

$\beta \in (0, 1)$ controls smoothness of the moments estimates. In other words, $\mathbb{E}\{y^k(n)\}$ is estimated using an exponential moving average (exponential smoothing). The result of the adaptive filter depends on the parameters μ and β, as well as on the initial filter. Many authors propose μ to be close to 0, often between 10^{-9} and 10^{-3} [8, 10]. β should be close to 1, e.g. $\beta = 0.99$. High β gives smoother estimate and low β might cause the estimator highly dependent on the current output of the adaptive filter, thus it might be unstable. The initial filter is often suggested to be the L-tap identity filter, i.e. $h(0) = [1, \ldots, 0]$ [8]. The flow chart of the algorithm is presented in Fig. 1.

Such number of parameters exploited by this algorithm might disturb the reader. In an industrial implementation it is highly undesirable if an algorithm has to be carefully calibrated many times during monitoring of the system. Thus, there are some attempts to make the number of subjectively chosen parameters lower by incorporating known properties of the signal (e.g. short-time stationarity) or to

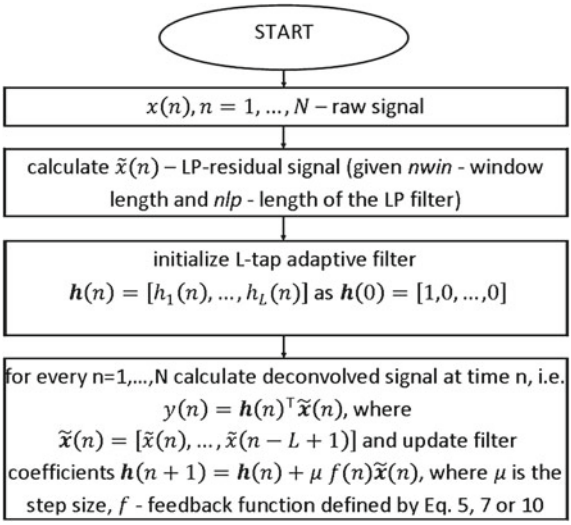

Fig. 1 Flow chart of the adaptive blind deconvolution algorithm

substitute them with parameters to which the result is less sensitive. Several researchers suggest that the time-domain implementation might provide poor results in terms of convergence and stability and provide the solution, which is the frequency-block implementation [10, 31]. The frequency-block implementation estimates $\mathbb{E}\{y^k(n)\}$ in a different way and the parameter β is substituted by block length. It allows to benefit from additional knowledge about the signal, because block length should follow length of a signal portion where the signal might be considered as stationary [8, 10]. In this approach also the output $y(n)$ is calculated block-by-block, thus it is updated once per block length instead of sample-by-sample. The parameter μ might be time-dependent and automatically fitted. The idea comes from [32] where the authors estimate the step-size in NLMS algorithm using temporary characteristics of the signal. Nevertheless, in this paper we present that the classical, time-domain implementation with appropriately chosen parameters might still provide interesting and motivating results, although the future work should be focused on automation of the methodology. This would make possible to implement it in real-time condition monitoring systems.

2.2 Generalization

In the literature related to filtering methods for signal of interest (SOI) extraction a lot of measures that quantify performance of the resulting SOI estimate might be found. One of the most classical ones is kurtosis, i.e. normalized fourth-order moment. Kurtosis is the basis of several method for indication of the IFB, i.e. Spectral Kurtosis, Kurtogram and Fast Kurtogram [33, 34]. This statistic has also been used to optimize parameters in the Morlet wavelet function [35]. Kurtosis is also used as the objective function for MED [14]—time-invariant equivalent of the adaptive filter based on kurtosis maximization that is described in Sect. 2. Over the years, researches found that kurtosis might not be the appropriate score function for certain applications. Thus, a number of alternative score functions have been introduced in the literature. For instance, one of the most general objective functions is the Gray's variability measure [16]. This function demonstrate many interesting properties, thus we refer to [16, 36] for them. Another interesting objective function is called D-norm, i.e. maximum of the absolute value of the normalized signal. It was used in [37] as an alternative to classical MED for seismic signal deconvolution. There are also other score functions that have been used in the literature related to damage diagnostics in gears and bearings, e.g. protrusion [38], sparsity [39], statistics based on quantiles or empirical cumulative distribution function, as well as the Jarque-Bera (JB) test statistic [40, 41]. In this paper we focus on the score functions driven by the Gray's variable norm, Jarque-Bera test statistic and the classical one—kurtosis. One of the most valuable properties of the JB test statistic is the fact that it incorporates not only kurtosis or only skewness, but both of them at the same time. Moreover, appropriate normalization of these

statistics takes into account different variance of kurtosis and skewness which is essential while signals of different length are compared [42, 43]. The cost function based on JB statistic is given by

$$J_{\mathrm{JB}}(n) = \frac{N}{6}\left(\left(\frac{\mathbb{E}\{y^3(n)\}}{\mathbb{E}^{\frac{3}{2}}\{y^2(n)\}}\right)^2 + \frac{1}{4}\left(\frac{\mathbb{E}\{y^4(n)\}}{\mathbb{E}^2\{y^2(n)\}} - 3\right)^2\right). \tag{7}$$

The constant $\frac{N}{6}$ does not change during adaptation, thus it might be omitted while only one signal is being analyzed. Such normalization might be usable when the equalization is applied to two or more signals of different lengths. The corresponding feedback function f_{JB} at time n related to the JB test statistic is as follows:

$$f_{\mathrm{JB}} = \frac{6\mathbb{E}^2\{y^3\}}{\mathbb{E}^4\{y^2\}}\left(\frac{\mathbb{E}\{y^2\}}{\mathbb{E}\{y^3\}}y^2 - y\right) + \left(\frac{2\mathbb{E}^2\{y^4\}}{\mathbb{E}^5\{y^2\}} - 6\frac{\mathbb{E}\{y^4\}}{\mathbb{E}^3\{y^2\}}\right)\left(\frac{\mathbb{E}\{y^2\}}{\mathbb{E}\{y^4\}}y^3 - y\right). \tag{8}$$

The time subscript has been omitted for simplicity of notation, although components of (8) depend on time point n.

The next cost function we analyze in this paper is the Gray's variable norm, which is defined as

$$J_{G(p,q)}(n) = \frac{\mathbb{E}\{|y|^p(n)\}}{\mathbb{E}^{\frac{p}{q}}\{|y|^q(n)\}}. \tag{9}$$

For interpretation and widely described properties of such norm we refer to [16]. When $p = 4$ and $q = 2$ it simplifies to well-known kurtosis. The feedback function $f_{G(p,q)}(n)$ related to $J_{G(p,q)}(n)$ is:

$$f_{G(p,q)}(n) = p\ \mathrm{sign}(y)\frac{\mathbb{E}\{|y|^p(n)\}}{\mathbb{E}^{\frac{p}{q}+1}\{|y|^q(n)\}}\left(\frac{\mathbb{E}\{|y|^q(n)\}}{\mathbb{E}\{|y|^p(n)\}}|y|^{p-1} - |y|^{q-1}\right). \tag{10}$$

Since (9) constitutes a family of measures, we only focus on particular p and q just to provide a general view on performance of the Gray's variable norm.

3 Application of Adaptive Blind Deconvolution

In this section we present results of application of the adaptive blind deconvolution driven by certain cost functions described in Sect. 2.2. The data we analyze is a vibration signal from a planetary gearbox used for to drive a bucket wheel in a bucket wheel excavator. This signal was analyzed in several previous works, e.g.

[44–48]. To avoid unnecessary redundancy we just recall basic parameters of the machine and signal. We refer to [44] for wider description. The excavation process is cyclic, during one cycle external load varies in wide range, so frequencies of components related to meshing phenomena vary in time, i.e. sinusoidal components are frequency modulated. Due to the average rotational speed of the sun gear and the numbers of teeth the fundamental gear mesh frequency is close to 435 Hz and variation generally does not exceed 5 %. The gearbox has not been inspected after the experiment, but the number of impacts in the acquired signal (11–12 impacts per 2.5 s) results in a fault frequency close to the arm frequency. The arm frequency is 4.67 Hz (upon an average rotational speed) and the task for a signal processing method is to extract a series of impulses that are spaced in time every 0.214 s.

The signal was acquired using an accelerometer, duration of the signal is 2.5 s and sampling frequency is 19,200 Hz. Every time series in the paper are normalized by their maximum absolute value. The time series and spectrogram are presented in Fig. 2. There are several high-energy harmonics related to gear mesh phenomena. Since frequency modulation of these components is barely visible here we refer to [47], where the frequency modulation property of a signal from a similar machine is widely described. There are also wideband cyclic excitations marked with arrows, mainly at 3000–5000 Hz. The impulses are different to each other, thus it is difficult to set a time-invariant frequency band for demodulation that covers all of the information and do not contain unnecessary noise. LP-residuals obtained using Hamming windows of length 10,000 samples and LP-filter order equal to 200 is presented in Fig. 3. It can be noticed that the harmonics related to gear mesh

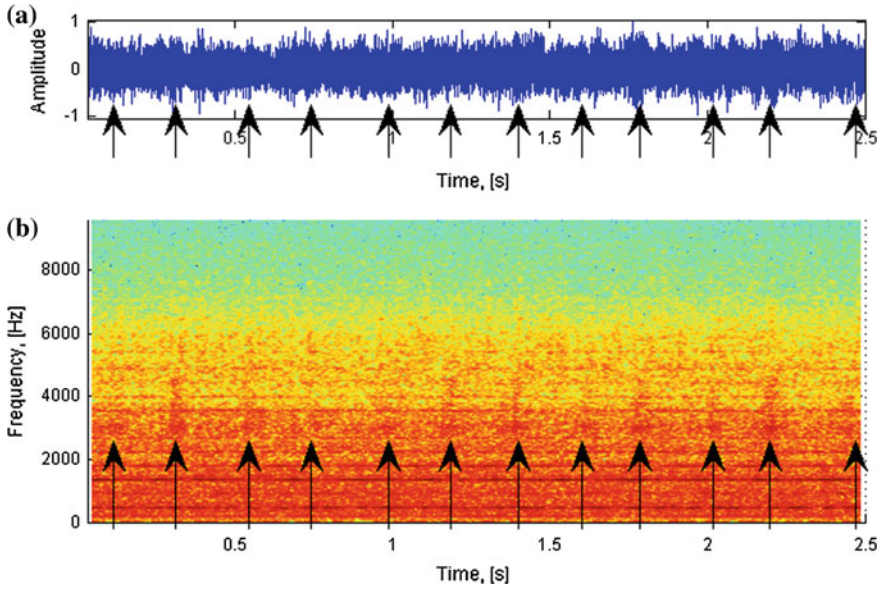

Fig. 2 Time series (**a**) and spectrogram (**b**) of the raw vibration signal from the planetary gearbox

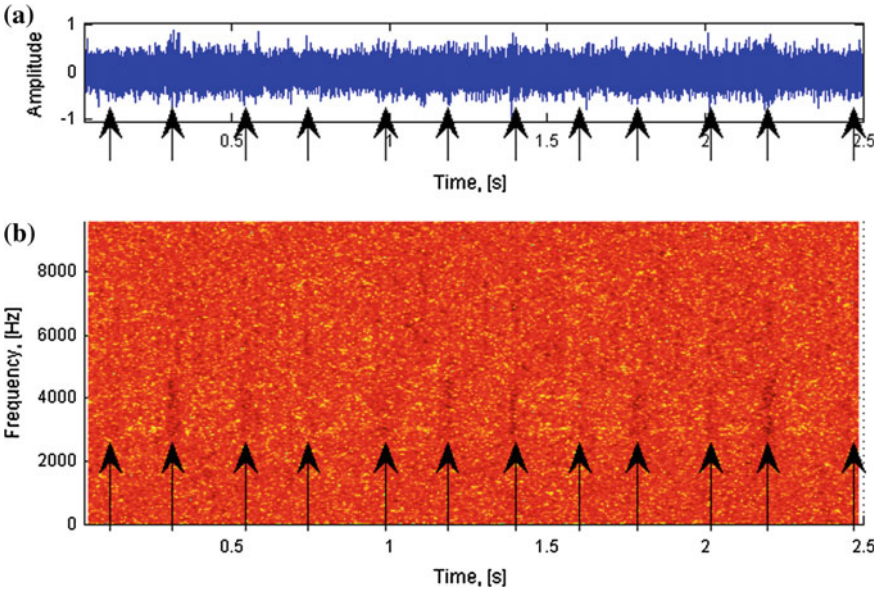

Fig. 3 Time series (**a**) and spectrogram (**b**) of the LP-residuals of the raw vibration signal from the planetary gearbox

phenomena are suppressed, but the signal is very noisy. This signal is the base for the blind deconvolution algorithms driven by several cost functions described in Sect. 2. Due to infinite number of cost functions described in Sect. 2 we present only results obtained using J_{JB} (Eq. 7) and Gray's variable norm with parameters $(p, q) \in \{(4, 2), (6, 2)\}$. Time series and spectrograms of the signals obtained using three mentioned cost functions are presented in Figs. 4 and 5, respectively.

In every case the starting filter is $h(0) = [1, \ldots, 1]$ and $\beta = 0.99$. The other parameters (μ, L) (L stands for length of the adaptive filter) of the adaptive filter are: $J_{\mathrm{JB}} - (0.05, 300)$, $J_{G(4,2)} - (0.02, 125)$ and $J_{G(6,2)} - (0.006, 150)$. The parameters are chosen to present the best results obtained for a particular method. The choice was preceded by comprehensive calculations using $\mu \in (2e-8, 1e-1)$ and $L \in (10, 1500)$, 720 pairs of parameters in total for every cost function. It can be noticed that the most impulsive time series with the smallest amount of noise is presented in Fig. 4c. It is worth to mention that most of these impulses actually follow the blurred impulses in the raw signal and LP-residuals. There are also some impulses that do not follow the time-spacing equal to 0.214 s. Their occurrence might be caused by artifacts due to the time-domain implementation of the algorithm (see [8, 31]) or another damage in early stage of development. Comparing spectrogram in Fig. 3b with spectrograms in Fig. 5 one can notice general behavior of the adaptive blind deconvolution algorithm for different step-sizes and different cost functions. Generally, the results follow the fact that some of impulses are wider in terms of their spectrum and some of them are narrower due to non-stationary

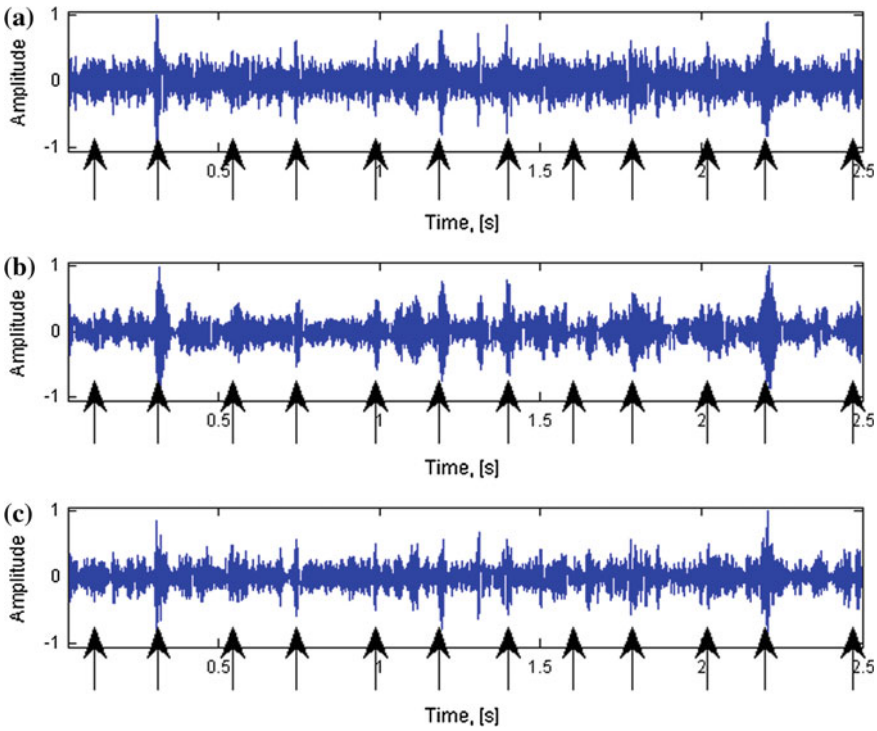

Fig. 4 Time series of the signals obtained using $J_{G(4,2)}$ (**a**), J_{JB} (**b**) and $J_{G(6,2)}$ (**c**)

operations of the considered planetary gearbox. The JB statistic value is larger for both kurtosis lower and higher that 3, thus its result looks different that others, e.g. at time points marked with the 2nd arrow (0.25 s) and 11th arrow (2.2 s). The results seems to be promising, but there is still some of issues that need an improvement before implementation of this method to industrial on-line monitoring system. To enhance the result and prove consistency with the SOI seen on the spectrogram in Fig. 2 in the band 3000–5000 Hz we performed additionally analysis of badnpassed signals. In Fig. 6 time series of all the previously presented signals are shown. These signals are bandpassed with cut-off frequencies 3000–5000 Hz. One can see that impulses marked with arrows appear in every signal, but the signals obtained using the adaptive blind deconvolution are much more impulsive than those in Fig. 6a, b. It is worth to mention that the arrows in every plot are in the same horizontal positions, although they are not equally spaced. Such dispersion might be caused by the fact that the rotational speed of the gearbox varies in time. It causes not only modulation of the deterministic components, but dispersion of time lapse between impulses as well.

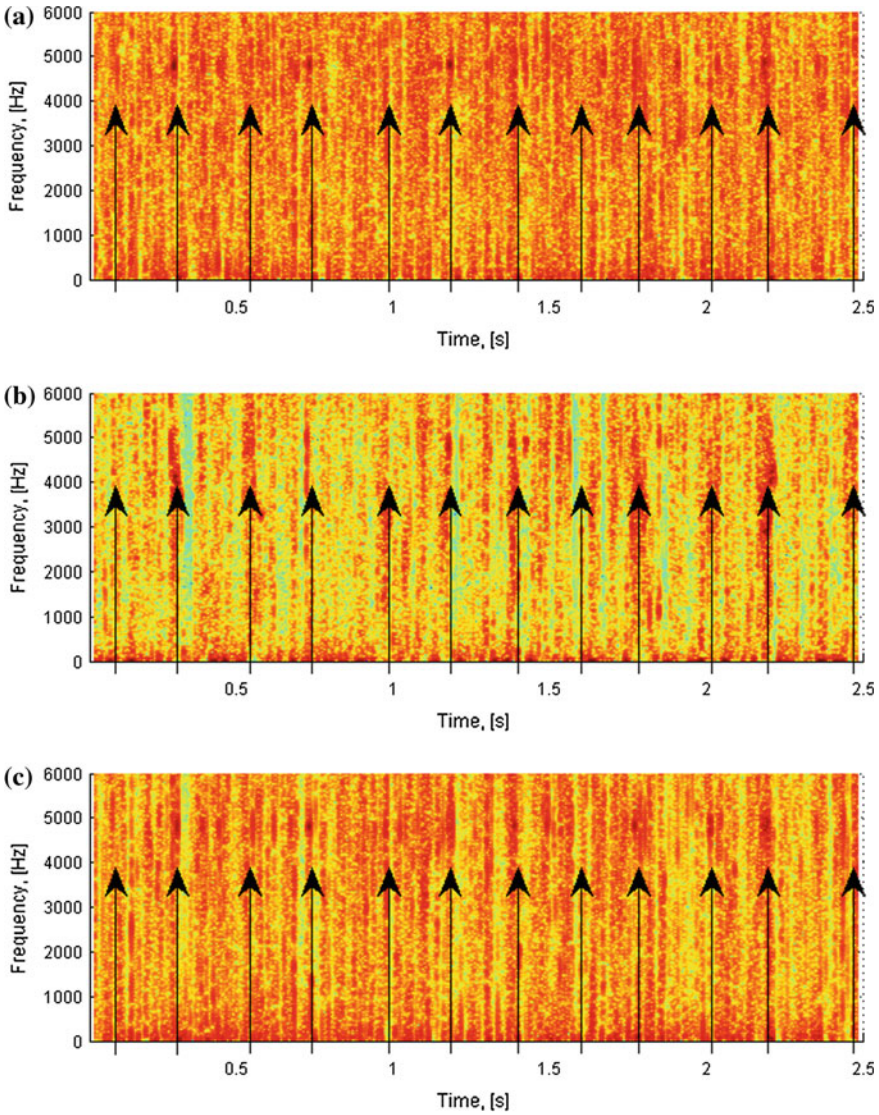

Fig. 5 Spectrograms of the signals obtained using $J_{G(4,2)}$ (**a**), J_{JB} (**b**) and $J_{G(6,2)}$ (**c**). Frequency axis is limited to 0–6000 Hz for better visibility

In the future it is crucial to provide an objective way to set the step-size and length of the filter. It would be also interesting to verify the adaptive blind deconvolution algorithm on a signal in which the IFB is narrow and highly varies in time.

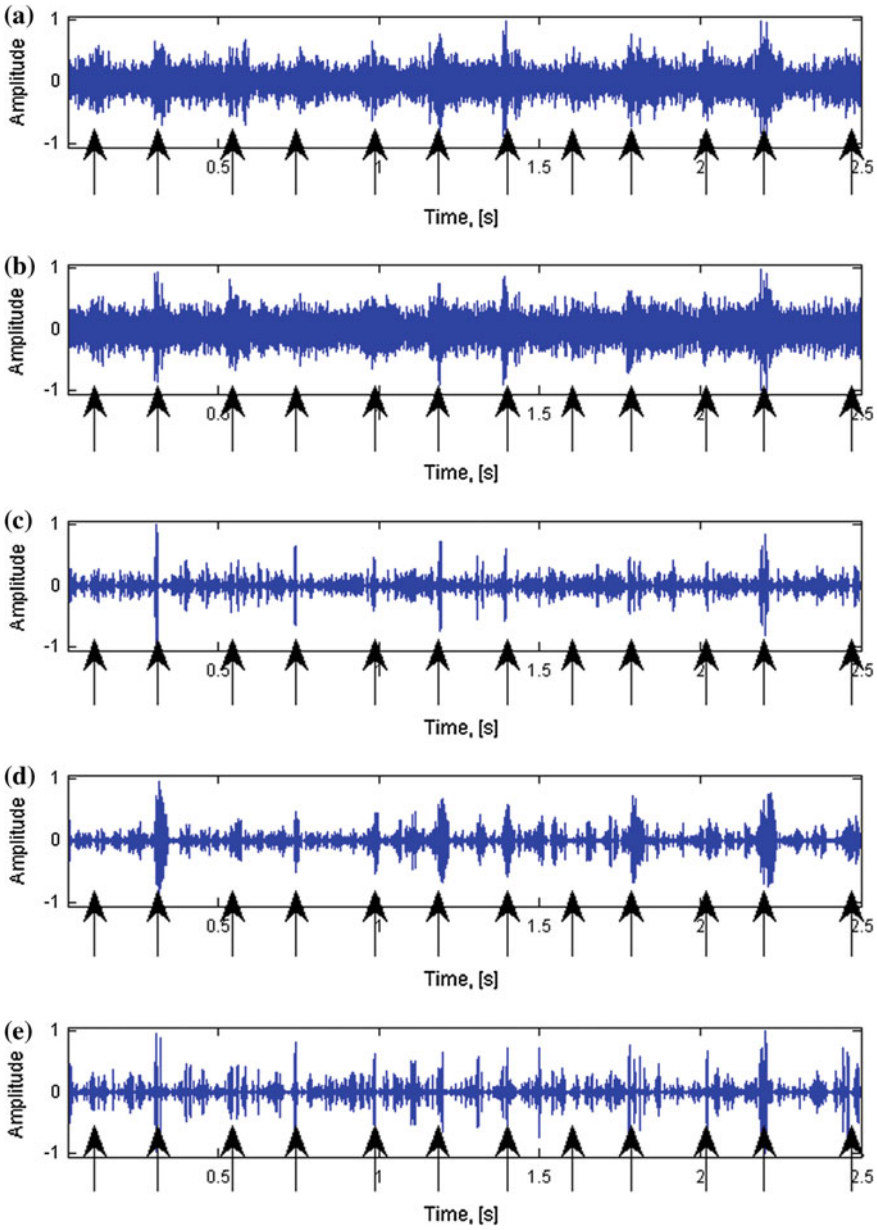

Fig. 6 Time series of band-pass filtered (3000–5000 Hz) signals: raw (**a**), LP-residual (**b**), signals obtained using $J_{G(4,2)}$ (**c**), J_{JB} (**d**) and $J_{G(6,2)}$ (**e**)

4 Conclusion

In this paper we presented application of the adaptive blind deconvolution to damage diagnostics in rotating machinery, namely a planetary gearbox that operates under a non-stationary regime. In the classical version, the algorithm searches for the time-varying filter that maximizes kurtosis of the residual signal. In the paper we recalled another criterion for adaptive blind deconvolution, as well as provided a gradient of a novel criterion based on the Jarque-Bera statistic. Such cost function incorporates not only a ratio of specific statistical moments, but it measures non-Gaussianity by incorporation of both skewness and kurtosis at the same time. The motivation for using the adaptive blind deconvolution algorithm is that it might extract the informative signal even if the impacts are not equally spaced in time and there are a lot of frequency modulated deterministic components that contaminate the damage signature. Since the algorithm implemented in time domain requires setting the step-size, filter length and parameters of LP filter, we just subjectively provided the best results obtained using kurtosis, Jarque-Bera statistic and Gray's variable norm with parameters $p = 6$ and $q = 2$ chosen among hundreds of parameters' combinations. Thus, it cannot be judged which criterion is the best for extraction of damage signature in the real vibration signal analyzed in Sect. 3. Every cost function lead to an impulsive signal in which the impulses meet the blurred impacts in the raw signal. However, it can be noticed that the Gray's variable norm ($p = 6$, $q = 2$) provided the most impulsive signal. The JB-driven adaptive deconvolution provided a signal which differs from two others in terms of time-frequency representation. It might be caused by the fact that the JB statistic is a general non-Gaussianity measure, i.e. it raises for kurtosis bot lower and larger than 3. Tu sum up, the results seems to be very promising and further work should be focused on objective criteria for parameters setting. It might be also interesting to analyze another cost functions which might exploit different signal characteristics than empirical moments.

Acknowledgements This work is partially supported by the statutory grant No. B40044 (J. Obuchowski). This research was supported in part by PL-Grid Infrastructure.

References

1. Randall RB, Antoni J (2011) Rolling element bearing diagnostics-A tutorial. Mech Syst Sig Proc 25:485–520
2. Samuel PD, Pines DJ (2005) A review of vibration-based techniques for helicopter transmission diagnostics. J Sound Vib 282:475–508
3. Martin N (1986) An AR spectral analysis of non-stationary signals. Signal Process 10:49–59
4. Poulimenos AG, Fassois SD (2006) Parametric time-domain methods for non-stationary random vibration modelling and analysis—a critical survey and comparison. Mech Syst Sig Process 20:763–816

5. Makowski RA, Zimroz R (2011) Adaptive bearings vibration modelling for diagnosis. Lecture notes in computer science (including subseries Lecture notes in artificial intelligence and lecture notes in bioinformatics), 6943 LNAI, pp 248−259
6. Makowski R, Zimroz R (2013) A procedure for weighted summation of the derivatives of reflection coefficients in adaptive Schur filter with application to fault detection in rolling element bearings. Mech Syst Sig Process 38:65–77
7. Makowski R, Zimroz R (2014) New techniques of local damage detection in machinery based on stochastic modelling using adaptive Schur filter. Appl Acoust 77:130–137
8. Gillespie BW, Malvar HS, Florencio DAF (2001) Speech dereverberation via maximum-kurtosis subband adaptive filtering. In: Proceedings 2001 IEEE International Conference on Acoustics, Speech, Signal Process. 6:3701−3704
9. Mosayyebpour S, Sayyadiyan A, Zareian M, Shahbazi A (2010) Single channel inverse filtering of room impulse response by maximizing skewness of LP residual. In: Proceedings of IEEE international conference on Signal Acquisition and Processing, pp 130–134
10. Mosayyebpour S, Sheikhzadeh H, Gulliver TA, Esmaeili M (2012) Single-microphone LP residual skewness-based inverse filtering of the room impulse response. IEEE Trans Audio Speech Lang Process 20(art. no. 6145617):1617–1632
11. Wu M, Wang DL (2006) A two-stage algorithm for one-microphone reverberant speech enhancement. IEEE Trans Audio Speech Lang Process 14:774–784
12. Yegnanarayana B, Murthy PS (2000) Enhancement of reverberant speech using LP residual signal. IEEE Trans Speech Audio Process 8:267–281
13. Paajarvi P, LeBlanc JP (2005) Online adaptive blind deconvolution based on third-order moments. IEEE Sig Process Lett 12:863–866
14. Wiggins RA (1978) Minimum entropy deconvolution. Geoexploration 16:21–35
15. Donoho DL (1981) On minimum entropy deconvolution. In: Findley DF (ed) Applied time series analysis. Academic, New York
16. Gray WC (1979) Variable norm deconvolution. Ph.D, thesis, Stanford University
17. Broadhead MK, Pflug LA (2000) Performance of some sparseness criterion blind deconvolution methods in the presence of noise. J Acoust Soc Am 107:885–893
18. Endo H, Randall RB, Gosselin C (2009) Differential diagnosis of spall vs. cracks in the gear tooth fillet region: experimental validation. Mech Syst Sig Proc 23:636–651
19. Barszcz T, Sawalhi N (2013) Fault detection enhancement in rolling element bearings using the minimum entropy deconvolution. Arch Acoust 37:131–141
20. Sawalhi N, Randall RB, Endo H (2007) The enhancement of fault detection and diagnosis in rolling element bearings using minimum entropy deconvolution combined with spectral kurtosis. Mech Syst Sig Process 21:2616–2633
21. Endo H, Randall RB (2007) Enhancement of autoregressive model based gear tooth fault detection technique by the use of minimum entropy deconvolution filter. Mech Syst Sig Proc 21:906–919
22. Ricci R, Borghesani P, Chatterton S, Pennacchi P (2012) The combination of empirical mode decomposition and minimum entropy deconvolution for roller bearing diagnostics in non-stationary operation. In: Proceedings of the ASME design engineering technical conference, Chicago, pp 723–730
23. Lee J-Y, Nandi AK (1998) Blind deconvolution of impacting signals using higher-order statistics. Mech Syst Sig Process 12:357–371
24. McDonald GL, Zhao Q, Zuo MJ (2012) Maximum correlated kurtosis deconvolution and application on gear tooth chip fault detection. Mech Syst Sig Process 33:237–255
25. Cichocki A, Amari S, Thawonmas R (1996) Blind signal extraction using self-adaptive non-linear Hebbian learning rule. In: Proceedings of international symposium on nonlinear theory and its applications, NOLTA-96, Kochi, Japan, pp 377–380
26. Cichocki A, Thawonmas R, Amari S (1997) Sequential blind signal extraction in order specified by stochastic properties. Electron Lett 33:64–65

27. Sawalhi N, Randall RB (2011) Vibration response of spalled rolling element bearings: observations, simulations and signal processing techniques to track the spall size. Mech Syst Sig Process 25:846–870
28. Sawalhi N, Randall RB (2005) Spectral kurtosis enhancement using autoregressive models. In: Australasian congress on applied mechanics, ACAM, pp 231–236
29. Cichocki A, Amari SI (2002) Adaptive blind signal and image processing: learning algorithms and applications. Wiley, New York
30. Tanrikulu O, Constantinides AG (1994) Least-mean kurtosis: a novel higher-order statistics based adaptive filtering algorithm. Electron Lett 30:189–190
31. Haykin S (2002) Adaptive filter theory, 4th edn. Prentice Hall, New York
32. Shin H-C, Sayed AH, Song W-J (2004) Variable step-size NLMS and affine projection algorithms. IEEE Signal Process Lett 11:132–135
33. Antoni J, Randall RB (2006) The spectral kurtosis: application to the vibratory surveillance and diagnostics of rotating machines. Mech Syst Sig Process 20:308–331
34. Antoni J (2006) The spectral kurtosis: a useful tool for characterising non-stationary signals. Mech Syst Sig Process 20:282–307
35. Lin J, Zuo MJ (2003) Gearbox fault diagnosis using adaptive wavelet filter. Mech Syst Sig Process 17:1259–1269
36. Lambert RH (1996) Multichannel blind deconvolution: fir matrix algebra and separation of multipath mixtures. University of Southern California, Los Angeles
37. Cabrelli CA (1985) Minimum entropy deconvolution and simplicity: a noniterative algorithm. Geophysics 50:394–413
38. Barszcz T, Jablonski A (2011) A novel method for the optimal band selection for vibration signal demodulation and comparison with the Kurtogram. Mech Syst Sig Process 25:431–451
39. Tse PW, Wang D (2011) The sparsogram: a new and effective method for extracting bearing fault features. In: Prognostics and system health management conference (PHM-Shenzhen), art. no. 5939587, p 6
40. Obuchowski J, Wylomanska A, Zimroz R (2014) Selection of informative frequency band in local damage detection in rotating machinery. Mech Syst Signal Process 48:138–152
41. Obuchowski J, Wylomanska A, Zimroz R (2013) Stochastic modeling of time series with application to local damage detection in rotating machinery. Key Eng Mat 569–570:441–448
42. Bera AK, Jarque CM (1981) Efficient tests for normality, homoscedasticity and serial independence of regression residuals. Monte Carlo Evid Econ Lett 7:313–318
43. Jarque CM, Bera AK (1980) Efficient tests for normality, homoscedasticity and serial independence of regression residuals. Econ Lett 6(3):255–259
44. Dybala J, Zimroz R (2014) Empirical mode decomposition of vibration signal for detection of local disturbances in planetary gearbox used in heavy machinery system. Key Eng Mat 588:109–116
45. Zimroz R, Bartkowiak A (2011) Investigation on spectral structure of gearbox vibration signals by principal component analysis for condition monitoring purposes. J Phys Conf Ser 305(art. no. 012075)
46. Zimroz R, Bartkowiak A (2013) Two simple multivariate procedures for monitoring planetary gearboxes in non-stationary operating conditions. Mech Syst Sig Process 38:237–247
47. Zimroz R, Millioz F, Martin N (2010) A procedure of vibration analysis from planetary gearbox under non-stationary cyclic operations for instantaneous frequency estimation in time-frequency domain. In: 7th international conference on condition monitoring and machinery failure prevention technologies 2010, CM 2010/MFPT 2010, 2, pp 1133–1145
48. Bartelmus W, Zimroz R (2009) Vibration condition monitoring of planetary gearbox under varying external load. Mech Syst Sig Process 23:246–257

Automatic and Full-Band Demodulation for Fault Detection—Validation on a Wind Turbine Test Rig

Marcin Firla, Zhong-Yang Li, Nadine Martin and Tomasz Barszcz

Abstract This paper proposes three algorithms for automatic diagnosis of mechanical system. First of all, an angular resampling with speed measurement correction is introduced. Secondly, a method for the association of detected spectral patterns with the characteristic frequencies of the investigated system is presented. This approach takes into consideration the slippage phenomenon of rolling element bearings. Thirdly, a full-band sideband demodulation method is proposed. It features with multi-rate filtering and offers new health indicators. All methods are applied on the real-world signals of a wind turbine test rig for diagnosis a bearing fault. The comparison of results shows the advantages of the proposed algorithms over well-known health indicators.

Keywords Signal processing · Demodulation · Condition monitoring · Angular resampling · Characteristic fault frequencies · Kinematic · Amplitude and frequency modulations · Wind turbine

M. Firla (✉) · Z.-Y. Li · N. Martin
Univ. Grenoble Alpes, GIPSA-Lab, F-38000 Grenoble, France
e-mail: marcin.firla@gipsa-lab.grenoble-inp.fr

Z.-Y. Li
e-mail: zhong-yang.li@gipsa-lab.grenoble-inp.fr

N. Martin
e-mail: nadine.martin@gipsa-lab.grenoble-inp.fr

M. Firla · Z.-Y. Li · N. Martin
CNRS, GIPSA-Lab, F-38000 Grenoble, France

T. Barszcz
Faculty of Mechanical Engineering and Robotics, AGH University of Science and Technology, al. Mickiewicza 30, 30-059 Kraków, Poland
e-mail: tbarszcz@agh.edu.pl

F. Chaari et al. (eds.), *Advances in Condition Monitoring of Machinery in Non-Stationary Operations*, Applied Condition Monitoring 4,
DOI 10.1007/978-3-319-20463-5_10

Contents

1 Introduction 128
2 Angular Resampling 129
3 Characteristic Fault Frequency Association 130
3.1 Association Algorithm 131
4 Sideband Demodulation 132
5 Case Study 133
5.1 Characteristic Frequency Association Results 134
5.2 Sideband Demodulation Results 135
5.3 Comparison with Traditional Health Indicators 135
6 Conclusions 137
References 138

1 Introduction

An automatic interpretation of a big amount of data is crucial for health monitoring of complex systems such as wind turbines. The Condition Monitoring System (CMS) is a solution using automated data acquisition to detect the change in the health of the investigated system [1–4]. Modern CMSs have to achieve a good balance between the precision of diagnosis and the amount of information taken into account. The proposition of relevant fault features is therefore essential.

In the case of wind turbines, components such as rolling element bearings, gearboxes, and generators have to be replaced during the lifetime of a wind turbine in order to achieve its assumed duration [1]. The faults of these components can be characterized on the spectrum by the modulation sidebands around the characteristic fault frequencies [5]. Therefore the sideband demodulation analysis is an efficient tool for the diagnosis in this context [6, 7].

In this paper, we propose two steps of an automatic fault diagnosis method. The first step is an association of the detected spectral patterns in the signal with the characteristic fault frequencies of the mechanical components. The second step is a sideband demodulation method to deduce health indicators highly indicative of faults. The proposed method is fully automatic since both steps are data-driven algorithms based on an automatic harmonic and sideband detection algorithm [8].

In order to cancel the non-stationarity caused by rotational speed fluctuation, we firstly propose a new angular resampling approach which can tolerate and correct the wrong tachometer measurements. It serves as a pre-processing step of the proposed method.

All the above mentioned algorithms belong to an automatic full-band spectrum analysis tool called AStrion. The data-driven property of the proposed method is consistent with the goal of AStrion—the independence of the functionality. The independence is a crucial issue for the implementation of AStrion in innovative CMSs.

The paper is organized as follows. Section 2 presents the angular resampling method. Section 3 elaborates on the automatic characteristic fault frequencies association and Sect. 4 describes an original approach to signal demodulation. Section 5 presents the results of the methods applied on real-world data and a comparison with the traditional diagnostic approaches. Section 6 gives the conclusions and future perspectives.

2 Angular Resampling

In order to cancel the non-stationary effect due to a varying rotational speed, the signal is usually resampled with an equidistant angular rate [9] using the tachometer signals from which we can extract the instantaneous phase. Note the impulsive raw tachometer signal as $I[n]$ (at instant $[n]$) which contains an impulse every $\Delta\phi$ radius of rotation, and n_i as the time instant of the ith impulse. The duration $\Delta T[i]$ between two neighborhood impulses can be obtained by differentiating n_i. The rotational speed $V[i]$ proportional to the real phase shift $\Delta\phi[i]$ as

$$V[i] = \Delta\phi[i]\frac{F_{s_I}}{\Delta T[i]} \tag{1}$$

with F_{s_I} the sampling frequency of the tachometer signal.

Since the rotational speed in a real machine cannot change drastically, the speed measurement errors can be detected by finding the outliers of the rotational speed.

Theorem 1 *The outlier $[i]$ in the rotational speed measurement is considered as wrong. We thus assume true rotational speed equals to the average rotational speed $\overline{V}$. The real phase shift should be $\Delta\phi[i] = \Delta\phi\frac{\Delta T[i]}{\overline{\Delta T}}$.*

Theorem 2 *For non-outlier measurements, the variations of the speed are considered as correct measurements, and can be calculated from $T[i]$ according to (1). Each waveform duration $\Delta\phi[i]$ corresponds to a unit phase shift $\Delta\phi$.*

Based on the above assumptions, we propose to distinguish the two types of variations of $V[i]$ by identifying and correcting the outliers of the measurements. The method gives a correct estimation of the phase shift $\Delta\phi[i]$ and the rotational speed $V[i]$ in an iterative way. In each iteration p the algorithm consists of 3 steps.

Step 1: Calculate the z-score of all the measurements,

$$Z_p[i] = \frac{V[i] - \bar{V}_p}{\sigma_{V_p}}, \quad i = 1, \ldots, N_\delta \tag{2}$$

where $\bar{V}_p$ and σ_{V_p} are respectively the mean and the standard deviation of all the correct waveform duration measurements $\mathbf{O}_p$

$$\mathbf{O}_p = [1, \ldots, N_\delta] \backslash \mathbf{X}_{p-1}, \tag{3}$$

where $\mathbf{X}_{p-1}$ is the set of waveform indices which are identified as wrong measurements (outliers) in the previous iteration $(p-1)$.

Step 2: If the variation of the speed $cv_p = \frac{\bar{V}_p}{\sigma_{V_p}}$ is inferior to a threshold η_{cv} (normally $10^{-6} \leq \eta_{cv} \leq 10^{-1}$), the speed measurement is considered outlier-free. Thus the algorithm terminates. Otherwise, it goes to Step 3.

Step 3: Locate the extrema x_p of the z-score $Z_p[i]$ and update the outlier set by $\mathbf{X}_p = \mathbf{X}_{p-1} \bigcup \{x_p\}$. Correct the angle shift $\Delta\phi[i]$ and the rotational speed $V[x_p]$ according to (1).

Finally, the interpolation of time domain signal $y[n]$ (sampled at F_{s_y}) is performed to obtain the resampled signal $y_\theta[\mu]$ in order domain [9].

3 Characteristic Fault Frequency Association

This section proposes an association algorithm of fault frequencies characteristic for investigated system with patterns detected in the analysed signal. For the pattern identification of harmonic series and modulation sideband series in the spectrum of a signal the method proposed by Gerber et al. [8] has been used. Its final results include fundamental frequency for harmonic series, central and modulation frequency for sidebands series, as well as energy and density of each series.

The rotating machinery under operation generates characteristic frequencies related to the rotational speed of the shaft V_r. The definition of characteristic frequencies corresponding to mechanical components such as shafts, gearboxes, and rolling elements bearings is presented in Table 1, where z is the number of teeth of gear, n_r is the number of rolling elements, d_r is the diameter of rolling element, d_p is the pitch diameter, and ϕ is the angle of the load from the radial plane.

Formulas presented in Table 1 allow for calculating theoretical values, however the real values can vary slightly. The important difference between calculated and measured values occurs in the case of rolling element bearings. The model used for calculation does not assume slippage phenomenon, which is always present in running bearings. According to [11] a random variation of theoretical characteristic fault frequencies is of the order 1–2 %.

Table 1 Formulas for calculating selected characteristic fault frequencies [10]

Fault frequency name	Formula
Shaft speed frequency	$\mathrm{SSF} = V_\mathrm{r}$
Gear mesh frequency	$\mathrm{GMF} = V_\mathrm{r} \cdot z$
Ball-pass frequency of outer race	$\mathrm{BPFO} = \frac{n_\mathrm{r} V_\mathrm{r}}{2}\left\{1 - \frac{d_\mathrm{r}}{d_\mathrm{p}}\cos(\phi)\right\}$
Ball-pass frequency of inner race	$\mathrm{BPFI} = \frac{n_\mathrm{r} V_\mathrm{r}}{2}\left\{1 + \frac{d_\mathrm{r}}{d_\mathrm{p}}\cos(\phi)\right\}$
Fundamental train frequency	$\mathrm{FTF} = \frac{V_\mathrm{r}}{2}\left\{1 - \frac{d_\mathrm{r}}{d_\mathrm{p}}\cos(\phi)\right\}$
Double ball spin frequency	$\mathrm{BSF2} = \frac{V_\mathrm{r} \cdot d_\mathrm{p}}{d_\mathrm{r}}\left\{1 - \left(\frac{d_\mathrm{r}}{d_\mathrm{p}}\cos(\phi)\right)^2\right\}$

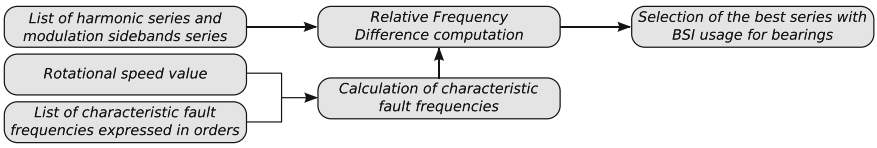

Fig. 1 Flowchart of the characteristic fault frequency association algorithm

3.1 Association Algorithm

Figure 1 presents the steps performed for each characteristic frequency in order to find the best suited series representing it.

In the case of shaft speed and gear mesh frequencies the association is done by finding the series with the lowest Relative Frequency Difference:

$$\mathrm{RFD}_i = \frac{f_{d,i} - f_{t,i}}{f_{t,i}} 100\,\% \tag{4}$$

where i is the index of the harmonic series, $f_{d,i}$ is the fundamental frequency of the series detected in investigated signal, $f_{t,i}$ is the theoretical frequency.

For rolling element bearing frequencies the additional parameter is calculated:

$$\mathrm{BSI}_i = \frac{\frac{E_i}{E_{\max,i}} + \mathrm{den}_i}{2} \tag{5}$$

where E_i is the energy of the series under investigation, E_max is the energy of the series with the highest energy among the series which met the condition $\mathrm{RFD}_i \leq 2\,\%$, and den_i is the density of the series. Finally, the series with the highest *BSI* is associated with characteristic fault frequency, which has been decided after inspecting numerous examples.

4 Sideband Demodulation

In this paper we propose a fully automatic demodulation method to investigate an arbitrary spectral band. The vibration signal $y[n]$ is considered as the sum of a wide-band random part $e[n]$ and a band-limited deterministic part $s[n]$. The latter is modulated in amplitude by $A[n]$ and in frequency by $F[n]$

$$A[n] = A_0(1 - \alpha \cos(2\pi f_a n)), \quad F[n] = f_0 + \beta f_\Phi \cos(2\pi f_\Phi n). \tag{6}$$

where A_0 represents the average amplitude, α is the amplitude modulation index and f_a the frequency of the amplitude modulation function. f_0 represents the carrier frequency which depends on the rotational speed and the resolution of the tachometer. β is the frequency modulation index and f_Φ is the frequency of the frequency modulation index.

The demodulation algorithm starts by applying a band-pass filter around the carrier frequency f_0 and end up by calculating the amplitude and the frequency modulation functions from the demodulated signal.

The filter is applied over a filter band $\mathbf{B} = [f_{\text{inf}}, f_{\text{sup}}]$, where f_{sup} the upper and f_{inf} the lower bounds are determined by

$$[f_{\text{inf}}, f_{\text{sup}}] = f_0 + [K_{\text{inf}}, K_{\text{sup}}] \times f_\Phi, \quad K_{\text{inf}} \in \mathbb{Z}^-, \quad K_{\text{sup}} \in \mathbb{Z}^+ \tag{7}$$

where f_Φ, f_0, K_{inf} and K_{sup} are estimated by an automatic sideband detection algorithm [8].

In order to design a stable filter which satisfies the desired performance even if the normalized bandwidth is very small or if the normalized filter band is very close to extreme values (0 and/or 0.5), we propose a new multi-rate filtering technique, which automatically decomposes a difficult filtering task into N_q iterations. Each of them is constituted by a chain of three essential operations:

Frequency shifting which applies a negative frequency shift $-\Delta f_q$ to the entire frequency contents; ***Filtering*** which filters over the target filter band $\mathbf{B}_q$; And ***down-sampling*** which decimates the signal by a factor D_q.

Based on these 3 operations, the iterations of the algorithm are arranged as follows

1. $q = 1$, $\mathbf{B}_0 = \mathbf{B}$, $y_0[n] = y[n]$ and $F_{s,0} = F_{s,y}$.
2. Verify if the stability criterion of the elliptic filter (0.005 dB of pass-band ripple and −80 dB of roll-off) is satisfied over $\mathbf{B}_q$. If so, perform a filtering operation over $\mathbf{B}_q$ on $y_{q-1}[n]$ to get the filtered signal $y_{\mathbf{B}}[n]$; $F_s = F_{s,q}$; and exit, otherwise go to Step (4).
3. Perform a frequency shifting operation: Apply a Butterworth filter over $\left[\Delta f_q, \frac{F_{s,q-1}}{2}\right]$ on $y_{q-1}[n]$ and carry out a frequency shifting by $-\Delta f_q$ to yield $y_{\text{shift},q}[n]$; $\mathbf{B}_q = \mathbf{B}_{q-1} - \Delta f_q$.

4. Perform a down-sampling operation: Apply a Butterworth filter over $\left[0, \frac{F_{s,q-1}}{2D_q}\right]$ on $y_{q-1}[n]$, and down-sample the signal by D_q; $F_{s,q} = \frac{F_{s,q-1}}{D_q}$.
5. Update the signal for the next iteration $y_{q+1}[n] = y_{\text{down},q}[n]$. Increment the iteration index $q \leftarrow q + 1$ and go to Step (2).

Such a method is able to automatically choose the optimal number of iterations and the configurations. The filters are designed at the highest orders which satisfy the stability criterion: the maximum modulus of all the poles does not exceed 0.996 for an elliptic filter, or 0.95 for a Butterworth filter. The filter band is considered too narrow if the highest order of a stable filter is below a given value. In this situation, the down-sampling and the frequency shifting operations are required.

The overall down-sampling rate D depends on the final sampling frequency $F_s = C \cdot \Delta B$ where C is a factor between 4 and 10. D is the closest integer to $\frac{F_{sy}}{F_s}$ factorized into $L^{(2)}$ factors of 2 and $L^{(3)}$ factors of 3. All the factors are alternatively arranged in a vector $\mathbf{d}$. The down-sampling rate D_q in each downsampling operation q is the product of L_q factors with L_q defining the narrowest band $\left[0, (F_{s,q-1})/(2D_q)\right]$ where a low-pass Butterworth filter satisfies the stability criterion. $\mathbf{d}$ is then updated by removing the first L_q factors.

The frequency shifting operations will carry the filter band $\mathbf{B}$ to $(\mathbf{B} - f_{\text{inf}})$ where the inferior frequency bound is 0. The total frequency shift $-f_{\text{inf}}$ is divided evenly into M smaller portions. In each iteration (q) the algorithm calculates M_q by finding the narrowest band $\left[\frac{M_q+1}{M} f_{\text{inf}}, (F_{s,q-1})/2\right]$ where a high-pass Butterworth filter satisfies the stability criterion, and updates $\Delta f \leftarrow \Delta f - \Delta f_q$.

To eliminate all the spectral contents which are incoherent to the period, the time synchronous averaging is applied on the filtered signal $y_{\mathbf{B}}[n]$ to yield a period-wise averaged signal $\overline{y_{T_{\mathbb{Z}}}}[\tau]$, where τ is the discrete time index. Then the amplitude $\hat{A}[\tau]$ and the frequency $\Phi[\tau]$ can be calculated from the analytical signal $\overline{y_H}[\tau]$ of $\overline{y_{T_{\mathbb{Z}}}}[\tau]$.

The scalar features can be derived from the demodulated functions $\hat{A}[\tau]$ and $\hat{F}[\tau]$ as mechanical fault indicators, such as the mean $\bar{A}$ and $\bar{F}$, The modulation index MI_A and MI_F, the root mean square RMS_A and RMS_F, The peak-to-peak magnitude PP_A and PP_F, The crest factor C_A and C_F and the Kurtosis Kurt_F. A further run of AStrion yields the number of peaks and the energy of harmonic series on the spectrum of the demodulated functions. These numbers contribute to 4 additional features.

5 Case Study

An advanced test rig, which simulates a wind turbine drive train, has been designed at CETIM (http://www.cetim.fr) as a part of the KAStrion project (http://www.gipsa-lab.fr/projet/KASTRION/). This test rig is equipped with hydraulic cylinders, which are installed to generate external forces on bearing corresponding to a wind turbine main bearing for its faster deterioration. In order to control the input speed

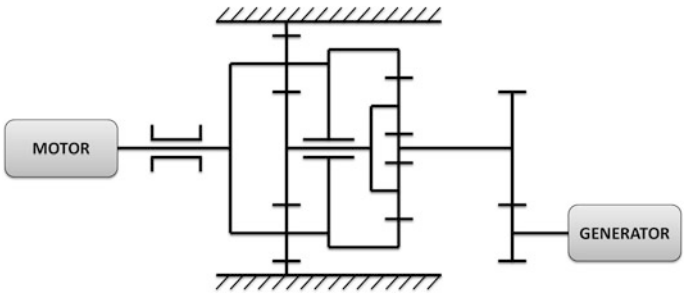

Fig. 2 Schematic representation of the test rig

of this test rig a 10 kW motor is installed in place of the blades of a wind turbine. Figure 2 presents the main mechanical components of the test rig.

The characteristic fault orders of the low speed shaft equals to $V_r = 0.01$ and the values for the main bearing are: BPFO = 0.076, BPFI = 0.103, FTF = 0.004, and BSF2 = 0.031.

All results presented in this paper are computed with signals sampled at 39062.5 Hz and 150 s long. The acquisition of signals is done with the rotational speed of the low speed shaft around 20 rpm and under the same load conditions. The test rig was working with the settings for fast deterioration of main bearing between measurements.

Signals presented in this paper were recorded with two accelerometers placed on the main bearing case in radial directions. One accelerometer Acc_H is situated in the horizontal plane and another Acc_V in the vertical plane. The set of data corresponds to a period from the beginning of degradation test until the 190th hour. There are 20 measurements for Acc_H and 16 for Acc_V. All signals used for computation of the results of the proposed methods were treated with angular resampling algorithm presented in Sect. 2. After this operation the angular sampling rate is equal to 1488 samples per revolution and its duration around 5000 revolutions.

5.1 Characteristic Frequency Association Results

Table 2 presents some results of association algorithm performed on one signal from Acc_V. Two harmonic series, which were associated with the main bearing, are presented. Moreover, the modulation sidebands of the series with the fundamental order value equal to 0.102 are listed. One sideband modulation series is not associated with any mechanical component, it is normal in case of real-world signals, since the pattern detection algorithm detects huge amount of series. The algorithm associated two sideband series with the low speed shaft, which appeared respectively around the fundamental frequency and around the second harmonic of main bearing BPFI harmonic series. The theoretical order value and the calculated RFD is also presented in the table.

Table 2 Example of harmonic and modulation sidebands series association on test rig data

Type	Order	Carrier	Modulation	Associated component	Model order	RFD
Harmonics	0.076	–	–	Main bearing BPFO	0.076	0.868
Harmonics	0.102	–	–	Main bearing BPFI	0.103	−0.645
Sidebands	–	0.102	0.02	–	–	–
Sidebands	–	0.102	0.01	Low speed shaft	0.01	0.041
Sidebands	–	0.205	0.01	Low speed shaft	0.01	−0.025

5.2 Sideband Demodulation Results

All health indicators proposed in Sect. 4 were computed from Acc_H and Acc_V data sets. Among them only three selected indicators are presented in Fig. 3. Although, the first sample used for the processing appeared in the 11th hour, the first results presented in Fig. 3 are computed at the 138th hour. The latter is due to the fact that there was no modulation sidebands series detected in prior signals [8]. Thus, this time-stamp is considered as the beginning of the fault in the inner ring of the main bearing. The early fault detection is thus the strength of the proposed methodologies.

The RMS_A and PP_A of Acc_H show a gradual increase of the parameters. On the other hand the MI_A of signals on this sensor starts with a high value and decreases until the 168th hour. Afterwards this parameter has a growing trend. The evolution of RMS_A and PP_A for the results of Acc_V is consistent. These features start with a dynamic increase followed by a fluctuation period until the 168th hour. Afterwards RMS_A and PP_A decreased rapidly and increased again in the end of the test. The values of MI_A of Acc_H are high at the beginning and decreases until the 168th hour. After noticing the different behaviour of the indicators before and after the 168th hour we can give additional information on the fault stage. From the presented results the conclusion can be deduced that the early stage fault is present until the 168th hour and subsequently it spreads.

Moreover, the fully automatic and data-driven demodulation method proposed in this paper is ready to use in CMS. Furthermore the method is robust thanks to not using the parameters defined a priori.

5.3 Comparison with Traditional Health Indicators

Using the same set of data, the popular health indicators for rolling element bearings were computed. In Fig. 4 crest factor and kurtosis calculated on the full-length vibration signals, as well as the narrow-band RMS over a band of ±2 % of the theoretical value of main bearing BPFI are presented.

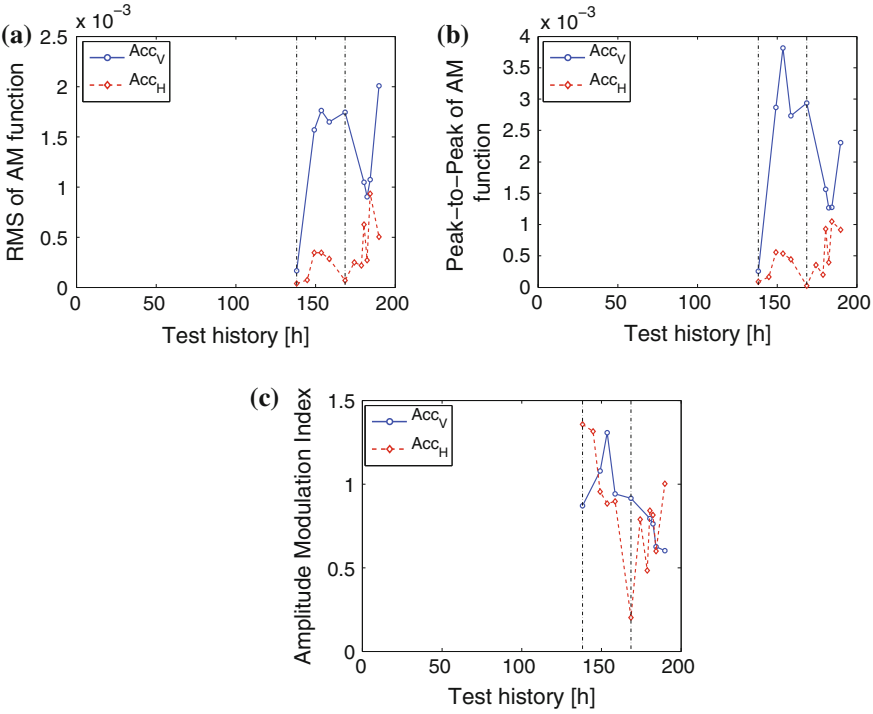

Fig. 3 Evolution of RMS_A, PP_A, and MI_A calculated on signals from Acc_H and Acc_V through the lifetime of the main bearing. **a** RMS_A. **b** PP_A. **c** MI_A

The fault of the main bearing is detected with the crest factor, but not earlier than in 175th hour for Acc_H and 182th hour for Acc_V. Moreover, using this method it is not possible to conclude which type of fault it is. Furthermore, it is impossible to determine a faulty bearing in case of multiple bearing in the investigated system. The kurtosis, presented in Fig. 4b, does not show sensitivity to investigated fault. The narrow-band RMS is the most precise among the classical health indicators, although it could happen that a band selected for this method will not correspond to the real characteristic fault frequency of bearing due to the slippage phenomenon described earlier. With a threshold value equal to 8×10^{-5} the detection of fault is possible in 149th and 144th hours for Acc_H and Acc_V respectively. It is important to notice that for Acc_H the fault detection is not obvious, since the value of parameter decreased below the threshold and again crossed it.

The presented traditional health indicators allow to detect the beginning of the fault of the main bearing, but later than above-proposed method. Another weakness of the traditional approach is the possibility of false alarms which are clear in Fig. 4a, c. In case of huge amount of data processed automatically the generated false alarms could make a conventional CMS unusable.

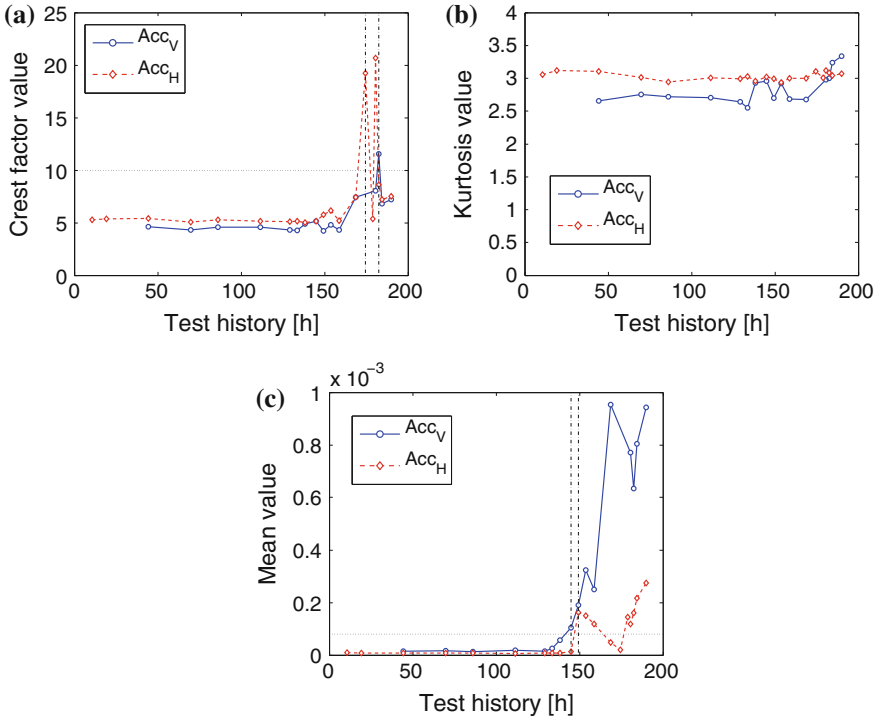

Fig. 4 Evolution of commonly used health indicators calculated on signals from 2 accelerometers through the lifetime of the main bearing tested at KAStrion test rig. **a** Crest factor. **b** Kurtosis. **c** Narrow-band RMS

6 Conclusions

This paper presents three data-driven methods in order to contribute to an automatic diagnosis of rotating machinery. First of all the adaptive angular resampling method with a correction of the speed signal. Moreover, the association of the patterns detected in the spectrum of the signal with characteristic fault frequencies is proposed. This method is robust against the slippage phenomenon present in rolling element bearings. Furthermore the automatic and full-band sideband demodulation method is introduced.

The results presented in this paper illustrate the interest of the proposed methods for the generation of automatic health indicators for CMS. Their comparison with a diagnosis parameters shows that the usage of the proposed approaches allows for an earlier detection of a main bearing fault of the test rig.

A further work will include tests of the proposed methods under varying speed and load conditions.

Acknowledgements All data are provided by CETIM, within KAStrion project, thanks to Sophie Sieg-Zieba.

The Innovation Project KAStrion has been supported by KIC InnoEnergy, which is a company supported by the European Institute of Innovation and Technology (EIT), and has the mission of delivering commercial products and services, new businesses, innovators and entrepreneurs in the field of sustainable energy through the integration of higher education, research, entrepreneurs and business companies.

This work has been supported by French Research National Agency (ANR) through EITE program (project KAStrion ANR-12-EITE-0002-01).

References

1. Hau E (2006) Wind turbines: fundamentals, technologies, application, economics. Springer, Berlin
2. Wiggelinkhuizen E, Verbruggen T, Braam H, Rademakers L, Xiang J, Watson S, Giebel G, Norton E, Tipluica MC, MacLean A, Christensen AJ, Becker E, Scheffler D (2007) CONMOW: condition monitoring for offshore wind farms. In: European wind energy conference (EWEC 2007), Milan, Italy
3. Jablonski A, Barszcz T, Bielecka M, Breuhaus P (2013) Modeling of probability distribution functions for automatic threshold calculation in condition monitoring systems. Measurement 46:727–738
4. Tavner PJ, Zappal D, Sheng S, Crabtree CJ (2014) Side-band algorithm for automatic wind turbine gearbox fault detection and diagnosis. IET Renew Power Gener 8:380–389
5. Antoni J (2009) Cyclostationarity by examples. Mech Syst Signal Process 23:987–1036
6. Barszcz T, Jabłoński A (2010) Selected methods of finding optimal center frequency for amplitude demodulation of vibration signals. Diagnostyka 2(54):2008–2011
7. Borghesani P, Ricci R, Chatterton S, Pennacchi P (2013) A new procedure for using envelope analysis for rolling element bearing diagnostics in variable operating conditions. Mech Syst Signal Process 38:23–35
8. Gerber T, Martin N, Mailhes C (2013) Identification of harmonics and sidebands in a finite set of spectral components. In: Tenth international conference on condition monitoring and machinery failure prevention technologies. CM 2013 and MFPT 2013, Kraków, Poland
9. Fyfe K, Munck E (1997) Analysis of computed order tracking. Mech Syst Signal Process 11 (2):187–205
10. Randall RB (2011) Vibration-based condition monitoring. Wiley, Chichester
11. Randall RB, Antoni J (2011) Rolling element bearing diagnostics–a tutorial. Mech Syst Signal Process 25:485–520

Robust Information Indices for Diagnosing Mechanical Drives Under Non-stationary Operating Conditions

Boštjan Dolenc, Pavle Boškoski and Đani Juričić

Abstract Reliable fault diagnosis of mechanical drives can become nontrivial task in case of restricted instrumentation and variable operating conditions. Under such circumstances changes in the calculated features can not be unambiguously associated with change in system condition. In this paper we propose a feature appropriate for diagnosing faults in mechanical drives that is robust to fluctuations in operating conditions. Therefore, its time evolution seems to be correlated only with the machine condition. Instead of relying on spectral properties of the vibration signal, we rather observe changes in the statistical patterns of the derived distribution functions. The effectiveness of the algorithm was evaluated on three datasets comprising both gear and bearing faults under constant and variable load.

Contents

1 Introduction 140
2 Fault Models 140
3 Application of the Jensen-Rényi Divergence for Diagnostic Purposes 141
3.1 Entropy: from Shannon to Rényi 141
3.2 Jensen-Rényi Divergence 142
3.3 The Influence of Weights w_i 143
3.4 JR Divergence as a Diagnostic Feature for Gear and Bearing Faults 144
4 Experimental Evaluation 145
4.1 The Experiment 145
4.2 Gear Experiments 145
4.3 Bearing Experiment 147
5 Conclusion 148
References 148

B. Dolenc (✉) · P. Boškoski · Đ. Juričić
Department of Systems and Control, Jožef Stefan Institute,
Jamova 39, Ljubljana, Slovenia
e-mail: bostjan.dolenc@ijs.si

B. Dolenc
Jožef Stefan International Postgraduate School, Jamova cesta 39,
SI-1000, Ljubljana, Slovenia

F. Chaari et al. (eds.), *Advances in Condition Monitoring of Machinery in Non-Stationary Operations*, Applied Condition Monitoring 4,
DOI 10.1007/978-3-319-20463-5_11

1 Introduction

Condition monitoring (CM) and diagnosis of mechanical drives aims to detect, localise and identify the onset of a fault on a machine. Traditional diagnostic techniques rely on monitoring of specific characteristic spectral components in measured vibrations [1]. These methodologies proved effective under constant operating conditions. However, without exact knowledge of the operating conditions it is not easy to determine the cause of the increased feature value.

By definition a feature should be related solely to the machine condition, while being insensitive to variations in the operating conditions. The currently available diagnostic approaches can be separated into three main groups. Those from the first group rely on features that require information about the operating conditions [2, 3]. The second group utilises statistical models for specifying gear health indices [4]. The approaches from the third group specify features that describe specific statistical properties of the generated vibrations [5]. A feature robust to the variations in operating conditions can be built by characterising the distribution of energy in the generated vibrations [6]. Firstly, the feature values show non-monotonic behaviour. Secondly, parameters required for feature calculation need to be estimated each time a new machine is applied.

This paper proposes a feature based on generalised Jensen-Rényi (JR) divergence of envelope distribution obtained from vibrations. Such a feature is shown to be practically insensitive to variations in the rotational speed and applied load. In particular, JR divergence is employed to measure the rate of change in the vibrational envelope due to evolving degradation.

The paper is organised as follows. Section 2 presents two conceptual models describing gear and bearing faults. The background of JR divergence and its properties as well as its applicability for cm of gears and bearings is presented in Sect. 3. Finally, the evaluation results are presented in Sect. 4.

2 Fault Models

Gears and bearings have different mechanisms that generate vibrations. At a first glance it seems that each component should be considered separately. However it will be shown that the distribution of the energy of the generated vibrations is sufficiently accurate indicator of their condition [6].

Gear fault signature The main source of vibration in fault-free gears is variation in the contact stiffness [7]. Under constant rotational speed the generated vibrations $x(t)$ can be represented as:

$$x(t) = \sum_{m=1}^{M} A_m(1 + a_m(t)) \cos\left(2\pi m f_{\text{gmf}} t + \beta_m + b_m(t)\right), \tag{1}$$

where f_{gmf} is gear mesh frequency, $a_m(t)$ is modulating signal due to incipient localized teeth damages, M is the highest harmonic of interest and A_m is the amplitude of the mth harmonic of the gear mesh frequency. The components $b_m(t)$ represent phase modulations, and β_m is the initial phase.

Faults in gears evolve through several stages: scuffing, initial pitting, pitting, spalling [8]. Regardless of the severity, localised gear faults influence only a limited number of teeth. Therefore, when these teeth mesh, the contact stiffness changes so that the amplitude modulation $a_m(t)$ in (1) changes accordingly. Hence, the amplitude modulation $a_m(t)$ contains all the essential diagnostic information [9].

Bearing fault signature Unlike gears, fault-free bearings produce negligible vibrations. When surface fault occurs, each time a rolling element passes across the damaged area, the impulse responses $s(t)$ are excited. The generated vibrations $x(t)$ can be represented as [10]:

$$x(t) = \sum_{i=-\infty}^{\infty} A_i s(t - \tau_i) + n(t), \tag{2}$$

where A_i is the amplitude of force that excites the entire structure and τ_i is the time of its occurrence. The term $n(t)$ defines an additive random component. The time moments τ_i can be considered as random and distributed with inverse Gaussian distribution [10]. Similarly, the amplitudes A_i of the impulses should be considered as random process [11].

The diagnostic information is contained in the time impacts τ_i. Under constant rotational speed, the frequency of their occurrence can be directly related to a localised bearing fault. From a macroscopic point of view, impacts can be considered as amplitude modulation of a carrier signal whose frequency is the same as the excited eigenfrequency.

3 Application of the Jensen-Rényi Divergence for Diagnostic Purposes

Changes in the envelope of vibrational signal can be associated with the change in condition. Here we will explore the potential of the generalised Jensen-Rényi (JR) divergence in quantifying the amount of change in envelope pdf due to change in machine's condition.

3.1 Entropy: from Shannon to Rényi

Entropy quantifies uncertainty involved in predicting the value of a random variable (r.v.). Shannon entropy reads:

$$H(\mathcal{P}) = -\sum_{i=1}^{N} p_i \ln p_i, \tag{3}$$

where $\mathcal{P}$ is probability distribution of a discrete r.v., i.e. $\mathcal{P} = \{p_1, \ldots, p_N\}$.

The results presented in this paper are based on a generalised version of the Shannon entropy i.e. the Rényi entropy [12]:

$$H_\alpha(\mathcal{P}) = \frac{1}{1-\alpha} \ln \sum_{i=1}^{N} p_i^\alpha \tag{4}$$

By proper selection of parameter α one can place focus on a particular part of the analysed probability distribution function. For $\alpha \to 1$, (4) reduces to Shannon entropy.

3.2 Jensen-Rényi Divergence

To quantify the distinction between two or more pdfs the relative entropy or *divergence* is often employed. Several divergence measures are applicable depending on the analysed data [13]. Here we employ the generalised Jensen-Rényi divergence JR_α^w to quantify dissimilarity among n pdfs:

$$\mathrm{JR}_\alpha^w(\mathcal{P}_1, \ldots, \mathcal{P}_n) = H_\alpha\left(\sum_{i=1}^{n} w_i \mathcal{P}_i\right) - \sum_{i=1}^{n} w_i H_\alpha(\mathcal{P}_i), \text{where} \sum_{i=1}^{n} w_i = 1. \tag{5}$$

In (5), H_α is Rényi entropy. The selection of weights w_i in (5) is in principle arbitrary. With w_i selected uniformly i.e. $w_i = 1/n$, the divergence reaches maximal value. As shown later on, the selection of weights w_i affects the behaviour of JR divergence significantly.

JR divergence quantifies shared information among n random variables. If they are identical, i.e. $\mathcal{P}_1 = \mathcal{P}_2 = \cdots = \mathcal{P}_n$, divergence is zero. However, if one of them deviates even slightly, the JR divergence becomes grater than zero. Therefore, JR divergence carries information about dissimilarity among n pdfs.

A simple example demonstrates the basic concept of JR divergence. Figure 1a shows three Rice pdfs with different scale and location parameters. Here we consider JR divergence in its simplest pairwise form where only two pdfs are considered and $w_i = \frac{1}{2}$:

$$\mathrm{JR}_\alpha^w(\mathcal{P}, \mathcal{Q}) = H_\alpha\left(\frac{1}{2}(\mathcal{P} + \mathcal{Q})\right) - \frac{1}{2}(H_\alpha(\mathcal{P}) + H_\alpha(\mathcal{Q})), \tag{6}$$

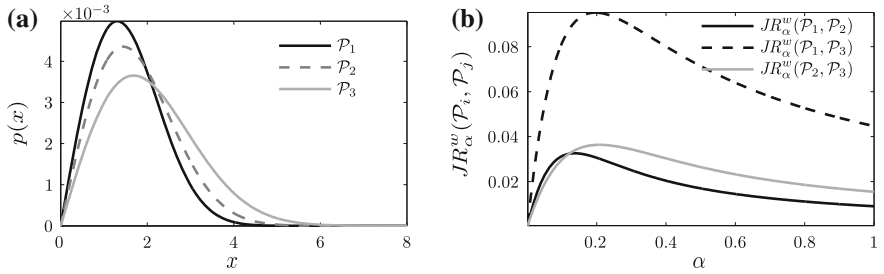

Fig. 1 Pdfs of the simulated signals and the resulting JR divergence. **a** Pdfs of the simulated signal. **b** Pairwise JR divergence as a function of α

where $\mathcal{P}$ and $\mathcal{Q}$ are pdfs of interest and $\alpha \in [0, 1]$. JR divergence between $\mathcal{P}_1$ and $\mathcal{P}_2$ from Fig. 1a is 0.017 ($\alpha = 0.5$). The dissimilarity between $\mathcal{P}_1$ and $\mathcal{P}_3$ is even grater, hence higher value of JR divergence (0.0714). Clearly the divergence is able to characterise relative dissimilarity among the analysed pdfs.

The effect of the parameter α is shown in Fig. 1b. Low value of $\alpha(\approx 0)$ emphasizes the dissimilarity among pdfs in low probable region ($x \in (6, 8)$ where pdfs do not differ much, hence low divergence values. In the middle region ($x \approx 4$, $\alpha \approx 0.2$) the pdfs differ the most, hence the highest values of JR divergence. Finally, for $\alpha \in (0.6, 1)$ which captures the region of the bulk probability masses the divergence value drops in a relatively linear manner.

3.3 *The Influence of Weights* w_i

The selection of weights w_i has significant influence on behaviour of the JR divergence. In this paper the exponential weights w_i are suggested. The weights w_i are calculated using the exponential function of the following form:

$$w_i = C \cdot \mathrm{e}^{-\frac{i}{n}i} \tag{7}$$

where λ is sensitivity parameter, n is the number of components in (5), $i = 1, 2, \ldots, n$ and C is normalising constant. One can easily see that (7) reduces to the uniform weighting for $\lambda \to 0$ and $n \to \infty$.

The influence of weights w_i on JR divergence can be illustrated by a simple simulated example. We first generate N sequences of a normal r.v. simulating abrupt change in shape of a pdf. Than we calculate JR divergence using (5) which results in divergence value after each measurement session i : $\mathrm{JR}^w_\alpha(\mathcal{P}_1, \mathcal{P}_2, \ldots, \mathcal{P}_i)$ for $i = 1 \ldots 21$.

The generated signals simulate an abrupt change in pdfs' shape. The corresponding pdfs are shown in Fig. 2a. The JR divergence is calculated after each measurement session. First 10 pdfs are identical, hence the measure of dissimilarity

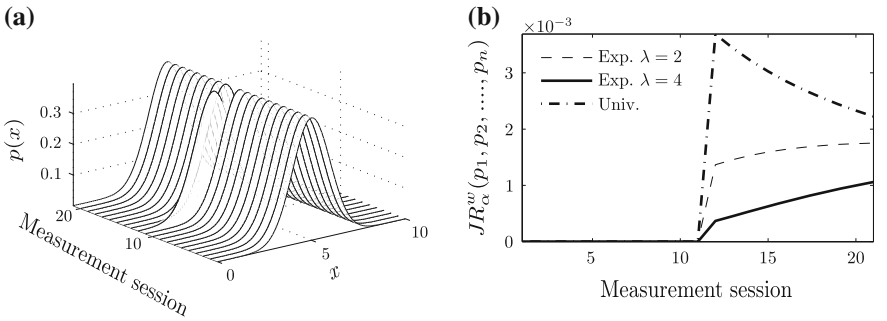

Fig. 2 The evolution of JR divergence after measurement sessions. Note that all pdfs are equal except the pdf #11. **a** Pdfs of the simulated signals associated to the measurement sessions $1, \ldots, 21$. **b** JR divergence

among them equals 0. Once the 11th pdf is included in the calculation of JR divergence (5) an increase in value is observed. The following 10 pdfs are identical to the first one, therefore dissimilarity among them decreases. The rate of change in JR divergence is conditioned with the selection of weights as shown in Fig. 2b. The most notable increase is observed if uniform weighting is applied, while exponential weighting alleviates the impact.

In this way the pdf belonging to the fault-free state have grater influence on JR divergence. For the JR divergence to increase significantly, several consecutive pdfs should be distinct in shape. Such a behaviour makes the proposed JR divergence robust to variations in the operating conditions with acceptable decrease of the fault sensitivity.

3.4 JR Divergence as a Diagnostic Feature for Gear and Bearing Faults

JR divergence as a dissimilarity measure among N pdfs can be successfully exploited as a feature for gear and bearing diagnostics. Vibrations caused by a fault in gear couple or bearing alter the shape of the envelope pdf. Therefore the generalised divergence among envelope pdfs is an ideal candidate for diagnostic purposes.

In a fault-free system the excited vibrational pattern does not vary significantly over time. The resulting envelope pdfs are almost equal. Consequently generalised JR divergence among these pdfs is zero. As soon as a fault occurs in the system the vibrational pattern is altered affecting the shape of the envelope pdf. In turn, the JR divergence among measured pdfs increases. With further system deterioration changes in the envelope pdf become even more apparent.

4 Experimental Evaluation

The proposed feature based on the generalised JR divergence was evaluated on three different experiments:

1. natural evolution of gear faults under constant operating conditions;
2. natural evolution of gear faults under variable load and
3. evolution of bearing faults under constant operating conditions.

In order to show the performance of the generalised JR divergence, classical spectral features were also calculated. It should be noted that the calculation of the proposed feature was done without any information regarding the operating conditions, although the employed experimental data include such information.

4.1 The Experiment

The first two experiments were performed using a motor generator test rig with one stage gearbox with spur gears. In the first experiment the torque was kept constant at 82 Nm, while for the second experiment the torque varied between 66 and 82 Nm as shown in Fig. 4a. The same type of gears were used in both experiments. For the third experiment the NASA data set [14] was used. Four bearings were subjected to excessive load and run-to-failure.

Pdfs were estimated by means of histogram. The divergence $\mathrm{JR}_{\alpha}^{w}(\mathcal{P}_1, \mathcal{P}_2, \ldots, \mathcal{P}_n)$ was calculated using (5). Parameter α in (4) was set to $\alpha = 0.9999$ for gear, and $\alpha = 0.8$ for bearing experiment. The JR divergence was calculated with exponential weights w_i according to (7) where $\lambda = 10$.

4.2 Gear Experiments

Vibrations generated by running gears are dominated by low-frequency content. Therefore, the generated vibrations were firstly low-pass filtered with cut-off frequency 2 kHz. The envelope pdf was estimated using the resulting signals.

Figure 3a shows the time evolution of two classical spectral features from the first gear experiment (under constant load). The first feature is the amplitude of the spectral component at the GMF. The second feature is the sum of the amplitudes of the side-bands around the GMF. As expected, the side-bands are more sensitive to the localised gear faults. The first increase in the side-band energy is visible around the 120th measurement. Although, an increasing trend is visible, both features show local non-monotonic behaviour, despite constant operating conditions.

Figure 3b shows the time evolution of the generalised JR divergence. In the beginning of the experiment, as the pdf of vibrations' envelope are similar, JR

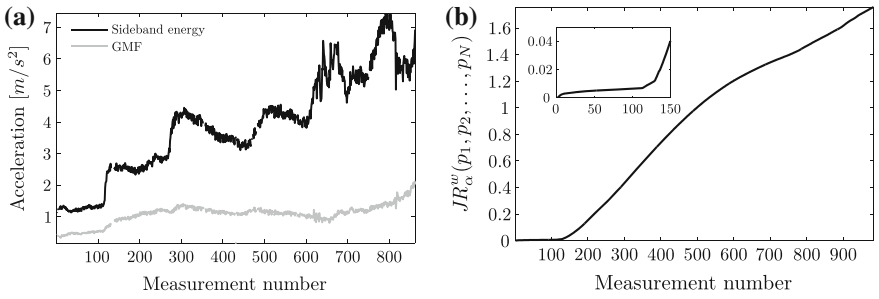

Fig. 3 Time evolution of features related to the gear experiment under constant load. **a** Classical spectral components. **b** Generalised JR divergence

divergence takes low value ($\sim 10^{-3}$). As soon as a fault occurs in the gear couple, its envelope changes and, unlike the classical spectral features, the value of the JR divergence monotonically increases.

In case of variable load, classical spectral features were calculated from generated vibrations in the same manner as before. The time evolution of cumulative side-band energy is shown in Fig. 4a. The influence of load variations is clearly visible. Although an increasing trend can be seen, without precise load measurements it is impossible to determine the proper cause for the abrupt changes in the features' values.

Conversely, the time evolution of the generalised JR divergence shows smooth and monotonic increase, as shown in Fig. 4b. Therefore, the generalised JR divergence can be considered as sufficiently robust to variations in the operating conditions while preserving the fault sensitivity.

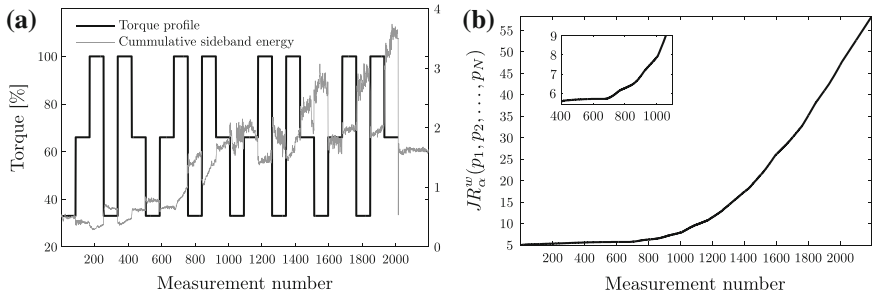

Fig. 4 Time evolution of features for gear experiment under variable load. **a** Classic features and torque profile. **b** JR divergence feature

4.3 Bearing Experiment

Generally, bearing's condition is estimated based on the amplitude of the characteristic spectral components such as: BPFO, BPFI, BSF and FTF. The time evolution of the first three is shown in Fig. 6a. The amplitudes were extracted from envelope of the band-pass filtered vibrations. The frequency interval was selected using spectral kurtosis. An example of envelope spectrum of the envelope is shown in Fig. 5, where characteristic frequency pattern of outer race fault can be recognised. The peaks of the spectrum belong to the BPFO and its harmonics.

In Fig. 6a it is noticeable that the outer race fault occurs soon after the 130th measurement session. However, the monotone behaviour of this feature is not preserved. Towards the end of the experiment its value changes in a non-monotonic manner. This can be attributed to the fixed band pass in which the envelope of the generated vibrations is calculated.

Since the frequency band containing eigenfrequency of the system is unknown prior to the fault initiation, the acquired vibration signals are filtered using 8 non-overlapping bandpass filters each spanning 1.25 kHz. Afterwards, the envelope pdfs and the corresponding JR divergence are calculated for each band separately,

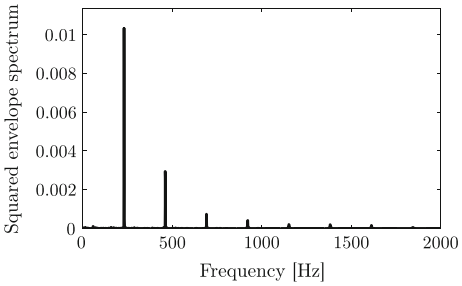

Fig. 5 Envelope spectrum of 300th measurement in frequency band $f \in (4-6)$ kHz: characteristic frequency BPFO and its harmonics are clearly visible indicating outer race failure

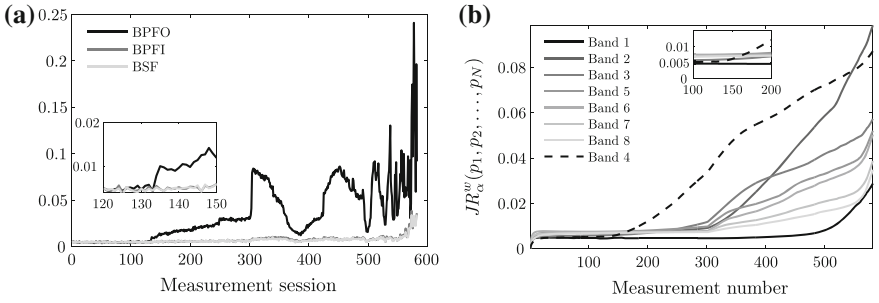

Fig. 6 Extracted features from the bearing dataset. **a** Classic features. **b** JR divergence feature

resulting in 8 JR divergence values. The time evolution of the JR divergence are shown in Fig. 6b.

As expected, at the beginning, the JR divergence is almost zero. As surface faults start to emerge, around the 150th measurement session, the JR divergence starts to increase. Unlike the standard features, the increase of the JR divergence is monotone. JR divergence covering the 4th frequency band includes the frequency band determined by the spectral kurtosis method. The same band covers frequencies where the squared envelope spectrum from Fig. 5 was calculated.

5 Conclusion

The generalised JR divergence seems to be a suitable feature for cm. It characterises changes in the pdf calculated from the envelope of the generated vibrations. As a result, the calculated feature is robust to variations of the operating conditions, while in the same time it preserves its monotone time evolution which seems to be correlated with component degradation. Additionally, feature shows great potential for remaining useful life estimation applicable to gears and bearings. This issue will be studied in a more detail in the follow up of this research.

Acknowledgment The authors acknowledge the financial support of the Slovenian Research Agency through the Research Program P2-0001 and the Ministry of Education, Science and Sport for support of the Eurostars project PRODISMON through grant 2130-13-090007.

References

1. Jardine AKS, Lin D, Banjevic D (2006) A review on machinery diagnostics and prognostics implementing condition-based maintenance. Mech Syst Signal Process 20:1483–1510
2. Bartelmus W, Zimroz R (2009) A new feature for monitoring the condition of gearboxes in non–stationary operating conditions. Mech Syst Signal Process 23(5):1528–1534
3. Zimroz R, Bartelmus W, Barszcz T, Urbanek J (2014) Diagnostics of bearings in presence of strong operating conditions non-stationarity—a procedure of load-dependent features processing with application to wind turbine bearings. Mech Syst Signal Process 46(1):16–27
4. Villa LF, Reñones A, Perán JR, de Miguel LJ (2012) Statistical fault diagnosis based on vibration analysis for gear test-bench under non-stationary conditions of speed and load. Mech Syst Signal Process 29:436–446
5. Chen P, Taniguchi M, Toyota T, He Z (2005) Fault diagnosis method for machinery in unsteady operating condition by instantaneous power spectrum and genetic programming. Mech Syst Sign Process 19(1):175–194
6. Boškoski P, Juričić Đ (2012) Fault detection of mechanical drives under variable operating conditions based on wavelet packet rényi entropy signatures. Mech Syst Signal Process 31:369—381
7. Wang W (2001) Early detection of gear tooth cracking using the resonance demodulation technique. Mech Syst Signal Process 15:887–903

8. GfT. Arbeitsblatt 7 tribologie definitionen, begriffe, prüfung (in german). Technical report 7, GfT, 2002
9. Randall RB (1982) A new method of modeling gear faults. J Mech Des 104:259–267
10. Boškoski P Juričić Đ (2014) Inverse gaussian mixtures models of bearing vibrations under local faults. Mech Syst Signal Process, page Under review
11. Antoni J, Randall RB (2003) A stochastic model for simulation and diagnostics of rolling element bearings with localized faults. J Vib Acoust 125(3):282–289
12. Rényi (1960) On measures of information and entropy. In: 4th Berkeley Symp Math Stat Prob 1:547–561
13. Basseville M (2013) Divergence measures for statistical data processing–an annotated bibliography. Signal Process 93:621–633
14. Lee J, Qiu H, Yu G, Lin J, Rexnord Technical Services (2007) Bearing data set, IMS, University of Cincinnati. NASA Ames, Moffett Field, CA

Empirical Mode Decomposition Combined with Empirical Wavelets for Extracting Bearing Frequencies in a Noisy Environment and Early Detection of Defects

Mourad Kedadouche, Marc Thomas and Antoine Tahan

Abstract The amplitude demodulation of a bearing signal allows for the extraction of component information-carrying defects on rotary machines. However, the quality of the demodulated signal depends on the selected frequency band for demodulation. Kurtogram is widely used to detect the frequency bandwidth which is the most excited by a defect. However in presence of high noises, the Kurtogram may be deficient in effectively detecting the resonances and it presents some instabilities. In the last decade, the Empirical Mode Decomposition (EMD) technique has been used by a lot of researchers for the signal decomposition. In this study, the EMD and Empirical Wavelet (EW) are used to generate a new feature. The EW is used to generate a filter bank which depends on the content of the component frequencies of the signal. A segmentation of the spectrum to define the support boundaries of the filter is proposed. The new indicator is proposed in order to track the frequency band that is more excited by a bearing fault. This study shows that the proposed technique can detect the resonances in all cases of simulation. On the other hand, the proposed method is able first to detect the resonance frequencies and secondly to detect on which Intrinsic Mode Function (IMF), the bearing default occurs. The proposed technique has confirmed its effectiveness by testing it on experimental signals obtained from a test bench with defects on a bearing outer race. A defect of only 40 μ on the outer race has been detected, which makes this method very effective for an early detection of bearing defects.

M. Kedadouche (✉) · M. Thomas · A. Tahan
Department of Mechanical Engineering, École de Technologie Supérieure, 1100, Notre-Dame street West, Montreal, QC H3C 1K3, Canada
e-mail: mourad.kedadouche.1@ens.etsmtl.ca

M. Thomas
e-mail: marc.thomas@etsmtl.ca

A. Tahan
e-mail: antoine.tahan@etsmtl.ca

F. Chaari et al. (eds.), *Advances in Condition Monitoring of Machinery in Non-Stationary Operations*, Applied Condition Monitoring 4,
DOI 10.1007/978-3-319-20463-5_12

Keywords Bearing fault · Demodulation · EMD (Empirical mode Decomposition) · Empirical wavelet transform (EWT) · Kurtogram · Early detection

Contents

1 Introduction 152
2 Empirical Mode Decomposition (EMD) 153
3 Empirical Wavelet Transforms (EWT) 154
4 A New Indicator Combining Energy, Kurtosis and ApEn 155
5 A Detection Method Based on EMD and EWT 155
6 Case Studies for Validating the Method 158
6.1 A Simulated Signal with One Resonant Frequency 158
6.2 A Simulated Signal with Gear and Bearing Signatures 160
6.3 Experiments on a Bearing Test Bench 162
7 Conclusions 164
References 164

1 Introduction

Bearing defects excite the resonance frequencies at their early stage of degradation. The High Frequency Resonance Technique (HFRT) allows for the extraction of component information representing defects on rotating machinery [1]. A band-pass filtering around the excited resonance frequency followed by an amplitude demodulation step results in a signal whose most of energy is concentrated around the fault frequency and its associated harmonics. However, the major challenge in the application of the HFRT technique is a proper selection of the center frequency and bandwidth of the band-pass filter. Many methods have been proposed for the selection of the frequency bandwidth that is the more excited by the faults. Among them, The STFT-based spectral kurtosis [2] has been proposed and applied to the fault detection of rolling element bearings and gears [3]. However, in the case of a strong and non-Gaussian noise with sudden high peaks, kurtosis shows extreme high values and doesn't really track the resonances [4]. Zhang and Randall [4] proposed an optimal resonance demodulation technique using the combination of the fast Kurtogram and genetic algorithm. Barszcz et al. [5] proposed a Portrugram. Qiu et al. [6] used the minimal Shannon entropy to select the proper bandwidth and Nikolaou et al. [7] and Lin et al. [8] selected the parameters of Morlet wavelet based on a kurtosis maximization criterion.

At the early stage of degradation of bearings, impulses are created when a defect on a rolling surface impacts with another surface. The impulses are generated almost periodically. The impact excites the structural resonance and we can observe

an increase of energy around the resonances [9]. For this reason, it is better to track the band frequency which presents a strong energy compared with a healthy bearing. Otherwise, High energy can be also related to other phenomena (gear meshing, high noise). So using only the energy as indicator to detect the frequency band excited by the defect is not a good way. The particularity of bearing defect is that the increase of energy is caused by the shocks (high level of the kurtosis). So, multiplying the energy by the kurtosis can make a difference between the energy caused by bearing defect and the energy associated to other phenomena.

In this study, EMD is used to decompose the signal into multiple components. The decomposition of a real signal gives some IMF with random shocks. So the kurtosis exhibits a higher value compared with the components from cyclic shocks. In this study, we propose to introduce a new indicator as an index which can distinguish between random shocks and cyclic shocks. Chen et al. [10] showed in their studies that the Spectral Kurtosis value of interference impulses is larger than from repetitive Impulses. If we select a frequency band according to the maximum value of SK, we cannot thus discover the defect frequency of interest even after an envelope demodulation. On other hand, they demonstrate that the entropy of interference impulses is less than from repetitive impulses. So they combined the two methods to better detection for the frequency band. In this study, we propose to combine energy, kurtosis and entropy to develop a new indicator.

In this study, the new method for selecting the optimal frequency bandwidth is thus presented. This new method is based on the Empirical Mode Decomposition (EMD) combined with the Empirical Wavelet method (EW). Specifically, this new indicator is aimed to track the frequency band that is more excited by the bearing fault. The advantage of this method is its ability to detect the resonances even in the presence of significant noise and also with low frequency signatures whose amplitudes are important. The filter bank is adaptive and it depends on each signature. The application of the proposed method is validated both on simulated and experimental data.

2 Empirical Mode Decomposition (EMD)

The EMD method can self-adaptively decompose any non-stationary signal into a set of intrinsic mode functions (IMFs) from high frequencies to low frequencies [11]. The decomposed signal may be written as:

$$x(t) = \sum_{i=1}^{N} \mathrm{IMF}_i(t) + r(t) \tag{1}$$

where $\mathrm{IMF}_i(t)$ indicates the ith IMF and $r(t)$ represents the residual of the sign $x(t)$.

3 Empirical Wavelet Transforms (EWT)

The Empirical Wavelet Transform (EWT) as developed by Gilles [12] presents a new approach for building adaptive wavelets. The main idea is to extract the different signal modes by designing an appropriate wavelet filter bank. The main concept of the EWT method consists in building a family of wavelets adapted to the processed signal. If we take the Fourier point of view, this construction is equivalent to build a set of band pass filters. One way to reach the adaptability is to consider that the filters' supports (w_c) depend on where the information in the spectrum of the analyzed signal is located. The method is based on two functions: The empirical scaling function and the EW are given by the Eqs. 2 and 3, respectively.

$$\hat{\emptyset_j}(w) = \begin{cases} 1 & \text{if } |w| \leq (1-\gamma)w_c(j=1) \\ \cos\left[\frac{\pi}{2}\beta\left(\frac{1}{2\gamma w_c(j=1)}(|w| - (1-\gamma)w_c(j=1))\right)\right] & \\ \quad \text{if } (1-\gamma)w_c(j=1) \leq |w| \leq (1+\gamma)w_c(j=1) & \\ 0 & \text{otherwise} \end{cases} \tag{2}$$

$$\hat{\varphi}_j(w) = \begin{cases} 1 & \text{if } (1+\gamma)w_c(j) \leq |w| \leq (1-\gamma)w_c(j+1) \\ \cos\left[\frac{\pi}{2}\beta\left(\frac{1}{2\gamma w_{n+1}}(|w| - (1-\gamma)w_c(j+1))\right)\right] & \\ \quad \text{if } (1-\gamma)w_c(j+1) \leq |w| \leq (1+\gamma)w_c(j+1) & \\ \sin\left[\frac{\pi}{2}\beta\left(\frac{1}{2\gamma w_c(j)}(|w| - (1-\gamma)w_c)\right)\right] & \\ \quad \text{if } (1-\gamma)w_c(j) \leq |w| \leq (1+\gamma)w_c(j) & \\ 0 & \text{otherwise} \end{cases} \tag{3}$$

The function $\beta(x)$ is an arbitrary $C^k([0,1])$ function defined as:

$$\beta(x) = \begin{cases} 0 & \text{if } x \leq 0 \\ \text{and } \beta(x) + \beta(1-x) = 1 & \forall x \in [0,1] \\ 1 & \text{if } x \geq 1 \end{cases} \tag{4}$$

Many functions satisfy these properties, the most used in the literature [13] is:

$$\beta(x) = x^4(35 - 84x + 70x^2 - 20x^3) \tag{5}$$

and γ is chosen by the Eq. 6 as defined by [12]:

$$\gamma < \min\left(\frac{w_c(j+1) - w_c(j)}{w_c(j+1) + w_c(j)}\right) \tag{6}$$

4 A New Indicator Combining Energy, Kurtosis and ApEn

As mentioned in the introduction, the bearing defect produces an increase of the energy around the resonance and of the Kurtosis level. The product of these parameters can be used as an indicator to track the frequency resonance. In our application, we used the EMD method to decompose the signal in multiple IMF. In some cases, we get components with interference impulses, especially in the case of acoustic emission signal. So, the kurtosis of random impulses is higher than from repetitive shocks [10]. The approximate entropy (ApEn) [14] seems to be an effective tool to distinguish between the random and the cyclic shocks. The ApEn of the repetitive shocks is higher than from random shocks. To reduce the effect of random impulses, we propose to multiply the kurtosis by the ApEn and to use the product of the energy, kurtosis and ApEn as an indicator for our investigation:

$$\text{Energy} = \sum x(f)^2 \tag{7}$$

The effectiveness of this new indicator has been tested on numerically simulated signals, based on [15]. The bearing signature is expressed as follows:

$$x(t) = \mathrm{e}^{-\alpha \times \mathrm{mod}\left(t, \frac{1}{F_m}\right)} \times \sin(2\pi f_1 t) + \text{noise} \tag{8}$$

where α is equal to 900, F_m is bearing fault characteristic frequency (equal to 100 Hz); F_s is sampling frequency (set to 12,000 Hz) and f_1 is carrier frequency (equal to 1800 Hz).

The simulated signals are shown in Fig. 1. Figure 1a shows a random signal, Fig. 1b shows a random impulse and Fig. 1c illustrates a bearing signal given by Eq. 3. In the three cases, the variance of noise is the same. Figure 1d shows the result for different indicators (Energy, Kurtosis and ApEn) applied to the simulated signals.

It is shown that ApEn can effectively distinguish between the random and cyclic impulses. The cyclic impulses are characterized by a higher ApEn compared with random impulses. It is revealed that the product of these three parameters gives an effective indicator which can make a difference between a random signal, a faulty bearing, and a random impulse. This indicator may then be used in all our investigations to track the bearing fault.

5 A Detection Method Based on EMD and EWT

As showed by Gao et al. [16], IMFs sometimes fail to reveal the signal characteristics due to the effect of noises. Hence, Combined Mode Function (CMF) may be used. With CMF, the neighboring IMFs are combined to obtain an oscillation

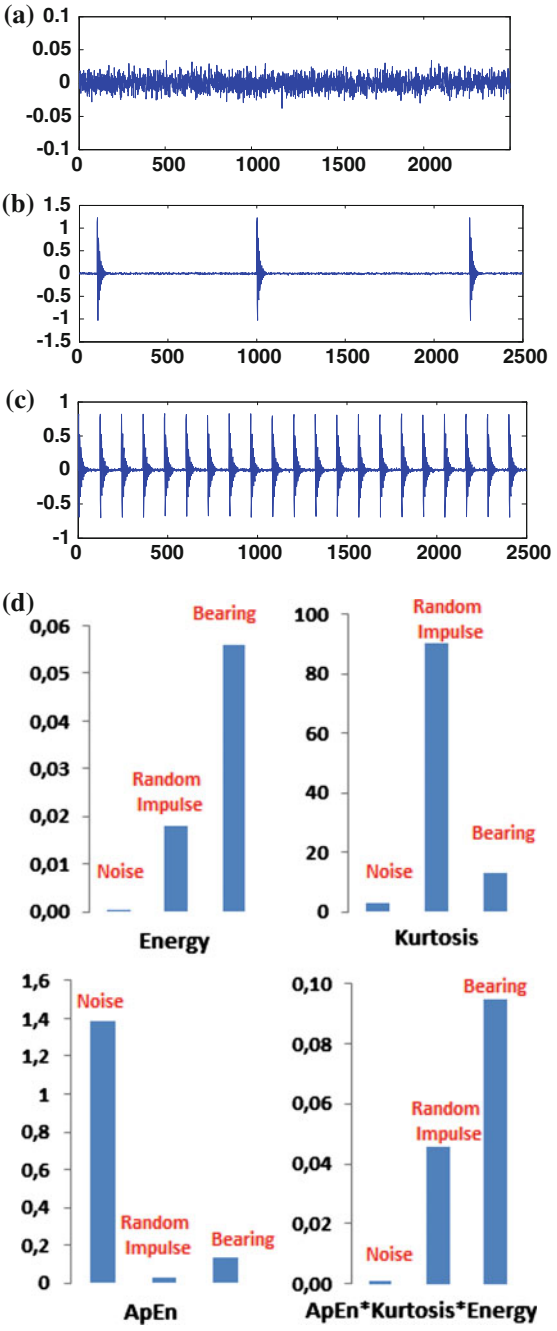

Fig. 1 Simulated signals, **a** random, **b** random impulse, **c** bearing signal, **d** value of indicators with signal type and method

mode depicting signal features more precisely. In the present application for bearing defects, we propose to only use the six first IMF of decomposition. Each IMF is added to the previous as shown in Eq. 9:

$$\mathrm{CMF}_i = C_i = \mathrm{IMF}_i + \mathrm{IMF}_{i+1} \tag{9}$$

After computing each CMF, by using EWT, we construct a series of filter-banks with different center frequencies properly for each CMF. The chart of our proposed method is shown in Fig. 2.

Each CMF is decomposed in four portions using the EWT. The supports boundaries for the filters defined by the EWT are shown in the algorithm (Table 1). After applying the algorithm, we get 3 cut frequencies $w_c(j = 1:3)$ for each CMF. The aim of the method consists in separating different portions of the spectrum which are centered on a specific frequency. The segmentation of the spectrum depends on the frequency w_n which presents the highest amplitude. The aim is to obtain a band-pass filter centered on the frequency w_n. The filtered component presents the highest energy and the other parts, a low energy.

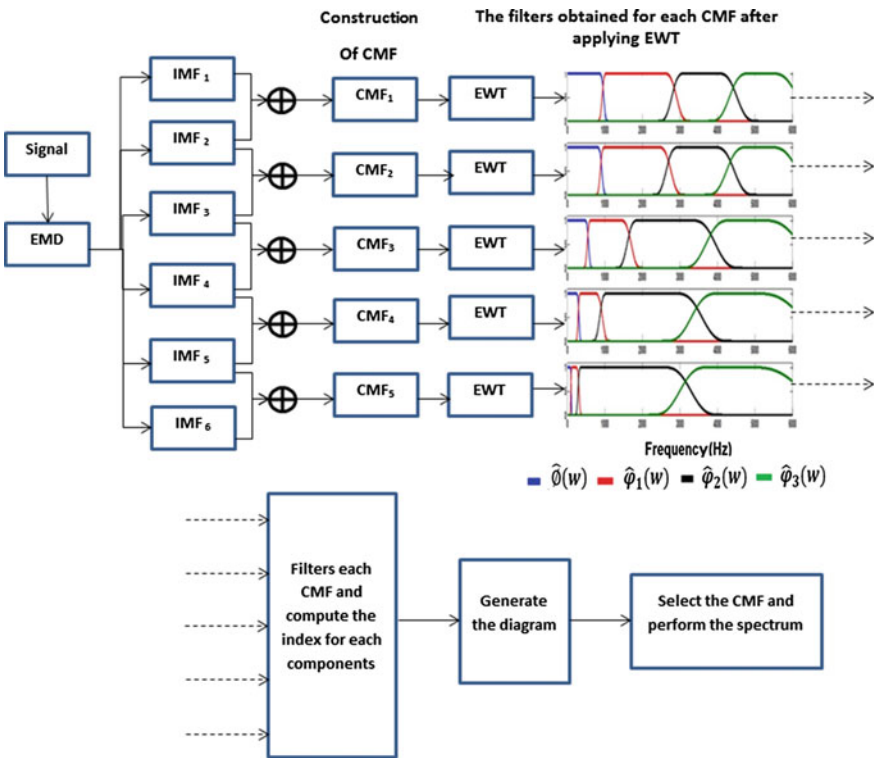

Fig. 2 The chart of the proposed method

Table 1 Algorithm of cut frequencies

$*F_e$: *Sample Frequency*
$*F_c = F_e / 2$
*Select the frequency w_n who present a higher amplitude spectrum
$*Let: \; w_c(1) = (w_n) / 2$
$w_c(2) = (w_n + F_c) / 2$
$Initialise: \quad j = 2$
if $|(w_c(j) - wn)| > |(w_c(j-1) - w_n)|$
$wc(j) = wn + |(wc(j-1) - wn)|$ $\qquad w_c(j+1) = (w_c(j) + F_c) / 2$
$w_c(j+1) = w_c(j)$
else $w_c(j) = w_n - |(w_c(j) - wn)|$
$w_c(j-1) = w_c(j) / 2;$
end

6 Case Studies for Validating the Method

6.1 A Simulated Signal with One Resonant Frequency

6.1.1 Case A: $\sigma^2_{\text{noise}} = 0.2$

The simulated signal is the same that the one used in Eq. 8 and only one natural frequency is used in this simulation. A normal distributed random signal with mean 0 and amplitude 0.2 is added to the simulated signal. The Combined Mode Function of the signal is displayed in Fig. 3a. We note that the signature of the bearing (cyclic shocks) is distributed on the CMF_1 and CMF_2. The filter bank obtained for each CMF_i, is exhibited in Fig. 3b.

$\hat{\emptyset}(w)$ represents the scaling function and $\hat{\varphi}_j(w)$ is the Empirical Wavelet. $\hat{\varphi}_{j=1}(w)$ is the frequency band which represents the highest energy compared to the others, and this band is centered around the frequency w_n. The diagram generated by our method is plotted in Fig. 4a. This diagram indicates that the combined CMF_1 has the deepest color value between [1000 and 2800] Hz. The fault excited frequency region is covered by the selected bandwidth. So, this indicates the expected resonance (1800 Hz). A demodulation, using the Hilbert Transform of the CMF_1 around this frequency band allows for identifying the defect frequency (BPFO (100 Hz) and its harmonics) as shown in Fig. 4b.

6.1.2 Case B: $\sigma^2_{\text{noise}} = 0.5$

The simulated signal is shown in Fig. 5. The diagram paved by our method is given in Fig. 6a. As in the previous simulations, we obtain similar results. The diagram

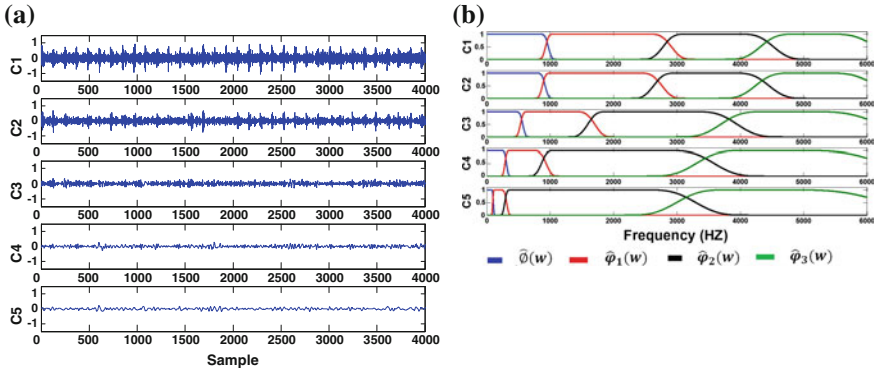

Fig. 3 **a** The combined mode function of the simulated signal, **b** the filter bank for each CMF

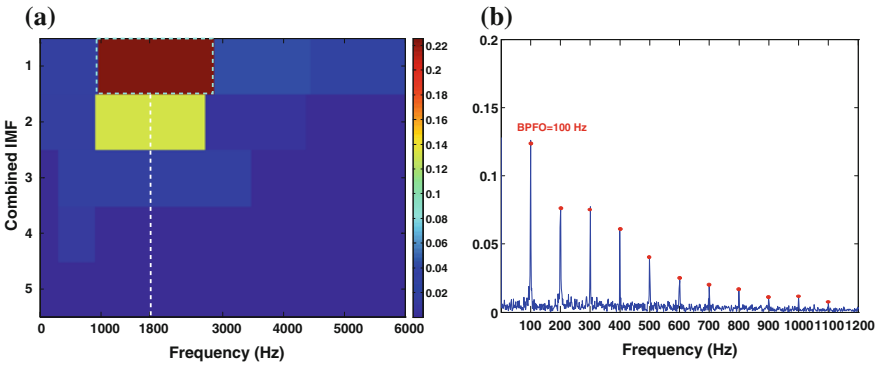

Fig. 4 **a** The diagram generated by our method for the simulated signal (variance o the noise is 0.2), **b** the envelope spectrum of CMF_1 around the frequency band as indicated by our method [1000–2800 Hz]

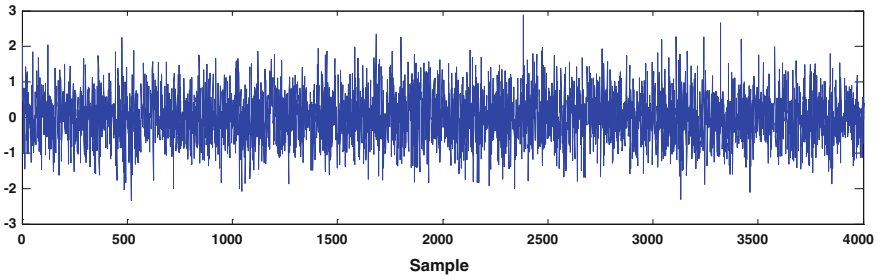

Fig. 5 The simulated signal $\sigma^2_{\text{noise}} = 0.5$

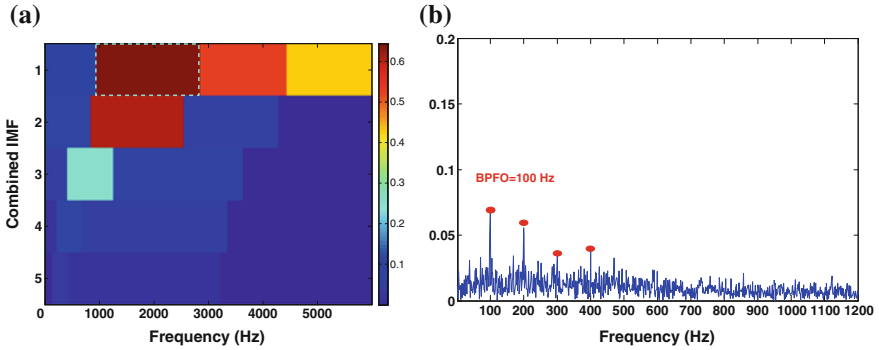

Fig. 6 **a** The diagram generated by our method for the simulated signal (variance o the noise is 0.5), **b** the envelope spectrum of CMF_1 around the frequency band as indicated by our method [1000–2800 Hz]

indicates that the CMF_1 has the deepest color value around the band [1000–2800] Hz. This proves the effectiveness of the proposed method even when the noise is high. A demodulation of the CMF_1 around the detected frequency bandwidth allows for detecting perfectly the defect harmonics (harmonic 1, 2, 3 and 4) (see Fig. 6b).

6.2 A Simulated Signal with Gear and Bearing Signatures

In order to simulate the vibratory signals of gearbox, a gear multiplicative model whose the meshing is modulated in amplitude has been used. The gear model as defined in [17] is used:

$$g(t) = \sum_{m=-\infty}^{+\infty} S_{r1}(t - m\tau_{r1}) + \sum_{m=-\infty}^{+\infty} S_{r2}(t - m\tau_{r2}) + \sum_{n=-\infty}^{+\infty} S_e(t - n\tau_e).\left(1 + \sum_{m=-\infty}^{+\infty} S_{r1}(t - m\tau_{r1})\right) \quad (10)$$

where τ_e, τ_{r1} and τ_{r2} represent the meshing period and the rotational periods; $S_e(t)$, $S_{r1}(t)$ and $S_{r2}(t)$ represents the meshing signal and its modulation. The gear signal is added to the simulated bearing signal (Eq. 8) with an added white noise with amplitude 0.2 and mean 0. Table 2 shows the frequency characteristics of the gear.

Table 2 Mesh frequencies of the gear

Fundamental mesh frequency (Hz)	Harmonic 1 (Hz)	Harmonic 2 (Hz)
330	660	990

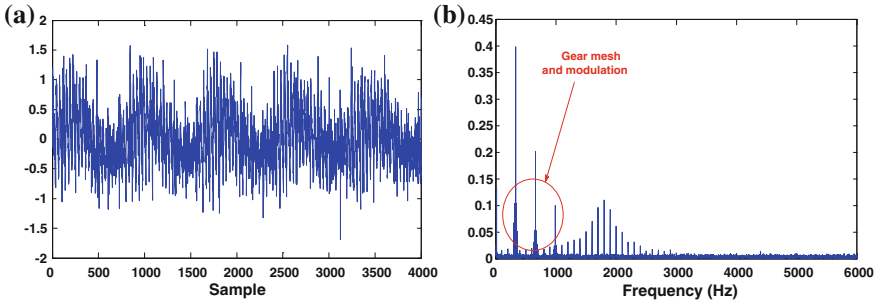

Fig. 7 **a** The simulated time gear and bearing signal, **b** its spectrum

The time signal is displayed in Fig. 7a and its spectrum in Fig. 7b. The aim of this section is to investigate the influence of the gear components on the proposed method, when the amplitude of the gear mesh is higher than the resonance excited by the bearing. The diagram paved by our method (Fig. 8a) allows for discriminating the natural frequencies from the two gear mesh frequencies when applying our method to this signal. The deepest color is in the expected bandwidth [1000–2800] Hz at CMF_1.

A demodulation of the CMF_1 around this bandwidth allows for the detection of the BPFO frequency and its harmonics as illustrated in Fig. 8b. This is due to the fact that the EMD decomposes the signal from fast to slow components. The components related to the gear are located in the CMF_2 and CMF_3.

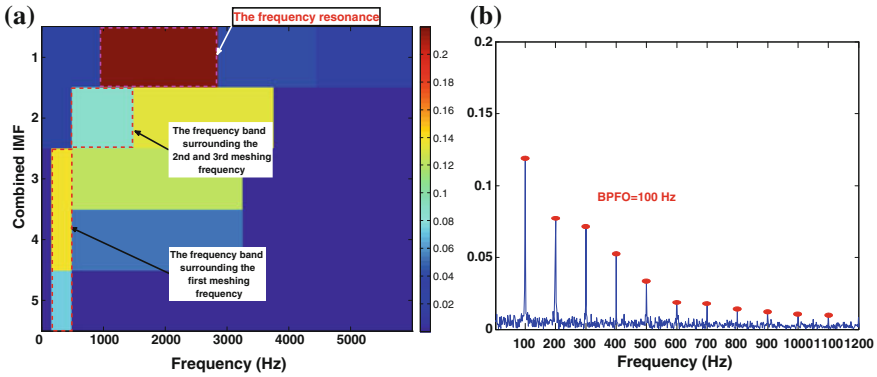

Fig. 8 **a** The diagram for the simulated signal with gear and bearing signature, **b** the envelope spectrum of the signal around the CMF_1 bandwidth

6.3 Experiments on a Bearing Test Bench

The test bench used in this study is described in Fig. 9(a). The shaft is supported by two bearings and connected to a motor with a coupling flange rubber. The bearings are double row ball (SKF, 1210 EKTN9). The defect is artificially caused on the outer ring by means of tool head carbide. The default size is only about of 40 μm as shown in Fig. 9b. The mechanical system can be imbalanced with a rotating radial load and a fixed axial load can be applied. The system was rotating at a speed of 300 rpm, and the frequency of default is then about 36.6 Hz (BPFO).

The measurements were conducted by acoustic emission. The equipment consists in an ultrasound detector (UE Systems UltraProb 10,000). The ultrasonic sensor used in this study operates in the lower ultrasonic spectrum from 20 to 100 kHz. A heterodyne circuit converts the high frequency AE signal as detected by the transducer around a central frequency Fc (here 30 kHz) into an audible signal

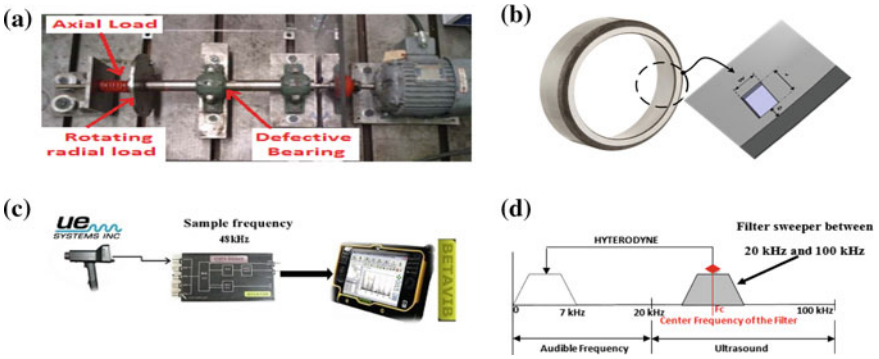

Fig. 9 **a** Test bench, **b** defect in outer, **c** race data acquisition system, **d** heterodyne principle

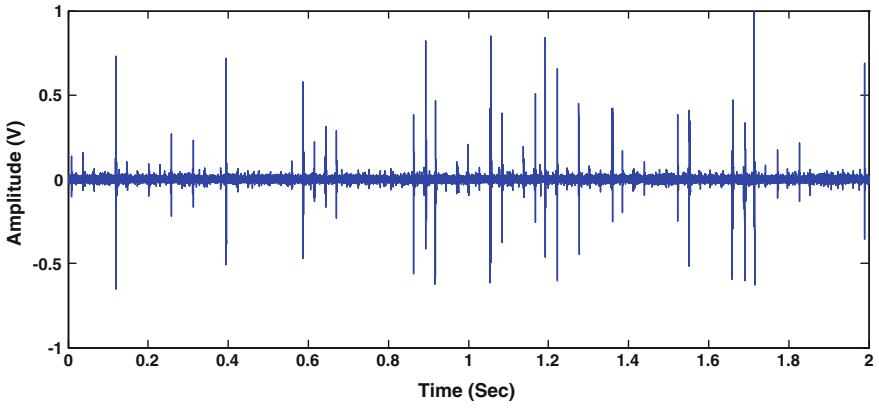

Fig. 10 A faulty bearing time signal

(0–7 kHz) (Fig. 9d) which may then be recorded through conventional data acquisition systems. It is connected to a collector-analyzer BETAVIB (See Fig. 9c). The sensor is connected to an analogue digital converter (THOR Analyzer PRO: DT9837-13310) with a sampling frequency of 48 kHz.

The time signal is shown in Fig. 10. The Combined Mode Function of the signal is displayed in Fig. 11a. The filter bank obtained for each CMF_i, is exhibited in Fig. 11b. The diagram paved by our method is shown in Fig. 12a. The result reveals a strong energy in the bandwidth [8000–18,000] Hz on CMF_1.

An analysis of the CMF_1 envelope around the bandwidth yields to the spectrum envelope as shown in Fig. 12b. This envelope spectrum shows clearly the presence of the fundamental peaks of the defect frequency (BPFO) and its harmonics until 800 Hz.

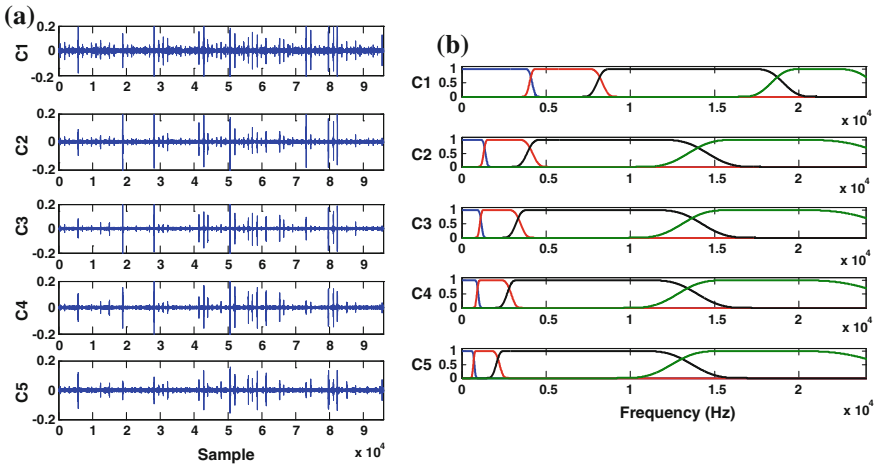

Fig. 11 **a** The combined mode function of the bearing signal, **b** the filter bank for each CMF

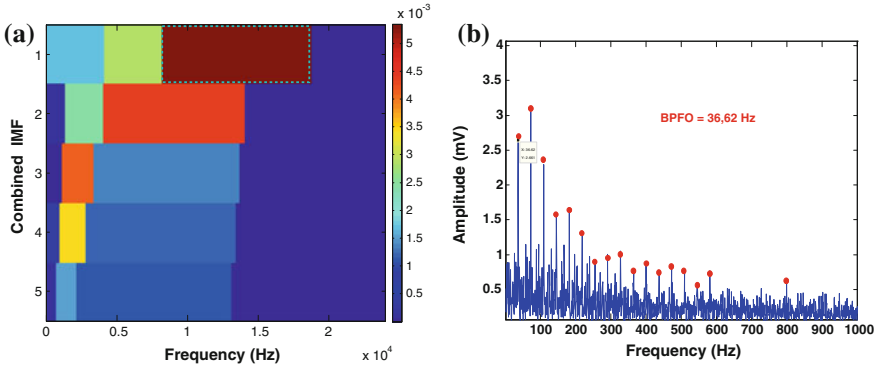

Fig. 12 **a** The diagram for bearing signal, **b** the envelope spectrum of the signal around the CMF_1 bandwidth

7 Conclusions

This study proposes a new concept based on the EMD and EW methods for early detection of bearing defects. The method was validated from numerical and experimental signals. From the results obtained in the studied cases, the proposed method can easily detect the resonances and bearing defects. Furthermore, the method has shown its efficiency to detect the most excited frequency bandwidth even in presence of very noisy signals. The results have shown that the identification of resonances or bearing defects is not perturbed by the frequencies coming from gear. Through experimental results, the proposed method has proven its ability to detect extremely low defect sizes (40 μm), which is essential for early detection. Finally, it should be emphasized that this new approach is not an optimal method for establishing the resonant frequency bandwidth but it is a quick way for detecting bearing defects, since we have two information in the same time: the useful frequency band and the CMF on which the default occurs.

References

1. Altmann J, Mathew J (2001) Multiple band-pass autoregressive demodulation for rolling-element bearing fault diagnosis. Mech Syst Sig Process 15(5):963–977
2. Antoni J, Randall RB (2006) The spectral kurtosis: application to the vibratory surveillance and diagnostics of rotating machines. Mech Syst Sig Process 20:308–331
3. Antoni J (2006) Fast computation of the Kurtogram for the detection of transient faults. Mech Syst Sig Process 21(1):108–124
4. Zhang Y, Randall RB (2009) Rolling element bearing fault diagnosis based on the combination of genetic algorithms and fast Kurtogram. Mech Syst Sig Process 23(5): 1509–1517
5. Barszcz T, Jabonski A (2011) A novel method for the optimal band selection for vibration signal demodulation and comparison with the Kurtogram. Mech Syst Sig Process 25:431–451
6. Qiu H, Lee J, Lin J, Yu G (2006) Wavelet filter-based weak signature detection method and its application on rolling element bearing prognosis. J Sound Vib 289:1066–1090
7. Nikolaou NG, Antoniadis IA (2002) Demodulation of vibration signals generated by defects in rolling element bearings using complex shifted morlet wavelets. Mech Syst Sig Process 16 (4):677–694
8. Lin J, Zuo MJ (2003) Gearbox fault diagnosis using adaptive wavelet filter. Mech Syst Sig Process 17:1259–1269
9. Tandon N, Choudhury A (1999) A review of vibration and acoustic measurement methods for the detection of defects in rolling element bearings. Tribol Int 32:469–480
10. Chen B, Yan Z, Chen W (2014) Defect detection for wheel-bearings with time-spectral kurtosis and entropy. Entropy 16:607–626. doi:10.3390/e16010607
11. Kedadouche M, Thomas M, Tahan A (2014) Monitoring machines by using a hybrid method combining MED, EMD, and TKEO. Adv Acoust Vib 2014, Article ID 592080, 10 pages. doi:10.1155/2014/592080
12. Gilles J (2013) Empirical wavelet transform. IEEE Trans Sig Process 61(16) (15 August)
13. Daubechies I (1992) Ten lectures on wavelets, ser. CBMS-NSF regional conference series in applied mathematics. Philadelphia, PA, USA: SIAM, 1992

14. Yan R, Gao RX (2007) Approximate entropy as a diagnosis tool for machine health monitoring. Mech Syst Sig Process 21:824–839
15. Sheen YT (2004) A complex filter for vibration signal demodulation in bearing defect diagnosis. Sound Vib 276:105–119
16. Gao Q, Duan C, Fan H, Meng Q (2008) Rotating machine fault diagnosis using empirical mode decomposition. Mech Syst Sig Process 22:1072–1081
17. El Badaoui M (1991) Contribution of vibratory diagnostic of gearbox by Cepstral analysis. Ph. D. thesis, Jean Monnet University of St Etienne (FR), p. 141 (in French)

Knife Diagnostics with Empirical Mode Decomposition

Michele Cotogno, Marco Cocconcelli and Riccardo Rubini

Abstract This paper deals with the condition monitoring of knives via the Empirical Mode Decomposition (EMD). The cutting process is basically transient, thus Fourier Analysis and similar signal processing tools aren't optimal because they treat signals as they were periodic. EMD is a signal analysis technique which is particularly suited for non-stationary and/or non-linear data, since it adaptively decomposes the signal in a sum of Intrinsic Mode Functions (IMFs). The knives under analysis are used inside an automated packaging machine; they are hydraulically actuated and are mounted on a moving support, so it's not possible to put sensors on them because of security reasons related to sensors wiring. Instead, the actuators control valve is hosted on a fixed machine part, so its pressure signal is the one analysed in this paper. The sum of two IMFs is used to estimate the knife state and to obtain a representation of the wearing process during a knife life.

Keywords Knife diagnostics · Empirical mode decomposition · Intrinsic mode functions · Pressure signal

Contents

1 Introduction 168
2 Empirical Mode Decomposition 169
3 Data Analysis and Results 170
4 Conclusions and Future Work 174
References 175

M. Cotogno (✉) · M. Cocconcelli · R. Rubini
Department of Science and Engineering Methods, University of Modena and Reggio Emilia, Via Amendola 2—Morselli Building, 42122 Reggio Emilia, Italy
e-mail: michele.cotogno@gmail.com

M. Cocconcelli
e-mail: marco.cocconcelli@unimore.it

R. Rubini
e-mail: riccardo.rubini@unimore.it

F. Chaari et al. (eds.), *Advances in Condition Monitoring of Machinery in Non-Stationary Operations*, Applied Condition Monitoring 4,
DOI 10.1007/978-3-319-20463-5_13

1 Introduction

Condition monitoring of knives is usually a demanding task, mainly because the cutting process is transient in its essence; because of this, Fourier Analysis and similar signal processing tools aren't optimal in this case because one of their basic assumptions is that the signal is periodic. In recent years the Empirical Mode Decomposition (EMD) has been developed [1], this being a signal decomposition technique which doesn't put any a priori assumption on the data and thus it's particularly suited for non-stationary data analysis. The knives analysed in this paper are used in an automated packaging machine where they cut the packaging material while it is moving, so they must be synchronized with the material flow and they are consequently hosted on movable supports. These supports also host other tools (such as a welding tool for the package sealing) and their movement is very wide, so it's not possible to put sensors on the supports because of security reasons concerning the sensors wirings. The knives are actuated by single effect hydraulic pistons (Fig. 1): both pistons are commanded by a common control valve which is hosted on a fixed part of the machine, so its pressure signal can be monitored and it is indeed used to perform the knives condition monitoring. The pistons perform the exiting movement of the knife, while its re-entering movement is performed by a spring tied to the knife by a spherical joint; the cutting happens without the blade making contact with an end of stroke.

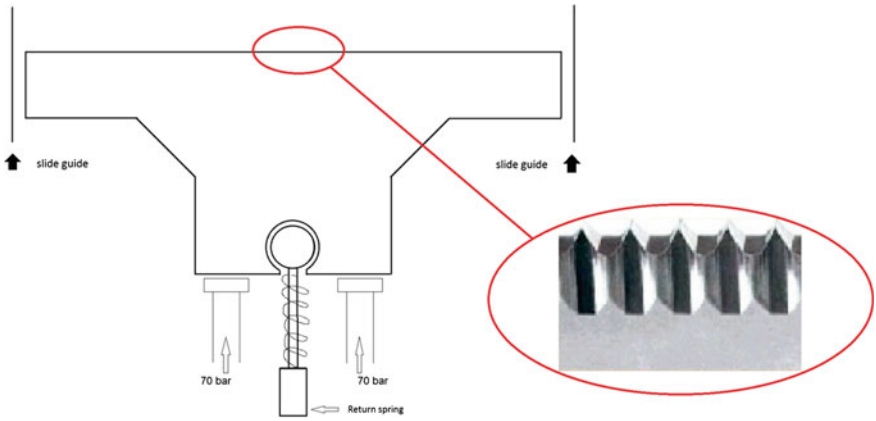

Fig. 1 Actuation scheme of the knives

2 Empirical Mode Decomposition

The EMD adaptively decomposes the signal in a set of intrinsic mode functions (IMFs), which often give very useful insights on the phenomena represented in the original signal (e.g. [2, 3]); indeed, an IMF represent a single oscillatory mode of the signal, and it's a function defined as follows:

- the number of extrema (i.e.: maxima and minima) and the number of zero-crossings must either equal or differ at most by one;
- at any point, the mean value of the envelope defined by the local maxima and the envelope defined by the local minima is zero.

In other words an IMF is almost symmetric with a unique local frequency, and ideally represent one of the signal "true" components, i.e. only one of the sources whose effects, summed up together, give the signal under analysis. The original EMD procedure is the following algorithm (also known as *sifting process*):

1. firstly, find out all the local maxima and the local minima of the signal under analysis $s(t)$, then the upper (lower) envelope can be get as the cubic spline interpolation of the maxima (minima);
2. compute the mean envelope $m(t)$ as the average of the upper envelope and the lower one. Let $h = s(t) - m(t)$ be the new input signal at step 1 and repeat the procedure above up to h satisfies the IMF definition, then set $c_i = h$;
3. separate the IMF from the signal, $r_{i+1} = s(t) - c_i$;
4. Let r_{i+1} be the new starting signal now (i.e. $s(t) = r_{i+1}$) and repeat steps 1–3 until the final residue $r_n(t)$ has at most one extreme or it is a constant or monotonic function.

By this process, the original signal $s(t)$ has been decomposed as the sum of n IMFs $c_i(t)$ and the final residue $r_n(t)$:

$$s(t) = \sum_{i=1}^{n} c_i(t) + r_n(t) \tag{1}$$

The IMFs form a local orthogonal basis as stressed in [1], although orthogonality can't be theoretically proved. In fact, the EMD method is totally data adaptive but still lacks of a firm mathematical background. This is the main cause of two of the principal problems of EMD process, which concern what in the EMD jargon are called the Convergence Criterion and the End-Effect. At step 2 of the sifting process, the Convergence Criterion declares if the result of the last completed sifting is an IMF or not: various stopping criteria were proposed (e.g.: [1, 4–6]), and here we made use of a combination of the SD Convergence Criterion [1] and the Fixed Siftings [6]. The SD criterion stops the sifting process at iteration k when the parameter SD_k is less than a predetermined value, which was set to 0.2 in this paper. SD_k is defined as follows:

$$\mathrm{SD}_k = \frac{\sum_{t=0}^{T}[h_{k-1}(t) - h_k(t)]^2}{\sum_{t=0}^{T}[h_{k-1}(t)]^2} \tag{2}$$

where t is the signal sample index and T is the signal's total samples number. The Fixed Sifting criterion simply stops the sifting after a predetermined number of iterations (which has been set to 23 in this work): this criterion comes from the observations that a good quality IMF is usually gathered after circa 10 iterations and that an excessive number of iteration (called *oversifting*) could distort the IMF. This distortion can come from several causes, including the Mode Mixing and the End Effect: Mode Mixing [7] is the spread of one "true" IMF in two or more IMFs due to intermittent or strongly non-stationary data; the End-Effect [8] is the corruption of the IMFs due to numerical errors in estimating the envelopes at the beginning and at the end of the signal. In this paper no action was taken against these two effects, i.e.: the original EMD was utilized.

3 Data Analysis and Results

The pressure data were acquired on a packaging machine used in an alimentary factory that experienced three problems concerning knives: the knives operational life was shorter than expected, and this caused many packages to be not complying with the requirements and therefore rejected. The pressure signals were acquired with National Instruments hardware and software. The acquisitions (sampling frequency: 10 kHz) were synchronized with the cutting; each record contains a sequence of 20 cuts (each cut has a duration of 0.7 s) and these sequences were acquired twice every hour. The available data encompass the complete life of three knives, which will be referred to as knife 1, 2 and 3: the larger dataset is relative to knife 1, while the smaller is relative to knife 3. It was chosen to apply EMD on the

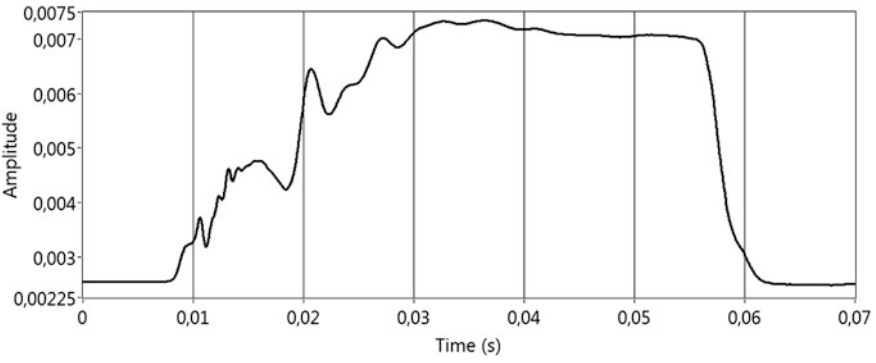

Fig. 2 Time synchronous average of the pressure signal of the actuating pistons control valve

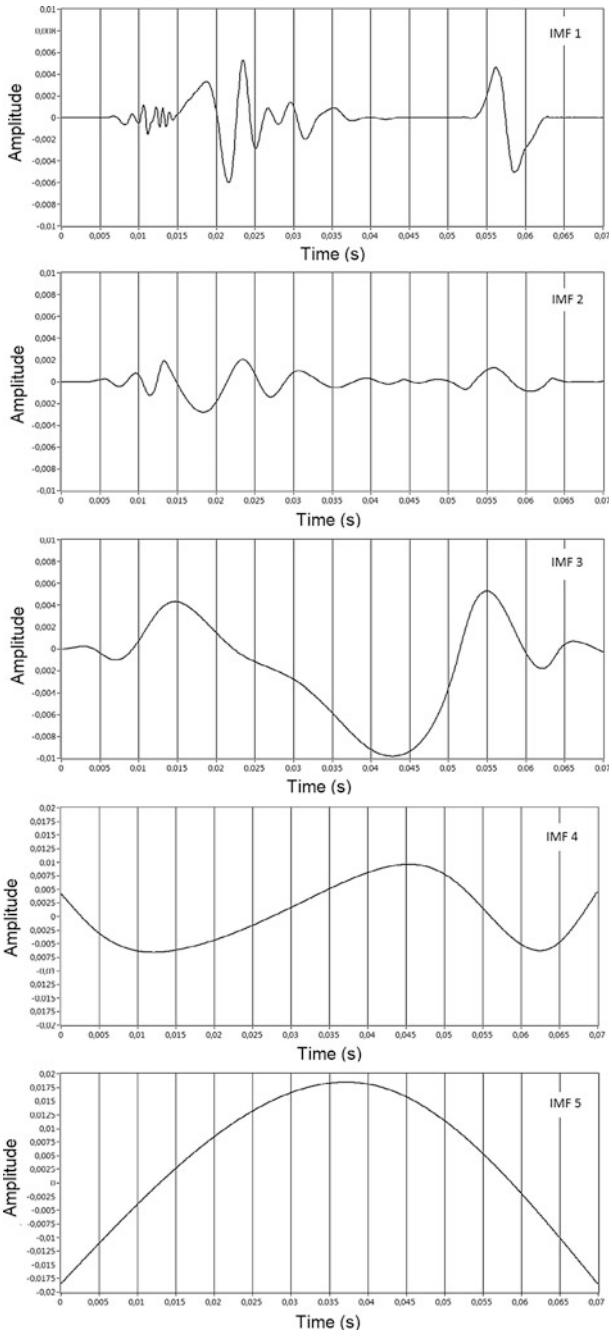

Fig. 3 EMD decomposition of the TSA pressure signal in Fig. 2

time synchronous average (TSA) [9] of the daily set of records in order to reject part of the noise that is naturally embedded in the data; Fig. 2 illustrates the TSA of the pressure signal. For the same reason, after examining the spectrum of the raw data it was chosen to lowpass filter the data before performing TSA, and the chosen cut-off frequency is 2300 Hz. Moreover, filtering the data this way allowed EMD to be stable in its decomposition: indeed, since the first IMF contains the higher frequency component [4] it often embodies the major part of the noise embedded in the data. Due to the aforementioned Mode Mixing, all this results in the fact that the same IMF may substantially differ from a decomposition to another, i.e.: the same simple oscillatory mode may reside in different IMFs. Since this outcome is unpredictable, it may prevent the use of this technique if repeatable (and thus reliable) results are requested, like in condition monitoring. This problem was resolved by the lowpass filtering of the data: by doing this, each IMF represents the same oscillatory mode in all the decompositions. In Fig. 3 the five IMFs extracted by the EMD process are reported. After analysing the EMD decomposition, the sum of the first two IMF was identified as the most communicative of the knife state: the instant of the minimum peak of this sum was noticed to occur gradually later along the knife life (Fig. 4), so this quantity was chosen as the diagnostic parameter.

In Fig. 5 the gradual shift of the instant of the minimum peak is shown along the entire life of knife 1: a logarithmic behaviour is recognizable, so it was chosen to fit these points with a curve described by the following equation:

$$y = a \ln[b(x + c)] \tag{3}$$

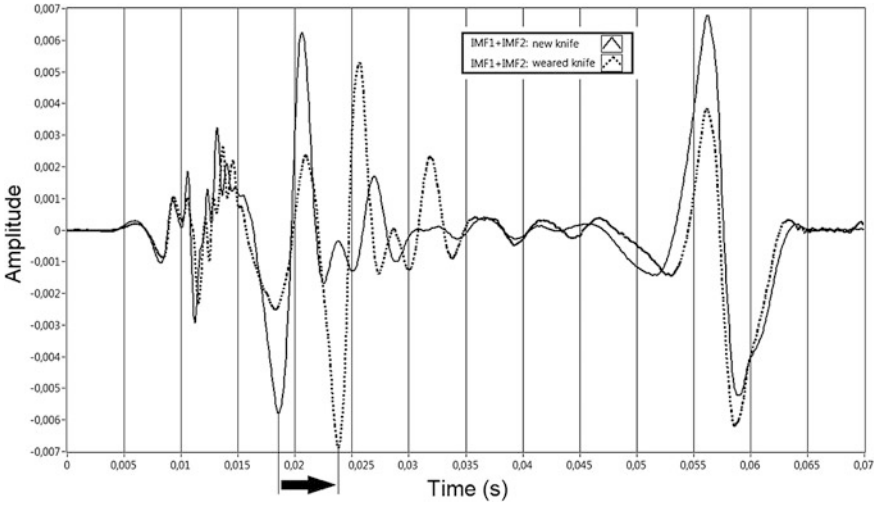

Fig. 4 Sum of the first and second IMFs in case of new knife (*solid line*) and weared knife (*dashed line*): the arrow highlight the change of the instant of the minimum peak

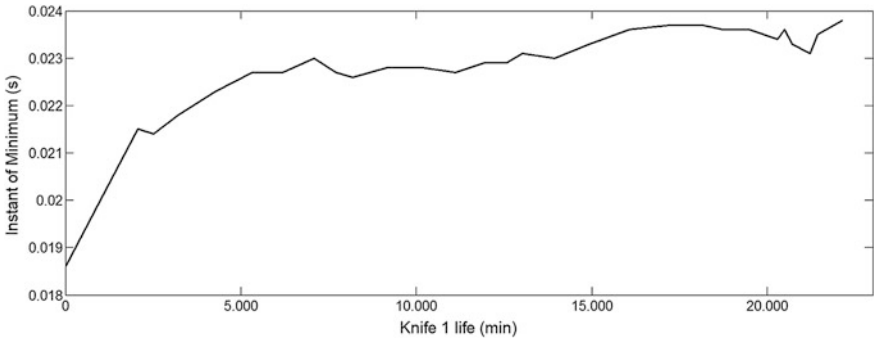

Fig. 5 Instant of minimum peak in the sum of the first 2 IMFs along the entire life of knife 1

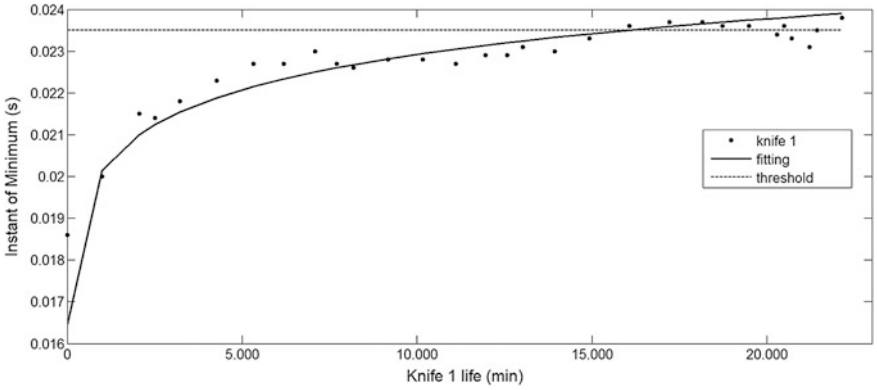

Fig. 6 Logarithmic fitting of knife 1 life. *x* axis is the knife working time in minutes, *y* axis is the instant (in seconds) of the minimum peak in the sum of the first two IMFs

where y is the instant of the minimum peak of the sum of the first two IMFs, x is the working minutes of the knife and a, b and c are fitting parameters. For the knife life showed in Fig. 6, the fitting gives $a = 123$ ms/min, $b = 1195$ min^{-1} and $c = 49.8$ min; this equation fits quite well the correspondent data from knife 2 (Fig. 7) but not so well for knife 3 (Fig. 8) for which only few recordings were made. Unfortunately, these are the only complete knife lives made available. Nevertheless, a value of 23.5 ms of the instant of the minimum peak can still be identified as a good indicator of excessive knife wear despite not in all the three cases. Considering this threshold in the case of knife 3 (Fig. 8), it can be seen that it is soon exceeded: therefore it can be deduced that either this knife was defective (or too weared too early) or that the available acquisitions encompassed only the final moments of the knife life; the latter case could explain the bad fitting exhibited by Eq. 3 for this knife.

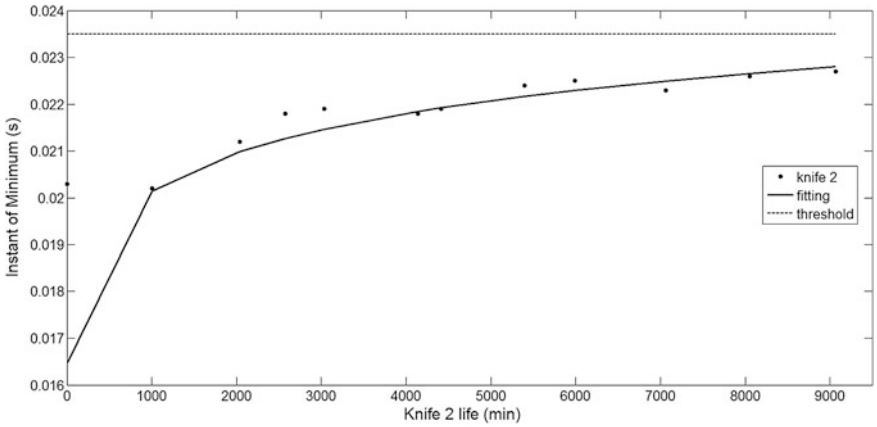

Fig. 7 Logarithmic fitting of knife 2 life. *x* axis is the knife working time in minutes, *y* axis is the instant (in seconds) of the minimum peak in the sum of the first two IMFs

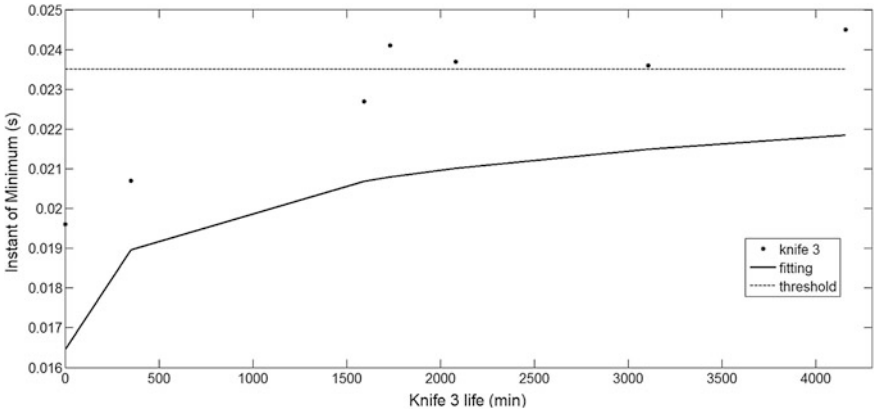

Fig. 8 Logarithmic fitting of knife 3 life. *x* axis is the knife working time in minutes, *y* axis is the instant (in seconds) of the minimum peak in the sum of the first two IMFs

4 Conclusions and Future Work

Condition monitoring of knives has been achieved by performing EMD on the pressure signal of the hydraulic control valve which feed the knife actuating pistons. EMD was applied on the daily TSA pressure signal after lowpass filtering the raw data, in order to reject noise and stabilize the EMD decomposition. The instant of the minimum peak of the sum of the first and second IMF was identified as the diagnostic parameter which shows a logarithmic behaviour, thus it was fitted by a 3 parameter logarithmic curve in case of knife 1, which is the knife with the largest dataset available. The obtained curve fit well the knife 2 data, while knife 3 isn't

fitted as well as the others. The results are encouraging despite the little amount of data available, since the fitting would probably improve its quality if more knife lives are taken into account; nevertheless, from this analysis is possible to identify a threshold (0.0235 s) which indicates the excessive wearing of the knife.

References

1. Huang NE, Shen Z, Long SR, Wu ML, Shih HH, Zheng Q, Yen NC, Tung CC, Liu HH (1998) The empirical mode decomposition and Hilbert spectrum for nonlinear and non-stationary time series analysis. Proc R Soc London Ser A 454:903–995
2. Ding H, Huang Z, Song Z, Yan Y (2007) Hilbert-Huang transform based signal analysis for the characterization of gas–liquid two-phase flow. Flow Meas Instrum 18(1):37–46
3. Huang NE, Shen Z, Long SR (1999) A new view of nonlinear water waves: the Hilbert spectrum 1. Annu Rev Fluid Mech 31(1):417–457
4. Flandrin P, Rilling G, Goncalves P (2004) Empirical mode decomposition as a filter bank. Signal Proc Lett IEEE 11(2):112–114
5. Huang NE, Wu M, Long SR, Shen SP, Qu W, Gloersen P, Fan KL (2003) A confidence limit for the empirical mode decomposition and Hilbert spectral analysis, Proc R Soc Lond A 459:2317–2345
6. Huang NE, Wu Z, Wang G, Chen X, Qiao F (2010) On intrinsic mode function. Adv Adapt Data Anal 2(3):277–293
7. Yang Y, Deng J, Wu C (2009) Analysis of mode mixing phenomenon in the empirical mode decomposition method, information science and engineering (ISISE), second international symposium on IEEE, pp 553–556
8. Cotogno M, Cocconcelli M, Rubini R, (2013) A window based method to reduce the end-effect in empirical mode decomposition, Diagnostyka 14, (2013)
9. Randall RB (2011) Vibration-based condition monitoring: industrial, automotive and aerospace applications. Wiley, West Sussex

Detection of Gear Faults in Variable Rotating Speed Using EEMD Decomposition and Instantaneous Frequency

Hafida Mahgoun, Ahmed Felkaoui, Semchedine Fedala and Fakher Chaari

Abstract When a local gear fault is presented, both the amplitude and phase of the tooth meshing vibration are modulated. If the rotating speed of the shaft is invariable, the gear-fault-induced modulation phenomenon which manifest as frequency sidebands equally spaced around the meshing frequency and its harmonics in vibration spectra. The Hilbert transform has been widely used in demodulation of such signals and has given good results. However, under variable rotating speed of the shaft, the meshing frequency and its harmonic and the sidebands vary with time and hence the vibration signal becomes non-stationary. The use directly of the Hilbert transform doesn't allow detecting the variation of the rotating machine and its harmonics which reflect the gear fault. In this study, we propose to use first the ensemble empirical decomposition (EEMD) which is particularly suitable for processing non stationary signals. By using EEMD the signal can be decomposed into a number of IMFs which are mono component, and then we use the Hilbert transform to calculate the instantaneous frequency and the envelope of each IMF. To identify the fault, we apply the ensemble empirical decomposition (EEMD) in second time to the instantaneous frequency to obtain mono component frequency and we calculate the spectrum of each IMF to evaluate the frequency. In this works, to validate this strategy, we analyze simulated signals for healthy and faulty gear boxes when the speed of machine is regular and variable; these models are based on the models of McFadden.

Keywords Vibration analysis · Non stationary operation · Time-varying frequency · EEMD · Instantaneous frequency

H. Mahgoun (✉) · A. Felkaoui · S. Fedala
Applied Precision Mechanics Laboratory, Institute of Optics and Precision Mechanics, Ferhat Abbas Sétif 1 University, Sétif 19000, Algeria
e-mail: mahafida006@yahoo.fr

F. Chaari
Mechanical Engineering Department, National School of Engineers of Sfax, Sfax, Tunisia

F. Chaari et al. (eds.), *Advances in Condition Monitoring of Machinery in Non-Stationary Operations*, Applied Condition Monitoring 4,
DOI 10.1007/978-3-319-20463-5_14

Contents

1 Introduction 178
2 EMD and EEMD Algorithms 179
2.1 EMD Algorithm 179
2.2 EEMD Algorithm 180
3 Hilbert Hang Transform 180
4 Simulation Studies 181
5 Conclusion 195
References 195

1 Introduction

Gears are mechanisms widely used for power transmission in rotating machinery. The malfunctions and defects of gears are inevitable in gear transmission system. The faulty gear is usually the major source of noise and vibration and may result in the abnormal operation and failure of the system. The early detection of gear faults is very important to prevent the system from damage. Vibration analysis is the most commonly used method for diagnosing gear faults since the vibration signals give plentiful information related to machines [1]. When a local gear fault is presented, both the amplitude and phase of the tooth meshing vibration are modulated. If the rotating speed of the shaft is invariable [1, 2], the gear-fault-induced modulation phenomenon which manifest as frequency sidebands equally spaced around the meshing frequency and its harmonics in vibration spectra.

The Hilbert transform has been widely used in demodulation and has given good results [1]. However, under variable rotating speed of the shaft, the meshing frequency and its harmonic and the sidebands vary with time and hence the vibration signal is non-stationary [3]. The use of the conventional fault diagnosis methods such the Fourier analysis and the Hilbert transform do not allow to good results. To avoid this problem, we propose to use first the ensemble empirical decomposition (EEMD) which is particularly suitable for processing non stationary signals [4]. This method was proposed by Huang et al. [4] for nonlinear and non-stationary signals and was recently applied in fault diagnosis of rotating machinery [2, 5–7]. It does not use a priori determined basis functions and can iteratively decompose a complex signal into a finite number of intrinsic mode functions (IMFs). Each resulting elementary component IMF can represent the local characteristic of the signal [4, 8]. Then, we can use the Hilbert transform to estimate the amplitude envelope and instantaneous frequency of the IMFs of interest and by using the EEMD and Hilbert transform, we can obtain a time- frequency representation [5, 8, 9]. The structure of the paper is as follows: Sect. 2 introduces the basic of EEMD. Section 3 is dedicated to Hilbert Huang transform method. In Sect. 4, we present a simulated signal to illustrate the non stationary phenomena due to the variation in the speed of the shaft. In Sect. 5, a conclusion of this paper is given.

2 EMD and EEMD Algorithms

2.1 EMD Algorithm

The EMD consists to decompose iteratively a complex signal into a finite number of intrinsic mode functions (IMFs) which verify the two following conditions:

(a) The number of extrema and the number of zeros of an IMF must be equal or differ at most by one,
(b) An IMF must be symmetric with respect to local zero mean.

For a given a signal $x(t)$ the EMD algorithm used in this study is summarized as follows [4, 8]:

Identify the local maxima and minima of the signal $x(t)$

1. Generate the upper $x_{\text{up}}(t)$ and lower $x_{\text{low}}(t)$ envelopes of $x(t)$ by the cubic spline interpolation of the all local maxima and the all local minima.
2. Average the upper and lower envelopes of $x(t)$ to obtain the local mean function:

$$m(t) = \frac{x_{\text{up}}(t) + x_{\text{low}}(t)}{2} \tag{1}$$

3. Calculate the difference

$$d(t) = x(t) - m(t) \tag{2}$$

4. If $d(t)$ verifies the above two conditions, then it is an IMF and replace $x(t)$ with the residual

$$r(t) = x(t) - d(t) \tag{3}$$

5. otherwise, replace $x(t)$ with $d(t)$

Repeat steps (1)–(5) until the residual satisfies the criterion of a monotonic function. At the end of this algorithm, the signal can be expressed as:

$$x(t) = \sum_{n=1}^{N} \text{IMF}_n(t) + r_N(t) \tag{4}$$

where $\text{LMF}_n(t)$ are IMFs, N is the number of IMFs extracted named and $r_N(t)$ is the final residue.

2.2 EEMD Algorithm

To alleviate the mode mixing effect of EMD, the EEMD was used. The EEMD decomposition algorithm of the original signal $x(t)$ used in this work is summarized in the following steps [4]:

1. Add a white noise $n(t)$ with given amplitude β_k to the original signal $x(t)$ to generate a new signal:

$$x_k(t) = x(t) + \beta_k n(t) \tag{5}$$

2. Use the EMD to decompose the generated signals $x_k(t)$ into N IMFs, $\mathrm{IMF}_{nk}(t), n = 1, \ldots, N$, where $\mathrm{IMF}_{nk}(t)$ is the nth IMF of the kth trial.

Repeat steps (1) and (2) K times with different white noise series each time to obtain an ensemble of IMFs: $\mathrm{IMF}_{nk}(t), k = 1, \ldots, K$.

Determine the ensemble mean of the K trials for each IMF as the final result:

$$\mathrm{IMF}_n(t) = \lim_{k\to\infty} \frac{1}{K} \sum_{k=1}^{K} \mathrm{IMF}_{nk}(t), n = 1, \ldots, N \tag{6}$$

The relationship among the amplitude of the added white noise and the number of ensemble trials is given by [4]:

$$\delta_k = \frac{\beta_k}{\sqrt{K}} \tag{7}$$

where K is the number of ensemble trials, β_k is the amplitude of the added noise and δ_k is the variance of the corresponding IMF(s).

3 Hilbert Hang Transform

The technique of Hilbert Huang transform (HHT) [5, 8, 9] is based on two methods: the empirical mode decomposition EMD and the application of the Hilbert spectral analysis method to the IMFs, we obtain the instantaneous frequency and the envelope of each IMF. By application of HHT, we obtain a time- frequency distribution of signal amplitude, which permits the identification of localized features.

The Hilbert transform for any signal $x(t)$ is:

$$y(t) = \frac{1}{\pi} \int_{-\infty}^{+\infty} \frac{x(\tau)}{t - \tau} \mathrm{d}\tau \tag{8}$$

With the Hilbert transform $y(t)$ of the function $x(t)$ we obtain the analytic function,

$$z(t) = x(t) + iy(t) = c(t)e^{i\theta(t)} \tag{9}$$

$$c(t) = \sqrt{(x^2 + y^2)} \tag{10}$$

$$\theta(t) = \tan^{-1}\left(\frac{y}{x}\right) \tag{11}$$

Here c is the instantaneous amplitude, and θ is the instantaneous phase function. The instantaneous frequency is:

$$\omega(t) = \frac{d\theta}{dt} \tag{12}$$

4 Simulation Studies

In this section first, we compare the model of a vibration signal generated by the normal gears and constant speed and the model of a vibration signal generated by the normal gears and variable speed. Secondly, we compare the model of a vibration signal generated by the faulty gears and constant speed and the model of a vibration signal generated by the faulty gears and variable speed. Then this section is divided in two parts:

(a) Normal gear

First, consider a normal pair of gears, meshing under a constant speed. The vibration signal generated by the normal gears and constant speed can be represented as [1]:

$$x_{nc}(t) = \sum_{m=0}^{M} X_m \cos(2\pi m Z f_r t + \varphi_m) \tag{13}$$

where M is the number of tooth-meshing harmonics, X_m and φ_m are, respectively, the amplitude and the phase of the mth meshing harmonic, Z is the number of gear teeth, t is the time, f_r is the shaft rotation frequency, and $f_m = Zf_r$ is the meshing frequency. Equation (13) indicates that the vibration signal acquired from a normal gearbox generally exhibits predominant frequency components at the meshing frequency and its harmonics.

Figure 1 shows the time domain and the spectrum of a simulated vibration signal from a normal gearbox which has the same features that the experimental test bench (a gear with 20 teeth and a constant rotational frequency equal to 20 Hz, and the meshing frequency is 400 Hz and the sampling frequency is 20,000 Hz). The spectrum exhibits the meshing frequency and its first harmonic for $M = 3$.

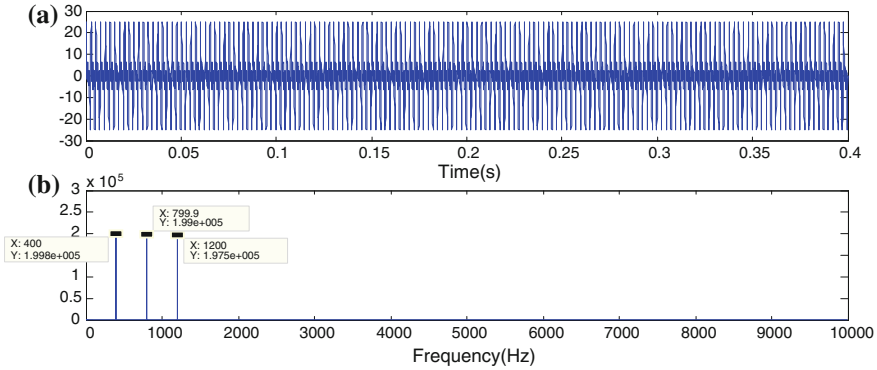

Fig. 1 Simulated vibration signal from a normal gearbox with a constant speed, **a** time domain, **b** spectrum

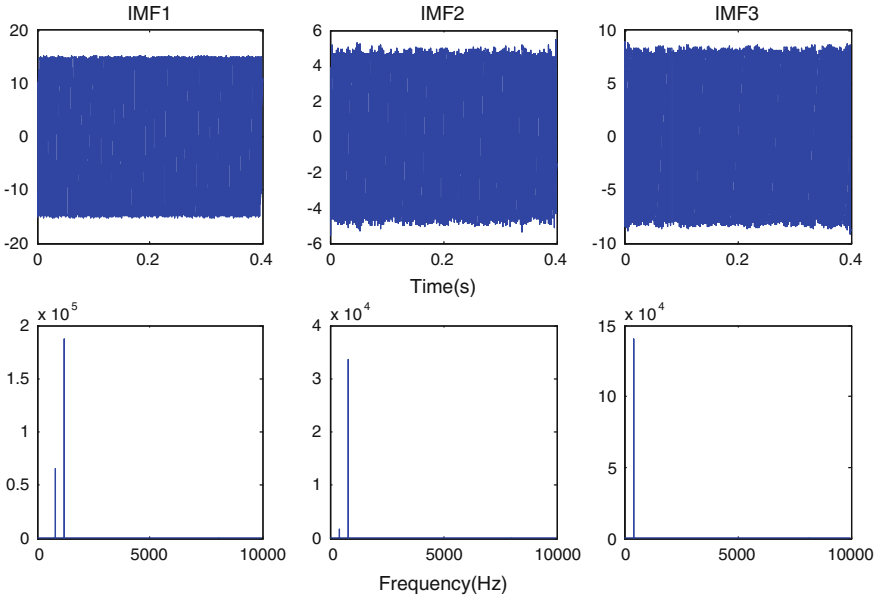

Fig. 2 IMFs obtained by EEMD of the simulated vibration signal from a normal gearbox with a constant speed and their spectrum

The EEMD method decomposes the signal in three IMFs which correspond to the meshing frequency and its harmonic (Fig. 2), we can see that this IMFs are not all mono components which explain the huge fluctuation of instantaneous frequency given in Fig. 3, this figure shows that the frequency doesn't change in time. To calculate exactly the value of each instantaneous frequency, we can use the Fourier transform. Figure 4 shows the spectrum of each instantaneous frequency of

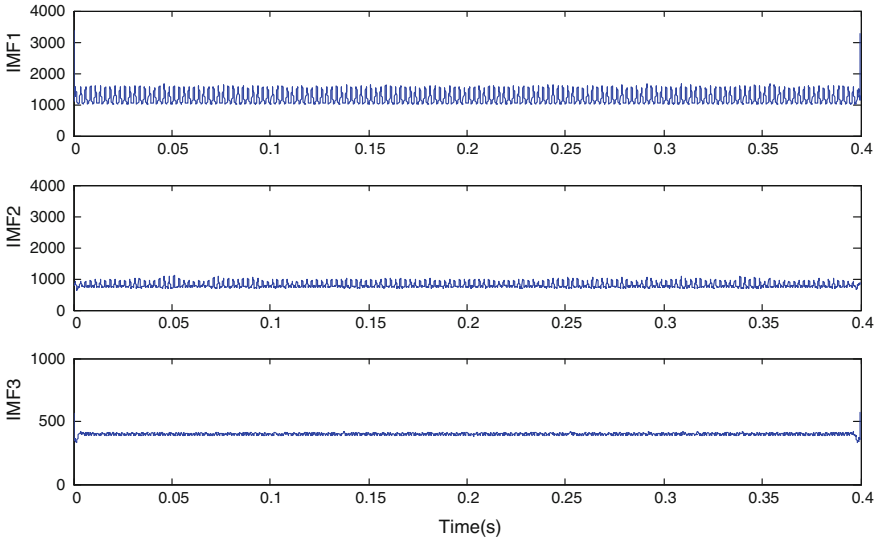

Fig. 3 The instantaneous frequencies of each IMF (Fig. 2)

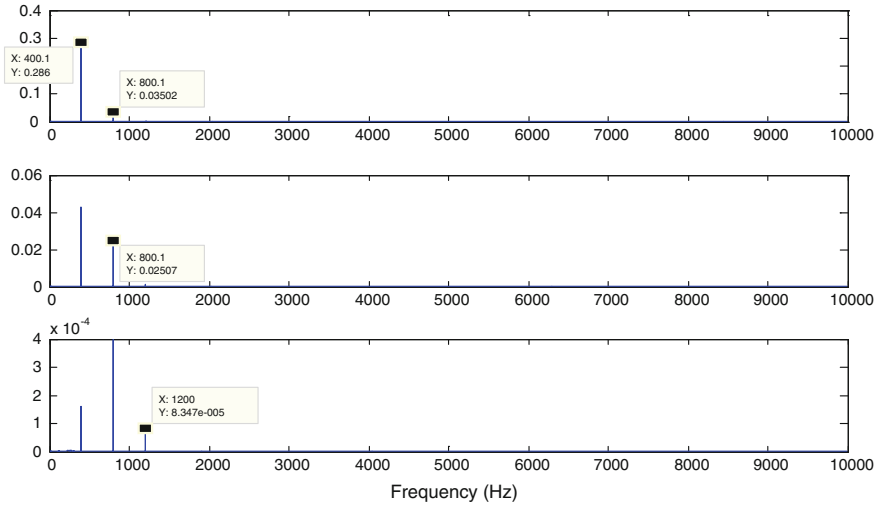

Fig. 4 The spectrum of the instantaneous frequency of each IMF

each IMF. We can see that each instantaneous frequency isn't a mono component but it was composed from a multiple frequency.

Now, we suppose that the normal pair of gears, meshing under a variable speed. The vibration signal generated by the normal gears and variable speed can be represented as:

$$x_{nv}(t) = \sum_{m=0}^{M} X_m \cos(2\pi m Z f_s t + \varphi_m) \tag{14}$$

where f_s is the variable shaft rotation frequency which varies with time. In this paper we suppose that:

$$f_s = f_r t \tag{15}$$

Figure 5 shows the time domain and the spectrum of a simulated vibration signal from a normal gearbox with a variable speed, from this two representations we can that there is a variation of the speed but we can't get more information about it. We can see also that the variation of the frequency is large band because the speed increase with time.

By using the EEMD method we can decomposes the signal also in three IMFs which correspond to the meshing frequency and its harmonics (Fig. 6). Figure 7 shows the variation of the instantaneous frequency of each IMF. We can see clearly that the three frequencies increase in time. This assumption can be clearly shown by the Hilbert Huang representation given in Fig. 8. The spectrum of each instantaneous frequency (Fig. 9) gives the bandwidth of each IMF and gives the variation of the frequencies, the instantaneous frequency and the HHT gives more information about this variation.

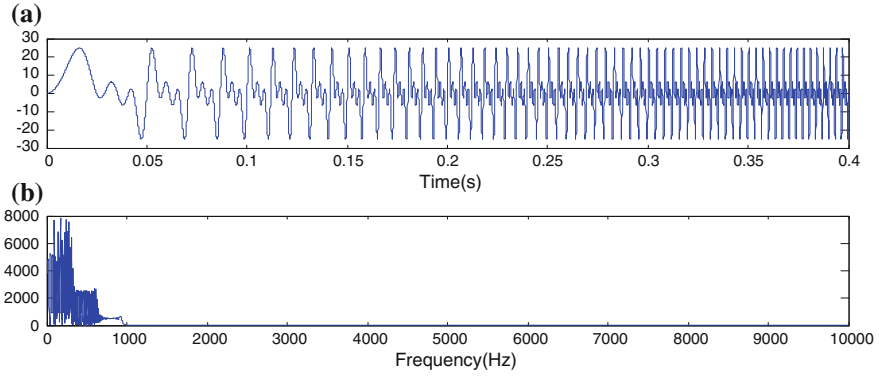

Fig. 5 Simulated vibration signal from a normal gearbox with a variable speed, **a** the time domain, **b** the spectrum

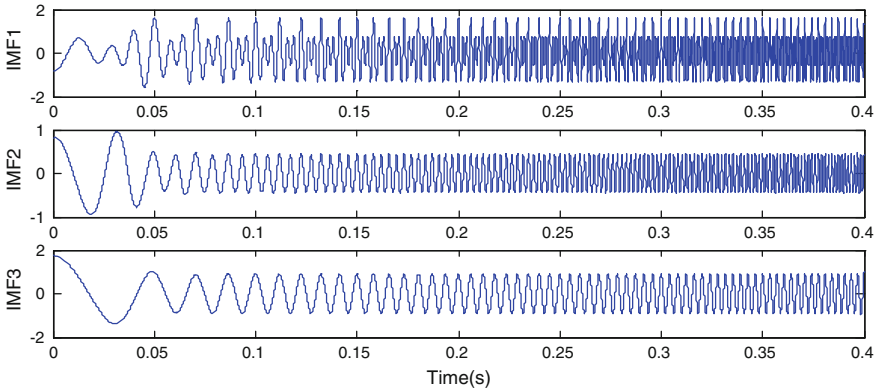

Fig. 6 IMFs obtained by EEMD of the simulated vibration signal from a normal gearbox with a variable speed

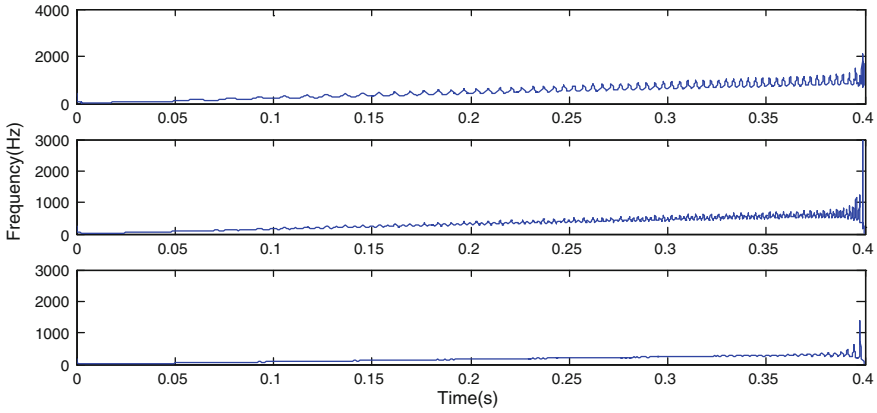

Fig. 7 The instantaneous frequencies of the IMFs (Fig. 6)

(b) Faulty gear

If the gearbox which is meshing under a constant speed has a tooth fault, the generated signal has been modulated by the unchanging rotating frequency and contains amplitude and phase modulations that are periodic with the rotating frequency of the gear. The modulation of the meshing frequency, as a result of faulty teeth, generates sidebands, which are frequency components equally spaced around the carrier frequency. Changes in vibration generated by a faulty gear tooth can be represented by the following amplitude and phase-modulating functions, $a_m(t)$ and $b_m(t)$, respectively:

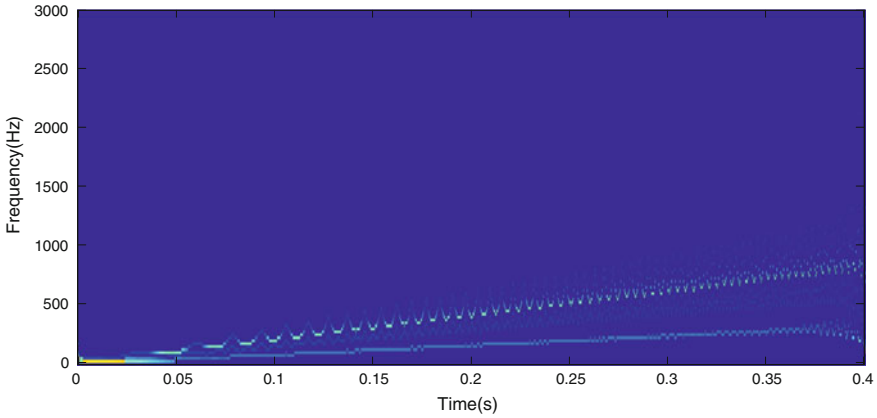

Fig. 8 The Hilbert Huang transformation of a simulated vibration signal from a normal gearbox with a variable speed

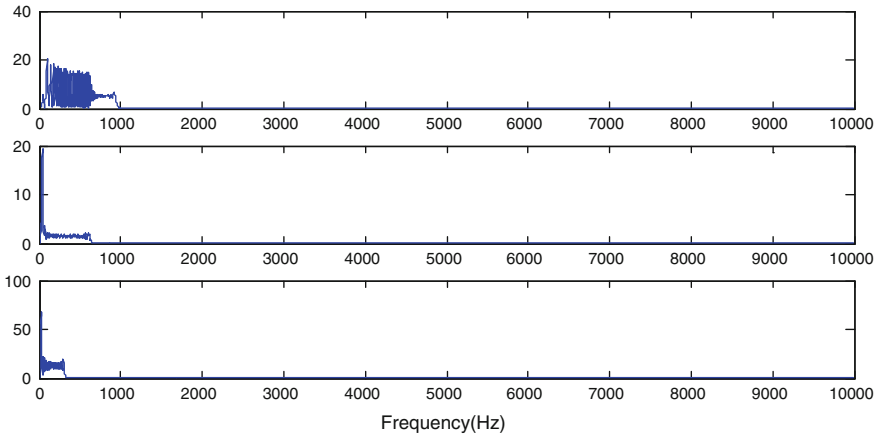

Fig. 9 The spectrum of the IMFs (Fig. 6)

$$\begin{cases} a_m(t) = \sum_{l=0}^{L} A_{ml} \cos(2\pi m Z f_r t + \alpha_{ml}) \\ b_m(t) = \sum_{l=0}^{L} B_{ml} \cos(2\pi m Z f_r t + \gamma_{ml}) \end{cases} \tag{16}$$

where L is the number of sidebands around tooth-meshing harmonics, A_{ml} and B_{ml} are amplitudes at the lth sidebands of amplitude and phase-modulating signals, respectively, around the mth meshing harmonic, α_{ml} and γ_{ml} are phases at the lth sideband of amplitude and phase-modulating signals, respectively, around the mth

meshing harmonic. The signal $x_{fc}(t)$, produced by a pair of meshing gears with a tooth fault in constant speed, is given by:

$$x_{fc}(t) = \sum_{m=0}^{M} X_m(1 + \mathrm{a}_m(\mathrm{t}))\cos(2\pi m Z f_r t + b_m(t)) \tag{17}$$

Figure 10 shows the time domain and the spectrum of a simulated vibration signal from a faulty gearbox for a constant speed and for $M = 3$. The time domain presents a modulated signal. In the same time the frequency present the mesh frequency and its harmonics surround by side bands.

Results obtained by using EEMD are presented in Fig. 11. The spectrum of each IMF shows that these IMFs are multi component and modulated (Fig. 12). The instantaneous frequency of each IMF are given in Fig. 13, which shows also that the meshing frequency and its harmonics are not a mono component they are composed by many frequencies, they are modulated by the frequency of rotation and its harmonics but the instantaneous frequency shows that the speed is constant, we can obtain more information about these frequencies if we calculate the spectrum of the instantaneous frequencies (Fig. 14), but this information is insufficient to describe the frequency of rotation and its harmonics. To obtain more information, we propose to decompose the instantaneous frequencies by EEMD and then we calculate the new instantaneous frequency of each new IMF, and finally we calculate the spectrum of each new instantaneous frequency. Figure 15 shows some new IMFs of the first instantaneous frequency described in Fig. 13. We can see from this figure that the first IMF has a shape of periodic impacts with a period equal to (0.05 s = 1/20 Hz), which correspond to the frequency of the shaft. The spectrum of each new IMF is given in Fig. 16. We can see from this figure clearly the frequency

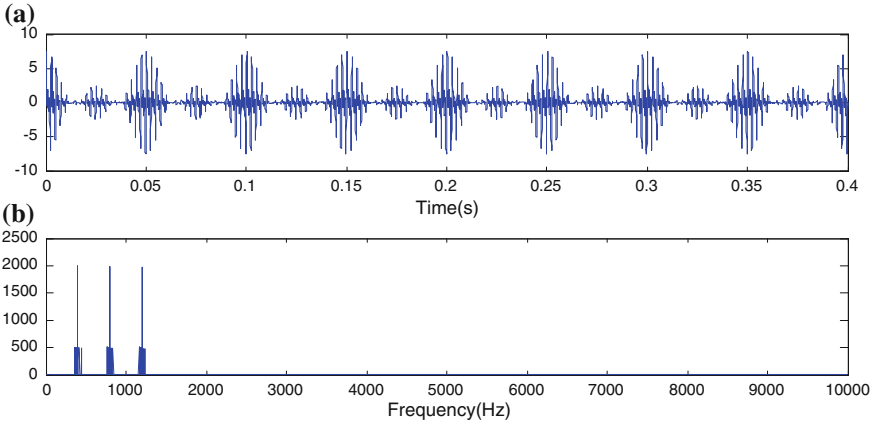

Fig. 10 Simulated vibration signal from a faulty gearbox with a constant speed, **a** the time domain, **b** the spectrum

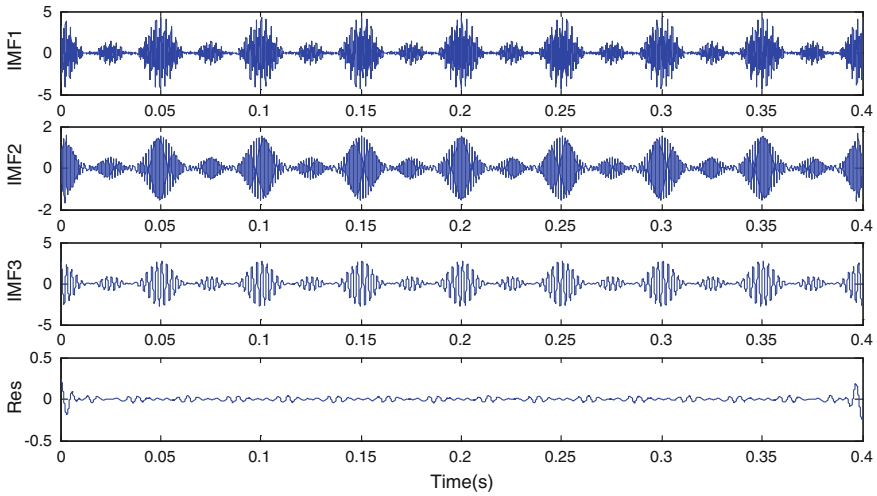

Fig. 11 IMFs obtained by EEMD of the simulated vibration signal from a faulty gearbox with a constant speed

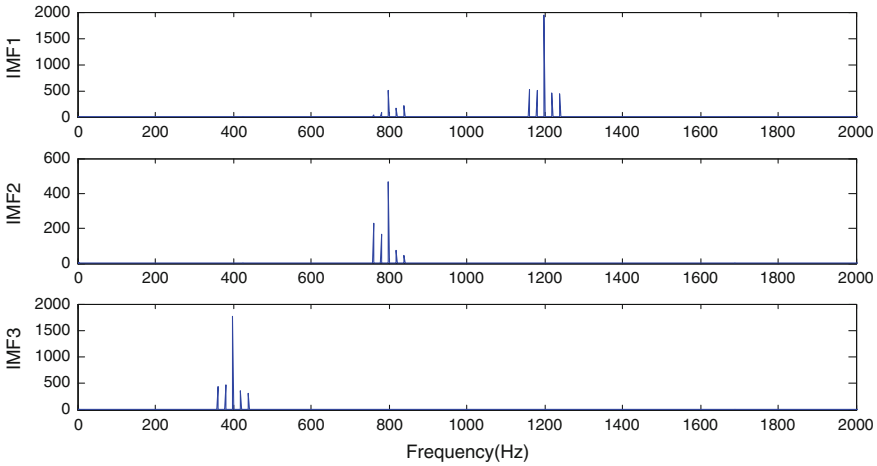

Fig. 12 The spectrum of IMFs (faulty gearbox with a constant speed)

of rotation and its harmonics (20, 40, and 60 Hz) and the mesh frequency (400 Hz) and its first harmonic (800 Hz).

Figure 17 shows the spectrum of the IMFs obtained by decomposition of the second instantaneous frequency, and Fig. 18 shows the spectrum of the IMFs obtained by decomposition of the third instantaneous frequency.

All these figures give the same information about the speed of the machine (constant speed) and give the values of the frequencies of modulation.

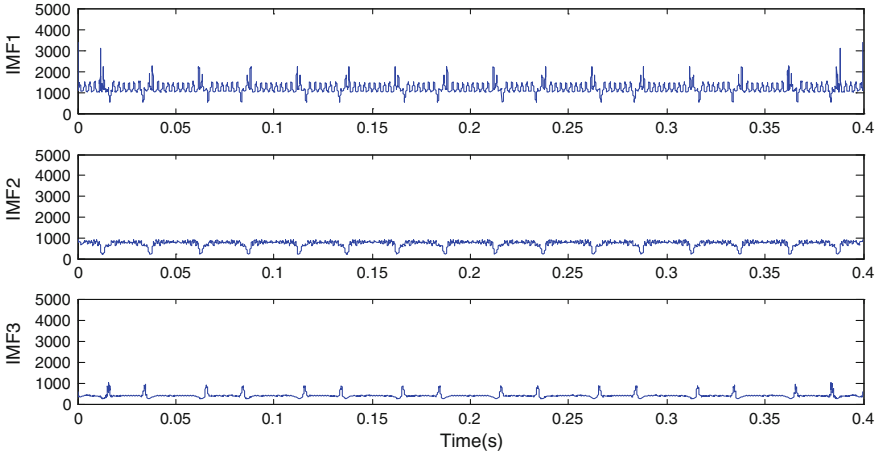

Fig. 13 The instantaneous frequencies of the IMFs (Fig. 11), (faulty gearbox with a constant speed)

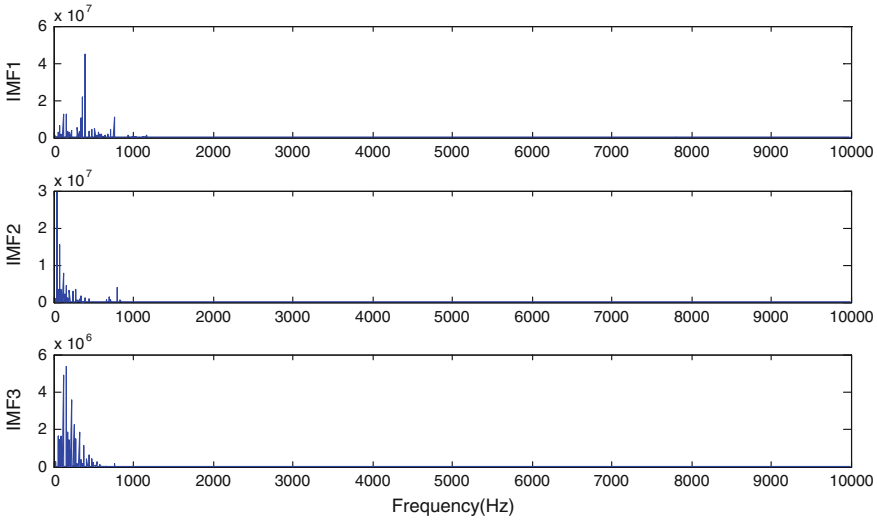

Fig. 14 The spectrum of the instantaneous frequencies, (faulty gearbox with a constant speed)

Now we suppose that the faulty pair of gears, meshing under a variable speed. The vibration signal generated by the faulty gears and variable speed can be represented as:

$$x_{fv}(t) = \sum_{m=0}^{M} X_m(1 + a_{mv}(t))\cos(2\pi m Z f_s t + b_{mv}(t)) \tag{18}$$

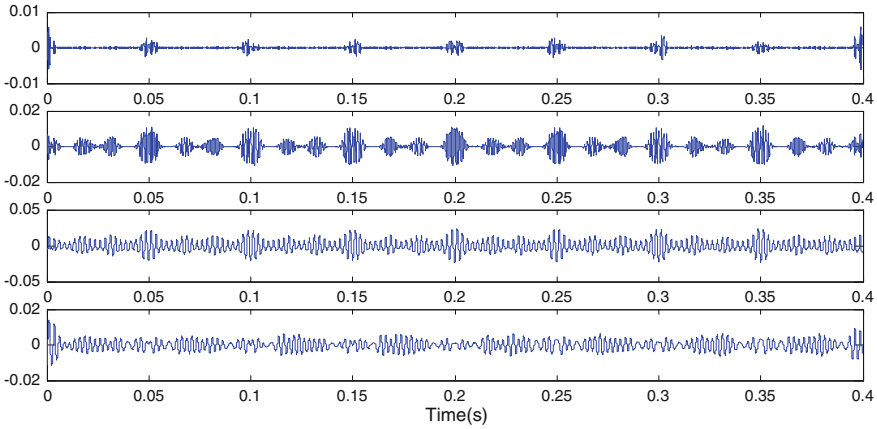

Fig. 15 EEMD of the first instantaneous frequency, (faulty gearbox with a constant speed)

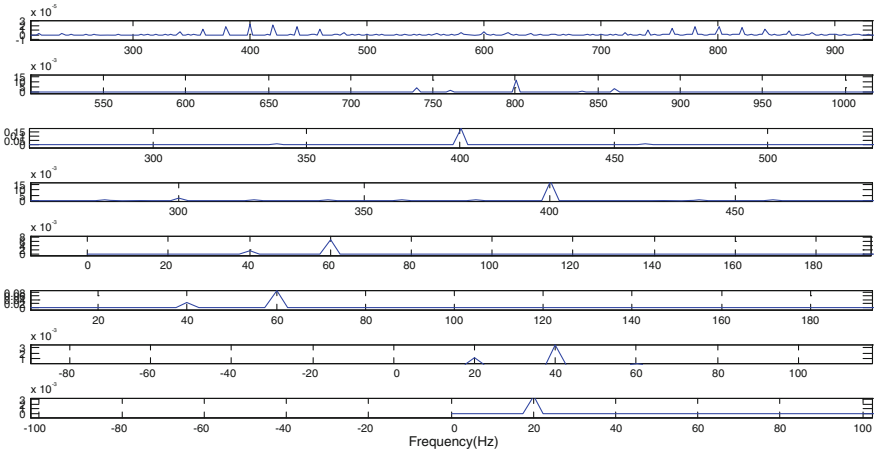

Fig. 16 The spectrum calculated for each IMF of the first instantaneous frequency, (faulty gearbox with a constant speed)

where $a_{mv}(t)$ and $b_{mv}(t)$ $b_{mv}(t)$ are respectively amplitude and phase-modulating functions:

$$\begin{cases} a_{mv}(t) = \sum_{l=0}^{L} A_{ml}\cos(2\pi mZf_s t + \alpha_{ml}) \\ b_m(t) = \sum_{l=0}^{L} B_{ml}\cos(2\pi mZf_s t + \gamma_{ml}) \end{cases} \tag{19}$$

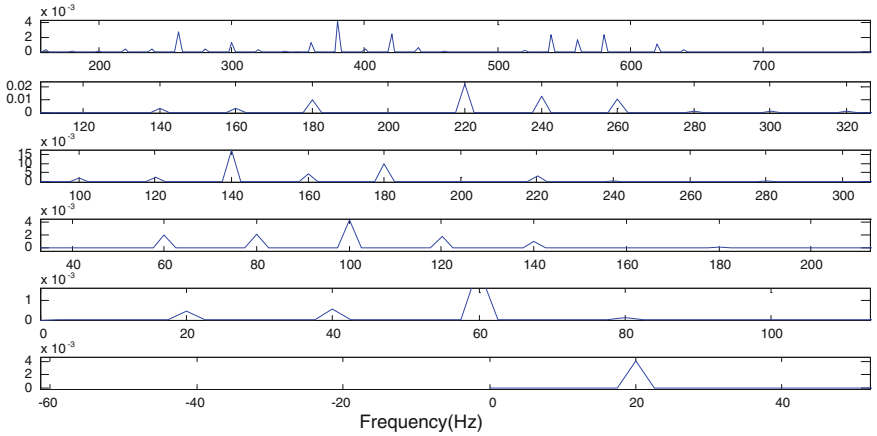

Fig. 17 The spectrum calculated for each IMF of the second instantaneous frequency

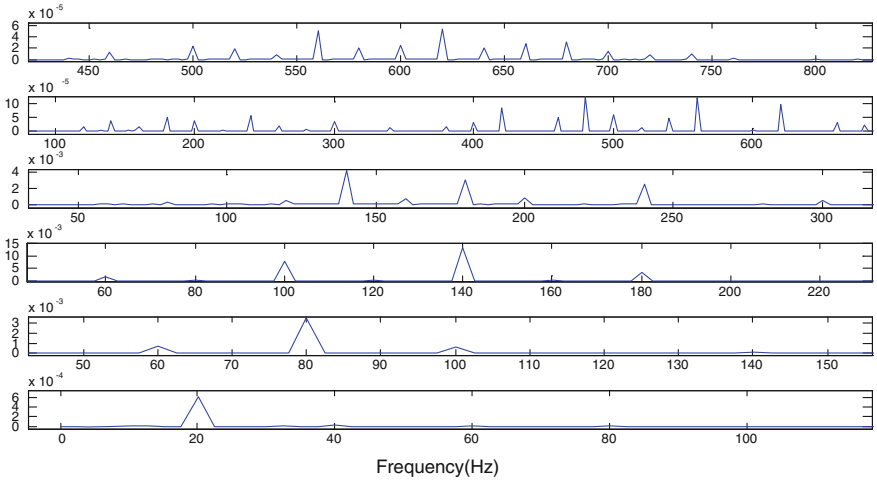

Fig. 18 The spectrum calculated for each IMF of the third instantaneous frequency

Figure 19 shows the time domain and the spectrum of a simulated vibration signal from a faulty gearbox for a variable speed $f_s = f_r t$, the time domain presents a modulated signal.

In the same time the spectrum present a large band of frequency. But the spectrum for the same length (0.4 s) does not show the third harmonic of the meshing frequency, for this reason we have increase the length of the signal to 0.8 s. Then for a variable speed, we shall take more samples than in the constant speed.

Results obtained by using EEMD are presented in Fig. 20. The instantaneous frequency of each IMF are given in Fig. 21, this figure shows that the meshing

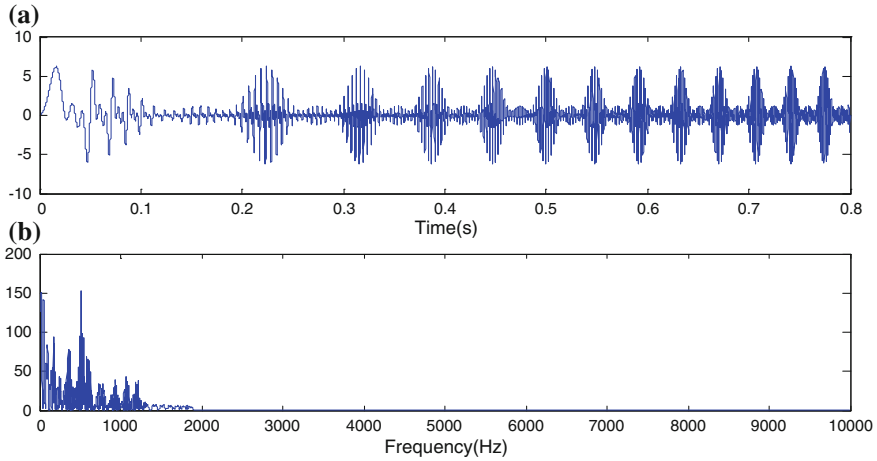

Fig. 19 Simulated vibration signal for a faulty gearbox with a variable speed, **a** the time domain, **b** the spectrum

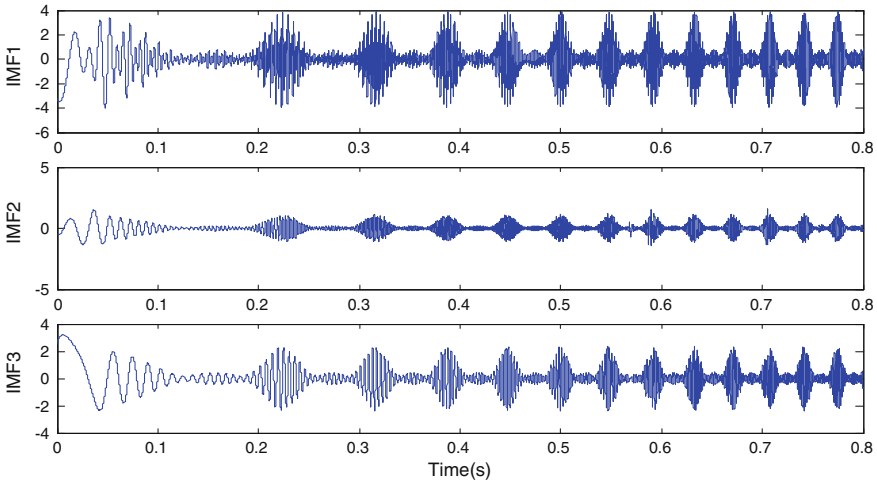

Fig. 20 IMFs obtained by EEMD of the simulated vibration signal from a faulty gearbox with a variable speed

frequency and its harmonics are modulated by many frequencies (frequency of rotation and its harmonics), and the meshing frequency decrease in time. The HHT given in Fig. 22 shows clearly this variation of the speed, we can obtain more information about this frequencies (frequency of rotation and its harmonics) if we calculate the spectrum of the instantaneous frequencies (Fig. 23).

The zoom of this figure (Fig. 24) shows large bands of frequency which explain the variation of the rotation frequency and its harmonics.

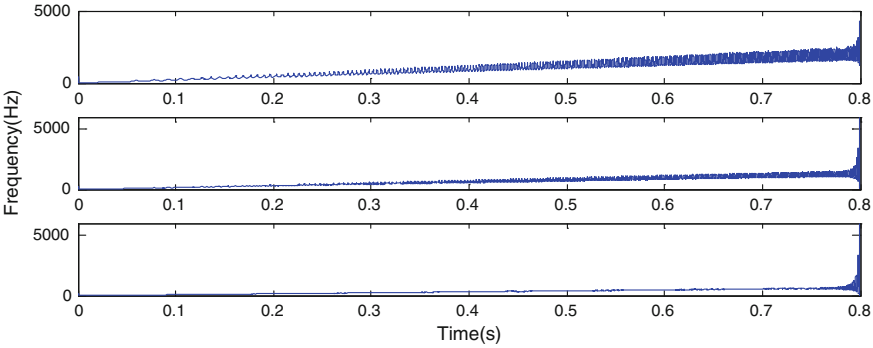

Fig. 21 The instantaneous frequencies of the IMFs (Fig. 21)

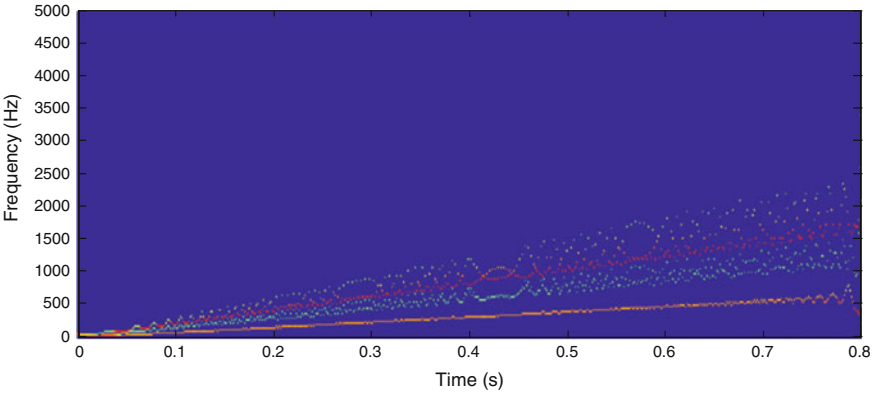

Fig. 22 The Hilbert Huang transformation of a simulated vibration signal from a faulty gearbox with a variable speed

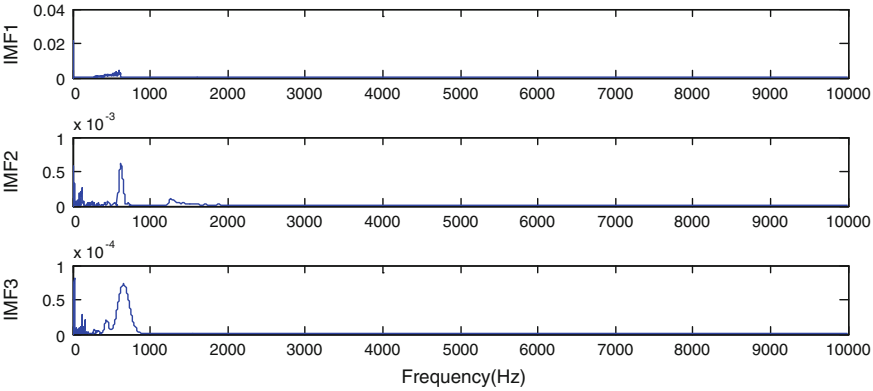

Fig. 23 The spectrum calculated of the instantaneous frequency (variable speed)

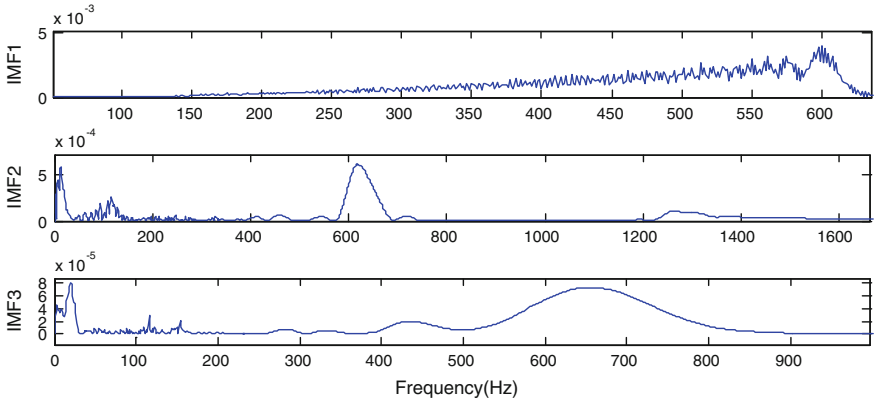

Fig. 24 Figure 23 zoomed

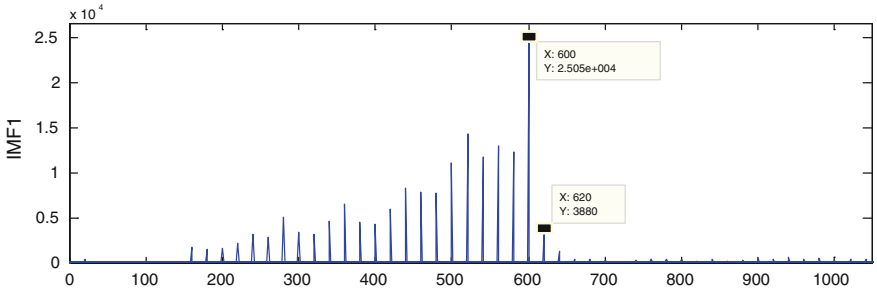

Fig. 25 Speed transformation of the first IMFs of the instantaneous frequency (Fig. 21)

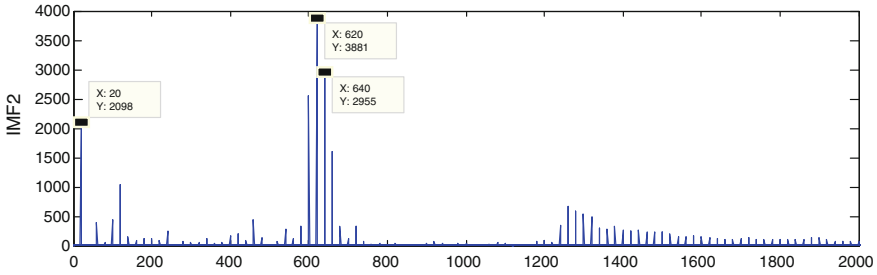

Fig. 26 Speed transformation of the second IMFs of the instantaneous frequency (Fig. 21)

To detect the rotation frequency and its harmonics, we propose to use the speed transform suggested by Capdessus et al. [10]. Figures (25, 26 and 27) show the results given by this method; we can see clearly the frequency of 20 Hz and its harmonics and we can see also that these figures have the same shape of the figures represented in Fig. 24.

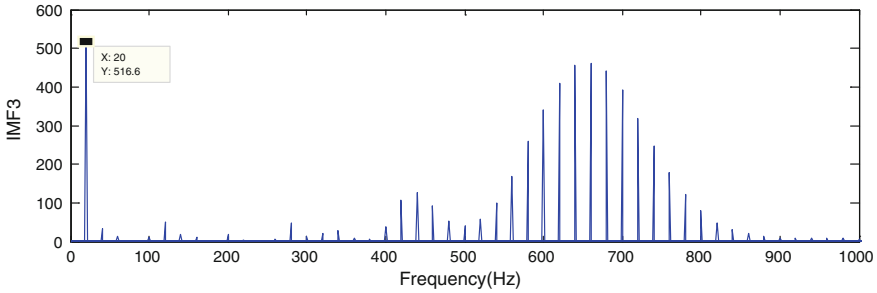

Fig. 27 Speed transformation of the third IMFs of the instantaneous frequency (Fig. 21)

5 Conclusion

In this study we have used a simulated signal to distinguish between a vibration signal from a machine which work in stable conditions and a vibration signal from another one which work at variable conditions like (variable speed and load). We have used the Hilbert Huang transformation based on EEMD to detect the variation of the speed. We also used the EEMD to decompose the instantaneous frequency which is considered as a non stationary signal, the IMFs given by the second decomposition was analyzed by using the FFT, the spectrum of the new IMFs show that the speed is variable, to detect the rotation frequency of the machine we have used the speed transform.

References

1. McFadden PD (1986) Detecting fatigue cracks in gears by amplitude and phase demodulation of the meshing vibration. Trans ASME, J Vibr, Acoust, Stress Reability, in Des 108:165–170
2. Wu TY, Chen JC, Wang CC (2012) Characterization of gear faults invariable rotating speed using Hilbert-Huang transform and instantaneous dimensionless frequency normalization. Mech Syst Sig Process 30(1):103–122
3. Luo J, Yu D, Liang M (2012) Application of multi-scale chirplet path pursuit and fractional fourier transform for gear fault detection in speed up and speed-down processes. J Sound Vib 331(1):4971–4986
4. Wu Z, Huang NE (2009) Ensemble empirical mode decomposition: a noise-assisted data analysis method. Adv Adapt Data Anal 1(1):1–41 (world scientific publishing company)
5. Liu B, Riemenschneider S, Xub Y (2005) Gearbox fault diagnosis using empirical mode decomposition and Hilbert spectrum. Mech Syst Sig Process 17(9):1–17
6. Mahgoun H, Bekka RE, Felkaoui A (2012) Gearbox fault diagnosis using ensemble empirical mode decomposition (EEMD) and residual signal. Mech Ind 13(01):33–44
7. Wu TY, Chung YL (2009) Misalignment diagnosis of rotating machinery through vibration analysis via hybrid EEMD and EMD approach. Smart Mater Struct 18(9):095004
8. Huang NE, Shen Z, Long SR (1998) The empirical mode decomposition and the Hilbert spectrum for nonlinear and non-stationary time series analysis. Proc R Soc Lond Ser 454:903–995
9. Huang NE, Shen SSP (2005) Hilbert-Huang transform and its applications. London
10. Capdessus C, Sekko E, Antoni J (2013) Speed transform, a new time-varying frequency analysis technique, CMMNO2013, Ferara 8–10 May

Multidimensional Signal Analysis for Technical Condition, Operation and Performance Understanding of Heavy Duty Mining Machines

Pawel K. Stefaniak, Radoslaw Zimroz, Pawel Sliwinski, Marek Andrzejewski and Agnieszka Wyłomanska

Abstract Continuous improvement of production efficiency, safety and reliability of machines' operation requires implementation of modern technology in the company, including monitoring systems, IT solutions, computer aided management tools etc. Gathering of data describing processes, extraction of information and knowledge discovery in automatic way seem to be key strategy in order to enhance company's performance in many contexts. In this paper we will refer to the current status of the system being developed in one of the biggest Polish mining companies. A special attention will be paid to signal validation, pre-processing and analysis in order to retrieve unknown knowledge about machine condition, processes executed on a daily basis and machine/operator performance.

Keywords Self-propelled mining machine · Mining industry · Monitoring system · Data processing · Data analysis

P.K. Stefaniak (✉) · R. Zimroz
KGHM Cuprum R&D, Wroclaw, Poland
e-mail: pkstefaniak@cuprum.wroc.pl; pawel.stefaniak@pwr.edu.pl

R. Zimroz
e-mail: rzimroz@cuprum.wroc.pl; radoslaw.zimroz@pwr.edu.pl

P. Sliwinski · M. Andrzejewski
KGHM PM S.A., Lubin, Poland
e-mail: p.sliwinski@kghm.pl

M. Andrzejewski
e-mail: m.andrzejewski@kghm.pl

P.K. Stefaniak · R. Zimroz · A. Wyłomanska
Wroclaw University of Technology, Wroclaw, Poland
e-mail: agnieszka.wylomanska@pwr.edu.pl

F. Chaari et al. (eds.), *Advances in Condition Monitoring of Machinery in Non-Stationary Operations*, Applied Condition Monitoring 4,
DOI 10.1007/978-3-319-20463-5_15

Contents

1 Introduction 198
2 Definition of Tasks and Expectations 200
3 Data Validation 200
4 Data Preprocessing 201
5 Signal Processing for Condition Monitoring Purposes 202
6 Signal Processing for Processes Monitoring Purposes 204
6.1 An Efficiency of Copper Ore Transport Using Loader 204
6.2 Quality and Efficiency of Drilling Process 205
7 Signal Processing for Performance Evaluation 206
8 Multidimensional Signals and Information Fusion 207
9 Conclusions 208
References 209

1 Introduction

Nowadays, there is a strong tendency to optimize—in wide sense—production efficiency, safety of operations, environmental impact etc. in mining industry. One can notice in different media that mining industry evolves to be green, intelligent, smart, invisible, safe and effective [1–4]. Different actions have been taken to achieve it. Undoubtedly, transfer of technology to mining industry that covers monitoring system, IT solutions, computer aided management systems, automation/robotics, etc. significantly helps in modernization of mining industry [5–13]. In this paper, we will present a brief description of one of such actions that is developing in one of the biggest underground mining companies in Poland. The aim of the project is to use advanced monitoring systems, modern IT solutions and so called data mining techniques to identify weak points in production chain and improve its efficiency. The production process is quite complex, it is understood here as excavating copper ore from underground mine and transporting it by LHD machines (involving drilling/bolting vehicles, loaders and trucks) to belt conveyor system located also underground.

Modelling, analyzing and optimizing of the entire process is a very difficult task. To achieve goals abovementioned the task has been decomposed into smaller sub-processes associated with given machine, operations or processes. To implement such system, one needs to consider technological issues (to equip each machine with on-board data acquisition system, to build telecommunication infrastructure in dozens of kilometres of mining excavations corridors including wireless technology to transfer data from mobile machines automatically, to create data storage and processing centre for more than 1000 machines from 3 different mines, etc.) as well as organizational and legal (mining regulations) specificity in the underground mine. In this paper we will focus on data processing context only.

Depending on the machine type, specified monitoring system (basic or advanced), number of acquired parameters might reach even up to 47 variables. They might represent instantaneous variation of different physical variables (temperatures, pressures, speeds, weights, torque) or flags (0/1) describing status of machine element/subsystem (for example: low level of oil). Furthermore, in order to reference signal to the location of machine in geographic space of mine, the location system has been developed. Next, these data are transferred via IT infrastructure in underground mine and stored in an advanced database structure of Business Intelligence System. From that point there is time for advanced data analysis. Structure of the entire system is illustrated in Fig. 1.

It is necessary to define number of essential, unique and dedicated algorithms for data validation/processing/analysis which lead to obtain information on the performance, appropriate usage and condition of the machine and operator's work. These algorithms can be simple, might be based only on one-dimensional data set or more advanced—when they are based on multidimensional data related to different characteristics of the machine. In this case it might be considered as the so called data fusion.

A list of information required to supporting decision making process related to particular management level is defined. It covers variety of issues: (i) Condition monitoring and fault detection purposes, (ii) Identification of machine operation regimes, (iii) Machine usage and efficiency analysis, (iv) Machine operator monitoring that can affect machine design (feedback to machine manufacturer), work organization, production performance, machine operation, operator's skills and training program, machine lifetime, safety of operation, etc. From signal processing point of view, there are a lot of challenging issues. The same problem (signal validation, segmentation, cycle/event identification, process understanding, change/anomaly detection etc.) might significantly differ for various variables and might require individual algorithms. At first stage of validated data processing we are

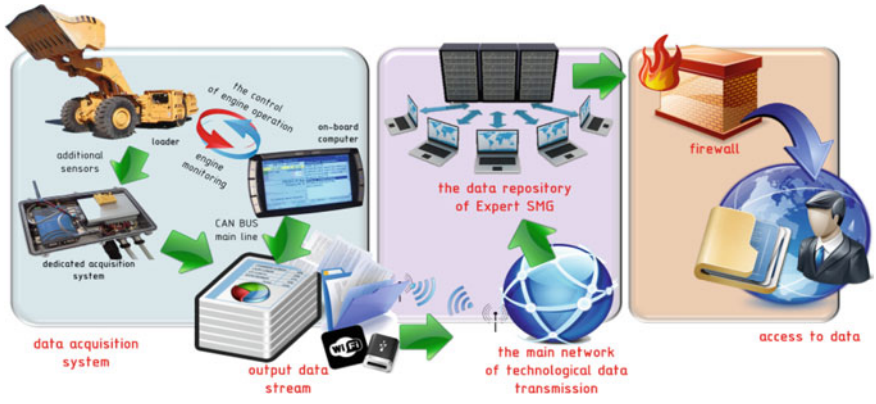

Fig. 1 Functional flow chart of the decision support system can be categorized following 3 layers. **a** Data acquisition, **b** data transmission, **c** data processing and presentation

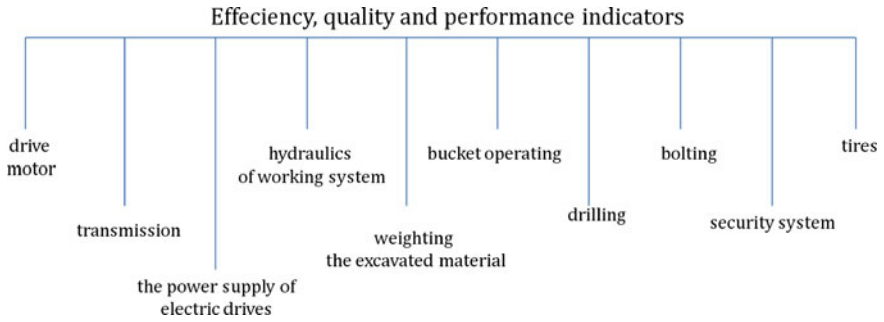

Fig. 2 Machine decomposition into subsystems

focusing on signal segmentation and identification of event or work cycles [13–17]. At second stage, we want to understand how important these events are (percentage-wise) for single shift, day, week, etc. by simple aggregation or advanced statistical analysis. Finally, we want to model extracted segments [15, 16] in order to analyze if there is any correlation between them (cyclic operation should be carried out in similar way). In the paper we are going to describe in detail mentioned issues and present selected examples from present actual examples from the industry.

2 Definition of Tasks and Expectations

In order to simplify the problem, the machine was decomposed into several key sub-systems as presented in Fig. 2. Depending on the machine, some of these systems might not exist (there is no weighting system in drilling machine and so on). For each sub-system there are groups of tasks related to signal analysis. They might be focused on condition monitoring, process monitoring (in order to increase safety, minimize processes of degradation and optimize process efficiency and production cost), machine's and its operator's performance analysis.

3 Data Validation

While measuring physical quantities such as temperature, pressure, rotational speed, engine torque, weight etc. one should be aware that in industrial conditions, a quality of the data might vary in time. If one consider single machine and on which the 2 h long experiment in the laboratory will be conducted, the problem of data validation nearly does not exist. When we extend data acquisition procedure to many variables, many machines, industrial conditions, especially underground mine

with severe environmental impact, problem of automatic, quick data validation becomes more serious than further processing. The problem of signal validation was mentioned by Ray [18]. Recently, significance of signal validation in industrial systems has been highlighted/recalled by Jablonski and Barszcz [19]. In our work, several stages of simple validation procedures have been applied. The project is in progress so validation might be still updating if new problems appear. The reason of multistage validation is that acquired variables are of different dynamics and types. First step was to analyze energy of each channel. If there is no energy, it means no data is acquired. However, some variables are flag-type (0 if no problem).

Another issue is null value. Many algorithms simply doesn't work if NaN/Null value appears. Missing single sample or single sample outlier is also frequent problem.

For some types of variables, taking into account experience/knowledge about machine, environmental issues, applied technology, used sensors and measurement techniques might significantly help during validation. As a result of validation procedures, different pieces of information might be obtained. The obtained information include whether the data package is correct or reveals some problems with detailed report on what kind of problem exists (e.g. no energy, missing values, outliers etc.). Such incomplete data will require further manual analysis.

4 Data Preprocessing

Basic knowledge about machines and processes performed by machines allows to define some preliminary tasks for signal processing. Due to used mining technology it is expected that signals should reveal cyclic nature. For vast amount of machines sequences of actions are repeatable for example loading, haulage and discharge of material, drilling a hole for blasting or bolting, starting and switching off engine at beginning/end of each mining shift, etc. Identification of these cycles and statistical analysis of their length, each cycle component or in general cycle performance analysis is one of the most important issues for processes and machine performance analysis. Another crucial task is machine regime identification. It might be generalized as cycle component analysis (time needed for petrol refuelling, time required to access the mining face, duration of idle mode/overloading mode etc.).

From signal processing perspective a key problem is related to segmentation procedures. These procedures may vary between machines and processes; segmentation might be conducted with regards to analysis of engine speed, engine torque, hydraulic pressure etc. In Fig. 3a, b, c examples of theoretical processes are presented altogether with their relation to engine operation regimes, drilling process regimes and loader operations regimes.

In the next section we will illustrate that identification of mentioned cycles and their components is possible. It will be done with utilization of different types of real data. Statistical parameterisation and analysis of these parameters might provide a number of information.

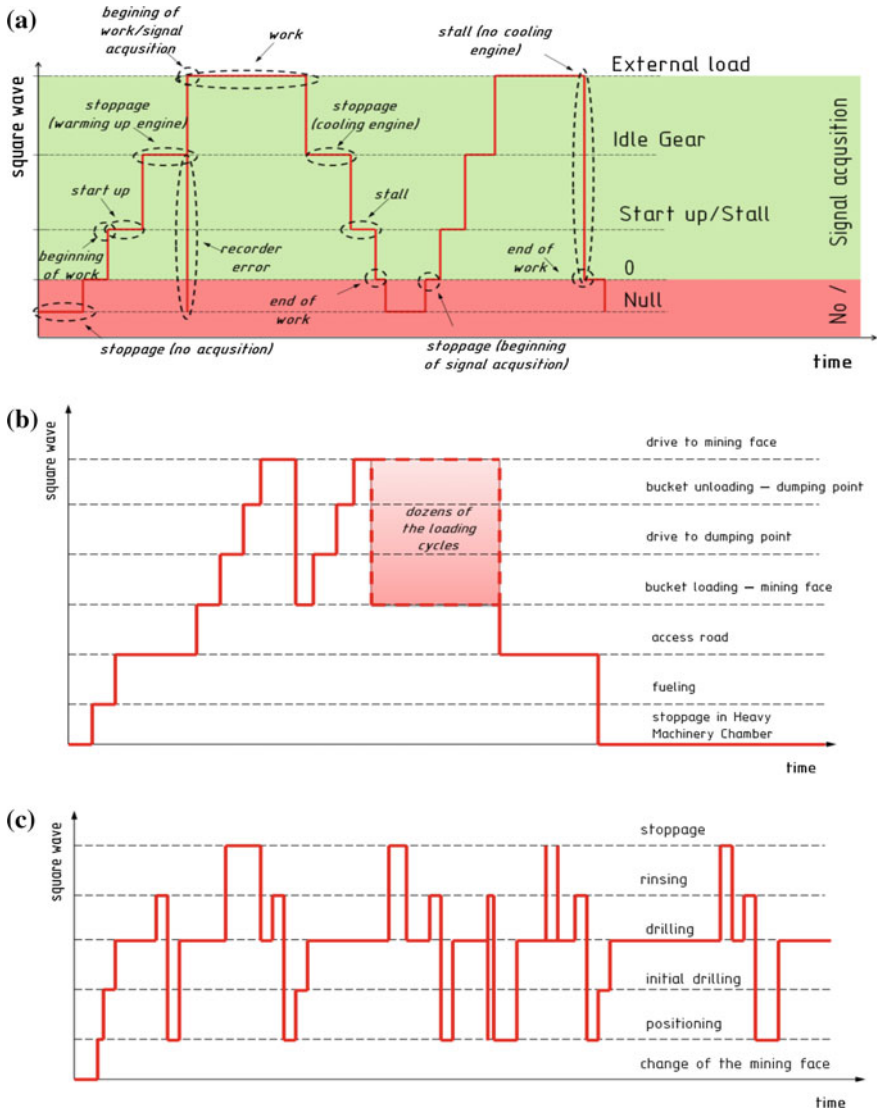

Fig. 3 **a** The graph of square wave showing sequence of basic engine operation regimes **b** theoretical drilling process and **c** loader operations

5 Signal Processing for Condition Monitoring Purposes

On board monitoring system is able to acquire many variables, mostly related to temperature, pressure, rotational speed, voltage, current. Detailed list of variables depends on type of machine. There are no vibration signals commonly used in

diagnostics of gears, bearings or combustion engines. However, simple diagnostic evaluation using temperature or pressure (hydraulic systems) can be easily done. A general algorithm related to temperature or pressure is basically searching for values exceeding the threshold, as defined by the manufacturer. Due to extremely harsh environmental conditions, detection of such situation is not necessarily going to indicate an alarm. Note that machine might operate under conditions where temperature is very close to the limit. Our experience is that single values are often exceeding the allowed value, however it is related to the measurement device problem. Moreover, temporary and insignificant overheating might be, for example, connected with entering to warmer zones without appropriate ventilation system near mining face. It should be indicated that all of these events will be aggregated in order to build daily report. This report will serve as a basis for evaluation of machine's condition, production volume but also performance and skills of the operator. To avoid inappropriate conclusions, advanced decision making scheme is required (Fig. 4).

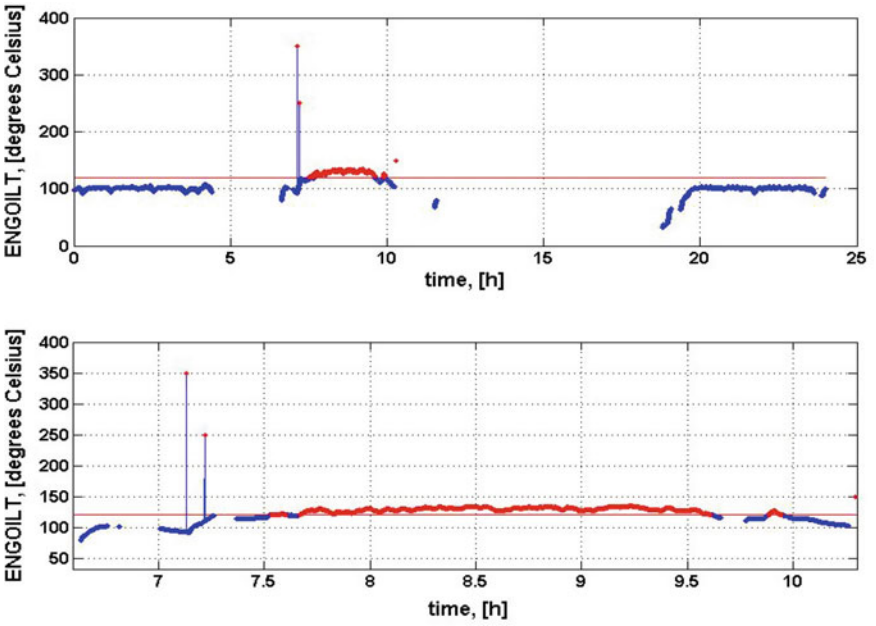

Fig. 4 Example of raw temperature signal and results of processing with detected temporary and regular overheating

6 Signal Processing for Processes Monitoring Purposes

Depending on type of the machine, it is possible to distinguish some key processes that might directly influence degradation processes in the machine as well as production volume (i.e. amount of transported material, number of drilled blasting holes, etc.). In this section two probably the most important processes will be discussed, namely copper ore transport from mining face to the nearest belt conveyor and blast hole drilling.

6.1 An Efficiency of Copper Ore Transport Using Loader

In the underground copper ore mine loaders are used to transport copper ore from point A to point B. The distance should not exceed a few hundred meters. Such a cycle (loading at A, haulage, dumping the material at B) should be repeated many times during one shift. Therefore certainly, the process of copper ore transportation should reveal cyclic nature. By signals segmentation, it is possible to investigate what is a cycle, how many cycles have been done during one shift, average duration of cycle and—in case of existence- deviations from average cycle. Building the cycle model, one might use many variables (multidimensional model) taking into account volume of material, duration of the cycle, effectiveness of loading procedure etc. Apparently, it might be easily noticed that set of features describing behaviour of signals will be redundant, i.e. will partially contain the same information. Signal redundancy in multichannel systems have been reported in [18]. There are many techniques for dimensionality reduction [20, 21].

Unfortunately, it was confirmed experimentally that each of the cycle components, particularly loading of copper ore, might take different amount of time. It has clear physical explanation. In order to transport all fragmented (after blasting procedure) ore it is expected to perform several cycles. The first cycle is usually requires the shortest period of time, whereas the last one lasts much longer. The operator should "clean" the mining excavation and more activities are required for loading purposes (moving forward/backward).

Figure 5 shows record of data from a few shifts (6 h each) with identified typical regimes of loader operation (machine is switched off, starting the engine, idle mode, normal operation, overloading). In Fig. 6 we present several variables to show that mentioned cycles for each loading/unloading operations exist. It is possible to observe these cycles based on several variables (engine torque, fuel usage, rpm speed…). Precise identification of each cycle allows to generate appropriate information for miners (no of cycles), for mechanical engineers (overloading of machine) and other professionals.

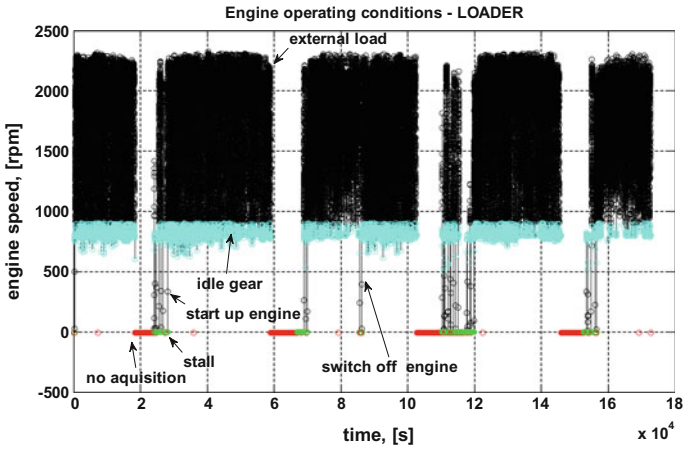

Fig. 5 Example of loader operations represented by engine rotational speed

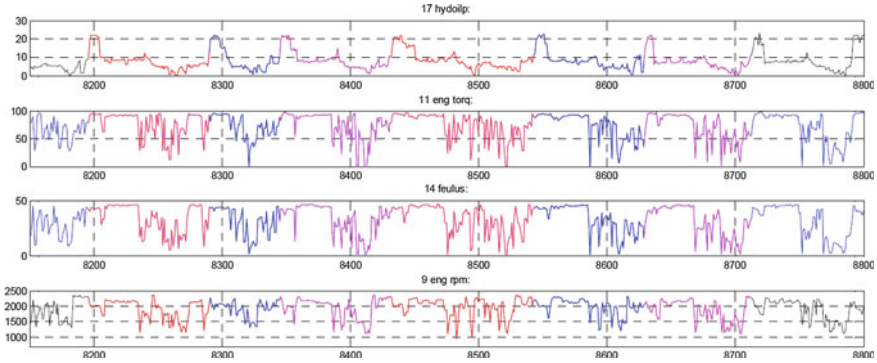

Fig. 6 Cycle identification for loader operations

6.2 *Quality and Efficiency of Drilling Process*

Drilling process is one of key processes in the mine. It is performed for blasting purposes as well as for bolting (in order to protect roof from collapsing). Due to a number of holes prepared daily, any improvement applied to this process could result in enormous savings.

The typical drilling process usually consists of following parts: positioning of the machine (for each mining face) and drilling tool (for each hole), initial drilling, regular drilling, cleaning of the hole. Figure 7a presents raw data describing length of a hole as an example of measurement. In Fig. 7b we show 4 examples—realizations of drilling process: two of them are incorrect (B, C —holes are too shallow, while A and D are correct). It can be easily realized that drilling process

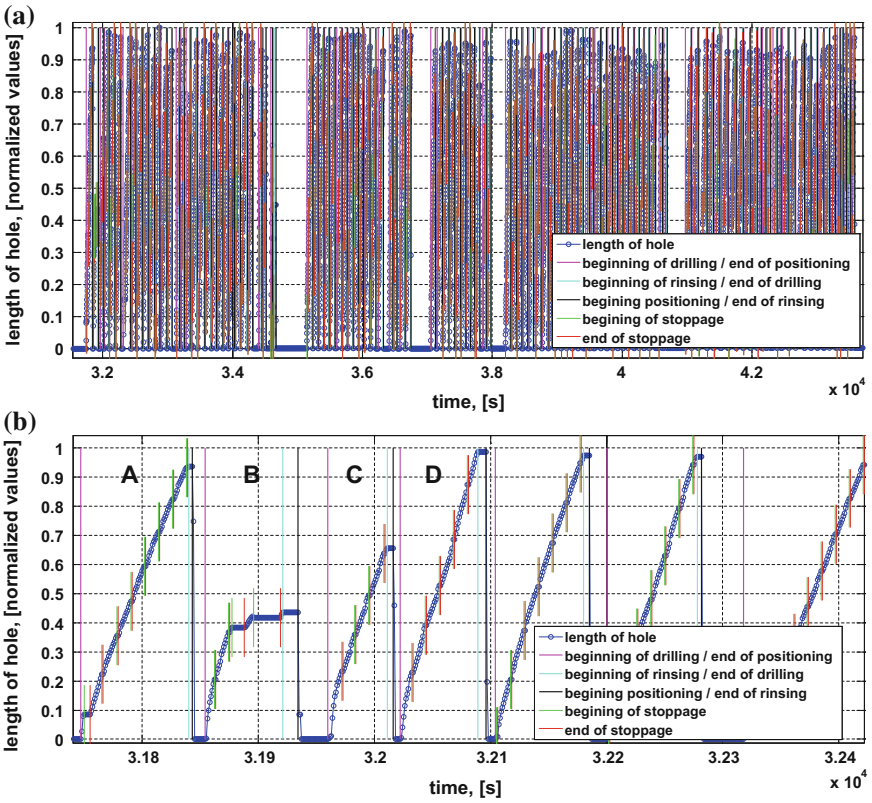

Fig. 7 **a** Variability of length of hole in correlation with main cycles of drilling process **b** zoom of Fig 7a

was not typical for a several cases. At this point, it should be considered why the drilling process happens to last longer than it ought to. The main reasons are related to operator's work and geological conditions, which are common cause of tool's jam. Multidimensional analysis of selected variables allows to recognize this phenomena.

7 Signal Processing for Performance Evaluation

From miners' point of view, volume of production is the most important aspect because it is a direct income source. Monitoring and statistical analysis of processes such as drilling, copper ore haulage etc.is critical. However, performance monitoring and evaluation depends strictly on type of machine. In this section we will show raw data and output parameters (which might be referred to Key Performance

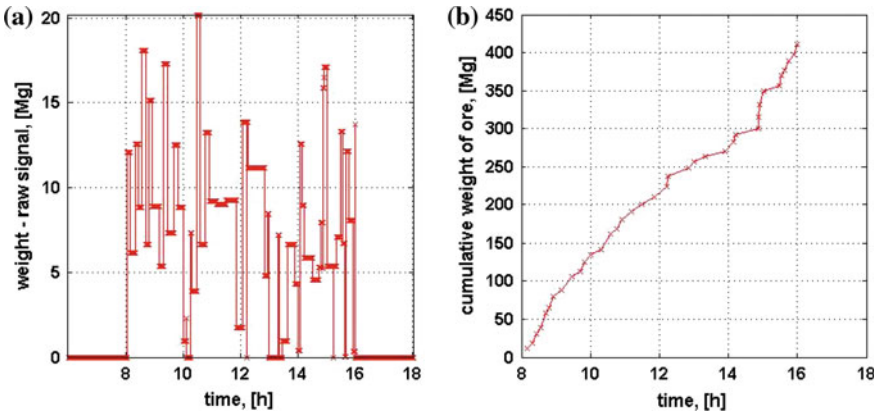

Fig. 8 Weighting of copper ore in the loader. **a** Raw signal, **b** aggregated cumulative weight of ore

Indicators) for material transport and drilling process. The first one is presented in Fig. 8. At given time (when bucket is raised to unload material) weighting process is conducted. Raw signal from Fig. 8a is pre-processed to obtain cumulative form of data showing current total amount of daily output and might be the basis for further advanced analysis.

Figure 9 is a pre-processed result of Fig. 5a. It can be easily seen that most of cycles related to drilling are very similar to each other. One might analyse in detail statistics of each component of drilling process (duration of initial drilling, regular drilling etc.). Several anomalies are connected with replacement of drilling tool or changing position of the machine (to another mining excavation). This is a regular situation in case of room-and-pillar mining system.

8 Multidimensional Signals and Information Fusion

To efficiently manage all of the machines and processes related to their operations there is a need to combine data/information from different sources. Good example of multidimensional signal analysis is tool's jam detection. It is necessary to monitor and analyze several variables (hole depth and pressures used for driving the drilling tool). Another example illustrating the need of multidimensional data analysis and information fusion is related to evaluation of performance and condition of machine. One needs to combine information related to location of the operating machine (position within the mine), environmental, geological etc. factors that could influence measured data and so on. Sources of mentioned information might be: localization system (*where the machine has been operated?*), SAP HR system (*who has been the theoperator of the machine?*), CMMS system etc. (*what kind of repair has been done?*, *what type of spare parts has been used*). At this

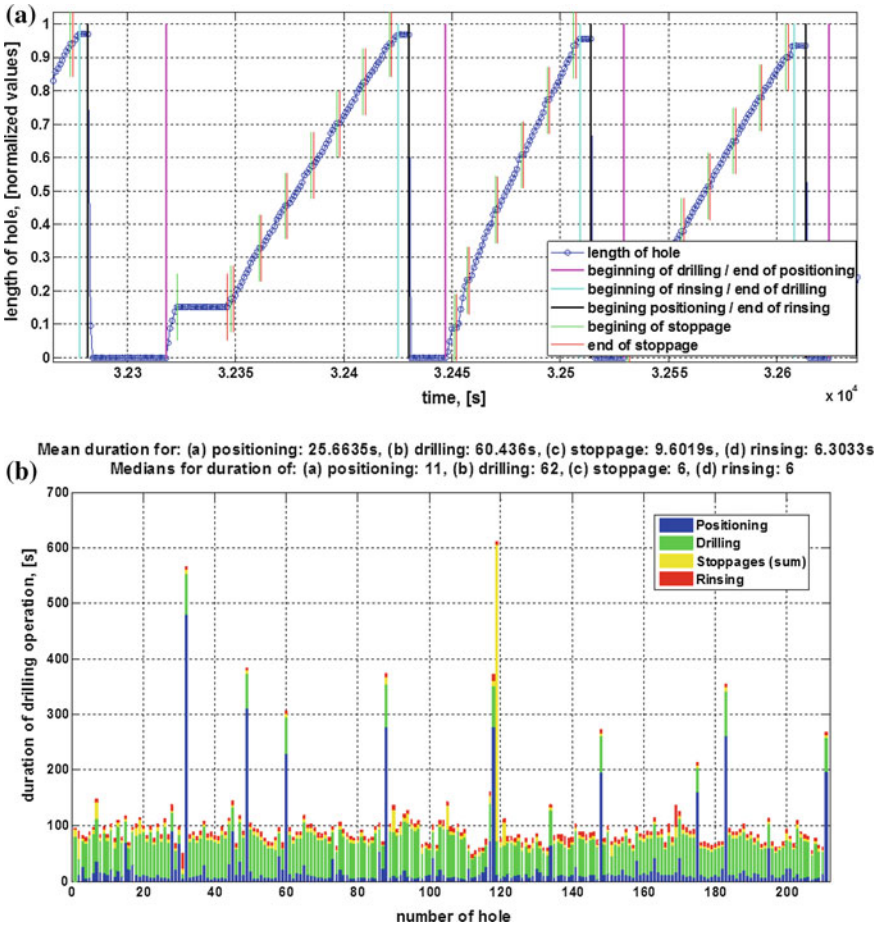

Fig. 9 Aggregated description of drilling process

stage, this type of data/information fusion is not automatically performed. It might be helpful in order to understand problematic/controversial results of daily/weekly performance/condition evaluation.

9 Conclusions

In this paper several important issues related to monitoring of machine condition and machine performance in underground mine have been discussed. General structure of the system is not overly complicated and might be found in other applications in the world. Unfortunately, specificity of the underground mine, local

organizational, technical mining and other conditions make the project very challenging and require high amount of effort in order to fulfil expectations of the company. In this paper we have focused on data processing issues. It was highlighted that particular attention should be paid during data validation. In most cases, the specialized algorithm related to identification of required information does not seem to be overly complicated. However there are several "keywords" known in the literature as *uncertainty, incompleteness*, *inaccuracy* that make processing very difficult. Serious inconveniency is related to lack of chance for experimental work in the laboratory. Due to mining regulations, financial and safety reasons no experiments are permitted in the mine during its normal operation. Therefore the proposed algorithm should be carefully tested and finally should be furtherly expanded. The need of multidimensional signal analysis and data fusion provides additional issues. Obviously all components of data stream should be correct in order to obtain proper information. When the data comes from different, independent sources, it is not that simple to accomplish.

From diagnostic perspective, proposed algorithms are focused on simple searching of periods with overheating, regimes or cycle extraction, their parametrisation/modeling and aggregation/statistical analysis of extracted segments. These algorithms are applied to real data in the context of condition monitoring, process monitoring as well as performance monitoring.

The project is still in progress, this paper is kind of current status description of challenging industrial project.

Acknowledgments Pawel Stefaniak and Radoslaw Zimroz are supported by I2Mine Project (KGHM Cuprum).

References

1. Description of SMIFU project. http://www.rocktechcentre.se/core-business/smifu/
2. The I2Mine Website (Innovative Technologies and Concepts for the Intelligent Deep Mine of the Future), i2mine.eu/
3. http://www.nrcan.gc.ca/mining-materials/green-mining/8178, Website of Natural Recourses of Canada
4. http://www.green-mines.eu/
5. Andrzejewski M, Sliwinski P, Zimroz R (2014) Monitoring Samojezdnych Maszyn Gorniczych, jako narzedzie do optymalizacji procesu wydobycia urobku w kopalniach KGHM Polska Miedz S.A. Proceedings of the 23rd School of Underground Mining, Krakow, 24–28/02/2014 / Instytut Gospodarki Surowcami Mineralnymi i Energia Polskiej Akademii Nauk, Katedra Gornictwa Podziemnego. Akademia Gorniczo-Hutnicza. Krakow : Szkola Eksploatacji Podziemnej, pp 1–10
6. Dyczko et al. Koncepcja monitoringu i transmisji danych technologicznych pracy samojezdnych maszyn górniczych w KGHM Polska Miedź S.A. (in Polish), unpublishedtechnical report prepared for KGHM PM SA
7. Kicki J, Dyczko A (2010) The concept of automation and monitoring of the production process in an underground mine. New Tech Technol Min Proc Sch Undergr Min, pp 245–253

8. Kohler JL, SottileJr J, Cawley JC (1994) On-board electrical diagnostic system to improve the availability of continuous mining machines. Min Eng 46(8):987–990
9. Luo C, Li W, Wang Y, Fan Q, Yang H (2013) A distributed positioning detection method of shearer under wireless sensor networks. J Comput Inf Syst 9(9):3619–3626
10. McBain J, Timusk M (2012) Software architecture for condition monitoring of mobile underground mining machinery a framework extensible to intelligent signal processing and analysis. In: IEEE conference on prognostics and health management (PHM), pp 1–12. doi:10.1109/ICPHM.2012.6299543
11. Okrent K, Studying the impact of the drilling process on the durability of cutting tools, PhD Thesis (in Polish), available at: http://winntbg.bg.agh.edu.pl/rozprawy2/10566/full10566.pdf
12. Ralston JC, Hainsworth, DW, McPhee RJ, Reid DC, Hargrave CO (2003) Application of signal processing technology for automatic underground coal mining machinery. In: Proceedings. (ICASSP'03). IEEE international conference on acoustics, speech, and signal processing, vol 2, pp 249–252. doi:10.1109/ICASSP.2003.1202341
13. Zimroz R, Wodecki J, Krol R, Andrzejewski M, Sliwinski P, Stefaniak PK (2014) Self-propelled mining machine monitoring system—data validation, processing and analysis mine planning and equipment selection. In: Carsten D, Raj S (eds) Proceedings of the 22nd MPES conference, Dresden, Germany, vol. 2, 14th–19th Oct 2013. Springer, Berlin, pp 1285–1294
14. Wyłomańska A, Zimroz R (2014) Signal segmentation for operational regimes detection of heavy duty mining mobile machines—a statistical approach. Diagnostyka 15(2):33–42
15. Wyłomańska A, Zimroz R (2014) Signals analysis from LHD mining machine on-board monitoring system. In: Proceedings of XIXth symposium VISHNO (Vibration, SHocks and Noise), France
16. Wyłomańska A, Zimroz R (2015) The analysis of stochastic signal from LHD mining machine. Stochastic models, statistics and their applications. Springer proceedings in mathematics & statistics, vol 122, pp 469–478
17. Wyłomańska A, Zimroz R (2014) Temperature signal analysis for processes and condition monitoring of LHD mining machines. In: 13th international technical systems degradation conference. Liptovski Mikulas, Slovakia
18. Ray A (1991) An introduction to sensor signal validation in redundant measurement systems control systems, IEEE 11(2):44–49
19. Jablonski A, Barszcz T (2013) Validation of vibration measurements for heavy duty machinery diagnostics. Mech Syst Signal Process 38(1):248–263
20. Bartkowiak A, Zimroz R (2011) Outliers analysis and one class classification approach for planetary gearbox diagnosis. J Phy Conf Ser 305(1):012031
21. Bartkowiak A, Zimroz R (2014) Dimensionality reduction via variables selection—linear and non-linear approaches with application to vibration-based condition monitoring of planetary gearbox. Appl Acoust 77:169–177

Part II
Data Mining

Analyzing State Dynamics of Wind Turbines Through SCADA Data Mining

Francesco Castellani, Davide Astolfi and Ludovico Terzi

Abstract Supervisory Control And Data Acquisition (SCADA) control systems have become ubiquitous in modern wind energy technology. Exploiting their potentialities is a keystone for performance optimization and to improve the operational control feeding smart electric grids. Yet, tackling the complexity of SCADA data sets is a challenging task. The philosophy underlying the present work is discretization of the continuous motion of machine states and error signals: doing this, one ends up with simplified databases, acting on which with statistical methods provide powerful insight. Indicators on the quality of turbine functionality and on the nature of error signals are formulated, and the distribution of errors as a function of wind intensity is studied. The methods are tested on the data of a wind farm in southern Italy, and it is shown that they are indeed capable of assessing performances and interpreting the nature of occurred errors.

Keywords Wind energy · Wind turbines · SCADA control system · Performance evaluation

Contents

1 Introduction 214
2 The Approach and the Wind Farm 215
3 Number Map and State Dynamics 217
4 Conclusions and Further Directions 222
References 222

F. Castellani (✉) · D. Astolfi
Department of Engineering, University of Perugia, Perugia, Italy
e-mail: francesco.castellani@unipg.it

D. Astolfi
e-mail: davide.astolfi.green@gmail.com

L. Terzi
Renvico srl, Milano, Italy
e-mail: ludovico.terzi@renvico.it

F. Chaari et al. (eds.), *Advances in Condition Monitoring of Machinery in Non-Stationary Operations*, Applied Condition Monitoring 4,
DOI 10.1007/978-3-319-20463-5_16

1 Introduction

In the latest years, the focus about wind energy has been considerably shifted from new installations into optimization of operating farms, for several reasons: the financial crisis, discouraging investments; the stagnation of economic growth in Europe, decreasing energy consumption; and the growth of the percentage of electric energy arising from renewable and stochastic sources, providing the necessity of accurate forecast and balancing, in order to build smart grids.

Wind turbines, due to their low density on the territory and the short-term variability of the source, are usually equipped with sophisticated control systems: Supervisory Control And Data Acquisition (SCADA). SCADA systems spread on 10-min time basis minimum, maximum, average, and standard deviation of several channels, providing a complete picture of machine functionality: details of the wind flow and turbine response to it, conversion of wind kinetic energy into active power, temperatures at meaningful parts of the machine, vibrational status, and so on.

Exploiting control systems potentialities has a direct economic return: in [1, 2], some estimates are provided. A sudden failure of 1.5 MW wind turbine causes, during wintertime, around €50,000 of missed production, while a judicious maintenance program can avoid sudden faults, resulting in 5 times smaller cost of energy loss. A complete optimization program of wind turbines, through SCADA data analysis, can decrease the cost of wind energy up to 20 %.

Scientific literature on SCADA data analysis for wind turbine optimization has become a fertile field, since it stands at the crossroad of engineering, physics, statistics, and computer science. Actually, the task is ambitious and challenging: digesting vast data streams, processing them smartly into knowledge and possibly integrating it into the control system, for automation of early diagnosis or performance evaluation.

For these reasons, methods basically demarcate in two categories, sharing capability of tackling complexity and big data: statistical approaches and Artificial Neural Network (ANN) techniques.

In [3], ANN is employed for investigating and preventing bearing faults, which are quite common: four months of data from 24 turbines are processed, and it is shown that the algorithm reliably predicts bearing faults 1.5 h before they occur. Bearing fault prediction through ANN techniques is also addressed in [4]. In [5], on the test case of Lillgrund wind farm, a machine learning approach is applied for structural health monitoring, and a comparison between ANN and Gaussian regression is made. In [6], ANN methods are employed for modeling temperature of generator bearing and cooling air, and are subsequently validated. In [7], an evolutionary strategy algorithm is applied to determine optimal control settings: it is shown that judicious fine tuning of blade pitch and generator torque improves sensibly the power coefficient.

Peculiar attention in the literature has been devoted to offshore wind farms, because of the copiousness of wake effects between nearby turbines, resulting in

decreased performance. The dynamics of wakes and polar efficiency of wind farms have therefore been studied both numerically and ex post. In [8], power losses due to wakes are analyzed on the test cases of offshore Horns Rev and Nysted wind farms, in Denmark. In [9], the analysis is focused on misalignment and yawing under downstream wake angles. In [10], the usual data set built on measurements on 10-min time basis is processed and replaced by a weighted average of several simulations covering a wide span of directions.

Previous work of the authors and the present work are based on a different approach to the complexity of SCADA measurements: the philosophy is processing the raw data sets into simplified ones, acting on which with simple statistical methods provides very meaningful indicators. In other words, with this approach, the difficulty lies at the very beginning, in the pre-processing phase: it must be as smart as possible, in order to smear out information which is unnecessary or extraneous to the kind of answer one is looking for. On the other way round, also post-processing which reduces the quality of the data sets is possible, if it simultaneously dramatically increases their simplicity; yet, very fine tuning must be applied in order not to lose precious information.

In [11], several post-processing methods are proposed for assessing wind farm performances; in [12], post-processing of SCADA temperature channels is applied for early fault diagnosis, and it is shown that the approach is useful for preventing even severe machine damages. In [13], polar efficiency is systematically addressed for onshore wind farms: it is shown intertwining of wake effects and complexity of the terrain forces to define it in a novel way, whose consistency is demonstrated. Further, on the test case of three wind farms on very different terrains, it is disentangled and quantified how complexity of the terrain, wake effects, and atmospheric stability affects polar efficiency.

The structure of the paper is as follows: in Sect. 2, the approach is sketched and the test case wind farm is introduced. In Sect. 3, the continuous state dynamics is analyzed by discretizing its motion on 10-min time basis, parallel to the SCADA database. The results on several monthly test cases are shown and discussed. Finally, in Sect. 4, the results are briefly summarized and further developments of the present work are sketched.

2 The Approach and the Wind Farm

As briefly discussed in Sect. 1, the complexity of the SCADA data stream, to be elaborated into knowledge, can be tackled with different approaches.

The philosophy of the present work is converting the continuous dynamics of relevant quantities into a discretized data set. At the cost of introducing some coarse-graining effect, which the consistency of the results should demonstrate being negligible, discretization provides data sets, acting on which with simple statistical methods leads to very meaningful indicators.

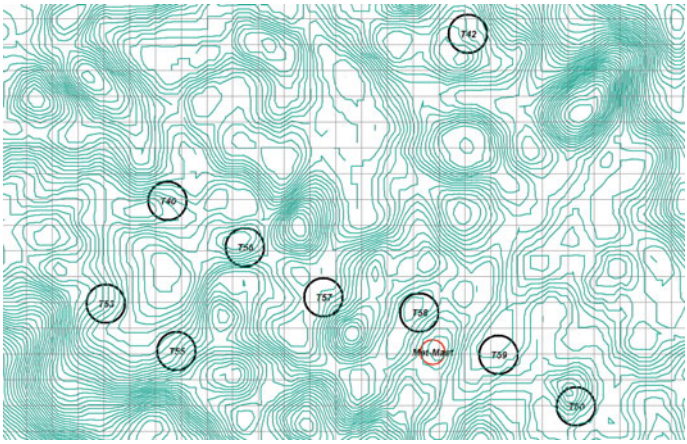

Fig. 1 The layout of the test case wind farm

The data sets at disposal have twofold nature: SCADA measurements are averaged and stored on 10-min time basis, and state histories are in the form of incoming or phasing out at given time stamps. By the point of view of time basis, the former kind of data is by construction discrete (the grain is 10 min), while state dynamics is recorded in its continuous motion.

The basic features of the proposed methods are here on summarized: the analysis of Sect. 3 is based on the discretization of the continuous dynamics of the states of the machines. We defer to Sect. 3 for the details of the method. Yet, the principle is as follows: building a data set, made of binary numbers, parallel to the SCADA measurements, and on the same 10-min time basis. The states of the machine under examination demarcate in classes: operating states, which are mutually exclusive and basically provide information about what each machine is doing, and status codes, which are not mutually exclusive and can have different degrees of severity (information, warning, and error). Status codes are the building blocks for reconstructing why the turbine behaves as dictated by the corresponding operating states. The principle is associating a digit to each operating state or status code for each 10-min interval: if this operation is performed judiciously, the data set built of binary numbers can be analyzed for classifying fault onsets, their severity, and reasons.

The approach above has been tested on the operational data of a Wind Farm sited in southern Italy. Nine turbines are installed on site, with a rated power of 2 MW each (Fig. 1, Table 1).

Table 1 Test case wind farm main features

Feature	Wind farm
Number of turbines	9
Rotor diameter	82 m
Hub height	80 m
Rated power	2 MW
Terrain	Flat

3 Number Map and State Dynamics

As introduced in Sect. 2, the state dynamics of the turbines of the test Wind Farm has been tackled by discretizing it on 10-min time basis, parallel to the SCADA measurements. Two number maps have been constructed: the former encodes the information contained in the operating states, i.e., what each turbine is doing, and the latter encodes the status codes, i.e., why each turbine behaves as dictated by the operating states.

To each operating state and status code, a digit has been associated for each 10-min time stamp, turning from 0 to 1 if the state activates during the interval. The only exception to this intuitive rule should be the operating state associated to power output production: actually, a 10-min interval should be considered productive if the production time exceeds a fairly high threshold. For the present work, this threshold has been chosen at 80 %, but it has also been checked that the results are poorly affected by this value, as long as it is consistently high.

The inspiring idea is trying to build a connection between what each turbine does and why, i.e., between the operating states and the status codes, crossing the simplified and discretized data sets, rather than the complete continuous dynamics. For this reason, status codes have been divided according to their severity and separate number maps have been built for information, warning, and error classes of status codes. The most urgent issue is therefore putting in relation the number map of error status codes with the one of the operating states: this operation should help in classifying errors according to their severity, in identifying clusters of status codes associated to the same malfunctioning, and in associating error status codes to each family of Brake Programs of the machine.

Yet, the discrete operating state number map is valuable on its own and provides insight to be subsequently put in relation with the error status code map. The idea is identifying a criterion for demarcating good and bad time steps, and quantifying the amount of them for each turbine on a same period. The absolute and relative classifications are both useful: the former relates to whether a turbine has been productive or not, and the latter relates to whether a turbine has deviated from the dominant farm behavior or not. We consider a time step good if the turbine has produced, or has been potentially but not actually productive due to inadequate wind strength. We consider a time step bad otherwise. Similarly, we consider a time step anomalous if the turbine has deviated from the farm trend.

With this classification at hand, two Indicators can be formulated for evaluating machine behavior. The former, Eq. 1, is the ratio of the number of not productive time steps to the number of anomalous time steps.

$$\left[I_{\mathrm{GL}} = \frac{N_{\mathrm{notprod.}}}{N_{\mathrm{anom.}}}\right] \tag{1}$$

The latter Indicator, Eq. 2, is the ratio of the number of anomalous not productive time steps to the number of anomalous productive time steps.

$$\left[I_{\mathrm{DET}} = \frac{N_{\mathrm{anom.\ notprod.}}}{N_{\mathrm{anom.\ prod.}}}\right] \tag{2}$$

Both Indicators are precious and have pros and cons: $[I_{\mathrm{DET}}]$ does not capture as malfunctioning a bad turbine behavior on a bad farm trend. If a farm undergoes long-term shutdowns, $[I_{\mathrm{DET}}]$ becomes not consistent. Yet, if as expected, the long-term dominant trend of the farm is power output production, $[I_{\mathrm{DET}}]$ brilliantly captures the details of one turbine against the other and is a precious tool for operational evaluation. The inconsistency of $[I_{\mathrm{DET}}]$ in the long farm shutdown limit is circumvented by $[I_{\mathrm{GL}}]$, because at numerator of Eq. 1, the absolute number of not productive time steps appears. Therefore, both Indicators are useful and should be unitarily employed for evaluating farm and machine behavior under each possible regime. Their consistency has been checked by computing them on the historical data of year 2013 of the test case Wind Farm: it arises that $[I_{\mathrm{DET}}]$ has an $[R^2]$ correlation coefficient of 0.98 against single turbine percentage of downtime, i.e., not productive nor potentially productive time. $[I_{\mathrm{GL}}]$ shows a slightly lower $[R^2]$. This strongly supports their consistency for evaluating wind farm behavior. On shorter time scales, yet, the Indicators provide more structured information with respect to the amount of downtime, with which they become not simply linearly correlated: $[I_{\mathrm{GL}}]$ and $[I_{\mathrm{DET}}]$ are therefore valuable on their own.

Further details of each turbine malfunctioning can be revealed by time analysis of the error database: the following step in building a connection between errors and operational behavior of the machines is therefore defining a criterion for severity classification of errors. This has been done as follows: an interval of variable amplitude, centered on the time step of error occurrence, has been considered, and it has been checked if the machine is productive before, during, and after the error signal has activated. A further distinction has been done, leading to two different and instructive limits: if during the considered interval, at least one time step of production appears, or rather if all the interval is productive. For the present work, an interval of 1 h forward and backward the activation time of the error has been considered. It has been observed that the results do not sensibly depend on the size of this threshold, when its order of magnitude is not altered. Severity magnitude has therefore been classified according to the following Table 2.

Table 2 Classification of the severity of error status codes

Degree of severity	Production before	Production during	Production after
0	✓	✓	✓
1	✗	✓	✓
2	✓	✗	✓
3	✗	✗	✓
4	✓	✓	✗
5	✓	✗	✗
6	✗	✓	✗
7	✗	✗	✗

The final step to relate status codes to operating states, i.e., why to what, is crossing the timesteps during which an error has been active for a given turbine against the map of operating state: the idea is inquiring whether an error is occurring while the turbine is in mode with the rest of the farm, or not. This allows to discriminate real alarms from, for example, planned maintenance programs which should be smeared out: actually, if the turbine is in error and in mode with the rest of the farm, it is likely that it is due to a service program, while if it is not, it is likely that it is a sudden and unexpected error. We therefore propose a Mode Index, Eq. 3, which is the ratio of the number of error time steps out of farm trend to the number of total error time steps.

$$\left[I_{\text{MODE}} = \frac{N_{\text{err. out. mode}}}{N_{\text{err. tot.}}} \right]. \tag{3}$$

We also propose an Error Index, Eq. 4, which is the ratio of the number of error time steps to the size of the data set.

$$\left[I_{\text{ERROR}} = \frac{N_{\text{err.}}}{N_{\text{tot.}}} \right] \tag{4}$$

In the following, we are going to provide a set of monthly test cases of the methods above. Figure 2 displays the values of $[I_{\text{ERROR}}]$ for a month during which

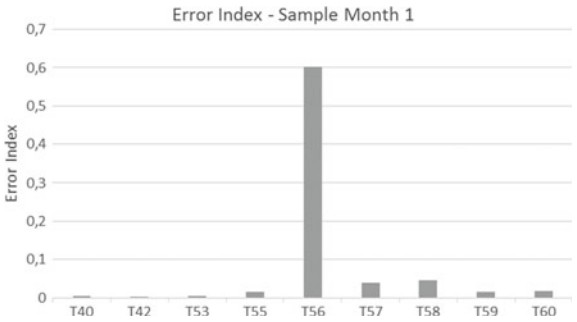

Fig. 2 Monthly test case 1: huge malfunctioning on turbine T56

turbine T56 has undergone a huge malfunctioning and a consequent shutdown. Actually, the value of $[I_{\mathrm{ERROR}}]$ far peaks with respect to other turbines and the time series of error activation vastly overlaps with a period of missed power output production. This shows that $[I_{\mathrm{ERROR}}]$ provides a first tool for identifying massive malfunctionings.

Figure 3 shows instead of the very opposite limit with respect to Fig. 2 a maintenance program on the wind farm, acting simultaneously on all the turbines. The methods above should help in recognizing that the errors appearing on the machines are rather false alarms due to planned shutdown, and no traumatic events happened. This is indeed the case: in Fig. 3, the distribution of $[I_{\mathrm{ERROR}}]$ is substantially flat, and so it is the distribution of $[I_{\mathrm{MODE}}]$, varying very little from turbine to turbine on the possible range (0–1) and being flattened to the lower limit. These features are clear indications that the error records of the month are not due to problematic situations on the machines, but rather to planned maintenance.

Yet, there are situations which, by the point of view of the Indicators $[I_{\mathrm{ERROR}}]$ and $[I_{\mathrm{MODE}}]$, are intermediate with respect to the examples above and cannot clearly be identified: common situations can be maintenance programs shifted in time from one turbine to the other, or acting on each turbine with slight differences. Both cases end up with values of $[I_{\mathrm{ERROR}}]$ (possibly considerably high) and $[I_{\mathrm{MODE}}]$ (possibly even tending to 1), which are indistinguishable from the case of real traumatic errors. A supplementary analysis is needed: this has been performed observing the distribution of error records as a function of wind intensity. If the error records are associated to false alarms associated to maintenance, we expect the shutdowns being wisely planned and performed during low wind intensity periods. If a traumatic shutdown has appeared, we expect it to be irrespective of wind intensity.

Figure 4a, b shows that the distribution of errors as a function of wind intensity (in this case as measured by the met mast of the wind farm) is a precious tool. In Fig. 4a, we observe an abrupt fall of each single turbine number of error signals for increasing wind speeds. The shape of the curves suggests that the farm has

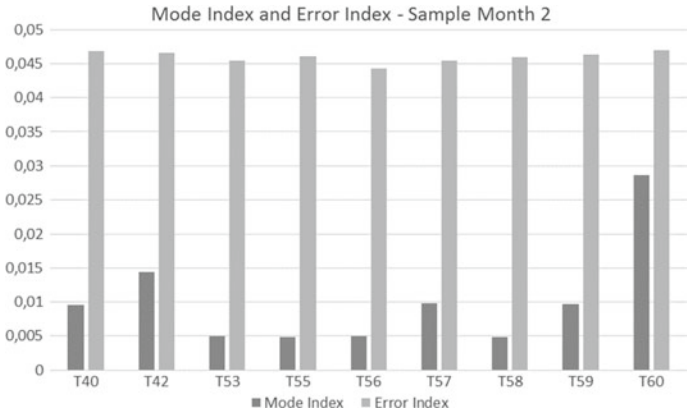

Fig. 3 Monthly test case 2: synchronized maintenance program on the wind farm

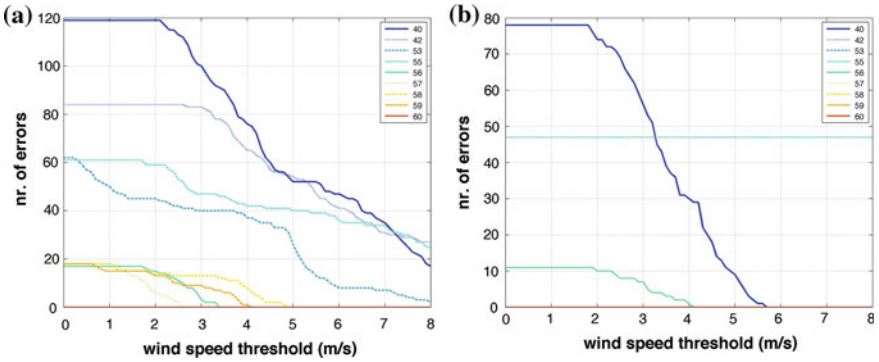

Fig. 4 Monthly test cases 3 and 4: number of errors against wind intensity. **a** Cluster maintenance program. **b** Traumatic stop

undergone a custom maintenance program for subclusters of turbines. Figure 4a allows thus to identify a false alarm, which the mere values of $[I_{\mathrm{ERROR}}]$ and $[I_{\mathrm{MODE}}]$ would not distinguish from a real problem to the wind farm. Figure 4b instead shows that the number of errors for turbine T55 does not flatten to 0 asymptotically for high wind speeds, suggesting that it has undergone a traumatic stop. This actually is confirmed by estimating the amount of producible energy which has been lost.

The test case of Fig. 4b has also been studied from the point of view of severity classification, as according to Table 2. In Fig. 5a, the severity of errors has been classified according to production for the whole interval around each error time step, while in Fig. 5b, the production condition is searched in at least one time step of the interval. It arises that the two histograms of Fig. 5 sensibly differ in the distribution of severity for turbines T55 and T56, which are the ones associated to traumatic stops (quite severe the former, almost negligible the latter). The lesson from the case above, and from others omitted for brevity, is that commonly traumatic stops of the machines are associated with oscillation of productive and not

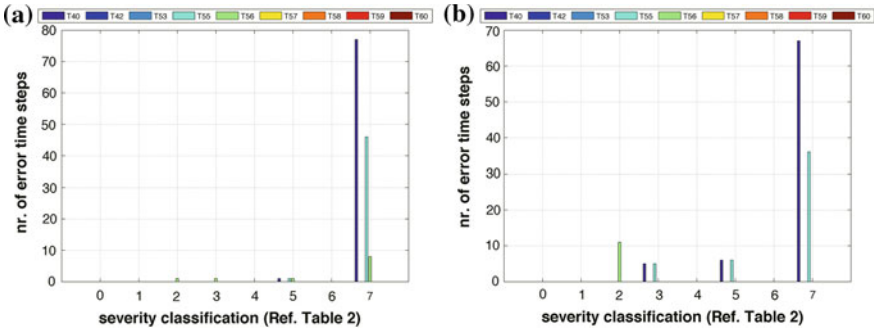

Fig. 5 Monthly test case 4: severity analysis, according to Table 2. **a** Severity: whole interval. **b** Severity: at least 1 time step

productive time steps on short time scales around error occurrence, while planned maintenances are more regular clusters, which the two different histograms of severity classification see as almost identical.

4 Conclusions and Further Directions

Therefore, summarizing, the present work is based on the discretization of the continuous motion of the states of wind turbines. Data sets parallel to the SCADA measurements, on 10-min time basis, have been built and they encode the basic features of what each turbine has done and why. Subsequently, acting with simple statistical methods on these simplified data sets, post-processing methods have been developed for crossing the error signal map against the state map and indicators have been formulated for quantifying goodness of operational behavior and, classifying the errors, their impact on the machines, and their severity. Consistence of the proposed methods has been tested on the data of an operating Wind Farm sited in southern Italy. Further directions of the present work include extending its approach, with a slight different philosophy: SCADA data sets are by itself a time discretization of (in principle) continuous quantities on 10-min time basis. The values they assume constitute, yet, a continuous set, which might be useful to discretize: we expect that the analysis of nacelle positions could provide very powerful insight on a complex phenomenon as clustering of turbines in alignment to wind direction (on large wind farms) and on its impact on power output production.

References

1. Wind Power Monthly (2013) Condition Monitoring. Expert report edition
2. Wind Power Monthly (2014) Wind Turbine Control Systems. Expert report edition
3. Kusiak A, Verma A (2012) Analyzing bearing faults in wind turbines: a data-mining approach. Renew Energy 48:110–116
4. Zhang ZY, Wang KS (2014) Wind turbine fault detection based on SCADA data analysis using ann. Advan Manuf 2(1):70–78
5. Papatheou E, Dervilis N, Maguire E, Worden K (2014) Wind turbine structural health monitoring: a short investigation based on SCADA data. In: Le Cam V, Mevel L, Schoefs F (eds) EWSHM—7th European workshop on structural health monitoring, Nantes. IFFSTTAR, Inria, Université de Nantes
6. Yan Y, Li J, Sun P, Zhang X (2014) Study on parameters modeling of wind turbines using SCADA data. Sens Transducers 176(8):237–243
7. Kusiak A, Zheng H (2010) Optimization of wind turbine energy and power factor with an evolutionary computation algorithm. Energy 35(3):1324–1332
8. Barthelmie RJ, Hansen KS, Pryor SC (2013) Meteorological controls on wind turbine wakes. Proc IEEE 101(4):1010–1019
9. Barthelmie RJ, Pryor SC, Frandsen ST, Hansen KS, Schepers JG, Rados K, Schlez W, Neubert A, Jensen LE, Neckelmann S (2010) Quantifying the impact of wind turbine wakes on power output at offshore wind farms. J Atmos Oceanic Technol 27(8):1302–1317

10. Hansen KS, Barthelmie RJ, Jensen LE, Sommer A (2012) The impact of turbulence intensity and atmospheric stability on power deficits due to wind turbine wakes at horns rev wind farm. Wind Energy 15(1):183–196
11. Castellani F, Garinei A, Terzi L, Astolfi D, Gaudiosi M (2014) Improving windfarm operation practice through numerical modelling and supervisory control and data acquisition data analysis. Renew Power Gener IET 8(4):367–379
12. Astolfi D, Castellani F, Terzi L (2014) Fault prevention and diagnosis through scada temperature data analysis of an onshore wind farm. Diagnostyka 15(2)
13. Castellani F, Astolfi D, Terzi L, Hansen KS, Rodrigo JS (2014) Analysing wind farm efficiency on complex terrains. J Phys Conf Ser 524:012142 IOP Publishing

Using SCADA Data for Fault Detection in Wind Turbines: Local Internal Model Versus Distance to a Wind Farm Reference

Alexis Lebranchu, Sylvie Charbonnier, Christophe Berenguer and Frédéric Prevost

Abstract The number of wind turbines is increasing each year, and with it, the need for methods of condition monitoring and predictive maintenance. During the last years, the number of techniques using 10 min SCADA data has grown and complex and efficient models are now available. Nevertheless, the non-stationary operating condition of wind turbines is still an issue. This paper will present a new approach using the similarity between the turbines behavior for fault detection. Then a more classical approach using data coming from a single turbine will be tested on two different generator failures to compare the results.

Keywords SCADA · Wind turbine · Local approach · Fault detection · Generator · Condition monitoring

Contents

1 Introduction 226
2 Presentation of the Two Methods 227
2.1 Comparison with a Wind Farm Reference 227
2.2 Regression Model 228
3 Presentation of the Data Set 229
4 Results 230
4.1 Comparison with a Wind Farm Reference 230
4.2 Regression Model 232

A. Lebranchu (✉) · S. Charbonnier · C. Berenguer
University of Grenoble Alpes & CNRS, GIPSA-lab, 38000 Grenoble, France
e-mail: Alexis.Lebranchu@gipsa-lab.grenoble-inp.fr

S. Charbonnier
e-mail: Sylvie.Charbonnier@gipsa-lab.grenoble-inp.fr

C. Berenguer
e-mail: Christophe.Berenguer@gipsa-lab.grenoble-inp.fr

A. Lebranchu · F. Prevost
Valemo S.A.S, 33323 Bègles, France

F. Chaari et al. (eds.), *Advances in Condition Monitoring of Machinery in Non-Stationary Operations*, Applied Condition Monitoring 4,
DOI 10.1007/978-3-319-20463-5_17

4.3 Comparison and Discussion 235
5 Conclusion 236
References 236

1 Introduction

The important growth in the wind power sector has led to the development of larger wind turbines, which are located into remote area. The importance of reducing any downtime coming from unexpected failures has then become critical. To do so, Condition Monitoring techniques have been developed using at first dedicated systems like vibration analysis of the drive train. Those condition monitoring systems (CMS) mainly use raw vibration signals acquired via added systems which can be expensive and working independently from the wind turbine PLC control system. In order to reduce the cost, research now focuses also on the use of low frequency data coming from Supervisory Control and Data Acquisition (SCADA) systems. For instance, in 2009, new proposals were published in [1], using data driven methods for automated fault detection. The SCADA provides an important amount of data using hundreds of sensors already present in the nacelle. Due to the complexity of the new turbines, manufacturers are now installing SCADA on each nacelle, allowing new techniques & methodologies to be developed.

The SCADA system provides low frequency data from all the sensors as well as alarms used for emergency action. Specific work on SCADA alarm processing has been done in [2]. An approach using both alarms and quantitative data was presented in [3]. This paper will make use of the quantitative data only. Automated techniques were developed in order to make the most of the sensors provided by the SCADA but they still could be improved. Some major issues remain unsolved. Due to frequent fluctuations in the wind speed, the wind turbines may operate under changing operation conditions. As shown in [4] CMS indicator such as RMS or peak-peak values are dependent of the turbine load. The same problem occurs for the indicator constructed with SCADA data. To solve this problem local approach were proposed in [5] where preprocessing are done in order to divide the data into several operation modes.

In this paper, we propose another way to solve the non-stationarity problem by comparing wind turbine behaviors in the same farm to detect early failure. In previous work [6] turbines were compared to monitor production performance. In this paper, we compare the temperatures, which are fault indicators for overheating. This new approach is tested on two failures that occurred on the generator, a faulty bearing and a failure in the cooling system. A method using a mathematical model describing the variations of the temperature as a function of other variables measured on one turbine is also presented and the results given by both methods are compared.

The method was initially proposed by [7] and obtained good result for overheating and fault detection in the main shaft bearing.

This paper is divided into 4 sections. In Sect. 2, both approaches are described. Section 3 gives further details on the database used for validation. The results of the methods on two different examples of failure are presented and discussed in Sect. 4.

2 Presentation of the Two Methods

Our goal is to develop methods able to detect on line faults that generated overheating on a turbine, using SCADA variables. Two different approaches are proposed. They are detailed in this section.

2.1 Comparison with a Wind Farm Reference

One of the main issues with wind turbine monitoring comes from the wind variability. Because of the frequent changes in the wind speed and nature, the turbines are almost never at steady state, thus the SCADA measured signals are non-stationary. Under the assumption that the wind farm is small enough to be passed through by a unique wind stream, we can consider that all the turbines in this farm are activated by a similar wind. Moreover, the wind turbines from the same farm are usually identical. As a result, they should react in the same way to the same solicitations, which means that all the sensors should measure similar values at the same time on all the turbines. This is obviously a strong assumption, and in the reality, due to landscape and different calibration of the sensors, differences between turbines can be measured. In this approach, we consider that those differences are independent of the SCADA variables and remain constant through time. The objective of this approach is to create a farm reference and use the distance between a turbine and this reference as a fault indicator that would be independent of the wind variability. The distance with the reference should remain constant for a healthy turbine and depend only on the specificity of landscape and calibration, considered as constant in this basic approach.

A fault in a bearing generally creates an increase in the bearing temperature. A temperature reference is then created by calculating the median of the bearings temperatures of all the wind turbines of the farm. Proceeding this way, the variation between the reference and any turbine should remain similar. The assumption of the method is that the temperatures should evolve in the same way. This is true provided that the turbines are in the same operating conditions. Thus, isolated events, such as a stop of a turbine, are filtered out. From the moment a turbine is stopped and until a short time after it has been restarted, its temperature is removed from the calculation of the wind farm reference. The latency period is chosen equal to 3 h. Thus, the number of turbines used to calculate the reference may change in time.

The temperature of each monitored turbine is compared to the farm temperature median. This farm temperature reference (median) is calculated using a leave one

turbine out method, i.e. the temperature of the turbine under consideration is not used to calculate the reference.

Let i be the number of the monitored turbine and $T^{\circ}_{Ai}(t)$ its corresponding temperature at time t of the bearing A. The reference temperature of bearing A for turbine i is:

$$T^{\circ}_{\mathrm{AREF}i}(t) = \mathrm{median}_{j=1 \text{ to } N}\left(T_{Aj}(t)\right) \tag{1}$$

with N the number of turbines in operation at time t, and with turbine i excluded.

The residual used as a health indicator is then:

$$\varepsilon_i(t) = T^{\circ}_{Ai}(t) - T^{\circ}_{\mathrm{AREF}i}(t) \tag{2}$$

The residual is calculated for each turbine when the T°_{Ai} and $T^{\circ}_{\mathrm{AREF}i}$ are relevant, i.e. when turbine i is in operational mode and when N is strictly higher than 2. Then the residual is filtered using a moving average on a window of size L equal to 1000 sampling periods, i.e. about one week. This length was chosen by a trial and error procedure. The detection of a failure is triggered when the residual is superior to a threshold, k_i. Under the assumption that this residual distribution follows a Gaussian law, a first threshold k_i can be proposed as follows:

$$k_i = 3\ \mathrm{std}_{\varepsilon_i} + \mathrm{mean}_{\varepsilon_i} \tag{3}$$

where $\mathrm{std}_{\varepsilon_i}$ represents the standard deviation and $\mathrm{mean}_{\varepsilon_i}$ the mean of the residual of the turbine i calculated on a healthy data set.

2.2 Regression Model

Some methods proposed in the literature [1, 5, 7, 8], focus on the use of internal models. Each turbine is considered independently of the other ones. The health indicator is created using mathematical relations between some variables measured on the same turbine. In [7], the temperature of the bearing A is described by:

$$T^{\circ}_{\mathrm{Aregi}}(t) = a_i T^{\circ}_{Ai}(t-1) + b_i n_i(t) + c_i P_i(t) + d_i T^{\circ}_{\mathrm{nacelle}i}(t) \tag{4}$$

where $T^{\circ}_{Ai}(t-1)$ represents the temperature of turbine i at time $t-1$ of the bearing A, $n_i(t)$ represent the rotation speed of the generator, $P_i(t)$ is the generated power, and $T^{\circ}_{\mathrm{nacelle}i}(t)$ is the nacelle temperature. $T^{\circ}_{\mathrm{Aregi}}(t)$ represents the theoretical temperature of the bearing A used as a reference for this approach. The constants a_i, b_i, c_i, d_i are determined using linear regression with historical data.

Each of the chosen variables contributes in the evolution of the bearing temperature in its own way. The power gives information on the energy transmitted via the wiring resistance to the bearing. The rotation speed gives information about the

heating coming from the friction between the mobile parts of the bearing. And finally the nacelle and bearing temperature at $t - 1$ give information about thermal inertia. The residual is then the difference between this model and the current temperature.

$$\varepsilon_i(t) = T^{\circ}_{Ai}(t) - T^{\circ}_{\text{Aregi}}(t) \tag{5}$$

The residual is calculated only when the turbine i is operating like in the median approach presented before. Nevertheless to calculate T°_{Aregi} all the variables need to have a valid value. For instance, the nacelle temperature sensor can be broken and then the reference cannot be calculated. Like in the previous method, a moving average with a window length L equal to 1000 sampling periods is used and then the thresholds of each turbine are calculated following Eq. (3).

3 Presentation of the Data Set

A data set formed of several variables recorded every 10 min on 6 identical 2 MW wind turbines from a French wind farm is available. Each data point comes from the SCADA and represents the average of the 10 last minutes of the measured variable. The selected variables are the:

- generated power (0–2 MW)
- rotation speed of the generator train (0–1800 r.p.m)
- bearing temperature (0–60 °C without failure)
- nacelle ambient temperature (0–40 °C)

The data were collected during 2 years from March 2010 to March 2012. During those 2 years two different faults occurred successively on two different turbines. The first failure occurred the 28/09/2010 and the second failure occurred from 8/10/2011 to 29/03/2012.

In order to train, validate and test the models, the data base is split in different time periods. The test periods are the 2 months period before a failure occurs. The training and validation periods are selected before the test periods. They are formed of two consecutives data set of the same length of 10,000 points as described in Fig. 1. The regression model and the detection thresholds are learnt on the learning period.

As described above, both approaches need specific conditions for the calculation of the residual. Filtering out all the irrelevant points will delete a large amount of data point and combined with usual connection loss, only 50 % of the data can be used for the regression method and only 30 % of the points can be used for the median method. Nonetheless the remaining data are distributed all along the data set, allowing us to create a relevant fault indicator.

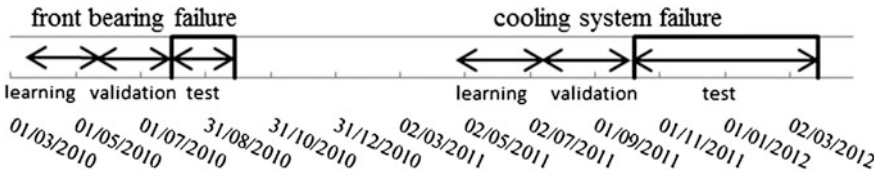

Fig. 1 Organization of data set

4 Results

Both methods presented are tested on two generator failures. The methods are presented separately and then compared. The first failure occurred on a bearing of the generator. The bearing was progressively damaged and finally stopped the turbine. The second failure is a break of the cooling system. It is a sudden failure that was not detected previously by the SCADA.

4.1 Comparison with a Wind Farm Reference

Bearing failure. Figure 2 represents the residual calculated over the two months preceding the bearing failure, without any filtering. It is calculated for two turbines, one healthy turbine in blue and one faulty turbine in red. The failure occurs at the end of the time period displayed. The machine is stopped the 28/09/2010, at the very end. One can see that, at the end of the observation period, the residual of faulty turbine is clearly higher than on the rest of the data set. Moreover, on the healthy turbine, this increase is not present. The value of thresholds calculated on those non-filtered residuals (as described in Sect. 2) are given the result in Table 1. The threshold is calculated using the mean and standard deviation [see Eq. (3)] calculated on the data of the learning period. The use of this threshold generates

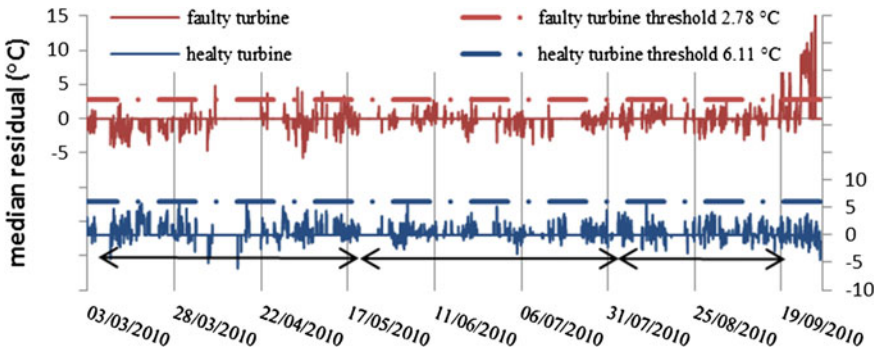

Fig. 2 Residual of the median approach on the first failure without filtering

Table 1 Threshold of the median approach on the bearing failure

	Before filtering			After filtering		
	Mean ε	Std ε	Threshold	Mean ε	Std ε	Threshold
Faulty turbine	−1.06	1.28	2.78	−0.399	0.659	1.58
Healthy turbine	1.41	1.57	6.11	1.368	0.763	3.66

several false alarms i.e. periods of time during the learning period when the residual is higher than the threshold value.

Because the residuals can be calculated when the turbines are in operational mode only, a large number of time periods are excluded. However, the periods when data are excluded are distributed all along the dataset. The large period of data exclusion around 15/04 or 16/07/2010 comes essentially from the fact that the turbines under consideration are not operational at those moments.

In Fig. 3, the residuals filtered using Eq. (2) are now displayed for the same turbines. The thresholds values are shown in Table 1. The number of false alarms is now equal to zero and only the faulty turbine has a residual that exceeds the threshold. The detection occurs the 19/09/2010, i.e. 10 days before the bearing failure.

Cooling system failure. Figure 4 represents the non-filtered residuals during the second failure period. Again the residuals are calculated on two turbines, one healthy turbine (i.e. the same as for the 1st studied case) and the faulty turbine where the cooling system failure occurs. Comparison between Tables 1 and 2 shows that the value of the mean and standard deviation of the residuals during the two learning periods are about the same, for the healthy turbine. Tables 1 and 2 also show that each turbine has a different mean and standard deviation, those differences between the turbines were expected. They are due to the landscape or the sensor calibration. Nonetheless, both residuals remain around the same mean all along the period preceding the occurrence of the fault. When applying the moving average filter proposed on the residuals, we obtain good results for the detection of this failure (Fig. 5). The number of false detection is equal to zero, and the cooling problem is detected the 24/10/2011. The cooling problem was present on this turbine during 5 months, but our fault indicator does not re-main above the

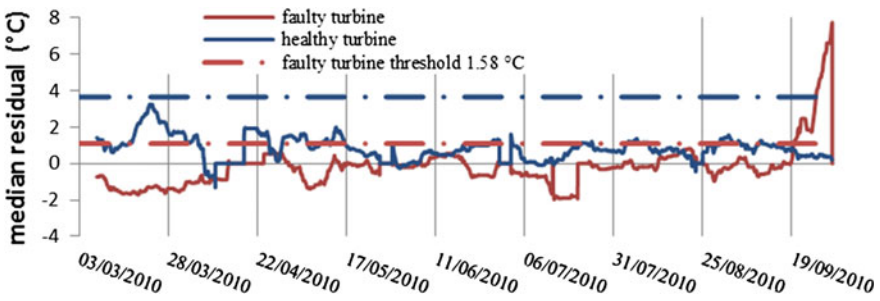

Fig. 3 Residual of the median approach on the bearing failure after filtering

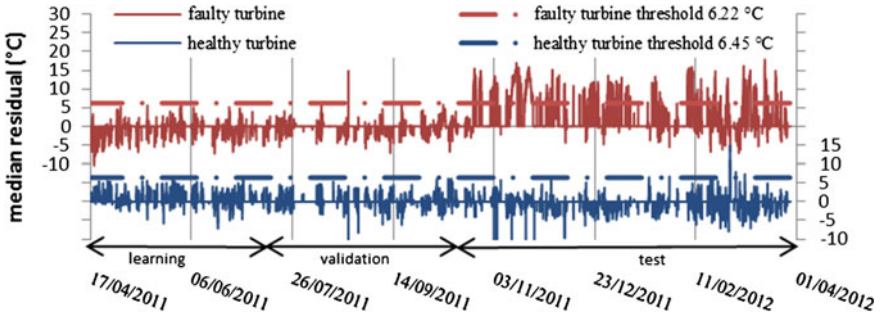

Fig. 4 Residual of the median approach on the cooling failure without filtering

Table 2 Threshold of the median approach on the cooling failure

	Before filtering			After filtering		
	Mean ε	Std ε	Threshold	Mean ε	Std ε	Threshold
Faulty turbine	−1.591	2.603	6.219	−1.366	1.091	1.906
Healthy turbine	1.170	1.760	6.451	1.140	0.687	3.201

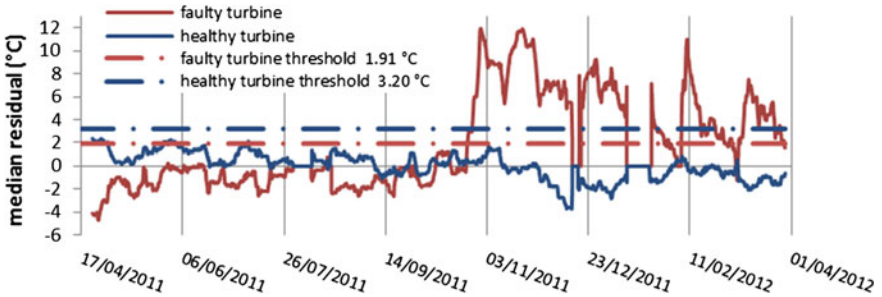

Fig. 5 Residual of the median approach on the cooling failure after filtering

threshold during all this period. The 29/01 and 28/03/2012 the residual decreased and stayed below the threshold during several days. This non-detection can be explained by the fact that the turbine stopped, which caused the temperature to decrease quickly. As expected, once the turbine is restarted, the residual increases quickly and the fault is once more detected.

4.2 Regression Model

Bearing failure. In Fig. 6 and Table 3, the unfiltered residual obtained with the regression method is presented for the bearing failure. The residual of the same

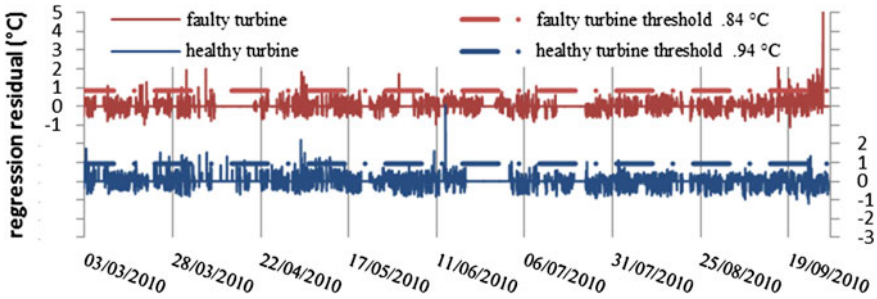

Fig. 6 Residual of the regression approach on the bearing failure without filtering

Table 3 Threshold of the regression approach on the bearing failure

	Before filtering			After filtering		
	Mean ε	Std ε	Threshold	Mean ε	Std ε	Threshold
Faulty turbine	0.03	0.27	0.84	−0.01	0.06	0.17
Healthy turbine	0.07	0.29	0.94	0.08	0.07	0.28

healthy turbine is also calculated for comparison purposes. The number of periods when the residual exceeds the threshold is also high with this method, which requires filtering the residuals. The increase in the residuals values at the end of the set, where the failure occurs, comfort us that a threshold can be calculated for the fault detection.

With the moving average filter, the bearing fault is detected firstly the 21/09/2010 then the residual decreases and increases again above the threshold the 25/09/2010 until the bearing breaks the 29/09/2010 as described in Fig. 7. Thus the real detection is considered to be only 4 days before the total and final bearing failure. No false detection is observed for the healthy turbine or the learning and validation part.

Cooling system failure. For the cooling system failure, the residual in Fig. 8 for the healthy turbine shows higher large values than the other test, especially around the 1st of March 2012. Again the number of those large values is still too high to

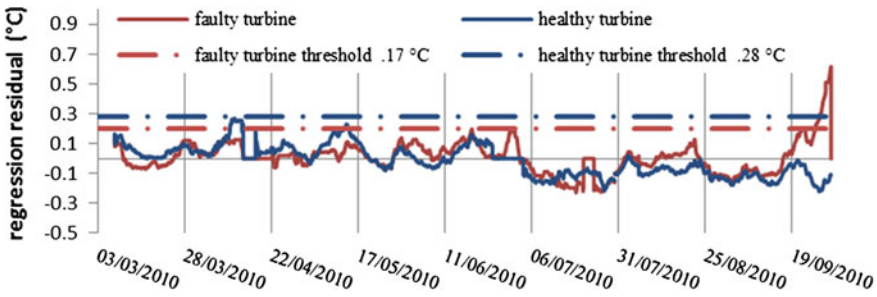

Fig. 7 Residual of the median approach on the bearing failure after filtering

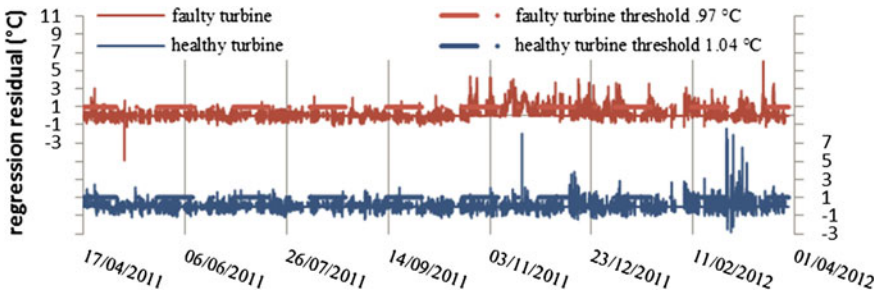

Fig. 8 Residual of the regression approach on the cooling failure without filtering

Table 4 Threshold of the regression approach on the cooling failure

	Before filtering			After filtering		
	Mean ε	Std ε	Threshold	Mean ε	Std ε	Threshold
Faulty turbine	0.016	0.318	0.969	0.001	0.098	0.296
Healthy turbine	0.004	0.345	1.038	−0.009	0.106	0.310

use this method without filter. We can observe in Tables 3 and 4 that the mean and standard deviation of the residuals of the healthy turbine are about the same, though the period of time used to learn them is different. This tends to show that the parameters of the model do not evolve in time.

In Fig. 9 the cooling system failure is detected on 24/10/2011 by using a filter on the regression residual. The first important information is that the healthy turbine is also considered as faulty since its residual reaches and exceeds the threshold. The residual of the faulty turbine does not remain above the threshold all the time until the end of the failure period. Three times during the failure period, the residual decreases because the wind turbine stops, which leads to a decrease of the bearing temperature. One possible explanation is that because of the duration and frequency of those stops, the number of points considered for the residual calculation and filtering dropped. Then the operational range considered for the calculation can be different.

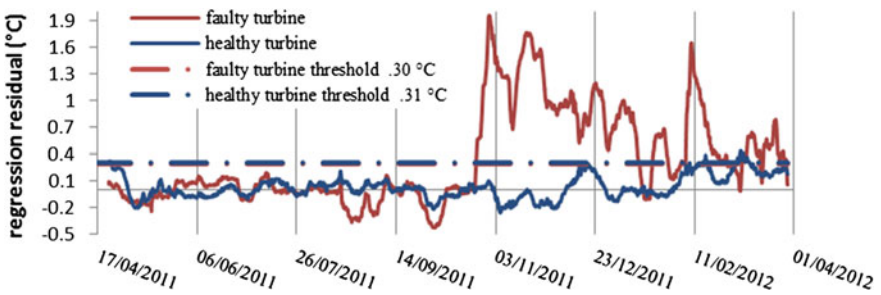

Fig. 9 Residual of the regression approach on the cooling failure after filtering

4.3 Comparison and Discussion

The methods presented are capable of detecting the bearing failure without any false alarm. For the cooling system second failure, only the first method turbine comparison does not raise any false alarm. Nonetheless the comparison of the residuals of the regression model with and without filtering (see Figs. 8 and 9) shows that all the false alarms are synchronised with a large amount of large values. This means that if we improve the ways to select the data (i.e. be more restrictive on the operating conditions), there is a hope that the false alarms could disappear.

If we compare the time of detection between the methods, the comparison with the farm reference method detects the bearing defect 10 days before the turbine is stopped by the actual bearing failure, against only 4 days for the regression method. According to the experts, to be warned 10 days ahead of time of the occurrence of a failure makes it possible to schedule the repair downtime so as to minimize the loss in production while 4 days ahead of time is too short to do anything but stop the machine for safety. In order to improve the detection time we could decrease the threshold level. Unfortunately the threshold is already close to the residual for the healthy turbine, which means that when decreasing it the number of false alarms will increase.

The second failure was detected at the same time by the two approaches, which is supposed to be the actual time the cooling failure occurred. Both methods were able to detect the problem while the SCADA system did not create any alarm since the temperature remained below the alarm threshold. However, both residuals did not remain above the detection threshold all the time during the faulty period. We can see that both approaches are still dependant on the operational conditions. The residual is a distance between a farm reference or a model and it is proportional to the amplitude of the temperature. When the turbine stops, the temperature decreases, and the residual also decreases, leading to the non-detection of the cooling failure.

Finally, the results show that both methods have detected the failures, but the regression model requires more variables than the median reference approach. This difference could be critical if all the variables are not available. For instance the temperature of the nacelle is not a crucial variable, which means that if the sensor fails, its replacement will not be a priority for the maintenance; as a result the regression could not be used any longer. The median approach compares variables from different turbines, and this comparison could be done on any kind of sensor, unlike the regression model that needs all the variables of the monitored process. This approach is very basic but proves its efficacy in two different failures. The wind and other environmental conditions are of course not the same for all the turbines. Future work will focus on the study of the correlation of environmental parameters between all the turbines resulting to a correlation of the process variable such bearing temperatures.

5 Conclusion

The new approach proposed permitted to detect two failures in a main component of a wind turbine, using only one variable per turbine. This new method has shown its potential interest for fault detection and especially for non-stationary systems like wind turbines. It has also shown that it could be deployed on any kind of sensors and by doing so keeping the wide scope of monitoring of the SCADA.

Future work will be dedicated to study the correlations between the turbines of a same farm in order to develop a more efficient method. With the same objective, the possibility of fusion between the internal model approach and the comparison between turbines approach could improve the robustness of the detection.

References

1. Zaher A, McArthur SDJ, Infield DG (2009) Online wind turbine fault detection through automated SCADA data analysis. Wind Energy 12:574–593
2. Qui Y, Feng Y, Tavner P, Richardson P, Erdos G, Chen B (2012) Wind turbine SCADA alarm analysis for improving reliability. Wind Energy 15:951–966
3. Kusiak A, Li W (2011) The prediction and diagnosis of wind turbine faults. Renew Energy 36:16–23
4. Zimroz R, Bartelmus W, Barszcz T, Urbanek J (2014) Diagnostics of bearings in presence of strong operating conditions non-stationarity—a procedure of load-dependent features processing with application to wind turbine bearings. Mech Syst Signal Process 46(1):16–27
5. Yang W, Court R, Jiang J (2013) Wind turbine condition monitoring by the approach of SCADA data. Renew Energy 53:365–376
6. McLaughlin D (2009) Wind farm performance assessment: experience in the real world. In: Proceedings of the renewable energy world conference & expo Europe, 26–28 May 2009, KoelnMesse, Cologne
7. Zhang Z (2014) Comparison of data-driven and model based methodologies of wind turbine fault detection with SCADA data, EWEA March 2014
8. Guo P, Infield D (2012) Wind turbine generator condition-monitoring using temperature trend analysis. IEEE Trans Sustain Energy 3(1):124

On Optimal Threshold Selection for Condition Monitoring

Đani Juričić, Nada Kocare and Pavle Boškoski

Abstract Well designed features and properly selected detection thresholds are important prerequisites for reliable performance of the condition monitoring systems. Ideally, thresholds should be selected in a way that the diagnostic system keeps alert to the appearance of fault with minimal delay while under normal conditions false alarms should be avoided. If the thresholds are set too high, missed alarms may occur while too low values implicate false alarms. In practice thresholds are often set heuristically by a skilled person for each component of the machine. The task is nontrivial as usually many thresholds need to be defined. Moreover, a feature may be related to diverse faults with different sensitivity levels. Motivated by this issue, the intention of this paper is to lay the basis for rigorous threshold selection that implies the need for minimal design parameters. The idea is to first elaborate the probabilistic model of the feature. In order to check the relative change in the probabilistic pattern, the statistical hypothesis tests are employed. The only required priors, needed to tune the diagnostic algorithm, are data records collected under nominal condition and the probability of false alarm (PFA) as a sole "tuning knob". Technically, the approach converts into the problem of statistical hypothesis testing. The performance of the algorithms is preliminarily confirmed via simulations and a real case study with a motor drive subjected to imbalance.

Đ. Juričić (✉) · P. Boškoski (✉)
Department of Systems and Control, Jožef Stefan Institute,
Jamova 39, Ljubljana, Slovenia
e-mail: dani.juricic@ijs.si

P. Boškoski
e-mail: pavle.boskoski@ijs.si

N. Kocare (✉)
Jožef Stefan International Postgraduate School, Jamova 39, Ljubljana, Slovenia
e-mail: nada.kocare@gmail.com

F. Chaari et al. (eds.), *Advances in Condition Monitoring of Machinery in Non-Stationary Operations*, Applied Condition Monitoring 4,
DOI 10.1007/978-3-319-20463-5_18

Contents

1 Introduction 238
2 Statistical Model of the Features 239
2.1 Data Acquisition Setup 239
2.2 Modelling Assumptions 240
2.3 Statistical Model of the Fourier Spectral Components 240
2.4 Parameter Estimation 242
3 Statistical Hypothesis Test 243
4 The Evaluation Study 245
4.1 A Simulated Example 245
4.2 EC Motor with Imbalance 247
5 Conclusion 248
References 249

1 Introduction

A systematic approach to the threshold selection renders important for the efficient realization of the diagnostic system commissioning. Usually a skilled person is needed to tune the values of the thresholds component by component.

Surprisingly, the problem of threshold selection for monitoring the rotational machines has attracted relatively limited attention, cf. [1]. Most likely, the reason is that during a diagnostic system design the majority of effort goes on feature extraction. Selection of the detection threshold for a well designed feature becomes the matter of heuristics and engineering pragmatism. In that sense the derivations often rely on assumption that the statistics of the collected features comply with the normal distribution. That such an approach is not quite correct, has been clearly pointed out by Bechhoefer and his co-workers [2]. They showed that the nature of the traditional condition indicators is non-Gaussian. Sticking to the simple Gaussian model of the condition indicator, and then selecting the threshold in accordance with the critical values derived from Gaussian distribution, can also result in high probabilities of false alarms.

The design of optimal threshold for change detection in signals has been researched in different monitoring and diagnostics contexts. In the well known book [3], the fundamental change detection algorithms for model based diagnosis are summarized based on hypothesis testing. However, in order to design a statistical decision rule, formulation of the probability density function (pdf) that describes data in nominal condition must be known. Unfortunately, in reality this is not the case. Unlike the above mentioned approach, in [4] an optimal threshold is designed on the basis of features and without a priori known statistics. It is assumed that features for shaft magnitude and bearing envelope are distributed according to the Rayleigh distribution. For a given component they are fused into one health indicator (HI), which is function of the distributions. However, to construct a function

of distributions, features must be independent and identically distributed from each other, which cannot be performed just with de-correlation as in [4]. In a novel approach [5] the authors suggest inference using only empirical distributions captured from data under nominal and current health condition. There is no need for knowing the parametric pdf's. Relative change in pdf patterns is obtained from change in the divergence function which is a measure for the dissimilarity among the empirical pdf's.

In this paper we question whether it is possible to deduce the parameterized pdf of a feature by employing the bottom-up physical modelling. The potential merit of the approach is that statistical decision making with parametric pdf's could be performed on substantially less data than methods relying on non-parametric statistics. Practically, this means that we can apply shorter data records compared to the heuristic approaches. Hence we are able to achieve shorter detection times in applications where high sensitivity of the detection is important.

The paper is organized as follows. In the next section we outline the derivation of the statistical model of the features. In this preliminary phase we focus on faults, which affect particular spectral components (like imbalance and eccentricity). Stationary operating conditions are presumed in this stage of the work. The problem of optimal threshold selection is then formulated as the problem of statistical hypothesis testing and is outlined in Sect. 3. Some preliminary simulation and experimental results serving to better insight are presented in Sect. 4.

2 Statistical Model of the Features

2.1 Data Acquisition Setup

Without loss of generality we assume periodical short sampling sessions are performed at high sampling rates. In most of the machines it is not needed to perform sampling at all times, unless the criticality conditions implicate continuous sampling. However in such a case the results below apply as well. Each sampling session is assumed to consist of N samples taken at sampling rate f_s.

As soon as a machine is brought to the stable operating conditions, say after the commissioning or the maintenance intervention, it is mandatory to get recordings that correspond to the *reference condition* of the machine. Hence the initial batch of sessions numbered $\mathscr{P}_{\text{ref}} = \{1, 2, \ldots, N_{\text{ref}}\}$, taken on the healthy machine under nominal condition, are said to belong to the *reference window*.

When the reference window is over, the comparison of the emerging recordings with the reference ones can start. For that purpose features obtained from recent sessions $\mathscr{S}_{\text{cur}} = \{K - N_{\text{cur}} + 1, \ldots, K\}$, where K is the last session in the *current window*, are employed. The number of session in the current window is N_{cur}.

2.2 Modelling Assumptions

The acquired vibrational signal $y(t)$ is assumed to be composed of random multiple sine waves and additive noise $n(t)$

$$y(t) = \sum_{r=1}^{R} A^{(r)} \cos(2\pi f_r t + \phi^{(r)}) + n(t) \tag{1}$$

$$n(t) \sim N(0, \sigma_n^2) \tag{2}$$

The noise term $n(t)$ is zero-mean with unknown variance σ_n^2. The amplitudes $A^{(r)}$ are assumed constant during a (short) sampling session but can take random values from session to session. We assume $A^{(r)}$ is Gaussian, i.e. $A^{(r)} = A_0^{(r)} + \Delta A^{(r)}$ where $\Delta A^{(r)} \sim \mathcal{N}\{0, \sigma^2_{\Delta A^{(r)}}\}$.

Remark 1 There are various disturbance sources that implicate fluctuations in amplitude A. For instance, variable load and speed (even when thought to be constant), variations in temperature, complex dynamics of forces in mechanical contacts etc. A plausible model for the resulting impact of several independent random inputs seems to be Gaussian pdf.

Also the phase $\phi^{(r)}$ is random variable uniformly distributed on interval $[0, 2\pi]$. The model (3) seems appropriate for explaining certain shaft faults in the rotating machineries.

In many applications feature extraction is performed by means of linear signal processing techniques, like Discrete Fourier Transform and Wavelet Transform [6]. Here we will assume stationary operating conditions, therefore we will restrict the analysis to the Discrete Fourier Transform. A further study, not addressed here, indicates that results obtained below hold even if the assumptions above are relaxed so that fluctuations in the operating conditions are allowed, for example because of varying rotational speed. In that case f_r should be treated as random variable as well.

We additionally assume that the sampling rate is high enough so that the noise band, remaining after anti-aliasing filtering, is significantly wide compared to the spectral components under investigation. The assumption of "whiteness" is thus somewhat conditional but simplifies technical manipulation.

2.3 Statistical Model of the Fourier Spectral Components

Let us assume that after a measurement session is completed, the Discrete time Fourier Transform (DFT) is applied to the signal $y(kT_s)$, where T_s is sampling time. Assume that the signal contains a spectral component f_c, which contains the

fingerprint of a fault and is therefore appropriate for feature extraction. Let f_c correspond to the mth spectral component meaning $f_c = m\Delta f$ where $\Delta f = \frac{f_s}{N}$ is frequency resolution. The mth component of the DFT reads

$$Y(m) = \frac{1}{N}\sum_{t=0}^{N-1} y(k)\mathrm{e}^{j2\pi\frac{mt}{N}} \tag{3}$$

Remark 2 Normalization with N in (3) is done in order to express the DFT components on the scale close to that of the Fourier series.

After introducing the notation $\theta = 2\pi\frac{m}{N}$ and

$$\boldsymbol{p} = [\,1 \quad \cos\theta t \quad \cos 2\theta t \quad \ldots \quad \cos(N-1)\theta t\,]^{\mathrm{T}}$$

$$\boldsymbol{q} = [\,1 \quad \sin\theta t \quad \sin 2\theta t \quad \ldots \quad \sin(N-1)\theta t\,]^{\mathrm{T}}$$

$$\boldsymbol{n} = [\,n(0) \quad n(1) \quad \ldots \quad n(N-1)\,]^{\mathrm{T}}$$

it follows from (3) that the mth spectral component reads

$$Y(m) = \frac{A}{2}\mathrm{e}^{j\phi} + \frac{1}{N}(\boldsymbol{n}^{\mathrm{T}}\boldsymbol{p} + j\boldsymbol{n}^{\mathrm{T}}\boldsymbol{q})$$

Note that indexes r are omitted for the sake of simplicity as we focus on the results obtained from a sampling session. The feature $\mathcal{F}$ will be the mth component in the power spectrum

$$\mathcal{F} = |Y(m)|^2 = \left(\frac{A}{2}\right)^2 + \frac{A}{N}\sum_{t=0}^{N-1} n(t)\cos(\theta t - \phi) + \boldsymbol{n}^{\mathrm{T}}\mathbf{Q}\mathbf{n} \tag{4}$$

where

$$\boldsymbol{Q} = \frac{1}{N^2}(\boldsymbol{p}\boldsymbol{p}^{\mathrm{T}} + \boldsymbol{q}\boldsymbol{q}^{\mathrm{T}}).$$

It is easily seen that $\boldsymbol{p}\boldsymbol{p}^{\mathrm{T}}$ and $\boldsymbol{q}\boldsymbol{q}^{\mathrm{T}}$ are each rank one matrix so that their sum results in a rank two matrix. Moreover, $\boldsymbol{Q} \geq 0$ is positive definite matrix.

Remark 3 If f_c is not a multiple of Δf then the result (4) becomes somewhat more complicated. However, due to fast sampling, f_c is nearly multiple of the frequency resolution Δf and the projection (3) results in a sufficiently accurate evaluation of the spectral content at f_c.

Even in a simple setup above we can see that rigorous characterization of the pdf of the feature $\mathcal{F} = |Y(m)|^2$ in (4) is not trivial. The first term $\left(\frac{A}{2}\right)^2$ should be

considered as random variable. Due to assumption $A \sim \mathcal{N}\{A_0, \sigma_{\Delta A}^2\}$ the first expression is weighted noncentral χ^2 distribution with one degree of freedom.

In what concerns the last term, one can take into account that $\boldsymbol{Q} = \boldsymbol{U}\boldsymbol{D}\boldsymbol{U}^{\mathrm{T}}$ with all singular values in $\boldsymbol{D}$ being zero with exception of the first two. Since transformation of the random vector $\boldsymbol{n}$ by the unitary matrix $\boldsymbol{U}$ results in uncorrelated random vector $z = \boldsymbol{U}^{\mathrm{T}}\boldsymbol{n}$ the quadratic form reduces to a weighted sum of centrally distributed random variables $\boldsymbol{n}^{\mathrm{T}}\boldsymbol{Q}\boldsymbol{n} = \frac{\alpha}{\sigma_n^2}\left(z_1^2 + z_2^2\right)$.

The analysis of the middle term reveals that its contribution to the first two moments of the random variable $\mathcal{F}$ is negligible. Since the phase can be assumed uniformly distributed on interval $[0, 2\pi]$ it follows that the expectation $\mathrm{E}_\phi \cos(\theta t - \phi) = 0$ and consequently

$$\mathrm{E}_\phi \sum_{t=0}^{N-1} n(t)\cos(\theta t - \phi) = 0$$

After dropping out the intermediate term, the expression (4) becomes a weighted sum of noncentral and 2 centrally distributed χ^2 variables, each with one degree of freedom. Such a sum can not be described by exact closed-form pdf [7].

The problem of approximation of the weighted sums of noncentral χ^2 variables has been addressed by a number of authors, cf. [7] for a comprehensive treatment. Here we adopt Pearson's approach [8] to show that the distribution of the expression (4) is similar to the distribution of the noncentrally distributed χ^2 variable with 3 degrees of freedom. Although this result looks rather obvious, it takes a rigorous procedure to show that the approximation is valid. The details will be omitted and we will mention the main result saying that

$$\mathcal{F} \sim \Omega \cdot \chi^2(v, \lambda) \tag{5}$$

where Ω is suitable scalling factor, $v = 3$ is the degree of freedom and λ is non-centrality parameter.

2.4 Parameter Estimation

Having a realization of the features $\{\mathcal{F}_1, \mathcal{F}_1, \ldots, \mathcal{F}_{N_r}\}$ over the reference window one can estimate the remaining parameters Ω and λ. We start from the fact that

$$\mathrm{E}\mathcal{F} = \Omega(v + \lambda) = a$$
$$\mathrm{E}(\mathcal{F} - a)^2 = \Omega^2(2v + 4\lambda) = b$$

If we use realization $\{\mathcal{F}_k, k = 1, \ldots, n_{\text{ref}}\}$ and put

$$a = \frac{1}{N_{\text{ref}}} \sum_{k=1}^{N_{\text{ref}}} \mathcal{F}_k$$

$$b = \frac{1}{N_{\text{ref}}} \sum_{k=1}^{N_{\text{ref}}} (\mathcal{F}_k - a)^2$$

the estimate for $\hat{\lambda}$ is positive root of the algebraic equation

$$\lambda^2 + \left(2v - \frac{4a^2}{b}\right)\lambda + v^2 - 2v\frac{a^2}{b} = 0$$

while the estimate of Ω reads

$$\hat{\Omega} = \frac{b}{a}\frac{v + \lambda}{2v + 4\lambda}.$$

3 Statistical Hypothesis Test

After the set of features is collected in a reference window under nominal machine condition, batches collected during operation of the machine, need to be checked to make sure whether they share the same statistical properties with those from the reference set. That means we have to compare two batches of the evaluated features. The first one contains N_{ref} values $\mathscr{P}_{\text{ref}} = \{\mathcal{F}_j, j = 1, \ldots, N_{\text{ref}}\}$ taken under the nominal health condition. The second one contains N_{cur} features from the current window $\mathscr{S}_{\text{cur}} = \{\mathcal{F}_i, i \in \{K - N_{\text{cur}} + 1, \ldots, K - 1, K\}\}$. The first set can be regarded as result of sampling from the weighted noncentral χ^2 distribution $\Omega_0 \cdot \chi^2(v_0, \lambda_0)$. In the similar way, the second set emerges from sampling $\Omega_c \cdot \chi^2(v_c, \lambda_c)$.

If there is no change in the system condition, then the statistical properties of samples in $\mathscr{S}_{\text{cur}}$ should be equal to the statistical properties of those in $\mathscr{S}_{\text{ref}}$. If the system condition deteriorates, the statistical properties of the feature change, which normally reflect in first two moments of the distribution. Let us now state the null hypothesis H_0 that the features in current window share the same statistical properties with those in the reference window. Take the sums $S_{\text{ref}} = \sum_{i=1}^{N_{\text{ref}}} \mathcal{F}_i$ and $S_{\text{cur}} = \sum_{i=K-N_{\text{cur}}+1}^{K} \mathcal{F}_i$. Under the hypothesis H_0 both expressions appear to be realisations of the sums of weighted, independent noncentrally distributed $\chi^2(v_0, \lambda_0)$ variables, resulting in the following distributions

$$S_{\text{ref}} \sim \Omega_0 \cdot \chi^2(v_{\text{ref}}, \lambda_{\text{ref}})$$
$$S_{\text{cur}} \sim \Omega_0 \cdot \chi^2(v_{\text{cur}} \lambda_{\text{cur}})$$

where $v_{\text{ref}} = N_{\text{ref}} v_0$, $\lambda_{\text{ref}} = N_{\text{ref}} \lambda_0$, $n_{\text{cur}} = N_{\text{cur}} v_0$, $\lambda_{\text{cur}} = N_{\text{cur}} \lambda_0$. Since S_{ref} and S_{cur} are statistically independent we propose the test statistic

$$\text{CI}_F = \frac{\frac{S_{\text{cur}}}{n_{\text{cur}}}}{\frac{S_{\text{ref}}}{n_{\text{ref}}}} = \frac{\frac{S_{\text{cur}}/\Omega_0}{n_{\text{cur}}}}{\frac{S_{\text{ref}}/\Omega_0}{n_{\text{ref}}}} = \frac{\frac{\chi^2(n_{\text{cur}}, \lambda_{\text{cur}})}{n_{\text{cur}}}}{\frac{\chi^2(n_{\text{ref}}, \lambda_{\text{ref}})}{n_{\text{ref}}}} \tag{6}$$

We get random variable CI_F which is described by *doubly noncentral F distribution*. To explain this, let us remind that if two central $\chi^2(v_1)$ and $\chi^2(v_2)$ are independent with v_1 and v_2 d.o.f. respectively, then $F = \frac{\chi^2(v_1)/v_1}{\chi^2(v_2)/v_2}$ has an F distribution. When only one of the χ^2 is noncentral, the ratio F has noncentral F distribution. If *both* χ^2 are noncentral then the ratio

$$F(v_1, v_2, \lambda_1, \lambda_2) = f = \frac{\chi^2(v_1, \lambda_1)/v_1}{\chi^2(v_2, \lambda_2)/v_2} \tag{7}$$

turns to what is referred to as *doubly noncentral F distribution* [9].

We are finally ready to define the null hypothesis

$$H_0 : \text{CI}_F \sim F(v_{\text{cur}}, v_{\text{ref}}, \lambda_{\text{cur}}, \lambda_{\text{ref}}) \tag{8}$$

versus the alternative hypothesis H_1 that CI_F is not compliant with the distribution (6). Hence we reject H_0 if

$$\text{CI}_F \geq h = F_\alpha(v_{\text{cur}}, v_{\text{ref}}, \lambda_{\text{cur}}, \lambda_{\text{ref}}) \tag{9}$$

where the term on the right side denotes the critical value of the distribution at the level of significance α (the tolerated PFA).

The distribution of f in (7) has a peculiar pdf [10]

$$p(f; v_1, v_2, \lambda_1, \lambda_2) = \frac{v_1}{v_2} \mathrm{e}^{-\frac{\lambda}{2}} \sum_{i=0}^{\infty} \sum_{j=0}^{\infty} \frac{\left(\frac{\lambda_1}{2}\right)^i \left(\frac{\lambda_2}{2}\right)^j \left(\frac{v_1 f}{v_2}\right)^{\frac{v_1}{2}+i-1}}{i! j! \left(1 + \frac{v_1 f}{v_2}\right)^{\frac{v_1+v_2}{2}+i+j} B\left(\frac{v_1}{2} + i, \frac{v_2}{2} + j\right)}$$

where $B(p, q)$ is beta-function. The pdf and cdf need to be evaluated numerically. To do so, we used the saddle point approximation algorithm according to [9].

Remark 4 Note that the d.o.f. v_{ref} and v_{cur} depend on whether in fault-free case there is a sine component at f_c or not. In the ideal case $A_0 = 0$ and $\sigma_{\Delta A}^2 = 0$ so that the pdf of (4) is χ^2 with only 2 d.o.f. and consequently $n_r = 2N_{\text{ref}}$ and $v_{\text{cur}} = 2N_{\text{cur}}$.

Hence we could also apply the noncentral F-test instead of (3). However, most often in applications some component at f_c is present so that $\nu_{\text{ref}} = 3N_{\text{ref}}$ and $\nu_{\text{cur}} = 3N_{\text{cur}}$ and some non-zero centrality parameters are present as well.

4 The Evaluation Study

4.1 A Simulated Example

We will take a mono-component signal with additive white Gaussian noise

$$y(t) = A_c \cdot \sin(2\pi \cdot f_c \cdot t + \phi) + n(t), \quad f_c = 2\text{Hz} \tag{10}$$

The feature $\mathcal{F}$ is component of the power spectrum at $f = 2$Hz.

By Monte Carlo simulation we obtain a realization of $N_{\text{MC}} = 1000$ signal waveforms and then calculate the required component of the power spectrum. Hence we get a realization of N_{MC} values of feature $\mathcal{F}$. First we want to show how nicely the noncentral χ^2 distribution fits the empirical distributions at any combination of noise parameters and amplitude of the sine component. Every fit is accompanied with the Kolmogorov-Smirnov (KS) test at 1 % of significance level with focus on p-values. It should be note that the KS test (mostly known from testing normality of distributions) is used here to "measure" the quality of fit of an empirical distribution described by a suitable χ^2 distribution.

In Fig. 1 we have two cases:

(a) $A_c = 0$, $\sigma^2_{\Delta A} = 0$, $\sigma^2_n = 1$ and then
(b) $A_c = 1$, $\sigma^2_{\Delta A} = 0.1$, $\sigma^2_n = 1$.

The first case resembles the situation with perfectly balanced machine. This is a quite special case as the distribution in (4) reduces to the central χ^2 distribution with 2 d.o.f. The p-value of the KS test is 0.63.

In the second case we have a signal composed of a sine wave with high additive noise. The degree of freedom of the random variable (4) now rises to 3. The quality of fit is confirmed by p-value 0.8 of the KS test. The next example illustrates the behaviour of the algorithm. The amplitude of the spectral component $f_c = 20$ Hz is defined by $A_c = 0.1$ and $\sigma^2_{\Delta A} = 0.01$ and apply to signals taken from 300 reference session, not shown in Fig. 2. The nominal conditions apply up to the session with number 350. From 350 on there is a slow drift in the amplitude A_c. The sliding window used for detection includes 150 sessions. Based on the fitted parameters of the pdf for the features in the reference window it follows that at $\alpha = 0.0006$ the threshold is $h = 2.4$. The evolution of the test statistics is shown in Fig. 2.

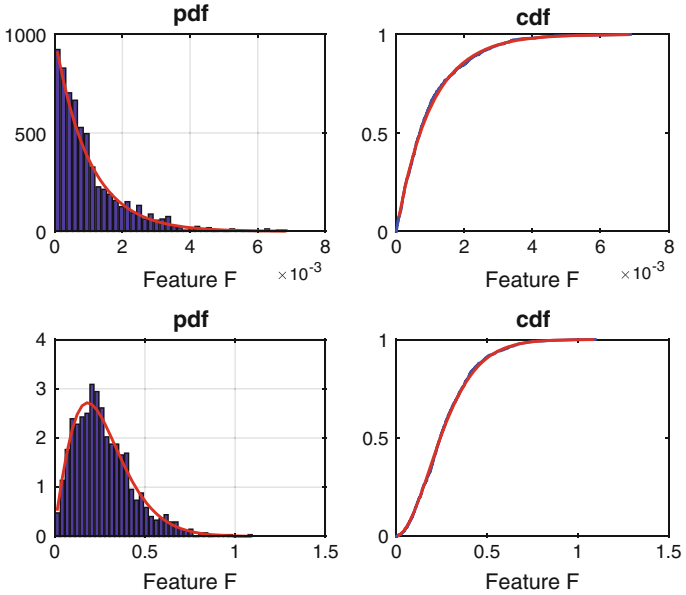

Fig. 1 The quality of fit of the χ^2 distribution: with 2 d.o.f and $A_0 = 0$, $\sigma^2_{\Delta A} = 0$ (*upper part*) and with 3 d.o.f. at $A_c = 1$, $\sigma^2_{\Delta A} = 0.1$ (*lower part*). In both cases $\sigma^2_n = 1$

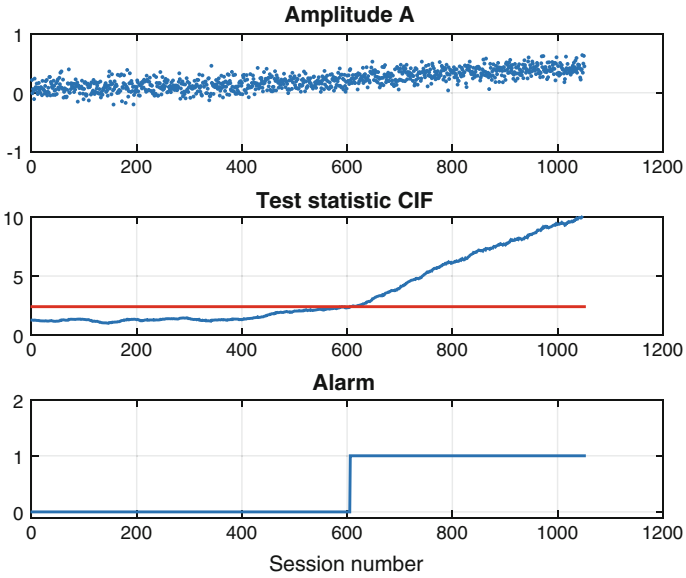

Fig. 2 The performance of the statistical test on simulated data

4.2 EC Motor with Imbalance

First experiments were done with imbalance on an EC motor, which serves to drive the fan in a ventilator for HVAC systems. The rig (Fig. 3) consists of a fixed pedestal on top of which a metal disk is positioned. The metal disk holds three rubber dampers that suspend the tested EC motor. The experiment starts by positioning the EC motor vertically on the rubber dampers in a way that the drive–end bearing is at the bottom. An accelerometer is mounted on the motor housing nearest to the bearings (lower side). Vibration signals were low–pass filtered with cut–off frequency at 22 kHz. Afterwards, both signals were sampled at 60 kHz. During the whole data acquisition process the nominal rotational speed of $f_{\text{rot}} = 30\,\text{Hz}$ was maintained. Each acquisition process lasted 8 s. Imbalance was generated artificially by gluing a mass with 0.5 g on the axis (at the bottom, cf. Fig. 3). To detect imbalance the spectral component at the rotational speed has to be analysed.

The results in Fig. 4 are preliminary since rather short reference and current windows are applied. It is essential to note that the pdf approximation of the data histogram are considered acceptable by KS test. Right is the time evaluation of the features after a sudden change in imbalance (caused due to a mounting error) (See Fig. 4).

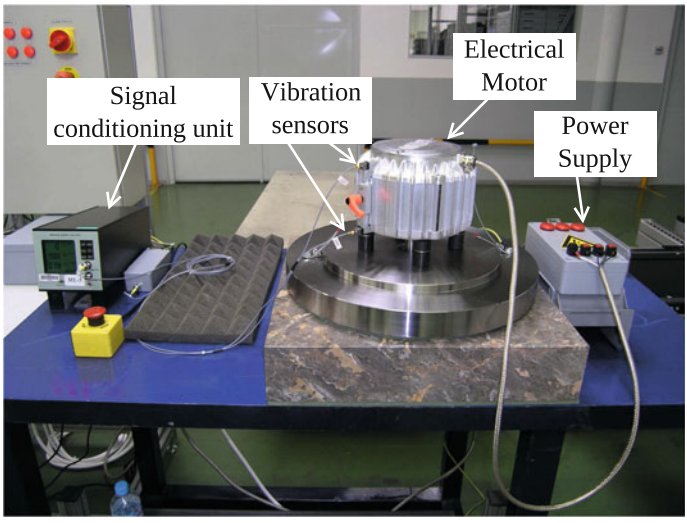

Fig. 3 The experimental setup centered around an EC motor. To create imbalance artificially, a small mass is glued on the axis of the motor (*the bottom part*)

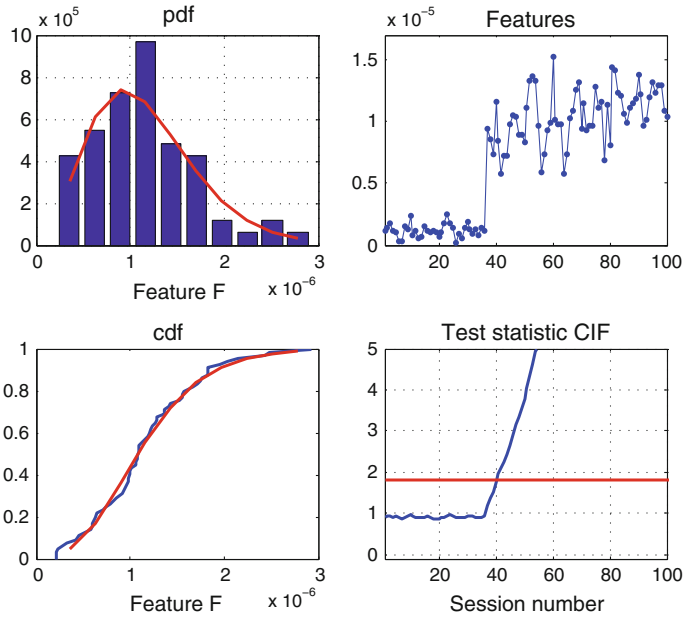

Fig. 4 Experimental results obtained on an EC motor with imbalance after session #35. The pdf and cdf fit of the reference data (*left*) and the performance of the statistical test (*right*)

5 Conclusion

The paper proposes an approach for setting the thresholds in monitoring of the rotational machines. The only "tuning knob" needed is the probability of false alarm (PFA). Fault detection builds on checking whether the normed sum of features complies with the a doubly noncentral F-distribution. If not, the alarm is triggered. Preliminary results are assessed on simulated examples and an EC motor. So far only stationary conditions are assumed although there are good indications that the results hold for fluctuating operating conditions as well. In the follow-up more focus will go on further practical assessments, analysis of other faults and potential robustness of the test with respect to disturbances.

Acknowledgments The authors acknowledge the financial support of the Slovenian Research Agency through the Programme P2-0001 and the Ministry of Education, Science and Sport for support of the Eurostars project PRODISMON through grant 2130-13-090007. The second author is indebted to the Slovene Human Resources Development and Scholarship Fund (Ad futura) for kind support.

References

1. Bechhoefer E, Bernhard APF (2006) Use of non-Gaussian distribution for analysis of shaft components. In: Proceedings IEEE Aerospace Conference, Big Sky, MT, p 9
2. Bechhoefer E, Bernhard APF (2007) A generalized process for optimal threshold setting in HUMS. In: Proceedings IEEE Aerospace Conference, 2007, pp 1–9
3. Basseville M, Nikiforov I (1998) Detection of abrupt changes: theory and applications. Prentice Hall, New Jersey
4. Bechhoefer E, He D, Dempsey P (2011) Gear health threshold setting based on a probability of false alarm. In: Proceedings of the 2011 Annual Conference of the Prognostics and Health Management Society, Montreal, Canada, 23–28
5. Dolenc B, Boškoski P, Juričić D (2014) Robust information indices for diagnosing mechanical drives under non-stationary operating conditions. In: International Conference on Condition monitoring of Machinery in non-stationary Operations, Lyon, p 11
6. Randall RB (2011) Vibration-based condition monitoring. Wiley, Chichester
7. Mathai AM, Provost SB (1992) Quadratic forms in random variables. Marcel Dekker, Inc., New York
8. Liu H, Tang Y, Zhang HH (2009) A new chi-square approximation to the distribution of non-negative definite quadratic forms in non-central normal variables. Comput Stat Data Anal 53:853–856
9. Paolella M (2007) Intermediate crobability: a computational approach. Wiley, New York
10. Walck C (1996) Handbook on statistical distributions for experimentalists, Internal Report SUF–PFY/96–01. Stockholm

Diagnostic Features Modeling for Decision Boundaries Calculation for Maintenance of Gearboxes Used in Belt Conveyor System

Paweł K. Stefaniak, Agnieszka Wyłomańska, Radoslaw Zimroz, Walter Bartelmus and Monika Hardygóra

Abstract Condition-Based maintenance (CBM) becomes more and more popular in industry. The idea is simple: measure raw data (vibrations, temperatures, etc.), extract features and make a right decisions regarding replacement of the whole machine or its component at appropriate time. Right decision might mean simple *if-then-else rule* or complex decision making scheme using multidimensional data. In any case mentioned rules require definition of appropriate thresholds for diagnostic parameters (i.e. decision boundaries). This is a key problem in CBM. The article presents the procedure for determining decision thresholds based on statistical modeling of diagnostic data. In the presented procedure first we fit the suitable distribution (Weibull) to data set for each gearbox. Next we calculate the fitting quality measure and select the distribution parameters for well fitted data. Finally, on the basis of the multidimensional analysis of those parameters we determine threshold values for the effective identification of the machines' condition and their components. It might be interpreted as training process of diagnostic system. From this phase of the procedure we can obtain thresholds for warning and alarm statuses and they can be used for classification of rest of the data (that did not pass modeling phase). Proposed procedure has been applied to relatively large diagnostic data set

P.K. Stefaniak (✉) · A. Wyłomańska · R. Zimroz · W. Bartelmus · M. Hardygóra
Wroclaw University of Technology, Wrocław, Poland
e-mail: pawel.stefaniak@pwr.edu.pl; pkstefaniak@cuprum.wroc.pl

A. Wyłomańska
e-mail: agnieszka.wylomanska@pwr.edu.pl

R. Zimroz
e-mail: radoslaw.zimroz@pwr.edu.pl; rzimroz@cuprum.wroc.pl

W. Bartelmus
e-mail: walter.bartelmus@pwr.edu.pl

M. Hardygóra
e-mail: monika.hardygora@pwr.edu.pl; mhardygora@cuprum.wroc.pl

R. Zimroz · M. Hardygóra
KGHM Cuprum R&D, Wrocław, Poland

F. Chaari et al. (eds.), *Advances in Condition Monitoring of Machinery in Non-Stationary Operations*, Applied Condition Monitoring 4,
DOI 10.1007/978-3-319-20463-5_19

that covers nearly 150 measurements acquired during several years in underground mine. The data describes gearboxes in different conditions—from nearly new or after repair to seriously damaged/worn just before failure.

Keywords Belt conveyor · Decision making · Maintenance · Weibull distribution · Diagnostics

Contents

1 Introduction 252
2 Belt Conveyors Network and Data Acquisition Module—Basic Information 253
3 Procedure of Decision Boundaries Estimation Using Weibull Distribution Modeling and Parameters Classification 255
4 Application to Real Data 257
5 Conclusions 261
References 262

1 Introduction

In Condition-Based Maintenance (CBM) one might point out two important issues: (i) how to detect and recognize change of machine condition; (ii) how to estimate residual lifetime. Term of residual lifetime is related to a period when machine should be replaced in order to avoid catastrophic failure and eventually repair of replaced machine will be financially reasonable. The second problem is still kind of open question. There are many factors that should be taken into account to build up the prognostic model for belt conveyor drive unit. As it was noticed by Bartelmus [1] design, production technology, operating conditions (variability of load/speed, their dynamics, frequent start up/stall of the machine etc.) and different degradation scenarios might affect gearbox vibration response and consequently provide family of lifetime curves. At this stage, critical problem is how to find reasonable values of simple diagnostic features, that might be used for decision making in practical maintenance management in underground mine. Unfortunately, there are just a few work available discussing similar problems. They are based on good/bad data sets statistical modeling for finding single thresholds value, analysis of behavior of data clouds to find border (hyperplane) between primary data sets or complex procedures that correlate some parameters with models of behaviors for machine during good and bad condition including influence of varying load [1–19].

How should it be done in ideal case? For stationary case, there are some works presenting experiments carried out in the lab, where fatigue test were done with visual inspection of actual condition of gear teeth. When any visual symptoms appear on the tooth surface, one might define early warning state, then after some

time of operation, just before failure, alarm threshold could be established. Using data acquired during experiments one might build a bath curve (known from reliability) and build mentioned before prognostic model [17, 20, 21].

How it works in real case? Let's consider an underground mine with nearly 100 gearboxes. There are several types of gearboxes, they are mounted in drive units with various technical configuration (different couplings, different drive units used for drive conveyors, different percentage of operation per day etc., different power…). It leads to set of design factors. Gearboxes operate in different mining zones, where assumed volume of transported materials, time of operation per day, temperature, humidity and level of dust might be very different for each zone and might vary in time. It leads to set of operational and environmental factors, that might significantly influence degradation processes. Finally, these gearboxes are two- or three-stages gearboxes. Maintenance staff is interested in detailed knowledge, which bearings/gears should be replaced. There is often a case when two or more degradation processes occur simultaneously (for different components of gearbox). Depending on mentioned operational and environmental factors, as well as design (bevel or cylindrical stage…) degradation processes might be fairly complex. What does it mean practically? There are many issues to consider during decision boundaries calculations. For sure, it is too expensive to do lab experiments for each case. So, one should base on passive experiments only (just observe and use data driven approaches). An automatic, simple procedure is expected.

The paper is organized as follow: first brief description of the belt conveyor and whole transportation system is provided including basic description of experiments, data acquisition/diagnostic tools and method and data set using in this work. Next, procedure of data processing for thresholds finding is presented. Finally, application of the method to real data with some discussion is provided.

2 Belt Conveyors Network and Data Acquisition Module—Basic Information

The belt conveyor network is a main continuous transportation system using in underground mines. For example, in one of them is exploited over 82 belt conveyors with total length of routes exceeding 50 km. Problem of management of this network deals both with its spatially distribution in extensive area and large amount of its key components. Let's imagine that this network is driven by over 220 drive units. So, in this reality the failure event of any component may cause directly stoppage of whole technological line—what is really unfavorable both from view point of economic and safety. Thus, the keeping the maintenance focusing on improvement of efficiency, reliability and reduction of repair costs seem to be justified. To maintain such a complex system there was a need to build a Decision Support System [15, 22] (called Diag Manager) using condition based maintenance approach. Data acquisition module (dedicated to Diag Manager system) consists of two layers: (a) sensors layer and (b) control and measurement layer. First of them is

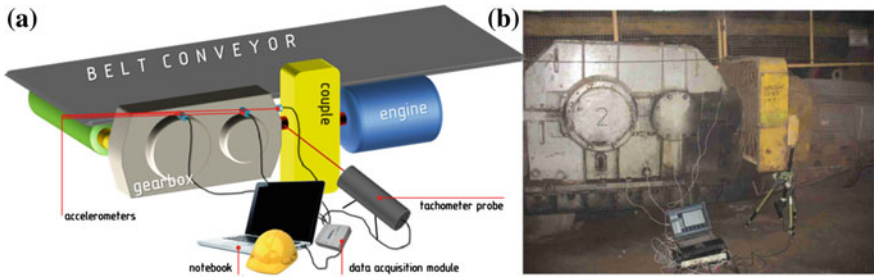

Fig. 1 **a** Diagram of the vibration data acquisition module with an exemplary arrangement of the measurement points. The measurement module consists of notebook and sensors layer, **b** real object in underground mine during measurement

composed of accelerometers placed on gearbox housing and tachometer probe directed toward gearbox input shaft in order to measure its rotational speed, Fig. 1.

Next, acquired vibration signals are processed for purpose of extraction of diagnostic feature. The procedure is based on Bartelmus method [2–4] and comes down to the three-way split of the signal spectrum (0–100 Hz range relates to shaft operation, 100–3500 Hz range relates to gears operations, over 3500 Hz range deals with bearings operations). Obtained 3 parameters are called DF1–DF3 (DF = Diagnostic Feature). In this paper we will discuss DF2 (describing gear pair) only.

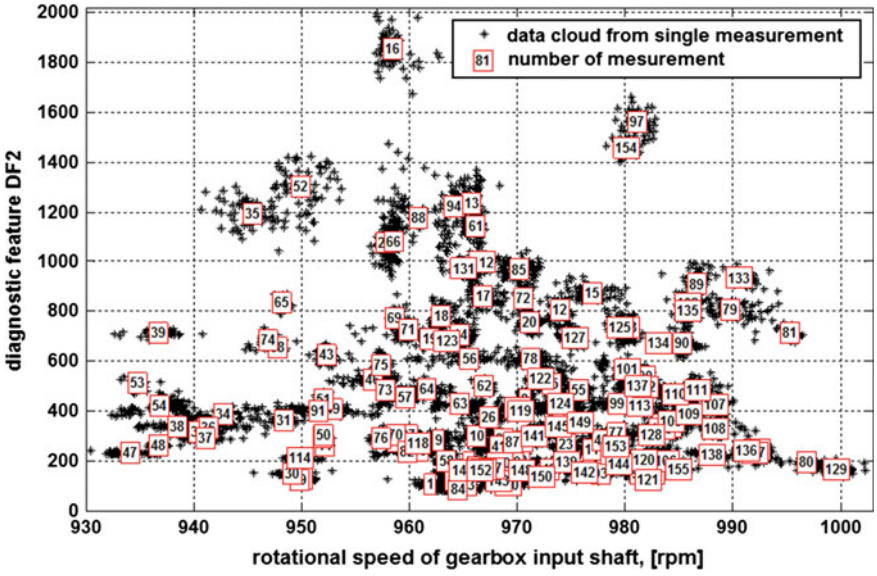

Fig. 2 The input data set: 155 measurements (60 samples of DF2 and rotational speed per single measurement). The diagnostic features' diversity is closely linked to external load and technical condition of gearboxes. It can be easily noticed, that depending on external load and technical condition both mean value of diagnostic features and scatters of their data clouds are different

In next step, spectral components in particular ranges are summed up (it might be interpreted as energy in these bands) and this way diagnostic features are extracted. Figure 2 shows population of 155 measurements of DF2 diagnostic feature describing technical condition of gears in function of rotational speed. These data clouds have been acquired from one type of gearboxes at irregular intervals in period 2010–2014. What is really important here is a disposal of knowledge about what data clouds represent gearboxes in good condition and which behaviors of these syndromes indicate an improper gearbox operation. It was proved in [2–4] that mining machines require to take into account the feature-external load relation in correlation with degradation process' progress. In Fig. 2 DF2 versus rotational input speed is shown.

3 Procedure of Decision Boundaries Estimation Using Weibull Distribution Modeling and Parameters Classification

The procedure of decision boundaries estimation is based on the modeling of the diagnostic features by using translated Weibull distribution and analysis of the quality of the Weibull distribution fit. The scheme of the proposed procedure is as follows:

First, for the diagnostic features we fit the translated Weibull distribution. Let us emphasize the translated Weibull distribution (called later Weibull) [7, 23] is defined through the probability density function as follows:

$$f(x) = \frac{\tau}{\beta}\left(\frac{x-m}{\beta}\right)^{\tau-1} \mathrm{e}^{-\left(\frac{x-m}{\beta}\right)^{\tau}}, \quad x \geq m. \tag{1}$$

The Weibull distribution (known also as Frechet distribution [8]) is therefore characterized by three parameters: shift parameter m, which can be any real number, scale parameter $\beta > 0$ and shape parameter $\tau > 0$. This distribution is an extension of the Pareto one. The Pareto distribution found interesting applications, for example it was used for distributions' modeling of diagnostic features in condition monitoring of mining machines [14]. We should mention here the right tail [24] of the Weibull distributed random variable X has the following form:

$$T(x) = P(X > x) = \mathrm{e}^{-\left(\frac{x-m}{\beta}\right)^{\tau}}, \quad x \geq m. \tag{2}$$

In the further analysis Eq. (2) is a starting point to estimate the parameters of Weibull distribution, as well as to check the quality of the Weibull distribution fit.

The main properties of Weibull distribution one can find for example in [7]. We only mention here all the moments of the Weibull distributed random variables exist and the moment generating function as well as characteristic function have explicit form.

In the first step of the estimation procedure of Weibull distributed random sample $X_1, X_2, \ldots X_n$ we estimate the parameter m which is equal to the minimum of the observed values. Next, the τ parameter is estimated. Namely, to the empirical right tail we fit the theoretical one given in Eq. (2). Since for large values of argument of tail function the expression $\left(\frac{x-m}{\beta}\right)$ behaves like $(x - m)$ then to the empirical tail we fit (by using the least squares method) the function $e^{-(x-m)^{\tau}}$ taking instead of m its estimator calculated in the first step. On the basis of the fitted function we calculate the τ parameter. Let us remind the empirical tail is an estimator of theoretical one calculated on the basis of random sample $X_1, X_2, \ldots X_n$ and takes the following form:

$$\widehat{T}(x) = \frac{1}{n}\sum_{i=1}^{n} 1_{\{X_i > x\}}, \tag{3}$$

where $1_{\{A\}}$ is an indicator of the set A.

In the last step we have to estimate the β parameter. In order to do this we calculate the empirical median on the basis of given random sample and compare it to the theoretical median of Weibull distribution that is given by:

$$me(X) = \beta \log(2)^{1/\tau}. \tag{4}$$

Taking instead of τ its estimator calculated in the previous step and instead of theoretical median its empirical counterpart we estimate the β parameter. In the next step of our procedure of decision boundaries estimation we analyze the quality of fit the Weibull distribution to the diagnostic features. More precisely, for each diagnostic feature we calculate the mean square error between the empirical tail calculated by using Eq. (3) and theoretical one given in (2) for estimated parameters of Weibull distribution. The mean square error is therefore calculated as:

$$\mathrm{MSE} = \frac{1}{k}\sum_{i=1}^{k}\left(T(x_i) - \widehat{T}(x_i)\right)^2, \tag{5}$$

where $x_1, x_2, \ldots x_k$ are arguments of the empirical tail.

Next, we choose such diagnostic features for which the calculated MSEs do not exceed the given threshold. For those features we plot the empirical tails. On the basis of empirical tails we can conclude on the decision boundaries.

In the last step we apply the same boundaries that we calculated for diagnostic features with small MSEs to the diagnostic features with MSEs that exceed the given threshold.

The scheme of the procedure is presented in Fig. 3.

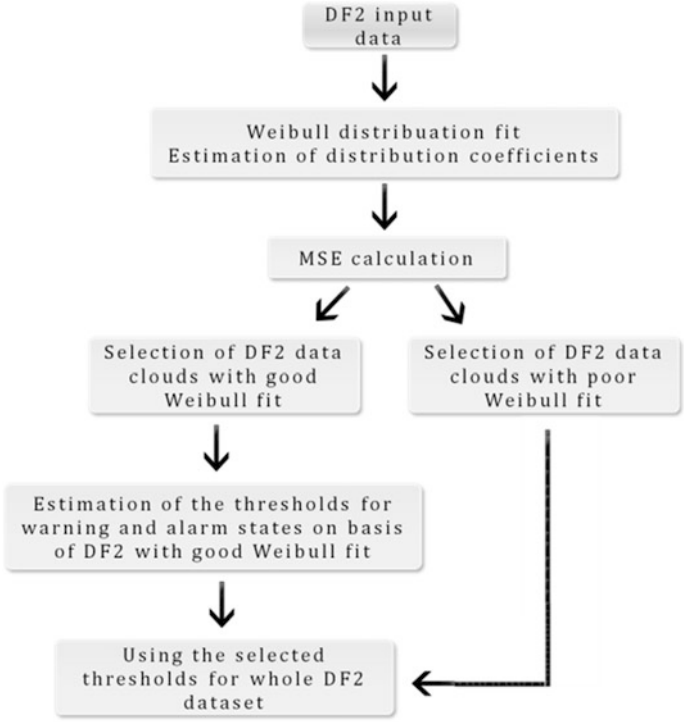

Fig. 3 Scheme of the procedure for definition of decision boundaries using Weibull distribution

4 Application to Real Data

In this section we present the application of described decision boundaries estimation procedure to real data i.e. diagnostic features DF2.

As it was mentioned in the previous section, to examined diagnostic features first we fit the Weibull distribution and estimate its parameters. In Fig. 4 we present the estimated parameters m, β and τ for 155 examined vector of observations.

Next, we analyze the mean square error of the Weibull distribution fit calculated on the basis of Eq. (5). In Fig. 5 we present the MSE as well as the chosen threshold that is equal to 0.08.

In Fig. 6 we show the empirical right tails for diagnostic features for which the MSEs are greater than the chosen threshold while in Fig. 7 we present the empirical right tails of diagnostic features with MSEs smaller than the given threshold. Moreover in Fig. 7 we indicate decision boundaries, i.e. 660 and 1100.

The empirical tails for the diagnostic features with good fit after application the decision thresholds we present in Fig. 8. The three presented groups correspond to good, warning and alarm state. In Fig. 9 we present the diagnostic feature DF2

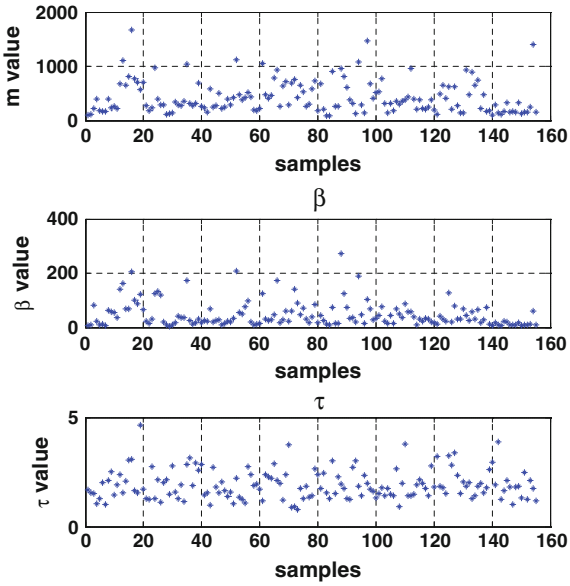

Fig. 4 Estimated parameters m, β and τ of Weibull distribution for diagnostic features DF2

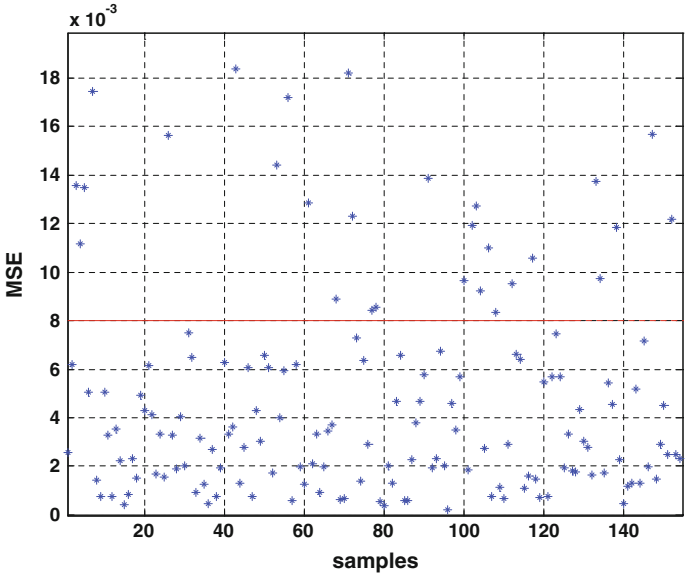

Fig. 5 The MSE of Weibull distribution fitting to the diagnostic features DF2

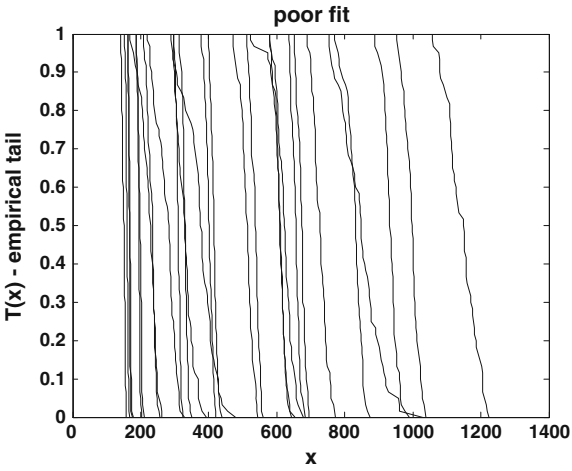

Fig. 6 The empirical tail of diagnostic features for which the MSEs of Weibull distribution fit are greater than chosen threshold

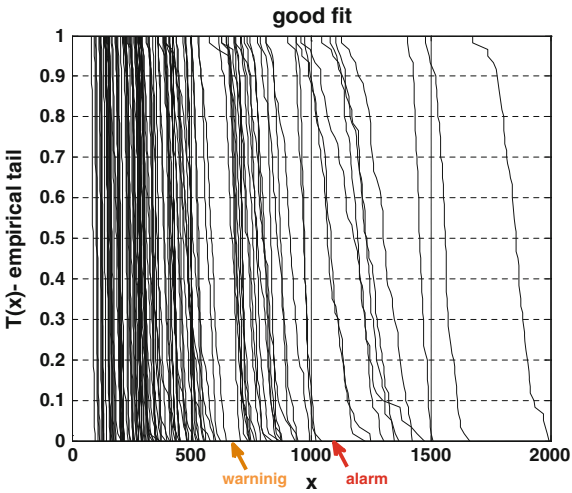

Fig. 7 The empirical tail of diagnostic features for which the MSEs of Weibull distribution fit are smaller than chosen threshold. The *arrows* indicate the decision boundaries

(with good fit) in rotational speed function after applying the decision threshold procedure.

As it was mentioned in the previous section, in the last step of our procedure we use the same thresholds calculated on the basis of empirical tails for DF2 diagnostic features of good fit and apply them to the DF2 with poor fit. In Fig. 10 we present the final result of classification for all DF2 diagnostic features.

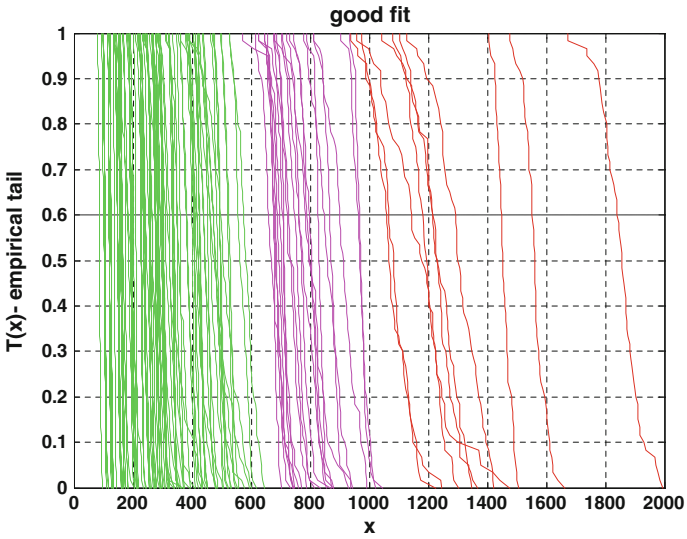

Fig. 8 The empirical tail of diagnostic features for which the MSEs of Weibull distribution fit are smaller than chosen threshold. The three selected groups correspond to good, warning and alarm state

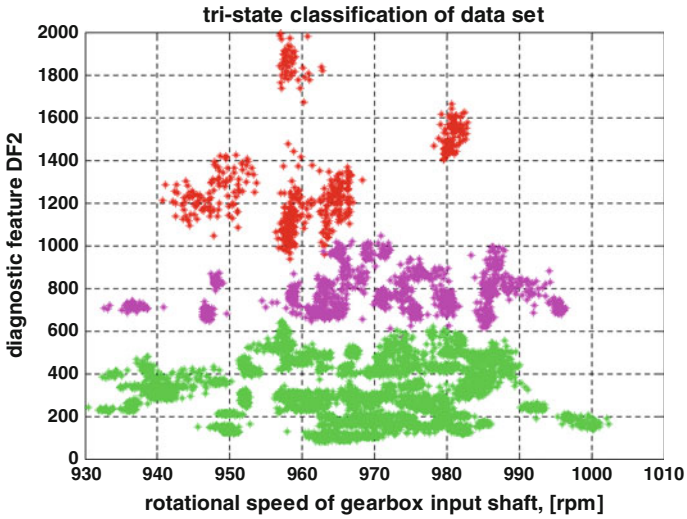

Fig. 9 The diagnostic feature DF2 (with good fit) in rotational speed function after applying the decision threshold procedure based on the Weibull distribution

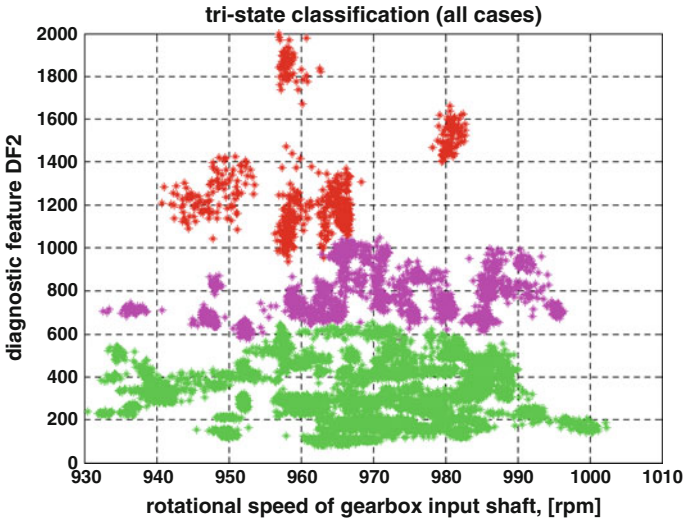

Fig. 10 The diagnostic feature DF2 (with good and poor fit) in rotational speed function after applying the decision threshold procedure based on the Weibull distribution

5 Conclusions

The problem of decision boundaries finding i.e. diagnostic thresholds for gearbox condition based maintenance is discussed. These gearboxes are used in belt conveyor driving units operated in underground mine. A core of the proposed method is statistical modeling of the diagnostic data set. For each data set describing single gearbox we have tried to fit Weibull distribution to real data. Obtained parameters plus a measure evaluating quality of such modeling (MSE) have been basis for next step of the procedure. We have noticed that empirical tails of diagnostic features create three separable groups of characteristics. We identified ID of each curve and used this information to group more intuitive data for engineers, namely diagnostic features DF2 plotted versus rotational speeds. The final conclusion is very positive, our result seriously converge to previous approaches. The advantage of this approach is that it might be realized in automatic way and doesn't require diagnostic intuition or experience.

Acknowledgments This work is partially supported by the statutory grant No. B40037 (P. Stefaniak).

References

1. Bartelmus W (2001) Mathematical modelling and computer simulations as an aid to gearbox diagnostics. Mech Syst Sig Process 15(5):855–887
2. Bartelmus W, Chaari F, Zimroz R, Haddar M (2010) Modelling of gearbox dynamics under time-varying non-stationary load for distributed fault detection and diagnosis. Eur J Mech A Solids 29(4):637–646
3. Bartelmus W (1992) Mach Vibr 1:178–189
4. Bartelmus W, Zimroz R (2009) A new feature for monitoring the condition of gearboxes in non-stationary operating conditions. Mech Syst Sig Process 23(5):1528–1534
5. Brooks R, Thorpe R, Wilson J (2004) A new method for defining and managing process alarms and for correcting process operation when an alarm occurs. J Hazard Mater 115:169–174
6. Cempel C (1990) Limit value in practice of vibration diagnosis. Mech Syst Sig Process 4 (6):483–493
7. Cizek P, Härdle WK, Weron R (2005) Statistical tools for finance and insurance. Springer, Berlin
8. Coles S (2001) An introduction to statistical modeling of extreme values. Springer, Berlin
9. Dybała J, Radkowski S (2007) Geometrical method of selection of features of diagnostic signals. Mech Syst Sig Process 21(2):761–779
10. Dybała J (2013) Vibrodiagnostics of gearboxes using NBV-based classifier: a pattern recognition approach. Mech Syst Sig Process 38(1):5–22
11. Galar D, Gustafson A, Tormos B, Berges L (2012) Maintenance decision making based on different types of data fusion. Eksploatacja I Niezawodnosc—Maintenance Reliab 14(2):135–144
12. Jablonski A, Barszcz T, Bielecka M, Breuhaus P (2013) Modeling of probability distribution functions for automatic threshold calculation in condition monitoring systems. Measurement 46(1):727–738
13. Lodewijks G (2004) Strategies for automated maintenance of belt conveyor systems. Bulk Solids Handling 24(1):16–22
14. Stefaniak PK, Wyłomańska A, Obuchowski J, Zimroz R (2015) Procedures for decision thresholds finding in maintenance management of belt conveyor system—statistical modeling of diagnostic data. Proceedings of the 12th international symposium continuous surface mining—Aachen 2014. Lecture notes in production engineering 2015, pp 391–402
15. Stefaniak PK, Zimroz R, Bartelmus W, Hardygóra M (2014) Computerised decision-making support system based on data fusion for machinery system's management and maintenance. Appl Mech Mater 683:108–113
16. Zimroz R, Bartelmus W, Barszcz T, Urbanek J (2012) Wind turbine main bearing diagnosis—a proposal of data processing and decision making procedure under non stationary load condition. Key Eng Mater 518:437–444
17. Zimroz R, Bartelmus W, Barszcz T, Urbanek J (2014) Diagnostics of bearings in presence of strong operating conditions non-stationarity—a procedure of load-dependent features processing with application to wind turbine bearings. Mech Syst Sig Process 46(1):16–27
18. Zimroz R, Bartkowiak A (2013) Two simple multivariate procedures for monitoring planetary gearboxes in non-stationary operating conditions. Mech Syst Sig Process 38(1):237–247
19. Zimroz R, Stefaniak P, Bartelmus W, Hardygóra M (2015) Novel techniques of diagnostic data processing for belt conveyor maintenance. Proceedings of the 12th international symposium continuous surface mining—Aachen 2014. Lecture notes in production engineering 2015, pp 31–40
20. Lim CKR, Mba D (2014) Switching Kalman filter for failure prognostic. Mech Syst Sig Process. http://dx.doi.org/10.1016/j.ymssp.2014.08.006i
21. Raad A, Antoni J, Sidahmed M (2008) Indicators of cyclostationarity: theory and application to gear fault monitoring. Mech Syst Sig Process 22(3):574–587

22. Stefaniak PK, Zimroz R, Krol R, Gorniak-Zimroz J, Bartelmus W, Hardygora M (2012) Some remarks on using condition monitoring for spatially distributed mechanical system belt conveyor network in underground mine—a case study condition monitoring of machinery in non-stationary operations: proceedings of the second international conference. Condition monitoring of machinery in non-stationary operations. CMMNO' 2012/ed. TaharFakhfakh [i in.] Springer, pp 497–507
23. Weibull W (1951) A statistical distribution function of wide applicability. J Appl Mech Trans ASME 18(3):293–297
24. Silverman BW (1986) Density estimation for statistics and data analysis. Chapman and Hall, London

Vertical Axis Wind Turbine States Classification by an ART-2 Neural Network with a Stereographic Projection as a Signal Normalization

Tomasz Barszcz, Andrzej Bielecki, Marzena Bielecka, Mateusz Wójcik and Mirosław Włuka

Abstract A common technique used to decrease a cost of wind turbine maintenance is a remote monitoring. Apart from the development of several advanced diagnostic methods for wind turbines there is a need to prepare an early warning tool which would work continuously in real-time and focus the attention on potentially dangerous cases. A research using the resonance neural networks made so far by the authors gave positive results. Systems based on the ART-2 networks were able to perform a classification of operational states of a horizontal axis wind turbine. In this paper the innovative idea of using the ART-2 network is applied to data from vertical axis wind turbines. The system, which were composed by ART-2 and new signal normalization procedures based on a stereographic projection, was implemented and tested. Simulations of a system operation showed that it is capable to perform an efficient state classification.

Keywords Vertical axis wind turbines · Operational states classification · ART-2 neural network · Input signals normalization · Stereographic projection

T. Barszcz
Faculty of Mechanical Engineering and Robotics, AGH University of Science and Technology, Cracow, Poland
e-mail: tbarszcz@agh.edu.pl

A. Bielecki · M. Wójcik (✉)
Faculty of Electrical Engineering, Automation, Computer Science and Biomedical Engineering, AGH University of Science and Technology, Cracow, Poland
e-mail: mateuszjanwojcik@gmail.com

A. Bielecki
e-mail: azbielecki@gmail.com

M. Bielecka
Faculty of Geology, Geophysics and Environmental Protection, AGH University of Science and Technology, Cracow, Poland
e-mail: bielecka@agh.edu.pl

M. Włuka
Anew Institute sp. z o.o, Cracow, Poland
e-mail: mpwluka@gmail.com

F. Chaari et al. (eds.), *Advances in Condition Monitoring of Machinery in Non-Stationary Operations*, Applied Condition Monitoring 4,
DOI 10.1007/978-3-319-20463-5_20

Contents

1 Introduction 266
2 ART-2 Network as Unsupervised Classifier 267
3 Input Signals Normalization 268
4 Adaptation of a Stereographic Projection to ART-2 Network with Data Scaling 270
5 Results 271
6 Concluding Remarks 274
References 274

1 Introduction

A common technique used to decrease a cost of wind turbine maintenance is a remote monitoring [1]. Large development of monitoring and diagnostic technologies for wind turbines has taken place in recent years. The growing number of installed systems created the need for analysis of gigabytes of data created every day by these systems. Apart from the development of several advanced diagnostic methods for this type of machinery there is a need to prepare an early warning tool which would work continuously in real-time and focus the attention on potentially dangerous cases. There were several attempts to develop such tools, in most cases based on various classification methods [2, 3]. A research using the resonance neural networks (ART networks) made so far by the authors gave positive results [4–6]. Systems based on the ART-2 networks were able to perform a classification of operational states of a horizontal axis wind turbine. In his paper the idea of using the ART-2 network is applied to data from vertical axis wind turbines. Application of neural networks in this area of research is innovative. It is shown that operational data from vertical-type wind turbine differ significantly from the ones obtained from horizontal turbines [4, 5]. This makes the classification of machine operational states difficult. It was shown that the ART-2 network is not able to work effectively on this kind of vertical data due to the network architecture limits. Therefore, two new signal normalization procedures were introduced. They are based on the idea of a stereographic projection which can transform data to a form appropriate for the ART-2 network processing. The system, which were composed by using the aforementioned procedures, was implemented and tested. Results of simulations of a system operation were analyzed.

The paper is organized in the following way. In the next section the architecture and basic properties of ART neural networks are briefly recalled. The input signal normalization procedure is discussed in Sect. 3 whereas its implementation details in the context of the input data processing for the ART network is described in Sect. 4. The results are shown in Sect. 5 and discussion is presented in the last section.

2 ART-2 Network as Unsupervised Classifier

Let us recall briefly basic properties of ART-2 neural network—see [4, 7, 8] for details. The ART-2 is an unsupervised neural network based on adaptive resonance theory (ART). A typical ART-2 architecture, introduced by Carpenter and Grossberg [7, 9], is presented in Fig. 1 (only one unit of each type is shown here). In the attentional sub-system, an input pattern s is first presented to the F1 layer, which consists of six kinds of units—the W, X, U, V, P and Q cells. It then undergoes a process of activation, including normalization, noise suppression and updating. This results in an output pattern p from the F1 layer. Responding to this output pattern, an activation is produced across F2 layer through bottom-up weights b_{ij}. As the F2 layer is a competitive layer with a winner-takes-all mode, only one stored pattern is a winner. It also represents the best matching pattern for the input pattern at the F1 layer. Furthermore, the pattern of activation on the F2 layer brings about an output pattern that is sent back to the F1 layer via top–down weights t_{ji}. For the orienting sub-system, it contains a reset mechanism R and a vigilance parameter q to check for the similarity between the output pattern from the F2 layer and the original input pattern from the F1 layer. If both patterns are concordant, the neural network enters a resonant state where the adaptation of the stored pattern is performed. Otherwise, the neural network will assign an uncommitted (inhibitory)

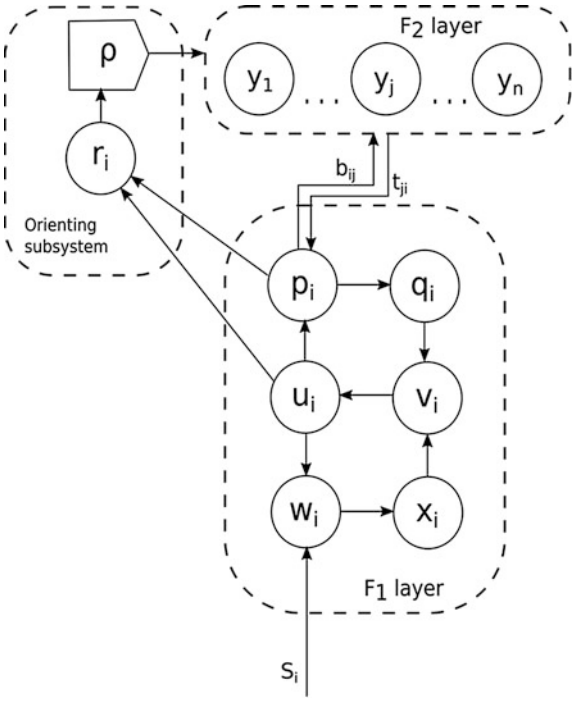

Fig. 1 ART-2 architecture

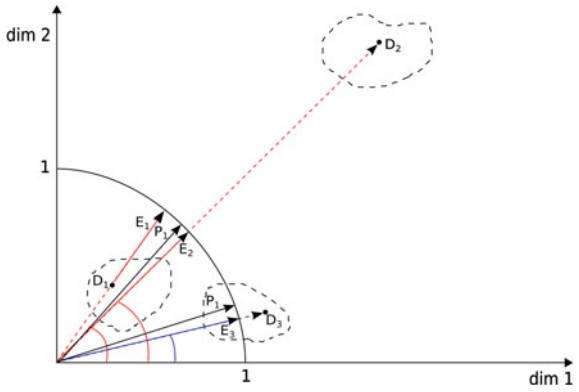

Fig. 2 The problem of clustering using ART-2 network. Data points D1, D2 and D3 are processed by ART-2 network as normalized vectors E1, E2 and E3. Vectors E1, E2 have similar angle distance then pattern P1, while E3 is close to P2. It means that the points D1 and D2 are classified as the same group which is differ then D3. Assuming Euclidean distance, the classification is incorrect—distance |D1D2| could be even several times greater than |D1D3| and D1 point is always classified as the same group as D2, but mostly differ then D3

node on the F2 layer for this input pattern, and thereafter, learn and transform it into a new stored pattern.

The ART-2 network had already been used by the authors to solve clustering problem in data from wind turbine monitoring [4–6]. It worked satisfactorily for available low-dimensional data from horizontal axis wind turbines, but encountered some barriers while clustering some new high dimensional data. The source and the specifics of mentioned barriers can be simply visualized in the case of two-dimensional data—see Fig. 2. When the network weights are interpreted as 2-d vector patterns, there is possibility that many input points, which can also be interpreted as vectors, are "similar" to one of network pattern even if the Euclidean distance between them is large. These difficulties are also observed for vertical axis wind turbines data and even if low-dimensional data, i.e. only operational states of turbines, were analyzed.

3 Input Signals Normalization

Let us describe the introduced normalization procedures. A normalization procedure corresponds to founding a mapping

$$F : R^n \supset A \ni X \rightarrow \tilde{x} \in R^k, \quad \text{where } \|\tilde{x}\| = 1$$

The most commonly used normalization is done according to the formula $\tilde{x} = \frac{x}{\|x\|}$. This formula defines the projection

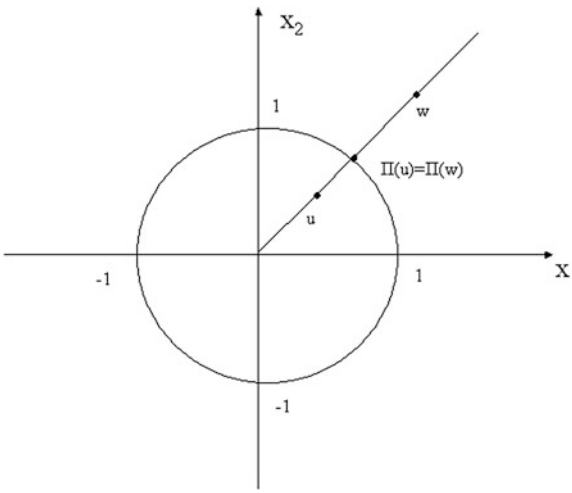

Fig. 3 Simple projection of R^2

$$\Pi : R^n \setminus \{0\} \rightarrow S^{n-1} \subset R^{\mathrm{n}},$$

Let us call it a simple projection, of $R^n \setminus \{0\}$ onto (n−1)-dimensional sphere S^{n-1}—see Fig. 3 for $n = 2$.

A simple projection, however, has crucial drawbacks. First of all data dimension is reduced. Secondly, the projection is not defined on the whole space—the mapping is undefined for 0. Furthermore, the space R^n that has an infinite measure is projected onto a sphere that has a finite measure. Additionally, the projection is not an injective mapping—if two points, say u and w, lie on the same radial line then $\Pi(u) = \Pi(w)$—see Fig. 3. This means that if two data clusters are situated along the same radial direction then, after normalization, they cannot be separated even they are well separated before normalization. Therefore, this method should be used only in such cases if it is a priori known that clusters in input signal space are situated in various radial directions. Therefore sometimes normalization which do not reduce the input signals space dimension is applied. The stereographic projection

$$S : R^n \rightarrow S^n \subset R^{n+1},$$

is an example of such a mapping. Geometric interpretation of the stereographic projection is visualized in Fig. 4 for the two-dimensional case. Stereographic projection is given explicitly by algebraic formulae for each natural n—see, for instance [10] p. 73. Let $P = (x_1, \ldots, x_{\mathrm{n}})$. Then $S(P) = \tilde{P} = (\tilde{x}_1, \ldots, \tilde{x}_{n+1})$ is given as

$$\tilde{x}_i = \frac{4x_i}{4 + s} \text{for } i = 1, \ldots, n$$

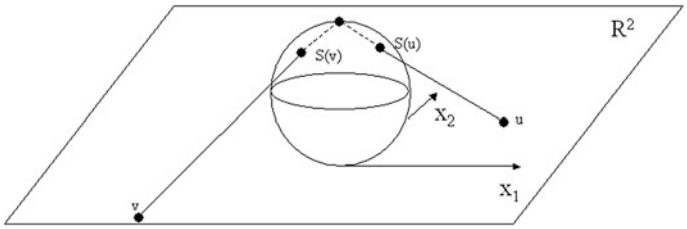

Fig. 4 Stereographic projection of R^2

$$\tilde{x}_{n+1} = \frac{s-4}{4+s}, \tag{1}$$

where $s := \sum_{i=1}^{n} x_i^2 \cdot$

As it has been aforementioned, the stereographic projection preserves the transformed space dimension and is defined on the whole R^n. Furthermore it is an injective mapping i.e. if $S(u) = S(v)$, then $u = v$. It transforms, however, a space which has infinite measure into space which has finite measure. This implied, among others, that points that are far from each other in R^n can be closed each to other on S^n. Therefore, two clusters which are well separated in R^n can be hardly separated after normalization. However such case can only take place if the clusters are far from the coordinate system origin—then they are transformed near to the north pole of the sphere. Since, in practice, norms of transformed vectors are limited, the minimal distance between clusters after signal normalization can be estimated.

4 Adaptation of a Stereographic Projection to ART-2 Network with Data Scaling

The described stereographic projection can be used as a normalization procedure of input data of neural networks that is able to process the full range of numbers from the set R. However, because the ART-2 networks are not able to recognize and store negative values, the input data should be additionally preprocessed just before the normalization. Use of a simple data in each dimension are scaled to a designated interval $[a, b]$ by the following formula:

$$V_i(k) := \frac{V_i(k) - \min(V(k))}{\max(V(k))}(b-a) + a \tag{2}$$

Optionally, before scaling, a following data transformation from $V^N \subset R^N$ to $\$V'^{2N} \subset R^{2N}$ is possible:

$$
\begin{aligned}
&\text{if } V_i(k) \geq 0 \text{ then} \\
&\quad V_i'(2k-1) := V_i(k) \\
&\quad V_i'(2k) := 0 \\
&\text{Else} \\
&\quad V_i'(2k-1) := 0 \\
&\quad V_i'(2k) := V_i(k)
\end{aligned}
$$

This kind of transformation increases a space's dimension twice, but allows to separate the negative values, what can save some additional information. Despite the data scaling to the interval $[a, b]$ such that the normalization defined by Eq. 1 presents the data in a positive part of a sphere, an interpretation of some of these data is opposite to the radial distance metrics. Patterns with values close to a are projected onto the equator so that their radial distances are large. In addition, if the value b is large then the patterns with large values, which, prior to the normalization are perpendicular to each other, after the normalization are not—radial distance between them can be small. Therefore, in addition to data scaling, the modification of classical stereographic normalization defined as Eq. 1 is needed to apply it to the ART-2 network. Such modification may be a reversal of the poles—of the projection's direction—Eq. 3. Vectors close to zero are then projected on a north pole. If the sphere has a radius equal to 1 and if the scaling range is, $\left[0, \frac{1}{\sqrt{2}}\right]$, then the largest values will be projected on the equator.

$$
\begin{aligned}
\tilde{x}_i &= \frac{2x_i}{1+s} \text{ for } i = 1, \ldots, n \\
\tilde{x}_{n+1} &= \frac{s+1}{s-1},
\end{aligned}
\tag{3}
$$

where $s := \sum_{i=1}^{n} x_i^2$

5 Results

The experiment was performed by using data from one of vertical axis of wind turbine prototypes. The data covering the period from 18.04.2014 till 24.04.2014 were recorded every 1 s by the online register system. The data set contained only the basic values that define the operational state of the turbine: wind speed, rotational speed of the rotor and the power generated by the turbine. They are related, but only to some extent and in fact they are all independent variables. The recorded data were not averaged. The data set included 500,000 measurements. In the experiment the results of classification, obtained by ART-2 network, were

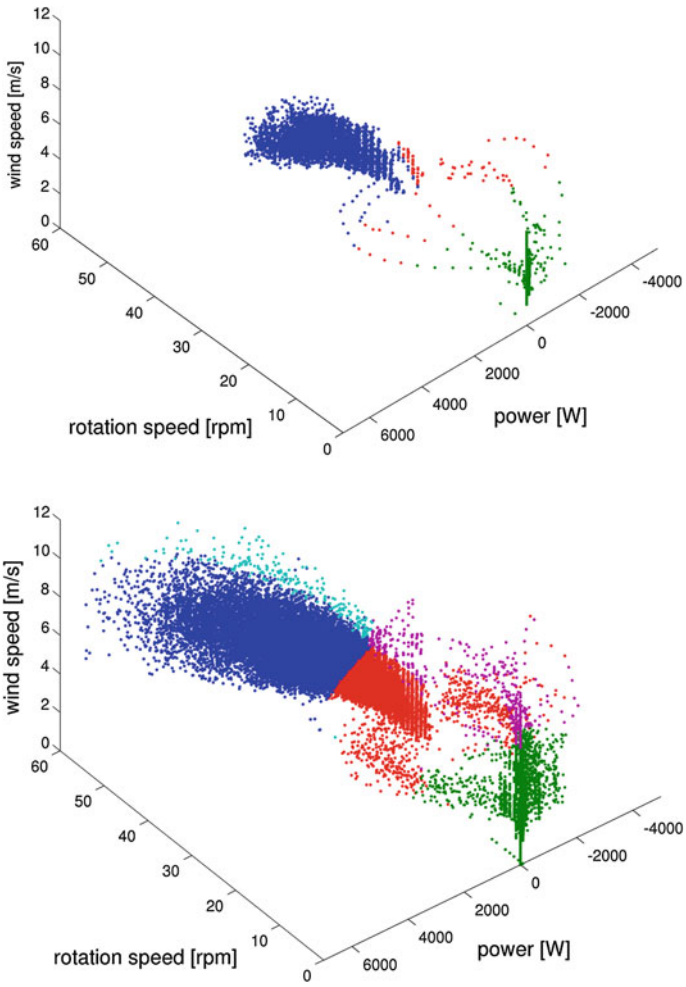

Fig. 5 Vertical axis wind turbine's operational states classification by the system of the ART-2 neural network and the stereographic projection normalization. The *upper plot* shows starting 10,000 data points of a full data set (500,000 points) placed in the *lower plot*

compared with the classification done by a human expert. Typically, the space of operation states of a wind turbine can be divided in a few distinct clusters: the stopped state, the idle load state, the low, the middle and the high generated power states. Very important advantage of the chosen data set is that it has only 3 variables and can be presented in a graphical way.

Thus, it can be easily visualized and a classification by a human expert can be done easily. The main idea of the research was to apply recorded data to the ART-2 network and to investigate what is its behavior i.e. how many states will be created in various time of processing. In all experiments the vigilance parameter ρ belongs

to the interval [0, 1]. The example of clustering performed by ART-2 network for vigilance parameter $\rho = 0.75$ with transforming input signals using stereographic projection including adaptation described in Sect. 4 is shown in Figs. 5 and 6 (projection on two dimensions—rotation speed and power). This example presents how the system of the ART-2 neural network processes data in a real-time scenario. Real-time processing was simulated by passing each data point to network only once, in a specified time order.

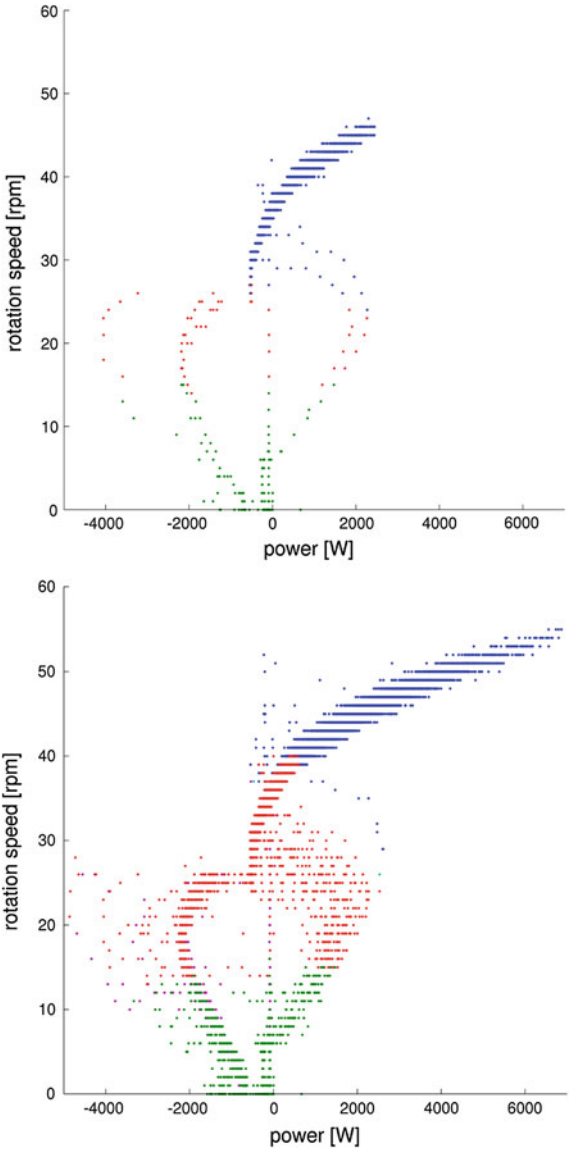

Fig. 6 2-D (rotation speed, power) projection of the classification presented in Fig. 5

6 Concluding Remarks

The presented results belong to a broader research activity, aimed at automatic monitoring of rotating machinery. We are interested in investigation of several approaches, which can be applied in the engineering practice [11–14]. The results described in this paper show that the ART-2 neural network is capable to classify typical states of a vertical axis wind turbine correctly. The ART-2 combined with the described preprocessing of input data has properly allocated classes corresponding to stopped state, idle load state, low and high generated power states. It turns out that the classification carried out by the used neural network and the one done by a human expert are much of a muchness.

Acknowledgments The paper was supported by the National Centre for Research and Development under grant no. WND-DEM-1-153/01

References

1. Hameeda Z, Honga YS, Choa TM, Ahnb SH, Son CK (2009) Condition monitoring and fault detection of wind turbines and related algorithms: a review. Renew Sustain Energy Rev 13:1–39
2. Shuhui L, Wunsch DC, O'Hair E, Giesselmann MG (2001) Comparative analysis of regression and artificial neural network models for wind turbine power curve estimation. J SolEnergy Eng 123:327–332
3. Kim YS (2010) Performance evaluation for classification methods: a comparative simulation study. Expert Syst Appl 37:2292–2306
4. Barszcz T, Bielecki A, Wójcik M (2010) ART-type artificial neural networks applications for classification of operational states in wind turbines. Lect Notes Artif Intell 6114:11–18
5. Barszcz T, Bielecki A, Wójcik M, Bielecka M (2013) "ART-2 artificial neural networks applications for classification of vibration signals and operational states of wind turbines for intelligent monitoring". Diagnostyka 14(4):21–26
6. Barszcz T, Bielecka M, Bielecki A, Wójcik M (2011) Wind turbines states classification by a fuzzy-ART neural network with a stereographic projection as a signal normalization. Lect Notes Comput Sci 6594:225–234
7. Carpenter GA, Grossberg S (1987) ART2: self-organization of stable category recognition codes for analog input pattern. Appl Opt 26:4919–4930
8. Shieh MD, Yan W, Chen CH (2008) Soliciting customer requirements for product redesign based on picture sorts and ART2 neural network. Expert Syst Appl 34:194–204
9. Carpenter GA, Grossberg S (1987) A massively parallel architecture for a self-organizing neural pattern recognition machine. Comput Vis Graph Image Process 37:54–115
10. Gancarzewicz J (1987) Differential geometry. PWN, Warszawa (in Polish)
11. Barszcz T, Bielecki A, Wójcik M (2013) Vibration signals processing by cellular automata for wind turbines intelligent monitoring. Diagnostyka 14(2):31–36
12. Barszcz T, Bielecka M, Bielecki A, Wójcik M (2012) Wind speed modelling using Weierstrass function fitted by a genetic algorithm. J Wind Eng Ind Aerodyn 109:68–78

13. Bielecki A, Barszcz T, Wójcik M (2014) Modelling of a chaotic load of wind turbines drivetrain. Mech Syst Signal Process. ISSN 0888-3270, http://dx.doi.org/10.1016/j.ymssp.2014.05.035
14. Bielecki A, Barszcz T, Wójcik M, Bielecka M (2014) Hybrid system of ART and RBF neural networks for classification of vibration signals and operational states of wind turbines. Lect Notes Comput Sci 8467:3–11

Electric Motor Bearing Diagnosis Based on Vibration Signal Analysis and Artificial Neural Networks Optimized by the Genetic Algorithm

Fenineche Hocine and Felkaoui Ahmed

Abstract The artificial neural networks (ANN) by their capacities of training, classification, and decision, give a solution to bearing diagnosis problem by the automatic classification of the vibratory signals corresponding to the various states the machines. They are intended to increase the precision(accuracy) and to reduce errors caused by subjective human judgments. However it is important to note that the ANNs in the aids to diagnosis must be set for optimum performance. The non-existence of predefined rules for ANNs parameters setting (number of hidden neurons in each hidden layers etc…) obstruct the achievement of optimal performances. The use of genetic algorithm (GA) can solve this problem by the parameters and structure optimization of ANN. This paper discusses the use of the ANN multilayer Perceptron (MLP), for the diagnosis of electric motor bearings, by the automatic classification of the various operating conditions the machine .The signals taken from the experimental test rig are processed by using various methods of signal processing. The calculated indicators were used to build the patterns vector, which is used for the following to train and test of the network. The GA are used to search(optimize) the structure and the various parameters of the network, which simplifies the neural network structure and makes the training process more efficient and giving the best performances of the network.

Keywords Diagnosis · Bearing defects · Vibration analysis · Artificial neural networks · Genetic algorithms

F. Hocine (✉)
Department of Mechanical Engineering, University of Jijel, Jijel 18000, Algeria
e-mail: fenihocine@yahoo.fr

F. Ahmed (✉)
Institute of Optics and Precision Mechanics, Setif-1 University, Setif 19000, Algeria
e-mail: a_felkaoui@yahoo.fr

F. Hocine · F. Ahmed
Laboratory of Applied Precision Mechanics (LMPA), Institute of Optics and Precision Mechanics, Setif-1 University, Setif 19000, Algeria

F. Chaari et al. (eds.), *Advances in Condition Monitoring of Machinery in Non-Stationary Operations*, Applied Condition Monitoring 4,
DOI 10.1007/978-3-319-20463-5_21

Contents

1 Introduction 278
2 Background 279
2.1 Rolling Element Bearings 279
2.2 Bearing Fault Diagnosis Techniques 280
2.3 MultiLayer Perceptron (MLP) 280
2.4 Genetic Algorithms (GA) 281
2.5 Artificial Neural Networks Optimized by the Genetic Algorithm 281
3 Materials and Methods 281
3.1 Data Acquisition 282
3.2 Fault Diagnosis Scheme 283
4 Results and Discussion 283
4.1 Preprocessing of Vibration Signals 283
4.2 Constitution of the Patterns Vector (Networks Input) 285
4.3 Choice of the Classes (Networks Output) 285
4.4 Data Normalization 286
4.5 The Neural Network Configuration 286
4.6 The Genetic Algorithms 287
4.7 Results 287
5 Conclusion 288
References 288

1 Introduction

Rolling element bearings are widely used elements in electric motors. Their failure is one of the most frequent reasons for electric motor breakdown. In order to enhance motor's reliability and reduce maintenance cost, bearing condition monitoring becomes an important measure to ensure machine safety [1].

Considerable research has been carried out previously to develop various algorithms and methods for bearing fault detection and diagnosis [2–6].

Nowadays, Artificial Neural Network (ANN) are proving their effectiveness in several research areas especially for classification problems in many different environments, including business, science and engineering. The ANN is an information processing paradigm inspired by biological nervous systems [7]. The human learning process maybe partially automated with ANN's. It can be configured for a specific application, such as pattern recognition or data classification, through a learning process. As the neural network theory is still in progress, there is not a set of ways to guide the design process. Now, the design of neural network and finding the optimal parameters in order to maximize the performance of ANN is one of the major challenges in the uses of ANN [8].

2 Background

2.1 Rolling Element Bearings

The main components of rolling bearings are: the inner ring; the outer ring, the rolling elements and the cage (Fig. 1). Typically, the inner ring of the bearing is mounted on a rotating shaft, and the outer ring is mounted to a stationary housing. Commonly rolling elements are balls or rollers. The roller elements transfer the load over a very small surface (ideally, point contact) on the raceways [9].

Local or wear defects cause periodic impulses in vibration signals. Amplitude and periodic of these impulses are related to the shaft rotational speed and fault location. The formula for the various defect frequencies is given by:

Ball pass frequency, outer race:

$$\mathrm{BPFO} = \frac{n\mathrm{fr}}{2}\left(1 - \frac{d}{D}\cos(\alpha)\right) \tag{1}$$

Ball pass frequency, inner race:

$$\mathrm{BPFI} = \frac{n\mathrm{fr}}{2}\left(1 + \frac{d}{D}\cos(\alpha)\right) \tag{2}$$

Fundamental train frequency (cage speed):

$$\mathrm{FTF} = \frac{\mathrm{fr}}{2}\left(1 - \frac{d}{D}\cos(\alpha)\right) \tag{3}$$

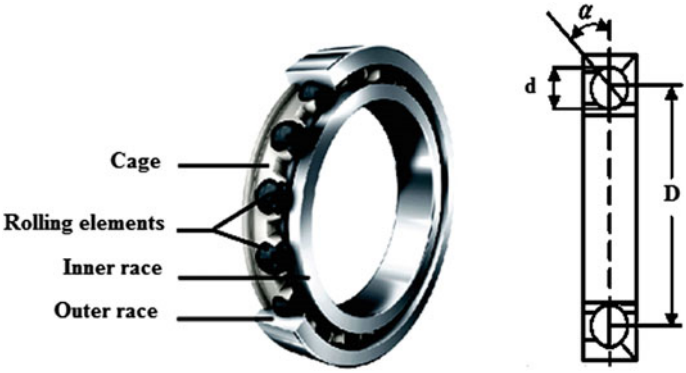

Fig. 1 Components of the bearing

Ball (roller) spins frequency:

$$\mathrm{BSF} = \frac{D}{2d}\left(1 - \frac{d}{D}\cos(\alpha)^2\right) \tag{4}$$

where *fr* is the shaft speed, *n* is the number of rolling elements, and α is the angle of the load from the radial plane. Note that the ball spin frequency (BSF) is the frequency with which the fault strikes the same race (inner or outer).

2.2 Bearing Fault Diagnosis Techniques

A wide variety of techniques, were developed for the detection and diagnosis of faults in rolling element bearings. They have been introduced to inspect raw vibration signals. These algorithms can be classified into time domain, frequency domain, time- frequency domain, higher order spectral analysis, and model based techniques [10, 11].

2.3 MultiLayer Perceptron (MLP)

The multilayer Perceptron (MLP) is the simplest and most known type of neural networks. Its structure, showed by Fig. 2, is relatively simple: an input layer, an output layer and one or more hidden layers. Each neuron is connected fully to the neurons of its preceding and the following layers [12].

MLP is one of the most successful feed-forward neural networks for diagnosis. A review of some works on fault diagnosis vibration based on ANN has been presented in [13].

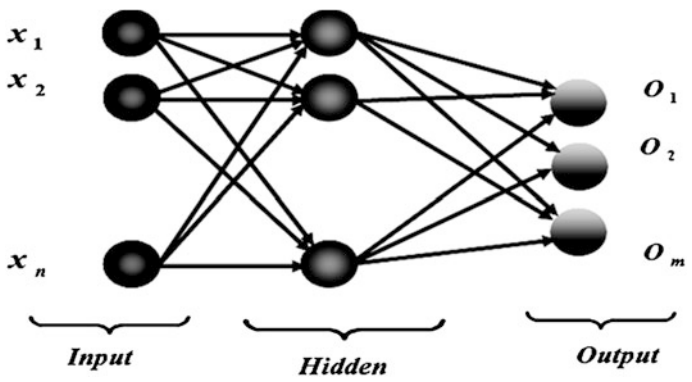

Fig. 2 Multi-layer perceptron

The challenges for constructing a MLP network are: the determination of a sufficient number of hidden layers; neurons within each layer; learning rate; the activation function, and the connections initial weights. These parameters have a great impact on the learning methods convergence. Although a formal methodology to express the number of hidden neurons does not been developed yet. Many studies on this subject were launched [14–20]. However, as a known fact more neurons and layers in the network result a longer training period and convergence problems.

2.4 Genetic Algorithms (GA)

The Genetic Algorithm (GA) has been introduced by J. HOLLAND to solve a large number of complex optimization problems. Each solution represents an individual coded in one or several chromosomes. These chromosomes represent the problem's variables. First, an initial population composed by a fixed number of individuals is generated; then, an operator of reproduction is applied on a number of individuals selected according to their fitness score. This procedure is repeated until the maximum number of iterations is reached. GA has been applied in a large number of optimization problems in several domains, telecommunication, routing, scheduling, and it proves its efficiency to obtain a good solution [21].

2.5 Artificial Neural Networks Optimized by the Genetic Algorithm

However it is important to note that the ANNs parameters (number of hidden neurons in each layer, number of hidden layers etc.) (Fig. 3), in the aids to diagnosis must be set for optimum performance.

These parameters are often chosen empirically seeking desired results, which makes the use of this method very difficult. In this work GA are proposed for the optimization and the search of the best(optimal)structure and parameters of ANN.

3 Materials and Methods

In this research work, the procedure of diagnosis consists of two stages, namely preprocessing using some signal processing methods for feature extraction, and the design of the appropriate neural network.

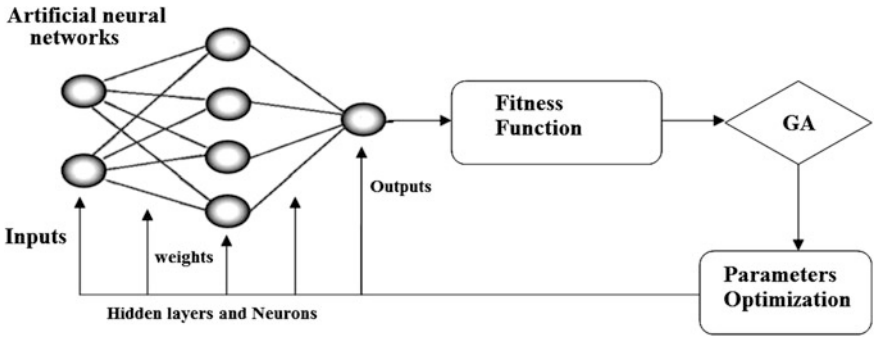

Fig. 3 Scheme of optimization of ANN by GA

3.1 Data Acquisition

The experimented data base was extracted from the test rig shown in Fig. 4.

The web site provides access to ball bearing test data for normal and faulty bearings [23]. Experiments were conducted using a 2HP Reliance Electric motor, and acceleration data was measured at locations near to and remote from the motor bearings. These web pages are unique in that the actual test conditions of the motor as well as the bearing fault status have been carefully documented for each experiment Motor bearings were seeded with faults using electro-discharge machining (EDM). Faults ranging from 0.17 mm in diameter to 0.71 mm in

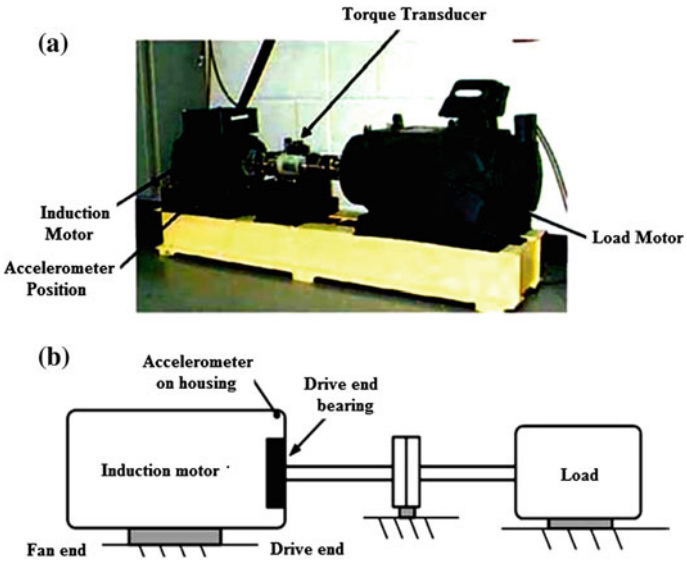

Fig. 4 **a** The bearing test rig. **b** The schematic description of the test rig. [22]

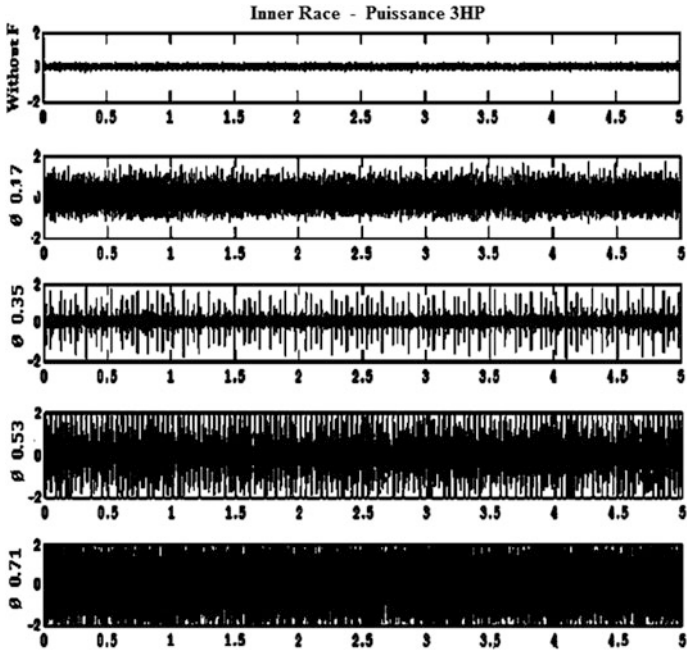

Fig. 5 The time domain signal

diameter were introduced separately at the inner raceway, rolling element (i.e. ball) and outer raceway. Faulted bearings were reinstalled into the test motor vibration data was recorded for motor loads of 0–3 horsepower (motor speeds of 1797–1720 RPM).Vibration data was collected using accelerometers, attached to the housing with magnetic bases. Accelerometers were placed at the 12 o'clock position at both the drive end and fan end of the motor housing. The time domain presentation of signal is shown in Fig. 5.

3.2 Fault Diagnosis Scheme

The flow chart of the Bearing fault diagnosis based on ANN is shown as Fig. 6.

4 Results and Discussion

4.1 Preprocessing of Vibration Signals

A signal conditioning step is required to remove useless information, and facilitate the task of indicators extraction from each signal the some of the most commonly

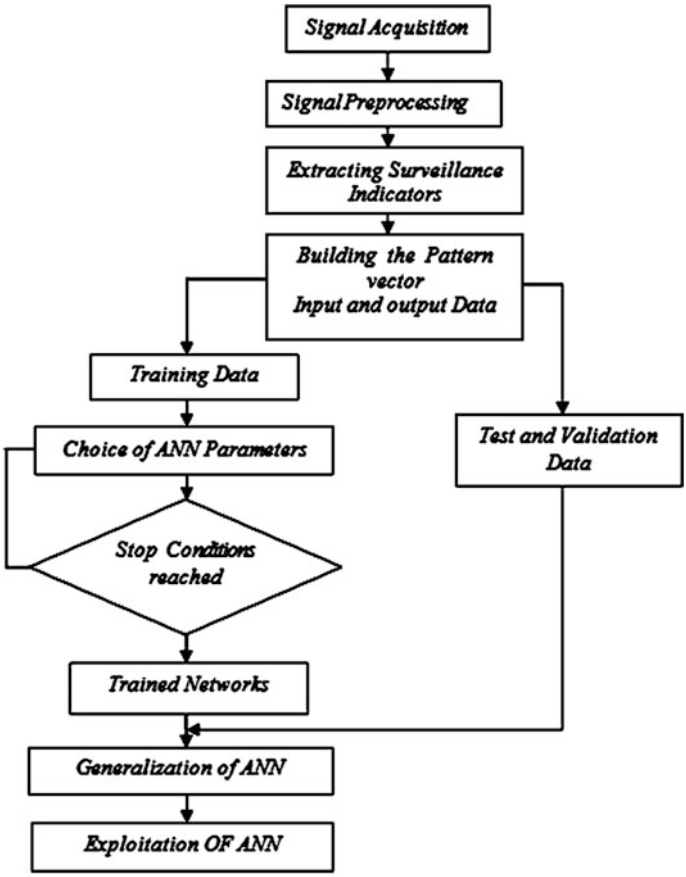

Fig. 6 Bearing fault diagnosis scheme

used indicators for bearing monitoring were extracted [24–27], namely: the RMS value, crest factor, peak to peak value, kurtosis, and the energy from the spectrum envelope.

After a preliminary analysis [28], we chose to calculate these indicators as follows:

Time domain indicators Each signal was pass band filtered in four adjacent 1.5 kHz band: [1–1500 Hz], [1500–3000 Hz], [3000–4500 HZ], [4500–6000 Hz] and [1–6000 Hz]. From each filtered signal were extracted: RMS, Crest factor, Crest-Crest Value and Kurtosis. Figure 7 presents the variation of time domain indicators.

Frequency domain indicators The frequencies domain indicators are calculated from the spectrum envelope in five frequency bands: [1–1000 Hz], [1000–2000 Hz], [2000–3000 Hz], [3000–4000 Hz], [4000–5000 Hz] and [1000–6000 Hz]. The variation of Frequency domain indicators are shown as Fig. 8.

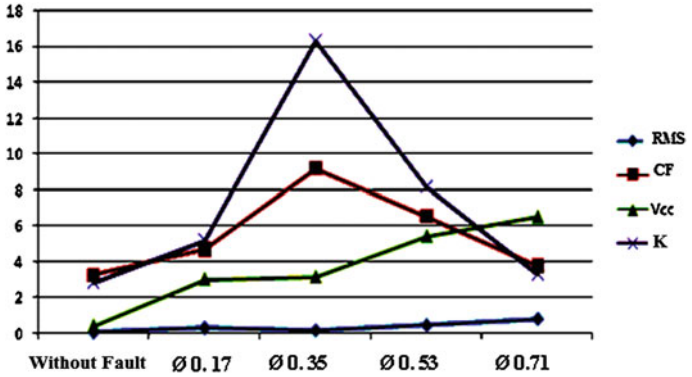

Fig. 7 Variation of time domain indicators

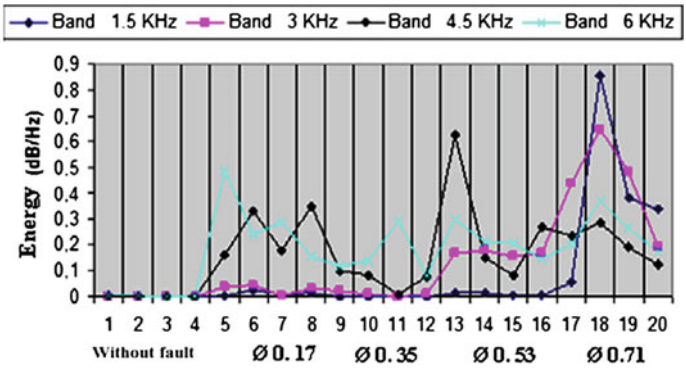

Fig. 8 Variation of frequency domain indicators

4.2 Constitution of the Patterns Vector (Networks Input)

The patterns vector is consisted of the described above time and frequency domain indicators. The data that have been be treated, categorized, and stored in an observations/variables array.

4.3 Choice of the Classes (Networks Output)

The networks output vector contains the various classes corresponding to each operating conditions from the experimental test rig. five classes fixed, each one of them corresponds to a defect diameter. Table 1 represents the labeling of the various studied classes.

Table 1 Labeling of the classes(Inputs)

Classes	Fault diameter	Labels
1	Without fault	10000
2	0.17 mm	01000
3	0.35 mm	00100
4	0.53 mm	00010
5	0.71 mm	00001

4.4 Data Normalization

To improve the performance of the MLP, normalization of patterns vector data was done. The obtained database was divided in three parts: training set, test and validation set. the used normalization formula is given below,

$$x_{ij} = \frac{x_{ij} - m_j}{\sigma_j} \tag{5}$$

where
σ_j is the standard deviation (SD) of du jth parameter
m_j Is the average

4.5 The Neural Network Configuration

The employed MLP was configured as follow (Table 2) [29, 30].

Table 2 Neural network configuration

Parameters	Value/type	Comment
Total set	140	–
Input	26	Monitoring indicators
Hidden layer	1	–
Output	5	Classes
Transfer function	tansig	Hidden layer
Transfer function	Purelin	Output layer
Learning algorithm	Backpropagation	–
Performance	Mse	Mean square error

4.6 The Genetic Algorithms

GA have been used in different ways in optimizing ANN; of the most common seeks the optimization the elements of the pattern vector (training data and test data) [31–33].

In our papers, GAs were applied to optimize the number of neurons in the hidden layer MLP. In this purpose, we created a fitness function whose formula is as follows [34].

$$F = C - (E \times H)/Hmax \tag{6}$$

C is a constant
E is the minimum error(performance)
H is the number of neurons in the hidden layer
Hmax is the maximum value of the neurons in the hidden layer

4.7 Results

The number of hidden neurons in the hidden layer range from 1 to 20, in order to obtain the optimal value that gives the best performance of classification.

So, for the GA we use the following parameters:

- 15 populations
- mutation rate 0.05
- crossover rate 0.9
- binary coding

Figure 9 shows that the value of the objective function is minimal for a number of hidden neuron equal 2.

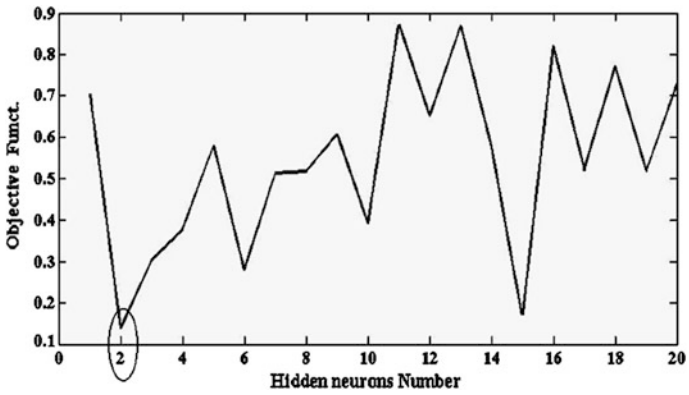

Fig. 9 Optimal hidden neurons number

So we can conclude that the number of neuron in the hidden layer that gives us the best performance is 2 neurons.

5 Conclusion

The present article describes the use of ANN to automate the electric motor bearing diagnosis, based on vibration signal analysis. Initially, the vibration signals collected from the test bench (Bearing Data Center) are preprocessed, to extract the monitoring indicators most appropriate to the health of the experimental device. Then we built the database used to training and testing the MLP. Various possible kinds of faults (five diameters) have been taken into consideration into this work. However, the ANN performance depending on the size of the training data set, the size of the ANN (the number of hidden layers and number of neurons per hidden layer). In order to finding the optimal value of the number of hidden neurons, we use the GA. That allow us to obtain the value that give us the best performance of ANN. We have stressed, that the efficiency of the optimization depends of the choice the GA parameters.

Acknowledgment The authors would like to thank Kenneth A. Loparo, from Bearing Data Center, Case Western Reserve University, Cleveland, for his experimental data provided.

References

1. Randall RB, Antoni J (2011) Rolling element bearing diagnostics—a tutorial. Mech Syst Signal Proc 25(2):485–520
2. Howard I (1994) A review of rolling element bearing vibration: detection, diagnosis and prognosis. DSTO-AMRL report, DSTO-RR-00113, pp 35–41
3. McInerny SA, Dai Y (2003) Basic vibration signal processing for bearing fault detection. IEEE Trans Educ 46(1):149–156
4. Sawalhi N (2007) Diagnostics, prognostics and fault simulation for rolling element bearings. Ph. D. thesis, School of Mechanical and Manufacturing Engineering, University of New South Wales, Australia
5. Nataraj C, Kappaganthu K (2011) Vibration-based diagnostics of rolling element bearings: state of the art and challenges. In: 13th world congress in mechanism and machine science, Guanajuato 19–25 June 2011
6. Kankar PK et al (2011) Fault diagnosis of ball bearings using machine learning methods. Expert Syst Appl 38:1876–1886
7. Haykin S (2001) Neural Networks—a comprehensive foundation, 2nd edn. Pearson Prentice Hall, India, p 823
8. Egriogglu E, Aladag CH, Gunay S (2008) A new model selection strategy in artificial neural networks. Appl Math Comput 195:591–597
9. McFadden PD, Smith JD (1985) The vibration produced by multiple point defects in a rolling element bearing. J Sound Vib 96(1):69–82
10. Khan AF (1991) Condition monitoring of rolling element bearings: a comparative study of vibration based techniques. PhD Dissertation, University of Nottingham
11. Chen P (2000) Bearing condition monitoring and fault diagnosis. Master of science thesis, The University of Calgary, Canada

12. Bishop CM (1995) Neural networks for pattern recognition. Oxford University Press, Oxford
13. Rao BKN et al (2012) Failure diagnosis and prognosis of rolling—element bearings using artificial neural networks: a critical overview. In: 25th international congress on condition monitoring and diagnostic engineering. Journal of physics: conference series vol 364
14. Miller GF, Todd PM, Hedge SU (1989) Designing neural networks using genetic algorithms. Proceedings of the 3rd international conference on genetic algorithms, Morgan Kaufmann, San Mateo
15. Onoda T (1995) Neural network information criterion for the optimal number of hidden units. In: Proceedings of the 1995 IEEE international conference on neural networks, vol 1
16. Ioan I, Corina R, Arpad I (2004) The optimization of feed forward neural networks structure using genetic algorithms. In: Proceedings of the international conference on theory and applications of mathematics and informatics—ICTAMI, Greece
17. Curry B, Morgan PH (2006) Model selection in neural networks: some difficulties. Eur J Oper Res 170(2):567–577
18. Liu Y, Starzyk JA, Zhu Z (2007) Optimizing number of hidden neurons in neural networks. In: Proceedings of the IASTED international conference on artificial intelligence and applications (AIA '07), pp 121–126
19. Shibata K, Ikeda Y (2009) Effect of number of hidden neurons on learning in large-scale layered neural networks. In: Proceedings of the ICROS-SICE international joint conference 2009 (ICCASSICE '09), pp 5008–5013
20. Sheela KG, Deepa SN (2013) Review on methods to fix number of hidden neurons in neural networks. Math Probl Eng Article ID: 425740, 11 pages, http://dx.doi.org/10.1155/2013/425740
21. Sivanandam SN, Deepa SN (2008) Introduction to genetic algorithms. Springer, Berlin
22. Huang Y, Liu C, Zha XF, Li Y (2010) A lean model for performance assessment of machinery using second generation wavelet packet transform and Fisher criterion. Expert Syst Appl 37:3815–3822
23. Case Western Reserve University, bearing data center (2006) http://www.eecs.cwru.edu/laboratory/bearing/download.htm
24. Alfredson RJ, Mathew J (1985) Time domain methods for monitoring the condition of rolling element bearings. Inst Eng Aust Mech Eng Trans 10:102–107
25. Claire B (2002) Éléments de maintenance préventive de machines tournantes dans le cas de défauts combinés d'engrenage et de roulements. INSA Lyon thesis
26. Chen P (2000) Bearing condition monitoring and fault diagnosis. Master of science thesis, The University of Calgary, Canada
27. SUN Q, XI F, Krishnappa G (1998) Signature analysis of rolling element defects. In: Proceeding of CSME forum, Toronto pp 423–429
28. Fedala S (2005) Le diagnostic vibratoire automatisé: comparaison des méthodes d'extraction et de sélection du vecteur forme. Magister thesis, University of Setif
29. Badri B, Thomas M, Sassi S, Lakis A (2007) Combination of bearing defect simulator and artifical neurl network of the diagnosis of damaged bearings. In: Proceedings of the 20th international congress on condition monitoring and diagnostic engineering management (COMADEM07), Faro, pp 175–185
30. Fenineche H (2008) Application des réseaux de neurones artificiels au diagnostic des défauts des machines tournantes. Magister Thesis. University of Setif
31. Li B, Chow MY, Tipsuwan Y, Hung JC (2000) Neural-network based motor rolling bearing fault diagnosis. IEEE Trans Industr Electron 47(51):1060–1067
32. Samanta B et al (2004) Bearing fault detection using artificial neural networks and genetic algorithm. EURASIP J Appl Signal Process 3:366–377
33. Jack LB, Nandi AK (2000) Genetic algorithm for feature extraction in machine condition monitoring with vibration signals. IEE Proc Vis Image Signal Process 147:205–212
34. Shifei D et al (2011) Studies on optimization algorithms for some artificial neural networks based on genetic algorithm(GA). J Comput—Mai

Gear Fault Diagnosis Based on Angular Measurements and Support Vector Machines in Normal and Nonstationary Conditions

Semchedine Fedala, Didier Rémond, Rabah Zegadi and Ahmed Felkaoui

Abstract Contrary to time-sampled acceleration signals (TA), angular measurements like instantaneous angular speed (IAS), transmission error (TE), and angular sampled acceleration (AA) represent all potential sources of relevant information in fault detection and diagnosis systems, but also to construct feature vector (FV) to make the methods of classification robust and effective even for different running speed or load conditions. In this work, we propose to use angular measurements and support vector machines (SVM) to detect and diagnose gear faults in normal and nonstationary conditions. For this purpose, features are extracted from angular and angle frequency domains of AA, TE, and IAS. Then, the classification is performed by SVM in order to improve the detection and identification of gear defects.

Keywords Fault diagnosis Gearbox · Angular measurements · Nonstationary conditions · Multiclass support vector machines

Contents

1 Introduction 292
2 Measuring Principle 293
3 Test Bed and Experimental Protocol 295

S. Fedala (✉) · R. Zegadi · A. Felkaoui
Applied Precision Mechanics Laboratory, Institute of Optics and Precision Mechanics, Sétif 1 University, Setif, Algeria
e-mail: semchedinef@yahoo.fr

R. Zegadi
e-mail: rzegadi@yahoo.fr

A. Felkaoui
e-mail: a_felkaoui@yahoo.fr

D. Rémond
LaMCoS UMR5259, CNRS, INSA-Lyon, University of Lyon, Lyon, France
e-mail: didier.remond@insa-lyon.fr

F. Chaari et al. (eds.), *Advances in Condition Monitoring of Machinery in Non-Stationary Operations*, Applied Condition Monitoring 4,
DOI 10.1007/978-3-319-20463-5_22

4 Experimental Part 297
4.1 Feature Extraction 297
4.2 Feature Vectors (FVs) 301
4.3 Classification Procedure 302
5 Classification Results and Discussions 304
6 Conclusion 306
References 307

1 Introduction

Condition monitoring of rotating machines is one of the areas of engineering that is gaining importance in industry. Its role is to ensure the continuity of operation of mechanical systems in factories, in order to limit production losses due to unexpected failures [1, 2]. This monitoring can be automated by implementing classification methods [3]. The performances of these methods are closely related to the relevance of fault indicators from response signals making up the feature vectors (FV) of these classification methods. The FV must be able to describe the different operation modes or system damage, and also reflect the precise definition of the classes that represent the different operation modes [4]. Generally, the indicators are based on analysis of signals provided by the sensors installed on the monitored system (accelerations, speeds, torques, currents, voltage, etc.) and must be also constructed automatically to ensure the most robust analysis (independent of speed and load variations). Current research on the automation of vibration diagnosis is mainly based on indicators extracted from the time-sampled acceleration signals (TA) [3, 4]. The major drawback of these signals is their sensitivity to operating speed conditions, particularly in nonstationary conditions. Therefore, there is a variation in the number of samples acquired by revolution but also changes in excitation frequencies related to the discrete geometry in rotation. In this context, it is difficult (or impossible in nonstationary conditions) to identify a characteristic frequency in the spectrum in an automated manner. One alternative is to have angularly sampled signals, which ensures a constant integer number of samples per revolution and by getting rid of speed fluctuations. Furthermore, the assessment of the interest frequency component level may be biased by the phenomenon of "picket fence effect" [5]. However, several possible solutions are proposed to obtain sampled angularly signals [6, 7]:

- Direct angular sampling, where the signal from encoder mounted on a shaft of the rotating machine is directly used to realize the angular sampling. This signal is used as an external clock for the data acquisition card. Each rising edge triggers the acquisition of the sample and the accelerometer signal conversion or any other analog signal. This technique remains costly and constraining on the experimental point of view (need of a DAQ and acquisition environment with this feature).

- The angular resampling, unlike the previous method, does not require to invest in an expensive instrumentation. It involves sampling the accelerometer and the encoder signals separately by conventional acquisition in time domain, usually at high frequency. Then it is sufficient to determine the instants corresponding to each angle position by interpolation, time locations where the acceleration signal is resampled by software interpolation. This method is limited in frequency.

Both solutions can advantageously be supplemented by an intermediate technique called counting which enables us to determine the time of appearance of the edges in signal delivered by the encoder(s) with a better precision.

Knowledge of the occurrence instants of angular events from one or more angular sensors also opens other perspectives since it allows access to new characteristic quantities of the operation of the rotating machine. The knowledge of these moments of angular sampling is indeed very interesting because

- It offers the possibility to calculate several other signals, in particular the transmission error (TE) [5] and instantaneous angular speed (IAS) [8–10]
- It allows to get a large number and a variety of indicators if one wants to build a FV to automate the diagnosis from these signals.

In this paper, several angular sampling signatures (AA, TE, and IAS) are determined to monitor different operating modes. For this purpose, features are extracted from angular and angle frequency domains. Then, the classification is performed by multiclass support vector machines (SVM) for the improvement of the detection and identification of gear defects. The methodology is applied in healthy conditions, then for five pinion faults with different running speed and load conditions. The experimental results prove the efficiency of angular indicators by increasing performance of the classification.

The first part of the paper provides an overview of existing angular techniques and measuring principle. Then, the description of the experimental device as well as the various test conditions are described. Afterwards, we present the analysis of the characteristics of the measured variables and the different indicators introduced as a FV. Finally, we compare the performances of the SVM classification for these different FVs in order to show the advantages of the proposed approach.

2 Measuring Principle

The use of high-resolution optical encoders, i.e., having a large number of pulses per revolution, offers the possibility to measure the angular displacement, and by consequence the TE as angular phase difference between the different shafts forming a gearbox. The principle of this measurement is based on counting the number of pulses supplied by a very high frequency clock between two rising edges of the signals from the two optical encoders. This count should be carried out simultaneously on both channels and with the same time reference, that is to say the

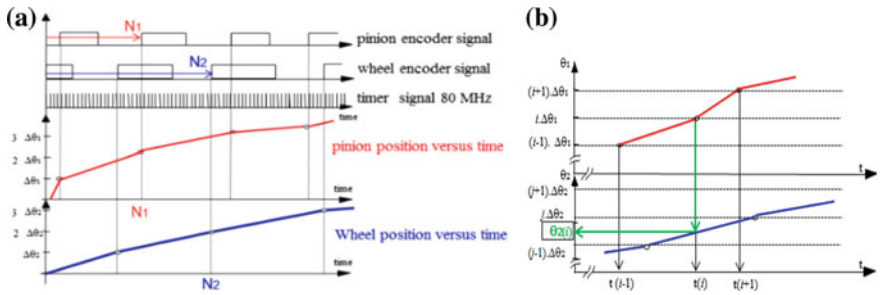

Fig. 1 Principle of angular measurement. **a** Building of angular position laws for the pinion and the wheel. **b** Angular method of reconstitution of the transmission error

same clock and the same counter. These allow us to get a solid time reference for each channel encoder and to measure the simultaneous difference between them [5]. Then it is possible to reconstruct the history of the angular positions of the encoders according to time or angular references and with a sampling given by the number of lines on each encoder Fig. 1a.

The reconstruction of TE signal occurs, for example, each time a new edge appears on encoder #1. It will thus be sampled at a constant angular spacing depending on the position of the shaft #1 and will be an estimate of the TE angularly sampled in reference to the shaft carrying encoder #1. To determine the value of the position of the shaft #2, it needs only to interpolate the position of the second shaft at the instant of appearance of the forehead on channel #1 Fig. 1b.

Expression of TE will be rebuilt taking into account the gear ratio numerically, at the instants corresponding to events of encoder 1, and may be written as follows [5]:

$$\Delta\theta_{a1}(i) = \theta_1(i) - \frac{Z_2}{Z_1}\theta_2(i) = i\Delta\theta_1 - \frac{Z_2}{Z_1}\theta_2(i) \tag{1}$$

with

Z_1 the number of teeth of the pinion,
Z_2 the number of teeth of the toothed wheel,
θ_1 the angular position of the pinion,
θ_2 the angular position of the toothed wheel.

Each encoder can also determine a variable with information on the presence of defects which is changes in IAS [8]. The clock counter counts the number of rising edges between two pulses Fig. 1a. The reconstruction of the IAS signal is directly calculated by the following formula [9]:

$$\omega_i = \frac{2\pi}{N_f}\frac{60\,f_h}{N_i}\,(\text{rd/min}) \tag{2}$$

with

N_i number of pulses of the clock at the frequency $f_h(\text{Hz})$ between two rising edges in the encoder signal,

N_f resolution of the encoder.

The resampling of the angular acceleration signal is performed by interpolating the acceleration signal at the instants corresponding to each angular position of the encoder and will be the signal called Angular sampled Acceleration (AA) [5].

As an example of construction of indicators and of automation of their extraction, the power spectral density is a very useful tool for the diagnosis of faults in rotating machinery. If one wants to get an accurate resolution in a spectral representation, it requires a high number of samples and thus a long recording time [1]. However, we know that the rotation speed varies continuously. Consequently, the peak that we hope observe will become inevitably a wide frequency band as the occurrence events frequency representing defects is proportional to the rotational speed in the case of a rotating discrete geometry. Therefore, the major risk is to stock information on bands superimposed on each other. The use of the Fourier transform on an angularly sampled rather than time-sampled signal overcomes the rotating speed variations and allows to consider directly the characteristic frequencies of the different signals. For instance, the frequencies of observation of the gears are no more changed by the rotational speed of the machine, but are directly observable peaks corresponding to the number of gear teeth [5]. Thus, the frequency channel of interest for the gear will be directly identified from the kinematics of the machine and the acquisition parameters (resolution of optical encoder and length of acquisition).

3 Test Bed and Experimental Protocol

The test bed Fig. 3 used in this study consists of two rotating shafts, on which are mounted a pinion and a spur gear offering a gear ratio of 25/56. To compare the effectiveness of methods of analysis, we used six pinions with different fault states. The first one is referred as Good (G), whereas the others have several different types of defects: a Root Crack (RC), a Chipped Tooth in Width (CTW), a Chipped Tooth in Length (CTL), a Missing Tooth (MT), and General Surface Wear (GSW) as shown in Fig. 2. Three pinions are simultaneously mounted on the input shaft of the gearbox, the engagement change is done by a simple axial movement of the wheel on its axis Fig. 3b.

The input shaft is driven by an electric DC motor controlled in rotational speed. The engine ensures a maximum speed of 3600 rpm. The output shaft is connected to a magnetic powder brake capable of generating different resistive torques. To record vibration signals, two accelerometers (sensitivity: 100 mV/g) are mounted radially, one vertically and the other horizontally on the outer surface of the bearing

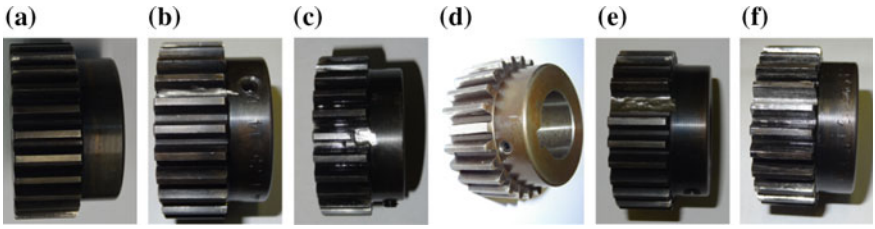

Fig. 2 View of six used pinions. **a** G. **b** RC. **c** CTW. **d** CTL. **e** MT. **f** GSW

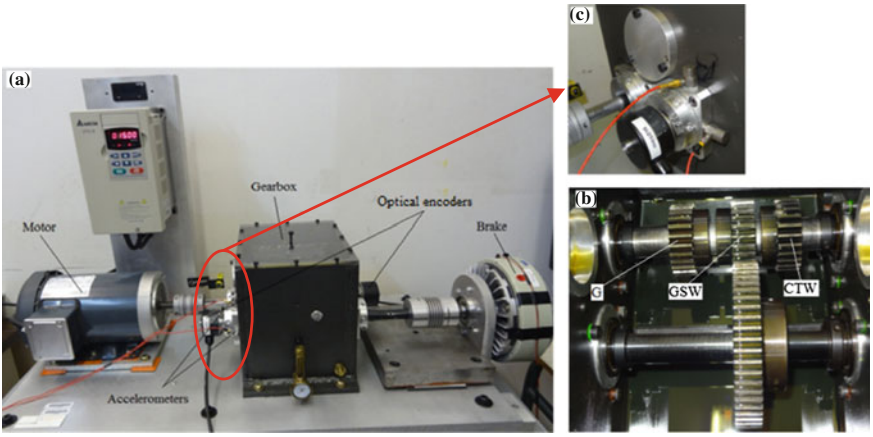

Fig. 3 The test bed (**a**), location of pinions (**b**) and sensors (**c**)

case of the output shaft of the gearbox as shown in Fig. 3c. To measure the angular positions of the shafts, two optical encoders of 2500 pulses per revolution are mounted at the free ends of the two shafts of the gearbox Fig. 3a. The clock frequency of the counting acquisition system is 80 MHz, generally considered sufficient to locate the rising edges of the encoder signals. The time sampling frequency of the accelerometer channels is 125 kHz. The cutoff frequency of the anti-aliasing filter is 27 kHz. The acquisition duration is 30 s. The accelerometer signals and the angular positions have been recorded for different operating conditions by varying the rotation speed and the resistant torque for each of the six gears used (Table 1). Each test is repeated ten times for normal conditions (Fig. 5 (1)) and five times for nonstationary conditions, in order to have a sufficient number of signals for the training and testing of SVM. In total, 1590 records have therefore been made, 265 records for each class of operation.

For the nonstationary running conditions two strategies have been used:

- Load variation: for the five RPMs used (Table 1) the load balances suddenly from the no-load to under load operation (Fig. 5(2)), repeated several times during the acquisition time. Two resistive torques are used, 5 and 8 Nm.

Table 1 Running conditions

Fault description	Conditions		RPMs (r/min)	Load (Nm)	Number of signals
Good	Normal (stationary)		900, 1200, 1500, 1800, 2400	0, 5, 8, 11	1200
Root crack					
Chipped tooth in width	Nonstationary	Load	900, 1200, 1500, 1800, 2400	Load variation	300
				– 0 and 5	
Chipped tooth in length				– 0 and 8	
Missing tooth		Speed	Speed variation	0, 5, 8	90
General surface wear					

- Speed variation: for the three couples used (0, 5, and 8 Nm), speed increases gradually until an approximated value of 50 Hz, then decreases with the same manner till the end of acquisition (Fig. 5(3)).

4 Experimental Part

The flowchart in Fig. 4 shows a complete overview of signals and analysis used in this study. From records made on the test bench, several signals are implemented in order to extract different types of indicators to build multiple FVs, which afterwards, will be used in classification procedure.

The full FV is composed simultaneously of all indicators extracted from all signals and ranked as follows:

$$\text{Full FV} = \{\text{FV1}(1 \text{ to } 15), \text{FV2}(16 \text{ to } 30), \text{FV3}(31 \text{ to } 45), \text{FV4}(46 \text{ to } 60)\}$$

4.1 Feature Extraction

The feature extraction stage is one of the most important stages in the pattern recognition process. The purpose of feature extraction is twofold; first, feature extraction is an attempt to reduce the dimensionality of the data presented to the classifier, without diminishing the content presented in the data. Second, feature extraction is intended to turn vibration signatures into indicators information that the classifier can use more usefully [3].

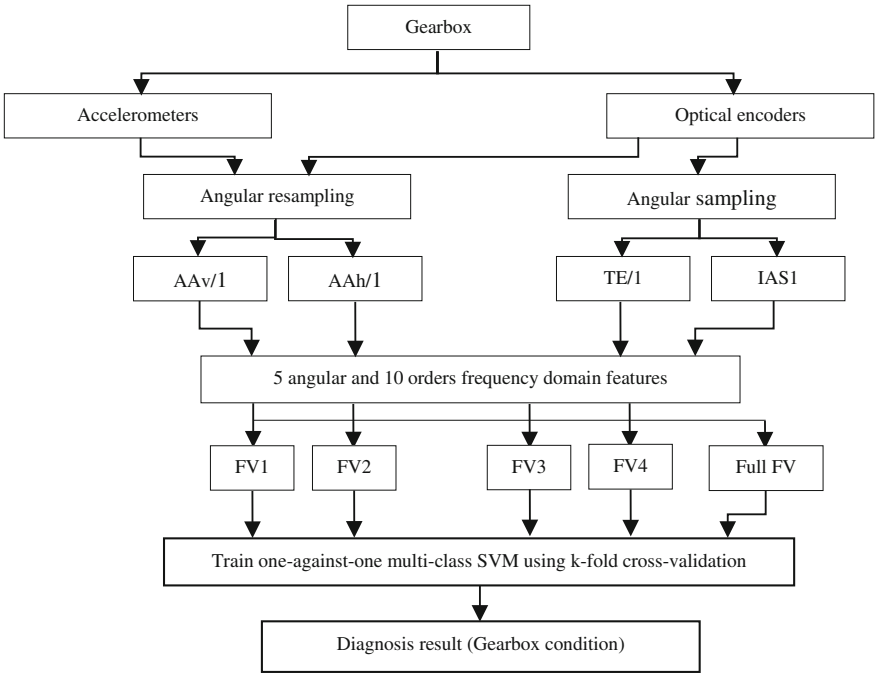

Fig. 4 Flowchart of preprocessing, FVs extraction and multiclass SVM-based faults diagnosis system

4.1.1 Signal Analysis (Angular Features Extraction)

Figure 5a 1, 2 and signals of the vertical accelerometer resampled in angular positions 3 represent the accelerometer of the input shaft (AAv/1): in normal conditions, load variation and speed variation, for the different pinions used.

The presence of defects on the pinion causes:

- A significant increase in the energy of the angular signals,
- As for localized defects, a presence of a shock repeated at every revolution period.

The angular sampling method in reference to the encoder #1 was used because it is the element affected by the defect, and we reconstructed the TE of the pinion from (1). The TEs signals (TE/1) shown in Fig. 5b 1, 2, and 3 clearly show low-frequency components corresponding to the rotation speed of the shaft, and the passage of the teeth at higher frequencies. We also note that the energy depends on the type of fault. The IAS1 signals are calculated from (2), using the encoder signal mounted on the input shaft of the gearbox where pinions with defects are mounted on. Figure 5c 1, 2, and 3 clearly shows the presence of a defect that is manifested by an increase in IAS. The used signals are processed to extract five angular domain

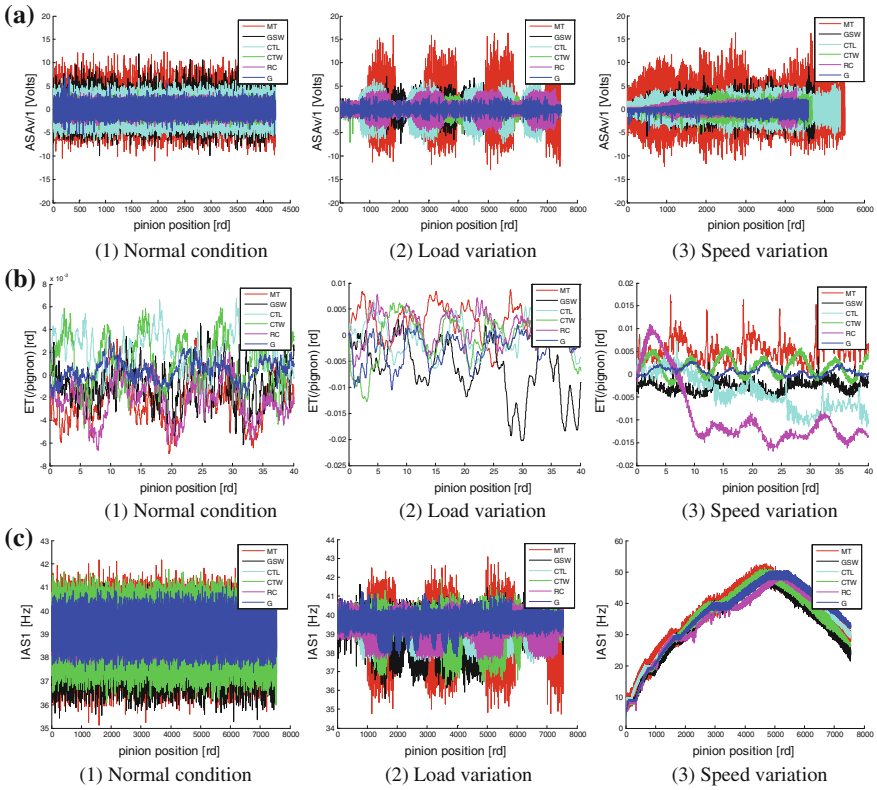

Fig. 5 Presentation of different signals in normal (1) and nonstationary conditions (2 and 3). **a** AAv/1, **b** TE/1, **c** IAS1. for pinions: Good (G), Root Crack (RC), Chipped Tooth in Width (CTW), Chipped Tooth in length (CTL), Missing Tooth (MT) and General Surface Wear (GSW)

features commonly used in literature, which are RMS, variance, crest factor, kurtosis, and skewness. The definitions of these features can be found in [2].

4.1.2 Spectral Analysis (Spectra Features Extraction)

Spectral data has been one of the most effective forms of feature extraction used in condition monitoring. As many of the machines monitored are rotational, many of the faults that exhibit themselves are frequency related. Where the construction of these machines is also known, it is a comparatively simple matter to calculate the frequencies at which certain defects would be likely to occur [1, 2]. However, reading frequency plots, identifying harmonic peaks, and giving confident diagnoses of problems are a skilled task and require experience. Spectral information is still very useful for providing information for classifiers, and as a result, it was used as one of the methods of features extraction.

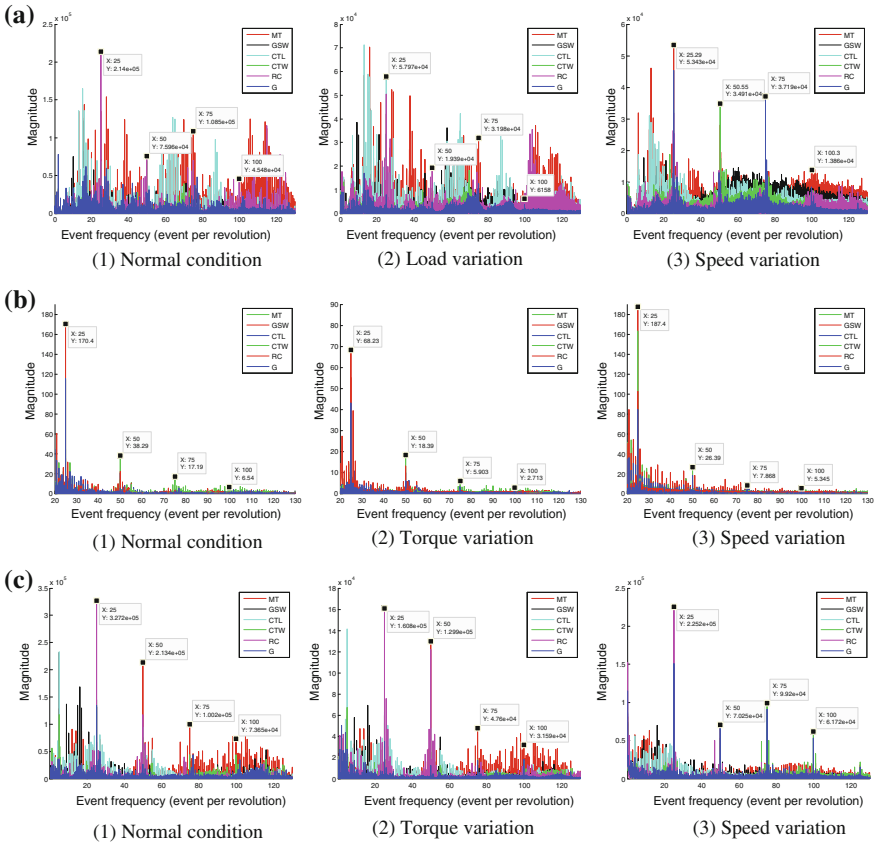

Fig. 6 Event spectra of angular signals in normal (*1*) and nonstationary conditions (*2* and *3*): **a** Event spectra of ASAv1. **b** Event spectra of TE/1. **c** Event spectra of IAS1, using pinions: Good (*G*), Root Crack (*RC*), Chipped Tooth in Width (*CTW*), Chipped Tooth in length (*CTL*), Missing Tooth (*MT*) and General Surface Wear (*GSW*)

The spectral field of the angular signals: AAv1, TE/1, and IAS1, presented, respectively, in Fig. 6a–c, give a considerable advantage, due to the frequency of observation of gears being not changed by the rotational speed, but are directly observable at the main orders:

- channel 1 and its harmonics for localized defects,
- channel 25 corresponding to the number of teeth of the pinion ($Z = 25$) and its harmonics, for generalized defects.

So, the presence of the fault on the pinion causes a number of events per revolution, the significant increase in the peak amplitude of the frequency channel corresponding either to the number of teeth of the pinion ($Z = 25$) for generalized defects, or on the frequency channel 1 for localized defects. We also remark an

increase in energy of the intermediate levels. It is found that the positions of these peaks will remain fixed despite variations in speed from one test to another, whereas the amplitudes vary in a different way from one frequency channel to another and depending on the type of fault. Consequently, it is a source of building highly relevant indicators. These figures are used to track with precision the frequency components associated to the different types of defects and to the supervised geometrics (number of teeth of the pinion), whether they are localized or generalized. These amplitudes are subsequently used as indicators in the FVs.

4.2 Feature Vectors (FVs)

We propose to use a several FVs of 15 features according to the flowchart given in Fig. 4. They are summarized in Table 2. All used signals are processed to extract:

- five angular domain features: RMS, variance, crest factor, kurtosis and skewness,
- ten orders frequency domain features from the angularly sampled signals.

Table 2 Description of the features

Indicators	Domain	AAv/1	AAh/1	TE/1	IAS1
1	Angular	RMS			
2		Variance			
3		Crest factor			
4		Kurtosis			
5		Skewness			
6	Frequency	The level of order 1			
7		The level of order 25			
8		The level of order 50			
9		The level of order 75			
10		The level of order 100			
11		The sum of the levels of the 2nd to 24th order			
12		The sum of the levels of the 26th to 49th order			
13		The sum of the levels of the 51st to 74th order			
14		The sum of the levels of the 76th to 99th order			
15		The sum of the levels of the 101st to 124th order			

4.3 Classification Procedure

After this learning step, the classification of the tested experiment is performed using multiclass SVM. First the detection is performed by testing if the FV belongs to the default class or to the healthy class. In case of default detection, the FV is compared with all the default classes for identification.

4.3.1 Support Vector Machine Theory

The SVM, proposed by Vapnik [11], is one of the most powerful algorithms in classification [12–17]. The basic principle of SVM is to separate two classes with optimal hyperplane which maximizes the margin between the separating hyperplane Fig. 7.

To describe the algorithm of SVM, let us consider the set P that trains the SVM classifier:

$$P = (x_i, y_i), \quad x_i \in R^m, y_i \in \{-1, 1\}_{i-1}^{n} \quad i = 1, 2, \ldots, n \tag{5}$$

where x_i represents an input vector containing m indicators of a n samples training set, while y_i is the desired output ($y_i = 1$ for positive class and $y_i = -1$ for negative class).

In the case of linearly separated data, the separating hyperplane $f(x) = 0$ can be expressed as

$$f(x) = w^{\mathrm{T}}x + b = \sum_{i=1}^{n} w_i x_i + b = 0 \tag{6}$$

where w is a weight vector and the scalar b is the bias.

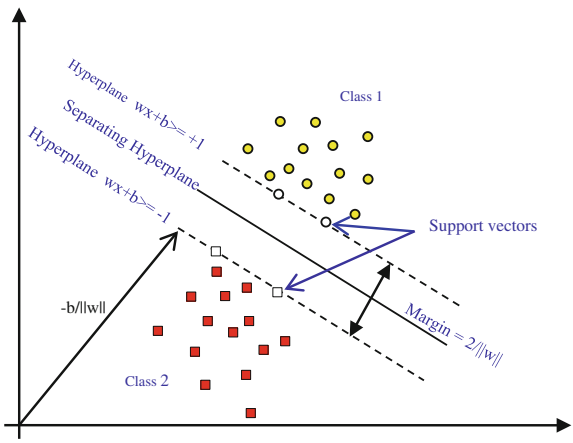

Fig. 7 Separation of two classes by SVM

The separating hyperplane must satisfy the equation,

$$y_i f(x_i) = y_i(w^{\mathrm{T}} x_i + b) - 1 \geq 1 \tag{7}$$

The Euclidean distance of any point that lies on either of the two hyperplanes is equal to $1/\|w\|$. Maximizing the margin $2/\|w\|$ is equivalent to minimizing $\|w^2\|$. The solution is found after solving the following quadratic optimization problem:

$$\begin{aligned} &\text{minimize} \quad \tfrac{1}{2}\|w^2\| + C\sum_{i=1}^{n}\xi_i \\ &\text{subject to} \quad \begin{cases} y_i(w^{\mathrm{T}} x_i + b) \geq 1 - \xi_i, & i = 1, \ldots, n \\ \xi_i \geq 0, \end{cases} \end{aligned} \tag{8}$$

where C is the regularization parameter and ξ is the slack variables.

Using the Lagrangian optimization method, the above equation can be presented as

$$\begin{aligned} &\text{maximize} \quad W(\alpha) = \sum_{i=1}^{n}\alpha_i - \tfrac{1}{2}\textstyle\sum_{i,j=1}^{n}\alpha_i\alpha_j y_i y_j (x_i, x_j) \\ &\text{subject to} \quad \begin{cases} 0 \leq \alpha_i \leq C \\ \sum_{i=1}^{n}\alpha_i y_i = 0 \end{cases} \quad i = 1, \ldots, N \end{aligned} \tag{9}$$

For the case of nonlinear separability in feature space, the kernel function is introduced in the last equation in order to transform the input vectors into a high-dimensional feature space, where the linear separation is possible. Thus, the inner product (x_i, x_j) (Eq. 6) is replaced by a kernel function $K(x_i, x_j)$, as shown in the following equation:

$$W(\alpha) = \sum_{i=1}^{n}\alpha_i - \frac{1}{2}\sum_{i,j=1}^{n}\alpha_i\alpha_j y_i y_j K(x_i, x_j) \tag{10}$$

Finally, based on the optimal hyperplane, the optimal classification function can be given as

$$f(x) = \operatorname{sign}\left(\sum_{i,j=1}^{n}\alpha_i y_i K(x_i, x_j) + b\right) \tag{11}$$

The kernel functions commonly used in SVM's formulations are: Linear, polynomial, sigmoid and radial basis function (RBF), etc. In this study, we opted for a *cubic polynomial kernel*.

4.3.2 Multiclass SVM

The discussion above deals with binary classification where the class labels can take only two values: 1 and −1. Generally, in the rotating machineries there are several fault classes such as gear faults, mechanical unbalances, misalignments, bearing faults, etc. In the gear fault also several faults appear like the wear of teeth, the MT, the chipped tooth, the RC, etc. Consequently, an appropriate multiclass method is needed. A number of possible methods for this purpose are as follows [18]:

- Modifying the design of the SVM to incorporate the multiclass learning directly in the quadratic solving algorithm,
- Combining several binary classifiers with two methods:
- One-against-one, which applies pair comparisons between classes
- One-against-all, which compares a given class with all the other classes.

According to a comparison study of Weston and Watkins [19], the accuracy of these methods is almost the same. Hsu and Lin [20] gave a detailed comparison of different methods for the multiclass SVM and concluded that one against-one (OAO) is a competitive approach.

5 Classification Results and Discussions

In the present work, we have several types of defects, so it is important to not only detect these defects (detection stage) but also to classify them (identification stage). For this, a SVM classifier is specifically used at each stage of diagnosis: the detection stage, where the training set consists only of examples in normal and fault conditions (2 classes) and the identification stage, where the training set consists only of examples in fault conditions (5 classes).

Here, we have applied the OAO approach for the multiclass classification using 10-fold cross-validation (CV). The data is divided arbitrarily into 10 portions. Every part is held out in turn and the learning scheme trained on the remaining nine-tenths, then its cross-validation accuracy (CVA) is calculated on the hold out set. Thus the learning procedure is executed 10 times on different training sets. Finally, the 10 CVA estimates are averaged to get an overall CVA estimate. The classification accuracy is the percentage of number of correctly predicted data with respect to the total number of testing data. The 10-fold CV is used to reduce the bias related with random sampling of the training and test sets. The CVA is the average of the k individual accuracy measures:

$$\mathrm{CVA} = \frac{1}{k}\sum_{j=1}^{k} A_j \tag{12}$$

where k (10 in our case) is the number of folds used,
and A_j is the accuracy measure of each fold, $j = 1,\ldots, k$
where N is the number of classes, $N\ (N-1)/2$ classifiers are constructed, and each one trains data from classification is considered to be a voting, where votes could be casted for two classes. In the identification stage, we use a voting strategy in which each binary all data points, x, at the end a point is designated to be in a class with the maximum number of votes [14, 18–20].

The CVA of SVM classification in detection and identification stages, in normal conditions, load variation, speed variation, and combined conditions, is shown respectively in Fig. 8a–d.

The results of Fig. 8 show the performance of the classification for detection and identification stages. It appears clearly that

- In the normal condition (Fig. 8a), we remark that all used FVs give high performances. Varying between a minimum value of 99.76 % for AA and a maximum value of 99.85 % for IASI (identification stage). This latest percentage is in fact higher than those of full FV.
- In nonstationary conditions:
- Load variation (Fig. 8b), for all used FVs, the diagnosis success is larger than 96.67 % and reaches a value of 100 % for IAS (detection stage).

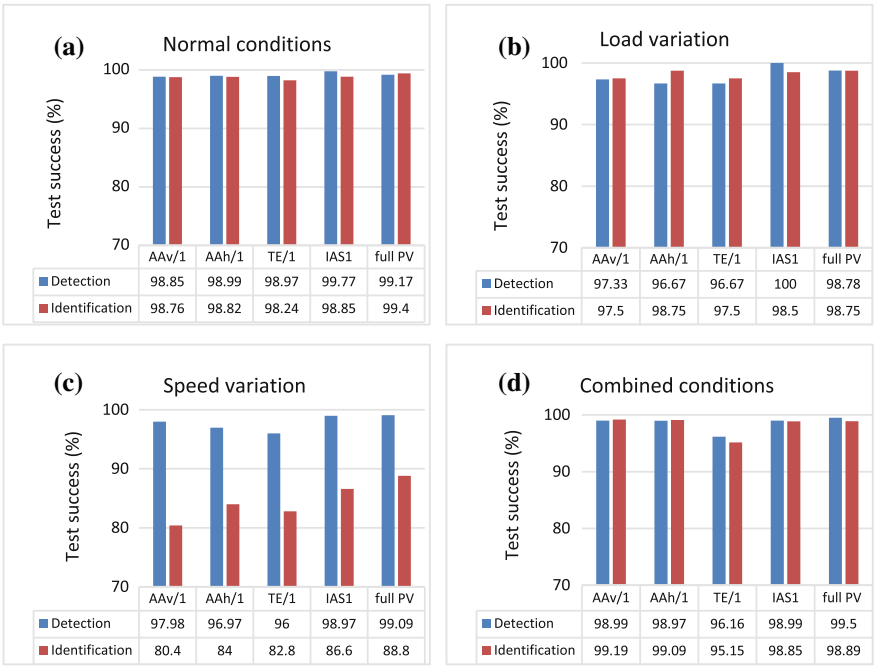

Fig. 8 Graphical representation of CVA of SVM classifiers. **a** Normal conditions. **b** Load variation. **c** Speed variation. **d** Combined conditions

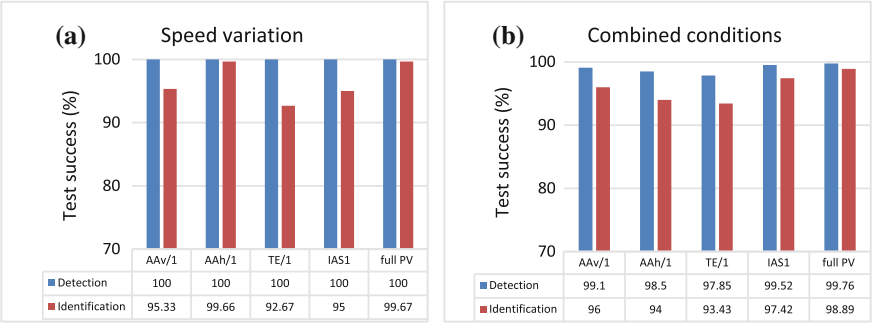

Fig. 9 Graphical representation of CVA of SVM classifiers without consideration of the unload mode. **a** Speed variation. **b** Combined conditions

– Speed variation (Fig. 8c), in the identification stage, the CVA achieves only 80.4 % for AA FV, and 88.8 % for full FV. The reason for this poor performance is not clear, it may be caused by:

  The randomness variation of speed during signals acquisition
  Vibrations signatures behave as the same way for certain:

    Gear faults (e.g., CTL and MT)
    No-load conditions (0 Nm)

  After the remove of all FVs of the unload mode from training and test databases, the performance levels rise significantly (Fig. 9a), 100 % in the detection stage and higher than 92.67 % for the identification stage.

– In the combined conditions (Fig. 8d), it is found that the designed SVM classifier can diagnose all gear faults accurately. Especially when we remove the unload mode (Fig. 9b)

Generally, The AA and TE give good performances in certain cases, but the IAS provides the best performances in all cases. Moreover, it ensures the same rates of detection given by FVs composed simultaneously of all indicators.

6 Conclusion

In this article, we showed that starting from two accelerometers and two optical encoders; it is possible to obtain several new signals representative of the behavior of the transmission, (i.e., TE and IAS of the two shafts). The techniques of angular sampling and resampling associated to the knowledge of the history of the angular positions of the shafts also make it possible to diversify the exploitation and the analysis carried out on the signals recorded in direct relationship with the discrete geometry in rotation (gears or bearings). The angular techniques are more robust in

nonstationary conditions. They indeed make it possible to locate precisely and in relation to the geometrical data of the mechanical components the frequential channels carrying information.

In a general way, the results obtained in operational phases of the diagnosis by multiclass SVM classifier using *k*-fold cross-validation, show that the gain in terms of effectiveness is significant in all cases while using FVs extracted from angular measurements. More especially, the IAS is relevant and produces better performances. The angular resampling of the accelerometer signals AA gives good performances. In consequence, using angular domain features extracted from IAS is recommended to the diagnosis of the gear faults in normal, nonstationary or combined conditions.

Acknowledgments This work was achieved at the laboratories LaMCoS (INSA-Lyon, France) and LMPA (IOMP, Sétif 1 University, Algeria). The authors would like to thank the French and Algerian Ministries of Higher Education and Scientific Research for their financial and technical support in the framework of program PROFAS 2011–2012.

References

1. Randall B (2011) Vibration-based condition monitoring; industrial, aerospace and automotive applications. Wiley, New York
2. Zwingelstein G (1995) Diagnostic des défaillances. Théorie et pratique pour les systèmes industriels, Editions Hermès
3. Dubuisson B (1990) Diagnostic et reconnaissance des formes. Traité des nouvelles technologies. Editions Hermès, Paris
4. Vachtsevanos G, Lewis FL, Roemer M, Hess A, Wu B (2006) Intelligent fault diagnosis and prognosis for engineering systems. Wiley, New Jersey
5. Rémond D (1998) Practical performances of high-speed measurement of gear transmission error or torsional vibrations with optical encoders. Meas Sci Tech 9:347–353
6. Bonnardot F, El Badaoui M, Randall RB, Danière J, Guillet F (2005) Use of the acceleration of a gearbox in order to perform angular resampling with limited speed fluctuation. Mech Syst Sign Proc 19:766–785
7. André H, Antoni J, Daher Z, Rémond D (2010) Comparison between angular sampling and angular resampling methods applied on the vibration monitoring of a gear meshing in non stationary conditions, (ed). In: Proceedings of the 2010 international conference on noise and vibration engineering, Leuven, Belgium, 20–22 Sept 2010
8. Renaudin L, Bonnardot F, Musy O, Doray JB, Rémond D (2010) Natural roller bearing fault detection by angular measurement of true instantaneous angular speed. Mech Syst Sign Proc 24:998–2011
9. Li Y, Gu F, Harris G, Ball A, Bennett N, Travis K (2005) The measurement of instantaneous angular speed. Mech Syst Sign Proc 19:786–805
10. Fedala S, Rémond D, Zegadi R, Felkaoui A (2013) Contribution of angular measurements in the diagnosis of gear faults by artificial neural networks. In: Surveillance 7, Chartre, France, 29–30 Oct 2013
11. Vapnik VN (1998) The statistical learning theory. Springer, Berlin
12. Widodo A, Yang B (2007) Support vector machine in machine condition monitoring and fault diagnosis. Mech Syst Sign Proc 21:2560–2574

13. Samanta B (2004) Gear fault detection using artificial neural networks and support vector machines with genetic algorithms. Mech Syst Sign Proc 18:625–644
14. Bordoloi DJ, Tiwari R (2014) Optimum multi-fault classification of gears with integration of evolutionary and SVM algorithms. Mech Mach Theory 73:49–60
15. Bordoloi DJ, Tiwari R (2014) Support vector machine based optimization of multi-fault classification of gears with evolutionary algorithms from time–frequency vibration data. Measurement 55:1–14
16. Yuan Sheng-Fa, Chua Fu-Lei (2007) Fault diagnostics based on particle swarm optimization and support vector machines. Mech Syst Sign Proc 21:1787–1798
17. Li Ning, Zhou Rui, Qinghua Hu, Liu Xiaohang (2012) Mechanical fault diagnosis based on redundant second generation wavelet packet transform, neighborhood rough set and support vector machine. Mech Syst Sign Proc 28:608–621
18. Chapelle O, Haffner P, Vapnik VN (1999) Support vector machines for histogram-based classification. IEEE Trans Neural Netw 10:1055–1064
19. Weston J, Watkins C (1998) Multi-class support vector machines. Technical Report CSD-TR-98-04, Royal Holloway, University of London, Department of Computer Science
20. Hsu CW, Lin CJ (2002) A comparison of methods for multi-class support vector machines. IEEE Trans. Neural Netw. 13:415–425

Diversity Measures in Classifier Ensembles Used for Rotating Machinery Fault Diagnosis

Wojciech Jamrozik

Abstract Recent progress in computational intelligence, sensor technology and soft computing methods permit the use of complex systems to achieve diagnostic process goal. Among many, machine learning and pattern recognition techniques are often applied. When dealing with complex machinery use of one classifier is often insufficient. It is known that classifier ensembles (combined prediction from several classifiers) have the capability to outperform single classifier, because ensemble results are less dependent on peculiarities of a single training set. Additionally a combination of multiple classifiers may learn a more expressive class. In the paper a comparative study of different diversity measures for the rotating machine common faults detection and isolation. The main premise was to investigate if there is a link between diversity measure and classification accuracy. Although in several cases the connection between diversity and fault detection as well as isolation performance was revealed, the generalization of the diversity measuring concept cannot be clearly formulated.

Keywords Classifier fusion · Information diversity · Dempster-Shafer theory · Rotating machinery diagnosing

Contents

1 Introduction 310
1.1 Overview of Dempster-Shafer Theory 311
1.2 Diversity Measures 311
1.3 Dependency Measure 312
2 Case Study 313
2.1 Test Setup 313

W. Jamrozik (✉)
Institute of Fundamentals of Machine Design, Silesian University of Technology, 18A Konarskiego St, 44-100 Gliwice, Poland
e-mail: wojciech.jamrozik@polsl.pl

F. Chaari et al. (eds.), *Advances in Condition Monitoring of Machinery in Non-Stationary Operations*, Applied Condition Monitoring 4,
DOI 10.1007/978-3-319-20463-5_23

2.2 Results 315
3 Conclusions 318
References 318

1 Introduction

Monitoring and diagnosing rotating machinery, especially in non-stationary operating conditions is a vital and very important issue. Diagnosing tasks is in general made by Fault Detection and Isolation (FDI) systems. First aim of this group of systems is to determine whether a fault has occurred (*fault detection*). When developing a diagnostic system, the interest is not only to accomplish the faults detectability but in many cases it is rather more desirable to specify the kind of the fault that has occurred in observing system, thus realizing the *fault isolation*.

Different methods to achieve demanded goal depending on the machine's complexity, the type of fault to be detected, etc. are proposed by various authors [1, 2]. The fault diagnosis (FDI) demands determining the relations existing between the measured symptoms and the faults pattern recognition approaches are used, and diagnosing is treated as a problem of classification. Unfortunately classifiers are often trained over limited data and required estimation of the target function [3]. To overcome limitations of individual classifiers combination (fusion) technique were introduced and also successfully applied into technical diagnostic domain [4–6].

There are various ways to build a classifiers ensemble: use of different subsets of features, use of different classification algorithms within the ensemble, variation of random parameters of the classification algorithm, use of different data set for each ensemble member. Regardless of the ensemble there is the aggregation (combination, fusion) stage required. Label outputs and continuous-valued outputs fusion can be perform. Among continuous-valued outputs fusion methods based on the belief function framework (Dempster-Shafer, Transferable Belief Model, Dezert-Smarandache) are popular and widely applied [7, 8].

In the area of classifier fusion the diversity among classifiers is well intuitively understood. There is no explicit measure of diversity involved in the process but it is assumed that diversity is a key factor for the success of this algorithm. Additionally when dealing with the classifier fusion that use techniques based on the belief functions theory there is another factor concerning the relationship among processed data namely dependence of sources of evidence.

In the paper research devoted to the problem how are the diversity measures related to the accuracy of the team. Additionally issues connected with the influence of the dependence of evidence sources on the team accuracy and its connection to the diversity terms are investigated.

1.1 Overview of Dempster-Shafer Theory

The belief functions theory, also called evidence theory or Dempster-Shafer theory (DS) [9, 10] is based on the use of functions defined on the power set 2^{Θ} (the set of all the subsets of Θ), where $\Theta = \{\theta_1, \theta_2, \ldots, \theta_n\}$ is the set of elements called frame if discernment (e.g. machinery conditions and faults). Objects of 2^{Θ} can be built upon $\cup$ operator, in other words if $A, B \in 2^{\Theta}$, then $A \cup B \in 2^{\Theta}$, wherefore two or mode elements of Θ cannot occur simultaneously. The restriction that elements of Θ are truly exclusive is one of cornerstones of so called Shafer's model. *Belief functions* or *basic belief assignments*, $m(\cdot)$ are defined by the mapping of the power set 2^{Θ} onto [0, 1] interval with: $m(\emptyset) = 0$, which is the hypothesis of a closed world [10], and $\sum_{X \in 2^{\Theta}} m(X) = 1$.

The first combination rule proposed by Dempster and Shafer is the normalized conjunctive combination rule given for two basic belief assignments m_1 and m_2 and for all $X \in 2^{\Theta}$, $X \neq \emptyset$ by:

$$m_{DS}(X) = \frac{1}{1-k} \sum_{A \cap B = X} m_1(A) m_2(B), \tag{1}$$

where $k = \sum_{A \cap B = \emptyset} m_1(A) m_2(B)$ is the global conflict of the combination.

Despite many successful applications of DS in many areas, the key element of theory, namely Dempster's rule can give in several cases counter-intuitive results, what was first pointed out by Zadeh [11] and more recently by Dezert et al. [12].

1.2 Diversity Measures

Intuitively, an ensemble of classifiers work the best when outputs of individual classifier are mostly good but at the same time there is a significant diversity among them. Thus the diversity is a vital factor of ensemble success, while in the case when all classifiers outputs are the same, aggregation will not lead to a solution that outperform the individual ensemble members. The main question is how to define an measure of diversity, how it reflects on classification results and how different measures are related to each other. In the area of general classification and clustering problems there were comprehensive studies made and many interesting measures of diversity elaborated, verified and validated [13–16]. The main conclusion that arise from already made research is that diversity is needed but there is no general and universal measure well suitable for all classification and clustering tasks.

In order to investigate whether diversity influences classifier fusion results in the field of rotating machinery FDI nine measures were chosen:

- Q-statistic (Q, $\downarrow$[1]), pairwise measure [13, 17],
- Correlation coefficient (ρ, $\downarrow$), pairwise measure [18],
- Disagreement measure (D, $\uparrow$), pairwise measure [19],
- Double-fault measure (DF, $\downarrow$), pairwise measure [20],
- Kohavi-Wolpert variance (KW, $\uparrow$), non-pairwise measure [21],
- Interrater agreement (κ, $\downarrow$), non-pairwise measure [22],
- Entropy measure (Ent, $\uparrow$), non-pairwise measure [23],
- Measure of difficulty (Dif, $\downarrow$), non-pairwise measure [24],
- Generalized diversity (GD, $\uparrow$), non-pairwise measure [25].

Although continuous valued outputs of classifier are possible to obtain all averaged diversity measures are dealing with oracle outputs. Thus some information provides is lost and does not took part in diversity calculation procedure.

1.3 Dependency Measure

When combination of classifier is made in the DS framework, beside diversity, the dependency of sources ia an important issue. The sources independence is one of the key foundations of belief function combination. Combining dependent belief, that give strong support to one element of frame of discernment that stands for one machine fault. Fusion using standard DS rules will artificially increase the belief in some fault hypothesis, that eventually can be a false one.

In this context it can be seen that multiple fusion of same belief function is made. When n identical the belief functions e are combined by conjunctive rule so called *autoconflict* increases [26]. According to that e tends to $\overline{e}(Y) = 1$ when $n \to \infty$.

To measure the degree of dependence between evidences the concept of handling dependent evidence proposed by Guralnik et al. [27] was adopted and transformed into a form of sources of evidence dependence factor. For the rotating machinery most common is the measuring of vibrations. When measuring same quantity, like vibration acceleration, following levels of dependency can be listed: measurement point, direction of measurement, signal feature and classifier. Considering case, when classifiers of the same type, with the same parameters are used, the transformation that lead to calculation of feature value (which have influence on the classifier output) can be formulated in the form of following equation: $ft = g_i\big(h_j(x_k)\big)$, where ft is the feature, $g_i(\cdot)$ is the transformation form raw signal to feature value, $h_j(\cdot)$ is the direction of vibrations and x_k stands for point of measurement. For the set of features $\boldsymbol{ft} = (ft_1, \ldots, ft_N)$ used to train individual

[1]The arrow specifies whether greater diversity is reflected in greater ($\uparrow$) or lower ($\downarrow$) diversity measure value.

classifiers of the ensemble, overall degree of dependence between N sources of evidence is defined as follows:

$$W_{nz}(\boldsymbol{ft}) = \frac{\sum_{a=1}^{N} w_a}{N} \tag{2}$$

where:

$$w_a = \begin{cases} 0 & \text{for } \mathrm{ft}_a \in \boldsymbol{ft} \quad \exists ft_b \in \boldsymbol{ft}(x_a \neq x_b) \\ 1/3 & \text{for } \mathrm{ft}_a \in \boldsymbol{ft} \quad \exists ft_b \in \boldsymbol{ft}(h_a(\cdot) \neq h_b(\cdot), x_a = x_b) \\ 2/3 & \text{for } \mathrm{ft}_a \in \boldsymbol{ft} \quad \exists ft_b \in \boldsymbol{ft}(g_a(\cdot) \neq g_b(\cdot), h_a(\cdot) = h_b(\cdot), x_a = x_b) \\ 1 & \text{otherwise} \end{cases} \tag{3}$$

Additionally $ft_a = g_a(h_a(x_a))$ and $ft_b = g_b(h_b(x_b))$, signals $h_a(x_a)$ and $h_b(x_b)$ were acquired in the same time.

2 Case Study

In order to investigate the connection between the classification accuracy, in machinery fault detection, isolation and diversity measures active experiment was prepared and carried out.

2.1 Test Setup

The method has been verified using a set of vibration signals recorded during active diagnostic experiments performed on laboratory stand containing a model of rotating machinery (Fig. 1). Following machinery conditions were simulated: ***S1***—no fault, ***S2***—small unbalance (6.21 g), ***S3***—large unbalance (12.43 g), ***S4***—misalignment (0.5 mm), ***S5***—pump with 10 % throttling. For each condition 20 realizations of signal were recorded. Unbalance was simulated by adding an additional mass (screw) to the balancing disk mounted on the rotor. Misalignment was also introduced in the Y-Z plane across the rigid coupling. In this scenario a steel shim was installed under the bearing housing B1, to obtain angular misalignment.

Fig. 1 Experimental test rig and computer station with signal analyser

Between all experiments there was a delay. It was required to cool down the test rig to ambient temperature.

Vibration signals were acquired on bearing housings. On the B1 housing triaxial piezoelectric accelerometer (PCB Piezotronics T356A32) and signals in axial and radial directions were taken. On B2 housing two accelerometers (PCB Piezotronics T338B30) were mounted, one in radial (Z) and second in axial (Y) direction. Signals were acquired by LMS Scadas Mobile and processed by LMS Test.Lab v12 software. Analysis were performed in Matlab environment. Acquired signals were assessed with use of several point estimators, widely used in the technical diagnostic: mean, absolute mean, squared mean, RMS, variance, standard deviation, absolute peak, maximum, minimum, peak to peak, form factor, crest factor, peak-to-average ratio (PTA), peak-to-sqrt ratio (PTS), asymmetry and kurtosis. After preliminary studies mean, RMS and kurtosis were chosen for further analysis.

For the classification simple k-Nearest Neighbour (k-NN) classifier was used. It was found, that the free parameter has to be $k = 5$. Because of small feature set, leave-one-out classification error estimation method was chosen. Classification was performed for all features separately and opinions from individual classifiers were obtained. 12 member classifiers were generated (marked $C1$–$C12$, Fig. 2). In order to determine mass assignment required, in other words to transform classifier output into the belief, the normalised class membership was extracted form k-NN [28] for each of considered classes. The frame of discernment $\Theta = \{\boldsymbol{S1}, \boldsymbol{S2}, \boldsymbol{S3}, \boldsymbol{S4}, \boldsymbol{S5}\}$ describing identified machinery conditions and an assumption was made that only one condition can be present in certain moment of time, what is required by DS to form 2^{Θ} set. Outputs from individual classifiers were combined with classical Dempster's rule. Outputs from three individual classifiers were used (Ca, Cb, Cc, Fig. 2.). According to that, for considered data set containing 12 features, 220 ensembles have been generated.

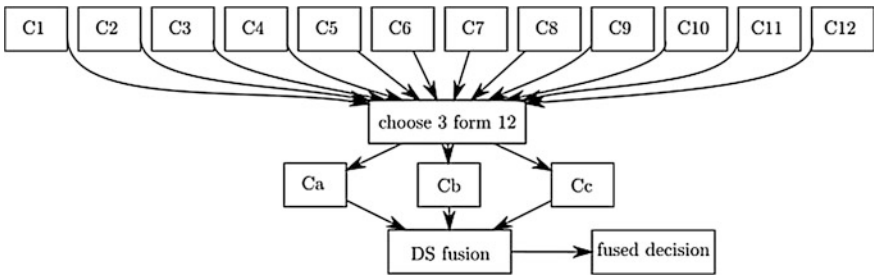

Fig. 2 Diagram of test procedure

2.2 Results

Distribution of kurtosis for all measurement points and vibration directions was gathered in Fig. 3. It can be noticed that for B2 bearing distinction between conditions ***S1***–***S3*** is difficult, while for B2_Y kurtosis for ***S3*** and ***S4*** is similar.

Overall classification accuracy was defined as follows: $a_{\text{all}} = N_c/N$, where N_c is the number of correct outputs and N is the number of all considered samples in the test set. Accuracies of FDI were gathered in Table 1. As expected in both cases accuracy of the ensemble was better then the base individual classifier. It must be stated that the improvement over the single best classifier was small.

The individual best accuracy in both FDI was for B2_Y_kurtosis feature. For aggregated it was for in the case of fault detection B2_Y_kurtosis, B2_Y_RMS and B2_Z_RMS features combination. In the diagnosis task the combination that led to best accuracy was B2_Y_RMS, B2_Z_RMS and B1_Z_RMS. It can be seen, that the best individual classifier trained over the B2_Y_kurtosis feature was not the member of the best diagnosing ensemble.

In Fig. 4 scatterplots of machinery condition detection accuracy gain against diversity are presented. In the case of ρ, D, KW, *Entropy* and *Dif* factors increase of accuracy gain results in decrease of the diversity. Opposite situation occurs for DF, κ and GD factors. Especially for double fault (DF) measure the relationship is

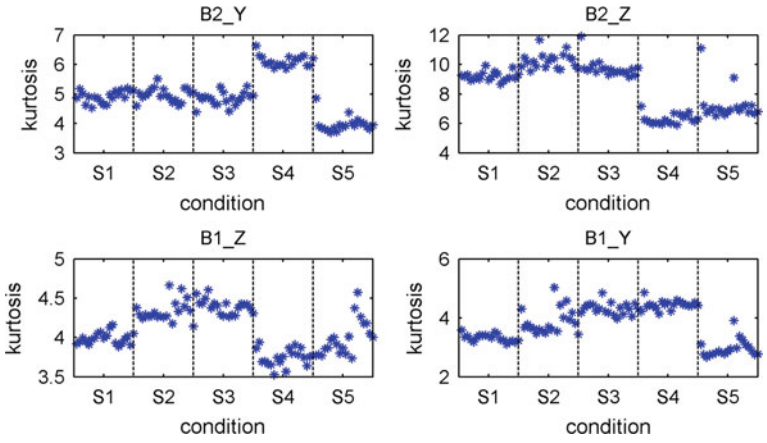

Fig. 3 Plot of kurtosis for considered measurement points for various vibration directions

Table 1 Results of machinery condition classification

Fault		Mean	Max	Min	Std
Detection	Individual	0.82	0.92	0.74	0.005
	Aggregated	0.84	0.95	0.77	0.042
Isolation	Individual	0.55	0.89	0.16	0.025
	Aggregated	0.55	0.91	0.12	0.173

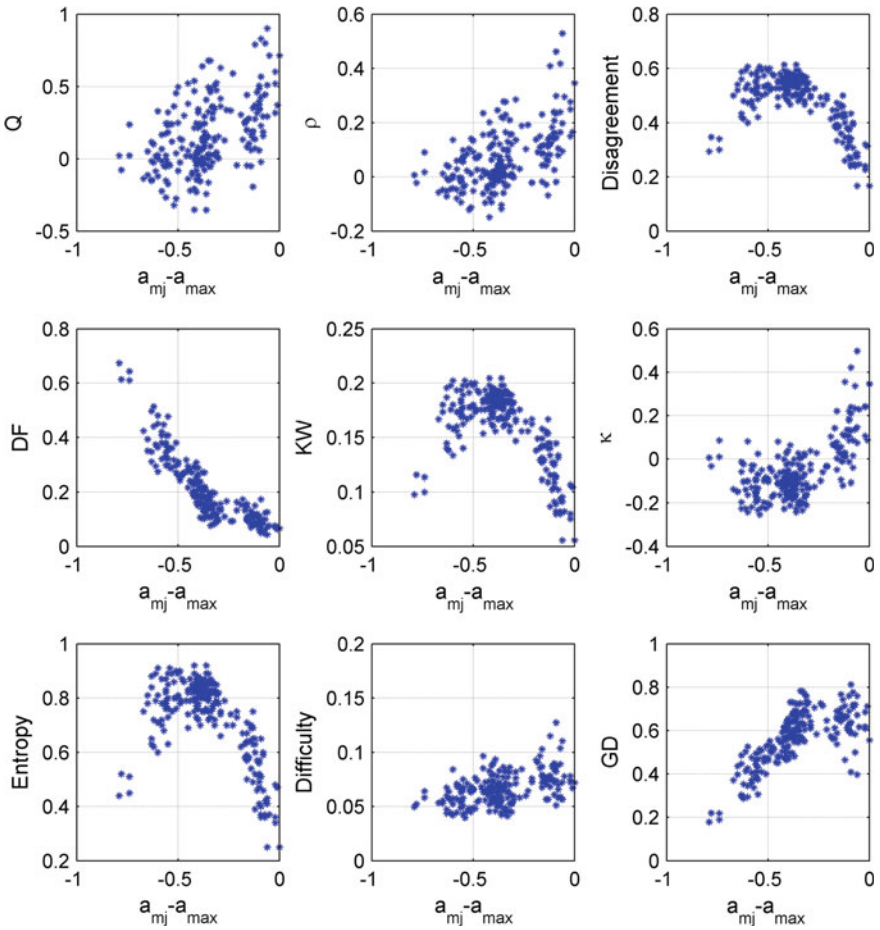

Fig. 4 Scatterplot of the diversity factors against improvement of the DS fusion over the single best classifier (a_{DS}–$a_{\max}$) for the fault isolation case

straightforward and dispersion of results is minimal. For Q the positive relation is noticeable but spread of results is significant.

To summarize and quantify data shown in Fig. 4 correlation between classification accuracy gain (a_{DS}–a_{max}) and diversity factors was calculated (Table 2). Obtained values have confirmed conclusions that arise from scatterplot analysis. In both cases (detection and isolation) double fault (DF) and generalized diversity (GD) factors seems to be the best choice in terms of best member classifiers selection for the ensemble. Correlation $p_{DF} = -0.89$ informs with high certainty that the lower the diversity factor is the higher the fault isolation accuracy will be. Moreover strong linear trend is clearly visible for DF factor.

Table 2 Correlation p between diversity measures and classification accuracy

	Q	ρ	D	DF	KW	κ	$Entropy$	Dif	GD
Detection	−0.46	−0.58	0.14	−0.77	0.14	−0.64	0.14	−0.78	0.71
Isolation	0.48	0.54	−0.59	−0.89	−0.59	0.62	−0.59	0.49	0.70

In Table 3 correlation between consecutive diversity factors calculated for the fault isolation task is presented. It can be seen that measures D, KW and $Entropy$ fully correlated and using all of them will not provide any additional useful information about classifiers that should be selected for the ensemble. DF and GD that were chosen as the best measures in term of relationship with classification accuracy, are strongly correlated among each other, moreover correlation with other factor is relatively low.

In Fig. 5 there are interesting results presented. Only when highest dependency was reached, the increase of classification accuracy has no chance to be maximal. In contrary, the minimal dependence led to largest increase of classification accuracy regarding maximal accuracy of the single classifier. Even more interesting is the

Table 3 Correlation p between diversity measures

	ρ	D	DF	KW	κ	$Entropy$	Dif	GD
Q	0.96	−0.63	−0.30	−0.63	0.73	−0.63	0.68	0.07
ρ		−0.71	−0.32	−0.71	0.83	−0.71	0.77	0.04
D			0.17	1.00	−0.92	1.00	−0.62	0.05
DF				0.17	−0.22	0.17	−0.18	-0.93
KW					−0.92	1.00	−0.62	0.05
κ						−0.92	0.85	−0.07
$Entropy$							−0.62	0.05
Dif								−0.11

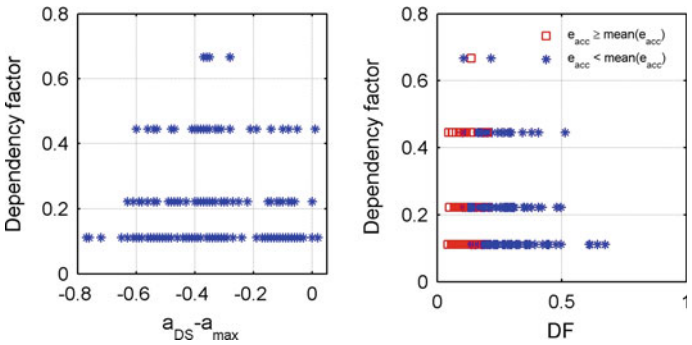

Fig. 5 Scatterplot of the dependence factor against improvement of the DS fusion over the single best classifier $(a_{DS} - a_{\max})$ and the dependence factor against DF diversity factor for machinery fault isolation

connection of source of evidence dependence factor with the *DF* diversity factor. Low dependency is does not guarantee that high diversity will be achieved (low *DF* factor). At the same time better classification results are obtained when dependency is low and diversity is high.

3 Conclusions

The study of nine diversity measures used in the task of rotating machinery FDI was presented in the paper. Experimental results were gathered and analysed to demonstrate how the accuracy of fault isolation can be improved by fusing information from multi-sensors. The search for the link between classification accuracy and diversity factor lead to one key conclusion, that diversity is strong connected do applied measure, while there is a large difference between factors that useful and unsuitable ones. Thus additional research should be performed in order to find or elaborate new measures that can be applied in wide range of not only diagnostic problems. As the fusion of classifier outputs was made in frame of Dempster-Shafer belief function theory the issue of sources of evidence dependence was also investigated. It has been found that straightforward relationship between classification accuracy and dependence of beliefs is limited, but independence of sources is connected with classification diversity and can has positive influence on quality of fault isolation and overall machinery diagnosis.

Acknowledgments Scientific work financed from resources assigned to statutory activity of Institute of Fundamentals of Machinery Design, Silesian University of Technology at Gliwice.

References

1. Assaad B, Eltabach M, Antoni J (2014) Vibration based condition monitoring of a multistage epicyclic gearbox in lifting cranes. Mech Syst Sig Process 42:351–367
2. Bartelmus W, Zimroz R (2009) A new feature for monitoring the condition of gearboxes in non-stationary operating conditions. Mech Syst Sig Process 23(5):1528–1534
3. Marciniak A, Korbicz J (2004) Pattern recognition approach to fault diagnostics. In: Korbicz J, Kowalczuk Z, Kościelny JM, Cholewa W (eds) Fault diagnosis. Springer, Berlin, pp 557–590
4. Oukhellou L, Debiolles A, Denoeux T, Aknin P (2010) Fault diagnosis in railway track circuits using Dempster-Shafer classifier fusion. Eng Appl Artif Intell 23(1):117–128
5. Wang X, Xu XB, Ji YD, Sun XY (2012) Fault diagnosis using neuro-fuzzy network and Dempster-Shafer theory. In: 2012 International conference on wavelet analysis and pattern recognition (ICWAPR)
6. Nembhard AD, Sinha JK, Pinkerton AJ, Elbhbah K (2014) Combined vibration and thermal analysis for the condition monitoring of rotating machinery. Struct Health Monit. doi:10.1177/1475921714522843
7. Yang BS, Kim KJ (2006) Application of Dempster-Shafer theory in fault diagnosis of induction motors using vibration and current signals. Mech Syst Sig Process 20(2):403–420

8. Basir O (2007) X.Y.: engine fault diagnosis based on multi-sensor information fusion using Dempster-Shafer evidence theory. Inf Fusion 8(4):379–386
9. Dempster AP (1967) Upper and Lower probabilities induced by a multivalued mapping. Ann Math Stat 38:325–339
10. Shafer G (1976) A mathematical theory of evidence. Princeton University Press, Princeton
11. Zadeh L (1979) On the validity of Dempster's rule of combination. In: Tech. Rep. UCB/ERL M79/24, University of California, Berkely
12. Dezert J, Wang P, Tchamova A (2012) On the validity of Dempster-Shafer theory. In: 2012 15th International conference on information fusion (FUSION). pp 655–660
13. Kuncheva L, Whitaker C (2003) Measures of diversity in classifier ensembles and their relationship with the ensemble accuracy. Mach Learn 51(2):181–207
14. Kuncheva LI (2005) Diversity in multiple classifier systems. Inf Fusion 6(1):3–4 (Diversity in Multiple Classifier Systems)
15. Hadjitodorov ST, Kuncheva LI, Todorova LP (2006) Moderate diversity for better cluster ensembles. Inf Fusion 7(3):264–275
16. Lysiak R, Kurzynski M, Woloszynski T (2014) Optimal selection of ensemble classifiers using measures of competence and diversity of base classifiers. Neurocomputing 126:29–35
17. Yule GU (1900) On the association of attributes in statistics. Philos Trans A(194):257–319
18. Sneath P, Sokal R (1973) Numerical taxonomy. The principles and practice of numerical classification. Freeman, San Francisco
19. Ho T (1998) The random space method for constructing decision forests. IEEE Trans Pattern Anal Mach Intell 20(8):832–844
20. Giacinto G, Roli F (2001) Design of effective neural network ensembles for image classification processes. Image Vis Comput J 19(9–10):699–707
21. Kohavi R, Wolpert D (1996) Bias plus variance decomposition for zero-one loss functions. In: Saitta L (ed) ICML. Morgan Kaufmann, Massachusetts, pp 275–283 (1996)
22. Dietterich TG (2000) An experimental comparison of three methods for constructing ensembles of decision trees: bagging, boosting, and randomization. Mach Learn 40(2):139–157
23. Cunningham P, Carney J (2000) Diversity versus quality in classification ensembles based on feature selection. In: de Mántaras RL, Plaza E (eds) ECML, Lecture Notes in Computer Science, vol 1810. Springer, Heidelberg, pp 109–116
24. Hansen LK, Salamon P (1990) Neural network ensembles. IEEE Trans Pattern Anal Mach Intell 12:993–1001
25. Partridge D, Krzanowski W (1997) Software diversity: practical statistics for its measurement and exploitation. Inf Softw Technol 39(10):707–717
26. Osswald C, Martin A (2006) Understanding the large family of Dempster-Shafer theory's fusion operators—a decision-based measure. In: IEEE FUSION, pp 1–7
27. Guralnik V, Mylaraswamy D, Voges H (2006) On handling dependent evidence and multiple faults in knowledge fusion for engine health management. In: 2006 IEEE aerospace conference, p 9
28. Han D, Han C, Yang Y (2007) Multiple k-nn classifiers fusion based on evidence theory. In: 2007 IEEE international conference on automation and logistics, pp 2155–2159

Diagnostics of Slow Rotating Bearings Using a Novel DAI Based on Acoustic Emission

Sylvester A. Aye, P. Stephan Heyns and Coenie J.H. Thiart

Abstract This study develops a novel integrated non-linear method for the effective feature extraction from an acoustic emission (AE) signal and the construction of a degradation assessment index (DAI) which is subsequently used for the fault diagnostics of slow rotating bearings. A slow rotating bearing test rig was developed to measure AE data under variable operational conditions. The aim of the study was to detect incipient damage and develop diagnostics which would be robust under changing operating conditions. The proposed model consists of a combination of polynomial kernel principal component analysis (PKPCA), a Gaussian mixture model (GMM) and an exponentially weighted moving average (EWMA). The proposed novel DAI is shown to be effective and suitable for monitoring the degradation of slow rotating bearings under investigation and is robust under variable operating conditions.

Keywords Diagnostics · Degradation assessment index · Polynomial kernel principal component analysis · Gaussian mixture model · Exponentially weighted moving average

Contents

1 Introduction 322
2 Methodology 323
3 Experimental Setup 324

S.A. Aye (✉) · P.S. Heyns · C.J.H. Thiart
Centre for Asset Integrity Management, Department of Mechanical and Aeronautical Engineering, University of Pretoria, Pretoria 0002, South Africa
e-mail: Sylvester.Aye@up.ac.za

P.S. Heyns
e-mail: Stephan.Heyns@up.ac.za

C.J.H. Thiart
e-mail: Coenie.Thiart@up.ac.za

F. Chaari et al. (eds.), *Advances in Condition Monitoring of Machinery in Non-Stationary Operations*, Applied Condition Monitoring 4,
DOI 10.1007/978-3-319-20463-5_24

4 Results and Discussion: Evaluation of the Proposed DAI Using Benchmark Studies.... 325
5 Conclusions..... 331
References..... 332

1 Introduction

There are many condition monitoring (CM) techniques for bearing diagnostics. These include vibration analysis, acoustic emission (AE), oil analysis, wear debris analysis and temperature analysis [1, 2]. Vibration analysis is the most commonly used technique but vibration-based methods have been shown to be effective when the defect in the bearings has already become severe. The vibration signal is generally not sensitive to the early stages of incipient faults. Furthermore, the vibration signal caused by bearing defects are often contaminated and distorted by other faults and mechanical noise [3]. Although it is possible to detect typical faults using vibration analysis, this is effective primarily in high-speed machinery [4].

Slow rotating bearings, which are the focus of this research, pose special challenges such as: being utilized at different rotational speeds, huge load variations, very high downtime costs, corrosion and contamination. AE seems to offer distinct advantages for monitoring slow rotating bearings. These include high rates of success in detecting damage in slow rotating bearings; earlier fault detection owing to its higher sensitivity; and application to a wide range of rotational speeds with significant advantages at slow rotational speeds [5].

In recent years, more and more researchers [6–12] have investigated the application of AE technique to the CM of bearings. Despite the distinct advantages of AE for monitoring the condition of slow rotating bearings, it has some shortcomings when processing the signal. One problem is the high frequencies that lead to large data files and the requirement for large memory space during the data acquisition phase. Another problem is the lack of periodicity that makes it inappropriate to process the signal in the frequency domain. Hence this study employs a time domain approach.

One of the challenges of bearing diagnostics is the effective evaluation of the degradation process, based on the features extracted. In spite of the fact that a large selection of extracted features can be used to depict the characteristics of AE signals, earlier studies have demonstrated that each feature is only effective for depicting specific defects at specific stages [13]. Moreover, it is difficult to quantitatively diagnose the severity of damage, especially at an early stage. The main diagnostic methods fall into two main approaches, namely the data-driven and model-based approaches. The data-driven approach is divided into statistical approaches [2, 14–16] and artificial intelligence (AI) approaches [17–19]. Several studies [20, 21] are applications of model-based approaches. Bayesian techniques which are mainly statistical are gaining widespread application in detecting damage to bearings, because these techniques can handle uncertainties better than the traditional statistical methods.

Some existing studies developed one or more CM indexes [22–30]. Though some studies implemented the dimensionality reduction of the original features, and hence reduced the large amount of correlation in the original features, others did not. Some of these studies considered the multimodal nature of the data but not the non-linearities. Others considered the non-linear nature of the data but did not consider the multimodal nature of the data. Others captured the dynamics of the system, filtered out noise and captured non-stationarities by using EWMA, others did not. The studies that used a Bayesian approach incorporated prior information and captured uncertainties in the data and parameters, others did not. Moreover, all these studies were conducted under constant operating conditions. Overall, no single study simultaneously captured the non-linearities and multimodal distribution of the extracted features, the dynamics of the system, noise filtering, non-stationarity and uncertainties in the data and the parameters of the model.

Against this background, this study used existing statistical data-driven Bayesian methods to develop a novel integrated methodology for slow rotating bearing fault diagnostics, based on AE data obtained from a run-to-failure experiment. The proposed model is capable of accounting for data dimensionality reduction and hence for the reduction of high feature correlation, non-linearities, noise filtering, non-stationarities, uncertainties, time variation (dynamics) and multimodal distribution in the data, under varying operating conditions. An index which accounts for these characteristics for the assessment of machine performance is vital for effective diagnostics. A number of studies, as listed previously, have developed CM indexes under different names, but to the best of our knowledge, no previous study has used the exact methodology proposed in this study for building a CM index. Hence, the proposed approach is considered a novel contribution to literature.

2 Methodology

The scheme used for developing the proposed degradation assessment index (DAI) for the diagnostics of slow rotating bearings is shown in Fig. 1.

The effectiveness of the proposed DAI is evaluated by comparing its performance with that of other monitoring indexes. To this end, the proposed model is

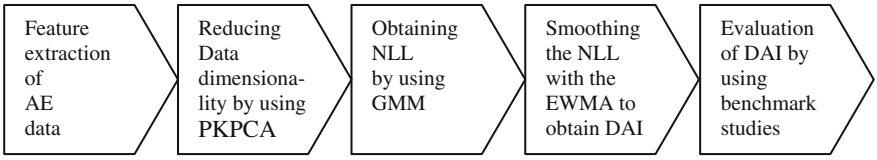

Fig. 1 Schematics for developing DAI for the diagnostics of slow rotating bearings *Key AE* Acoustic emission; *PKPCA* Polynomial kernel principal component analysis; *NLL* Negative log likelihoods; *GMM* Gaussian mixture models; *EWMA* Exponentially weighted moving average; *DAI* Degradation assessment index

reordered to form three other different submodels which essentially correspond to some of the models that may have been used in other studies for developing CM indexes. In other words, each submodel misses at least one component that is utilised in the proposed model. The models consist of the DAI model, the PKPCA-EWMA model, the PKPCA-GMM model and the GMM-EWMA model.

3 Experimental Setup

An experimental setup was used in this research to collect AE signals from a slow rotating bearing. The test setup was designed so that it would be able to test slow rotating bearings. The experimental test setup is shown in Fig. 2 below and was used in this study to collect the AE signals generated by slow rotating bearings.

A controller controlled the rotational speed of the bearing. The system was driven by an AC servo motor with the speed set at 70, 80 and 100 rpm for bearings 1, 2 and 3 respectively. An AE sensor was mounted on the housing of the test Timken bearing.

The life of the slow rotating bearings was tested until failure, which occurred on the outer race for all the bearings considered here. Ground metal debris was introduced gradually into Bearing 1 at the openings between the outer race, rollers and inner race to accelerate the initiation of damage. Bearings 2 and 3 were simply not lubricated from the start to the end of the measurement process in order to speed up the bearing degradation. The slow rotating bearing was loaded at various dynamic loads by using an electrodynamic shaker. Bearing 1 was sinusoidally loaded over a range from 1.6 to −1.0 kN. Bearing 2 was loaded between 1.8 and −1.4 kN, whereas Bearing 3 was loaded between 2.0 and −1.7 kN. The excitation frequency was approximately 2 Hz.

The major components of the slow rotating bearing test setup are the Zonic Xcite 1100-4-FT System hydraulic shaker (load actuator), the load cell, the Timken

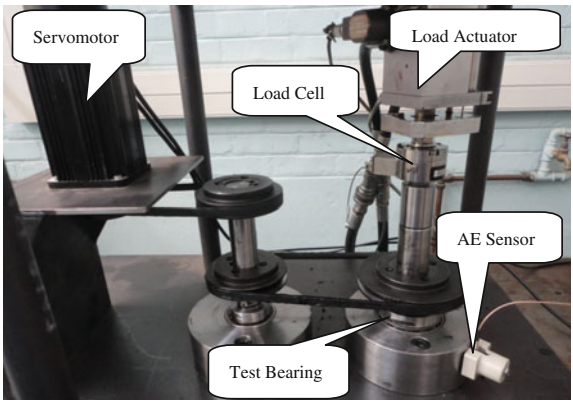

Fig. 2 Test setup

tapered roller test bearings with bearing number HR 30307 J, the AC servo motor with model number 80MT-M04025, the speed controller and a National Instruments data acquisition card with a shielded BNC Connector Block.

The Soundwel AE sensor with model number SR 150 M was used for collecting the data in an analogue form. This broadband piezoelectric AE transducer was connected to a 40-dB gain pre-amplifier. The AE transducer was mounted on the bearing housing.

The AE signal was recorded at a sampling frequency of 200 kHz over a sampling period of 1 s, using the NI PCI 6110 data acquisition card with the model occupying one of the ISA slots in a host computer. Data records were taken every 20 min until all three bearings failed, using the National Instruments Lab View software. The function for capturing the time domain and the pre-selected sampling time and interval was used. The recorded data was subsequently processed by means of dedicated Matlab programs.

4 Results and Discussion: Evaluation of the Proposed DAI Using Benchmark Studies

Normal slow speed bearings were run until failure in this study. Figure 3 presents the AE signals for the healthy, slightly degraded and severely degraded states of Bearing 1.

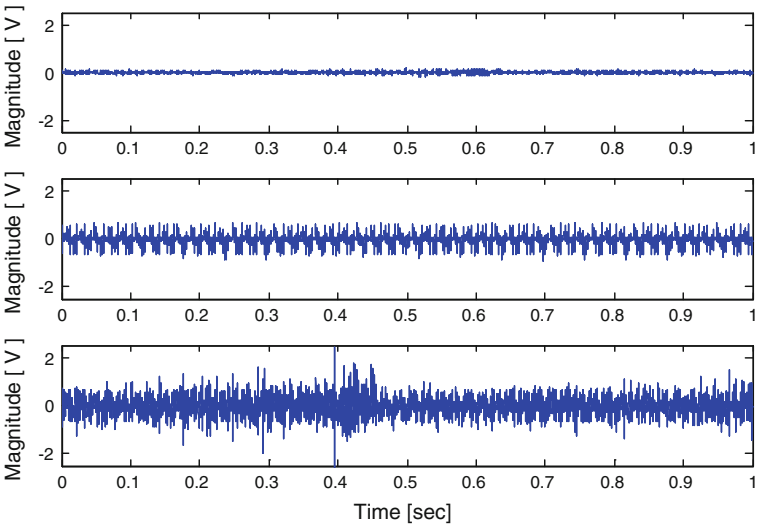

Fig. 3 AE signal for bearing 1: *topmost* (healthy state); *middle* (slightly degraded state) and *bottom* (severely degraded state)

The effectiveness of the proposed DAI was evaluated by comparing its performance with that of other CM indexes. To this end, the proposed model was reordered to form three additional different submodels which basically represent some of the models that may have been used in other studies for developing CM indexes. In order words, each submodel misses at least one component that is captured in the proposed model. The different models and their capabilities are shown in Table 1.

The DAI (PKPCA-GMM-EWMA) was the model proposed for this study. Since it is a combination of the polynomial kernel principal component analysis (PKPCA), the Gaussian mixture model (GMM) and the exponentially weighted moving average (EWMA) models, it combines all the features of the three individual models. When bearings are run under varying operating conditions, there is a high likelihood that the extracted features will have non-linear and or multimodal (multiple modes) distribution [28]. The PKPCA submodel is capable of reducing the dimension of the extracted AE features (kurtosis, RMS, crest factor, skewness and peak-to-peak) from a non-linear high-dimensional data space to a linear low-dimensional data space, in this way reducing the high correlation existing in the original features. The PKPCA model neither accounts for noise in the various AE features nor does it permit an incorporation of external knowledge (priors) about the model. Moreover, the PKPCA model is a static model as it does not capture the dynamics of the system (i.e. the historical time evolution of the monitoring statistics). Hence, the PKPCA model does not account for time variation in the data.

After extracting the features from the high-dimensional data via PKPCA, the multimodal features in the low-dimension can still be preserved. Therefore, for the effective diagnosis of bearing faults and assessment of performance degradation, the GMM submodel is used to describe the multimodal distribution of the data. The GMM is accordingly capable of handling the multimodal and non-linear features of the data by using a mixture of Gaussian components. Moreover, as the GMM is a Bayesian technique, it allows one to combine external information with the information in the data through a prior density function. Hence, all variables and parameters are considered as random or stochastic and their behaviour is described by a probability density function. This enables the GMM to handle uncertainties in the data and parameters. Like the PKPCA, the GMM model is a static model. However, the EWMA model developed by Wold [31] is a dynamic non-linear model that includes a memory function by using historical data for monitoring a bearing or any other systems [23]. This makes it capable of improving the sensitivity and reliability of monitoring techniques to detect a slight degradation or shifts in the performance of bearings [28]. It also smoothens and filters out noise in the data and is therefore capable of capturing non-stationarity.

Following the above features of the three submodels, the DAI model can handle the non-linear and multimodal distribution of the data, incorporates prior knowledge, accounts for uncertainty in both the data and the parameters of the model and is dynamic. The PKPCA-EWMA is a combination of the PKPCA and EWMA models so it is capable of handling non-linearities and the dynamic characteristics in the extracted features. However, it does not handle multimodal distribution nor

Table 1 Model reordering

PKPCA-GMM-EWMA		Handles non-linear data	Handles multi-modal distribution	Incorporates prior knowledge	Handles uncertainties	Dimensionally reduction	Dynamic or time variation and filters noise	
PKPCA	PKPCA	✓	×	×	×	✓	×	PKPCA-EWMA
PKPCA-GMM	GMM	✓	✓	✓	✓	×	×	
GMM-EWMA	EWMA	✓	×	×	×	×	✓	

account for uncertainties in the parameters of the model and it does not incorporate prior information. The PKPCA-GMM model has all the features or capabilities of the DAI model except that it is not dynamic, but static. The GMM-EWMA model also has all the capabilities of the DAI model, except that the concept of dimensionality reduction is not involved, meaning that the model uses all the extracted features.

There are several methods for selecting the optimal number of principal components from the PKPCA-EWMA model. These include the use of scree plots, the cumulative percentage variance explained, cross–validation and the PCs with eigenvalues equal to or greater than the average eigenvalue. This study employs the cumulative percentage variance explained [32] where the number of principal components that explain a cumulative percentage variance of between 70 and 90 % is selected. Two principal components were selected in the present study as they accounted for over 78 % of the cumulative variance. These two retained principal components were subsequently used either to construct the traditional monitoring statistics Hotelling's T^2 and squared prediction error (SPE) as inputs into the GMM model.

The effectiveness of the proposed model was tested by comparing its degree of accuracy in discriminating between healthy and faulty bearing conditions with that of the submodels. The evaluation of performance can be reported by using the false alarm rate and the detection rate criteria. The false alarm rate gives information about the robustness of each model to healthy system changes. The detection rate gives information about the sensitivity and efficiency of detecting faults. The rates are obtained by counting the percentage of samples that fall outside the 99.7 % confidence level used in setting the thresholds. Since two thresholds have been defined, the detection rate was also classified into a slightly degraded detection rate and a severely degraded detection rate.

The plots showing the monitoring indexes obtained from the different models are discussed before discussing the qualitative assessment. Figure 4 shows the results for Bearing 1 including the slight and severe degradation thresholds (DTs). The slight and severe DTs were obtained by using the kernel density estimation methods on the healthy and faulty bearing data respectively. Once slight DT is exceeded this indicates the commencement of incipient damage whereas once the severe DT is exceeded it indicates the start of final failure. A number of observations emerge from these figures. The monitoring indexes from the DAI, PKPCA-EWMA-T^2 and PKPCA-EWMA-SPE models appear to perform better than the index from the GMM-EWMA model, in terms of less volatility (stability or stationarity) and also the ability to discriminate between faulty and normal operating working conditions, with the exception of the PKPCA-GMM that appears to be as volatile as the GMM-EWMA. This is not surprising, given that the inclusion of all the original extracted features in the GMM-EWMA model can obscure its ability to monitor the degradation trends effectively. The PKPCA-GMM's non-stationarity can be attributed to the absence of the EWMA smoothening and noise filtering in this model. It can also be observed that the PKPCA-EWMA-SPE statistic shows a

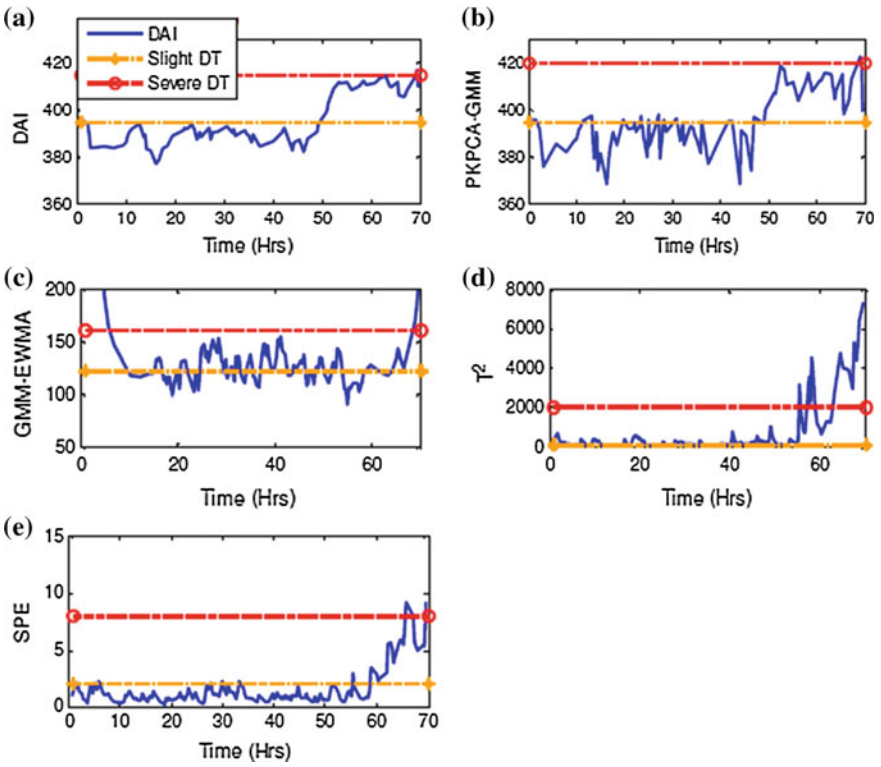

Fig. 4 CM indexes for bearing 1 **a** DAI **b** PKPCA-GMM **c** GMM-EWMA **d** PKPCA-EWMA-T^2 and **e** PKPCA-EWMA-SPE

clearer distinction between the normal operating condition and the faulty state than its counterpart T^2 statistic.

The quantitative assessment of the effectiveness of each model in assessing the health states of each of the slow rotating bearings requires a comparison of its fault alarm rates, the slight degradation detection rates and the severe degradation detection rates with those of the submodels. The results of the comparison are presented in Table 2 for Bearings 1, 2 and 3.

First, by focusing on Bearing 1, it can be seen that the proposed index from the DAI model has the least fault alarm rate (1.97 %), meaning that in the normal bearing operating region, the index crosses the 99.7 % confidence level 1.97 times out of 100, whereas the worst index (GMM-EWMA) crosses the threshold about 55 times out of 100 when the bearing is actually healthy. The proposed model could perfectly detect a slight fault and remained within the threshold of the slight degradation state 100 % of the time, followed by PKPC-GMM with a slight degradation detection rate of 75 %. The proposed model's performance was poor in terms of its ability to detect severe degradation as it missed 50 % of the time. In this case, the PKPCA-EWMA-T^2 performed better. For Bearing 2, the proposed model had a

Table 2 False alarm and degradation detection rates of the three bearings (%)

Bearings	False alarm and fault detection rate	PKPCA-GMM-EWMA	PKPCA-GMM	GMM-EWMA	PKPCA-EWMA	
					T^2	SPE
Bearing 1	False alarm rate	1.97	25.45	55.45	42.31	4.23
	Slight degradation detection rate	100.00	75.00	42.31	61.54	60.87
	Severe degradation detection rate	50.00	50.00	50.00	60.00	42.86
Bearing 2	False alarm rate	0.00	25.00	20.00	65.48	20.53
	Slight degradation detection rate	100.00	77.78	29.73	84.21	94.12
	Severe degradation detection rate	54.55	53.85	50.00	62.00	65.00
Bearing 3	False alarm rate	7.50	32.43	12.36	72.22	7.62
	Slight degradation detection rate	88.89	76.92	56.25	75.00	83.33
	Severe degradation detection rate	100.00	100.00	80.00	92.31	60.00

0 % false alarm rate whereas no other model did as well. In terms of the ability to detect a slight degradation, the proposed model performed better and had a detection rate of 100 % whereas the second-best model, PKPC-EWMA-SPE, had a detection rate of 94 %.

For Bearing 3, the proposed model still had the lowest fault alarm rate (7.50 %) followed by the PKPC-EWMA-SPE model with a fault alarm rate of 7.62 %. In terms of detecting a slight degradation, the detection rate was approximately 89 % for the proposed model followed by the PKPCA-EWMA-SPE model; whereas it performed as well as the PKPCA-GMM model in terms of detecting severe degradation. The quantitative analysis confirms the analysis of the visual plots. Overall, the proposed model performed better than the other models in terms of the fault alarm rate and the fault detection rates.

The overall superiority of the monitoring performance of the DAI can be attributed to the fact that it uses fewer kernel principal components from the original features, thus reducing redundancies in the data. In addition, it incorporates the dynamics of the slow rotating bearings, making it more sensitive to and reliable in detecting slight faults via EWMA; accounts for non-linearities and multimodal distribution in the data, thus eliminating the bias arising from wrong model specifications; handles adequate filtering of noise; allows for smooth characteristics of the features through both GMM and EWMA subcomponents; reduces uncertainties in the measurement of the data as well as in the estimations of the parameters of the model; and permits the incorporation of external knowledge via the prior density function characterisation in the GMM component.

5 Conclusions

The effectiveness of the DAI was investigated by comparing its performance with other CM indexes and it was found to outperform them. The DAI was the only model with all these properties: it uses fewer kernel principal components from the original features thereby reducing redundancies in the data, incorporates the dynamics of the slow rotating bearings thereby making it more sensitive to and reliable in detecting slight faults via EWMA, accounts for the non-linearities and multimodal distribution in the data thus eliminating the bias arising from wrong model specifications, filters noise, allows for the smooth characteristics of the features through both the GMM and EWMA subcomponents, reduces the uncertainties in the measurement of the data as well as in estimations of the parameters of the model, and permits the incorporation of external knowledge via the prior density function characterisation in the GMM component. In this investigation, the proposed DAI has been proven to be effective in the CM of slow rotating bearings under varying operating conditions.

References

1. Tandon N, Choudhury A (1999) A review of vibration and acoustic measurement methods for the detection of defects in rolling element bearings. Tribol Int 32:469–480
2. Jardine AK, Lin D, Banjevic D (2006) A review on machinery diagnostics and prognostics implementing condition based maintenance. Mech Syst Sig Process 20(7):1483–1510
3. He Y, Friswell MI, Zhang X (2009) Defect diagnosis for rolling element bearings using acoustic emission. J Vibr Acoust 131(6):1–10
4. Kim EY, Tan ACC, Yang B, Kosse V (2007) Experimental study on condition monitoring of low speed bearings: time domain analysis. In: Proceedings of the 5th australasian congress on applied mechanics (ACAM 2007), Brisbane, Australia, 10–12 December 2007
5. Mba D (2003) Acoustic emissions and monitoring bearing health. Tribol Trans 46(3):447–451
6. Nienhaus K, Boos FD, Garate K, Baltes R (2012) Development of acoustic emission (AE) based defect parameters for slow rotating roller bearings. In: 25th International congress on condition monitoring and diagnostic engineering, IOP Publishing, Journal of Physics: conference series, 364. 012034. doi:10.1088/1742-6596/364/1/012034
7. Yoshioka T (1992) Detection of rolling contact subsurface fatigue cracks using acoustic emission technique. J Soc Tribologists Lubr Eng 49:303–308
8. Li CJ, Li SY (1995) Acoustic emission analysis for bearing condition monitoring. Wear 185:67–74
9. Shiroishi J, Li Y, Liang S, Kurfess T (1997) Bearing condition diagnostics via vibration and acoustic emission measurements. Mech Syst Sig Process 11(5):693–705
10. Mba D, Bannister RH, Findlay GE (1999) Condition monitoring of low-speed rotating machinery using stress waves: parts I and II. Proc Inst Mech Eng 213(E):153–185
11. Mba D (2005) Prognostic opportunities offered by acoustic emission for monitoring bearings and gearboxes. In: Twelfth international congress on sound and vibration, Lisbon, 11–12 July 2005. http://www.iiav.org/archives_icsv/2005_icsv12/content/papers/pdf-files/FP1009_Mba.pdf
12. Elforjani M, Mba D (2011) Condition monitoring of slow-speed shafts and bearings with acoustic emission. Strain 47(2):350–363
13. Yu J-B (2011) Bearing performance degradation assessment using locality preserving projections. Expert Syst Appl 38:7440–7450
14. Phelps E, Willett P, Kirubarajan T (2001) A statistical approach to prognostics. Component and systems diagnostics, prognosis and health management, Bellingham 4389:23–34
15. Wang W (2002) A model to predict the residual life of rolling element bearings given monitored condition information to date. IMA J Manage Math 13:3–16
16. Vlok P-J, Wnek M, Zygmunt M (2004) Utilising statistical residual life estimates of bearings to quantify the influence of preventive maintenance actions. Mech Syst Sig Process 18:833–847
17. Zhang S, Ganesan R (1997) Multivariable trend analysis using neural networks for intelligent diagnostics of rotating machinery, transactions of the ASME. J Eng Gas Turbines Power 119:378–384
18. Yam RCM, Tse PW, Li L, Tu P (2001) Intelligent predictive decision support system for condition-based maintenance. Int J Adv Manuf Technol 17:383–391
19. Wang WQ, Golnaraghi MF, Ismail F (2004) Prognosis of machine health condition using neuro-fuzzy systems. Mech Syst Sig Process 18:813–831
20. Bolander N, Qiu H, Eklund N, Hindle E, Rosenfeld T (2009) Physics-based remaining useful life prediction for aircraft engine bearing prognosis. In: Annual conference of the prognostics and health management society, San Diego, CA, 27 Sept 2009–1 Oct 2009
21. Camcia F, Medjaher K, Zerhounib N, Nectoux P (2012) Feature evaluation for effective bearing prognostics. Qual Reliab Eng Int 1–15. doi:10.1002/qre.1396
22. Lee J-M, Yoo C, Choi SW, Vanrolleghem PA, Lee I-B (2004) Nonlinear process monitoring using kernel principal component analysis. Chem Eng Sci 59:223–234

23. Yoo CK, Lee IB (2006) Nonlinear multivariate filtering and bioprocess monitoring for supervising nonlinear biological processes. Process Biochem 41:1854–1863
24. Shu-kai Q, Xue-peng F, Xiao-bo C (2008) Fault diagnosis method based on the EWMA dynamic kernel principal component analysis. In: Proceedings of the IEEE 2008 Chinese control and decision conference (CCDC), pp 463–467
25. Sun C, Zhang Z, Cheng W, He Z, Shen Z, Chen B, Zhang L (2013) Manifold subspace distance derived from kernel principal angles and its applications to machinery structural damage assessment. Smart Mater Struct 22:1–12
26. Qiu H, Lee J, Yu G (2003) Robust performance degradation assessment methods for enhanced rolling element bearing prognostics. Adv Eng Inf 17:127–140
27. Ma J (2012) Development of integrated prognostics application to bearing and bevel gear life prediction. Ph.D. thesis, Industrial engineering and operations research, University of Illinois at Chicago
28. Yu J (2011) Bearing performance degradation assessment using locality preserving projections and Gaussian mixture models. Mech Syst Sig Process 25(7):2573–2588
29. Shen Z, He Z, Chen X, Sun C, Liu Z (2012) A monotonic degradation assessment index of rolling bearings using fuzzy support vector data description and running time. Sensors 12:10109–10135
30. Dong S, Luo T (2013) Bearing degradation process prediction based on PCA and optimised LS-SVM model. Measurement 46:3143–3152
31. Wold S (1994) Exponentially weighted moving principal components and projections to latent structures. Chemometr Intell Lab Syst 23:149–161
32. Martinez L, Martinez A (2004) Exploratory data analysis with matlab. CRS Press, USA

Development of Expert System Shell for Coal Mining Industry

Piotr Przystałka, Wojciech Moczulski, Anna Timofiejczuk, Mateusz Kalisch and Marek Sikora

Abstract The paper deals with the design of an expert system shell for the decision support system that is developed to be used in coal mining industry. A proposed architecture of the system allows reasoning by means of multi-domain knowledge representations and multi-inference engines. The implementation of the system is based on data mining software (RapidMiner) which makes possible to acquire domain-specific knowledge and its application in the expert system shell. In this study, the preliminary verification is presented using DAMADICS simulator that was proposed to compare different fault diagnosis methods. The obtained results show the merits and limitations of the proposed approach.

Keywords Diagnostic expert systems · Knowledge representations · Machine learning · Data mining · Fault detection and isolation

P. Przystałka · W. Moczulski · A. Timofiejczuk (✉) · M. Kalisch
Institute of Fundamentals of Machinery Design, Silesian University of Technology, Konarskiego 18A, 44-100 Gliwice, Poland
e-mail: anna.timofiejczuk@polsl.pl

P. Przystałka
e-mail: piotr.przystalka@polsl.pl

W. Moczulski
e-mail: wojciech.moczulski@polsl.pl

M. Kalisch
e-mail: mateusz.kalisch@polsl.pl

M. Sikora
Institute of Innovative Technologies EMAG, Katowice, Poland
e-mail: m.sikora@emag.pl; marek.sikora@polsl.pl

M. Sikora
Institute of Computer Sciences, Silesian University of Technology, Akademicka 16, 44-100 Gliwice, Poland

F. Chaari et al. (eds.), *Advances in Condition Monitoring of Machinery in Non-Stationary Operations*, Applied Condition Monitoring 4,
DOI 10.1007/978-3-319-20463-5_25

Contents

1 Introduction 336
2 Related Work 337
3 Description of the DISESOR System 338
4 Model of the Proposed Expert System Shell 340
5 Expert System Implementation 341
6 A Case Study 343
6.1 Diagnostic Tests for Fault Detection and Isolation 344
6.2 Example of Verification Studies 345
7 Conclusions 347
References 347

1 Introduction

Nowadays, expert systems are frequently applied for solving real-world problems. Expert systems were successfully employed in many areas such as medicine, education, entertainment, risk management and fault diagnosis [1, 2]. In the area of mining engineering, expert systems also play a very important role, what is observed in the activity of scientists and engineers. The state of the art analysis in this domain shows that the propositions of expert systems for coal mining industry are quite different from each other and they are not developed taking into account all aspects of management of mining companies (they are in majority subject-oriented). In this paper, the authors proposed the idea of an expert system shell which is very similar to a solution described in [3], where multiple knowledge models and hierarchical reasoning were suggested to eliminate the limitations of traditional expert systems. The novelty in our approach depends on that the expert system is not only used for fault diagnosis but it can also be employed for other purposes corresponding to the coal mining industry. Hence, the overall goal of the research is to design a more generic and complete expert system shell environment in comparison to previous expert system engines which are known from the literature. Moreover, the core of the proposed expert system shell is not designed as a new tool but the data mining software is adopted. The proposed solution is motivated by the fact that users usually prefer to work with already known tools instead of learning how to apply completely new means.

The development of the diagnostic expert system shell with multi-domain knowledge representations and multi-inference engines is realized within the frame of the DISESOR project. The DISESOR is an acronym of a decision support system designed for fault diagnosis of machinery and other equipment operating in underground mines as well as for monitoring potential threats that can occur in such kind of industry. This system is designed by the authors of the paper in collaboration with researchers and engineers from Institute of Innovative Technologies EMAG, Silesian University of Technology, University of Warsaw and Sevitel company.

2 Related Work

In 1990s, a more attention has been duly focused on development of expert systems for mining industry, and it was the cause to initiate expanding different methodologies in this field. Grayson et al. [4] applied a knowledge-based expert system for better managing underground coal mines. Their system concentrated on capturing the complex body of knowledge needed to enhance efficient management of a mine and therefore it encompassed information and preferred rules on work scheduling, work practices, responses to operating problems, etc. Another knowledge based expert system was developed by [5] for the combat of fires and also pollution due to fires by analysing the different causes of fires in underground conditions with the help of certainty factor techniques.

Zhang and Zhao [6] developed a system called Coal Mining Expert and Optimization Consultation System. The system was a preliminary attempt to combine expert systems and optimization techniques in the Chinese coal mining industry. It was applied to determine the underground mining methods, open-pit mining and transportation systems, etc. The proposed approach was developed using AI language Prolog and software engineering principles and methods. In the paper [7], the authors designed and applied a kind of expert system based on a function detection for supervision workstations of coal mines. Their system adopted production rules to expert's knowledge, and the inference process was based on forward and backward reasoning. The design and implementation of a safety expert information management system for coal mine was proposed in Wang and Z. Wang [8]. The authors developed the safety information processing system according to a fault tree, which run under the way of web site technology. At present the system is being applied in Zibo mining industry group and Xu Chang coal plants in China. The paper [9] gives a concept of an expert system for estimation and optimization of coal mines in terms of their eco-efficiency. The proposed solution was not a classical expert system, but rather a set of computer tools for management of a mining company. The more complementary discussion on the survey on the application of expert systems in the mining industry can be found for example in Chekushina et al. [10].

As it is mentioned in the previous section the expert systems for coal mining industry are limited due to the facts that they are developed without taking into account all aspects of management of mining companies as well as their engines and user interfaces are completely different from each other. Therefore, there is a need to elaborate a much more advanced expert system shell based on the well known tools which will be easy to apply by end users.

3 Description of the DISESOR System

The DISESOR system can be used for different purposes, e.g. to assess seismic hazard probabilities in the area of a coal mine, to forecast a dangerous increase in the methane concentration in mine shafts, to detect and localize endogenous fires, and also to conduct the fault diagnostics of machines working in such environment. A diagram of data flow in the DISESOR system is presented in Fig. 1. This scheme shows an idea of an expert system in the context of other modules. The description explains functionalities of all components of the designed system.

The data repository is proposed to integrate the data coming from varied dispatches and supervisory systems of coal mines, for instance THOR [11], SMoK [12] systems, etc. The data repository together with interfaces such as Extract, Transform, Load (ETL) module and data cleansing are necessary for validation and processing the input data and information provided by other components of the system. The structure of the repository is designed in such a way that it is possible to feed a wide spectrum of data obtained from measurements. Moreover, different

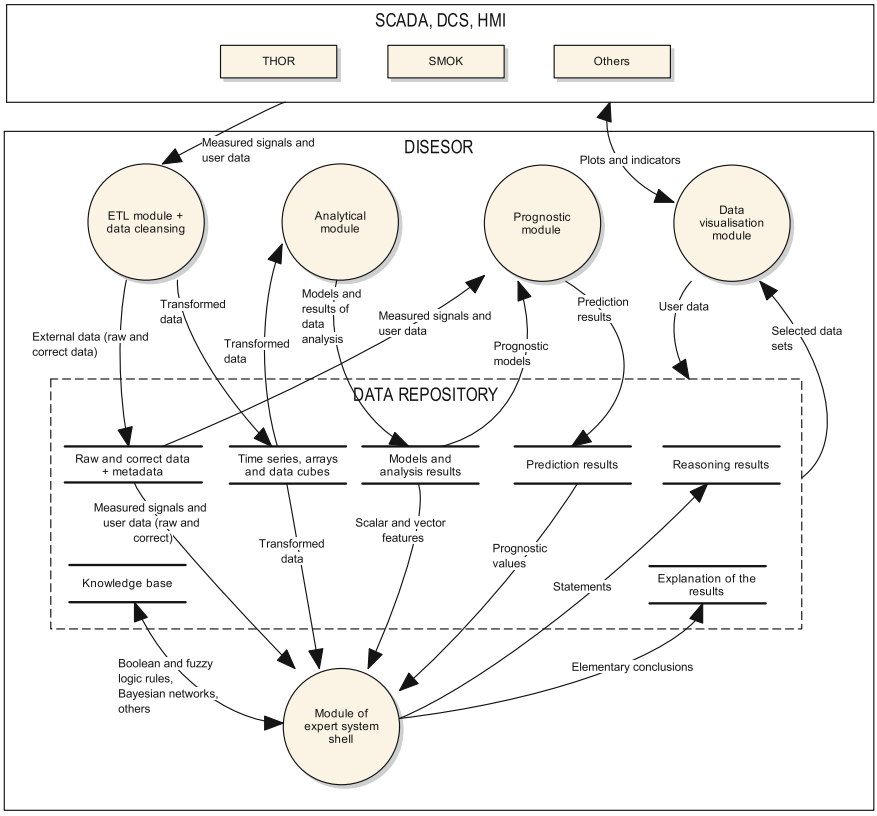

Fig. 1 A data flow diagram of the DISESOR system

layers of metadata describe the structure of a monitoring object in order to have the exact locations of actuator devices and sensors. Due to the heterogeneity of the dispatches and supervisory systems it is required to possess an independent description of the individual measuring systems of coal mines. The main functionality of the repository is to provide data to other components of the system, in particular, to analytical module, prognostic module, expert system shell and data visualization module.

The prognostic module is used for a task of incremental on-line learning of models on measured values of specified signals with a given horizon and frequency. This is also proposed for tracking trends in incoming data. In case of the prognostic models the adaptive tuning based on the input data stream in combination with a comparative analysis of previously learnt patterns of the historical data was applied. The module provides interfaces which let us choose dependent variables (subject to forecasting) as well as independent variables (supporting forecasting) and determine the preferred forecast horizon and its threshold which is needed to define the minimum quality of the prognosis. The choice of a method for data analysis together with the selection of primary and derived variables (e.g. delay) is performed automatically. In cases when the quality of prediction is in the range of threshold values specified by an user, results of the forecast can be treated as virtual data (virtual measurements) and can be used as a source of information for other modules. An important factor in the approval of the forecasts is that the elaborated model should be as transparent as possible for the end user. The analytical module is applied for executing tasks of analysis of the historical data (off-line) and reporting the identified significant relationships and trends in registered signals. The results generated by this module are used by the end user to supply the data repository. Therefore this is conformed to support the user in deciding on what kind of variables should be also monitored and forecast. It helps also to provide additional information that can be employed to enrich the knowledge base of the expert system or to carry out more advanced comparative analyses.

The main purposes of the analytical module can be characterised as follows. This module is required to obtain information about measured values (original or aggregated). It is important to know whether the information is associated with a particular aspect of the monitored process aimed at a desired or undesired direction. These values are related to other ones, and from the point of view of data it is necessary to identify the cause of the recorded changes. In the module a number of basic tasks was defined (e.g. “Follow trend”, “Compare because of”, “What if”). They can initiate analytical tasks by a choice and parametrization of predefined operations (including the choice of variables to be compared, the method of aggregation of available measurement data, the thresholds of attractiveness of discovered relations, the selection of a frequency of the comparisons, etc.). The presented functionality is not only used for aiding identification of changes in the monitored processes and devices, but also for comparing work of machine operators and dispatchers. The fundamental representation of discovered relations are rules, facts, and readable statistical indicators that let us illustrate a type and

strength of identified dependencies. The results of the analysis task made by the module are presented similarly to the natural language.

The expert system shell module is used for on-line and off-line diagnosing of technical objects and for monitoring processes. Another task of the module is to support domain experts in taking decision either on terms of the technical condition of the objects or on risk managing e.g. in situations when the process is going to an undesirable direction. The main assumption in case of operation of this module is to allow the user acquire intuitively the knowledge and store the knowledge with use of different types of representations. The expert system shell is designed in such a way that the reasoning can be based on elementary methods such as boolean and fuzzy logic, Bayesian networks, etc.

The last module was elaborated for data visualizing and reporting. The task of this part of the system is to show the measured data and information computed by other modules of the system. The visualization is realized by means of predefined charts and maps plotted with the proper graduations. The module is also equipped with tools for creating report.

4 Model of the Proposed Expert System Shell

The case diagram of the proposed expert system shell is given in Fig. 2. The system consists of two layers. The first layer is called a management layer and it is used to supervise the whole system. There are included several functionalities such as a mode selection that can be used to switch the system into one of three different modes. The on-line mode serves in situations when the scheduler of the reasoning process is created. In this mode an user (a knowledge engineer) is able also observe the parallel execution of the scheduler logic. The off-line mode is often applied for ad hoc reasoning on historical data. The last mode is necessary for editing the knowledge base.

The engine of the system is implemented in the second layer (the execution layer). The user is able to clearly edit the knowledge base using three different knowledge representations which are Boolean logic, fuzzy logic and Bayesian networks. The user can also define the vocabulary of statements in order to prepare the description of a monitored object. The execution layer applies multi-domain knowledge representations for reasoning by means of the multi-interference engine. The inference procedures are executed using selected reasoning mechanisms in order to prepare a conclusion. It is also assumed that a context may be taken into account in the condition part of the rules or input nodes of the Bayesian network (it is an extended use case). In the next step the elementary conclusions are results of a fusion process. The output of the system (statements) is obtained for measured and user data. The last use case of the system is the possibility to record the results of the reasoning in order to realize the explanation interface.

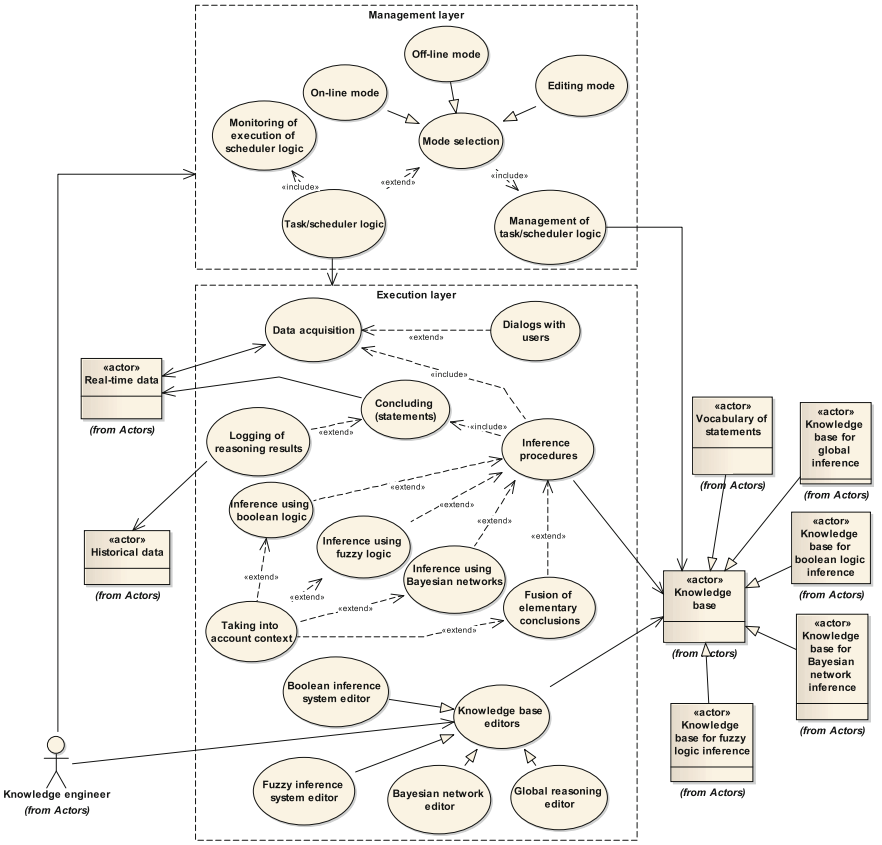

Fig. 2 A use case diagram of the proposed expert system shell

5 Expert System Implementation

The authors of the DISESOR project decided to apply RapidMiner software as an engine of their decision support system. There are many free and commercial applications created by developers to solve data mining and classification problems, e.g.: Weka [13], R language [14], Orange [15], Statistica [16], Angoss Knowledge Studio [17]. Most of them have an user interface which is helpful in building data mining processes. In contrast to these applications, the main environment of R language is a text editor. R language is a very popular open source tool which is developed by a large community of researchers. RapidMiner is a partially free software developed to solve data mining problems [18]. It has a clear interface based on drag and drop mechanism. The application allows users to make a modification in a source code and add plug-ins created by other people to extend a functionality of the program. The authors decided to use this software since

implemented methods of ensemble learning can be used for knowledge acquisition. An additional factor is that the architecture presented in Fig. 2 can be obtained in a direct way by creating new plug-ins for this software.

Due to the early stage of the system design, in this paper the authors decided to show how the applied software can be used to create different types of classification schemes which will be subsequently used in the knowledge base of the developed system. The application allows the users to implement basic methods of ensemble learning like stacking, voting, bagging, AdaBoost and others. The main purpose of this approach is to obtain a better general result than results of each of base classifiers. In a stacking operator the user is able to apply any number of base classifiers and one meta-classifier. The user decides what kind of data meta-classifier can use as its input. The voting is another method used to combine many classifiers and extract from them a single output. The voting can be divided into a few classes like unanimous voting, majority voting and weighted majority voting [19]. The unanimous voting requires the same output class from all considered classifiers. It should be only used when a number of classes is small because in case of a large number of classes it could be difficult to reach the same answers from all classifiers. In a majority voting final answer is based on the class with the highest number of votes. In case of draw, a result is randomly chosen among wining classes. Other methods like e.g. bagging and boosting create a group of classifiers based on the same method of classification [19, 20]. The main purpose of a method called bagging is to create a random data set as long as a base dataset. The probability of selecting a single value from data is the same for all values. It means that each of the row from the base dataset can be added to the output dataset many times. The new random dataset is prepared for each classifier in the group. This approach was the basis for new methods like e.g. AdaBoost. In AdaBoost algorithm each value in the base dataset has weight which determines relevance of this value. At the beginning all values have the same weight equal to 1 and the first classifier is trained on random dataset where each of the value has the same probability of drawn. Then the first classifier is tested on the same dataset. The weights of correct estimated values are decreased and the probability of drawn of incorrect values for the next classifier is higher. Each next classifier is learnt on data which contains values more difficult to classify. The final result is chosen during weighted majority voting. Another reason to use the ensemble learning is when a classifier is weak and a small change in the a learning dataset can significantly affect its efficiency [19].

The RapidMiner is equipped with many basic classifiers e.g. k-nearest neighbour, naive bayes, neural network, decision tree, linear regression, SVM, etc. [19]. All mentioned classifiers are available in the application as operators which can be connected to other operators of process and full process looks like a data flow diagram. The main result of most classifiers is a label. Another value returned by a classifier is the degree of belief for class occurrence and it is a numerical value from 0 to 1. For some classifiers the level of belief is calculated during the learning process (e.g. decision tree, rules induction) and for other classifiers during testing process and when the classifier is used (e.g. k-nearest neighbour, naive bayes).

6 A Case Study

In this section the authors give an example of usage of base classifiers and various ensembles of classifiers to solve a fault detection and isolation problem. The case study is investigated using DAMADICS project which was elaborated for scientists and engineers to simplify the process of evaluating and comparing different methods of fault detection and isolation for industrial systems [21]. In the literature there were available several papers where case study results dealing with this problem were presented, see e.g. [22–24]. The numerical model is used to simulate an electropneumatic valve (Fig. 3) which was a part of the production line in Lublin Sugar Factory in Poland.

The model was created in MatLAB/Simulink software and was on a careful study of the physical phenomena that gave the origin of faults in the actuator system. This simulator generated the following signals of the process variables: CV —process control external signal, P1—inlet pressures on valve, P2—outlet pressures on valve, X—valve plug displacement, F—main pipeline flow rate, T—liquid temperature, f—standard diagnostic signal. All of these signals are normalized to the range between 0 and 1.

The DAMADICS simulator allows to choose only one from nineteen available faults. A part of them is considered only as incipient faults or as abrupt faults (there are three sizes of abrupt faults: small, medium and big) and some of them as both. A list of all available faults is as follows: f1—valve clogging, f2—valve or valve seat sedimentation, f3—valve or valve seat erosion, f4—increase of valve friction, f6—internal leakage, f7—medium evaporation or critical flow, f8—twisted

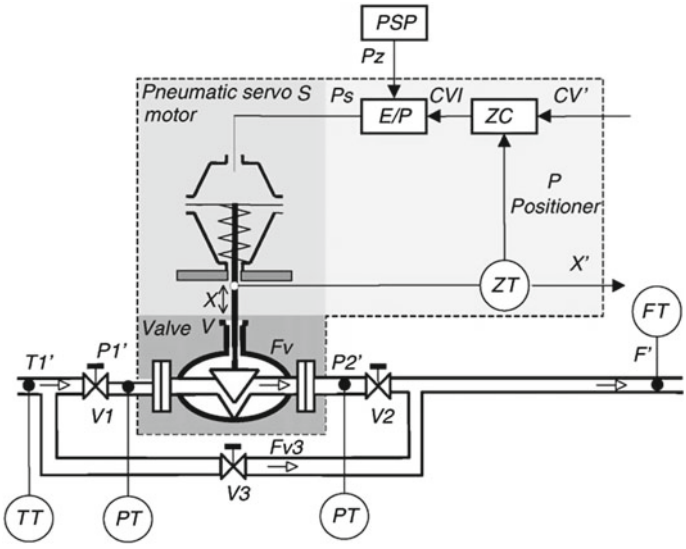

Fig. 3 Structure of benchmark actuator system [21]

servo-motor stem, f9—servomotor housing or terminal tightness, f10—servomotor diaphragm perforation, f11—servomotor spring fault, f12—electro-pneumatic transducer fault, f13—stem displacement sensor fault, f14—pressure sensor fault, f15—positioner spring fault, f16—positioner supply pressure drop, f17—unexpected pressure change across valve, f18—fully or partly opened bypass valves, f19—flow rate sensor fault. In this case the valve was controlled by a harmonic signal in which the frequency was equal to 0.01 Hz. During a simulation the device was working correctly until about 800 s than a chosen fault occurred and lasted until the end of the simulation.

A form of obtained raw signals is difficult to use directly in prepared classifiers. The control signal is harmonic and its period is equal to 100 s so the authors decided to calculate a few features of available signals in a moving window and its width was equal to a period of the control signal. During this specific fault, the minimum value of plug displacement is very useful, but for other faults only one feature can be not enough. The authors chose four basic features such as the minimum value, maximum value, average value and median, each of them was calculated in the window (the width was equal to 100 s).

6.1 Diagnostic Tests for Fault Detection and Isolation

The RapidMiner software allows us to create data mining processes with the use of a visual programming language. This tool gives the opportunity for developing different classification schemes using so-called drag and drop methodology. In this way the classification processes can be viewed as data-flow graphs. One process may contain many classifiers which allows users to create custom ensembles of classifiers. This software contains also predefined operators supporting the ensemble learning and in this paper the authors compared them with others. It is possible to use various methods to estimate efficiency of the classification such as the splitting method where dataset is divided into learning and testing datasets. Thanks to this a classifier is learnt on the first data set and tested with another dataset. This approach is used in order to avoid an over fitting problem. The over fitting problem occurs when classifier is learnt and tested on the same dataset, then an estimated efficiency can be very high, but a real efficiency for a classifier working with a new dataset can be much lower. It can be difficult to use a splitting method when the size of data is small and various. Therefore, the user can apply other methods like X-validation and leave-k-out. In these methods data is divided into learning and testing datasets a few times. At each time a new classifier is learnt and tested on a new prepared data. The general result is calculated as the average efficiency of all classifiers with the standard deviation. In this paper X-validation method was used.

6.2 Example of Verification Studies

The software used to build the system has an operator which allows the users to apply a meta-classifier. To use this method the user is obligated to select a few base classifiers and meta classifier. The user may decide if the meta-classifier should use only outputs of the base classifiers or it should use also original signals. At the beginning of a verification process the authors used single classifiers to check how well they can isolate faults. Results are shown in Table 1 (rows 1, 2, 3, 4). A single classifier based on the decision tree is characterised by the highest result equal to 85.56 %. The meta-learning tool implemented in RapidMiner software enabled to obtain the result that was 4 % higher than the best result for a single classifier.

In the experiment the naive bayes was a meta-classifier and the random tree, decision tree and naive bayes (kernel) were base classifiers. The second example of the ensemble learning was based on voting. In RapidMiner the user can apply an operator called Vote where the final decision is reached by majority voting. It is possible to use many different classifiers or the same classifiers but learnt on various data. The authors tested this method using mentioned above four classifiers and all of them were treated the same. In this case the result was a little bit worse than the result of the decision tree. Another method of the ensemble learning implemented in RapidMiner is bagging and AdaBoost. In this paper the authors chose a decision tree classifier. They used it in AdaBoost operator and compare its result with results of other methods. Thanks to the decision tree it was possible to compare a level of complexity (the number of nodes) of classifiers created by AdaBoost algorithm. The general result is a little bit worse than the result of the meta-classifier but it is also better then the result of a single decision tree. Table 2 shows a level of complexity for each of the classifier created by AdaBoost method. The classifiers created in the

Table 1 Results of various methods of classification

	Classifier	Efficiency (%)
1.	Random tree	50.07
2.	Naive bayes	84.19
3.	Decision tree	85.56
4.	Naive bayes (kernel)	84.20
5.	Meta-classifier	89.55
6.	Majority voting	85.00
7.	AdaBoost (decision tree)	87.39
8.	Custom meta-classifier	90.00

Table 2 Level of complexity of classifiers created by AdaBoost algorithm

Iteration	Level of complexity
1	22
2	22
3	36
4	44

following iterations have a higher level of complexity which means that data drawn by the algorithm in each next iterations contained elements which were more difficult to classify. The last example of the ensemble learning is based on the meta-classification without using methods implemented in RapidMiner which have some limitations.

The default output value of the classifier is a label which informs the user about an estimated class of a specific element of data. Another information returned by the classifier is a vector which contains levels of belief that belong to each of the class. But this information basically can be shown in the screen as e.g. a plot and cannot be used by other operators. RapidMiner has an operator which can freely modify data by usage of java language. In this case the operator was used to change a role of degrees of beliefs of base classifiers then this information can be used as the input data of a meta-classifier. This custom meta-classifier was based on a concept of the first meta-classifier described above. There were three different base classifiers and one meta-classifier. But this time base classifiers returned the vector of levels of beliefs instead of labels. This method obtained the highest result among all tested algorithms. Results of all tested methods are quite similar, especially the best results which were based on the meta-learning method. Only the random tree as a single classifier reaches clearly the worst result.

The authors decided to verify the influence of classifier order in the meta-learning operator and a type of input signals into the final efficiency of the classification. It was decided to use an operator implemented in RapidMiner called Stacking. At this time a meta-classifier had the same type of base classifiers so it was important to differentiate input signals for each base classifier. The authors grouped signals by a signal type and feature type. In both cases there were four base classifiers but in the first case each of them had four different features calculated for the same signal, e.g. the first classifier used features of signal X, the second classifier used features of signal F and so on. In the second case each of the base classifier used the same features calculated from all signals, e.g. the first classifier used average values of all types of input signals for the second classifier input signals contains the maximum value of all types of process variables and so on. Table 3 shows the results of eight different configurations of meta-learning.

At this part of the case study, the authors changed three parameters: a type of signal grouping, type of base classifiers, as well as type of meta-classifier. The text

Table 3 Results of various methods of meta-classification

	Meta-classifier	Efficiency (%)
1.	Features NB → NB	88.81
2.	Signals NB → NB	80.67
3.	Features DT → DT	89.69
4.	Signals DT → DT	68.02
5.	Features NB → DT	89.84
6.	Signals NB → DT	86.81
7.	Features DT → NB	86.18
8.	Signals DT → NB	81.33

in the second column of Table 3 describes a type of the configuration, e.g. Features DT → NB means that an input signals were grouped by features, base classifiers were the decision trees and meta-classifier was naive bayes. The best result for configuration Features NB → AT is almost as good as the custom meta-classifier described above.

7 Conclusions

In this paper the authors proposed the model of an expert system shell as a part of the DISESOR system that is designed to be used in the coal mining industry. The implementation of the engine of the system is based on a data mining software called RapidMiner. Thanks to this, it was possible to elaborate a much more advanced engine of the expert system shell based on a well known tool which can be easily applied by the end users. Moreover, in this paper the authors mainly showed the methodology of diagnostic tests creation based on a machine learning approach in the context of using it in the developed system. The authors compared different machine learning methods and proved that usage of the ensemble learning could improve the efficiency of classification (classifiers created in this way could be directly used as a knowledge representation in the knowledge base of the system). It was also showed how changes in data grouping and in order of classifiers could influence the final efficiency.

Taking into account the promising results of the research it is planed to use more complex classification approaches e.g. based on rough set [25] and fuzzy-rough set [26] methods, mainly due to the possibility of using some existing packages that can be potentially integrated or partially rewritten. The authors also view the proposed environment as a tool that can be employed for a wider spectrum of applications, and therefore it is considered to apply this software for solving analogues problems/tasks, e.g. in supporting a fire commander [27] or for leakage detection and localization [28].

Acknowledgements The research presented in the paper was partially financed by the National Centre of Research and Development (Poland) within the frame of the project titled "Zintegrowany, szkieletowy system wspomagania decyzji dla systemów monitorowania procesów, urzadzeń i zagrożeń" (in Polish) carried out in the path B of Applied Research Programme—grant No. PBS2/B9/20/2013. The part of the research was also financed from the statutory funds of the Institute of Fundamentals of Machinery Design.

References

1. Cholewa W (2004) Expert systems in technical diagnostics. In: Korbicz J, Kowalczuk Z, Kościelny J, Cholewa W (eds) Fault diagnosis. Springer, Berlin, pp 591–631
2. Liebowitz J (1997) The handbook of applied expert systems. CRC Press LLC, Boca Raton

3. Yang J, Ye C, Zhang X (2001) An expert system shell for fault diagnosis. Robotica 19:669–674
4. Grayson RL, Watts CM, Singh H, Yuan S, Dean JM, Reddy NP, Nutter RS Jr (1990) A knowledge-based expert system for managing underground coal mines in the us. IEEE Trans Ind Appl 26(4):98–604
5. Sahu HB, Pal BK (1996) Knowledge based expert system to assess fires and pollution to fires in underground coal. J Min Met Fuels 44(6–7)
6. Zhang H, Zhao G (1999) CMEOC an expert system in the coal mining industry. Expert Syst Appl 16:73–77
7. Yingxu Q, Hongguo Y (2010) Design and application of expert system for coal mine safety. In: Second IITA international conference on geoscience and remote sensing
8. Wang C, Wang Z (2010) Design and implementation of safety expert information management system of coal mine based on fault tree. J Softw 5(10):1114–1120
9. Golak S, Wieczorek T (2014) Koncepcja system ekspertowego do oceny i poprawy ekoefektywności kopalń. Studia Informatica 116(2):213–222
10. Chekushina EV, Vorobev AE, Chekushina TV (2013) Use of expert systems in the mining. Middle-East J Sci Res 18:1–3. doi:10.5829/idosi.mejsr.2013.18.1.12345
11. THOR main control system website, February 2015. Available at http://www.sevitel.pl/product,25,THOR.html
12. SMoK system website—monitoring system for machinery and equipment, February 2015. Available at http://www.somar.com.pl/products/smok,18,2,48
13. Weka project website, October 2014. Available at http://www.cs.waikato.ac.nz/ml/weka/
14. R project website, October 2014. Available at http://www.r-project.org/
15. Orange software website, October 2014. Available at http://orange.biolab.si/
16. Statistica software website, October 2014. Available at http://www.statsoft.pl/
17. Angoss knowledge studio website, October 2014. Available at http://www.angoss.com/
18. Akthar F, Hahne C (2012) Rapid Miner 5 Operator Reference. Rapid-I GmbH. Available at http://www.rapid-i.com
19. Kuncheva LI (2004) Combining pattern classifiers: methods and algorithms. Wiley, New Jersey
20. Woźniak M, Grana M, Corchado E (2014) A survey of multiple classifier systems as hybrid systems. Inf Fusion 16:3–17 (Special Issue on Information Fusion in Hybrid Intelligent Fusion Systems)
21. Bartyś M, Patton R, Syfert M, de las Heras S, Quevedo J (2006) Introduction to the damadics actuator fdi benchmark study. Control Eng Pract 14(6):577–596
22. Korbicz J, Kowal M (2007) Neuro-fuzzy networks and their application to fault detection of dynamical systems. Eng Appl Artif Intell 20(5):609–617,doi:10.1016/j.engappai.2006.11.009
23. Mrugalski M, Witczak M, Korbicz J (2008) Confidence estimation of the multi-layer perceptron and its application in fault detection systems. Eng Appl Artif Intell 21:895–906
24. Puig V, Witczak M, Nejjari F, Quevedo J, Korbicz J (2007) A GMDH neural network-based approach to passive robust fault detection using a constraint satisfaction backward test. Eng Appl Artif Intell 20:886–897
25. Kabiesz J, Sikora B, Sikora M, Wróbel Ł (2013) Application of rule-based models for seismic hazard prediction in coal mines. Acta Montanist Slovaca 18(4):262–277
26. Riza LS, Janusz A, Bergmeir C, Cornelis C, Herrera F, S'lezak D, Benítez JM (2014) Implementing algorithms of rough set theory and fuzzy rough set theory in the r package ŕoughsets. Inf Sci 287:68–89
27. Krasuski J, Jankowski A, Skowron A, Ślezak D (2013) From sensory data to decision making: a perspective on supporting a fire commander. In: Web intelligence/IAT workshops, pp 229–236
28. Wyczółkowski R (2008) Intelligent monitoring of local water supply system pp 3–36

Part III
Condition Monitoring Techniques

Analysis of a Planetary Gearbox Under Non-stationary Operating Conditions: Numerical and Experimental Results

Cristián Molina Vicuña and Fakher Chaari

Abstract Planetary gearboxes are used in a large variety of mechanical systems. Several of these systems undergo variable operating conditions, producing non-stationary features of measured variables typically used for condition monitoring purposes, such as vibrations. Benefits can be obtained from these signals only if the consideration of the non-stationary features is properly made. For this purpose it is necessary to conduct numerical investigation and experimental study on the dynamic behaviour of planetary gearboxes under variable operating conditions. In this paper we address the problem of a one-stage planetary gearbox driven by an asynchronous motor in open-loop control configuration and subjected to periodically variable load. The dynamic response is obtained by integrating the equation of motion using implicit Newmark algorithm. For validation, test bench measurements are performed on a planetary gearbox subjected to the same conditions simulated. The results show good agreement between the model and actual system.

Keywords Planetary gearbox · Variable operating conditions · Vibration

Contents

1 Introduction 352
2 Experimental Setup 353
2.1 Test Rig Description 353
2.2 Instrumentation and Data Acquisition 354
2.3 Test Description and Experimental Results 354

C.M. Vicuña
LVM-UdeC, Universidad de Concepción, Concepción, Chile
e-mail: crimolin@udec.cl

F. Chaari (✉)
Laboratory of Mechanics, Modeling and Production, National School of Engineers of Sfax, BP 1173, 3038 Sfax, Tunisia
e-mail: fakher.chaari@gmail.com

F. Chaari et al. (eds.), *Advances in Condition Monitoring of Machinery in Non-Stationary Operations*, Applied Condition Monitoring 4,
DOI 10.1007/978-3-319-20463-5_26

3 Model of the Gearbox 357
4 Simulation Results 359
5 Conclusions 361
References 361

1 Introduction

Planetary gears can be found in several mechanical systems with application in aerospace, automotive, and heavy industries. The main objective is to allow the transmission of large torques. However, noise and vibration remain key concern in all planetary gear industrial applications. Operating conditions such as load and speed can alter the dynamic behavior of planetary gears. If these conditions are time varying and non-stationary, vibration signals will be complex to process and analyze and the monitoring will be more difficult than for transmissions running under stationary conditions.

Diagnostic of transmissions running under non-stationary conditions is becoming one of hot topics for researchers. In fact, simultaneous load and speed variation changes vibration signal structure leading to both amplitude and frequency modulation [1] so that pure spectral analysis is no longer efficient.

Our case study is a planetary gear transmission which is frequently subjected to time varying loading conditions such as in mining machines or wind turbines. Randall [2] showed that load fluctuation modulate the vibration signals issued from meshing process. Bartelmus [3] and Bartelmus and Zimroz [4] related load level in gear transmission to vibration amplitude by linear function. They [5] showed that the presence of defects will lead to an increase of the slope of this function concluding about the necessity to use proper signal processing techniques in order to monitor and diagnose correctly planetary gearboxes.

Zimroz et al. [6] used automatic segmentation algorithm of vibration signals issued from gearbox in time frequency to estimate instantaneous rotational speed.

Khabou et al. [7] was interested in the start-up of a gearbox which is an extremely non-stationary running regime. He described the speed-load variation using the motor mechanical characteristic. Chaari et al. [1] used this procedure for a single stage spur gear transmission running under varying loading conditions and highlighted amplitude and frequency modulations in time signals using time frequency analysis.

Bouchaala et al. [8] showed that during start-up of defective gearbox transmission, high vibration levels are observed.

Chaari et al. [9] presented a model of a planetary gear transmission subjected to time varying loading and speed conditions. They simulated the dynamic behavior and highlighted the frequency modulation observed in vibration signals.

This paper is dedicated to both experimental and model based approaches to describe the dynamic behavior of planetary gear transmission subjected to time

varying loading conditions. The experimental setup is first described. Results issued from test rig for variable load and at two nominal rotational speeds of the driving motor are discussed. A model of the studied test rig is then presented. The objective is to explain the behavior of the system under non-stationary conditions.

2 Experimental Setup

2.1 Test Rig Description

Experimental measurements are taken from a planetary gearbox test rig, Fig. 1. The asynchronous motor (3 phases, 3 kW IP55, 400 V/50 Hz, class F, 4 poles) runs in open-loop configuration and is controlled by a frequency converter. The rotational speed of the motor shaft is measured by means of an optical encoder coupled to the motor shaft on the fan side. Since the motor is operated in open-loop, the relation between load and speed is determined by the motor curve, which was available from the manufacturer.

The test object is a single-stage spur gear planetary gearbox with transmission ratio of 1:5. The gearbox is used in reduction mode, which means the motor shaft is coupled to the sun gear shaft and the carrier shaft is coupled to the load unit. The gearbox has three planetary gears, each mounted on bolts and supported by needle bearings. Available details of the gearbox are listed in Table 1.

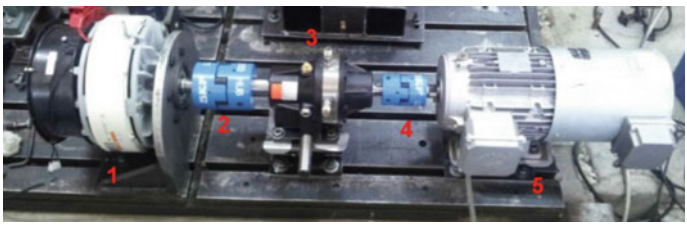

Fig. 1 Planetary gearbox test rig. (*1*) magnetic particle brake, (*2*) low-speed coupling, (*3*) planetary gearbox, (*4*) high-speed coupling, (*5*) asynchronous motor

Table 1 Planetary gearbox parameters

Parameter	Sun gear	Planet gear	Ring gear	Carrier plate	Planet bolt
Tooth number	18	26	72	–	–
Module	1.5	1.5	1.5	–	–
Mass (kg)	0.178	0.129	1.711	0.810	0.070
Pitch diameter (mm)	27	39	180	–	–
Number of planets	3, equally distributed				

The load unit is a magnetic particle brake. The maximum braking torque is limited by heat dissipation capabilities, which depend on rotational speed. For example, maximum torque at motor speed of 600 RPM is 55 Nm; at 1000 RPM is 35 Nm; etc. However, these limits can be exceeded for short periods. The braking torque is produced by creating a magnetic field between the rotor and stator. The field produces the magnetic particles to arrange and the magnetic forces between them and the rotor and stator result in the braking torque. Based on this functioning principle, it is possible to adjust the braking torque by controlling the intensity of the magnetic field, which is done by regulating the current on the stator. In this case, we use a current power supply with remote control capability by means of a 0–10 V signal. The relation between current and braking torque is obtained from the manufacturer's brake curve. The voltage/current relation is calibrated previous to the measurements. The voltage signal is generated using a D/A converter. All this arrangement allows the generation of time variable braking torque with magnitude and shape controlled by software.

2.2 Instrumentation and Data Acquisition

The vibration sensor is a 100 mV/g accelerometer, installed on the top outer part of the ring gear. A flat surface was milled on the outer ring to provide appropriate mounting surface for the sensor. The sensor is attached to the ring gear by using a stud.

Measurements were done using data acquisition hardware from National Instruments and routines programmed in LabVIEW. Separate devices with synchronized clocks were used for digitizing the signals from the accelerometer and motor optical encoder (2048 pulses/rev). The measurement system is used for simultaneous measurement of acceleration vibration and motor instantaneous angular speed.

2.3 Test Description and Experimental Results

The planetary gearbox was driven at different nominal rotational speeds. At each speed, varying braking torque in shape of a sinusoidal was applied. Figure 2 shows the result of a measurement taken at 1500 RPM and load variation between 10 and 50 Nm with a frequency of 5 Hz. As it can be seen, the varying load influences the rotational speed of the complete system, producing a periodic variation of the motor rotational speed between 1435 and 1480 RPM. As expected, the frequency of the speed variation matches the frequency of the load variation, and does have much of a sinus-like shape. On the other hand, the acceleration signal presents amplitude modulations due to the load variation. These are more clearly evidenced in Fig. 3, which shows the measured signals for a nominal motor speed of 1200 RPM and

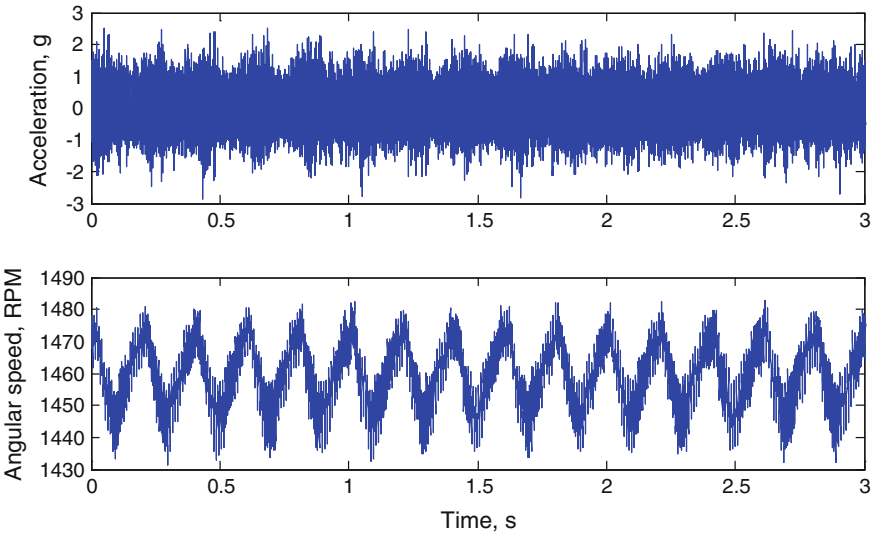

Fig. 2 Measurement of acceleration vibration of the ring gear (*top*), and motor instantaneous speed (*bottom*). Nominal motor speed is 1500 RPM and load is a 5 Hz sinusoidal varying between 10 and 50 Nm

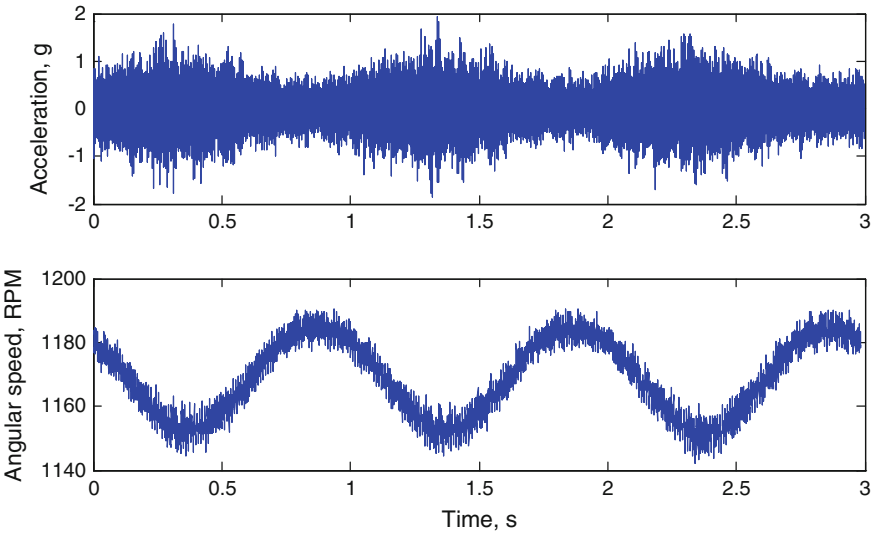

Fig. 3 Measurement of acceleration vibration of the ring gear (*top*), and motor instantaneous speed (*bottom*). Nominal motor speed is 1200 RPM and load is a 1 Hz sinusoidal varying between 10 and 50 Nm

sinusoidal load variation between 10 and 50 Nm with frequency of 1 Hz. Note that the vibration amplitude is higher when the speed is lower. Since the motor is controlled in open-loop, the speed reduces when the load increases and vice versa, so the larger vibration amplitudes are obtained when load is higher. Under these conditions, the resulting acceleration vibration is amplitude and frequency modulated with corresponding modulating functions sharing essentially the same frequency content.

Let us further analyze the case where nominal motor rotational speed is 1500 RPM and sinusoidal load variation between 10 and 50 Nm with 5 Hz frequency. Figure 4 presents the spectrum of the motor instantaneous angular speed, showing that the speed variation is dominated by the lower harmonics of the load variation frequency.

The planetary gearbox has three equally spaced planets and all gear mesh progressions occur simultaneously inside the transmission and are in-phase. Planetary gearboxes with these characteristics are classified as planetary gearboxes of Group A according to [10]. For planetary gearboxes of this group, and for constant speed, the spectral structure of the vibrations measured by a sensor on the ring gear theoretically corresponds to spectral lines at the gear mesh frequency (GMF) with symmetrical sidebands spaced at Nf_C, where N is the number of planet gears and f_C is the rotational frequency of the carrier plate. The same structure is expected for higher harmonics of the GMF.

In addition to the specific features of planetary gearbox vibrations explained above, the effects of amplitude and frequency modulation must be considered. Independently, both modulation effects result in the appearance of a symmetrical family of sidebands around each carrier frequency, spaced at the frequency of the modulating function. When amplitude and frequency modulation simultaneously take place, asymmetry in the sidebands generally follows. Figure 5 shows a zoom of the magnitude spectrum of the acceleration vibration around the GMF showing sideband asymmetry. The central line corresponds to the mean gear mesh frequency (GMF, which acts as the carrier frequency of the modulation). Detailed analysis shows that there are actually two families of sidebands with close frequencies. One

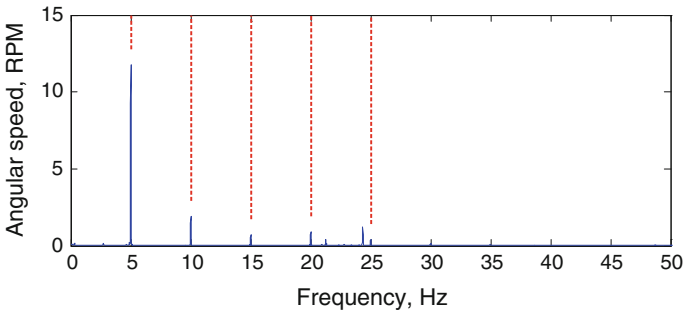

Fig. 4 Magnitude spectrum of the motor instantaneous angular speed. *Dashed lines* indicate multiples of 5 Hz

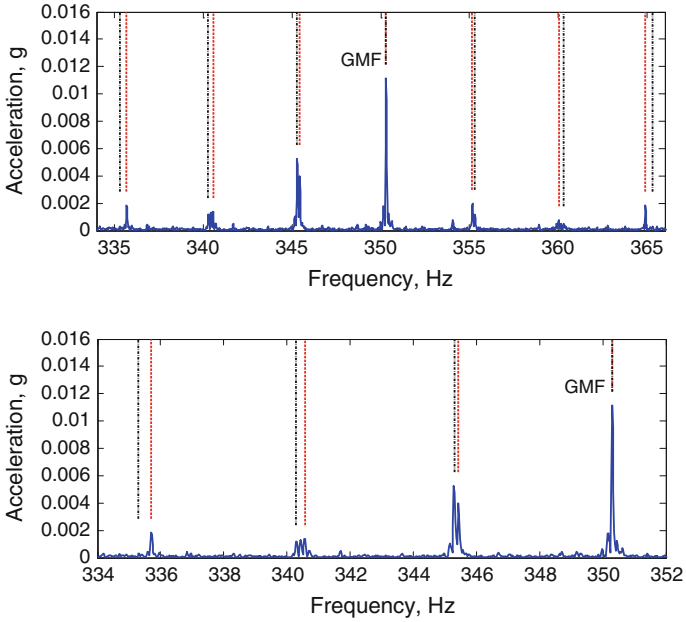

Fig. 5 Magnitude spectrum of the acceleration vibration. *Top* Zoom around the gear mesh frequency (*central line*). *Bottom* Second zoom portion to distinguish the different sidebands. *Red dashed lines* label sidebands spaced at $3f_C$; *black dot-dash lines* label sidebands spaced at 5 Hz (load and speed variation frequency)

has the frequency of the load variation (5 Hz). The second has a frequency of 4.87 Hz and corresponds to the average frequency of the carrier plate during the measurement, f_C. Note that for a planetary gearbox of Group A sidebands at f_C are not predicted by phenomenological models; however, they are typically observed in practice. Note also in Fig. 5 (bottom), that the sideband at Nf_C is present, as theoretical models predict ($N = 3$) [10, 11].

3 Model of the Gearbox

In order to understand the dynamic behavior of the planetary gear subjected to time varying loading conditions as tested in the last section, a dynamic lumped parameter model is developed (Fig. 6). Ring gear (r), sun gear (s), planet gears (p) and a carrier (c) are considered as rigid bodies that can translate in two directions and rotate around their rotational axis. Mesh phenomena are modeled by suitable mesh stiffness functions. In total there are $(3N + 9)$ degrees of freedom, where N is the number of planets [12]. Damping is introduced in parallel to each

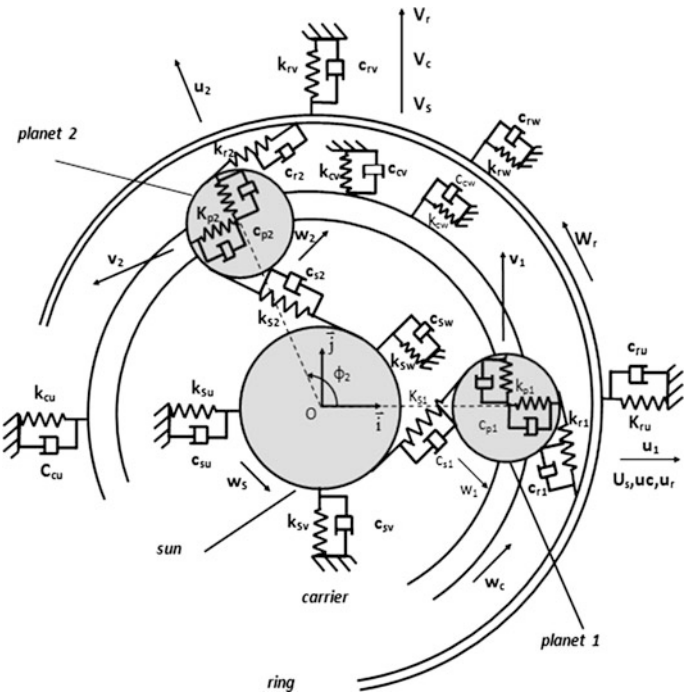

Fig. 6 Model of the planetary gear

stiffness. Neglecting gyroscopic effects (low rotational speeds) the equation of motion can be written as:

$$[M]\{\ddot{q}\} + ([C_b] + [C_m])\{\dot{q}\} + ([K_b] + [K_m(t)])\{q\} = \{T(t)\} \tag{1}$$

where q is the degree of freedom vector, $[M]$ is the mass matrix, $[C_b]$ is the bearing damping matrix, $[C_m]$ is the mesh damping matrix, $[K_b]$ is the bearing stiffness matrix, $[K_m(t)]$ is the time varying mesh stiffness matrix and $\{T(t)\}$ is the external torque vector applied on the system. Expressions of these matrices can be found in [1].

The asynchronous motor driving the system has a mechanical characteristic, which relates the driving torque to the rotational speed, expressed by [13]:

$$T_m = \frac{T_b}{\left(1 + (s_b - s)^2\right)\left(\frac{a}{s} - bs^2\right)} \tag{2}$$

where T_b is the torque at break point, a and b are constant properties of the motor, s_b is the slope at break point, and s is the slope of the motor expressed by:

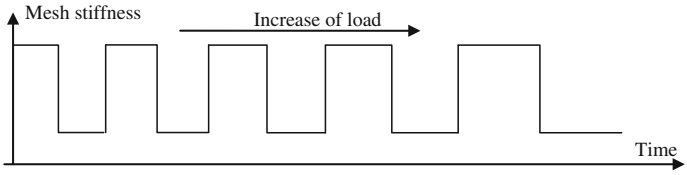

Fig. 7 Model of the time varying mesh stiffness

$$s = \frac{(N_s - N_1)}{N_s} \tag{3}$$

where N_s is the synchronous speed of the motor and N_1 is the rotational speed of the motor, which is also the rotational speed of the sun gear.

The mechanical characteristic used for simulations is provided by the motor manufacturer. When there is no speed controller, the motor speed is sensitive to loading conditions. In fact, an increase of load will lead to a decrease of speed and vice versa. As a consequence, if load increases, the motor has to overcome it by supplying the adequate torque but the speed in this case will decrease and vice versa. This situation leads to time varying mesh frequency which can be expressed by:

$$f_m(t) = \frac{Z_s Z_r}{Z_s + Z_r} f_s(t) \tag{4}$$

where $f_s(t)$ is the varying sun shaft rotational frequency (motor rotational frequency), Z_s is the tooth number of the sun and Z_r is tooth number of the ring. Figure 7 shows the evolution of mesh stiffness function as load is increasing.

4 Simulation Results

The modeled gearbox is subjected to the same operating conditions of the experiments. We present here the results for 1500 RPM motor nominal speed and 10–50 Nm, 5 Hz sinusoidal load variation. Figure 8 shows on top a portion of the acceleration time history showing clear evidence of the amplitude modulation effect of the load variation. Figure 8 (center) displays the speed variation of the sun gear, showing sinusoidal speed variation between 1437 and 1475 RPM and frequency of 5 Hz. This evolution was obtained after intersecting the mechanical characteristic of the driving asynchronous motor with the loading values. Similar values and behaviour were observed in the measurements (Fig. 2). Figure 8 (bottom) shows the portion of magnitude spectrum of the acceleration vibration around the mean GMF. The central dot-dashed line marks the GMF and the rest of the markers are spaced at the frequency of the load variation (5 Hz). As explained, the presence of asymmetrical sidebands spaced at the load variation frequency is a result of the frequency and amplitude modulation.

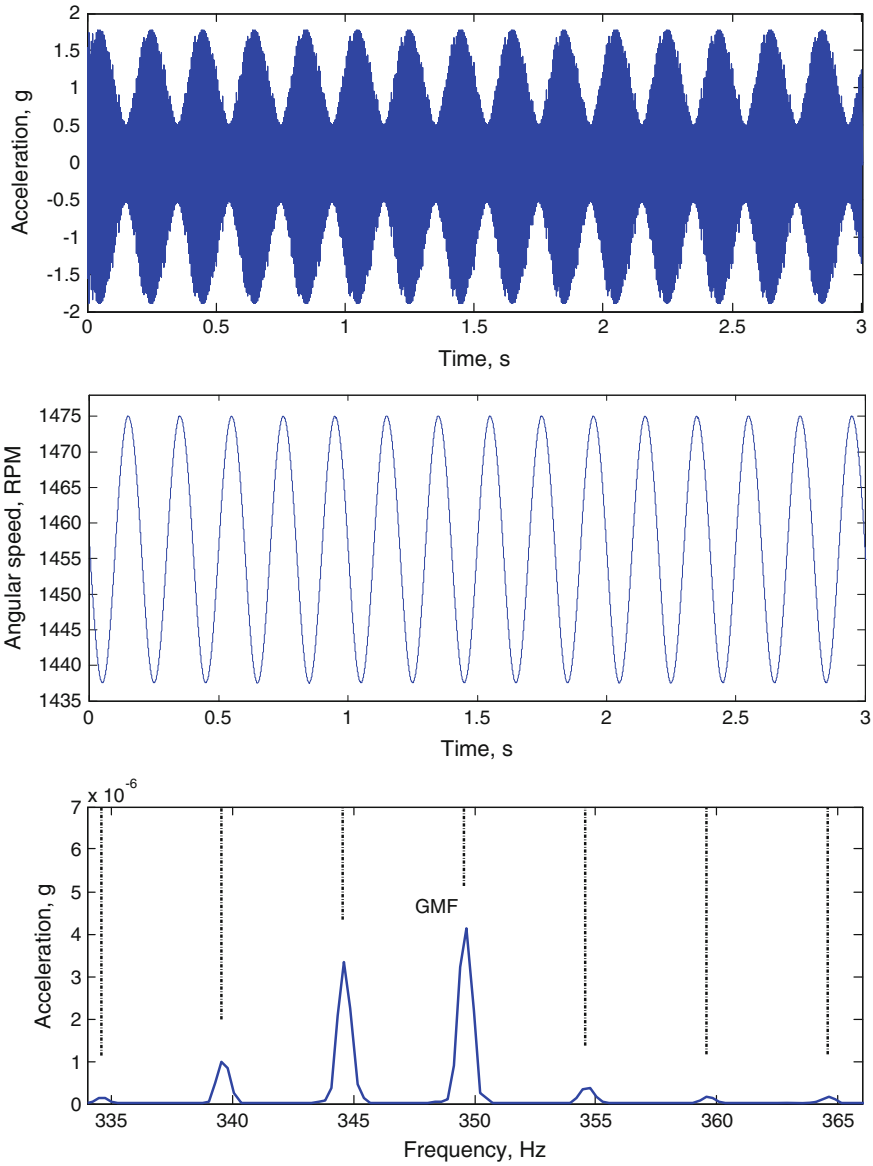

Fig. 8 Simulation results. *Top* Time history of acceleration vibration. *Center* Instantaneous angular speed of the sun gear shaft. *Bottom* Portion of magnitude spectrum around the gear mesh frequency. *Black dot-dash lines* label sidebands spaced at 5 Hz (load and speed variation frequency)

Note that the resolution of the spectrum (0.29 Hz) of Fig. 8 does not allow investigating the presence of sidebands spaced at multiples of f_C (as in Fig. 5). However, they should not be present in the simulation results, because the reference

frame used for the degrees-of-freedom of the model is a rotating frame fixed to the carrier plate. Thus, there is no varying transmission path effect [14] and, therefore, no additional sidebands. Taking this consideration into account, the simulation results are in full agreement with the experimental results.

5 Conclusions

In this paper a planetary gear transmission running under non-stationary operating conditions was investigated using two approaches: experimental and model-based. The non-stationary operating condition studied was modeled by time varying loads imposed on the carrier (output of the system). The experimental setup was described and results issued from varying loading cases were analyzed. Dynamic model of the test rig was then developed including the main excitation sources. Numerical and experimental results can be summarized as follows:

- Rotational speed is sensitive to load variation. Motor speed variability follows intimately the mechanical characteristic.
- It is clear that variation of load leads to amplitude and frequency modulations in vibration signals. This was observed in the simulation and experimental results.
- Asymmetric sidebands are observed in vibration spectra around GMF and its harmonics, due to the simultaneous frequency and amplitude modulation.
- Simulation results show similar results excepting the absence of sidebands at Nf_c. This was explained by the fact that simulated time signals are obtained according to a rotating frame fixed to the carrier.

This last point leads us to think that it is necessary to adapt the developed model in order to express the vibration signals according to fixed frame. This task is under development by the authors.

Acknowledgments Cristián Molina Vicuña thanks CONICYT-FONDECYT for the support of Project 11110017.

References

1. Chaari F, Bartelmus W, Zimroz R, Fakhfakh T, Haddar M (2012) Gearbox vibration signal amplitude and frequency modulation. Shock Vib 18:1–18
2. Randall RB (1982) A new method of modeling gear faults. J Mech Des 104:259–267
3. Bartelmus W (1992) Vibration condition monitoring of gearboxes. Mach Vib 1:178–189
4. Bartelmus W, Zimroz R (2009) Vibration condition monitoring of planetary gearbox under varying external load. Mech Syst Sig Proc 23:246–257
5. Bartelmus W, Chaari F, Zimroz R, Haddar M (2010) Modelling of gearbox dynamics under time-varying non stationary load for distributed fault detection and diagnosis. Eur J Mech A/Sol 29:637–646

6. Zimroz R, Millioz F, Martin N (2010) A procedure of vibration analysis from planetary gearbox under non-stationary cyclic operations for instantaneous frequency estimation in time-frequency domain. In: Conference on condition monitoring and machinery failure prevention technologies (CM and MFPT 2010). Stratford-upon-Avon, UK
7. Khabou MT, Bouchaala N, Chaari F, Fakhfakh T, Haddar M (2011) Study of a spur gear dynamic behavior in transient regime. Mech Syst Signal Process 25(8):3089–3101
8. Bouchaala N, Chaari F, Khabou MT, Fakhfakh T, Haddar M (2011) Influence of the nonlinear Hertzian stiffness on the dynamics of a spur gear system under transient regime and tooth defects. Int J Veh Noise Vib 7(2):149–177
9. Chaari F, Abbes MS, Rueda FV, del Rincon AF, Haddar M (2013) Analysis of planetary gear transmission in non-stationary operations. Front Mech Eng 8(1):88–94
10. Vicuña CM (2012) Theoretical frequency analysis of vibrations from planetary gearboxes. Forschungim Ingenieurwesen 76(1):15–31
11. Inalpolat M, Kahraman AA (2009) Theoretical and experimental investigation of modulation sidebands of planetary gear sets. J Sound Vib 323(3–5):677–696
12. Lin J, Parker RG (1999) Analytical characterization of the unique properties of planetary gear free vibration. J Vib Acoust 121:316–321
13. Wright D (2005) Class notes on design and analysis of machine elements. Department of Mechanical and Materials Engineering, The University of Western Australia
14. McFadden PD, Smith JD (1985) An explanation for the asymmetry of the modulation sidebands about the tooth meshing frequency in epicyclic gear vibration. Proc Inst Mech Eng 199(C1):65–70

Model-Based Estimation of Elevator Rail Friction Forces

Ekaitz Esteban, Oscar Salgado, Aitzol Iturrospe and Inge Isasa

Abstract This paper presents a model-based monitoring approach for the estimation of the elevator rail friction forces. This model-based monitoring approach is based on a Linear Parameter Varying (LPV) model of a 1:1 elevator installation, comprising both the mechanical and the electrical subsystems. The Extended Kalman algorithm (EKF) is then employed as an observer for the joint estimation of the elevator LPV states and parameters. Finally, the estimated rail friction forces are evaluated and energy efficiency indicators describing elevator performance during the ride are obtained.

Keywords Linear parameter varying model · Extended kalman filter · Performance indicator

Contents

1 Introduction 364
2 Elevator Model 365
2.1 Car-Rail Force Model and the Mechanical Subsystem Dynamics 366
2.2 Model of the PMSM 367
2.3 Model of the Field Oriented Control 368

E. Esteban (✉) · O. Salgado
Mechanical Engineering, IK4-Ikerlan, J.M. Arizmendiarrieta 2, 20500 Mondragon, Spain
e-mail: eesteban@ikerlan.es

O. Salgado
e-mail: osalgado@ikerlan.es

A. Iturrospe
Department of Electronics and Computer Sciences, Mondragon Goi Eskola Politeknikoa, Loramendi 4, 20500 Mondragon, Spain
e-mail: aiturrospe@mondragon.edu

I. Isasa
Mechanical Engineering, Orona EIC S. Coop, Pol. Lastaola s/n, 20120 Hernani, Spain
e-mail: iisasa@orona-group.com

F. Chaari et al. (eds.), *Advances in Condition Monitoring of Machinery in Non-Stationary Operations*, Applied Condition Monitoring 4,
DOI 10.1007/978-3-319-20463-5_27

3 Estimation of Elevator Rail Friction Forces by EKF 369
4 Energy Efficiency Indicators 370
5 Simulation Results 370
6 Conclusions 373
References 373

1 Introduction

Maintenance and modernization services account for more than a 46 % of the total revenue in some elevator manufacturing companies [1]. It is highly important to accurately estimate and analyze the energy efficiency of the elevators [2]. Elevator maintenance services usually involve periodical in situ inspections, which are generally conducted employing commercial equipment designed specifically to evaluate the performance using energy efficiency indicators [2, 3]. An energy efficient elevator can make a long lasting and effective contribution to a safer environment in the future through its lower environmental impact [3].

Currently, the energy efficiency indicators applied in the elevator industry are based on the evaluation of the energy consumption following the industry standard as the one described in the VDI 4707 guideline [3]. Using the VDI 4707 guideline, the total energy consumption of an elevator can be known through the direct measurement of the voltage and current signals from the machine. However, the losses of the consumed energy can not be identified. The mechanical energy losses are mainly due to the rail friction forces which are difficult to measure with already installed sensors in the elevator. However, the rail friction forces can be indirectly estimated based on existing signals as proposed in the literature [4].

The aim of this paper is to estimate the mechanical energy losses due to the rail friction forces during the ride. We apply a model-based identification procedure [5], as shown schematically in Fig. 1. The EKF algorithm [6] estimates step by step the model states and the rail friction forces based on an electromechanical model of a 1:1 elevator installation [4] and the existing signals: the regulator signature, the voltage and current signals from the machine, the machine encoder and the draw-wire encoder of the elevator car. Then, three elevator energy efficiency indicators are calculated.

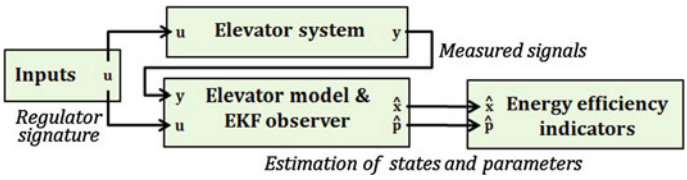

Fig. 1 Model-based approach for the estimation of rail friction forces

The rest the paper is organized as follows. In Sect. 2, both the dynamics of a 1:1 elevator installation and its model are described. In Sect. 3, the model-based algorithm is applied for estimating elevator rail friction forces. Then, the energy efficiency indicators are described in Sect. 4. In Sect. 5, the model-based estimation procedure is tested by simulations based on a 1:1 elevator installation model and several conclusions are discussed in the last section.

2 Elevator Model

An elevator installation comprehends both a mechanical subsystem and an electrical subsystem, as it is shown in Fig. 2. The mass of the elevator car is balanced by a counterweight in order to reduce the torque demanded to the machine. An electrical machine drives through a pulley onto the suspension ropes which interconnect the elevator car and the counterweight. Both the car and the counterweight move vertically, constrained by a pair of rails each.

The installation modeled in this paper is driven by a Permanent Magnet Synchronous Machine (PMSM) with a three-phase wye-wound stator which is controlled using a Field Oriented Control (FOC), where the velocity signature profile is generated for each ride, depending on the starting car position and its final destination.

The imbalance between the elevator car and the counterweight exerts a mechanical torque that is actively balanced with the electromagnetic torque applied by the machine. The mechanical and the electrical subsystems are coupled by the following torque balance equation

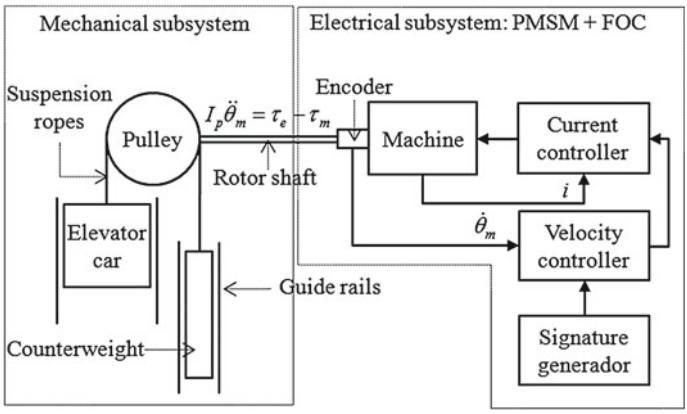

Fig. 2 Simplified schematic description of the 1:1 elevator installation modeled in Sect. 2

$$\frac{\mathrm{d}}{\mathrm{d}t}\dot{\theta}_m = \frac{\tau_e - \tau_m}{I_p} \tag{1}$$

where I_p is the inertia of the driving pulley, the angular velocity of the rotor shaft is denoted with $\dot{\theta}_m$, the electromagnetic torque exerted by the machine is denoted with τ_e and the resulting mechanical torque is τ_m.

2.1 Car-Rail Force Model and the Mechanical Subsystem Dynamics

In this subsection the car-rail guide force model and the mechanical subsystem dynamics are explained, as shown in Fig. 3. The free body diagram of the elevator car is shown in Fig. 3a. In z axis, the inertial force is applied at the car center of gravity whereas the rope elastic force f_c, is applied at the top of the car. Due to the imbalance caused by these forces, the self-balanced rail guide reaction forces f_x and f_y appear as a reaction to this imbalance in each contacting elements. Considering the coulomb friction model [7] for each car sliding elements, the self-balanced rail guide reaction forces produces a proportional rail friction forces f_{rc} in z axis. Assuming that the angular rotation and the lateral translation of the car is constrained by a pair of rails, the force balance model can be simplified as,

$$\begin{aligned} \sum \mathbf{f}_i &= m_c\,\mathbf{a} \\ \sum \mathbf{r}_i \times \mathbf{f}_i &= \mathbf{0} \end{aligned} \tag{2}$$

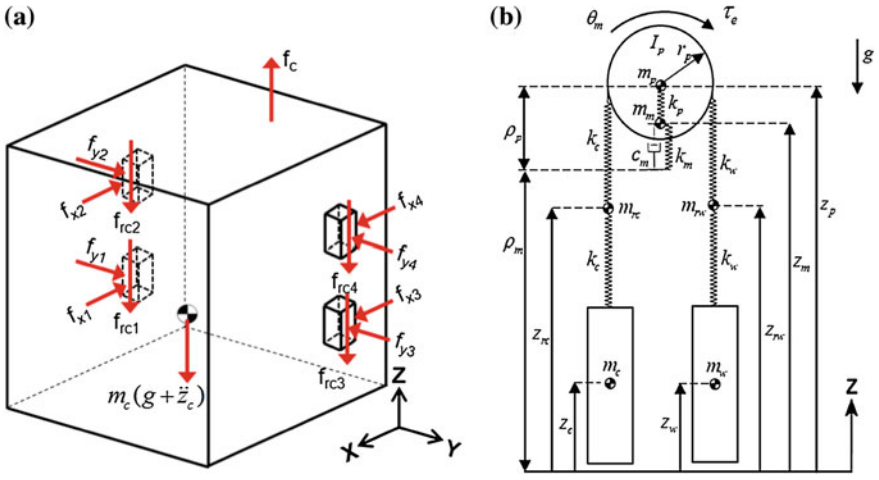

Fig. 3 Car-rail force model and the mechanical subsystem dynamics **a** Free body diagram of the elevator car. **b** Lumped parameter model of a 1:1 elevator vertical dynamics

where the vectors $\boldsymbol{f}_i$, $\boldsymbol{a}$ and $\boldsymbol{r}_i$ are the forces, accelerations and the distance with respect to a fixed reference point of the car in three axis, respectively. Given these simplifying assumptions, we can note that the friction forces are proportional to the elastic force, which is in turn proportional to the inertial force. Therefore, it can be assumed that the rail friction force is proportional to the inertial force as follows

$$f_{rc} \equiv \gamma_c \, m_c \, (g + \ddot{z}_c) \quad f_{rw} \equiv \gamma_w \, m_w \, (g + \ddot{z}_w) \tag{3}$$

where, the proportionality between the load of the car and the rail friction force is denoted by the parameter γ_c. Note that the same assumptions are made for the calculation of the counterweight rail friction forces f_{rw}.

The equations describing the car-rail force model Eq. (3) are coupled into a 1:1 vertical dynamic model of the elevator [4, 8], as shown in Fig. 3b. Based on the force balance in each inertial element, the linear second order differential equations that govern the mechanical subsystem dynamics including the car-rail lateral force model Eq. (3) are expressed as,

$$\frac{\mathrm{d}}{\mathrm{d}t}\begin{bmatrix} \dot{z}_m \\ \dot{z}_p \\ \dot{z}_{rc} \\ \dot{z}_{rw} \\ \dot{z}_c \\ \dot{z}_w \end{bmatrix} = \begin{bmatrix} \frac{-c_m \dot{z}_m - k_m z_m - k_p (z_p - z_m) + k_m \rho_m - k_p \rho_p}{m_m} \\ \frac{-k_p (z_p - z_m) + k_c (z_{rc} - z_p) + k_w (z_{rw} - z_p) + k_p \rho_p + 2\,EA}{m_p} \\ \frac{-\dot{m}_{rc} \dot{z}_{rc} - k_c (2\, z_{rc} - z_c - z_p)}{m_{rc}} \\ \frac{-\dot{m}_{rw} \dot{z}_{rw} - k_w (2\, z_{rw} - z_p - z_w)}{m_{rw}} \\ \frac{-k_c (z_c - z_{rc}) - EA}{m_c (1+\gamma_c)} \\ \frac{-k_w (z_w - z_{rw}) - EA}{m_w (1-\gamma_w)} \end{bmatrix} - \begin{bmatrix} g \\ g \\ g \\ g \\ g \\ g \end{bmatrix} \tag{4}$$

where the lumped masses, stiffness and damping elements of each j-inertial elements are denoted by m_j, k_j and c_j, respectively. The position, velocity and acceleration of each j-inertial elements are denoted by z_j, $\dot{z}_j$ and $\ddot{z}_j$, respectively and r_p is the pulley radius. The mechanical torque obtained as a result of the response of the mechanical subsystem is,

$$\tau_m = r_p k_w (z_{rw} - z_p) - r_p k_c (z_{rc} - z_p). \tag{5}$$

2.2 Model of the PMSM

The linear first order differential equations that govern the electric dynamics of a PMSM can be expressed in the dq0 reference frame assuming the magnetic symmetry of the machine and the same inductances ($L_d \approx L_q$) among other simplifications as in [9],

$$\frac{\mathrm{d}}{\mathrm{d}t}\begin{bmatrix} i_d \\ i_q \end{bmatrix} \cong \begin{bmatrix} V_d/L_d \\ V_q/L_q \end{bmatrix} - \begin{bmatrix} R/L_d & 0 \\ 0 & R/L_q \end{bmatrix}\begin{bmatrix} i_d \\ i_q \end{bmatrix} - \begin{bmatrix} 0 \\ p\,\lambda/L_q \end{bmatrix}\dot{\theta}_m \tag{6}$$

where V, i and L denote the voltages, currents and inductances respectively. The subscripts d and q denote the direct and quadrature axis respectively. The resistance of the stator is denoted by R, λ is the magnetic flux linkage and p is the number of machine pole pairs. The electromagnetic torque τ_e is assumed to be proportional to the quadrature axis current as,

$$\tau_e \cong \frac{3}{2} p\,\lambda\, i_q = K_t\, i_q \tag{7}$$

where the machine torque constant is denoted by K_t.

2.3 Model of the Field Oriented Control

The aim of a FOC strategy is to control the direct and quadrature axis current independently, maximizing the active power and minimizing the reactive power. This is achieved by minimizing i_d and maximizing i_q by means of two different PI current controllers, as shown in Fig. 4. In the outer loop, the rotor angular velocity $\dot{\theta}_m$ is controlled by means of another PI control. For an ideal FOC control, $i_{d_{\mathrm{ref}}}$ is set to zero in order to minimize the consumed reactive power by the machine and $i_{q_{\mathrm{ref}}}$ is the output of the velocity control.

This FOC strategy can be represented as a linear first order differential equations analogously to [10] as follows

$$\frac{\mathrm{d}}{\mathrm{d}t}\begin{bmatrix} i_{q_{\mathrm{ref}}} \\ V_d \\ V_q \end{bmatrix} = \begin{bmatrix} K_{ps} & 0 & 0 \\ 0 & K_{pd} & 0 \\ 0 & 0 & K_{pq} \end{bmatrix}\begin{bmatrix} \dot{\omega}_{\mathrm{ref}} - \ddot{\theta}_m \\ \dot{i}_{d_{\mathrm{ref}}} - \dot{i}_d \\ \dot{i}_{q_{\mathrm{ref}}} - \dot{i}_q \end{bmatrix} + \begin{bmatrix} K_{is} & 0 & 0 \\ 0 & K_{id} & 0 \\ 0 & 0 & K_{iq} \end{bmatrix}\begin{bmatrix} \omega_{\mathrm{ref}} - \dot{\theta}_m \\ i_{d_{\mathrm{ref}}} - i_d \\ i_{q_{\mathrm{ref}}} - i_q \end{bmatrix} \tag{8}$$

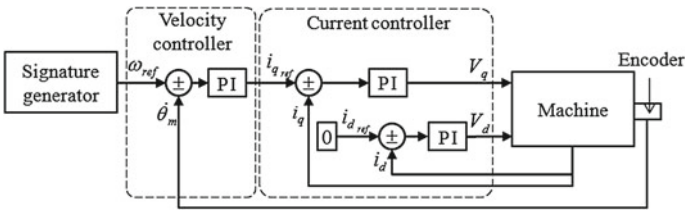

Fig. 4 Field oriented control scheme

where the proportional gain and integral gain of a PI control are denoted with K_p and K_i respectively. The subscript s, d and q represent the velocity, direct current and quadrature current controller respectively.

Finally, substituting the Eqs. (5 and 7) in Eq. (1), and rewriting the linear differential equations from Eqs. (1, 4, 6 and 8) in state-space domain as described in [11] we get,

$$\dot{\mathbf{x}}(t) = \mathbf{A}(t)\mathbf{x}(t) + \mathbf{B}(t)\mathbf{u}(t) \tag{9}$$

where the state matrix is denoted by $\mathbf{A}(t)$ and the input matrix is $\mathbf{B}(t)$. The state vector $\mathbf{x}(t)$ and input vector $\boldsymbol{u}(t)$ are detailed as follows

$$\begin{aligned} \mathbf{x} &= \left[z_m \; z_p \; z_{rc} \; z_{rw} \; z_c \; z_w \theta_m \; \dot{z}_m \; \dot{z}_p \; \dot{z}_{rc} \; \dot{z}_{rw} \; \dot{z}_c \; \dot{z}_w \; \dot{\theta}_m \; i_d \; i_q \; i_{qref} \; V_d \; V_q \right]^{\mathrm{T}} \\ \mathbf{u} &= \left[\dot{w}_{ref} \; w_{ref} \; \dot{i}_{def} \; i_{def} \; g \; 1 \right]^{\mathrm{T}}. \end{aligned} \tag{10}$$

As the rope stiffness parameters of the state matrix k_c and k_w depends on its instantaneous length, the elevator model above can be considered a LPV system.

3 Estimation of Elevator Rail Friction Forces by EKF

The estimation of the rail friction forces requires to estimate the $\ddot{z}_c$ and $\ddot{z}_w$ states in order to identify the γ_c and γ_w parameters in Eq. (3). This joint estimation can be accomplished by using the EKF, and adding the identified parameters to the state vector in Eq. (9) as described in [6],

$$\mathbf{x}_{\text{aug}} = \begin{bmatrix} \mathbf{x} \\ \mathbf{p} \end{bmatrix} \quad \mathbf{p} = \begin{bmatrix} \gamma_c \\ \gamma_w \end{bmatrix}. \tag{11}$$

Therefore, the new model that identifies friction parameters is,

$$\dot{\mathbf{x}}_{\text{aug}} = \begin{bmatrix} \mathbf{A} & \mathbf{O} \\ \mathbf{O} & \mathbf{O} \end{bmatrix} \mathbf{x}_{\text{aug}} + \begin{bmatrix} \mathbf{B} \\ \mathbf{O} \end{bmatrix} \mathbf{u} + \mathbf{w}(t) \quad \mathbf{w}(t) \sim N(\mathbf{0}, \mathbf{Q}) \tag{12}$$

$$\mathbf{y} = [\mathbf{C} \quad \mathbf{O}]\mathbf{x}_{aug} + \mathbf{v}(t) \quad \mathbf{v}(t) \sim N(\mathbf{0}, \mathbf{R}) \tag{13}$$

where the process noise vector denoted by $\boldsymbol{w}(t)$ is assumed to be a zero mean Gaussian noise with covariance matrix $\mathbf{Q}$; the measurement noise vector denoted by $\mathbf{v}(t)$ is assumed to be a zero mean Gaussian noise with covariance matrix $\boldsymbol{R}$ and the output matrix $\boldsymbol{C}$ outputs the estimated state variables for the draw-wire encoder position and velocity, the machine encoder position and velocity and the machine quadrature current and the quadrature voltage as,

$$\mathbf{C} = \begin{bmatrix} 0 & 0 & 0 & 0 & 1 & 0 & 0 & 0 & 0 & 0 & 0 & 0 & 0 & 0 & 0 & 0 & 0 & 0 \\ 0 & 0 & 0 & 0 & 0 & 0 & 1 & 0 & 0 & 0 & 0 & 0 & 0 & 0 & 0 & 0 & 0 & 0 \\ 0 & 0 & 0 & 0 & 0 & 0 & 0 & 0 & 0 & 0 & 0 & 1 & 0 & 0 & 0 & 0 & 0 & 0 \\ 0 & 0 & 0 & 0 & 0 & 0 & 0 & 0 & 0 & 0 & 0 & 0 & 1 & 0 & 0 & 0 & 0 & 0 \\ 0 & 0 & 0 & 0 & 0 & 0 & 0 & 0 & 0 & 0 & 0 & 0 & 0 & 0 & 1 & 0 & 0 & 0 \\ 0 & 0 & 0 & 0 & 0 & 0 & 0 & 0 & 0 & 0 & 0 & 0 & 0 & 0 & 0 & 0 & 0 & 1 \end{bmatrix}. \quad (14)$$

4 Energy Efficiency Indicators

The estimated states from Eq. (12), $\hat{\tilde{z}}_c$, $\hat{\tilde{z}}_w$, $\hat{\gamma}_c$ and $\hat{\gamma}_w$ are then employed to estimate the rail friction forces $\hat{f}_{rc}$ and $\hat{f}_{rw}$ from Eq. (3). These estimated rail friction forces are then applied to obtain three energy efficiency indicators during the ride. The first energy efficiency indicator, η_m is the ratio between the friction energy losses and the consumed active energy by the motor, [2]:

$$\eta_m = 1 - \frac{\text{friction energy losses}}{\text{motor active energy}} = 1 - \frac{r_p \int_0^{\omega_m} (\hat{f}_{rc} + \hat{f}_{rw}) \mathrm{d}\omega_m}{3/2 \int_0^t (V_q i_q + V_d i_d) \mathrm{d}t} \quad (15)$$

where, the numerator of the Eq. (15) represents the energy work obtained for the rail friction forces and the denominator is the time-integral of the electrical active power.

The second energy efficiency indicator, η_e is the ratio between the consumed active energy and the total energy consumption by the motor:

$$\eta_e = \frac{\text{motor active energy}}{\text{consumed energy}} = \frac{3/2 \int_0^t (V_q i_q + V_d i_d) \mathrm{d}t}{\int_0^t (V_a i_a + V_b i_b + V_c i_c) \mathrm{d}t} \quad (16)$$

where the subscripts a, b and c denote the measured three-phases of a wye-wound stator PMSM, respectively.

Finally, the third energy efficiency indicator, η_t is defined as an indicator of the whole installation efficiency:

$$\eta_t = \eta_e \, \eta_m. \quad (17)$$

5 Simulation Results

The proposed procedure in Sect. 4 has been tested by three simulations. The different values of the rail friction parameters are $\gamma_c = \gamma_w = 0.073$, $\gamma_c = \gamma_w = 0.082$ and $\gamma_c = \gamma_w = 0$ for each simulation respectively. These selected values correspond to

Table 1 Elevator model parameter values

Parameter	Value
ρ_m	9 m
m_m	225 kg
m_w	145 kg
k_m	1.3×10^6 N/m
K_{ps}	0.83 A/rad/s
K_{id} and K_{iq}	404 Ω/s
L_q	18.175 mH
ρ_p	0.125 m
m_p	10 kg
I_p	0.34 kg m^2
k_p	2×10^5 N/m
K_{is}	59.5 A/rad
R	1 Ω
K_t	15.936 Wb
r_p	5.75 cm
m_c	220 kg
EA	10^6 N
c_m	0 Ns/m
K_{pd} and K_{pq}	6.1 Ω
L_d	18.175 mH
g	9.81 m/s^2

equivalent friction scenarios obtained experimentally in [12]. The other elevator model parameter values are summarized in Table 1.

We define the same reference signature for the three simulations where the elevator car moves upwards, as shown in Fig. 5. The reference signature is calculated with the following values: ride distance d = 5.2 m, maximum velocity v = 0.58 m/s, maximum acceleration a = 0.38 m/s^2 and jerk j = 1 m/s^3 respectively. More details about the continuous time equations for the reference signature can be found in [13].

The EKF algorithm for joint estimation, as described in Sect. 3, is tuned by setting the process error covariance matrix $\boldsymbol{P} = \boldsymbol{I}_{21}$, the process noise covariance matrix $\mathbf{Q} = 0.01\mathbf{I}_{21}$ and the measurement noise covariance $\mathbf{R} = 0.64\mathbf{I}_6$ for the three simulations. The initial values for the state estimates are statically obtained (at t = 0) by considering the input vector as $\mathbf{u} = [0 \quad 0 \quad 0 \quad 0 \quad g \quad 1]^{\mathrm{T}}$ and considering that the elevator car is still, that is $\dot{\mathbf{x}} = \mathbf{0}$. The estimation was carried out using Matlab and ReBEL[1] The estimation of the rail friction force for the first simulation in the car and counterweight side during the ride are shown in Fig. 6. The solid line

[1]ReBEL is a Matlab toolkit for Sequential Bayesian inference.

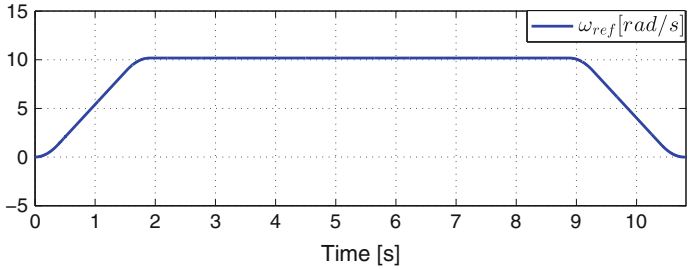

Fig. 5 Velocity reference signature

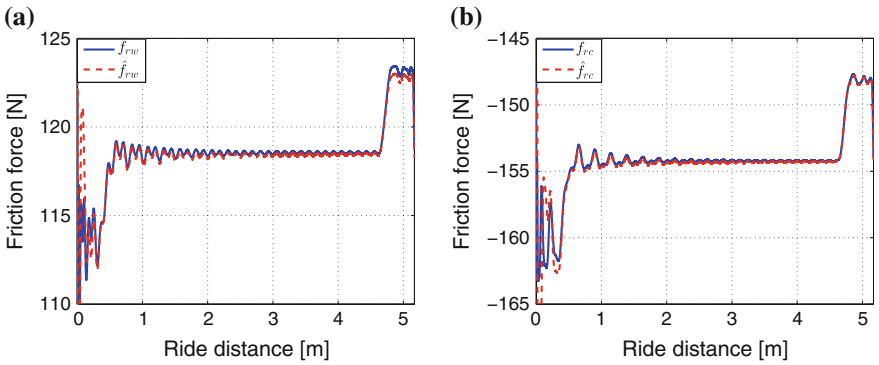

Fig. 6 Estimation of the friction forces during the ride for the first simulation **a** Ride friction force in the counterweight. **b** Ride friction force in the car

Table 2 Comparison of the energy efficiency indicators with the VDI indicators

Indicator name	Sim. (1)	Sim. (2)	Sim. (3)
η_e (%)	93.7	92.5	95.6
η_m (%)	72.9	67.8	100
η_t (%)	68.3	62.8	95.6
VDI energy (mWh/kg m)	1.246	1.357	1.046
VDI rank	A	A	A

is the simulated rail friction force employing Eq. (9), and the dashed line is the estimation of the rail friction force by the EKF algorithm.

Finally, we compare the energy efficiency indicators in Sect. 4 with the energy efficiency evaluation following the VDI 4707 guideline. Table 2 contains the values of the energy efficiency indicators obtained from the simulated three different rail friction scenarios. The VDI 4707 guideline defines different ranks (from lower G to higher A) that classify the elevator installations in different ranges of energy efficiency. Despite of the friction forces are different for the three simulations, the VDI

4707 indicator has assigned to them a range of maximum efficiency A. We can conclude that, contrary to the proposed energy efficiency indicators, the VDI rank is unable to distinguish the three different friction energy losses.

6 Conclusions

A LPV model for a elevator, including the dynamics of a PMSM controlled by a FOC strategy has been proposed. According to the results presented in simulation, the model is valid for estimating the rail friction forces based on the Extended Kalman Filter in real-time. Moreover, these rail friction forces are estimated employing already existing signals in the elevator installation.

The proposed three energy efficiency indicators allows to evaluate the friction energy losses, as well as the whole installation efficiency during the ride. Moreover, the proposed energy efficiency indicators are able to distinguish different rail friction scenarios whereas the VDI 4707 is unable.

Acknowledgments This work has been supported in part by the project ETORTEK MECOFF, economically supported by The Basque Government under project No. IE13-379. Any opinions, findings and conclusions expressed in this article are those of the authors and do not necessarily reflect the views of funding agencies. The authors also gratefully acknowledge Orona EIC S. Coop. for supporting this research line.

References

1. Kone Q4 financial statement bulleting 2013 (2014). Tech Rep, Kone
2. Adak MF, Duru N, Duru HT (2013) Elevator simulator design and estimating energy consumption of an elevator system. Energy Build 65:272–280
3. VDI 4707 (2007) Lifts—energy efficiency. Association of German Engineers
4. Kang J, Sul S (2000) Vertical-vibration control of elevator using estimated car acceleration feedback compensation. Trans Indus Electron IEEE 47(1):91–99
5. Isermann R, Munchhof M (2011) Identification of dynamical systems: an introduction with applications. Springer, Verlag
6. Van Der Merwe R (2004) Sigma-point Kalman filters for probabilistic inference in dynamic state-space models. Ph.D. thesis, Oregon Health & Science University
7. Andersson S, Söderberg A, Björklund S (2007) Friction models for sliding dry, boundary and mixed lubricated contacts. Tribol Int 40(4):580–587
8. Zhou Y (1997) Models for an elevator hoistway vertical dynamic system. In Intenational congress on sound and vibration, no. 5, Adelaida, Australia, pp 2673–2680
9. Grzesiak L M, Tarczewski T, Mandra S (2008) Permanent magnet synchronous servo-drive with state position controller. In Proceedings of power electronics and motion control conference—13th EPE-PEMC, pp 1071–1076
10. Venu K, Rushikesh C, Rajasekhar V (2013) Design and analysis of DC motor with PID controller—a state space approach. Transac Electr Electron Eng (ITSI-TEEE) 1:11–14
11. Ogata K (2003) Modern control engineering. Prentice Hall

12. Zhang XG, Guo KJ, Li HG, Meng G (2008) A new friction model for the slide guide in elevator systems: experimental and theoretical investigations. Proc Inst Mech Eng, Part C J Mech Eng Sci 222(11):2177–2189
13. Peters R D (1995) Ideal lift kinematics. In Barney GC (ed) The international congress on vertical transportation technologies. Elevcon, Elevator Technology, pp 175–184

Modelling and Simulation of Gear Systems Dynamics for Supporting Condition Monitoring Using Mathematica

Walter Bartelmus and Juliusz Grabski

Abstract Modelling and simulation of gear system dynamics to support the condition monitoring is one of the most important issues which should be properly developed. There are many papers on the subject of gearbox dynamic modelling however they are not coherent. Only in few papers a "complete system", which consist of a drive, gearbox and a driven machine is considered. The system which is going to be considered in this paper is complete and its parameters are based on a real system. To present different gear system dynamics problems a nonlinear time-varying model is analysed using *Mathematica* software. In the model the torsional vibration of the rotating system is considered. The model includes time-varying gear mesh stiffness, gear errors of each meshing tooth pair and nonlinearities due to tooth separations. Numerical solution of the system is obtained by *Mathematica*. Highly optimized superfunctions used in *Mathematica* analyse model equations and automatically select the right algorithms to get accurate results quickly. Other computation systems (e.g. MATLAB) require manual selection of solution algorithm to apply, whereas in *Mathematica* we use NDSolve and the risk of wrong results is minimal. The aim of the study is to show that mathematical modelling and computer simulation using *Mathematica* enable detailed investigation of the dynamic properties of a gearing system.

Keywords Gear system · Modelling · Dynamic · Acceleration · Load susceptibility characteristics

W. Bartelmus (✉)
Wroclaw University of Technology, Wroclaw, Poland
e-mail: walter.bartelmus@pwr.edu.pl

J. Grabski
Lodz University of Technology, Lodz, Poland
e-mail: juliusz.grabski@p.lodz.pl

F. Chaari et al. (eds.), *Advances in Condition Monitoring of Machinery in Non-Stationary Operations*, Applied Condition Monitoring 4,
DOI 10.1007/978-3-319-20463-5_28

Contents

1 Introduction 376
2 Model Description in *Mathematica* 378
3 Simulation Results 379
3.1 Simulation Results for Gear Pitch Error e_{1max} = 0.00002 m 379
3.2 Results Comparison for Different Values of Gear Pitch Error (e_{1max} = *0.00002* m, e_{1max} = *0.000022* m, e_{1max} = *0)* 382
3.3 Acceleration Amplitudes Estimation for e_{1max} = *0.00002* m, e_{1max} = *0.000022* m and e_{1max} = *0* 382
4 Conclusions 383
References 383

1 Introduction

The paper includes short discussion on mathematical modelling and computer simulation of one stage gear system as shown in Fig. 1. The bases for the modelling are described in papers [1–4]. In paper [2] model of one stage gearbox complete system Fig. 1 is described which consist of an electric motor, represented by its rotor inertia J_s, two gears represented by its inertia J_{p1} and J_{p2} and driven machine represented by its inertia J_r. More model parameters are given below. The incomplete model of a gearbox is understood as one which consists of only two gears and driving and driven elements of the system are not taken into consideration. Thorough investigations on the modelling of a complete system (as shown in Fig. 1) is given in papers [1] and [2], where gear imperfections, inter-teeth friction and backlash and only torsional vibration are considered. More sophisticated models including lateral vibrations are presented in paper [3], where double stage gearboxes are considered with torsional and lateral vibrations. The paper is cited 70 times according to Scopus including papers [5] and [6]. If one wants to consider varying load transmitted by a system the load susceptibility characteristic should be considered as in paper [4] and [6]. In paper [6] results obtained by measurements on a real industrial object are presented. There the susceptibility characteristic for a planetary gear gearbox is evaluated, which is incorporated into a complicated gearbox system. The load susceptibility characteristic is thought as an universal characteristic for a gearbox system. The investigations undertaken in this paper are directed to obtain the load susceptibility characteristics of investigated system shown in Fig. 1.

Model parameters used in numerical simulations:

- average gearing's stiffness $k_z = 2.4 \times 10^9$ N/m,
- minimum gearing's stiffness $k_{zd} = 2.3 \times 10^9$ N/m,
- maximum gearing's stiffness $k_{zg} = 2.5 \times 10^9$ N/m,
- stiffness of shafts $k_{s1} = 3 \times 10^6$ N/m, $k_{s2} = 3.3 \times 10^7$ N/m,
- gear radii $r_1 = 0.122$ m, $r_2 = 0.493$ m,

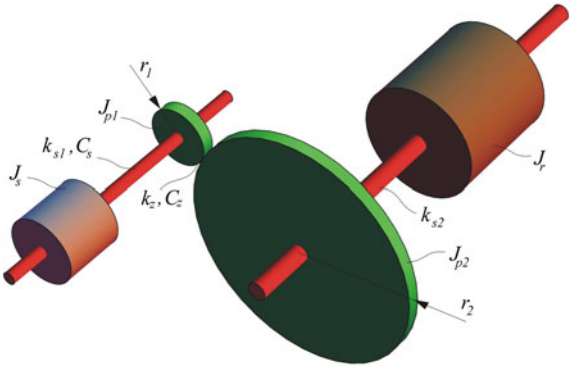

Fig. 1 Model of one-stage gearbox (*details below*)

- teeth numbers $z_{11} = 23$, $z_{12} = 93$,
- moments of inertia $J_s = 12.2$ kgm^2, $J_{p1} = 1$ kgm^2, $J_{p2} = 200$ kgm^2, $J_r = 1140$ kgm^2,
- damping coefficients $C_z = 10{,}000$ Ns/m, $C_s = 10{,}000$ Ns/m,
- inter-tooth backlash $l = 0.0003$ m,
- maximum of gear pitch error $e_1 = 0.00002$ m.

Inter-tooth forces according to [2] are described by Eq. (1a) when gear imperfections $E_r(t) = 0$ and by (1b) when imperfections $E_r(t) > 0$.

$$F[t] = \begin{cases} k_{zm}(r_1\varphi_2[t] - r_2\varphi_3[t] + l_u & \text{for} \quad r_1\varphi_2[t] - r_2\varphi_3[t] - l_u > 0 \\ k_{zm}(r_1\varphi_2[t] - r_2\varphi_3[t] - l_u & \text{for} \quad r_1\varphi_2[t] - r_2\varphi_3[t] + l_u < 0 \\ 0 & \text{for} \quad -l_u \le r_1\varphi_2[t] - r_2\varphi_3[t] \le l_u \end{cases} \tag{1a}$$

or

$$F[t] = \begin{cases} k_{zm}(r_1\varphi_2[t] - r_2\varphi_3[t] + l_u + E_r[t] & \text{for} \quad r_1\varphi_2[t] - r_2\varphi_3[t] - l_u + E_r[t] > 0 \\ k_{zm}(r_1\varphi_2[t] - r_2\varphi_3[t] - l_u + E_r[t] & \text{for} \quad r_1\varphi_2[t] - r_2\varphi_3[t] + l_u + E_r[t] < 0 \\ 0 & \text{for} \quad -l_u \le r_1\varphi_2[t] - r_2\varphi_3[t] + E_r[t] \le l_u \end{cases} \tag{1b}$$

Equations of motion are described by Eqs. (2)–(5).

$$J_s\ddot{\varphi}_1[\mathrm{t}] + k_{s1}\left(\varphi_1[t] - \varphi_2[t]\right) + C_s\left(\dot{\varphi}_1[t] - \dot{\varphi}_2[t]\right) = M_s \tag{2}$$

$$J_{p1}\ddot{\varphi}_2[t] - \mathrm{k_{s1}}(\varphi_1[t] - \varphi_2[t]) - C_s\left(\dot{\varphi}_1[t] - \dot{\varphi}_2[t]\right) + C_z r_1(r_1\dot{\varphi}_2[t] - r_2\dot{\varphi}_3[t]) = -F[t]r_1 \tag{3}$$

$$J_{p2}\ddot{\varphi}_3[t] + k_{s2}(\varphi_3[t] - \varphi_4[t]) - C_s\left(\dot{\varphi}_1[t] - \dot{\varphi}_2[t]\right) + C_z r_2(r_1\dot{\varphi}_2[t] - r_2\dot{\varphi}_3[t]) = F[t]r_2 \tag{4}$$

$$J_m\ddot{\varphi}_4[t] - k_{s2}(\varphi_3[t] - \varphi_4[t]) = M_r \tag{5}$$

2 Model Description in *Mathematica*

The basics for the model description is presented in papers [2] and [3], basic principle is described by Eqs. (1a, b) to (5).

Few code fragments in *Mathematica* syntax [7] are presented below.

Data preparation—model characteristics (external moments, gear pitch error function, gearing's stiffness function, inter-tooth force):

```
Ms=Interpolation[Table[{ωrads[[i]], Msiln[[i]]},{i,1,wymtabω]];

Mr=Interpolation[Table[{czass[[i]], Mrzew[[i]]},{i,1,wymtabcz}]];

If[i4==1,Er(t)=((t-tf1n) (blzaz[[2]]-blzaz[[1]]))/(tfbz-tf1n)
  +blzaz[[1]];ptfpbz=tf1n;ktfpbz=tfbz];

If[i4==1,kzm(t)=((t-tf1n) (sztyzeb[[i4+1]]-sztyzeb[[i4]]))/(tf2n-
  tf1n)+sztyzeb[[i4]];ptfp=tf1n;ktfp=tf2n];

Fbl1(t_)=kzm(t) (Er(t)-luz+r1 φ2(t)-r2 φ3(t));

Fbl2(t_)=kzm(t) (Er(t)+luz+r1 φ2(t)-r2 φ3(t));
```

Dynamics equations and numerical solution function:

```
row1=Cs (φ1'(t)-φ2'(t))+Js φ1''(t)+ks1 (φ1(t)-φ2(t))-Ms;

row2=r1 Cz (r1 φ2'(t)-r2 φ3'(t))-Cs (φ1'(t)-φ2'(t))+r1 Fbl(t)+
  Jp1 φ2''(t)-ks1 (φ1(t)-φ2(t));

row3=-r2 Cz (r1 φ2'(t)-r2 φ3'(t))+r2 (-Fbl(t))+Jp2 φ3''(t)+ks2 (φ3(t)-
  φ4(t));

row4=Jm φ4''(t)-ks2 (φ3(t)-φ4(t))+Mr;

roz=NDSolve[{row1==0,rown2==0,rown3==0,rown4==0,φ1(tp)==φ10,φ2(tp)==φ20,
  φ3(tp)==φ30,φ4(tp)==φ40,φ1'(tp)==φ1p0,φ2'(tp)==φ2p0,
  φ3'(tp)==φ3p0,φ4'(tp)==φ4p0},{φ1(t),φ2(t),φ3(t),φ4(t),φ1'(t),
  φ2'(t),φ3'(t),φ4'(t)},{t,tp,tk},MaxSteps->∞,
  MaxStepSize->maxstepsize,Method->{"EventLocator","Event"->
  event1(t) event2(t) event3(t) event4(t) eventluz(t),
  "EventAction":>Throw[end=t,"StopIntegration"]}];
```

3 Simulation Results

In Fig. 2 electric motor characteristic, input moment M_s [Nm] as a function of a rotation speed in [rad/s] and an output moment M_r [Nm] as function of time [s] are plotted. The gear system transmits the rated power 1000 [kW]. Most simulations presented in papers [8–18] are made for gearboxes of very low transmitted power. Some of them refer to the back to back rigs. It is always uncertain if the results obtained for low power gearboxes can be expected to be the same for high power gearboxes. This paper is devoted to modeling and simulations of high power gearboxes.

Figure 3 gives a gear stiffness characteristic k_{zm} [N/m] as a function of time [s] and an imperfection/error function characteristic as a function of time.

3.1 Simulation Results for Gear Pitch Error $e_{1max} = 0.00002$ m

Figure 4 shows variations of inter-tooth force $F(t)$ and variations of angular rotation speed [rad/s] of the first gear with mass inertia J_{p1}. The variations are caused by variations of stiffness and variations of imperfections shown in Fig. 3.

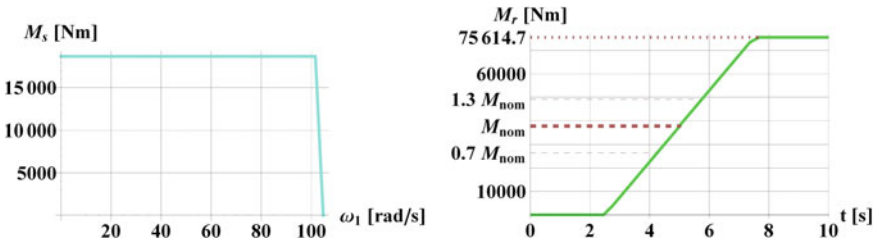

Fig. 2 Electric motor characteristic and output moment characteristic

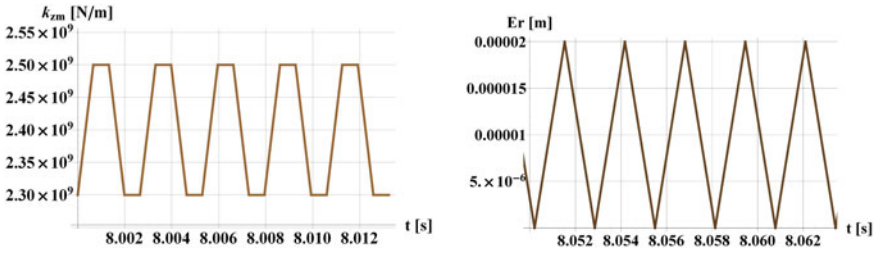

Fig. 3 Gearing's stiffness $k_{zm} = k_z(t)$ and error mode function $Er = e_1(t)$

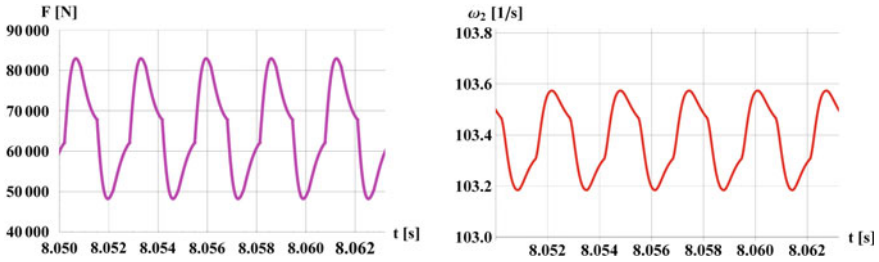

Fig. 4 Inter-tooth force $F(t)$ and angular velocity $\omega_2(t)$

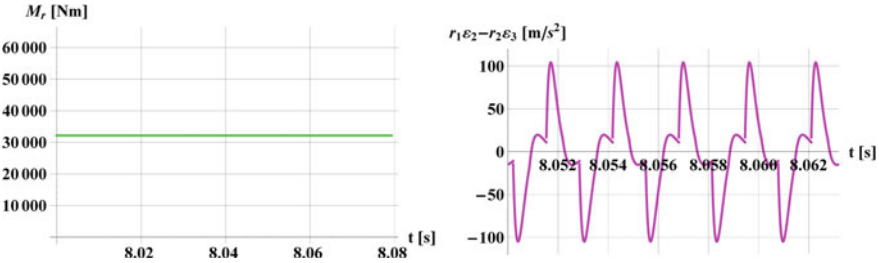

Fig. 5 Moment $M_r(t)$ and acceleration differences $r_1\varepsilon_2(t)$–$r_2\varepsilon_3(t)$

In Fig. 5 acceleration differences $r_1\varepsilon_2(t)$—$r_2\varepsilon_3(t)$ are presented, where $\varepsilon_2(t)$, $\varepsilon_3(t)$ are rotational accelerations of the first and second gear (pin and wheel). The maximum value of the acceleration differences are proportional to the inter-tooth dynamic force acting in the direction of line of a gear action. The external moment M_r is constant. The variations of accelerations are caused by variations of inter-tooth stiffness and gear imperfections.

Figure 6 shows acceleration comparison for maximum imperfection value 0.000022, 0.00002 m and 0—with variable and constant inter-tooth stiffness. It is well seen that acceleration variations are mainly caused by gear imperfections.

Figures 7 and 8 show respectively the course of random error mode of imperfections and the course of acceleration comparison.

It ought to be mentioned that an external/output moment is constant M_r as a function of time [s] as one can see in Fig. 5. Figure 5 also shows variation of acceleration in [m/s^2]. The acceleration can be treated as a measure of design parameters which are expressed in Fig. 3. The inter-tooth force not only cause inter-tooth variation of acceleration but is also transmitted through the bearing on the gearbox case. As it is stated in [2] and [3] the change of the gearing condition can cause increase of imperfections that can cause an increase of the amplitude in the error mode function (Fig. 3). In paper [4] it is stated that inter-tooth acceleration is also a function of external/output load of a gearbox. To illustrate this influence of imperfections, change of a gear condition and influence of an external/output load, the load susceptibility characteristics are given in Fig. 9 showing a change of the

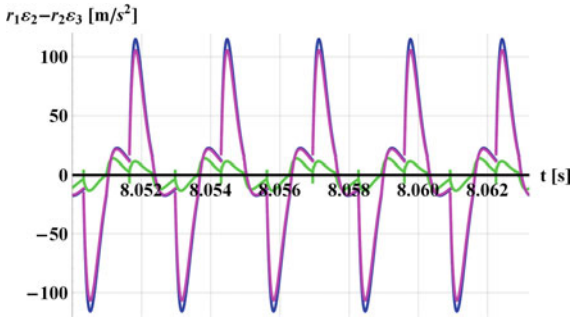

Fig. 6 Accelerations comparison $r_1\varepsilon_2(t)$–$r_2\varepsilon_3(t)$ for some values of $e_{1\max}$ ($e_{1\max}$ = 0.00002 m—*magenta line*, $e_{1\max}$ = 0.000022 m—*blue line*, $e_{1\max}$ = *0*—*green line*, $e_{1\max}$ = *0* and k_{zm} = *const*—*black line*)

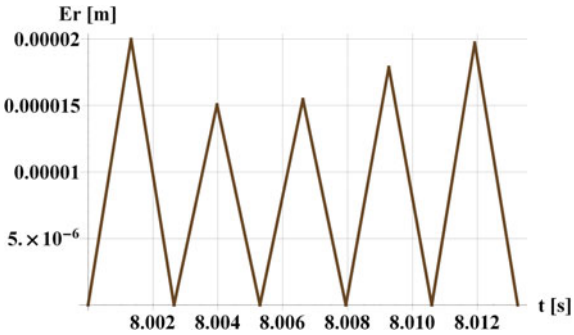

Fig. 7 Random error mode function $Er = e_1(t)$ ($e_{1\max}$ = 0.00002 m)

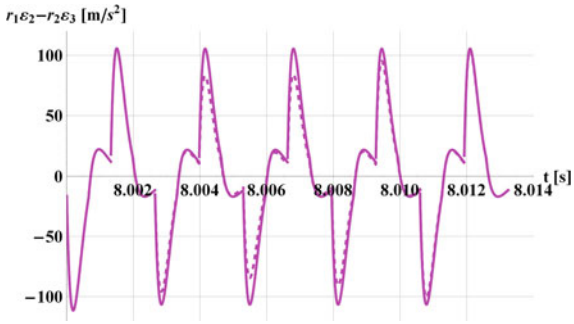

Fig. 8 Accelerations comparison $r_1\varepsilon_2(t)$–$r_2\varepsilon_3(t)$ for constant (*solid line*) and random (*dashed line*) error mode function ($e_{1\max}$ = 0.00002 m)

inter-tooth acceleration. On the Fig. 9 three lines are plotted and approximated by linear regression functions. The regression lines of acceleration are functions of the external/output load expressed by moment M_r [Nm]. The blue line is obtained for

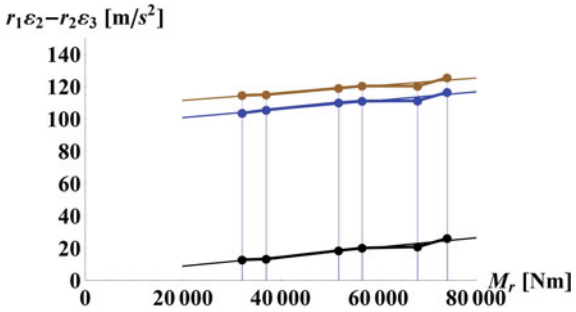

Fig. 9 Load susceptibility characteristics to acceleration differences $r_1\varepsilon_2(t)$–$r_2\varepsilon_3(t)$ for few values of $e_{1\max}$ ($e_{1\max}$ = 0.00002 m—*blue line*, $e_{1\max}$ = 0.000022 m—*brown line*, $e_{1\max}$ = *0—black line*)

an of error $e_{1\max}$ = 0.000020 [m]. In this case an acceleration is caused by variation of the gear pitch error and variations of the gear stiffness. The brown line is obtained for the error $e_{1\max}$ = 0.000022 [m]. This change of the error is a result of gear condition change. This small increase of the error can cause an increase of acceleration of about 10 [m/s^2]. The black line shows the results when the error is $e_{1\max}$ = 0.0, in this case there is only the influence of inter-tooth stiffness, and this causes a drop of the acceleration by 94 [m/s^2]. It is seen that the main cause of the change of inter-tooth acceleration are imperfections. Furthermore, it may be inferred that it is also the main cause of the inter-tooth dynamic force variation.

3.2 *Results Comparison for Different Values of Gear Pitch Error* (e_{1max} = 0.00002 *m*, e_{1max} = 0.000022 *m*, e_{1max} = 0)

See Fig. 9.

3.3 *Acceleration Amplitudes Estimation for* e_{1max} = 0.00002 *m*, e_{1max} = 0.000022 *m and* e_{1max} = 0

Linear estimation of the acceleration amplitudes are as follows:

- for $e_{1\max}$ = 0.00002 m

$$\Delta a = r_1\varepsilon_2(t) - r_2\varepsilon_3(t) = 94.553 + 0.000297M_r, \tag{6}$$

- for $e_{1\max}$ = 0.000022 m

$$\Delta a = r_1\varepsilon_2(t) - r_2\varepsilon_3(t) = 104.395 + 0.000284M_r, \tag{7}$$

- for $e_{1\max}$ = *0*

$$\Delta a = r_1\varepsilon_2(t) - r_2\varepsilon_3(t) = 0.553 + 0.000344M_r. \tag{8}$$

As it is seen from the Eqs. (6) to (8) the load susceptibility characteristic Δa is a linear function of external moment M_r. It is coherent with results obtained in papers [4] and [6] both for simulation and experimental results.

4 Conclusions

The paper presents the possibility to use *Mathematica* for modelling and computer simulations of gearbox systems dynamics. Gearbox system which consists of one stage gear, driving and driven elements—such system is defined as complete system. For the final verification of the system load the susceptibility characteristics have been evaluated. The characteristics have been presented as a linear function of external load represented by external/output moment M_r [Nm]. The results of computer simulations presented are in accordance with results described in papers [4] and [6] showing linearity of the load susceptibility characteristics. Presentation of the final results in the form of the load susceptibility function is very important when the system works in non-stationary operation condition which occurs in most industrial cases. It ought to be stressed that the paper presents introductory results and it is planned to make further developments leading to model multistage gear systems including planetary gear systems.

References

1. Bartelmus W (1999) Transformation of gear inter teeth forces into acceleration and velocity. In: Conference proceedings of the 7th international symposium on transport phenomena and dynamics of rotating machinery Hawaii USA 1998 and International Journal of Rotating Machinery 5, 3, pp 203–218
2. Bartelmus W (2000) Mathematical modelling of gearbox vibration for fault diagnosis. Int J COMADEM 3:4
3. Bartelmus W (2001) Mathematical modelling and computer simulations as an aid to gearbox diagnostics. Mech Syst Signal Process 15(5):855–871
4. Bartelmus W, Chaari F, Zimroz R, Haddar M (2010) Modelling of gearbox dynamics under time varying non-stationary operation for distributed fault detection and diagnosis. Eur J Mech 29:637–646
5. OD Mohamed and others (2014) Dynamic modelling of a one-stage gear system and vibration based tooth crack detection analysis. Mech Syst Signal Process

6. Bartelmus W, Zimroz R (2009) A new feature for monitoring the condition of gearboxes in non-stationary operation conditions. Mech Syst Signal Process 23:1528–1534
7. Wolfram Research, Inc., (2012) Mathematica, Version 9.0, Champaign, IL
8. Wu S, Zuo M, Parey A (2008) Simulation of spur gear dynamics and estimation of fault growth. J Sound Vib 317:608–624
9. Haddar CF (2014) Mohamed modelling of gear transmissions dynamics in non-stationary conditions conference: 6th workshop on cyclostationary systems and their applications, Poland, 09, 2013 In: Chaari F, Leskow J, Napolitano A et al. (ed) Cyclostationarity: theory and methods book series: lecture notes in mechanical engineering, pp 109–124
10. Tian Z, Zuo MJ, Wu S (2012) Crack propagation assessment for spur gears using model-based analysis and simulation. J Intell Manuf 23(2):239–253
11. Chaari F, Zimroz R, Bartelmus W et al (2012) Model based investigation on a two stages gearbox dynamics under non-stationary operations. In: Fakhfakh T, Bartelmus W, Chaari F et al (eds) 2nd International conference on condition monitoring of machinery in non-stationnary operations (CMMNO). Hammamet, Tunisia, 26–28 Mar 2012. Condition monitoring of machinery in non-stationary operations, pp 133–142
12. Ren Y, Tian Z (2012) Dynamic modelling of two-stage gearbox for condition monitoring. In: Pham H (ed) 18th ISSAT international conference on reliability and quality in design location: Boston, MA, 26–28 Jul 2012, pp 136–140 (Sponsor(s): Int Soc Sci Appl Technol Proceedings 18th ISSAT International Conference on Reliability & Quality in Design)
13. Zhou X, Shao Y, Zuo MJ (2010) Features of early cracks in a gear based on a 16dof nonlinear time-varying stiffness dynamic model book group. In: ASME international design engineering technical conferences/computers and information in engineering conference, San Diego, CA, 30 Aug–02 Sep 2009 (Sponsor(s): ASME, Design Engn Div; ASME, computers & Info Engn Div Proceedings of the ASME international design engineering technical conferences and computers and information in engineering conference, 1, pp 349–354)
14. Randall RB (2009) The Application of fault simulation to machine diagnostics and prognostics. Int J Acoust Vib 14:81–89
15. Tian Z, Zuo MJ (2009) Spur Gear Crack Propagation Assessment Using Model Based Analysis and Simulation Edited by: Chu, F; Ouyang, H; Silberschmidt, V; et al. Conference: 8th International Conference on Damage Assessment of Structures (DAMAS 2009) Location: Beijing, Peoples R China, Aug 03–05, 2009 Sponsor(s): Natl Sci Fdn China; Inst Phys; State Key Lab Tribol Damage Assessment of Structures VIII Book Series: Key Engineering Materials 413-414, 299-304 (2009)
16. Lazarz B, Wojnar G, Madej H et al (2009) Evaluation of gear power losses from experimental test data and analytical methods By. Mechanika 6:56–63
17. Wu S, Zuo MJ, Parey A (2008) Simulation of spur gear dynamics and estimation of fault growth. J Sound Vib 317(3–5):608–624
18. Parey A, El Badaoui M, Guillet F et al (2006) Dynamic modelling of spur gear pair and application of empirical mode decomposition based statistical analysis for early detection of localized tooth defect. J Sound Vib 294(3):547–561

Wind Turbine Generator Bearing Fault Diagnosis Using Amplitude and Phase Demodulation Techniques for Small Speed Variations

Ehsan Mollasalehi, Qiao Sun and David Wood

Abstract Vibration analysis of the generator bearing of a large wind turbine using demodulation techniques is discussed in this paper. The purpose of this paper is to show how capable these techniques are for small shaft speed variations. Highest energy band was calculated by wavelet packet transform for amplitude and phase demodulation. Results from the vibration analysis were consistent with a localized outer-race bearing fault. They were then validated by cutting the bearing with water jet machine. A significant localized fault was found on the outer race.

Keywords Condition monitoring · Amplitude demodulation · Envelope analysis · Phase demodulation · Generator bearing · Wind turbine · Outer race fault · Short record

Contents

1 Introduction 386
2 Vibration Analysis Methods 387
2.1 Amplitude Demodulation 387
2.2 Phase Demodulation 388
3 Results and Discussions 389
3.1 Vibration Data 390
3.2 Bearing Characteristic Frequencies 390
3.3 Vibration Analysis—Amplitude Demodulation 391

E. Mollasalehi (✉) · Q. Sun · D. Wood
Department of Mechanical and Manufacturing Engineering, Schulich School of Engineering, University of Calgary, Calgary, AB, Canada
e-mail: emollasa@ucalgary.ca

Q. Sun
e-mail: qsun@ucalgary.ca

D. Wood
e-mail: dhwood@ucalgary.ca

F. Chaari et al. (eds.), *Advances in Condition Monitoring of Machinery in Non-Stationary Operations*, Applied Condition Monitoring 4,
DOI 10.1007/978-3-319-20463-5_29

3.4 Vibration Analysis—Phase Demodulation 393
3.5 Visual Inspection 394
4 Conclusion 396
References 397

1 Introduction

Rolling element bearings have received great attention in the field of condition monitoring. A robust machinery condition monitoring system is very beneficial to capture a defect so as to prevent machinery performance malfunctions, or even catastrophic failures by subsequent root cause analysis. Fault detection can be performed based on information including acoustic emission, stress waveform, oil analysis, temperature variation, vibration, etc. The most common technique for fault detection is vibration signature analysis. Vibration monitoring in rotating machines offers very important information about defects formed inside the structure of the machine. The information gained by vibration analysis enables the planning of maintenance. Vibration signature based diagnostics are mainly concerned with the extraction of those features from a diagnostic signal, which can be related to a good or a defective state of the component.

A survey of over 1000 failed wind turbine generators showed that bearing failure is the dominant cause of wind turbine generator failure as shown in the Fig. 1. This stresses the need of a special monitoring system to maintain the system proactively and avoid any huge damage. The online vibration analysis and proactive

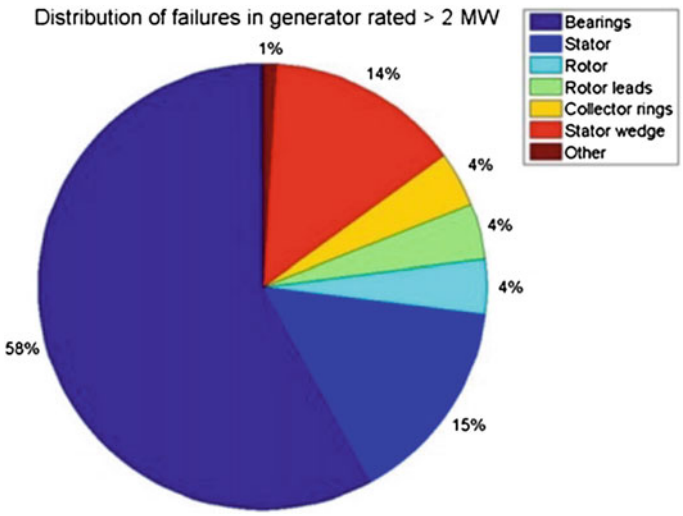

Fig. 1 Failure in wind turbine generator [1]

maintenance cost a fraction of the total cost of replacement and required man-hours and most importantly the indirect cost of the turbine shut down. This paper reflects analysis conducted on the operational data received from the generator bearing of a 1.5 MW wind turbine. The bearing malfunction was identified by ear from the bottom of the tower at the time of operation.

2 Vibration Analysis Methods

Vibration analysis is by far the most prevalent method for machine condition monitoring as it has a number of advantages compared with other methods. One main advantage is that vibration responds without any intervening time to changes in machine condition. Therefore it can be used for both permanent and intermittent monitoring. Vibration analysis has superior characteristics for industrial use and is thus chosen to be the type of analysis in this paper. Due to rotating elements such as shafts and bearings, vibration signals tend to be periodic. Modulating frequencies are produced by specific faults of rotating elements including gears, bearing, and shaft. As a result, the key task to diagnose bearing faults is to detect these modulating signals. Demodulation is an important step in bearing fault detection and thus in the most of machine condition monitoring. The theory behind this method is well described in the literature such as [2] and [3], and is not the purpose of this paper.

Sidebands occur when a signal is under the effect of modulation, a phenomena that occurs when a so-called carrier signal, has its amplitude or frequency to vary with time. The first case, when the amplitude varies with time, is known as Amplitude Modulation (AM) and the latter case, when the frequency varies with time, is called Frequency Modulation (FM) or Phase Modulation (PM), where the FM simply is the time derivative of the PM. As the name implies, the carrier frequency carries the intelligence which is called the modulator. For example in gear vibration signals, the gear mesh frequency and its harmonics are the carriers and the shaft rotating speeds of the meshing gears are the modulators.

2.1 Amplitude Demodulation

Vibration signals with bearing faults can be modeled as an AM of a carrier signal at the resonance frequency by periodic pulses. In so-called Envelope Analysis the signal envelope is extracted by amplitude modulation and frequency analyzed to reveal the repetition frequencies even when these have a small random fluctuation. In the next section, one of the common approaches that can be used for demodulation is briefly presented.

2.1.1 Narrow-Band Amplitude Demodulation

Narrowband demodulation techniques select an interesting frequency band for further analysis as an alternative to analyzing the entire frequency-domain signal. This is performed by plotting the spectrum, and then select the frequency band in frequency-domain (which usually has the highest energy). Therefore, bandwidth filter is applied on the FFT of the signal instead of the signal in time-domain. The algorithm for narrowband amplitude demodulation is now briefly described:

- Apply the FFT on the input signal.
- A frequency band of interest is selected.
- New zero spectrum is generated.
- The new spectrum is filled with the selected frequency band by shifting it to the left hand end of the new spectrum, i.e. the lower limit of the selected band starts at the zero frequency.
- Apply inverse FFT on the spectrum.
- The narrowband amplitude demodulated signal in time-domain is then calculated by taking the absolute value of the complex analytic signal.
- The spectrum of the narrowband amplitude demodulated signal is calculated via absolute value of FFT.

Note that the narrowband selection does not change the length of the signal in the time domain.

2.2 Phase Demodulation

Phase-modulated signal refers to a signal where there is a phase variation with respect to time. For instance, a sine wave whose phase is modulated by another sine wave. The simplest form is described as:

$$x(t) = A\cos[\omega_1 t + \beta\sin(\omega_2 t)] \tag{1}$$

where A is the amplitude of the signal. ω_1 is the carrier frequency, and ω_2 is the phase modulating frequency. β is amplitude of the modulating component.

The signal needs to be reconstructed such that modulated signal's phase is characterized with respect to time. Equation 1 can be written as:

$$x(t) = Ae^{j(\omega_1 t + \beta\sin(\omega_2 t))} \tag{2}$$

Phase at any time instant can be calculated by the angle between the real and imaginary part of the complex signal. Therefore, the idea is to convert the real signal into a complex signal, where the real part is the original signal. This can be achieved by the Hilbert transform.

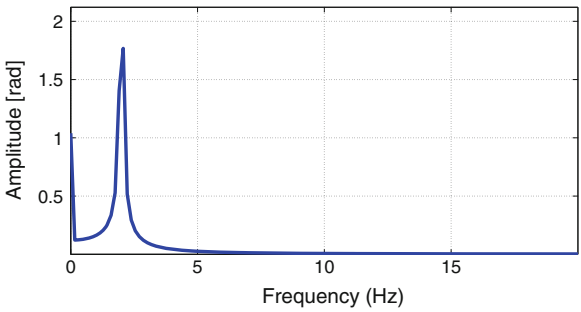

Fig. 2 Spectrum of the phase modulating signal after subtracting the linear fit of the carrier frequency

By taking the signal into the frequency domain by Fourier transform, setting negative frequency to zero and doubling all positive frequencies, the real signal with the complex multiplied Hilbert transform of the same signal is constructed, which is called analytic signal. To summarize, the procedure for phase demodulation can be described as:

- Fourier Transform the signal
- Fix negative frequencies to zero
- Double positive frequencies, except zero frequency
- Reconstruct the complex signal by transform back to the time domain. Analytic signal is then created
- Calculate the instantaneous angle of the analytic signal
- Unwrap instantaneous phase of the original signal to obtain $\omega_1 t + \beta \sin(\omega_2 t)$
- $\omega_1 t$ can be estimated by linear fit of the unwrapped phase. Subtract the linear phase to obtain $\beta \sin(\omega_2 t)$.

To verify the procedure, let's assign values to Eq. 1 as:

$$A = 1, \omega_1 = 32 \text{ Hz}, \omega_2 = 2 \text{ Hz}, \text{ and } \beta = 5$$

Figure 2 shows how the procedure described earlier can detect the instantaneous phase of the modulated signal. The peak shown 2 Hz which is equal to ω_2.

3 Results and Discussions

The main purpose of this paper is to show the simple but useful condition monitoring system for generator bearings which could reduce the cost of repair or maintenance by early indication of the problem and scheduling the maintenance on a proper time. For instance, in many cases, the owner of the wind turbine, replaced a bearing in spring/summer which leads to a higher revenue loss than winter. This late replacement due to the fault associated with an early indication in vibration signature could have been completed in winter when the price of electricity is usually lower than summer.

3.1 Vibration Data

This section reflects the vibration data analyzed. The data was recorded from the on-line vibration monitoring systems on the 80 m 1.5 MW wind turbine:

1. Sensor locations:
   - Drive End Axial (DE-Axi)
   - Drive End Vertical (DE-Ver)
   - Drive End Vertical (DE-Ver)
2. Sampling Frequency:
   - DE-Axi: 5.12 kHz in 3.2 s, and 25.6 kHz in 0.64 s
   - DE-Ver: 0.512 kHz in 16 s, and 5.12 kHz, 3.2 s
   - NDE-Ver: 5.12 kHz in 3.2 s, and 25.6 kHz, 0.64 s
3. Averaged rotational speed of the shaft during the data collection period.
4. The operational data were collected in the period of two months.

This paper does not reflect any results from highest and lowest sampling frequency rates. Vibration results from non-drive end sensor are not reflected here as well. The only set of data shown is associated with 5.12 kHz. It should be noted that the drive-end bearing was connected to the high speed bearing attached to the gearbox by a semi-flexible coupling. Both generator bearings were observed to be making noise and scheduled for replacement.

3.2 Bearing Characteristic Frequencies

Faults on the inner race, outer race, and rolling elements (balls) of a bearing show peaks, called characteristic frequencies. They can be calculated and compared with the peaks in the power spectrum of the demodulated signal to identify the source of the bearing faults. In order to perform the calculations, the following parameters are required [3]:

- Diameter of balls: $d = 4.5$ cm
- Pitch diameter: $D = 23.5$ cm
- Contact angle between the ball and the race: $\alpha = 0$
- Shaft rotational frequency: f
- Number of balls: $n = 9$

Having these values, the following equations are used:

- Ballpass frequency, outer race:

$$\text{BPFO} = \frac{n \times f}{2}\left(1 - \frac{d}{D}\cos\alpha\right) \tag{3}$$

- Ballpass frequency, inner race:

$$\text{BPFO} = \frac{n \times f}{2}\left(1 + \frac{d}{D}\cos\alpha\right) \tag{4}$$

- Fundamental train frequency (Cage speed):

$$\text{FTF} = \frac{f}{2}\left(1 - \frac{d}{D}\cos\alpha\right) \tag{5}$$

- Ball spin frequency:

$$\text{BSF} = \frac{D \times f}{2 \times d}\left(1 - \left(\frac{d}{D}\cos\alpha\right)^2\right) \tag{6}$$

3.3 Vibration Analysis—Amplitude Demodulation

To select the bandwidth of interest to perform envelope analysis, wavelet transform was used to select the highest energy band. Its complete theory and further explanations are discussed in many texts on signal processing such as [4]. Briefly, wavelet transform breaks down the signal to separate frequency bands, called detail and approximation. Each approximation and detail then is split into another approximation and detail, and so on. As the signal energy is proportional to the squared magnitude, then, Root Mean Square (RMS) values for different bands will be calculated. Considering the sampling frequency of 5120 Hz, the frequency bands are:

$$0 - 640 \text{ Hz}, 640 - 1280 \text{ Hz}, 1280 - 1920 \text{ Hz}, 1920 - 2560 \text{ Hz}$$

Figure 3 shows the result of DE-Axi signal at the rotational speed of 868.5 rpm. The wavelet decomposition and RMS showed the highest energy band of 1280–1920 Hz. The primary frequency refers to 52 Hz which is the ball passing frequency outer race (BPFO) harmonic associated with the other harmonics.

Figure 4 shows the result of DE-Axi signal at the rotational speed of 1046 rpm. The wavelet decomposition and RMS calculations showed the highest energy band of 640–1280 Hz. The primary frequency refers to 63.4 Hz which is BPFO harmonic associated with the other harmonics.

Figure 5 shows the result of DE-Axi signal at the rotational speed of 1181 rpm. The wavelet decomposition and RMS calculations showed the highest energy band

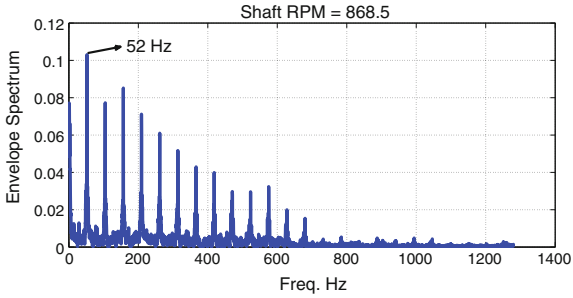

Fig. 3 Envelope spectrum, DE-Axi at 868.5 RPM

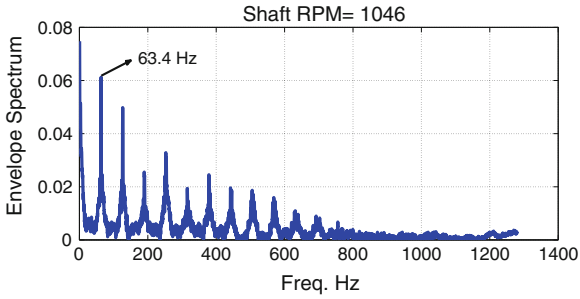

Fig. 4 Envelope spectrum, DE-Axi at 1046 RPM

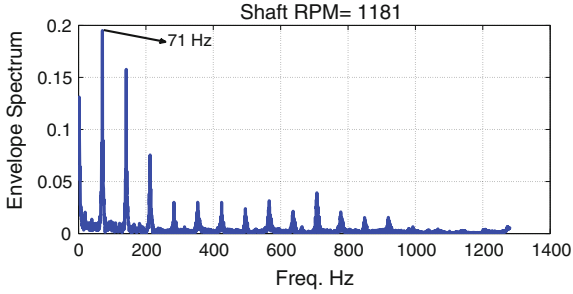

Fig. 5 Envelope spectrum, DE-Axi at 1181 RPM

of 1920–2560 Hz. The primary frequency refers to 71 Hz which is BPFO harmonic associated with the other harmonics.

Figure 6 shows the envelope analysis of DE-Ver signal at the rotational speed of 1125 rpm. The wavelet decomposition and RMS calculations showed the highest energy band of 1920–2560 Hz. However none of the peaks are associated with any of bearing characteristics frequencies. The magnitude is also much lower than the ones calculated from DE-Axi signals. The other signals of DE-Ver also showed the same pattern. As it was mentioned earlier, drive end bearing (DE) is close enough to the gearbox to receive noise (gear mesh signals). Without gearbox configuration information including tooth number of each gear, supporting bearing models and speed (constant or variable speed), vibration signal from the bearing cannot be de-noised. This needs further investigation and analysis.

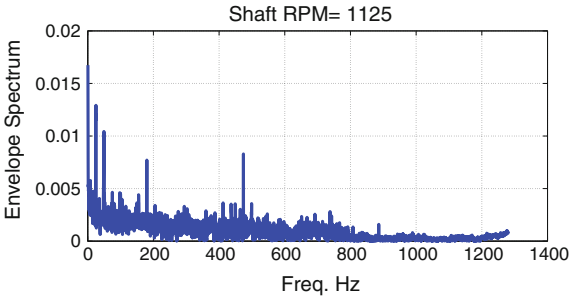

Fig. 6 Envelope spectrum, DE-Ver at 1125 RPM

3.4 Vibration Analysis—Phase Demodulation

Phase demodulation technique is widely used for the application of gearbox fault detection rather that bearing diagnosis. However, in this section it is shown that the phase demodulation can be performed on bearing signals where the shaft speed is nearly constant. The main purpose of performing phase demodulation on a bearing signal could be estimating the shaft speed, where it is not available due to the constrains on the speed measurement. For instance, in terms of the wind turbine generator, industry usually does not install any tachometer on the shaft. Therefore, the shaft speed needs to be calculated either by power generation log or phase calculation for a specific shaft harmonic. Another benefit of bearing phase demodulation is to isolate the unwanted gearbox noise, specially for the bearing close to the gearbox, i.e. drive-end bearing. In any event, narrow-band phase demodulation is recommended, which is not the purpose of this paper, and would be the outcome of the authors upcoming works. That being said, authors try to show the general application of fault detection for bearings in parallel with Amplitude demodulation, as described in Sect. 2.1.

The time signal used for this section has the following features:

- Sampling frequency: 5120 Hz
- Drive-end bearing
- Data collection time period: 3.2 s
- Average shaft speed: 1181 RPM = 19.7 Hz

Figure 7 shows the the spectrum of the phase angle after applying the procedure described in 2.2.

The dashed lines correspond to the bearing outer race characteristic frequency and its harmonics, starting from 71 Hz. In Fig. 7, there are many other peaks whose source are unknown. They could be generated and induced to the system from the gearbox.

To be able to reduce and minimize the unwanted information, narrow-band phase demodulation is performed. The theory behind the narrow-band phase demodulation is similar to the one described in 2.2, however, only applies to the frequency band of interest. Appropriate frequency band can be selected considering

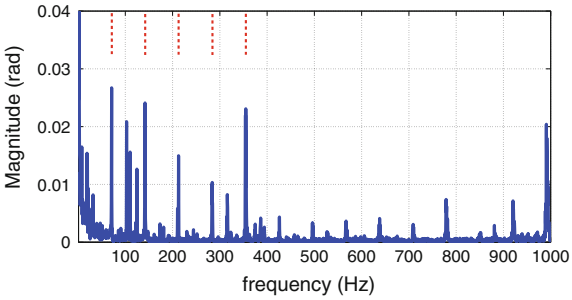

Fig. 7 Spectrum of the modulating phase signal, after phase demodulation. Vertical *dash lines* refer to outer race frequency and its harmonics

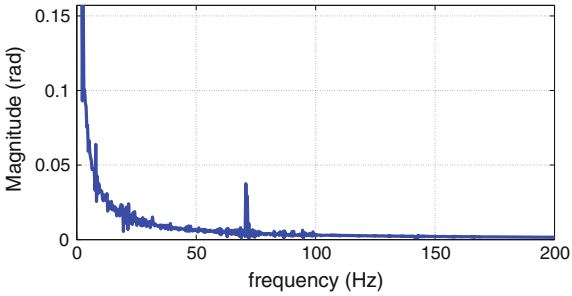

Fig. 8 Spectrum of the modulating phase signal, after Narrow-band phase demodulation

the shaft rotational speed. In other words, one of the shaft speed harmonics can be chosen as the center/carrier frequency. Due to the relative low rotational speed in this application and that it is masked in the spectrum, this method could lead to erroneous results. Instead, as described in 3.3, wavelet transform can be used to calculate the highest energy band which potentially has the maximum required fault information.

Figure 8 shows the spectrum of the phase angle after narrow-band phase demodulation, clearly identifying the outer-race frequency with minimum unwanted peaks. The magnitude scale is dropped due to the band filtration.

3.5 Visual Inspection

In the last section, it was shown that there is a high potential of a fault/defect presenting on the outer race. Analysis was blind, and were not aware of any actual fault at the time of analysis. To validate this conclusion, the bearings disassembled by water jet cutter at the machine shop. As shown in Fig. 9, only the outer race was cut. The bearing was a basic type ceramic insulated bearing, up to 3 kV voltage

Fig. 9 Bearing while water jet cutting

resistance. The races and balls were made of steel. The cage and the housing were made of brass and cast iron, respectively.

Water jet cutting machine do not generate any heat, therefore the bearing was not affected and no new defects/faults were introduced. Figure 8 shows the outer race which has a defect on it. The defect is a localized-type. Faults in this category maybe produced by excessive load, normal fatigue failure, or misalignment. On the other hand, the defect in Fig. 10 is a burned-out type. Generally, this type of fault is generated either by electrical discharge, lack of proper lubrication, or shaft/bearing misalignment. Misalignment which could cause an excessive load on the races/balls, introduced by the shaft or housing, seems to be more possible. The misalignment produced a very high local load on the area and consequently high heat. Therefore the lubrication was burned out. The location of the melted area is shown by a red oval in the left picture in Fig. 8 and zoomed in the right picture. There is some evidence of off-track raceways as well.

This assumption was derived based on the available information and visual inspection. That being said, the root cause analysis at this stage with the provided vibration data would not yield any firm conclusions. Root cause analysis requires

Fig. 10 Fault on the outer race

much complicated analysis with more information. This is the next step which is vital for any maintenance and scheduling the inspection.

4 Conclusion

This paper briefly demonstrated the application of demodulation analysis on the operational vibration signals. Only drive-end data from the generator bearing of a wind turbine were chosen to be reflected in the paper. The results from both amplitude and phase demodulation analyses indicated the presence of fault(s) on the outer race before any inspection to be done by the authors.

To validate the results, the bearing was cut by a water jet cutting machine. Water jet cut was chosen since no heat is introduced to the rolling elements. It was shown that there was a local fault on the outer race. Although there was not enough information to perform the root cause analysis, this type of fault most likely comes from misalignment which can cause very high loads. The misalignment and load could be due to either the shaft or housing, however it is not certain. Further investigations and inspections are required.

An online condition monitoring system with a reliable analysis could reduce the maintenance cost (cost of new parts, man-hour at site, loss of production, etc.) and generally the revenue loss by an early indication of the fault, primarily with a scheduled and proactive maintenance at a proper time. In addition, when a localized outer race fault has been diagnosed by the monitoring system, for example, the faulty bearing does not need to be replaced but only to be rotated 180°; the bearing can operate as new to save cost. The cost of the analysis is small. It is suggested that collecting additional data such as torque/load will provide supplementary

information regarding the status of the bearing, and will lead to firm results. This information could be either collected by torque sensors or calculated by having power and rotational speed.

Still, more sophisticated analysis is required to be able to develop a comprehensive analysis tool. For instance, gearbox data/information will be essential in order to isolate the gear vibration signatures (as shown in Fig. 6), so that the monitoring system can handle all typical mechanical faults.

Acknowledgements The authors would like to thank the TransAlta Corporation, specially Tracy Duncan, for providing the operational data and the bearings, and the Natural Sciences and Engineering Research Council (NSERC) of Canada for financial support under the Industrial Research Chair and Engage programs.

References

1. Rabe U, Janser K, Arnold Wt (1996) Vibrations of free and surface-coupled atomic force microscope cantilevers: theory and experiment. Rev Sci Instrum 67(9):3281–3293
2. Randall R (2012) Vibration based condition monitoring. Wiley, New York
3. Chui CK (1992) An introduction to wavelets. Academic Press, New York, pp 1–200
4. Alewine K, Chen W (2010) Wind turbine generator failure modes analysis and occurrence, Windpower 2010, Dallas, Texas, 24–26 May 2010

Diagnostics of a Defective Bearing Within a Planetary Gearbox with Vibration and Acoustic Emission

Faris Elasha, Matthew Greaves and David Mba

Abstract Whilst vibration analysis of planetary gearbox faults is relatively well established, the application of Acoustic Emissions (AE) to this field is still in its infancy. For planetary-type gearboxes it is more challenging to diagnose bearing faults due to the dynamically changing transmission paths which contribute to masking the vibration signature of interest. The present study is aimed at developing a series of signal processing procedures to reduce the effect of background noise whilst extracting the fault feature from AE and vibration signatures. Three signal processing techniques including an adaptive filter, spectral kurtosis and envelope analysis, were applied to AE and vibration data acquired from a simplified planetary gearbox test rig with a seeded bearing defect. The results show that AE identified the defect earlier than vibration analysis irrespective of the tortuous transmission path.

Keywords Planetary gearboxes · Acoustic emission · Vibration analysis · Signal processing

Contents

1 Introduction 400
2 Signal Processing and Data Analysis 401
2.1 Adaptive Filter 401
2.2 Envelope Analysis 403
3 Experimental Setup 403
4 Observations of Vibration Analysis 406
5 Acoustic Emission Observations 407
6 Discussion and Conclusion 409
References 410

F. Elasha (✉) · M. Greaves
School of Engineering, Cranfield University, Cranfield, UK
e-mail: f.elasha@cranfield.ac.uk

D. Mba
School of Engineering, London South Bank University, Southwark, UK
e-mail: mbad@lsbu.ac.uk

F. Chaari et al. (eds.), *Advances in Condition Monitoring of Machinery in Non-Stationary Operations*, Applied Condition Monitoring 4,
DOI 10.1007/978-3-319-20463-5_30

1 Introduction

Planetary gearboxes are important components of rotating machines due to their high transmission ratio, higher torque to weight ratio and high efficiency [1]. As such this type of gearbox is widely used in many industries such as aerospace, wind turbines, mining and heavy trucks [2–6]. Different planetary gearbox configurations and designs allow for a range of gear ratios, torque transmission and shaft rotational characteristics. The planetary gearbox generally operates under severe conditions, thus the gearbox components are subject to different kinds of fault conditions such as gear pitting, cracks, etc. [7–10]. Recent investigations on wind turbine applications of planetary gearboxes have shown that failures initiate at a number of specific bearing locations, which then progress into the gear teeth. In addition bearing debris and the resultant excess clearances cause gear surface wear and misalignment [10]. The accident to G-REDL [11], resulting in the loss of 16 lives, was caused by degradation of a planet gear bearing, resulting in the failure of the planet gear and, as a result, the loss of the aircraft.

Several authors have proposed numerous diagnostic approaches for planetary gearboxes, with vibration analysis the most commonly employed monitoring technology [1, 7, 9, 12–14]. However, fault detection of bearings within the planetary gearbox is one of the most challenging diagnostic scenarios, as the resulting vibration signatures are influenced by the variable transmission paths from the bearing to the receiving externally mounted sensor. This leads to strong background noise which can mask the vibration signature of interest. This task is compounded by the fact that the gear mesh frequencies typically dominate the resultant vibration signal [7, 13, 15].

More recently, signal separation techniques have been applied in the diagnosis of bearing faults within gearboxes. The separation is based on decomposing the signal into deterministic and random components. The deterministic part represents the gear component and the random part represents the bearing component of the measured signal. The bearing contribution to the signal is expected to be random due to slip effects [8, 16–18]. A number of methods for signal separation are available, each having relative advantages and disadvantages [16, 19–21]. Techniques such as Linear Prediction (LP) have been employed for separation, allowing the separation of the deterministic (or predictable) part of a signal from the random background noise using the information provided by past observations [22, 23]. The results of such techniques depend on the number of past observations considered. Smaller values of past observation produce a poor prediction, giving a result of negligible improvement in the signal-to-noise ratio, while very high values compromise computation time, over-constrain the prediction and tend to reduce even the main components of the signal (both deterministic and non-deterministic parts) [24, 25]. Interestingly LP is applied only to stationary vibration signatures.

In addition to the vibration analysis, the Acoustics Emissions (AE) technology has emerged as a promising diagnostic approach. AE was originally developed for non-destructive testing of static structures, however, in recent times its application

has been extended to health monitoring of rotating machines and bearings [26–29]. AE signal processing is challenged by the attenuation of the signal and as such the AE sensor has to be close to its source. However, it is often only practical to place the AE sensor on the non-rotating member of the machine, such as the bearing housing or gearbox casing. Therefore, the AE signal originating from the defective component will suffer severe attenuation and reflections, before reaching the sensor. Challenges and opportunities of applying AE to machine monitoring have been discussed by Sikorska et al and Mba et al. [30, 31]. To date, most applications of machine health monitoring with AE have targeted single components such as a pair of meshing gears [32], a particular bearing or valve [33–35]. This targeted approach to application of AE has on the whole demonstrated success. However the ability to monitor components that are secondary to the main component of interest such as a bearing supporting a gear, as is the case with planetary gears in an epicyclical gear box, has not been well-explored. This is the first known publication to explore the ability to identify a fault condition where the AE signature of interest is severely masked by the presence of gear meshing AE noise. This paper discusses the analysis of vibration and AE data collected from a simplified planetary gear test rig, and compares their effectiveness in diagnosing a bearing defect in the simplified planetary gearbox. The data was collected for various bearing fault conditions and processed using an adaptive filter algorithm to separate the non-deterministic part of the signal and enhance the signal-to-noise ratio for both AE and vibration. The resultant signatures were then further processed using envelope analysis to extract the fault signature.

2 Signal Processing and Data Analysis

2.1 Adaptive Filter

An adaptive filter is used to model the relationship between two signals in an iterative manner; the adaption refers to the method used to iterate the filter coefficient. The adaptive filter solution is not unique; however the best solution is that which is closest to the desirable response signal [36]. FIR filters are more commonly used as adaptive filters in comparison to IRR filters [37]. The adaptive filter principle is based on Wold theorem which proposes that the vibration signal can be decomposed into two parts, deterministic $P(n)$ and random $r(n)$. This decomposition process can be represented by the following formula [38]:

$$x(n) = P(n) + r(n) \tag{1}$$

The process of separation begins by applying adaptive noise cancellation (ANC). The fundamentals of this method have been detailed in [38, 39]. In application of the self-adaptive Least Mean Square (LMS) algorithm, the reference signal in the application of ANC algorithm is replaced by a delayed version of the input signal.

In this algorithm, the signal is filtered using a Wiener filter, the coefficients of which should be updated for each step. As a consequence, feedback from the filter output is required to estimate the filter coefficients. This process is repeated for each filter step until the prediction error reaches the minimum value. The adaptive filter is a special case of FIR filter expressed by the following relation:

$$Y_i = \sum_{i=0}^{n-1} h_i * x(t-i) \tag{2}$$

where, h_i is the filter coefficient, $x(t-i)$ is corresponding sample of time series signal, and n denotes the number of samples in the input signal. Equation (2) is similar to linear prediction, however the difference is the filter coefficient in this case is estimated recursively based on Least Mean square Error (LMS). In order to optimize filter parameters and minimize prediction error, the prediction error ε_t should be estimated by [39]:

$$\varepsilon_t = d_t - h_i * x(t-i) \tag{3}$$

where, d_t denotes the desirable signal. The filter coefficient should be adjusted to minimize this error function. The error might be random in distribution and as such the expectation of the square error signal is used. This leads to the cost function presented in Eq. (4), which should be minimised in order to find the optimum filter coefficients. This function is defined by:

$$E(\text{MSE}) = E(\frac{1}{2}\sum(d_t - h_i * x(t-i))^2) \tag{4}$$

To optimize the mean square error, the cost function should be minimized.

$$\frac{\partial \text{MSE}}{\partial h} = 0 \tag{5}$$

The solution of this optimization problem leads to the estimation of the optimum coefficients, this solution known as the Wiener–Hopf filter equation [40]:

$$h_{\text{opt}} = [R_{xx}]^{-1} R_{dx} \tag{6}$$

where, R_{xx} is the autocorrelation function of the input signal, and R_{dx} is cross-correlation between input signal and desirable output. However, in the case of the gearbox signal there is no reference signal; instead a delayed version of the input signal is used, therefore the Weiner-Hopf equation is written as:

$$h_{\text{opt}} = [R_{xx}(t-\Delta)]^{-1} R_{xx} \tag{7}$$

where, $R_{xx}(t-\Delta)$ is the autocorrelation of the delayed signal.

In practice, the filter size is very large and the Weiner-Hopf equation is difficult to solve. As a result, an approximated adaptive LMS algorithm is proposed [36], such that the coefficients are updated by:

$$h_{t+1} = h_t + 2\mu\, x(t)\varepsilon \tag{8}$$

In which h_{t+1} denotes the updated filter coefficient, and μ denotes the step size of the filter.

2.2 *Envelope Analysis*

Envelope analysis is applied extensively in vibration analysis for the diagnosis of bearings and gearboxes [9, 15, 41]. As impacts due to the defects excite resonance at higher frequencies, it is possible to identify the frequency of the impacts with the use of envelope analysis. In application, the vibration signal is filtered at high frequencies (structural resonance frequencies) and then the signal is passed through an envelope detector and a low pass filter. The enveloped signal is either presented in the time domain or transformed into the frequency domain in order to identify fault frequency components [42]. In order to detect fault signatures it is important to select filter parameters carefully [43]. In addition, Spectral Kurtosis (SK) has been applied to select such filter parameters [44, 45]. The basic principle of the SK method is to determine the Kurtosis at different frequency bands in order to identify the energy distribution of the signal and to determine where the high impact (transient) energy is located in the frequency domain. Obviously the results obtained strongly depend on the width of the frequency bands Δf [46]. The Kurtogram [22] is a representation of the calculated values of the SK as a function of f and Δf. However, exploration of the entire plane (f, Δf) is a complicated computational task, though Antoni [46] suggested a methodology for the fast computation of the SK.

3 Experimental Setup

A simplified model of a planetary gearbox was employed with gears arranged to represent a typical epicyclic configuration of a planet gear and bearing (see Fig. 1). The input gear of the test rig represents the sun gear in the epicyclic configuration with the idler gear representing a single planet gear and the output gear acts as the ring gear in the epicyclic configuration. The gearbox was driven by electric motor (15 kW) at a rotation speed of 1500 rpm. A load of 10 kW was applied by a dynamometer. Synthetic AeroShell Turbine Oil 555 was employed for the gearbox lubrication, see Table 1.

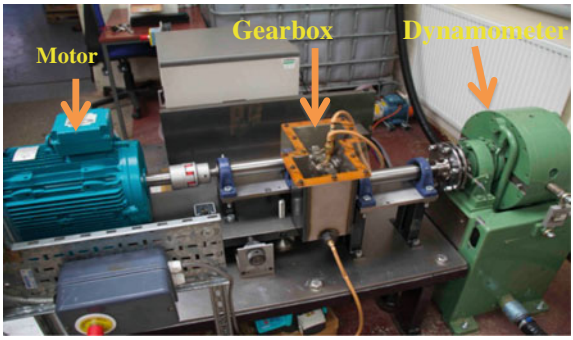

Fig. 1 Test rig layout

Table 1 Gears specification

Gear	Input gear	Idler gear	Output gear
Number of teeth	17	18	19
Module (mm)	4		
Pitch diameter (mm)	77.94	81.94	85.28
Helix angle (°)	25		
Facewidth (mm)	90		
Material	EN36c steel, ground case harden to give a case depth core tensile strength of 1080 Nmm^2		
Oil	Ester synthetic, kinematic viscosity@ 40 °C 11,000 mm^2/s		

The gears were supported by a single row deep groove ball bearings (SKF SYJ 507) whilst the idler gear bore was machined to accommodate two single row tapered roller bearing (SKF 32005 X/Q). As such the outer race of the bearing was in direct contact with the gear inner bore and the outer race rotated with the gear whilst the inner race was stationary, similar to planetary gears employed in epicyclic gearboxes.

Bearing faults were seeded on the idler gear bearing to simulate a planet gear bearing fault. Outer race bearing defects of different sizes were seeded. In total three fault conditions were considered, which included fault free condition, a small defect of 2 mm diameter and 0.5 mm depth and a large defect simulated as a slot across the bearing outer race (2 mm wide and 1 mm deep); see Fig. 2. To aid diagnosis, all characteristic vibration frequencies were determined, see Table 2. These included the shafts speed with its harmonics and the bearing defects frequencies. The bearing defect frequencies were calculated and referenced to the rotating speed. Vibration data was acquired with a triaxial accelerometer (type PCB Piezotronics 356A03) at a sampling frequency of the 51.2 kHz. The accelerometer had an operating frequency range of 2–8 kHz. The acquisition system employed was a National Instruments (NI) cDAQ-9172 chassis fitted with a 9234 module. A 60s sample was

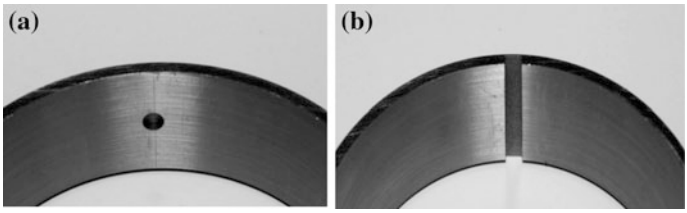

Fig. 2 Seeded fault cases **a** small defect **b** large defect

Table 2 Spectrum frequency components

Component	Frequency (Hz)
Motor shaft	25
Intermediate shaft	23.6
Dynamometer shaft	22.4
Gear mesh frequency GMF	425
Outer race defect frequency	192

recorded for each fault case. The accelerometer was installed on the idler shaft, which runs through the idler gear, as this was not rotating, see Fig. 3. The Y-axis of the tri-axial accelerometer arrangement was oriented parallel to idler shaft direction; the X-axis refers to the vertical axis perpendicular to the idler shaft axis, and the Z-axis is the horizontal axis perpendicular to the idler shaft axis, see Fig. 3. In addition, a Physical Acoustics Corporation (PAC) PICO commercial sensor was placed adjacent to the vibration sensor, see Fig. 6. AE data was acquired at a sampling rate of 5 MHz using a PAC PCI-2 card and a 2/4/6 pre-amplifier, with gain set at 40 dB.

Fig. 3 Vibration (*left*) and AE (*right*) sensor location

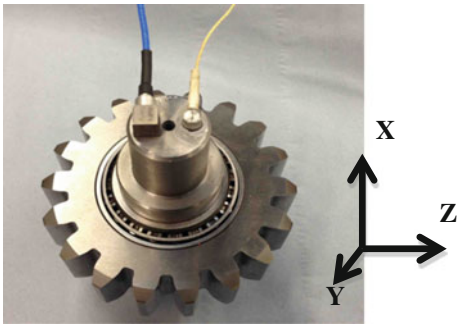

4 Observations of Vibration Analysis

The measured vibration data was processed to estimate the power spectrum of the vibration signal for both damaged and fault-free conditions,. This analysis was performed to assess the ability of FFT spectrum to determine the fault signature. The results show clearly that no distinctive differences can be identified between faulty and fault-free bearing conditions, simply because the defect frequencies were not evident in the spectrum. Therefore the data was further processed using signal separation and Spectral Kurtosis to identify the fault signature as described earlier. The Spectral Kurtosis analysis was undertaken on data sets collected from the gearbox for the different fault cases and this yielded the frequency bands and center frequencies which were then used to undertake the envelope analysis. An example kurtogram used to estimate filter characteristics for different defect conditions is shown in Fig. 4. Spectral plots of enveloped vibration signals following filtration, whose characteristics were determined with the aid of the kurtogram, are shown in Fig. 5.

Observation from the spectra of the enveloped signal in the X-direction, see Fig. 5, showed the presence in the spectrum of the large defect. Typical outer race defect frequency (192 Hz), the 2nd harmonic (384 Hz), the 3rd harmonic (576 Hz)

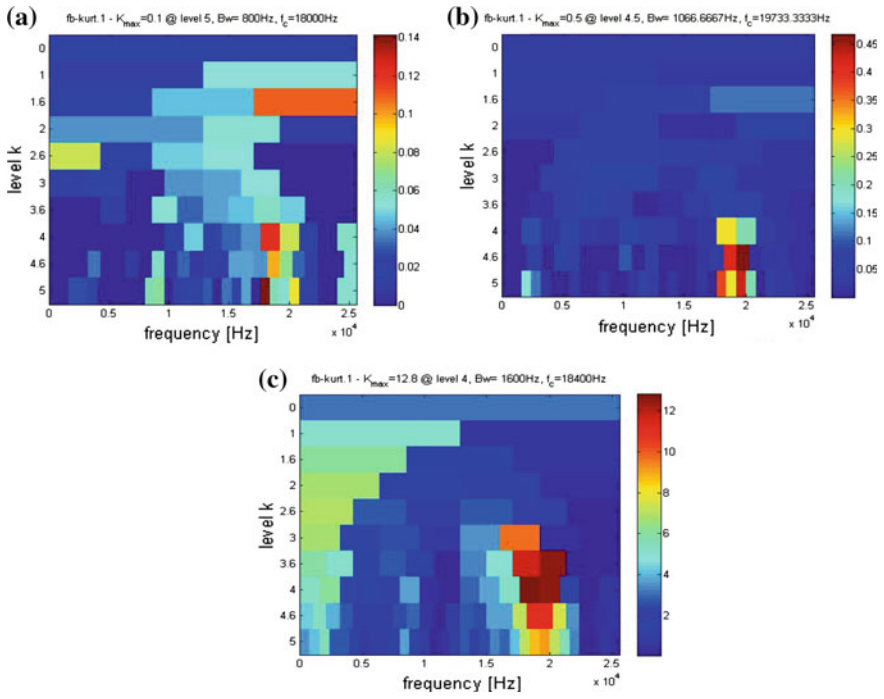

Fig. 4 SK of of non-deterministic signal for **a** Fault-free **b** small defect **c** large defect

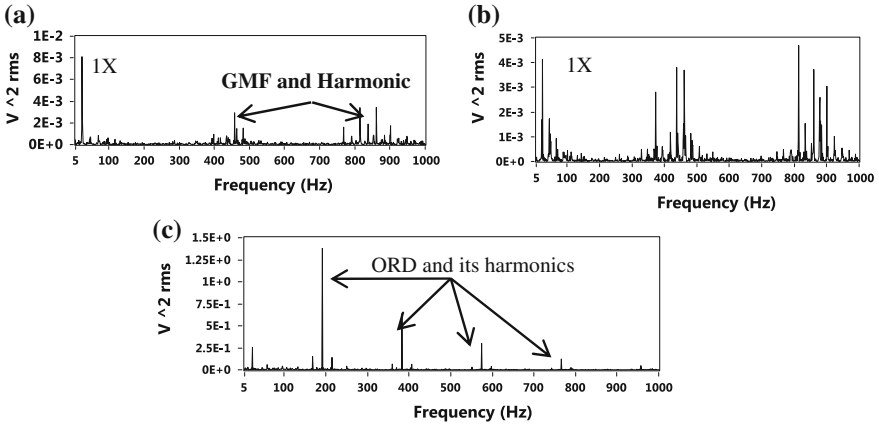

Fig. 5 Enveloped Spectra of non-deterministic signal for **a** Fault-free **b** small size defect **c** large size defect conditions

and 4th harmonics (768 Hz) were detected for large defect. However the small fault condition was not identified by this analysis. It is apparent that the signal separation still had not completely removed the gear mesh and shaft frequencies, which were detected by envelope analysis.

5 Acoustic Emission Observations

Figure 6a shows the AE signature prior to, and after signal separation of the deterministic components. Figure 6b clearly exhibited periodic shocks events that were masked by background noise in the original time trace, Fig. 6a.

The Spectral Kurtosis was employed to extract the filter characteristics which were utilised for envelope analysis on the non-deterministic component of the AE signature. Associated typical kurtograms of SK analysis are shown in Fig. 7. The overall maximum kurtosis for defective bearing conditions was significantly higher compared to fault-free condition which was 3, the maximum kurtosis increased by 600 % for the small outer race defect (18.5) and 3000 % for severe defect condition (91.7) in comparison to the fault-free condition (3).

The envelope analysis was undertaken using the central frequency Fc and bandwidth (Bw) estimated by SK analysis. Observations of Fig. 8b showed the presence of the bearing outer race defect frequency (192 Hz) for the small defect condition. In addition, the outer race defect frequency, and its harmonics, were observed for large defect condition (192 and 384 Hz).

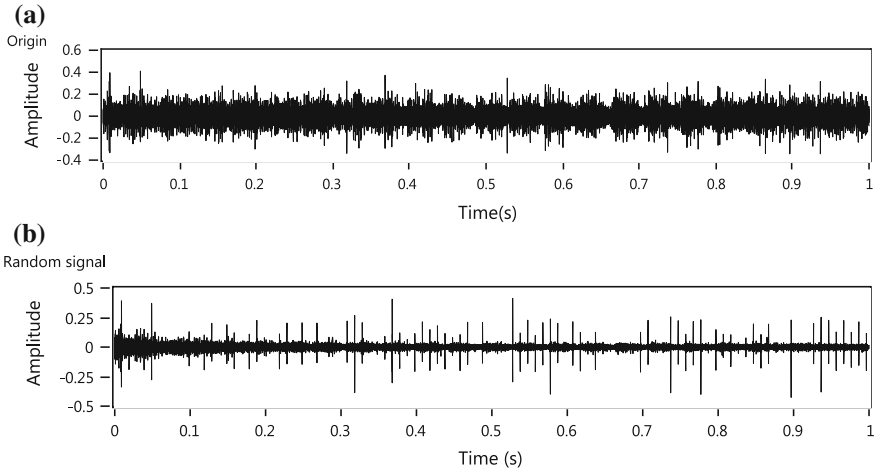

Fig. 6 Time waveform of AE signal **a** before and **b** after separation

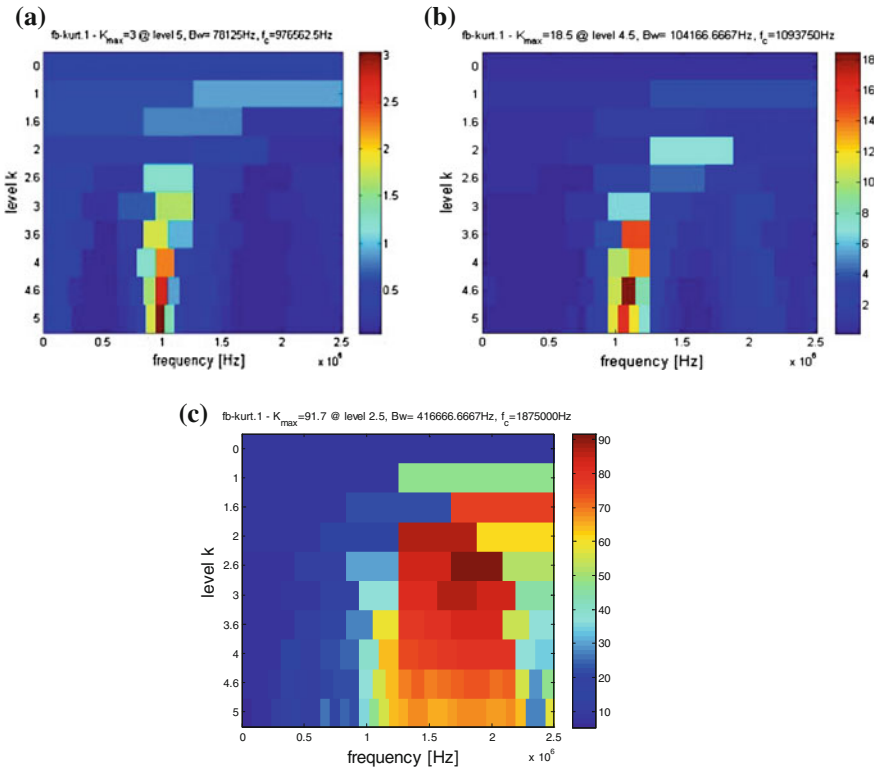

Fig. 7 SK kurtograms **a** Fault-free **b** small **c** large bearing defects

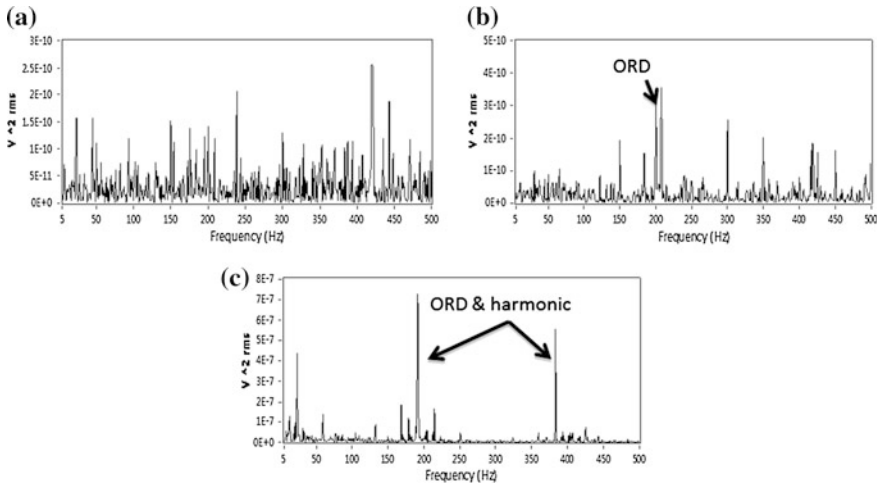

Fig. 8 Enveloped spectra of AE signal **a** Fault-free **b** small **c** large bearing defects

6 Discussion and Conclusion

The techniques used in this paper are typically used for applications where strong background noise masks the defect signature of interest within the measured vibration signature. The AE signal is more susceptible to background noise and in this case, the arduous transmission path from the outer race through the rollers to the inner race and then the shaft makes the ability to identify outer race defects even more challenging. Therefore, the use of signal separation to offer further insight into diagnostic information is deemed necessary for application of AE in the diagnosis of planetary gearboxes.

A comparison of the vibration and AE analysis showed both measurements were able to identify the presence of the large bearing defect based on observations in the enveloped spectra. For the small defect condition however, the enveloped spectrum was dominated by the gear mesh frequencies and their harmonics, and as such the bearing defect frequencies were not evident. However AE analysis was able to identify both the small and large defect conditions. Detection of the small bearing defect gives the AE an indisputable diagnosis advantage over the vibration analysis. The ability of applied signal processing techniques to identify the presence of bearing fault is based on removing the masked signal and the identification of particular frequency regions with high impact energy; these impacts are due to presence of bearing defect which affect bearing sliding motion.

In summary an investigation employing vibration and AE to identify the presence of a bearing defect in a planetary type arrangement has been undertaken. A series of signal processing techniques were applied to extract the bearing fault signature, which included adaptive filter, Spectral Kurtosis, and envelope analysis. The combination of these techniques demonstrated the ability to identify the

presence of the various defect sizes of bearing in comparison to a typical frequency spectrum. From the results presented it was clearly evident that the AE offered much earlier indication of damage than vibration analysis. In addition, the signal processing techniques demonstrated the capability to successfully separate the bearing signal within an AE signal, enhancing the application of AE to gearbox fault diagnosis.

Acknowledgements This work was conducted as part of EASA study 2012.OP.13 into improved detection techniques for helicopter main gearbox defects.

References

1. Cotrell JR (2002) A preliminary evaluation of a multiple-generator drivetrain configuration for wind turbines. In: ASME 2002 Wind Energy Symposium, American Society of Mechanical Engineers, p 345
2. Lynwander P (1983) Gear drive systems: design and application. CRC Press, Boca Raton
3. Kahraman A (1994) Planetary gear train dynamics. J Mech Des 116(3):713–720
4. Huang C, Tsai M, Dorrell DG, Lin B (2008) Development of a magnetic planetary gearbox. Magn IEEE Trans 44(3):403–412
5. PR (2012) Dudley's Handbook of practical gear design and manufacture, 2nd edn. CRC press, USA. ISBN 9781439866016
6. Lu B, Li Y, Wu X, Yang Z (2009) A review of recent advances in wind turbine condition monitoring and fault diagnosis. In: IEEE power electronics and machines in wind applications. PEMWA, Denver, p 1
7. McFadden PD (1987) A revised model for the extraction of periodic waveforms by time domain averaging. Mech Syst Signal Process 1(1):83–95
8. Randall RB (2004) Detection and diagnosis of incipient bearing failure in helicopter gearboxes. Eng Fail Anal 11(2):177–190
9. Wang W (2001) Early detection of gear tooth cracking using the resonance demodulation technique. Mech Syst Signal Process 15(5):887–903
10. Musial W, Butterfield S, McNiff B (2007) Improving wind turbine gearbox reliability, In: Proceedings of the European wind energy conference
11. Department for Transport (2011) Report on the accident to aerospatiale (Eurrocopter) AS332 L2 Super Puma, registration G-REDL 11 nm NE of Peterhead, Scotland, on 1 Apr 2009, 2/2011, Air Accident Investigation Branch, Aldershot, UK
12. Samuel PD, Pines DJ (2005) A review of vibration-based techniques for helicopter transmission diagnostics. J Sound Vib 282(1–2):475–508
13. McFadden PD, Toozhy MM (2000) Application of synchronous averaging to vibration monitoring of rolling elements bearings. Mech Syst Signal Process 14(6):891–906
14. Sawalhi N, Randall RB, Forrester D (2014) Separation and enhancement of gear and bearing signals for the diagnosis of wind turbine transmission systems. Wind Energy 17(5):729–743
15. McFadden PD, Smith JD (1984) Vibration monitoring of rolling element bearings by the high-frequency resonance technique—a review. Tribol Int 17(1):3–10
16. Randall RB, Sawalhi N, Coats M (2011) A comparison of methods for separation of deterministic and random signals. Int J Condition Monit 1(1):11
17. Antoni J, Randall RB (2001) Optimisation of SANC for separating gear and bearing signals. Condition Monit Diagn Eng Manage 1:89–99
18. Ho D, Randall RB (2000) Optimisation of bearing diagnostic techniques using simulated and actual bearing fault signal. Mech Syst Signal Process 14(5):763–788

19. Antoni J (2005) Blind separation of vibration components: principles and demonstrations. Mech Syst Signal Process 19(6):1166–1180
20. Li Z, Yan X, Tian Z, Yuan C, Peng Z, Li L (2013) Blind vibration component separation and nonlinear feature extraction applied to the nonstationary vibration signals for the gearbox multi-fault diagnosis. Measurement 46(1):259–271
21. Barszcz T (2009) Decomposition of vibration signals into deterministic and nondeterministic components and its capabilities of fault detection and identification. Int J Appl Math Comput Sci 19(2):327–335
22. Randall RB (2011) Vibration-based condition monitoring, 1st edn. Wiley, UK
23. Wang W (2008) Autoregressive model-based diagnostics for gears and bearings. Insight Nondestr Test Condition Monit 50(8):414–418
24. Makhoul J (1975) Linear prediction: a tutorial review. Proc IEEE 63(4):561–580
25. Satorius EH, Zeidler JR, Alexander ST (1979) Noise cancellation via linear prediction filtering. In: IEEE international conference on ICASSP '79 acoustics, speech, and signal processing, vol 4, p 937
26. Holroyd T (2000) Acoustic emission as a basis for the condition monitoring of industrial machinery. In: Proceedings of the 18th machinery vibration seminar, Canadian machinery vibration association, pp 27
27. Eftekharnejad B, Carrasco M, Charnley B, Mba D (2011) The application of spectral kurtosis on acoustic emission and vibrations from a defective bearing. Mech Syst Signal Process 25 (1):266–284
28. Kilundu B, Chiementin X, Duez J, Mba D (2011) Cyclostationarity of acoustic emissions (AE) for monitoring bearing defects. Mech Syst Signal Process 25(6):2061–2072
29. Ruiz-Cárcel C, Hernani-Ros E, Cao Y, Mba D (2014) Use of spectral Kurtosis for improving signal to noise ratio of acoustic emission signal from defective bearings. J Fail Anal Prev 14 (3):363–371
30. Mba D, Rao RB (2006) Development of acoustic emission technology for condition monitoring and diagnosis of rotating machines; bearings, pumps, gearboxes, engines and rotating structures. Vibration Institute, Chennai
31. Sikorska J, Mba D (2008) Challenges and obstacles in the application of acoustic emission to process machinery. Proc Inst Mech Eng Part E J Process Mech Eng 222(1):1–19
32. Eftekharnejad B, Mba D (2009) Seeded fault detection on helical gears with acoustic emission. Appl Acoust 70(4):547–555
33. Elforjani M, Mba D (2008) Monitoring the onset and propagation of natural degradation process in a slow speed rolling element bearing with acoustic emission. J Vib Acoust 130 (4):041013
34. Al-Balushi KR, Addali A, Charnley B, Mba D (2010) Energy index technique for detection of acoustic emissions associated with incipient bearing failures. Appl Acoust 71(9):812–821
35. Kedadouche M, Thomas M, Tahan A (2013) Cyclostationarity applied to acoustic emission and development of a new indicator for monitoring bearing defects, 3ième Congrès International sur l'Ingénierie des Risques Industriels, France, July 3–5 2013
36. Douglas SC (1999) Introduction to adaptive filters. CRC Press, Boca Raton
37. Douglas SC, Rupp M (1999) Convergence issues in the LMS adaptive filter. In: Madisetti VK (ed) The Digital signal processing handbook, 2nd edn. CRC Press, Atlanta, USA
38. Widrow B, Glover JR Jr, McCool JM, Kaunitz J, Williams CS, Hearn RH, Zeidler JR, Eugene Dong J, Goodlin RC (1975) Adaptive noise cancelling: principles and applications. Proc IEEE 63(12):1692–1716
39. Widrow B, McCool J, Ball M (1975) The complex LMS algorithm. Proc IEEE 63(4):719–720
40. Simon H (1991) Adaptive filter theory, 2nd edn. Prentice-Hall International Inc, USA
41. Randall RB, Antoni J (2011) Rolling element bearing diagnostics—a tutorial. Mech Syst Signal Process 25(2):485–520
42. Alan D (1998) Handbook of the condition monitoring techaniques and methodology, 1st edn. Chapman and Hall, London

43. Elasha F, Ruiz-Cárcel C, Mba D, Kiat G, Nze I, Yebra G (2014) Pitting detection in worm gearboxes with vibration analysis. Eng Fail Anal 42:366–376
44. Sawalhi N, Randall RB, Endo H (2007) The enhancement of fault detection and diagnosis in rolling element bearings using minimum entropy deconvolution combined with spectral kurtosis. Mech Syst Signal Process 21(6):2616–2633
45. Antoni J, Randall R (2006) The spectral kurtosis: application to the vibratory surveillance and diagnostics of rotating machines. Mech Syst Signal Process 20(2):308–331
46. Antoni J (2007) Fast computation of the kurtogram for the detection of transient faults. Mech Syst Signal Process 21(1):108–124

Methodology for the Estimation of the Fatigue Life of Rolling Element Bearings in Non-stationary Conditions

Urko Leturiondo, Oscar Salgado, Diego Galar and Madhav Mishra

Abstract The estimation of the life of rolling element bearings (REBs) is crucial to determine when maintenance is required. This paper presents a methodology to calculate the fatigue life of REBs considering non-stationary conditions. Instead of taking a constant value, the paper considers cyclic loading and unloading processes, as well as increasing and decreasing values of the speed of rotation. It employs a model-based approach to calculate contact loads between the different elements of the bearing, with a finite element model (FEM) used to calculate the contact stresses. Using this information, it then performs a fatigue analysis to study overloading in faulty bearings.

Keywords Rolling element bearing · Life estimation · Non-stationary conditions · Fatigue

Contents

1 Introduction 414
2 Fatigue Life Estimation Procedure 417
2.1 Bearing Properties and Operating Conditions 417
2.2 Results 418

U. Leturiondo (✉) · O. Salgado
Mechanical Engineering, IK4-Ikerlan, 20500 Arrasate-Mondragon, Gipuzkoa, Spain
e-mail: uleturiondo@ikerlan.es

O. Salgado
e-mail: osalgado@ikerlan.es

U. Leturiondo · D. Galar · M. Mishra
Division of Operation and Maintenance Engineering, Luleå University of Technology, 971 87 Luleå, Sweden
e-mail: diego.galar@ltu.se

M. Mishra
e-mail: madhav.mishra@ltu.se

F. Chaari et al. (eds.), *Advances in Condition Monitoring of Machinery in Non-Stationary Operations*, Applied Condition Monitoring 4,
DOI 10.1007/978-3-319-20463-5_31

3 The Effect of a Damage in the Fatigue Life Estimation 420
4 Conclusions 422
References 423

1 Introduction

The estimation of the life of rolling element bearings (REBs) is very important as these are key components in many rotary systems. A conservative estimation suggests part of the REB life is not used, leading to excessive and unnecessary maintenance; this, in turn, results in the overstocking of spare parts and excessive labour costs. In contrast, a more optimistic estimation suggests there is a risk of system failure, making earlier maintenance essential. In the end, both safety and economic issues have to be taken into account when estimating the life of a REB.

The typology of failure modes that can appear in the various elements of a REB is extensive. For instance, Harris and Kotzalas [1] proposed the following classification of failure and damage modes: failure due to faulty lubrication, fracture of rings due to fretting, failure due to excessive thrust loading, cage fracture, incipient failure due to pitting or indentation of the rolling contact surfaces, failure due to wear, micropitting and failure due to surface- and subsurface-initiated fatigue. To this, Tallian [2] contributed a complete study of numerous damage types. According to the origin of damage, Tallian identified two groups: defects and failure. The first group refers to damage whose origin is in either manufacturing or assembling, whereas the second refers to operation damage. Tallian's list of failures includes the following: mild wear, galling and skidmarking, fretting wear, spalling, surface distress, denting, heat imbalance failure, corrosion and electric erosion, bulk cracking, fracture, permanent deformation, and lubricant failure.

As there are different criteria for classifying the different failure modes, the International Organization for Standardization presented the standard ISO 15243 [3] with the aim of unifying the classification. The ISO list includes six failure modes: fatigue, wear, corrosion, electrical erosion, plastic deformation, and fracture and cracking.

Ferreira et al. [4] analysed 47,030 failed roller bearings used in railway ore transportation and found fatigue is the most common failure mode: almost the 80 % of the REBs in their study failed for this reason. The repeated stress occasioned by the contacts between the elements of a REB implies changes in their surfaces, such as spalling.

The standard ISO 281 [5] is the main document employed for REB selection based on operating life, in which life is defined as the number of revolutions until the first evidence of fatigue develops in any of the elements of a REB. This standard presents a methodology to calculate the rating life, i.e., a prediction of the life of a REB based on a constant stationary load, obtained by means of two variables: basic dynamic radial (or axial) load rating C_r (or C_a) and dynamic equivalent radial

(or axial) load P_r (or P_a). The first represents the constant radial load which a REB can support for a rating life of one million revolutions with 90 % reliability. The second is the constant stationary radial load under the influence of which a REB would have the same life as under the applied load conditions.

Given this, the basic rating life, L_{10}, that is the rating life associated with 90 % reliability, can be calculated as:

$$L_{10} = \begin{cases} \left(\frac{C_r}{P_r}\right)^3 & \text{for radial REBs} \\ \left(\frac{C_a}{P_a}\right)^3 & \text{for thrust REBs} \end{cases} \quad (1)$$

For railway application, SKF [6] modifies Eq. 1 to obtain the basic rating life expressed in operating mileage as:

$$L_{10s} = \frac{\pi \cdot D}{1000} \cdot \left(\frac{C_r}{P_r}\right)^3 \quad (2)$$

where D is the diameter of the wheel.

However, a prediction for the rating life can be done for a different level of reliability than 90 %, thus obtaining what is called the modified rating life, L_{nm} [5]. It can be obtained as:

$$L_{nm} = a_1 \cdot a_{\text{ISO}} \cdot L_{10} \quad (3)$$

where a_1 is the life modification factor for reliability and a_{ISO} is the life modification factor based on a systems approach to life calculation. Expressions for other kinds of REBs can be obtained in [5].

The standard ISO 281 only considers REBs in stationary conditions. In fact, many REBs experience variable operating conditions, with changes in loads (magnitude and direction), speed, lubricant conditions, temperature and level of contamination. There are various methodologies to calculate the life of a REB in non-stationary conditions, based on the simplification of the operating conditions. For example, Ferreira et al. [4] proposed the use of a mean equivalent dynamic load for a wagon experiencing different loading conditions along the track. This mean equivalent dynamic load F_m is expressed as:

$$F_m = \sqrt[3]{\frac{\sum_{i=1}^{k} (F_i^3 \cdot u_i)}{\sum_{i=1}^{k} u_i}} \quad (4)$$

where k is the number of loading conditions, F_i is the ith loading condition and u_i is its respective period of operation. Then, the value of L_{10} is obtained by substituting P_r for the value of F_m.

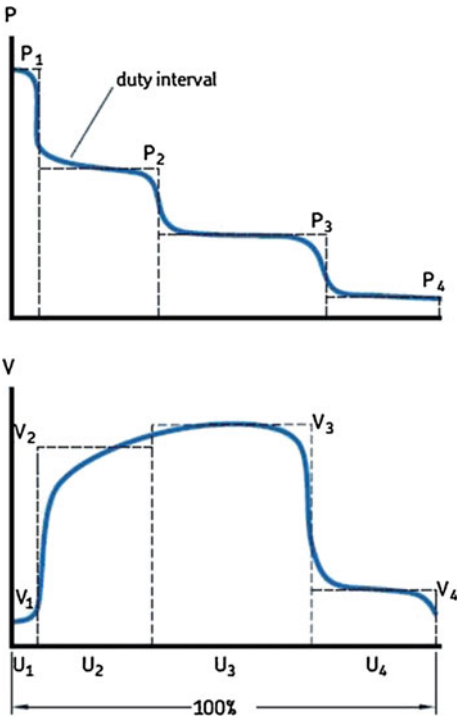

Fig. 1 Variable operating conditions [7] (load at the *top* and speed at the *bottom*)

SKF [7] proposed the reduction of the operating conditions to a limited number of constant load blocks, as shown in Fig. 1. Thus, the life for the variable operating conditions L_{10m} is calculated as

$$L_{10m} = \frac{1}{\sum_{i=1}^{k} \frac{u_i}{L_{10m_i}}} \tag{5}$$

where L_{10m_i} is the basic rating life of a REB given the ith operating conditions.

However, these methodologies are all based on simplifications to constant variable conditions, whether in load or speed, with the aim of applying the theory proposed by the ISO 281. Consequently, the approaches are approximations of the non-stationarity but lose some information, which implies the estimations are conservative. This paper presents a methodology to calculate the fatigue life of a REB in both stationary and non-stationary conditions using a physical modelling approach to take advantage of the whole fatigue life of the REB. It also studies the effect of a fault in the fatigue life.

This paper is structured as follows. Section 2 shows how the fatigue life estimation can be carried out in detail for non-stationary conditions; then, Sect. 3 discusses the effect of faults when estimating the fatigue life; finally, conclusions are presented in Sect. 4.

2 Fatigue Life Estimation Procedure

In order to estimate the fatigue life of a REB in non-stationary conditions, the stress evolution is calculated. For that purpose, we have used two physical models. First, we carry out a dynamic simulation of a REB using the model proposed by Leturiondo et al. [8]. Next, we develop a finite element model (FEM) with the aim of studying the stress in a specific zone of a ring when a unitary load is applied in different positions of that ring. Rather than analysing just the contact stress in one ellipse of contact due to that contact as in Romanowicz and Szybiński [9], we calculate the maximum stress in an ellipse, considering the effect of the contact between all the rolling elements and rings and assuming they are independent of each other.

In this section, we begin by presenting the dimensions of the REB as along with the operating conditions. We then give the results for our fatigue life estimation.

2.1 Bearing Properties and Operating Conditions

A single-row deep-groove ball bearing is selected for this analysis. It has eight balls, and its dimensions shown in Table 1. The REB is made of steel with the following properties: modulus of elasticity E of 207 GPa, Poisson number v of 0.3, density ρ of 7830 kg/m^3, tensile ultimate strength σ_u of 460 MPa and tensile yield strength σ_y of 250 MPa. Table 2 shows the properties of the lubricant. The inner ring is the rotating one; the outer ring is located in rigid housing. A constant value of 30 °C is chosen as the operating temperature T.

Table 1 Dimensions of the simulated REB

Dimension	Value (mm)
Ball diameter, D_w	22.46
Outer raceway diameter, d_o	147.73
Inner raceway diameter, d_i	102.79
Pitch diameter, D_{pw}	125.26
Outer groove radius, r_o	11.6792
Inner groove radius, r_i	11.6792

Table 2 Properties of the lubricant

Property	Value
Dynamic viscosity, η_0	0.04 Pa s
Viscosity-pressure coefficient, c_{η_P}	1.2×10^{-8} Pa^{-1}
Viscosity-temperature coefficient, c_{η_T}	0.05 °C^{-1}
Thermal conductivity, K_c	0.125 J/(kg K)

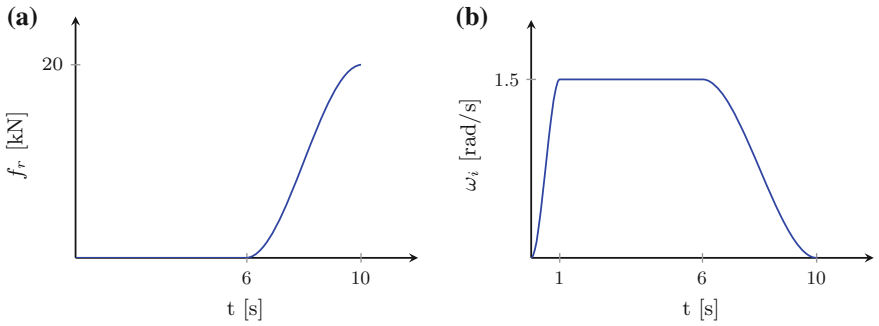

Fig. 2 Non-stationary conditions. (a) Radial force (b) Shaft speed

Non-stationary conditions are applied to both the loading and the speed. Figure 2 shows the time evolution of the radial load f_r and the shaft speed ω_i used in this paper. The defined load and speed profiles try to represent the operating conditions of the loading process of a press.

2.2 Results

In order to obtain the time evolution of the stress in a ring, we calculate two variables. First, we obtain the time evolution of the contact loads between each rolling element and the ring, $Q_j(t, \theta)$, using the dynamic model in the aforementioned operating and REB conditions. Second, using the FEM, we estimate the Von Mises stress $\bar{\sigma}_j(\theta)$ produced in the most loaded zone when a unitary load is applied in different angular positions θ of the ring. Thus, the time evolution of the cumulative Von Mises stress $\sigma_{\mathrm{VM}}(t)$ is calculated as

$$\sigma_{\mathrm{VM}}(t) = \sum_{j=1}^{Z} \left[Q_j(t, \theta) \cdot \bar{\sigma}_j(\theta) \right] \tag{6}$$

where Z is the number of rolling elements.

Figure 3 shows the values of $\sigma_{\mathrm{VM}}(t)$. Using this information, we now apply high-cycle fatigue theory [10] to obtain a life estimation for the REB. First, different loading conditions are defined from that stress signal using the rainflow technique and are summarised in Table 3; n_i is the number of cycles for each loading condition, and $\sigma_{\mathrm{max},i}$ and $\sigma_{\mathrm{min},i}$ are the maximum and the minimum stress for each loading condition, respectively.

Then, we calculate mean and alternate stress (σ_m and σ_a, respectively) for each loading condition as

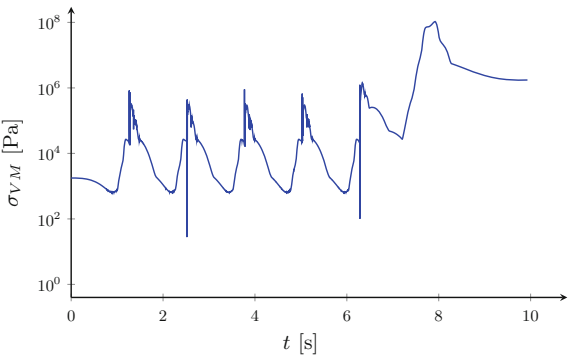

Fig. 3 Time evolution of the Von Mises stress

Table 3 Loading conditions defined by the stress evolution

Case i	n_i (cycles)	$\sigma_{\max,i}$ (Pa)	$\sigma_{\min,i}$ (Pa)
1	0.5	1.062×10^8	632
2	0.5	1773	632
3	4	2.988×10^5	632
4	1	1.332×10^6	2.714×10^4
5	0.5	1.062×10^8	1.74×10^6

$$\sigma_m = \frac{(\sigma_{\max} + \sigma_{\min})}{2} \tag{7}$$

$$\sigma_a = \frac{(\sigma_{\max} - \sigma_{\min})}{2} \tag{8}$$

Once mean and alternate stress are calculated for each loading condition, we use the Goodman fatigue criterion to calculate the equivalent stress σ_{eq} using the following expression:

$$\frac{\sigma_m}{\sigma_u} + \frac{\sigma_a}{\sigma_{\text{eq}}} = 1 \tag{9}$$

where σ_u is the tensile strength of the material.

We now calculate the fatigue life prediction N_i for each loading condition. For that purpose the fatigue curve of the material shown in Fig. 4 is used. Taking the value of the equivalent stress for each loading condition $\sigma_{\text{eq},i}$ as an input in the Y axis, a horizontal line is drawn until the material curve is reached. The value in the X axis for that intersection is the value of N_i. The values of the fatigue life for each loading condition, as well as the values of the equivalent stress, are given in Table 4.

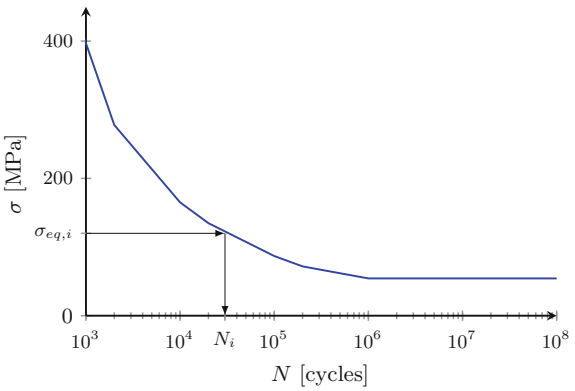

Fig. 4 Stress—life curve of the material

Table 4 Fatigue life prediction for each loading condition

Case i	n_i (cycles)	$\sigma_{\text{eq},i}$ (Pa)	N_i (cycles)
1	0.5	6.003×10^7	7.386×10^5
2	0.5	570	∞
3	4	1.491×10^5	∞
4	1	6.534×10^5	∞
5	0.5	5.917×10^7	7.777×10^5

Finally, Miner's rule [10] is applied to calculate the number of blocks N:

$$\sum_{i=1}^{p} \frac{n_i}{N_i} = \frac{1}{N} \tag{10}$$

where p is the number of loading conditions, in this case equal to 5. This results in a life estimation of 7.576×10^5 cycles under the explained procedure.

3 The Effect of a Damage in the Fatigue Life Estimation

As a bearing operates, the alternating loads caused by the non-stationary conditions and by the pass of the rolling elements leads to fatigue damage. These faults appear progressively, from microcracks producing first flacking, then spalling, and finally, peeling.

The appearance of this kind of fault amplifies the contact stress. In this work, we model the outer ring of a REB with a damaged area at the most loaded zone using a FEM. We then use the model to calculate the stress concentration factor k_f due to the fault in the outer ring, as in Kršćanski and Turkalj [11] for fillet welded CHS-plate T-joints. Figure 5 shows the evolution of k_f, defined as a function of the angular distance to the fault, θ.

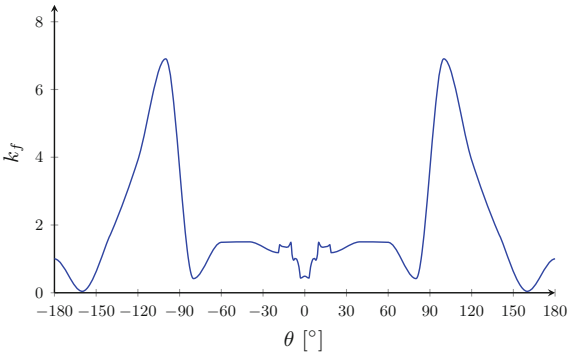

Fig. 5 Stress concentration factor

As the figure shows, the maximum values occur at near 90; this occurs because bending is produced in the fault when a load is applied in these angular positions. Moreover, the effect of traction/compression in the stress is almost negligible as the value of k_f for a distance of 180° is equal to 1.

Besides the effect on the faulty zone itself, a damaged area has a great impact on other contact areas. Leturiondo et al. [8] showed that when a rolling element reaches a fault, the contact between this rolling element and the ring is lost. Consequently, the rear and front rolling elements suffer from overloading to maintain the applied load.

We now consider the effect on the fatigue life of the overloading produced due to the loss of contact between a rolling element and a ring when the former reaches the damage. As the selected bearing has eight balls, the overloaded zones are located at an angular distance of 45°. As we are studying a symmetric case, the result is the same for both positions. The damage is defined by means of two cubic curves, as shown in Fig. 6; its dimensions are the following: 1 mm depth (h) and $\pi/45$ rad of angular length (ψ).

The stress evolution is shown in Fig. 7 and the information on the different loading conditions obtained from this signal appears in Table 5.

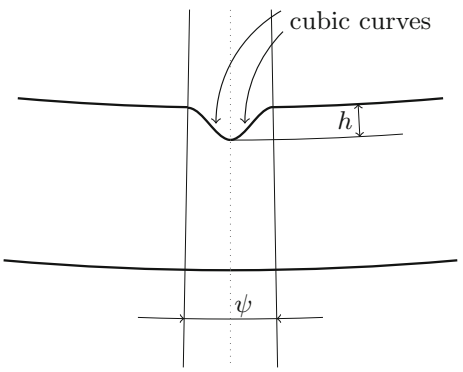

Fig. 6 Fault scheme

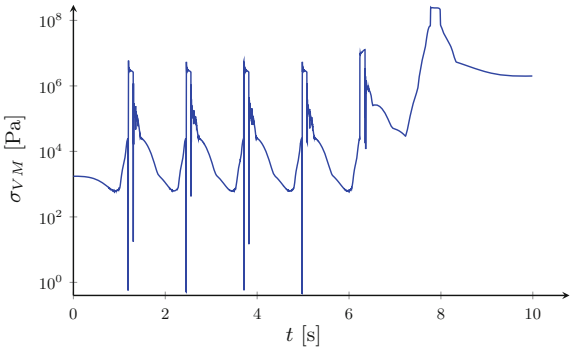

Fig. 7 Time evolution of the Von Mises stress for the faulty REB

Table 5 Loading conditions defined by the stress evolution for the faulty REB

Case i	n_i (cycles)	$\sigma_{\max,i}$ (Pa)	$\sigma_{\min,i}$ (Pa)	$\sigma_{\text{eq},i}$ (Pa)	N_i (cycles)
1	0.5	2.481×10^8	606	1.699×10^8	9.67×10^3
2	0.5	1745	606	569	∞
3	4	3.52×10^6	606	1.767×10^6	∞
4	1	1.286×10^7	2.929×10^4	6.507×10^6	∞
5	0.5	2.481×10^8	2×10^6	1.69×10^8	9.721×10^3

This faulty condition leads to a fatigue life of 9.69×10^3 cycles. Therefore, the loss of contact between a ring and a rolling element when the latter reaches the fault directly affects to the REB life of the outer ring corresponding to the front and rear rolling elements position. In this case, the overloading produced in this area implies the fatigue life is reduced by approximately 78 times.

4 Conclusions

The literature provides a number of approaches to estimating the fatigue life of a REB. Besides the standardised methodology given by ISO 281 for constant operating conditions, some methods offer to calculate the fatigue life for non-stationary conditions. But these are based on obtaining one or a series of constant equivalent conditions in order to apply the standardized technique to each equivalent condition.

This paper proposes the use of the knowledge of the dynamics of a REB in non-stationary conditions with appropriate knowledge of the stress evolution in the different components. This yields to a stress evolution that can be evaluated using classic fatigue theory. Thus, an estimation of the fatigue life of a REB can be done in non-stationary conditions.

Our results show the effect of a fault in the life of a REB. Specifically, we analyse the fatigue due to the overloading caused by the loss of contact between a ring and a rolling element when the latter reaches the fault. We find this overloading is important enough to reduce the life of the REB considerably.

Acknowledgments This work has been supported in part by the project ETORTEK MECOFF, economically supported by The Basque Government under project No. IE13-379. Any opinions, findings and conclusions expressed in this article are those of the authors and do not necessarily reflect the views of funding agencies. The authors would also like to thank Fundación de Centros Tecnológicos—Iñaki Goenaga.

References

1. Harris TA, Kotzalas MN (2006) Essential concepts of bearing technology, 5th edn. Taylor & Francis, New York
2. Tallian TE (1992) Failure atlas for Hertz contact machine elements, 1st edn. ASME Press, New York
3. ISO 15243:2004 (2004) Rolling bearings—damage and failures—terms, characteristics and causes. International Organization for Standardization, Geneva
4. Ferreira JLA, Balthazar JC, Araujo APN (2003) An investigation of rail bearing reliability under real conditions of use. Eng Fail Anal 10:745–758
5. ISO 281:2007 (2007) Rolling bearings—dynamic load ratings and rating life. International Organization for Standardization, Geneva
6. SKF (2012) Axle boxes, wheelset bearings, sensors, condition monitoring, subsystems and services. Railway technical handbook, vol 1. SKF Group, Gothenburg
7. SKF (2012) Drive systems: traction motor and gearbox bearings, sensors, condition monitoring and services. Railway technical handbook, vol 2. SKF Group, Gothenburg
8. Leturiondo U, Mishra M, Salgado O, Galar D (2014) Nonlinear response of rolling element bearings with local defects. In: Proceedings of the eleventh international conference on condition monitoring and machinery failure prevention technologies, Manchester, United Kingdom
9. Romanowicz P, Szybiński B (2014) Estimation of maximum fatigue loads and bearing life in ball bearings using multi-axial high-cycle fatigue criterion. App Mech Mat 621:95–100
10. Budynas R, Nisbett K (2014) Shigley's mechanical engineering design, 10th edn. McGraw-Hill, New York
11. Kršćanski S, Turkalj G (2012) FEM stress concentration factors for fillet welded CHS-plate T-joint. Eng Rev 32(3):147–155

Adaptive Vibration Diagnostic Technique for Bearings Condition Monitoring of Complicated Machines

Alexey Mironov, Pavel Doronkin and Alexander Priklonsky

Abstract A new approach to monitoring of rolling bearings called adaptive vibration diagnostic technique is discussed in the paper. Diagnostic methods currently used for bearings monitoring have problems with damage identification caused by its insufficient effectiveness that is illustrated by industrial research study. It is briefly described the basic model of rolling bearing operation and new approach to its condition evaluation using operational transfer function. There is consideration of results of research study on laboratory test bench and trial applications for bearings of jet engine helicopter and swash plate. Results of the technique application on industrial aggregates are discussed. Main benefits of the adaptive technique are analyzed and its input to condition-based maintenance (CBM) is considered.

Keywords Condition monitoring · Vibration diagnostic · Adaptive methods · Bearing · Machines

Contents

1 Introduction 426
2 Efficiency Estimation of a Conventional Technique 426
3 Adaptive Technique and Model of Operating Bearing Vibration Signal 428
4 Tests and Trial Applications of Adaptive Technique 432

A. Mironov (✉) · P. Doronkin · A. Priklonsky
D un D centrs, Riga, Latvia
e-mail: aleksei@ddcentrs.lv

P. Doronkin
e-mail: pavel@ddcentrs.lv

A. Priklonsky
e-mail: alexander@aviaresearch.eu

F. Chaari et al. (eds.), *Advances in Condition Monitoring of Machinery in Non-Stationary Operations*, Applied Condition Monitoring 4,
DOI 10.1007/978-3-319-20463-5_32

4.1 Laboratory Test Rig 432
4.2 Trial Applications 435
4.3 Industrial Research 437
5 Conclusion 438
References 438

1 Introduction

Rolling bearing are obligatory units of practically all rotary mechanisms taking up all static and dynamic loads from a rotor. However, its operational condition could be complicated by abnormal loading, lubricating, or elevated temperatures. So the technical condition of bearings often limits workability of the whole machine.

To increase lifetime and reliability of rotary mechanisms as well as to reduce maintenance costs it is necessary to monitor bearings' technical condition during all its life cycle. Vibration methods of bearings monitoring and diagnostics became the most popular in the last decades. The reason is that vibration signal reflects most of mechanism operation aspects including technical condition of the bearings. The theory and practices of vibration signal analysis are developed well up to moment providing adequate information about technical condition of bearings [1, 2]. Actual diagnostic techniques apply mean-square values, peak/noise ratio, spectral density peaks, and spectrum of an envelope. However, for complicated machines (especially in transport and energy sectors) efficiency of above methods is still low and main problems of these methods are:

- vibration path from a bearing to a sensor is complex, also extrinsic vibration sources may mask bearing signals, so useful signal is lost in the noise;
- application of practically all actual methods to each bearing of specific machine requires its preliminary tests and high-skill expertise to achieve reliable diagnosis.

2 Efficiency Estimation of a Conventional Technique

As a typical tool for bearing monitoring the SKF-manufactured device CMAS 100-5L was selected for assessment of widely used diagnostic technique. SKF is a leading global supplier of products and services associated with roller bearings. For bearing monitoring this device applies *gE* parameter obtained through the envelope detection method. The device generates two kinds of diagnostic messages within measurement process: "Alert"—recommendation to halt the aggregate and investigate its state, and "Danger"—the message signalizing a fault of the bearing.

To estimate effectiveness of the device and its technique we applied it to the reference set of bearings of 12 operating industrial aggregates having different technical states. The efficiency of the technique realized was evaluated using comparison of measured parameters with actual bearings' technical state based on its investigation applying the microscope. Research study included 3 stages: initial measurement of gE parameter of each industrial aggregate equipped by bearing with working life of 2–20 years, repeated measurement after replacement of used bearing for a new one, and laboratory investigation of replaced bearings. The last one allows to separate 12 replaced bearings in two groups: bearings without visible traces of wear (6 pieces) and another 6 bearings having visible faults, as it is illustrated on Fig. 1a.

Comparing the bearings' technical state and signal messages of SKF device, one may come to the conclusion that the device has made errors of first kind (false alarm) and second kind (non-detection or missing target). For example, in 12 tests where vibration of brand-new bearings was investigated, the device had reported a fault (Danger) three times and once more prevention signal (Alert).

For group of 6 replaced bearings with no visible traces (practically healthy state) the device issued Danger twice and Alert—once. Therefore, the device incorrectly identified technical state in 39 % of cases. For another group formed by 6 replaced bearings with substantial faults the device has taken the correct decision in three cases: two times by issuing "Alert" and once—"Danger." In regards to the remaining three bearings with substantial defects, the device has even failed to issue the signal "Alert," so it was interpreted as target missing. Therefore, with respect to that group of bearings, the probability of correct identification of their technical state by SKF device constituted 50 % only.

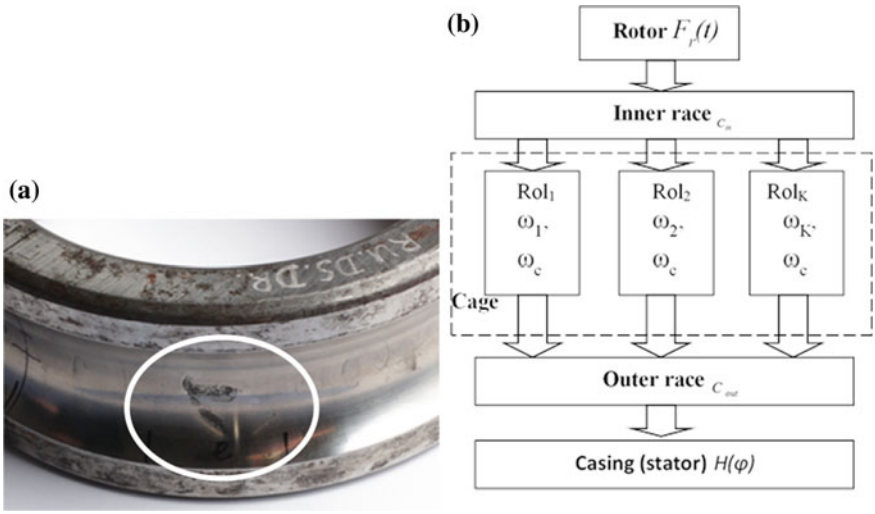

Fig. 1 **a** Visible fault of inner race; **b** bearings component interaction chart

These results suggest that applied traditional technique cannot provide reliable monitoring of machines, since a high percentage of errors of the first and the second kind leads to unsubstantiated prevention maintenance jobs and uncontrolled failures, which ultimately increases the operating costs for the plant maintenance. The problem of the applied technique is that their parameters depend on structural and operational factors that differ for variety of industrial bearings. As a result, two same new bearings in two different industrial plants may show different measures.

3 Adaptive Technique and Model of Operating Bearing Vibration Signal

The new technique, called *adaptive,* settles most of above problems using new approach for extraction of useful components from common vibration signal. This technique considers phase ratios between rotating elements of a bearing (rollers, inner ring, and cage) that allows its extraction. Adaptive technique [3] uses physical model that based on well-known assumption for pulse-mode interaction between rollers/balls and bearing rings. Subjects and order of bearing interaction are illustrated by Fig. 1b. Rotor through inner ring affects balls by inertial dynamic forces $F_r(t)$ caused by both rotating unbalance and housing response. Rotating balls transfer these quasi-periodical forces to outer ring and then to a casing. All rollers (or balls) (Rol_1, Rol_2, …, Rol_K) rotate together with cage (separator) around the rotor axis. By the way, each of them is spinning at its own rate $(\omega_1, \omega_2, \ldots \omega_K)$. Surfaces of ball races are not ideal as its shape has waviness and roughness.

Uneven balls roll along races with its own unevenness and generate pulsed forces acting to a rotor and a stator both. Such pulsed interaction has random mode and looked as a continuous sequence of micro-impacts. However, quasi-periodical motion of rotating components modulates this random process by that creating opportunity for extraction of useful information. The specialty of interaction is though all balls interact with outer ring concurrently, only two of them participate in transmittance of rotor loads to an outer ring (in single-row bearing).

Any fault appearing in a bearing's component increases unevenness of races so the main disgnostic task is to evaluate such unevenness. Unevenness distribution in relation to phase of body revolution $C(\varphi) = 1 + \Delta C(\varphi)$ is called irregularity profile and is used for measurement of race unevenness of bearing component. Phase of component (ball, inner, or outer race) revolution in its rotation is an argument of this function. Irregularity is measured in relative scale and fluctuates by ΔC around 1, which means ideally even race. Sensor on a casing measures momentary vibration that may be described by the expression (1a) that is mathematical model of vibration signal

$$a(t) = \sum_{k=1}^{K} \left\{ \begin{array}{l} H(\varphi_k) * P_r(\omega_r t + \varphi_0^r) * f_k[K\omega_c, \Delta r] \\ *C_{\text{in}}(\varphi) * C_{\text{out}}(\varphi) * C_k^{\text{rol}}(\varphi) \\ +H(\varphi_k) * F_{\text{rol}}^k(m_k, \omega_c) * C_{\text{out}}(\varphi) * C_k^{\text{rol}}(\varphi) \end{array} \right\} \quad (1a)$$

where

$H(\varphi_k)$	stator transfer function between contact point of ball k and outer ring, from one side, and sensor on a casing, from other side;
$P_r(t)$	rotor inertial force transmitted through inner ring to balls;
ω_r	rotation speed of a rotor;
$f_k[K\omega_c, \Delta r]$	lumbering function that is subject of balls quantity K, cage turning rate ω_c and radial clearance Δr;
$C_{\text{in}}(\varphi) = \left[1 + \Delta C_{\text{in}}(\omega_{\text{in}} t + \varphi_0^c)\right]$	inner ring (race) irregularity;
$C_{\text{out}}(\varphi) = \left[1 + \Delta C_{\text{out}}(\omega_{\text{out}} t + \varphi_0^c)\right]$	outer ring (race) irregularity;
$C_k^{\text{rol}}(\varphi) = \left[1 + \Delta C_k^{\text{rol}}(\omega_{\text{rol}}^k t + \varphi_0^{k\text{rol}})\right]^2$	race irregularity of ball No k;
F_{rol}^k	inertial force of ball No k to outer ring;
m_k	mass of ball No k;
ω_{rol}^k	turn rate of ball No k;
$\varphi_0^{r,c,k\text{rol}}$	initial phase of any bearing component

Two augends of (1a) describe two types of inertial forces generated when bearing operates:

- rotor forces transferred by inner ring to outer ring, and
- inertial forces of balls rotating with a cage.

For most of bearings the rotor forces multiply exceed the forces created by balls, so the first augend plays dominant role, but the second one is close to negligible. That is why further consideration will be related for this part of equation only.

$$a'(t) = \sum_{k=1}^{K} \left\{ \begin{array}{l} H(\varphi_k) * P_r(\omega_r t + \varphi_0^r) * f_k[K\omega_c, \Delta r] * \\ *C_{\text{in}}(\varphi) * C_{\text{out}}(\varphi) * C_k^{\text{rol}}(\varphi) \end{array} \right\} \quad (1b)$$

Applying above model for consideration of actual bearing vibration it is necessary to keep in mind that at any moment of time only pair of ("loaded") balls transfers rotor forces to a stator. Weak centrifugal forces acting to other balls and radial clearance do not facilitate sufficient contact, so these (unloaded) balls slide. Such sliding reduces turn rate of unloaded balls that breaks a cage and its rotation speed slightly decreases. Occasional sliding of unloaded balls creates uncertainty of its phases that means any recontacting between specified points of the ball and the

ring will happen with arbitrary phase. Such uncertainty is the main source of occasional component of vibration.

Transfer function $H(\varphi_k)$ is determined by mass-elastic properties of the stator and independent to bearing state and operation mode (1a). Rotor generated forces $P_r\left(\omega_r t + \varphi_0^r\right)$ are considered as quasi-periodical. Lumbering function $f_k[K\omega_c, \Delta r]$ depends of cage turn rate (related by kinematic with rotor speed), phase angle between balls (determined by balls quantity K) and radial clearance in the bearing. This nonlinear function transposes dynamic rotor forces to higher frequency zone ($K \times f_r$). By this, the product of first three multipliers in first raw (1b) is quasi-deterministic and it is not related to race unevenness.

Occasional component of vibration is generated by interaction of balls and races irregularities under rotor forces impact. Three multipliers in second raw (1b) describe this component. The unevenness profile $\Delta C(\varphi)$ is an arbitrary; however, relative rotation periodically repeats occasional micro-impulses and modulates them.

Nonlinear interaction between balls and rings may be presented as multifactor transfer function by those a bearing transfers dynamic forces to a stator

$$\mathrm{MF}(t) = f_k[K\omega_c, \Delta r] * C_{\mathrm{in}}(\varphi) * C_{\mathrm{out}}(\varphi) * C_k^{\mathrm{rol}}(\varphi). \tag{2}$$

This function (called *MF*) transforms dynamic forces induced by a rotor to the sequence of occasional micro-impulses modulated by quasi-periodical motion of an inner ring, a cage, and balls. *MF* function depends on bearing's kinematics, radial clearance, and technical condition of its components, including balls, a cage, and ring races. This function is not related to rotor's motion and forces as well as to stator transfer function.

Replacing multinomial (product of ball races unevenness profiles) in (1b) by MF (t) from (2) we have equation

$$\bar{a}'(t) = \sum_{k=1}^{K} \left\{ H(\varphi_k) * \bar{P}_r(\omega_r t + \varphi_0^r) \right\} * \overline{\mathrm{MF}}(t) \tag{3a}$$

from which we could find estimation of the bearing transfer function

$$\overline{\mathrm{MF}}(t) = \frac{\bar{a}'(t)}{\sum_{k=1}^{K} \left\{ H(\varphi_k) * \bar{P}_r(\omega_r t + \varphi_0^r) \right\}} \tag{3b}$$

Equation (3b) shows that *MF* function could be calculated from vibration vector divided by the product of this casing transfer function and rotor force time vector.

To determine bearing unevenness following data is to be provided:

- measured vibration vectors $A(N)$ and rotation speed signal vector $T(N)$ in digital form (N samples length),
- bearing relative frequencies or construction data for its calculation (type, ball quantity and diameter, ball races diameters).

Using above noted data it is possible to calculate ratio of bearing components' turn rates and order K of modulating function $f_k[K\omega_c, \Delta r]$. Then time vector of rotor forces and casing (stator) transfer function should be found. For this purpose iteration approach may be applied to reduce uncertainty. At first, momentary acceleration values to be measured in three orthogonal directions in order to form time vector of magnitudes. Then synchronized averaging is applied to the vector of magnitudes. Averaged vector acts as the divisor for *MF* function vector calculation, which length N will be the same as raw data vector $A(N)$.

MF transfer function allows estimating technical condition of a bearing at whole. Any reason that causes growth of micro-impulses intensity will increase *MF* function values. In case if bearing vibration dominates, *MF* function may be used for bearing state monitoring. *MF* function could be easily obtained and widely used; however, its application is limited. *MF* function cannot detect the source of bearing operation abnormality, for instance, radial clearance increased or inner ring race is damaged. Another limitation is influence of extrinsic sources of dynamic excitation.

To eliminate above limitations further *MF* function processing is needed that provides separate evaluation of each bearing component condition. Spatial Time Domain Distribution (STDD) developed in our laboratory provides such separate assessment based on *MF* function vector and using calculation routines originating from Eq. (2). Parameters needed for STDD are based from one side on the specific bearing kinematics, and from other side on the knowledge about motion specialties of bearing components dependent on operation mode, lubricating, damaging, etc. To obtain such knowledge the extensive experimental program was carried out. Specially constructed test rig and high-speed camera have been used to study kinematics of operating bearings in different operation modes and technical states.

Above considered approach, including estimation of bearing's transfer function and STDD, has provided some important advantages in contrast with typical diagnostic methods of bearings.

Using *MF* function instead of vibration signal adaptive technique becomes universal for technical condition evaluation of any bearing independently to a type, size, rotation speed and operation mode. This capability appears because condition parameters of adaptive technique are based on assessment of rotor loads transferring quality but not on vibration amplitudes. As irregularity parameters of adaptive technique have relative scale, they are compatible for bearings of different types. This means that parameters' statistics is common for most of bearings types, and being collected for one type may be applied to other types with similar faults.

Adaptive technique has low sensitivity to noise generated by other vibration sources, including frequency components that are multiple for rotation speeds of bearing components. External vibration sources cannot mask diagnostic signs of bearing faults, thanks for considering ball's and cage's motion specialties and utilizing wide frequency range vibration. Using this feature adaptive technique does not require preliminary tests in contrast to conventional methods of bearing diagnostics, which need preliminary research and tests of the object in wide range of its operational modes in order to choose optimal frequency zone for specific bearing mounted in specific aggregate.

Above-mentioned benefits of adaptive technique provide reliable diagnostics of complicated aggregates and machines, where no opportunities to locate a sensor close to a bearing, but there are plenty of external sources of vibration. Such benefits are important especially for gearboxes, turbomachines, piston engines, pumps, and other machines that are widely applied in transport and energy. By adaptive technique it is possible to monitor condition of multiple bearings of the machine using only one vibration sensor that is mounted on machine's exterior part.

Effectiveness of adaptive technique was tested in different research studies and trial applications. Bearings of aviation engines, the drive train, the main rotor of a helicopter or a wind generator and a swash plate have been tested in healthy and faulty conditions. Also the adaptive technique was applied to a wide variety of industrial bearings. Some results are briefly considered below.

4 Tests and Trial Applications of Adaptive Technique

4.1 Laboratory Test Rig

Laboratory test rig was used for the technique approval and for research of bearing components motion (Fig. 2).

This facility includes electric drive, mechanical part, and high-speed camera. Electric drive provides operation of the rotor on two supports in wide range of rotation speed. Mechanical part of facility provides variable conditions of tested bearing operation. High-speed camera (up to 150,000 frames/s) allows measuring parameters of cage and balls motion, which have marking on the end faces of rollers, cage, and inner ring (Fig.2b). Research study had the task to approve effectiveness of adaptive technique to detect healthy or faulty states of the operating bearing as well as states of its components separately. Here below brief results of this study are considered. Three single-row roller bearings had been consequently tested. Each bearing was tested in healthy and faulty states alternately. Test faults have been made by local damages of inner or outer ring races as well as one of rollers. There were 7 technical states of one type of bearings:

- healthy state of each of three same type bearings (*init*1, *init*2, *init*3);
- local damage as a notch crossing inner ring race: depth 0.5 mm, width 1 mm, length 3 mm (*inner*);
- local damage as a notch crossing outer ring race: depth 0.5 mm, width 1 mm, length 3 mm (*outer*);
- damage of one roller as milling with depth 0.8 mm (*roller*);
- combined fault: inner and outer races as well as one roller are damaged (*combB*4).

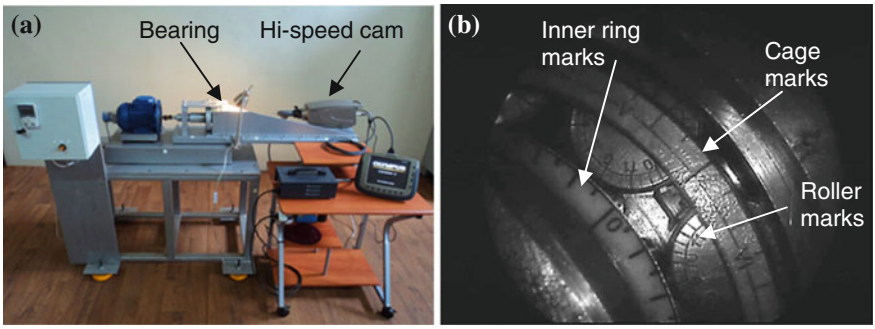

Fig. 2 Experimental test rig for bearing research: **a** common view; **b** typical frame of high-speed camera with marked rollers, cage, and inner ring

4.1.1 Diagnostic Abilities of *MF* Parameters

Diagnostic parameters were calculated using adaptive technique and are presented on Fig. 3.

Figure 3a illustrates in dB scale evaluation of max*MF* parameter to bearing state modification. This most simple parameter calculates maximum value of transfer function in each state. Bearings in healthy conditions had its max*MF* in range 15, 8, …16.9 dB. Faulted inner race of the 1st bearing caused 6 dB growth of the parameter. Outer race fault had affected stronger (13 dB growth), but ball's fault influenced a bit less—9 dB. So, max*MF* parameter certainly separates faulted conditions of a bearing from healthy ones.

The set of parameters inner*MF*, outer*MF*, and roller*MF* have been calculated using STDD and are able to diagnose each component of bearings separately. Diagram on Fig. 2b characterizes race's condition of inner, outer rings, and rollers. As each of these parameters measures only part of total bearing unevenness described by max*MF*, their values are less. Therefore, for healthy components its values vary between 5 dB and 8 dB. Each type of fault caused growth of

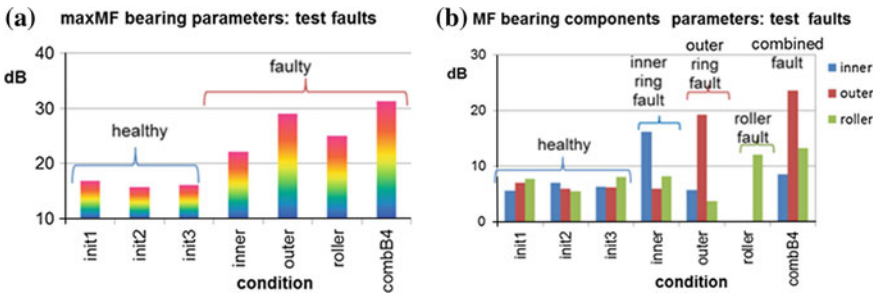

Fig. 3 *MF* parameters diagram of bearing condition: **a** max*MF* parameter for bearing states; **b** *MF* parameters of bearing's components

corresponding parameter. Damaged inner ring of the 1st bearing had uplifted inner*MF* value up to 16.8 dB that means 10 dB (3 times) increase as against healthy state. Same scale fault of the 2nd bearing outer race caused outer*MF* growth up to 19.5 dB, that is, 12 dB higher than initial value. Smaller growth of roller*MF*—up to 12.1 dB was observed when a single roller of the 3rd bearing was damaged. Smaller response to roller's fault is stipulated by rollers motion specialties considered earlier in this paper. It is important that specific *MF* component parameters responding to "its" fault almost do not react to faults of other components. Combined fault caused much greater growth of the parameters with *outerMF* dominating. This fact illustrates transfer function nonlinear dependency of factors combination. In this case decisive influence has radial clearance variation created by interaction of all three faults in one bearing. Such interaction amplifies rollers interaction with outer ring but attenuates it with inner one.

Thus, the set of *MF* parameters provides reliable detection of bearing faults at its early stages, even if a fault appears on one of the components only. The most important benefit of adaptive technique is that it may assess the bearing condition in relative scale without any background. Compatibility of *MF* parameters for most of bearing types means any bearing could be diagnosed by single measurement. Based on the results of the laboratory study the threshold of healthy state (6–8 dB) was preliminary accepted for all *MF* parameters.

4.1.2 *MF* Parameters for Monitoring

MF parameters may provide accurate monitoring of individual bearing's condition using comparing of current appraisals with initial ones. *MF* monitoring allows prognosis of lifetime, maintenance, and repair planning. Figure 4 illustrates *MF* monitoring parameters calculated as difference between faulted and healthy bearings states. The diagram shows definite detection of any fault using *MF* parameters as the tools for monitoring purpose. Indirect assessment of method error may be

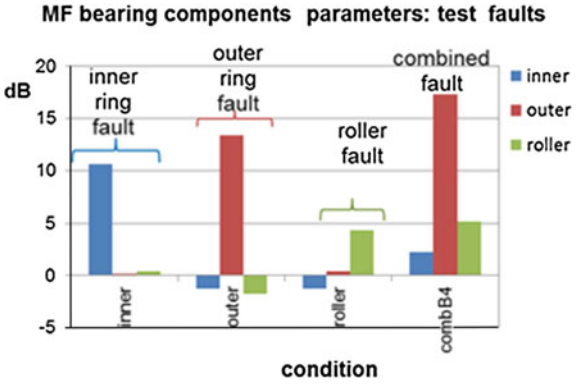

Fig. 4 **a** Diagram: application of *MF* parameters as monitoring tool

estimated by scatter of *MF* parameters for unharmed component of bearings that varies from −1.8 dB to +0.4 dB.

So, experimental check of adaptive technique by laboratory tests has proved its ability to diagnose faults of bearing components separately. This technique could be applied to both monitoring of bearing condition as well as diagnosis of bearings with no "vibration" history of its parameters in initial state.

4.2 Trial Applications

4.2.1 Compressor's Bearing of Aviation Jet Engine (Test Bench)

Trial application on aviation jet engine was aimed to check effectiveness of adaptive technique for diagnosis of the bearing that operates in complicated machine with multiple extrinsic sources. Tested aviation turboprop engine is a part of test bench, where terms of bearings' operation could be approximated to actual ones. The engine operates in "cold" mode being driven by powerful electric motor (Fig. 5a).

To measure vibration signal of front support bearing the 3-axial accelerometer was mounted on intermediate casing of the engine. Preliminary spectral analysis of vibration signal has determined dominating sources of vibration that were: epi-cyclical 2-stage gearbox, gears of lubricating pump, hydraulic, pneumatic, and electric systems as well as aerodynamic vibration generated by compressor's blade wakes. Such combination of sources is typical not only for jet engine but also for helicopter or wind generator main rotor and other machines.

After testing in healthy state the engine has been dismantled. The roller bearing of front support was taken out, and its outer ring has been slightly damaged. Initial scale of damage was minimized to small cross scratch (0.08 mm depth and 1 mm width) aiming to find lower threshold of the technique sensitivity. Then, after testing in the 1st faulty condition the engine has been dismantled again and the scratch has been deepened up to 0.2 × 2 mm. So, the 2nd faulty testing was with

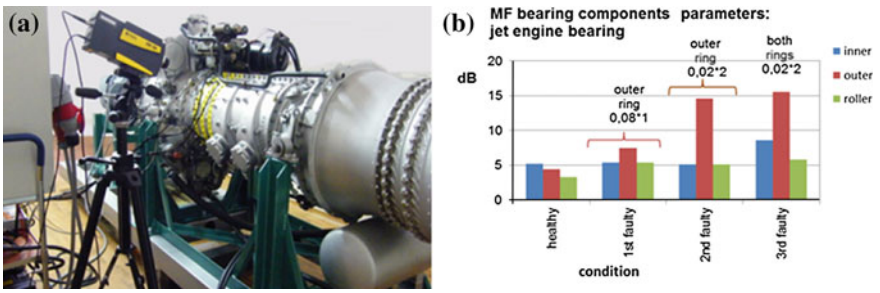

Fig. 5 **a** Aviation turboprop engine test bench; **b** *MF* parameters response to condition modifications of the turboprop engine's bearing

more damaged outer ring. For the 3rd faulty test the bearing was more damaged by adding the same scale damage (0.2 × 2 mm) onto the inner ring. Diagram on Fig. 5b presents testing study results as calculated *MF* parameters for above considered bearing states. Diagram demonstrates that healthy components of this bearing also do not exceed the range 4…6 dB, as it was in the laboratory study. Visible response of *outerMF* parameter (red) to smallest scratch was few (7.5 dB) but doubling of scratch increased growth of the parameter up to 14.6 dB. Such change of the parameter (10 dB in comparison to healthy state) to the typical damage scale at early stage could be considered as satisfactory. It should be noted that other parameters of healthy bearing components did not change practically.

Further development of damage was simulated by same size fault on the inner ring. *OuterMF* almost does not react. *InnerMF* has risen fairly but smaller because of nonlinear influence of both damaged rings.

4.2.2 Swash Plate Bearing of Helicopter Rotor

A bearing of helicopter swash plate operates in specific conditions caused by both: bladed rotor dynamic forces and extrinsic vibration sources like meshing frequencies of a gearbox. To trial the adaptive technique in such conditions the helicopter main gearbox test bench was used (Fig. 6a). Adaptive technique was applied to data collected from the bearing in healthy (initial) operation state, and then in damaged state. In contrast to many others the swash plate bearing has its outer ring as rotating but inner ring as stationary. Another specialty is very low rotation speed that did not exceed 240 rpm in the testing session. Cross scratch of 0.15 mm depth and 1.5 mm width on the inner ring played role of test damage. The bearing responded to the damage by growth of *innerMF* with practically unchanged *outerMF* and *ballMF* parameters (Fig. 6b). Results of experiments on the engine and main helicopter rotor demonstrated technique's high sensitivity to faults on early stage and insensibility to extrinsic influence.

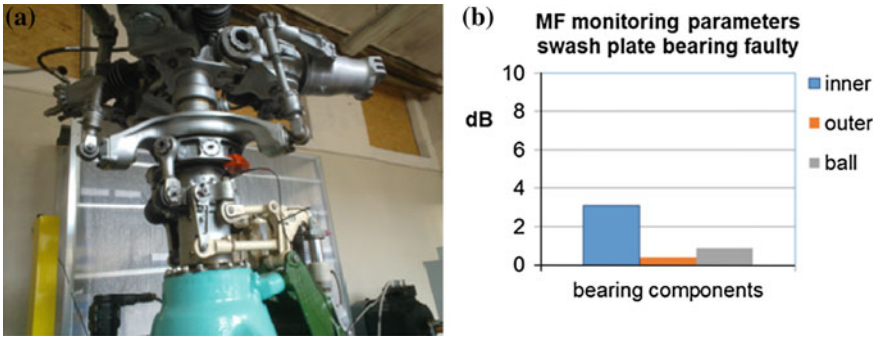

Fig. 6 **a** Helicopter main gearbox and rotor test bench; **b** *MF* parameters of swash plate bearing in faulty state

4.3 Industrial Research

One of the most important benefits of adaptive technique is its universality allowing condition monitoring of any bearings within common scale. Aiming to check this feature on natural scale machines and technique's sustainability in "field" conditions the extensive research program was carried out with some industrial partners. Twelve medium and small size industrial aggregates mentioned in p. 2 have been used as objects for researches.

Figure 1 showed typical fault on replaced bearing but Fig. 7 demonstrates corresponding *MF* parameter diagrams for removed and new bearing of this aggregate. Two local damages on the inner race (Fig. 1) and smaller ones on the outer ring provided 13.4 dB *innerMF* and 11.8 dB *outerMF* (Fig. 7a)—both higher than earlier fixed threshold of healthy state (6–8 dB). Bearing's balls survived with a good state and its parameter remained as for new ones. Replacement with a new bearing returned MF parameter values of this aggregate to "healthy" zone—less than 6 dB (Fig. 7b).

In a similar way, technical state of bearings of all industrial aggregates has been investigated. As optimal for estimation of whole bearing technical condition was used *comb adaptive* parameter, that is, derivative of *MF* parameters for all three components. Diagram on Fig. 8 demonstrates such parameters effectiveness for condition monitoring of whole bearing. It is clear that removed *worn-out* bearings (red color) of all aggregates have parameter values higher than *new* ones.

Six parameters related to aggregates with light worn (no visible traces) are located from left side of diagram (Sper 50 fan—RU st2 pump). Red *comb adaptive* values of above aggregates slightly exceed parameter values of new bearing. Right located six parameter values (RU deg pump—Daina motor) relate to bearings with visible traces of wear. These parameter values of "retired" bearing essentially exceed (8 …22 dB) related new bearing values of the same aggregates.

In contrast to conventional method the adaptive technique in the same set of investigated bearings demonstrated high efficiency. As Fig. 8 demonstrates, the *comb adaptive* parameter of used bearing all the time is higher than of new one in each pair of new and used bearings in the same industrial plant.

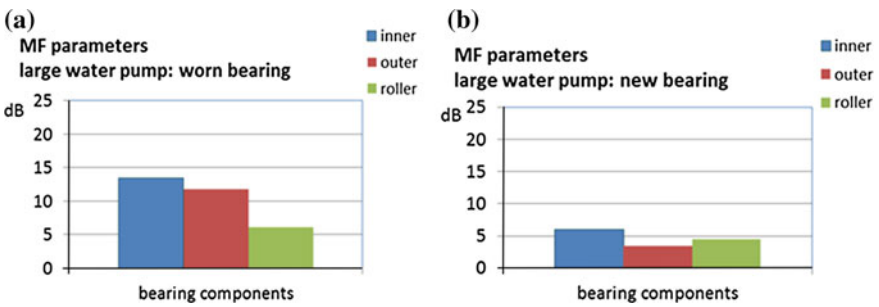

Fig. 7 Sample of deteriorated bearing of water pump: **a** MF parameters of deteriorated bearing; **b** MF parameters of new bearing

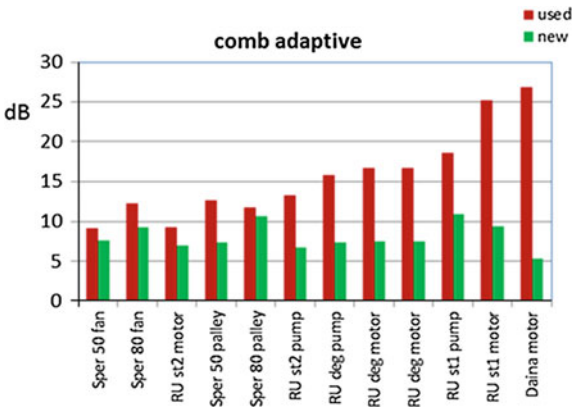

Fig. 8 Diagram: c*omb adaptive* parameters for replaced worn-out bearings (*red*) and new ones (*green*) on 12 industrial aggregates

5 Conclusion

Tests and applications demonstrate weighty proofs of adaptive technique's abilities for bearing diagnostics, especially for complicated machines and aggregates. Universality of the technique regardless of the type, size, rotation speed and operation mode is based on transfer function but not on vibration levels. Relative scale of condition measures makes the technique compatible for different types of bearings that were demonstrated by trial applications. Another benefit is that the technique does not require preliminary research and testing of observed objects. High robustness of adaptive technique to extrinsic vibration sources is maintained by phased synchronization. This approach accounts specialties of rollers/cage motion and use wide frequency range of vibration that assure technique's application to complicated machines and aggregates. Adaptive technique is available for condition monitoring of bearing during its life cycle as well as for diagnosis in one-time survey.

Acknowledgments The paper uses materials related to research study No. 1.26 project of the project "Establishment of Transport Mechanical Engineering Competence Center" L-KC-11-0002 in cooperation with Investment and Development Agency of Latvia.

References

1. Sohoel EO (1985) Method and instrument for determining the condition of an operating bearing. Patent: US 4528852 A
2. Butler DE (1973) The shock-pulse method for the detection of damaged rolling bearings. Non-Destr Test 6(2):92–95
3. Mironov A et al (2014) Adaptive technology application for vibration-based diagnostics of roller bearings on industrial plants. Trans Telecommun 15(3):233–242. doi:10.2478/ttj-2014-0009

Study on Rotating Machine Vibration Behavior Using Measured Vibro-Acoustic Signals

Akilu Yunusa-Kaltungo, Jyoti K. Sinha and Adrian D. Nembhard

Abstract Literatures have shown that there is a significant rise in the use of measured vibro-acoustic signals for faults diagnosis in rotating machines. This is particularly based on the premise that affluent information about a rotating machine's operating conditions is usually conveyed by the sounds of the machine. Several earlier studies have already shown the usefulness and capabilities of amplitude spectra for faults diagnosis. However, very limited analyses of rotating machine's vibro-acoustic signals are available in literatures. Hence, the current study compares the fused amplitude spectra of measured vibration signals from a flexibly supported rotating machine with different faults, using accelerometers and microphones. The experiments, spectra computations and observations are presented here.

Keywords Vibro-acoustic signals · Poly coherent composite spectrum · Data fusion · Faults diagnosis · Condition monitoring · Rotating machines · Flexible foundation

Contents

1 Introduction 440
2 Machine Setup and Faults Initiation 441
3 Data Analysis and Observations 441
4 Concluding Remarks 445
References 445

A. Yunusa-Kaltungo (✉) · J.K. Sinha · A.D. Nembhard
School of Mechanical, Aerospace and Civil Engineering, University of Manchester, Oxford Road, Manchester M13 9PL, UK
e-mail: akilu.kaltungo@postgrad.manchester.ac.uk

J.K. Sinha
e-mail: jyoti.sinha@manchester.ac.uk

A.D. Nembhard
e-mail: adrian.nembhard@postgrad.manchester.ac.uk

F. Chaari et al. (eds.), *Advances in Condition Monitoring of Machinery in Non-Stationary Operations*, Applied Condition Monitoring 4,
DOI 10.1007/978-3-319-20463-5_33

1 Introduction

Although the general concept of data fusion is not particularly new, however, the recent advances in signal processing hardware and techniques have significantly enhanced the practicability of the concept [1]. In general, multi-sensor data fusion involves the merging of measured data from several condition monitoring (CM) sensors (e.g. vibration, sound, temperature, pressure, etc.) installed on an equipment, so as to obtain precise and comprehensive faults diagnosis features that could eventually simplify the overall CM process [2–6]. The current research effort similarly involves the frequency domain fusion of measured CM data (vibration and vibro-acoustic) from several measurement locations of a typical rotating machine with flexible foundations, through the construction of a single representative poly coherent composite spectrum (pCCS) [7] for the entire machine, with the sole aim of reducing the complexities often associated with performing separate analysis at individual measurement locations. The recently developed pCCS method is an enhancement of the earlier introduced composite spectrum (CS) [8] method that offered only amplitude information at individual frequencies. Earlier studies [7] have adequately demonstrated that the retention of both amplitude and phase information by pCCS significantly enhances faults diagnosis as well as eliminates the rigor associated with the application of numerous harmonic components during faults diagnosis.

All previous researches involving the application of CS [8] and pCCS [7] frequency domain data fusion techniques have been restricted to measured vibration signals from rotating machines, probably owing to the maturity and popularity of the techniques for analyzing vibration signals [9–13]. In comparison to vibration analysis, the shift towards the application of vibro-acoustic signals alone and in combination with other popular CM techniques for monitoring the operational condition of rotating machines can be considered to be relatively recent [14–20], however, the study of the different sound patterns emitted by rotating machines under different operating conditions has significantly grown with time. This is perhaps based on the awareness that extensive information about the operating state of a rotating machine can be extracted from its measured sound characteristics [21, 22]. Also, when compared to vibration monitoring which requires contact sensors (e.g. accelerometers), a very significant advantage of faults diagnosis with vibro-acoustic signals is the possibility for non-intrusive measurements, using non-contact sensors such as microphones [23]. In the current study however, a comparison between the pCCS features of vibration signals measured using PCB accelerometers and vibro-acoustic signals measured with microphones installed in close proximity to the bearing pedestals of a flexibly supported rotating machine with different faults and at different speeds, so as to further expose the usefulness of CM using vibro-acoustic signals.

2 Machine Setup and Faults Initiation

The rig shown in Fig. 1 consists of two rigidly coupled 0.02 m diameter mild steel shafts (1 and 0.5 m lengths respectively), and the 1 m shaft is flexibly coupled to the electric motor. Three similarly dimensioned balance discs (outside diameter of 0.125 and 0.015 m thickness) are also distributed along the lengths of the two rigidly coupled rotors. Two of the balance discs are installed on the 1 m shaft at distances of 0.3 and 0.19 m from the flexible coupling and bearing 2 respectively, while the third balance disc is installed midway (i.e. 0.21 m) between bearings 3 and 4 on the 0.5 m shaft. The entire rotor assembly is then supported by four anti-friction ball bearings. Each anti-friction ball bearing is mounted through the aid of four 0.01 m mild steel threaded bars, so as to simulate a flexible foundation.

On the flexibly supported rig in Fig. 1, four commonly encountered machine operating conditions, namely; healthy with residual misalignment, bent shaft, loose bearing and shaft rub were experimentally simulated at two separate machine speeds (1800 RPM and 2400 RPM). Table 1 shows the descriptions, abbreviations, severities and locations of all the four cases studied in the current study.

3 Data Analysis and Observations

Owing to the extensive description of the computational approach for pCCS already provided in an earlier study [7], details of such computations have been omitted from the current study. Hence, a MATLAB code was applied in accordance with

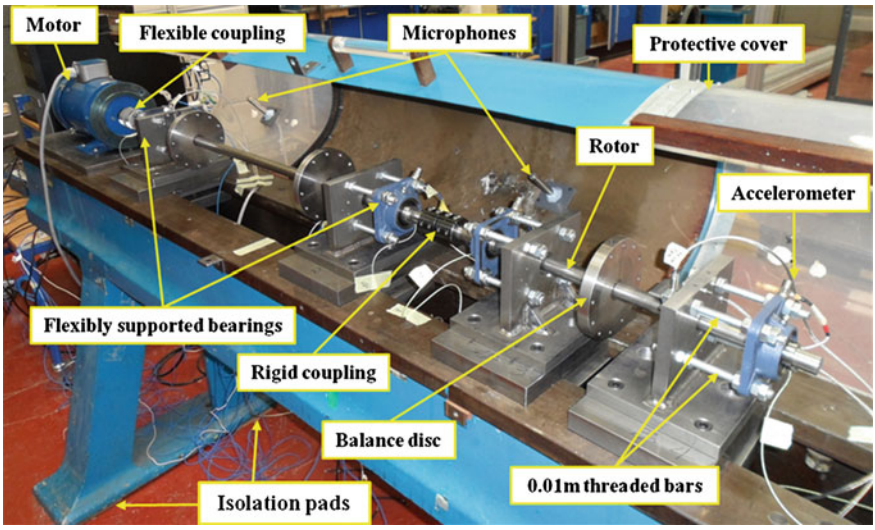

Fig. 1 Machine setup

Table 1 Experimentally simulated cases

Case	Description	Abbreviation	Severity and location
1	Healthy with residual misalignment	HRM	Some residual misalignment, possibly at couplings
2	Bent shaft	BS	0.0034 mm run-out was created at the centre of the 1 m shaft
3	Loose bearing	LB	Loosening some of the bearing 3 threaded bar nuts
4	Shaft rub	SR	Rub using a brass sleeve of 0.021 m on the 1 m shaft near balance disc 2

the previously described pCCS [7] computational approach for the measured vibration and vibro-acoustic data at both machine speeds (1800 RPM and 2400 RPM), using the signal processing parameters shown in Table 2.

The computed pCCS amplitude spectra and phase plots for separately measured vibration and vibro-acoustic data, on the flexibly supported experimental rig (Fig. 1) at two speeds (1800 RPM and 2400 RPM) are respectively displayed in Figs. 2 and 3. From these figures (Figs. 2 and 3), both vibration (Figs. 2a, c, e, g and 3a, c, e, g) and vibro-acoustic (Figs. 2b, d, f, h and 3b, d, f, g) pCCS amplitude and pCCS phase plots exhibit variations in features for each of the experimentally simulated cases at both machine speeds, which provides an indication of the potential of the proposed technique for faults diagnosis with either of the measured data (vibration and vibro-acoustic). For instance, the HRM cases for both signals (vibration and vibro-acoustic) at both speeds [1800 RPM (Fig. 2a, b) and 2400 RPM (Fig. 3a, b)] only possessed prominent peaks at the first (1x) and second (1x) harmonics of the machine speed, which is due to the residual misalignment associated with this case. However, all other higher harmonic peaks (3x, 4x, 5x, 6x, etc.) associated with this case (HRM) for both signals at all speeds were of negligible amplitudes when compared to other cases. On the contrary, the faulty cases (BS, LB and SR) for both measured vibration and vibro-acoustic signals at both machine speeds possessed very prominent higher harmonic component peaks (e.g. 4x, 5x, 6x, etc.) which were more dominant than 1x and 2x peaks for the SR case (Figs. 2g, h and 3g, h). Although the BS case also possessed 4x, 5x and 6x peaks, however,

Table 2 Signal processing parameters

Parameter(s)	Type of signal	
	Vibration	Vibro-acoustic
Sampling frequency (fs) (Hz)	10,000	10,000
Number of data points (*N*)	16,384	16,384
Frequency resolution (df) (Hz)	0.6104	0.6104
Number of averages	148	148
Segment overlap (%)	95	95

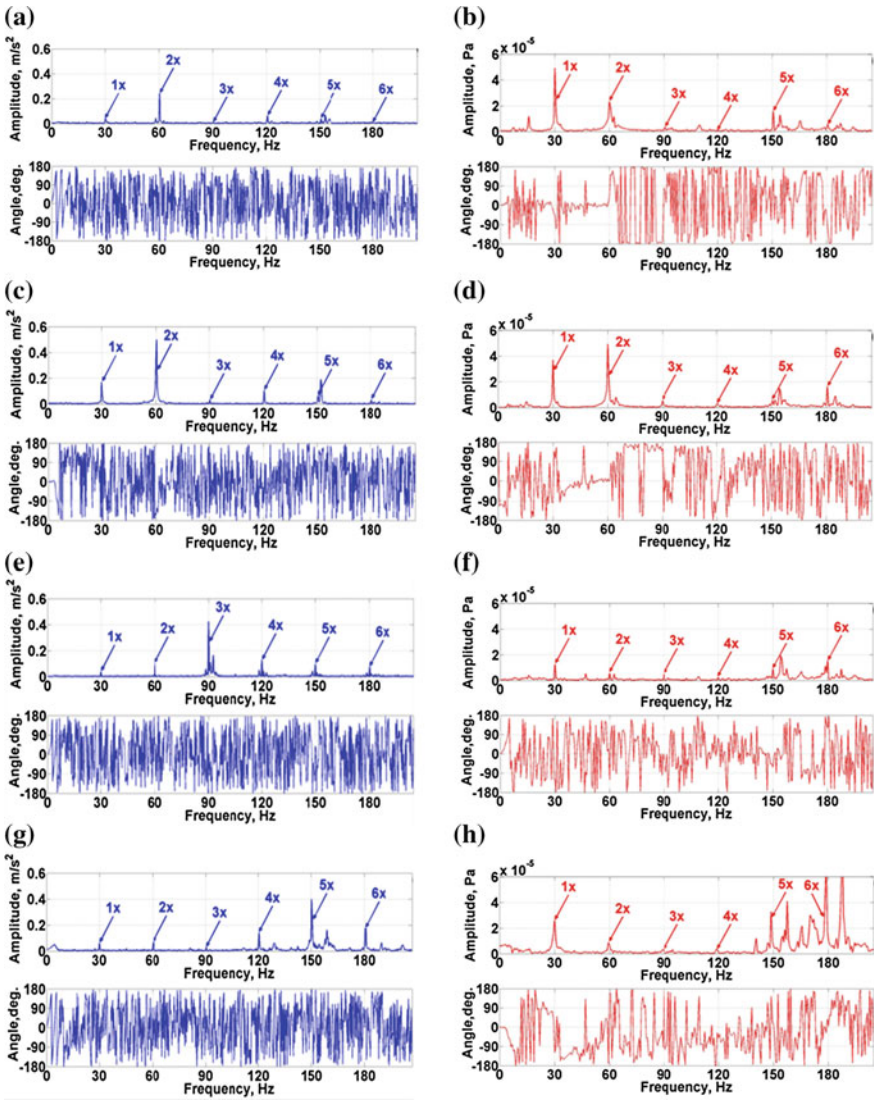

Fig. 2 Typical pCCS and phase plots at 1800 RPM; **a** vibration-HRM, **b** vibro-acoustic-HRM, **c** vibration-BS, **d** vibro-acoustic-BS, **e** vibration-LB, **f** vibro-acoustic-LB, **g** vibration-SR, **h** vibro-acoustic-SR

the magnitude of 3x peaks were relatively low, which was the reverse of the features observed for the LB case (Figs. 2e, f and 3e, f) where 3x peaks were dominant. In addition to the pCCS amplitude spectra, the pCCS phase plots for each of the cases at both machine speeds for measured vibration and vibro-acoustic signals also provide distinctive features, which may further enhance faults diagnosis.

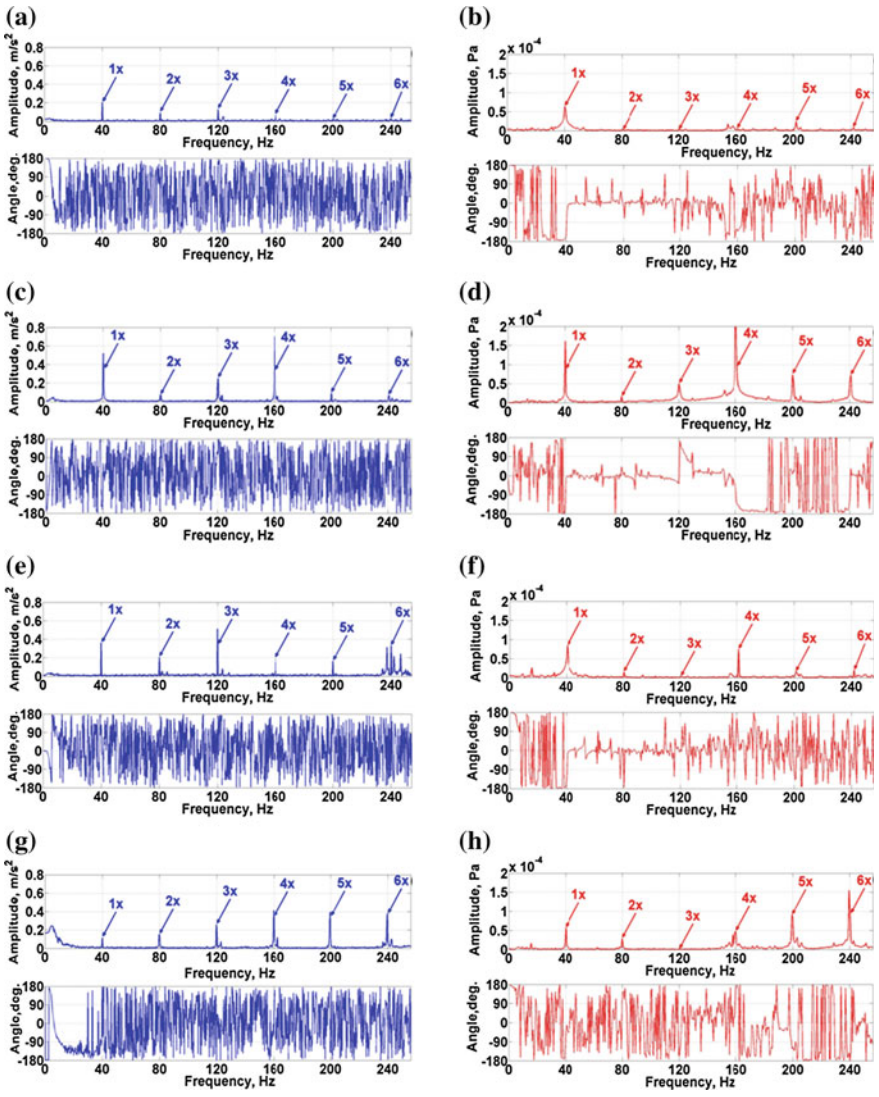

Fig. 3 Typical pCCS and phase plots at 2400 RPM; **a** vibration-HRM, **b** vibro-acoustic-HRM, **c** vibration-BS, **d** vibro-acoustic-BS, **e** vibration-LB, **f** vibro-acoustic-LB, **g** vibration-SR, **h** vibro-acoustic-SR

From Figs. 2 and 3, it can be seen that the computed pCCS for both vibration (measured on bearing pedestals) and vibro-acoustic signals (measured near bearing pedestals with microphones) provide distinctive features for each of the experimentally simulated cases. However, due to the appearance of several peaks for the different cases at both machine speeds, direct comparison of the features from the two classes of signals could become difficult. Therefore, in order to further enhance

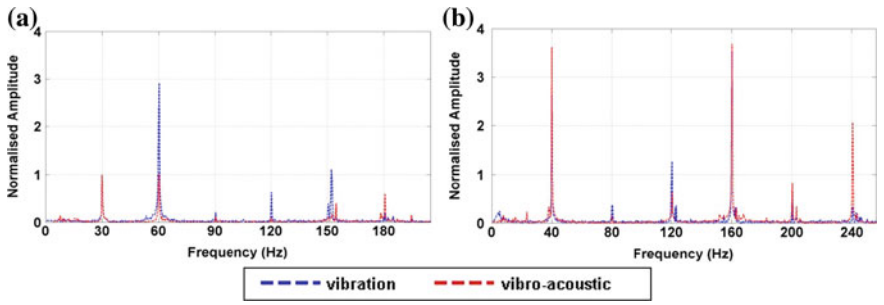

Fig. 4 Typical normalized pCCS for BS case; **a** 1800 RPM, **b** 2400 RPM

the visualization of the similarities between the pCCS diagnosis features for both measured vibration and vibro-acoustic signals, the amplitudes of a typical case (BS) have been normalised by the amplitude of the first harmonic component at both machine speeds (1800 RPM and 2400 RPM), as shown by Fig. 4. It can be seen that the pCCS features for both signals at both machine speeds appear similar. Although the amplitudes vary slightly for some harmonic components, however, the spectral features and patterns are very similar. This however provides an indication of the potentials of applying pCCS of vibro-acoustic signals measured with just two microphones installed near bearing locations for rotating machines faults diagnosis.

4 Concluding Remarks

The pCCS spectrum was found useful for faults diagnosis, particularly with measured vibration data in earlier studies. In the current study, a similar concept is applied to vibro-acoustic data measured from a flexibly supported rotating machine, using just two microphones. The observations appear to be identical for both classes of signals. The investigation of the possibilities of applying fused vibro-acoustic signals for rotating machines' faults diagnosis was particularly driven by the ability to conduct non-intrusive measurements using non-contact sensors such as microphones, which is of significant advantage over the use of contact type accelerometers, especially when dealing with extremely hazardous machines.

References

1. Hall DL, Llinas J (1997) An introduction to multisensor data fusion. Proc IEEE 85(1):6–23
2. Basir O, Yuan XH (2007) Engine fault diagnosis based on multi-sensor information fusion using Dempster-Shafer evidence theory. Inf Fus 8(4):379–386
3. Niu G, Han T, Yang BS, Tan ACC (2007) Multi-agent decision fusion for motor fault diagnosis. Mech Syst Signal Process 21(3):1285–1299

4. Zhang J (2007) Improved on-line process fault diagnosis through information fusion in multiple neural networks. Comput Chem Eng 30(1):558–571
5. Boutros T, Liang M (2007) Mechanical fault detection using fuzzy index fusion. Int J Mach Tools Manuf 47(11):1702–1714
6. Niu G, Yang BS, Pecht M (2010) Development of an optimized condition-based maintenance system by data fusion and reliability-centered maintenance. Reliab Eng Syst Safety 95(7):786–796
7. Yunusa-Kaltungo A, Sinha JK (2014) An improved data fusion technique for faults diagnosis in rotating machines. Measurement 58:27–32
8. Elbhbah K, Sinha JK (2013) Vibration-based condition monitoring of rotating machines using a composite spectrum. J Sound Vib 332(11):2831–2845
9. Wang J, He Q, Kong F (2013) Automatic fault diagnosis of rotating machines by time-scale manifold ridge analysis. Mech Syst Signal Process 40(1):237–256
10. Gubran AA, Sinha JK (2014) Shaft instantaneous angular speed for blade vibration in rotating machine. Mech Syst Signal Process 44(1–2):47–59
11. Al-Badour F, Sunar M, Cheded L (2011) Vibration analysis of rotating machinery using time-frequency analysis and wavelet techniques. Mech Syst Signal Process 25(6):2083–2101
12. Pennacchi P, Vania A (2008) Diagnostics of a crack in a load coupling of a gas turbine using the machine model and the analysis of the shaft vibrations. Mech Syst Signal Process 22(5):1157–1178
13. Yunusa-Kaltungo A, Sinha JK (2014) Combined bispectrum and trispectrum for faults diagnosis in rotating machines. Proc Inst Mech Eng Part O J Risk Reliab 228(4):419–428
14. Kilundu B, Chiementin X, Duez J, Mba D (2011) Cyclostationarity of acoustic emissions (AE) for monitoring bearing defects. Mech Syst Signal Process 25:2061–2072
15. Tan CK, Irving P, Mba D (2007) A comparative experimental study on the diagnostic and prognostic capabilities of acoustic emission, vibration and spectrometric oil analysis for spur gears. Mech Syst Signal Process 21:208–233
16. Tandon N, Yadava GS, Ramakrishma KM (2007) A comparison of some condition monitoring techniques for the detection of defect in induction motor ball bearings. Mech Syst Signal Process 21(1):244–256
17. Loutas TH, Sotiriades G, Kalaitzoglou I, Kostopoulos V (2009) Condition monitoring of a single-stage gearbox with artificially induced gear cracks utilizing on-line vibration and acoustic emission measurements. Appl Acoust 70:1148–1159
18. Li W, Parkin RM, Coy J, Gu F (2002) Acoustic based condition monitoring of a diesel engine using self-organising map networks. Appl Acoust 63:699–711
19. Garcia-Perez A, Romero-Troncoso RJ, Cabal-Yepez E, Osornio-Rios RA, Lucio-Martinez JA (2011) Application of high-resolution spectral analysis for identifying faults in induction motors by means of sound. J Vib Control 18(11):1585–1594
20. Cernetic J (2009) The use of noise and vibration signals for detecting cavitation in kinetic pumps. Proc Inst Mech Eng Part C J Mech Eng Sci 223:1645–1655
21. Shibata K, Takahashi A, Shirai T (2000) Fault diagnosis of rotating machinery through visualisation of sound signals. Mech Syst Signal Process 14(2):229–241
22. Lin J (2001) Feature extraction of machine sound using wavelet and its application in faults diagnosis. NDE&T Int 34:25–30
23. Loutas TH, Roulias D, Pauly E, Kostopoulos V (2011) The combined use of vibration, acoustic emission and oil debris on-line monitoring towards a more effective condition monitoring of rotating machinery. Mech Syst Signal Process 25(4):1339–1352

A Probabilistic Approach to the Crack Identification in a Beam-like Structure Using Monitored Mode Shapes and Their Curvature Data with Uncertainty

Sergey Shevtsov, Igor Zhilyaev, Paul Oganesyan and Vladimir Akopyan

Abstract This work, which has been carried out for defects in aircraft structures diagnosis, is considering of measurement errors, different accelerometers positioning and numerical differentiation of the natural vibrations mode shapes as the sources of uncertainty, which affects on the crack identification results. A physical theory to solve the forward identification problem assumed the Timoshenko beam model with opened crack. With 1D cracked beam finite element (FE) model at the different position and depth of the crack we reconstruct the first 5 mode shapes, using vibration amplitudes measured on the fixed uniformly distributed points on the beam surface. All measured amplitudes are noisy by randomly distributed errors. Once these modes reconstructed, we determine their curvatures using central schemes for the first and second spatial finite differences. To obtain the probabilistic means for decision about the damage existence, the multiple numerical simulations of the FE models have been carried out for both intact and defected beams with different damage severity. Using results of these simulations we reconstruct the probability density functions for maximum difference between vibration amplitudes of intact beam and beam with known damage that allow us to separate the damaged and undamaged cases. Next, we calculate the empirical probability distributions, which allow to estimate a probability of the crack location and to distinguish the cases of presence and absence of defect. Then, we compare the sensitivity and robustness of crack parameters predictions by the mode shapes and modal curvatures analysis at the different instrumental precision using known and identified cracks' characteristics. We established that damage identification using mode shape curvatures data is less reliable because increased noise caused by twofold numerical differentiation of amplitudes measured on the discrete set of points, whereas the

S. Shevtsov (✉) · I. Zhilyaev · P. Oganesyan
South Center of Russian Academy, Southern Federal University, Rostov on Don, Russia
e-mail: sergnshevtsov@gmail.com

V. Akopyan
Institute of Mechanics and Applied Mathematics, Rostov on Don, Russia
e-mail: akop@math.rsu.ru

F. Chaari et al. (eds.), *Advances in Condition Monitoring of Machinery in Non-Stationary Operations*, Applied Condition Monitoring 4,
DOI 10.1007/978-3-319-20463-5_34

mode shapes are more suitable for distinguish perfect intact and damaged state of a structure. Our results confirm that each vibration mode is most sensitive to the damage within the own specific intervals along the beam, and besides, such the sensitivity increases along with mode's number.

Keywords Structural health monitoring · Timoshenko beam · Crack identification · Damage sensitivity · Probabilistic analysis

Contents

1 Introduction 448
2 The Timoshenko Beam with the One Opened Crack 450
3 The Finite Element Implementation of the Forward Problem 452
4 Probabilistic Analysis of Resolution and Sensitivity of the Vibration Modes and Their Curvatures to Damage Existence, Severity and Location 455
5 Conclusions 459
References 460

1 Introduction

Structural damage prediction and identification attracts a relentless attention of engineers and scientists because the unpredicted structural failure may cause catastrophic loss, especially at the cases of flying aircrafts. The state of this problem has been considered in very detailed surveys [1–5], etc. These surveys categorized all vibration-based damage identification methods as global nondestructive evaluation technique because these methods do not require a priori information about the possible damage location. Different kinds of the vibration-based method are widely used in aerospace and civil engineering. Regular diagnostics to on-line possible damage detection of aircraft [6–8], rotorcraft [9–12], UAVs [13], aerospace engines [14] has been studied and reported. Despite the fact that a damage diagnosis problem is topical for the different civilian structures, including bridges, buildings, towers, pipes, plate-like and shell-like structures, the beam-like structures are particularly studied. Most often such the objects are described by the Euler-Bernoulli theory [5, 10], and relatively seldom by the Timoshenko beam equations [15–19], which allow to take into account the effects of shear deformation and rotational inertia. The beam's defects are modeled by the spring with rotational stiffness [3, 15, 20], by the local bending stiffness due to decrease of the Young module or moment inertia of the beam cross-section [16–19, 21–26], by attached auxiliary mass [6, 12, 13, 27], or by notch in FE model of the beam [23, 27]. In this work, we use the advantageous that provide the Timoshenko beam equations. In contrast to other studies, which modeled the damage as relatively wide region with

the reduced flexural stiffness or by the zero length spring whose rotational stiffness is assigned quiet arbitrarily, we accurately describe an opened crack as a very narrow local change of the beam cross-section according the approach firstly developed in [16].

Most authors [1–4] classified all damage identification methods as 'model-based methods' or 'response based methods'. The model-based method assumes that some mathematical model of the structure is available for damage identification, while the response-based method depends only on experimental response data from structures. A wide range of problems that state as 'model-based' can be considered as inverse problems. In inverse problems, data from indirect measurements used to estimate unknown parameters of physical systems, in the considered cases to estimate geometric location and/or severity of the damage [1]. Among the main approaches to solve such the problems are use some assurance criteria that assume a comparison between the processed experimental data and model response [1–4, 12] etc., the model-updating methods [21] that utilizing some analytical optimization algorithm (gradient-based, most often) [21, 28], wavelet analysis [9, 29], soft methods, including artificial neural network [6, 30], fuzzy logic [25] and genetic algorithm [7, 22, 27, 31], and also approach that consider the studied vibrated structure as a closed-loop controlled system whose faults can cause the destabilization and variation of control performance [23, 32,37]. A common feature of such problems and cause a variety of methods for solving them is that they are ill-posed.

There are many reasons that make the inverse problem underdetermined (non-unique). In the considered example of damaged structure, two different models of this structure may predict the same measurements data and the finite bandwidth of these data never allow to resolve the very small features of the models, and there are always experimental uncertainties that allow different models to be 'acceptable' [33]. Many investigations that have been devoted to the influence of uncertainty on the solution of inverse damage identification problem, confirmed a very high sensitivity of such the solution to experimental noise or numerical errors [7, 15, 19, 25, 26, 31, 32, 34–36].

In this article, we use the probabilistic approach [30], which is widely used for uncertainty analysis of mathematical models [6, 14, 19, 22, 35, 38, 39]. This approach, which assumes a large number of *samples* or *experiments* with the studied object, and the probability of an event (damaged or undamaged state, damage severity etc.), is defined as the ratio of the number the event occurs to the total number of samples or experiments. So, using a probabilistic approach to the damage detection, we no longer consider of each variable as a single value or number. Instead, we consider each variable in terms of its probability distribution.

The survey papers [1, 4] classify the vibration-based methods by the monitored value into four major categories: natural frequency-based methods [24, 27, 35, 40], mode shape-based methods [10, 26, 31, 34, 41, 42], curvature mode shape-based methods [17, 25, 43], and methods using both mode shapes and frequencies [16]. The modal strain energy-based method [12, 30, 38] is very similar to these methods. Some authors proposed also to monitor the time domain response of vibrated structure to extract damage sensitive characteristics [32, 44]. Based on the

successful results of identification using vibration mode shapes and their curvatures presented in our previous papers [16, 19], we use here these dynamic characteristics of the potentially damaged mechanical structures. Because this investigation is oriented to the aircraft structural health monitoring the utilizing of the accelerometers array instead of set of the surface bonded strain gages is preferred due to specific prohibitions for the flying vehicles. However, such the monitoring, which allow to measure the accelerations in the points of the accelerometers installation, requires to twice integrating the electric signals in the time domain to obtain the vibration amplitudes from electric signal, which is proportional to acceleration, and next, requires to twice differentiating in the space domain to obtain the local curvature. In the papers [1, 25, 43] it is pointed out that for the higher modes, the difference in modal curvature calculated using the data acquired from the intact and damaged structures shows several peaks not only at the damage location but also at the other positions, which may lead to a false indication of damage. This is due to experimental and numerical reasons. Indeed, if we use the mode shape curvature as an indicator of the damage, the inherent uncertainty caused by the measurements errors and environmental action is increased after double numerical differentiation. Hence, the resulting uncertainty (i.e. noise) will be associated with both the number and spatial positions of sensors. The damage localization accuracy depending on the set of sensors has been studied in [8, 23, 36, 44], where it is proved that the number of sensors and the choice of sensors coordinates may have a crucial effect on the accuracy of the damage detection procedure. In our previous work [19], where we modeled three cases with 20, 40, and 80 sensors uniformly distributed along the beam span it has been established that 40 sensors is the optimum number. This number is agreeing with the experimental results presented in [12], and it used here.

2 The Timoshenko Beam with the One Opened Crack

The most attractive feature of the Timoshenko beam equations at the modeling of defected structures with crack is its ability to describe correctly the narrow variation of the mechanical properties and cross-section along the beam. Moreover, these equations satisfy the main requirements to the model used to simulate the forward problem [16]. Among these requirements are the small number of parameters, which fully characterize a crack, the model of the damaged structure is continuously modified to the model of perfect structure at decreasing of the damage severity, and also the minimum computation cost that is very important at the multiple simulations. The Timoshenko beam equations, which take into account the effects of shear and the section rotation even at quite high frequencies of flexural vibrations, has the form

$$\begin{aligned}(EJ\psi_x)_x + kGF(w_x - \psi) &= \rho J\psi_{tt}\\ [kGF(w_x - \psi)]_x + q &= \rho F w_{tt},\end{aligned} \tag{1}$$

where E, G, ρ, J, F, L are the Young module, shear module, material density, section moment inertia, section area, and beam length respectively; w, ψ are beam axis deflection and angle of the section rotation; q is distributed load; and k is form-factor equal to 6/5 for rectangular cross section. The subscripts x and t designate the space and time differentiation. It is important that the assumption about uniform cross-section of the beam with the exception of the crack location, which adopted here, do not lead to the loss of generality for the following consideration.

The boundary conditions for the cantilever beam with the free load tip are

$$w|_{x=0} = \psi|_{x=0} = 0; \quad \partial\psi/\partial x|_{x=L} = (\partial w/\partial x - \psi)|_{x=L} = 0\,. \tag{2}$$

Expressing the spatial distribution of the section moment inertia and section area

$$J(x) = J_0 \cdot \zeta(x); \quad F(x) = F_0 \cdot \eta(x), \tag{3}$$

where J_0 and F_0 are the section moment inertia and section area along the defectless parts of the beam, and introducing the dimensionless variables

$$\xi = x/L \Rightarrow \partial/\partial x = 1/L \cdot \partial/\partial\xi; \quad \tau = t/T \Rightarrow \partial/\partial t = 1/T \cdot \partial/\partial\tau; \quad u = w/L\,, \tag{4}$$

where dimensionless coordinate ξ, time τ and displacement u and pseudo period T, system (1) is transformed to the dimensionless representation

$$\begin{aligned}\eta u_{\tau\tau} - B(\eta u_\xi)_\xi + B(\eta\psi)_\xi &= \Phi\\ \zeta\psi_{\tau\tau} - \left(\zeta\psi_\xi\right)_\xi - A\eta u_\xi + A\eta\psi &= 0\end{aligned} \tag{5}$$

In Eq. (5) a pseudo-period T is defined as $T = L\sqrt{\rho/E}$, and the dimensionless coefficients A, B, Φ are

$$A = 6kL^2/\left[h^2(1+v)\right]; \quad B = k/(1+v) \quad \Phi = qL/(bhE), \tag{6}$$

and the spatial distributions of the dimensionless beam thick η and section moment inertia ζ

$$\eta(\xi) = 1 - \delta(\xi); \quad \zeta(\xi) \approx 1 - 3\delta(\xi) \cdot (1 - \delta(\xi))^2 = 1 - 3\delta(\xi) \cdot \eta^2(\xi)\,, \tag{7}$$

that depend on the delta-like opened crack, which has depth $d \in [0; 1)$, half width ε and is placed at the dimensionless distance l from the clamped end

$$\delta(\xi) = d \cdot \begin{cases} \cos[\pi(\xi - l)/2\varepsilon]; & \xi \in [l - \varepsilon, l + \varepsilon] \\ 0; & \xi \notin [l - \varepsilon, l + \varepsilon], \end{cases} \tag{8}$$

At performing of frequency response and modal analysis both u and ψ (see Eq. 5) assumed as harmonic oscillations with amplitudes $U(\xi), \Psi(\xi)$, and the boundary value problem for the damaged cantilevered beam is formulated in the form

$$\begin{aligned} -\eta\tilde{\omega}^2 U - B(\eta U_\xi)_\xi + B(\eta \Psi)_\xi &= \Phi \\ -\zeta\tilde{\omega}^2 \Psi - (\zeta \Psi_\xi)_\xi - A\eta U_\xi + A\eta \Psi &= 0 \\ U|_{\xi=0} = \Psi|_{\xi=0} = \Psi_\xi|_{\xi=1} = (U_\xi - \Psi)|_{\xi=1} &= 0, \end{aligned} \tag{9}$$

where the dimensionless angular eigenfrequency $\tilde{\omega}_i$ and eigenfrequency v_i that expressed in the natural frequency units are linked by the relationships

$$\tilde{\omega}_i \tau = 2\pi v_i t \Rightarrow v_i = \tilde{\omega}_i \sqrt{E/\rho}/2\pi L. \tag{10}$$

The numerical implementation of the boundary value problem (9) was carried out in the Partial Differential Equation (PDE) mode of FE soft tool Comsol Multiphysics.

3 The Finite Element Implementation of the Forward Problem

One-dimensional FE mesh of the beam model consisted of 1000 knots, and near 5000 degree of freedom. For the model testing and validation we used the experimentally studied steel beam with dimensions 4 cm × 5 cm × 1 m and artificially introduced "cracks"—notches with depth: 0.25, 0.4, 0.55, and 0.7 of thick and randomly distributed along the beam. First 5 vibration modes have been calculated and next normalized by dividing the points displacement amplitude on the maximum displacement at the free end. To obtain the curvatures of the modes shape the 3 and 5-points symmetric finite differences schemes for the first and second derivatives were used. For these calculations we used 40 points on the beam surface, separated by the identical distance h. Comparison of this FE model simulation results with the experimental data and with the results of 3D FE simulation confirmed the ability to successfully reconstructing the dynamic properties of damaged beams [16]. Some examples of the mode shapes and their curvatures without noise are shown in a Fig. 1. A visual analysis of these plots demonstrates that at absence of the experimental noise the sensitivities of the mode shapes and their curvatures are comparable.

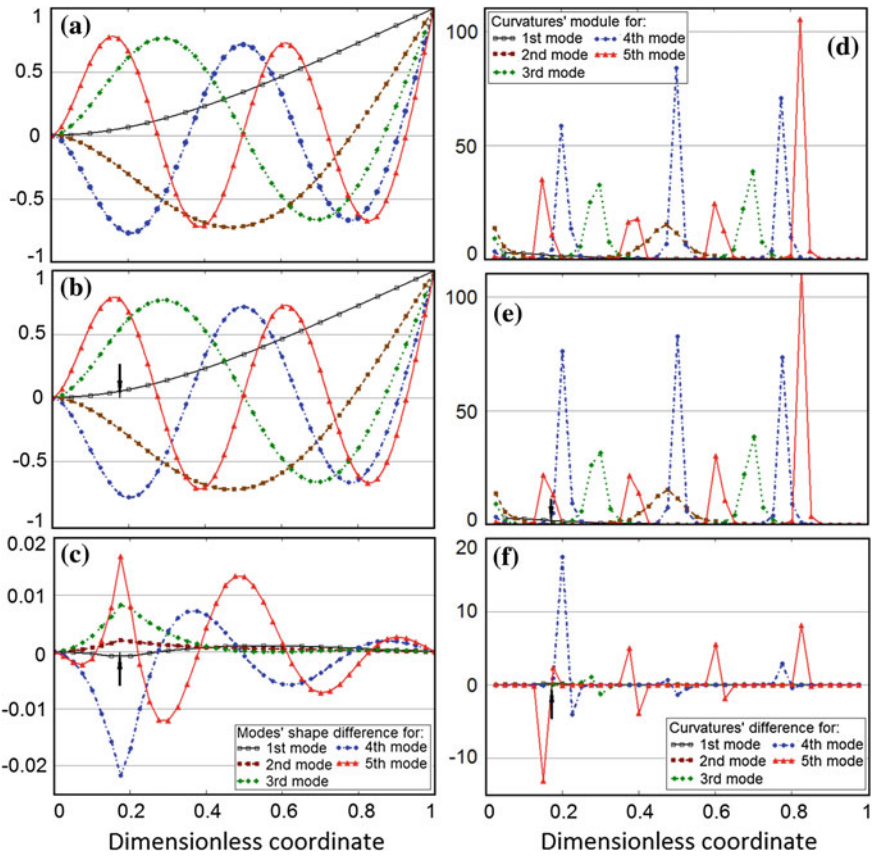

Fig. 1 The normalized mode shapes (**a**, **b**), curvatures' modules calculated from these mode shapes (**d**, **e**) for intact beam (**a**, **d**) and beam with the crack at $l = 0.18$; $d = 0.25$ (**b**, **e**), and differences between these dependencies for the damaged and undamaged beam (**c**, **f**). Calculation was performed using 40 uniformly distributed points along the beam assuming no any measured noise

Last statement is because the maximum discrepancies between mode shapes and their curvatures are in a vicinity of the known crack location $l = 0.18$. Nevertheless, deviations of lesser magnitude are also observed far from the location of the defect. Obviously, these deviations are due to the numerical differentiation on a discrete set of points. Since all second derivatives are calculated for the normalized modes, the amplitude of the curvatures increases with the number of mode, and mode (curvature) sensitivity to the presence of the defect is better in the areas of the larger curvature.

The artificial noise was introduced by adding to the displacement of each point the "measurements error" as a random value, according to normal distribution. We studied two cases when measuring error is enclosed within the ranges ± 0.01 and

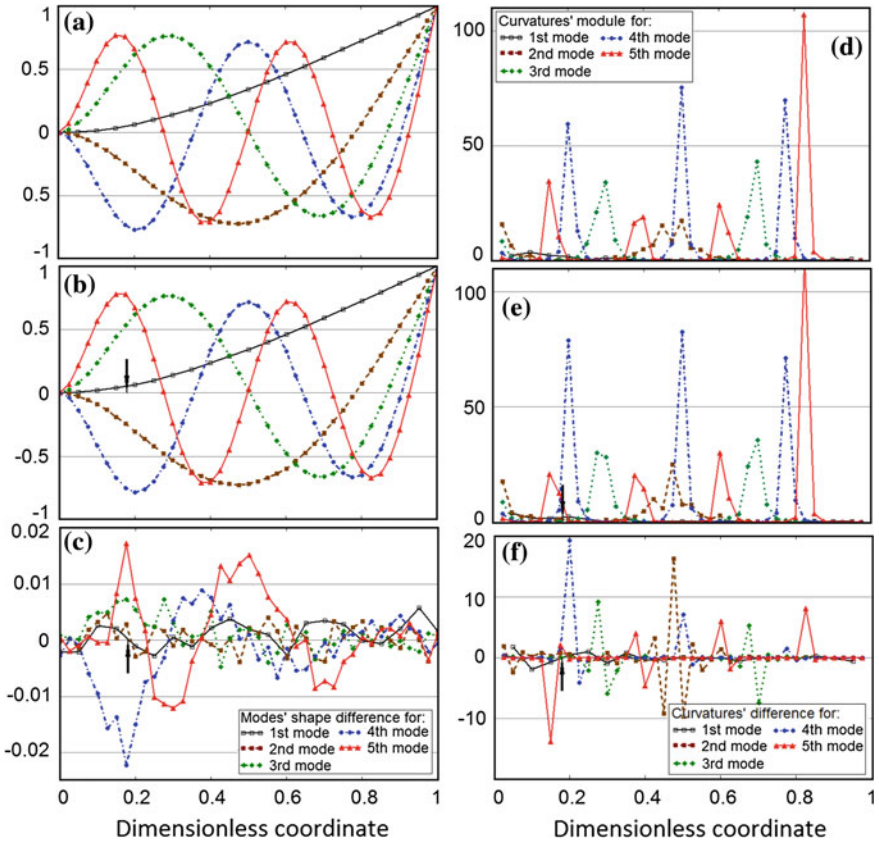

Fig. 2 The normalized mode shapes (**a**, **b**), curvatures' modules calculated from these mode shapes (**d**, **e**) for intact beam (**a**, **d**) and beam with the crack at $l = 0.18$; $d = 0.25$ (**b**, **e**), and differences between these dependencies for the damaged and undamaged beam (**c**, **f**). Calculation was performed using 40 uniformly distributed points along the beam assuming measured noise within the interval ±0.005

±0.005. Figure 2 demonstrates the corresponding examples of the mode shapes and their curvatures with noise ±0.005 that corresponds to the workable precision of vibration measurement equipment. The resolution of both modes and curvature significantly deteriorated. Furthermore, some erroneous peaks (see peaks at $l = 0.25$ for the 3rd mode and at $l = 0.45$ for the 2nd mode in Fig. 2f) can appear.

Plots on Figs. 1 and 2 confirm the local sensitivity for each mode shape. Therefore, it must be assumed that different vibration modes (or their curvatures) should be less or more sensitive to the damages, which are localized in the different segments of the beam length. Introducing even small measuring error worsens the sensitivity and resolution of the modes shape and their curvatures. At the existence of the measuring error, the erroneous peaks can arise on the different positions making difficult to localize damage and making less obvious fact of its existence or absence.

In order to obtain the probabilistic estimations for the defected as well as for the perfect beams we simulated a pairs of beams (both beams with the artificial noise), and then compared the maximum discrepancies between these beam axis deflections (and their curvatures) along the beams for the five natural vibration modes. In the cases of intact beam analysis, both simulated beams are intact, and each defected beam with known damage severity was compared with the intact beam. All modeled 500 defects realization was stored in a text file for the further statistical analysis.

4 Probabilistic Analysis of Resolution and Sensitivity of the Vibration Modes and Their Curvatures to Damage Existence, Severity and Location

Two different types of analysis were performed. First type was a reconstruction of empiric distribution of maximum discrepancies along the beam in the form of histograms for all five modes shape and their curvature for intact beam and for the beams with different damage severity, then calculation of parameters for matching probability density distribution. In order to approximate the obtained empiric distributions by the probability density functions used in practice we chose the normal distribution and modified beta distribution, which was defined on interval $[a; b]$ as follow

$$\hat{B}(a, b, x, m, n) \equiv \begin{cases} B\left(\frac{x-a}{b-a}, m, n\right) & \text{if } x \in [a; b] \\ 0, & \text{otherwise,} \end{cases} \tag{11}$$

where probability density for beta distribution is

$$B(x, m, n) \equiv \frac{\Gamma(m+n)}{\Gamma(m) \cdot \Gamma(n)} \cdot x^m \cdot (1-x)^{n-1}. \tag{12}$$

Figure 3 demonstrates two examples of such probability distributions. These results allow us to estimate ability of the vibration modes and their curvatures to determine severity of possible damage and make decision about absence of damage. For example, a maximum discrepancy of the 1st mode curvature for a perfect beam cannot exceed value 80.

Second type of analysis was performed to determine the sensitivity of studied vibration modes and their curvatures to the presence of damages with different levels, when this damage locates randomly along the beam. As a result, the spatial distributions of correct crack localization by each mode and its curvature have been obtained for the different part of the beam. The length of studied damaged beams has been divided on ten identical intervals. Then a number of correct predictions percentage and distribution of deviations from the true crack positions have been

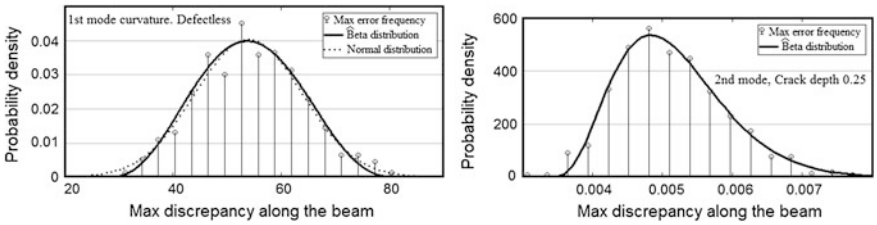

Fig. 3 Two examples of the empiric distribution of the maximum discrepancies along a beam

calculated. These deviations are illustrated in Fig. 4 by the confidence intervals for their expected values. Two examples of these results, which are presented in Fig. 4, show the distributions of the localization errors and percentage of correct crack localization for the cracked beam ($d = 0.25$) according to the analysis of second vibration mode and curvature of the first vibration mode.

Both Figs. 3 and 4 correspond to the amplitude's measuring error $\pm 1\,\%$. Two graphs in Fig. 3 demonstrate the tendency to transform the probability distribution from the symmetric normal to the modified beta distribution together with increasing a damage severity.

Figure 4 demonstrates the best reliability of the crack localization of the mode shapes comparing to the curvature, which is dependent with very big uncertainty. Our numerical experiments convincingly demonstrate higher reliability of the predictions based on the vibration natural mode shapes in comparison with the results given by their curvatures. This conclusion cast doubt on the assertion of works, such as [26, 32, 34] in which the good capabilities of the modal curvatures method were communicated. It is obvious; such dissimilarity can be explained by the assumption about the smoothness of the curvatures, accepted in the mentioned papers. Therefore, the information in Figs. 5 and 6 corresponds to the natural mode shapes only.

The probability distributions for the sensitivity the natural modes to the damages with the different severity at the measuring errors ± 1 and $\pm 0.5\,\%$, which are presented in Fig. 5, show the magnification of sensitivity and ability to separate the intact and damaged cases with an increase of the mode number. Such increase of

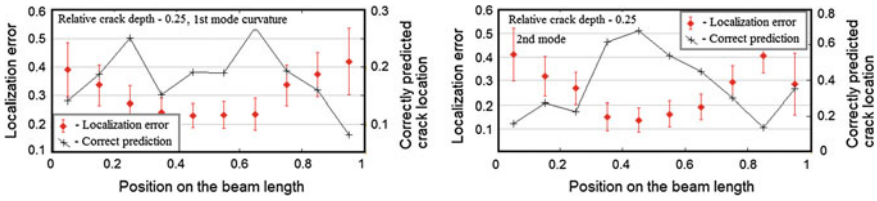

Fig. 4 Two examples of the spatial distributions of correct crack localization by the first mode shape curvature (*left*) and by the second natural vibration mode (*right*)

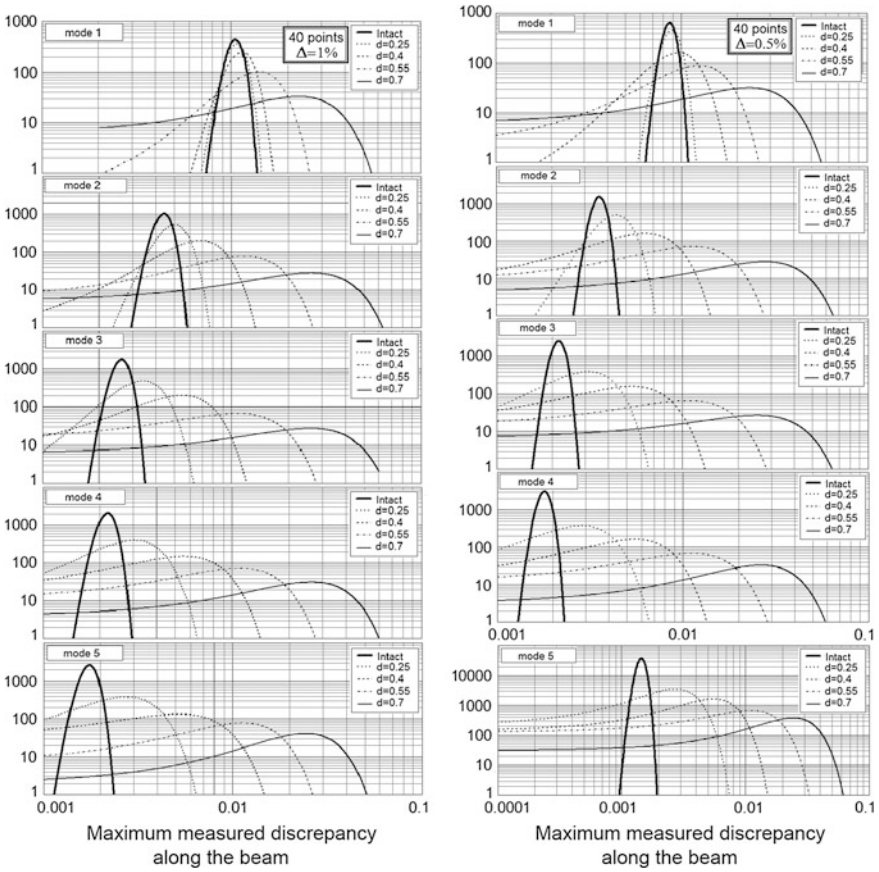

Fig. 5 Two kinds of the empiric probability distribution for the crack detection, which depend on the damage severity and measuring errors

the sensitivity of the 3rd, 4th, and 5th modes is particularly noticeable at the small damages, while the first natural mode is almost not possible to separate intact state from damage with $d = 0.25$. The crack detection sensitivity also increases at the improving of the measuring precision.

Figure 6, which depicts the spatial distribution of the correct forecasting for the crack localization, shows the different sensitivity of analyzed mode shapes in the different area of a beam. The exactitude of the crack's location forecasting increases along with the number of the flexural vibration modes, but this exactitude is localized in the areas, specific for each mode. Dependence of the crack's localization exactitude on the measuring precision is relatively week. Comparison of diagrams in Fig. 6 shows that the zones of better crack's localization correspond to the beam areas with greatest curvature, especially for the 3rd, 4th, and 5th modes.

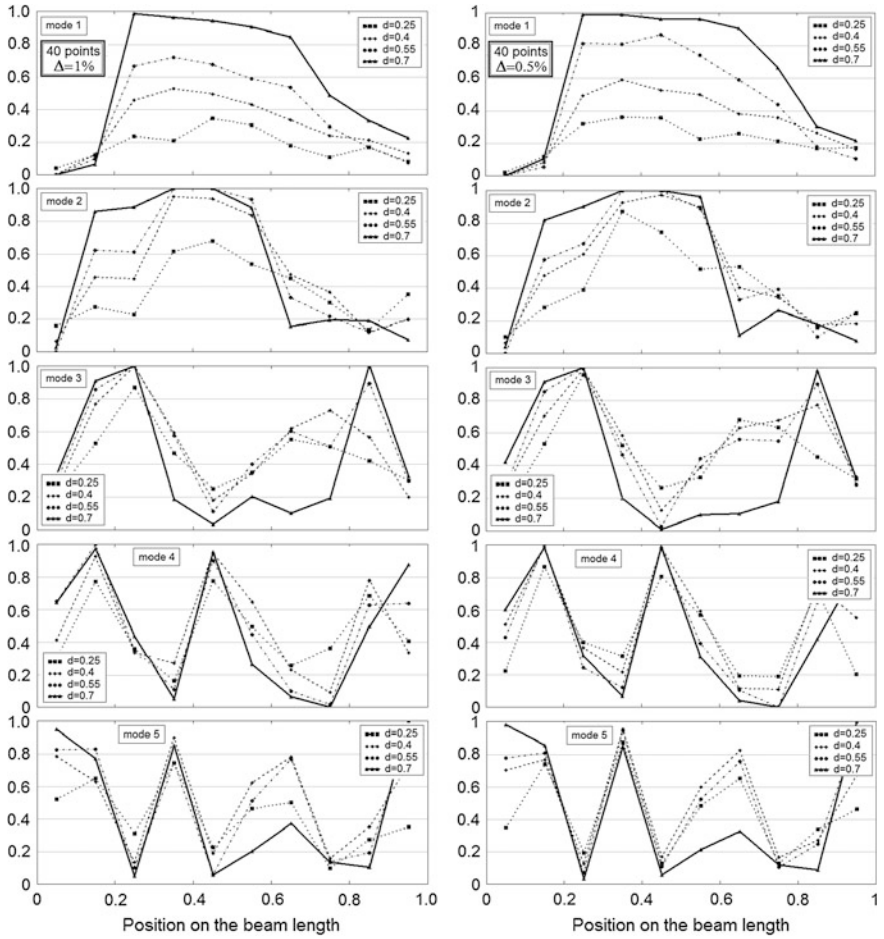

Fig. 6 Two kinds of the empiric probabilities for the correct crack localization, which depend on the damage severity and measuring errors

For all considered vibration modes even at the better measuring precision, the sensitivity near beam-ends is minimal. The small crack can be identified by using a comparative study of the several mode shapes with the different spatial sensitivity. This fact confirms the weak efficiency of t early-developed simple damage indices to identify the damage state in the beam-like structures correctly. Our results show unsatisfactory resolution and sensitivity to the damage of the mode shape curvatures determined as the second finite differences of the noisy mode shape that is due to high additional numerical errors.

5 Conclusions

The studied cracked Timoshenko beam model confirms its efficiency to many times numerical simulation of the forward problem at the solving the inverse problem of the damage identification of potentially defected beam-like structures using mode shape-based monitoring with the set of accelerometers uniformly distributed along the beam. In our study, we used the cantilever beams, intact and with the randomly distributed narrow delta-like notch, which simulates an opened crack. The primary feature of our consideration is accounting of vibration amplitudes' measurements error, which is random value, determined by the precision of the vibration monitoring equipment, and such error corrupt the measurements vibration amplitudes on the beam surface. Each simulation of such a model results the 5 first modes shape as the discrete set of amplitudes values. This discrete-valued function then is used to numerically calculate the spatial distribution of the mode shape curvature.

Our results show big scatter of the curvatures value due to discrete definition of the modes shape and due to calculation of curvature using twofold numerical differentiation. Such numerical reconstruction of the curvatures is caused by restricted use of the strain gauges bonded on the surface of aircraft structures for the direct measurement of bending strains.

To obtain the probabilistic estimations of the possible damage in the studied structure we performed multiple numerical simulations, whose output is the set of discrete modes shapes for intact beams and for beams with randomly distributed defects. Then, for each pair of beams (with known crack depth and a priori intact, both with the artificial noise), we compared the maximum discrepancies between these beam axis deflections (and their curvatures) along the beams for the five natural vibration modes. For these maximum discrepancies, we built the probability density functions that allow estimating the probability of the damage existence and damage severity is used as the damage index, whose value and location along the beam give a probable estimate for the damage existence, the ranges of its location and severity. Our estimations of the probability of true damage location using data for the different vibration modes shows that best results can be obtained using 2nd and next modes, and besides, each vibration mode is most sensitive within the own specific intervals along the beam. These results confirm that for the correct defect identification, we need to take account of measurement errors, the probability distributions of maximum dispersion amplitudes on each vibration mode of beam with different damage severity, and spatial variation of sensitivity to defect for each vibration mode.

Acknowledgments The authors wish to acknowledge the partial financial support from the Russian Foundation for the Basic Research (Grants 14-08-31612, 15-08-00849).

References

1. Carden EP, Fanning P (2004) Vibration based condition monitoring: a review. Struct Health Monitor 3(4):355–377
2. Humar J, Bagchi A, Xu H (2006) Performance of vibration-based techniques for the identification of structural damage. Struct Health Monitor 5:215–242
3. Del-Grosso A, Lanato F (2008) A critical review of recent advances in monitoring data analysis and interpretation for civil structures. In: Proceedings of 4th European conference on structural control, vol 1. Saint–Petersburg, Russia, 12–15 Sept 2008, pp 320–330
4. Fan W, Qiao P (2011) Vibration-based damage identification methods: a review and comparative study. Struct Health Monitor 10(1):83–111
5. Jassim ZA, Ali NN, Mustapha F, Abdul Jalil NA (2013) A review on the vibration analysis for a damage occurrence of a cantilever beam. Eng Failure Anal 31:442–461
6. De Moura JDRV Jr, Steffen V Jr (2006) Impedance-based health monitoring for aeronautic structures using statistical meta-modeling. J Intel Mater Syst Struct 17:1023–1036
7. Meruane V, Heylen W (2010) Damage detection with parallel genetic algorithms and operational modes. Struct Health Monitor 9:481–497
8. Georgiou IT (2011) Advanced processing of collocated acceleration signals in symmetric beam-like structures with applications to damage detection in a propeller. J Intel Mater Syst Struct 22:1371–1395
9. Ghoshal A et al (2001) Damage detection testing on a helicopter flexbeam. J Intel Mater Syst Struct 12:315–330
10. Kiddy J, Pines D (2001) Experimental validation of a damage detection technique for helicopter main rotor blades. J Syst Cont Eng 215:209–221
11. Pawar PM, Ganguli R (2007) Helicopter rotor health monitoring—a review. Proc Inst Mech Eng Part G J Aero Eng 221:631–650
12. Santos FLM, Peeters B, Van der Auweraer H, Góes LCS (2013) Experimental damage detection of a helicopter main rotor blade based on modal properties. In: Proceedings of international conference on engineering structural dynamics ICEDyn-2013. Sesimbra, Portugal, 17–19 June 2013, 7 p
13. Wallace M, Azzam H, Newman S (2004) Indirect approaches to individual aircraft structural monitoring. Proc Inst Mech Eng Part G J Aero Eng 218:329–346
14. King S, Bannister PR, Clifton DA, Tarassenko I (2009) Probabilistic approach to the condition monitoring of aerospace engines. Proc Inst Mech Eng Part G J Aero Eng 223:533–542
15. Chang CC, Chen L-W (2003) Vibration damage detection of a Timoshenko beam by spatial wavelet based approach. Appl Acoust 64:1217–1240
16. Shevtsov SN, Akopyan VA, Rozhkov EV (2011) An Approach to the problem of damage identification in an elastic rod based on the Timoshenko beam model. Rus J Nondes Test 47 (7):480–490
17. Radzienski M, Krawczuk M, Palacz M (2011) Improvement of damage detection methods based on experimental modal parameters. Mech Syst Sign Proc 25:2169–2190
18. Dincal S, Stubbs N (2013) Damage evaluation of Timoshenko beams using invariant stress resultants. Eng Struct 56:2052–2064
19. Shevtsov S, Zhilyaev I, Akopyan V, Flek M (2013) Crack identification in a beam-like structure using the probabilistic approach and Timoshenko beam model. In: Proceedings of the 11th international conference on vibration problems ICOVP-2013. Lisbon, Portugal, 9–12 Sept 2013, 10 p
20. Afshari M, Inman DJ (2013) Continuous crack modeling in piezoelectrically driven vibrations of an Euler-Bernoulli beam. J Vibr Contr 19:341–356
21. Kolakowsky P, Mujica LE, Vehi J (2006) Two approaches to structural damage identification: model updating versus soft computing. J Intel Mater Syst Struct 17:63–80

22. Mehrjoo M, Khaji N, Ghafory-Ashtiany M (2013) Application of genetic algorithm in crack detection of beam-like structures using a new cracked Euler-Bernoulli beam element. Appl Soft Comp 13:867–880
23. Chomette B, Sinou J-J (2012) Crack detection based on optimal control. J Vibr Contr 18:1737–1750
24. Yang Z, Wang L (2010) Structural damage detection by changes in natural frequencies. J Intell Mater Syst Struct 21:309–320
25. Chandrashekhar M, Ganguli R (2009) Structural damage detection using modal curvature and fuzzy logic. Struct Health Monitor 8:267–283
26. Baneen U, Kinkaid NM, Guivant JE, Herszberg I (2012) Vibration based damage detection of a beam-type structure using noise suppression method. J Sound Vibr 331:1777–1788
27. Kuang KSC, Maalej M, Quek ST (2006) An application of a plastic optical fiber sensor and genetic algorithm for structural health monitoring. J Intel Mater Syst Struct 17:361–379
28. Urgessa GS (2011) Vibration properties of beams using frequency-domain system identification methods. J Vibr Contr 17:1287–1294
29. Wu N, Wang Q (2011) Experimental studies on damage detection of beam structures with wavelet transform. Int J Eng Sci 49:253–261
30. Pawar PM, Reddy KV, Ganguli R (2007) Damage detection in beams using spatial fourier analysis and neural networks. J Intel Mater Syst Struct 18:347–359
31. Srinivas V, Ramanjaneyulu K, Jeyasehar CA (2010) Multi-stage approach for structural damage identification using modal strain energy and evolutionary optimization techniques. Struct Health Monitor 10(2):219–230
32. Rébillat M, Hajrya R, Mechbal N (2014) Nonlinear structural damage detection based on cascade of Hammerstein models. Mech Syst Sign Proc 48:247–259
33. Mosegaard K, Tarantola A (2002) Probabilistic approach to inverse problems. Int Handb Earthq Eng Seismolog 81A:237–265
34. Pai PF, Young LG (2001) Damage detection of beams using operational deflection shapes. Int J Solid Struct 38:3161–3192
35. Hios JD, Fassois SD (2014) A global statistical model based approach for vibration response-only damage detection under various temperatures: a proof-of-concept study. Mech Syst Sign Proc 49:77–94
36. Majumder L, Manohar CS (2003) A time-domain approach for damage detection in beam structures using vibration data with a moving oscillator as an excitation source. J Sound Vibr 268:699–716
37. Lew JS (2011) Structural damage identification with performance-based uncertainty quantification and feedback control. J Intel Mater Syst Struct 22:1317–1326
38. Bahlous SE-O, Abdelghani M, Smaoui H, El-Borgi S (2007) A modal filtering and statistical approach for damage detection and diagnosis in structures using ambient vibrations measurements. J Vibr Contr 13:281–308
39. Xu YL, Zhang J, Li JC, Xia Y (2009) Experimental investigation on statistical moment-based structural damage detection method. Struct Health Monitor 8:555–572
40. Gillich G-R, Praisach Z-I (2014) Modal identification and damage detection in beam-like structures using the power spectrum and time–frequency analysis. Sign Proc 96:29–44
41. Wang J, Qiao P (2008) On irregularity-based damage detection method for cracked beams. Int J Solids Struct 45:688–704
42. Dixit A, Hanagud S (2010) Comments on: 'curvature mode shape-based damage assessment of carbon/epoxy composite beams'. J Intel Mater Syst Struct 21:659–663
43. An Y, Ou J (2014) A signal energy change-based damage localization approach for beam structures. Measurement 48:208–219
44. Mendrok K, Uhl T (2011) Experimental verification of the damage localization procedure based on modal filtering. Struct Health Monitor 10:157–173

Condition Monitoring of Aircraft Engine Rotor System with Stiffness Anisotropy of Rotor Supports. Comparative Analysis of Accelerometers Mounting Schemes

S.V. Semenov, M.Sh. Nikhamkin, N.A. Sazhenkov and I.V. Semenova

Abstract Elimination of dangerous vibration modes is one of the major issues in Modern aircraft engines designing. The main source of vibrations in gas-turbine engines is rotors (Khronin in Vibrations in aircraft engines. Mashinostroenie, Moscow, 1980). Aircraft engines weight reducing and applying of new engineering solutions (Inozemtsev et al. in Fundamentals of aircraft and power plants gas turbine engines construction, 2008) lead to appearing of shaft and case units stiffness decreasing tendency. This may cause a problem with supports stiffness anisotropy which leads to complexity of vibration modes. It is known that standard (in vertical plane of engine) accelerometer mounting scheme is not effective for detecting anisotropy of supports stiffness. Therefore it might be more useful to place sensor at the angle of 45 degrees to the weak and strong stiffness axes. Comparison of both mounting schemes was made on the base of experiments performed on the rotor test rig. During experimental investigation, supports accelerations, shaft displacements and shaft rotational speeds were obtained and analyzed. Comparative qualitative analysis for both mounting schemes was provided.

Keywords Rotor dynamics · Stiffness anisotropy · Sensors mounting schemes · Accelerometers · Gas-turbine engines

S.V. Semenov (✉) · M.Sh. Nikhamkin · N.A. Sazhenkov
Department of Aircraft Engine, Perm National Research Polytechnic University, Perm, Russia
e-mail: sergey.semyonov@mail.ru

M.Sh. Nikhamkin
e-mail: nikhamkin@mail.ru

N.A. Sazhenkov
e-mail: sazhenkov_na@mail.ru

I.V. Semenova
Department of Applied Mechanics, VSB-TUO, Ostrava, Czech Republic
e-mail: semenova-irina-v@mail.ru

F. Chaari et al. (eds.), *Advances in Condition Monitoring of Machinery in Non-Stationary Operations*, Applied Condition Monitoring 4,
DOI 10.1007/978-3-319-20463-5_35

Contents

1 Introduction 464
2 Mounting Schemes Comparison Using Experimental Rotor Test Rig 465
2.1 Test Rig Description 465
2.2 Mounting Schemes Comparative Analysis 467
3 Real Gas Turbine Engine Testing 468
4 Conclusion 470
References 470

1 Introduction

Ensuring of the gas turbine engines dynamic strength is one of the most important issues in modern aircraft engines design process. Due to the tendency of the engine weight reduction, application of modern materials and sophisticated designs, engine vibration characteristics tend to be difficult to analyze [1, 2]. One of possible reasons of this is rotor supports stiffness anisotropy [3]. The anisotropy appears when support stiffness is not even in radial directions. Generally it leads to additional critical modes and rotor backward precession appearance. Moreover it may complicate rotor balancing procedures and rotor vibration behavior analyzing [4, 5].

It is known that standard (in vertical plane of engine, Fig. 1a) accelerometer mounting scheme is not effective for detecting anisotropy of supports stiffness [6, 7]. The main reason of that is an "ellipticity" of orbits (which can vary their shape from nearly circular to linear depending on rotation speed). Since orbits are non-circular, measured vibration amplitude depends on the sensor mounting orientation. The solution is likely to place sensors at the angle of 45° to the weak and strong stiffness axes (see Fig. 1b) [6]. The main goal of the work is to check the ability of new sensor mounting scheme to detect critical regimes (1X splitting resonance) caused by supports stiffness anisotropy.

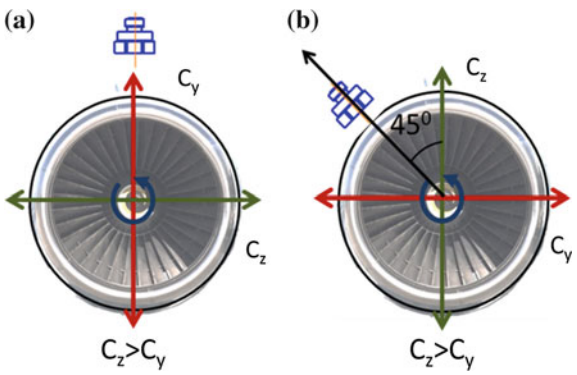

Fig. 1 Gas turbine engine accelerometer mounting scheme (**a**—basic, **b**—alternative)

The problem of accelerometers mounting scheme sensitivity validation using real gas turbine engine tests lies in a complexity of its vibration spectrum [8]. Therefore, it seems to be rational to use special test rig to simulate needed gas turbine engine rotor characteristics and to analyze influencing factors separately. At the first stage of investigation a comparative analysis of two mentioned accelerometers mounting schemes was made using rig test. After the comparative analysis the alternative mounting scheme was validated on a real gas turbine engine during its development testing.

2 Mounting Schemes Comparison Using Experimental Rotor Test Rig

2.1 Test Rig Description

Experimental test rig consists of a rotor with one load disk, two supports and flexible coupling with AC motor which is controlled via AC drive (see Fig. 2).

The test rig allows changing its parameters (weight and position of the loading disk, arrangement of supports, unbalance value). In experiment with accelerometers position at the angle of 45° to the weak and strong stiffness axes, one of the supports was equipped with specially prepared bush (see Fig. 3) to simulate two-axis support stiffness anisotropy.

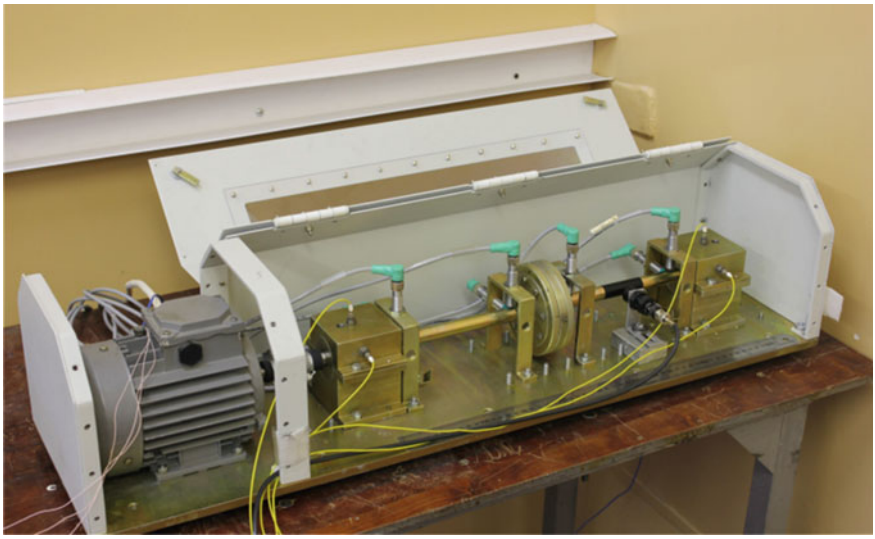

Fig. 2 Experimental test rig

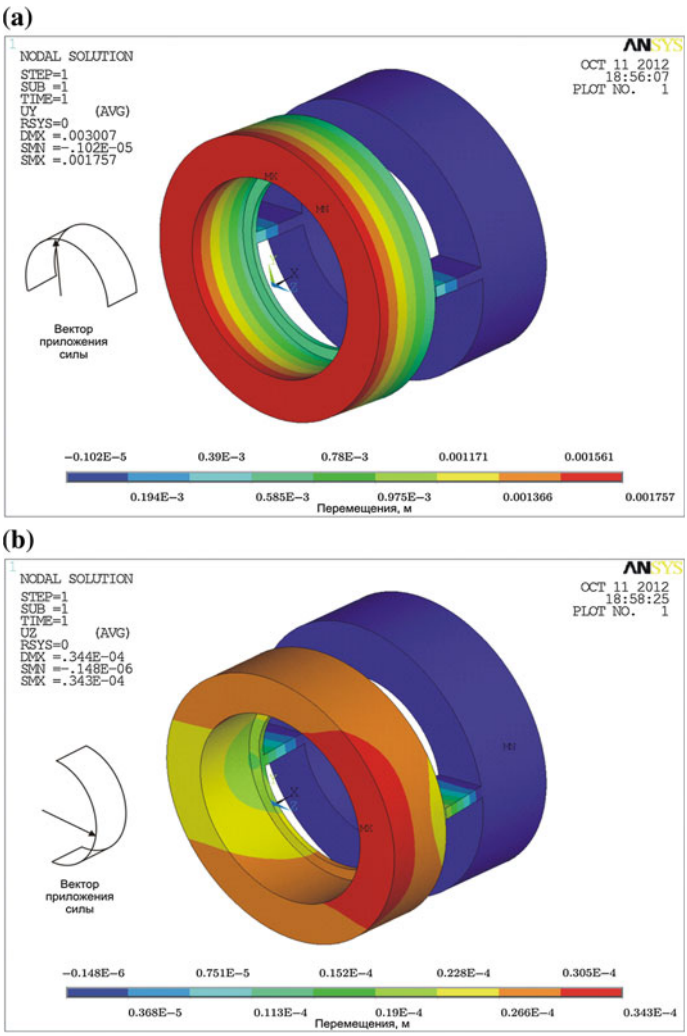

Fig. 3 Deformations of bush with two-axis stiffness anisotropy (**a**—deformation towards weak direction, **b**—deformation towards strong direction)

During experimental investigation supports acceleration, dynamic displacement of the shaft (via inductive proximity sensors) and rotational speed during speed up from 0 to 6000 rpm were measured. All this data were analyzed via Fast Fourier Transform (FFT). Critical speeds and shaft rotating orbits were determined. Measurements and control system was based on National Instruments (LabView) and LMS SCADAS Mobile (Test.Xpress) equipment [9, 10].

2.2 Mounting Schemes Comparative Analysis

Analysis of rotor dynamics with two-axis stiffness anisotropy of rotor supports was provided. Resonance frequency splitting and reverse orbiting were obtained. Two following mounting schemes were tested: the basic and the alternative.

According to the basic scheme of mounting accelerometers were positioned along the weak and the strong stiffness axes (see Fig. 4).

For this scheme the values of critical speeds were 4368 rpm (72.8 Hz) and 4620 rpm (77 Hz). It is shown that the scheme allows detecting both critical peaks using two accelerometers. Reversal orbiting between the peaks of split resonance was also obtained (see Fig. 5).

At the second scheme (alternative) accelerometers were placed at the angle of 45° to the weak and the strong stiffness axis (see Fig. 6a). This was made by rotation of the bush 45° counterclockwise (see Fig. 6b).

In this case the values of critical speeds were 4266 rpm (71.1 Hz) and 4590 rpm (76.5 Hz). It is shown that the scheme allows detecting split resonance using only one accelerometer (see Fig. 7). Besides, it should be noticed that critical speeds values are slightly less than in previous scheme, because of support stiffness decreasing.

Comparative analysis of the both schemes was performed. It was ascertained that standard scheme allows detecting only one resonance peak corresponding to bending mode in plane of each accelerometer. In real aircraft engine accelerometer mounting scheme, where the only one accelerometer is used, it is not possible to identify effects caused by supports anisotropy.

Alternative mounting scheme allows detecting both resonance peaks even by the one accelerometer placed at the angle of 45° to the weak stiffness axis against direction of rotor rotation (see Fig. 7b), but to identify all anisotropy effects it is recommended to use a set of two sensors [7].

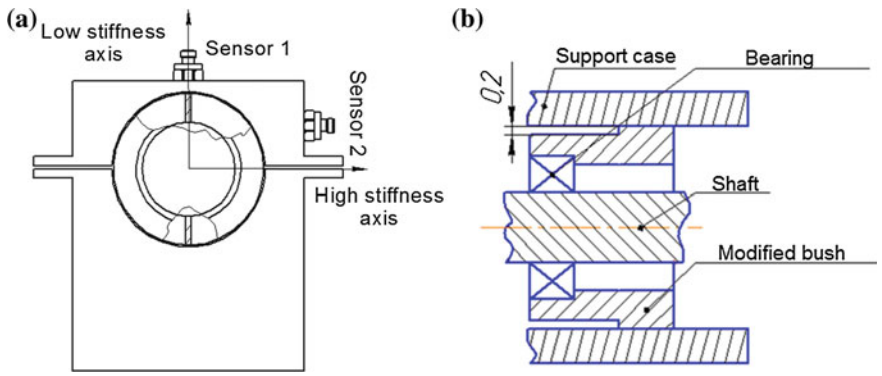

Fig. 4 The basic sensors mounting scheme

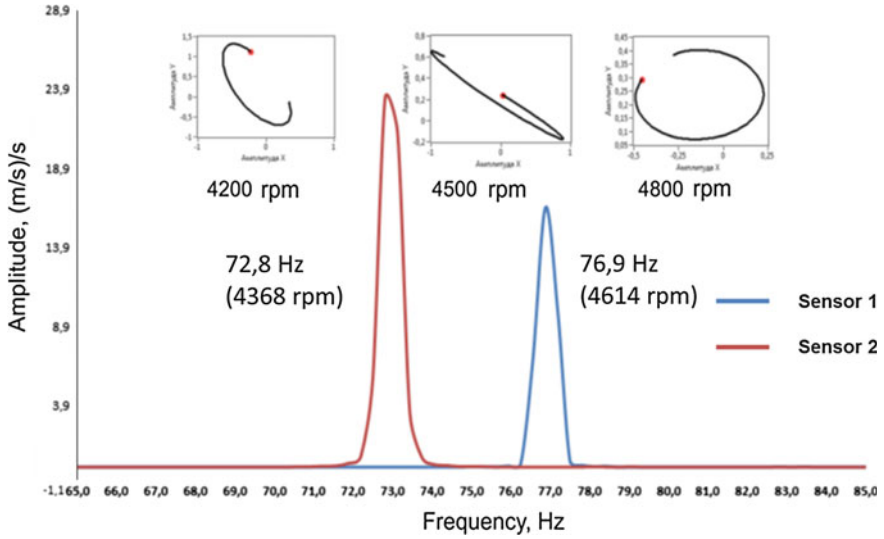

Fig. 5 The basic sensors mounting scheme investigation results (accelerometers signal FFT, *red*—horizontal vibration component, *blue*—vertical vibration component)

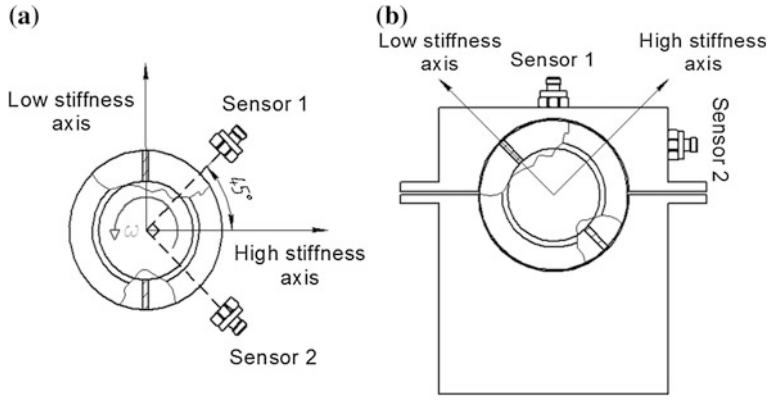

Fig. 6 The alternative sensors mounting scheme with bush

3 Real Gas Turbine Engine Testing

The efficiency of alternative mounting scheme was checked during full-scale gas turbine engine testing. The engine was equipped by additional vibration sensors placed on the fan supports and on the case near front and rear suspensions. Due to

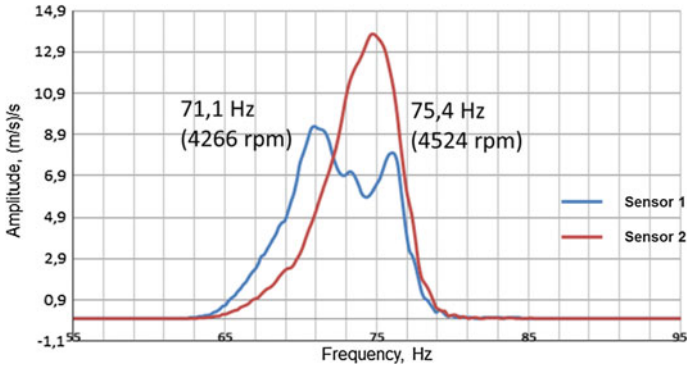

Fig. 7 The alternative sensors mounting scheme investigation results (accelerometers signal FFT, *red*—horizontal vibration component, *blue*—vertical vibration component)

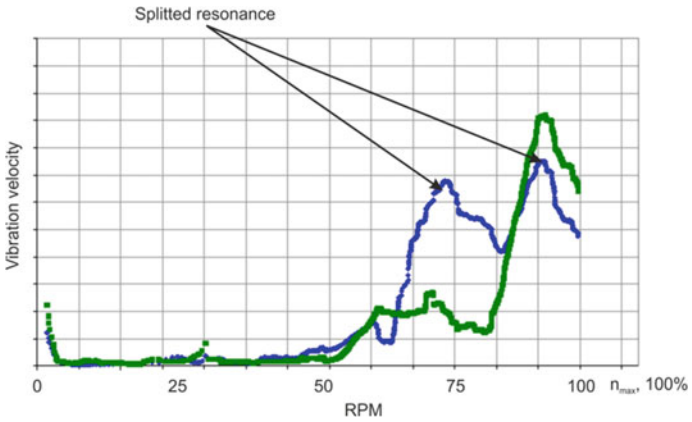

Fig. 8 Example of amplitude-frequency diagram. *Green*—sensor placed in vertical plane of engine, *blue*—sensor placed at 20° to vertical plane of engine

construction restrictions additional sensors were mounted at the angle of 20° (instead of 45° angle which was used in investigation via test rig) to the vertical plane of engine.

The experimental investigation of full-scale gas turbine engine rotor dynamics consisted of frequency response and trajectory of fan supports vibration displacement analysis. Analysis of data gathered by additional vibration transducers shows that there are following signs of supports stiffness anisotropy in engine: the presence of splitting resonance (see Fig. 8), ellipsoidal orbits, degeneracy of fan supports vibration displacement trajectory (locus) to line (see Fig. 9).

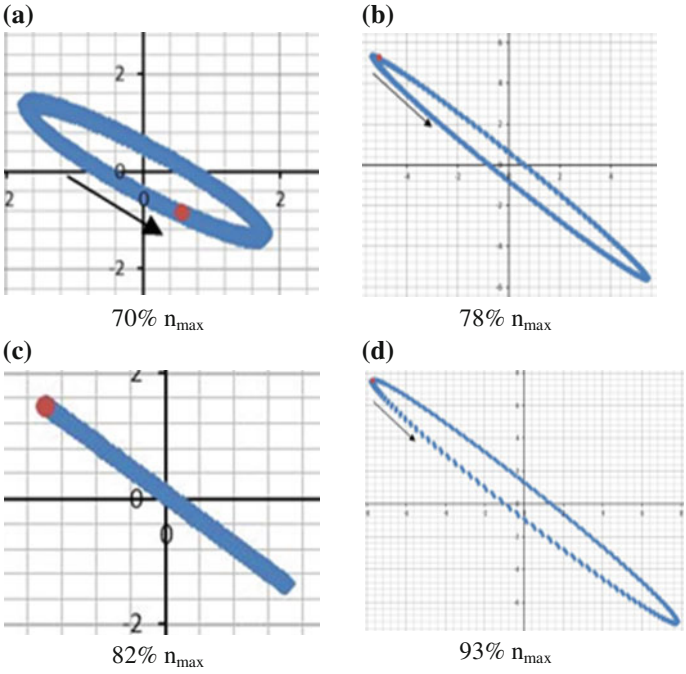

Fig. 9 Example of fan supports vibration displacement trajectory alterations during speed up (**c**—moment of degeneracy to line)

4 Conclusion

The investigation shows that there is possibility to improve sensitivity of traditional accelerometers mounting scheme. Also received data can be used for specific vibration transducers mounting schemes justification and for mathematical models verification.

Acknowledgements The work was supported by Grant № 9.576.2014/K "Development of numerical and experimental methods for twin-shaft aircraft engines vibration safety providing".

References

1. Khronin DV (1980) Vibrations in aircraft engines. Mashinostroenie, Moscow (in Russian)
2. Inozemtsev AA, Nikhamkin MSh, Sandratskiy VL (2008) Fundamentals of aircraft and power plants gas turbine engines construction (in Russian)
3. Kelzon AS, Zhuravlev YN, Yanvarev NV (1977) Numerical analysis and designing of rotor systems. Mashinostroenie, Moscow (in Russian)

4. Childs D (1993) Turbomachinery rotordynamics: phenomena, modeling and analysis. Wiley, New York
5. Dimentberg FM (1964) Vibration of machines. Mashinostroenie, Moscow
6. Agnieszka Muszyńska (2005) Rotordynamics. Taylor & Francis, London
7. Bently DE (2002) Fundamentals of rotating machinery diagnostics. Bently Pressurized Bearing Company, Minden
8. Sidorenko MK (1968) Vibrometry of gas-turbine engines. Mashinostroenie, Moscow (in Russian)
9. Semenov SV, Mekhonoshin GV (2013) Control-measuring system of model twin-shaft rotor system, Innotech 2013. http://conference.msa.pstu.ru/arhiv/mezhdunarodnaya%20konferenciya%20studentov%202013.pdf (in Russian)
10. Semenov SV, Mekhonoshin GV (2014) Gas turbine engine twin shaft rotor system experimental investigation/fundamental investigations, no 11, part 2, 280–284 p (in Russian)

Operational Safety of Steel-Cord Conveyor Belts Under Non-stationary Loadings

Ryszard Blazej, Leszek Jurdziak and Witold Kawalec

Abstract To ensure the safe work of a conveyor high values of a conveyor belt safety factor (BSF) are applied for obtaining peak tensions and belt strength. The BSF of steel-cord conveyor belts is derived from the splice dynamics fatigue strength (as identified by the laboratory tests that were made almost half a century ago), as well as degradation from age, factory and field installation error factors and non-steady momentary factors. The users' experience suggests that the steel-cord belt tensile strength is overestimated, especially for the long, high capacity conveyors. The authors propose the use of the recently implemented complex methods of steel-cord belts in situ condition monitoring methods for identification of the actual belt tensile strength and the accurate methods of calculation of a conveyor's resistances to motion and belt tension in order to identify and monitor the operational belt safety factor (OBSF) for steel-cord belts.

Keywords Belt conveyors · Steel-cord belts · Belt safety factor · Condition monitoring · Non-stationary operations · Belt tension identification

Contents

1 Introduction 474
2 Definition of the Operational Belt Safety Factor 475
2.1 The OBSF Formula 475
2.2 Identification of the Actual Belt Strength 476

R. Blazej (✉) · L. Jurdziak · W. Kawalec
Faculty of Geoengineering, Mining and Geology, Wroclaw University of Technology, Wroclaw, Poland
e-mail: ryszard.blazej@pwr.edu.pl

L. Jurdziak
e-mail: leszek.jurdziak@pwr.edu.pl

W. Kawalec
e-mail: witold.kawalec@pwr.edu.pl

F. Chaari et al. (eds.), *Advances in Condition Monitoring of Machinery in Non-Stationary Operations*, Applied Condition Monitoring 4,
DOI 10.1007/978-3-319-20463-5_36

2.3 Identification of the Top Belt Tension 479
3 Guidelines to The Control of the OBSF 480
References 481

1 Introduction

The established standards for calculating belt conveyors (ISO5048, DIN22101 [1]) employ the simplified concept of rolling resistance of the belt on idlers. Determining the coefficient of the main resistance f upon guidelines provided by these standards is still more a matter of experience than of an exact calculation supported by theoretical and experimental scientific research. All forces induced by resistances to motion, lifting the transported bulk material and starting (accelerating) or stopping of the loaded belt are compensated by the belt tension. To ensure the safe work of a conveyor the conservative Belt Safety Factor (BSF) of near 7:1 (following the standards) is applied for obtaining peak tensions and belt strength requirements of steel-cord belts (Fig. 1) which are usually designated for the high capacity belt conveyors. The BSF, used for calculation of a required conveyor belt tensile strength, has not been modified for many years. The BSF is derived from the splice dynamics fatigue strength (36 % of the nominal belt strength—the value identified from laboratory tests that were made almost half a century ago) and the estimated overloading caused by factory and field installation errors, belt ageing and non-steady momentary peak tensions (adding 140 % to the maximum tensions during steady operations). The obtained figure 2.4/0.36 = 6.67 has been set as the base BSF for steel-cord belts. With regard to the additional factors representing operational conditions adopted in the subsequent releases of technical standards [1], the base BSF could be either raised to 8 or even 9.5 (in the case of uphill, high output conveyors with frequent stops and starts) or decreased to mere 5 (in the case of long-distance, overland conveyors that are usually well maintained and operated without unexpected stoppages [2, 3]).

The values of BSF are so high due to difficulties of credible assessment of peak tensions in a belt. There are several reasons for these difficulties. Belt conveyors

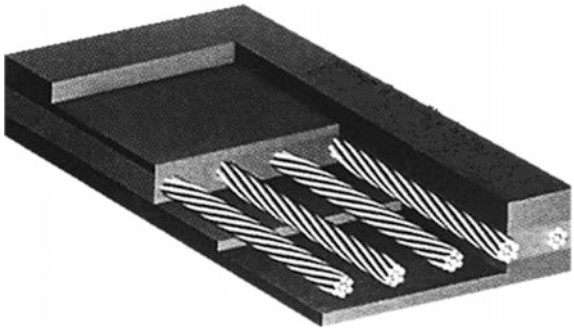

Fig. 1 Conveyor belt with steel-cord core

work in changing operating conditions which have a great impact on their resistances to motion. The uneven distribution and misalignment of transported bulk material, belt mistracking, varied idlers rolling resistance and caused by stoppages and starts instantaneous accumulation of belt tension at drive pulleys result in significant variations of top belt tension on a given belt conveyor [4–6]. All these phenomena together cause that the operation of a belt conveyor is a non-stationary process—hence the high values of the BSF adopted many years ago. However, there are now evidences for a serious reconsideration of the BSF:

- The actual values of resistances to motion of a belt conveyor with regard to changing operational conditions can be more precisely calculated on the basis of the detailed analysis of the energy dissipation processes in a conveyor belt and in the transported material, as well as the analysis of the interaction between the belt and idlers [7, 8];
- The residual tensile strength of steel-cord belt splices, due to technology improvement, is now higher than 50 years ago, even after applying the most rigorous six sigma quality criterion [9];
- Conveyor belts can now be monitored on-line to provide with the diagnose of their actual condition [10–12].

Utilising the results of belt diagnostics basing upon its condition monitoring allows to calculate the actual Operational Belt Safety Factor (OBSF) which represents the real value of the safety factor of a given belt conveyor working under its specific operating conditions. Though such idea has been already proposed [13, 14], only recently the necessary conditions have been achieved.

2 Definition of the Operational Belt Safety Factor

2.1 The OBSF Formula

The operational safety of a steel-cord conveyor belt working on a given belt conveyor is identified by its OBSF. The OBSF is defined as a ratio:

$$\text{OBSF} = K_T / T_Z \tag{1}$$

where:
K_T actual breaking strength of the installed conveyor belt,
T_Z maximum operating belt tension on the conveyor.

The ratio has to be greater than 1 in order to maintain the safe work of a conveyor. Both values on the right side of the equation have to be identified and controlled throughout the operation. On a contrary to the conservative high values of constants in established standards, the proposed method bases on results of

condition monitoring of conveyor belts as well as computations based on the actual mathematical model of the conveyor operation.

2.2 Identification of the Actual Belt Strength

The steel-cord belts' tensile strength depends on the actual condition of steel ropes inside the belt core (Fig. 1). With the help of magnetic NDT methods after scanning the whole belt loop on a conveyor and then processing the obtained signals, the condition of the belt core can be diagnosed [10–14]. As the belt loop is built of the individual belt segments connected together with vulcanized splices, the actual breaking strength of the installed conveyor belt can be expressed as follows:

$$K_T = \min_{i=1}^{k}\{\min\{K_{is1}, K_i, K_{is2}\}\} \tag{2}$$

where:

k	number of belt segments in the whole belt loop,
K_{is1}, K_{is2}	actual breaking strength of both splices between the "i" belt segment and its preceding, succeeding belt segment,
K_i	actual breaking strength of the "i" belt segment

Belt segments and their splices have to be treated separately as different procedures of control the actual condition are available. The strength of a belt splice can be expressed as the minimum of the following:

$$K_{is} = \min\{t(K_{is}), \mathrm{d}(K_{is}), \mathrm{r}(K_{is})\} \tag{3}$$

where:

$t(K_{is})$	actual breaking strength of the belt splice tested in the laboratory,
$d(K_{is})$	diagnosed actual breaking strength of the belt splice upon the results of condition monitoring,
$r(K_{is})$	residual breaking strength of the belt splice upon the results of the splice dynamics fatigue strength (49 % of the nominal belt strength—see Fig. 2 [9])

The diagnosis of the actual breaking strength of the belt splice upon the results of condition monitoring ($d(K_{is})$) has been assumed by the authors as not reliable yet despite some publication on this topic. The investigations in this area are now pending and then the calculated value of $d(K_{is})$ should be available.

The actual breaking strength of a belt segment can be now successfully identified with the use of diagnostics results obtained from the in situ belt condition monitoring. Assuming that scans of a belt loop are done (see Fig. 3) and analysed on a regular basis with regard to the known speed of fatigue processes, for the each belt

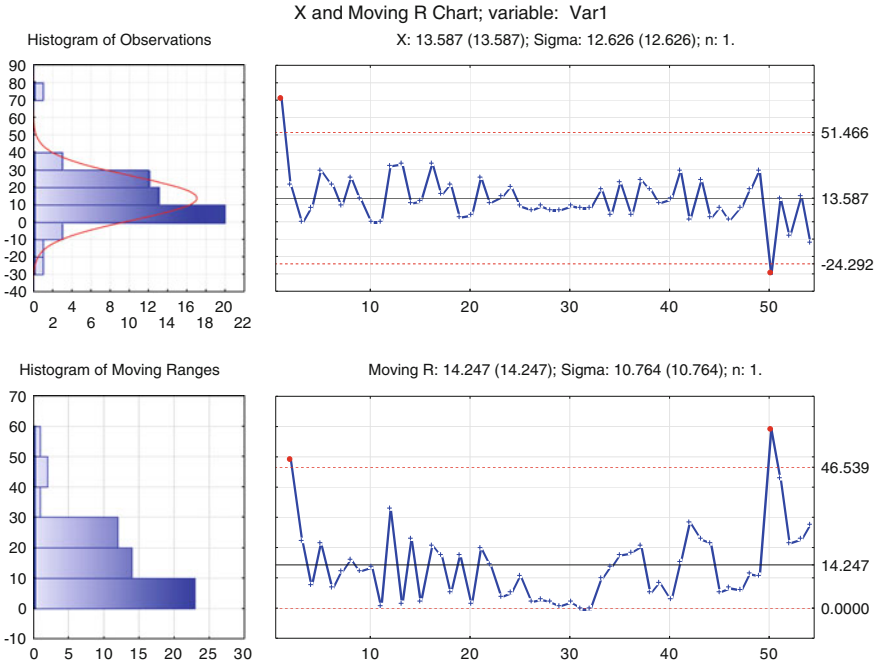

Fig. 2 Quality control chart of the analysed loss of belt tensile strength within belt splices; 6σ area marked (Statistica), based on the results of unpublished laboratory tests reports [9]

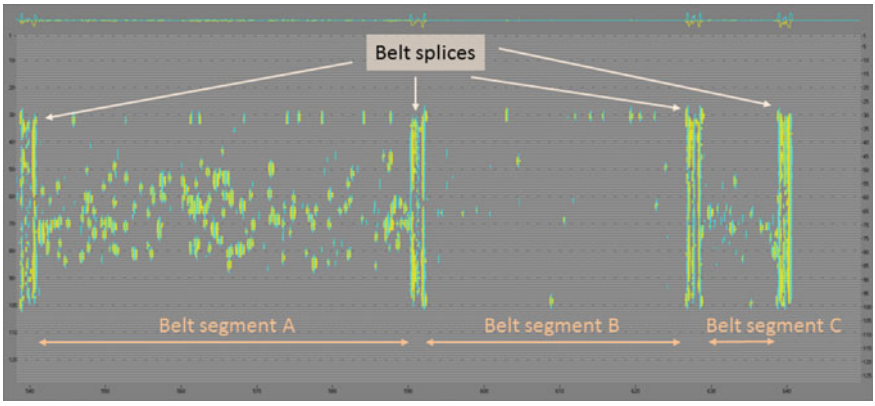

Fig. 3 Recorded sample scan of 3 belt segments and belt splices of an investigated belt loop—raw data for belt diagnostics; irregular spots represent discontinuities (in the area of splices) or damages (in the area of segments) of steel cords—different density of spots in segments *A*, *B* and *C* indicates the different level of the wear of these belt segments [11]

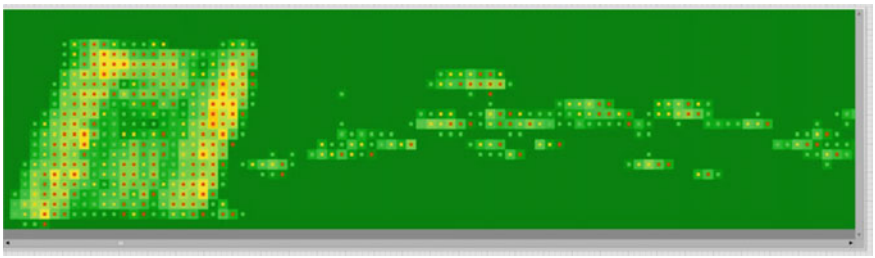

Fig. 4 Visualisation of the condition of a scanned belt segment; the level of damage is presented on the square grid where colours of a square indicate the averaged level of damage, *dots*—registered maximum values of damage within rectangles; *heavily dotted area* on the left side of the top chart represents a belt splice that is to be processed separately [10, 11]

segment areas of a damage (corrosion or discontinuity of a belt cord) can be identified and marked (see Fig. 4). Not only the number of damaged cords but also their position is important for the need of identification of a tension concentration factor (TCF) as described and analysed with regard to layout of damaged areas by Harrison [14].

The strength of a belt segment can be therefore expressed as the minimum value of the following:

$$K_{\mathrm{i}} = \min\{\mathrm{d}(K_{\mathrm{is}}), \mathrm{r}(K_{\mathrm{is}})\} \tag{4}$$

where:
$\mathrm{d}(K_{\mathrm{is}})$ diagnosed actual breaking strength of the belt segment,
$\mathrm{r}(K_{\mathrm{is}})$ residual breaking strength of the belt segment

The diagnosed actual breaking strength of a belt segment is expressed as the ratio:

$$d(K_i) = \frac{K_N}{TCF} \tag{5}$$

where:
K_{N} nominal (rated) belt breaking strength.

The TCF is calculated upon the spatial distribution of damaged areas and their scale. The neighbouring areas of damage are treated separately only if the distance between their borders is greater than the recognized impact radius otherwise they are put together into a resultant, combined area [14]. The supplied data are processed automatically to provide with the aggregated actual breaking strength of the belt segment.

The residual breaking strength a belt segment is computed with the use of the algorithm of fatigue analysis and described in the chapter "Condition monitoring of conveyor belts as a tool for proper selection of their replacement time".

2.3 Identification of the Top Belt Tension

The maximum operating belt tension on a conveyor can be identified with the use of the specialized software which bases upon the well proven algorithms of individual calculating the main resistance force components. In the Wroclaw University of Technology theoretical and experimental (done both in the laboratory and in situ) investigations in the field of belt conveyors main resistances to motion have been carried out for many years. The algorithms depend on the analysis of the energy dissipation processes in a conveyor belt and in the material load stream and the analysis of the interaction between the belt and idlers with regard to a large set of technical, physical and operational parameters [4, 5, 7]. The algorithms have been eventually implemented into the comprehensive, specialised program for detailed belt conveyor modelling and calculation—QNK-TT [3]. The accuracy of the computational results obtained for various configurations of the conveyor and verified by in situ measurements, has confirmed the reputation of the QNK-TT software as a reliable tool [15]. For the calculations the following parameters (apart from the standard design data of a conveyor) are taken into account:

- the actual configuration of a conveyor: the profile of its route, arrangement of the conveyor main elements (drive units, take-up equipment, pulleys layout, loading and discharge points, idlers spacing and layout;
- parameters of the main conveyor elements: belts (type and thickness of carcass, covers thickness and elasticity modulus, damping factors and flexural rigidity), idlers (rotational resistance to motion);
- parameters of a transported bulk material: density, angle of repose, internal friction coefficient, material-to-belt friction angle, distribution of the transported material along the conveyor;
- operational conditions: ambient temperature, belt and transported material mistracking; belt conveyor route misalignment;
- control parameters of starting and stopping operations.

The actual maximum operating belt tension T_Z for the given belt conveyor can then be computed against its worst operational parameters by a specialist (a Competent Engineer) much more accurately than with the use of established standards. As the resulting figure depends on a wide set of input parameters, in an instant need of decreasing T_Z, it can be achieved by adjusting the available factors (e.g.: lowering the start peak tension by setting the main drive soft-start control or temporary limiting the loadings by reduction—if it is possible—the volumes of conveyed material which is discharged onto the conveyor) (Fig. 5).

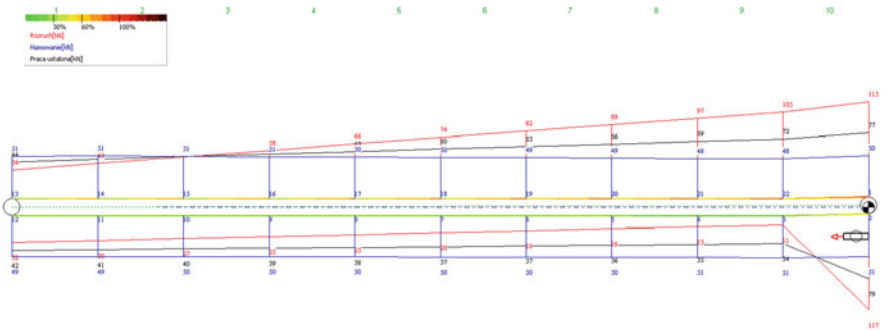

Fig. 5 An example of a belt tension chart along a conveyor route for the steady and non-steady conveyor operations—during start and stopping (QNK-TT) [16]

3 Guidelines to The Control of the OBSF

Following the definition of the OBSF, its identification requires the procedure that allows to control the investigated belt conveyor: the actual values of the actual breaking strength of the installed conveyor belt and the maximum operating belt tension.

The implementation of the OBSF for a given belt conveyor assumes that the following activities have been done:

- The whole loop of the conveyor belt is scanned on a regular basis with the use of dedicated NDT equipment to recognize the failures. Each signal of a failure is automatically processed and desurveyed to build the map of belt damage from which the diagnosed actual breaking strength of belt segment and the whole belt loop is derived.
- Belt conveyors layout and loadings in any large transportation system are changing. Therefore the data of the analyzed belt conveyor should be regularly updated and then processed with the use of the specialized software to calculate the maximum operating belt tension. As the calculation depends on a wide set of parameters (including the assessment of the most difficult actual operational conditions), it should only be performed by a certified personnel (the Competent Engineer).
- The OBSF for each belt segment should be recalculated after updating any of the above.

The obtained results of the OBSF can be used for the alternative maintenance decisions (replacement of damaged segments, decreasing of the belt tension) that would allow to continue the safe operation of a conveyor.

As the whole procedure of the described above condition based conveyor belt maintenance requires a substantial knowledge of designing and use of conveyors, it

is recommended that an individual procedure for the given belt conveyor should be developed and checked by a Competent Person—a specialist in the field of steel-cord conveyor belt maintenance.

Acknowledgments This work is supported by the Applied Research Programme (PBS): "Intelligent system for automated testing and continuous diagnosis of the conveyor belt".

References

1. Technical Standard: Gurtfoerderer fuer Schuettgueter—DIN 22101
2. Fiscor S, Carter RA (2007) Conveyor technology rolls ahead to keep pace with industry demands. Eng Mining J 208:34
3. Lawrie E, Rasul MG, Gilroy T (2007) Coal land transport economics of options in Eastern Australia, Bulk Solids Handling 27, 8
4. Gladysiewicz L, Kawalec W (2001) Modelling chosen operating conditions of a belt conveyor. Proceedings of the International Symposium Mine Planning & Equipment Selection, New Delhi
5. Gladysiewicz L, Kawalec W (2006) Optimised selection of a belt conveyor loaded by a BWE. In 8th international symposium continuous surface mining, RWTH Aachen
6. Harrison A (1998) Modelling belt tension around a drive drum. Bulk Solids Handling 18 (1):75–80
7. Gladysiewicz L (2003) Belt conveyors. Theory and calculations. Wroclaw University of Technology Publishing House, Wroclaw (in Polish)
8. Gladysiewicz L, Hardygora M, Kawalec W (2009) Determining belt resistance. Bulk handling today, no 5
9. Hardygora M, Komander H (2002) Analysis of tensile tests of steel-cord conveyor belt splices, Wroclaw University of Technology, Report of the Belt Transportation Laboratory, nr arch. Z-4/33/02 (in Polish, not published)
10. Blazej R (2012) Review of the newest NDT equipment for conveyor belt diagnostics. Diagnostyka, 4(64)
11. Blazej R, Jurdziak L, Zimroz R (2013) Novel approaches for processing of multi-channels NDT signals for damage detection in conveyor belts with steel cords. Key Eng Mater 569:978–985
12. Blazej R, Zimroz R, Jurdziak L, Hardygóra M, Kawalec W (2013) Conveyor belt condition evaluation via non-destructive testing techniques, mine planning and equipment selection: proceedings of the 22nd MPES conference, Dresden, Germany
13. Harrison A (1996) 15 years of conveyor belt nondestructive evaluation. Bulk Solids Handling 16(1):13–19
14. Harrison A (1990) Safety factor calculations for high-strength inclined belts based on NDT signal analysis. International coal handling and utilizing conference, Sydney, 19–21 June 1990
15. Kulinowski P (2013) Simulation studies as the part of an integrated design process dealing with belt conveyor operation. Maint Reliab 15(1):83–91
16. Kawalec W, Kulinowski P (2007) Computations of belt conveyors. Transport Przemyslowy 1 (27) (in Polish)

Condition Monitoring of Conveyor Belts as a Tool for Proper Selection of Their Replacement Time

Ryszard Błażej, Leszek Jurdziak and Witold Kawalec

Abstract Condition monitoring of steel cord belts using magnetic scanners is known since late 70s however it has not been widely used in Polish mines due to difficult interpretation of signals and cost of services and diagnostic devices. Recent integrated diagnostic tool developed in Machinery Systems Division at Wroclaw University of Technology showing 2D/3D state of belts core and calculating aggregated measures (e.g. wear density of belt segments) allows on better interpretations and prediction of remaining belt life and optimal selection of their time for replacement. Proposed approach utilise experience and models of belt wear developed and verified statistically on belts durability data. Now addition of new dimension (current belt condition) allows on observation of increasing belt degradation process (belt wear density trajectory) which extrapolation allows on prediction of remaining life and replacement time.

Keywords Visual inspection · Belt diagnostics · Magnetic scanner

Contents

1 Introduction—The Value of Belts in Poland 484
2 Lack of Belt Condition Monitoring Creates Costs and Losses 484
3 Non Stationary Load of Belt Conveyors 485
4 Belt Degradation Processes 486
4.1 Influence of Conveyor Length on Belt Degradation and Its Durability 487
4.2 Influence of Conveyor Belt Load on Belt Durability 487

R. Błażej · L. Jurdziak (✉) · W. Kawalec
Faculty of Geoengineering, Mining and Geology, Wroclaw University of Technology, Wroclaw, Poland
e-mail: leszek.jurdziak@pwr.edu.pl

R. Błażej
e-mail: ryszard.blazej@pwr.edu.pl

W. Kawalec
e-mail: witold.kawalec@pwr.edu.pl

F. Chaari et al. (eds.), *Advances in Condition Monitoring of Machinery in Non-Stationary Operations*, Applied Condition Monitoring 4,
DOI 10.1007/978-3-319-20463-5_37

5 The Increasing Need to Create an Own Diagnostic Device for Condition Monitoring of Conveyor Belts 488
6 An Intelligent System for the Automatic Examination and Continuous Diagnosis of the Condition of Conveyor Belts 489
7 Forecasts of Remaining Life of St Belts Based on Individual Trajectory of Belt's Core Condition 490
8 Conclusions 490
References 492

1 Introduction—The Value of Belts in Poland

Belt conveyors are common devices used for material transportation in Polish coal mines (both surface lignite mines and underground hard coal mines). They are also used in underground copper ore mines. The total length of belt conveyors installed there is greater than 1000 km and the length of belts is twice as much due to belts work as close, continuous loops rewound oneself around conveyors. Belts (esp. steel cord) are the most expensive replacement part in conveyors which one meter can costs up to 200 euros [1, 2]. So the value of installed conveyor belts can be estimated at about 200 million euros. Such expensive parts undergo very rough treatment in mines due to heavy materials is discharged on belts in loading points causing belt punctures. Belts transporting coal/ore for long distances are wearing out in particular points (drives, returning drums, cleaning devices) and along the conveyor rout (idlers, self-trainings idlers, constructions, and movement of materials against belt surface).

2 Lack of Belt Condition Monitoring Creates Costs and Losses

Such valuable parts are observed only visually during discrete evaluations. Human inspection of belt conditions, extensively used in Polish mines, takes a lot of time and gives only subjective information about their state [3, 4]. In order to manage huge amount of information about each belt segment special databases were created with computer aided belt management programs [5–8]. Even with the help of computers only selected data are kept and processed—mostly event data connected with belts: purchase, tests, assembly, repairs and cuts, disassembly, recondition or scrap and operational data like working time (calendar or effective), number of cycles around conveyor or carried mass/volume (last two are almost not used [7]). Data about belt condition and their changes with time are restricted to necessary action alarms and belt cover thickness measurements. Introduced in one of mines

the uniform classification of conveyor belt failures and their intensity [3, 4, 9] was used only for description of condition of dismantled belts. In order to take economic reliable decisions about belt segments or their parts such as do nothing, repair or disassembly for economic valuable refurbishment decision taker aided by computer needs more precise data about current condition of all belt segments, their covers, edges and cord as well as splices. Unfortunately belt management computer systems are not popular. Only in two lignite surface mines such systems are used. In underground mines recently one system were applied [8] aimed more on condition monitoring of mechanical conveyor parts such as engines, couplings, gear boxes etc. then focusing specifically on conveyor belts and their condition.

Only in two mines a special steel cord condition monitoring devices are being used instead of human inspections [10–12] even such methods are known since dozens of years [13] and on neither conveyor real time continuous monitoring is applied even if with belt failures not only losses of belts value are connected but also costs of emergency stops (costs of removing spilled out materials, repair costs of damaged construction, costs of putting on belt loop and its splicing, etc.) [1, 14]. Frequently the most important are losses of production due to emergency stops take much longer time than planned repairs. In case of copper and silver ore mining or even lignite excavation each hour of standstill can costs the mine dozens thousand dollars (e.g. in Consol Energy they estimated that one hour of underground hard coal mines standstill costs the company 60,000 USD [15]).

3 Non Stationary Load of Belt Conveyors

The stochastic process of conveyors load is definitely not stationary due to bucket wheel excavators (BWEs), mining shearers or continuous miners are working with different output depending on working conditions, place of the head according to mining face and the cycle of its work. Several analysis [16–18] shows that utilization of conveyor output in average is very low but sometimes for a while can access as high level as 135 % of theoretical output [19].

For example analysing operation of BWEs it can be seen that they work with different efficiencies, what could be a consequence of cut design, applied targets (e.g. in connection with coal blending) or working conditions. Expected value $E\{U_n\} = U$ is constant only locally and even then actual output is oscillating according to different BWE cycles of work and is different for different cycle phases (Fig. 1). The shortest cycle is the discharge of material from buckets within time $60/n$ (n = the number of buckets discharged within 1 min). A bit longer is the excavation of one slice in a terrace (about 3 min), then excavation of one terrace in a block (about 1 h), and then excavation of full block (few hours), full short wall (several weeks) and full level. For the dimensioning of belt conveyors important are cycles shorter than their loading periods due to cyclical reduction (sometimes even

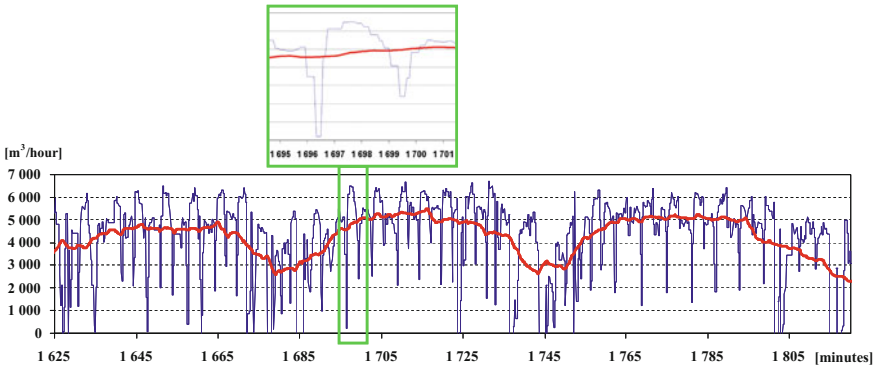

Fig. 1 Different cycles of work of BWE SRs2000—terraces excavation (1 h, 14-min moving average) and slices excavation (3 min, actual efficiency measured every 5 s) [20]

to zero) of actual volume capacities (Fig. 1) what is connected with cyclical movements of BWE or its parts [20]. Joint output stream from 2 BWEs on collective conveyor also is not stationary [16].

4 Belt Degradation Processes

Variable conditions of belts operations creates threats for sudden accidents causing catastrophic belt failures such as transverse belt rapture, longitudinal rips, tearing out edges, punctures with wires pulling out. Process of belt degradation, when there is no sudden accidents, may have cumulative character of gradual wearing out connected with abrasion of the covers, wiping out of edges, fatigue weakening of core strength and increasing number of core punctures (both textile plies as well as steel cords).

In the last thirty years several analysis determining belt reliability [21] were undertaken in order to establish economically optimal belt replacement strategies [22–24] basing on statistical data about belts operating time till belt replacement for refurbishments or sending it to waste [24]. The only detail information about belt condition was registered at the end of belt's life after its dismantling from conveyor. These data was sufficient to establish the influence of the conveyor length and its load on belt's operating time. All economic calculations and forecasts [23] were built based on statistical data about belt operational time and were not corrected according to changes in belt quality. For better belts the estimated belt's life was too short and for worse belts too long. The trials to reduce subjectivity in belts wear assessment based on linguistic variables and fuzzy sets required too much time and could not be automated [3] without special software [4]. Therefore special diagnostic devices used in western countries were evaluated and the work on own solutions has started.

4.1 Influence of Conveyor Length on Belt Degradation and Its Durability

Factors contributing to belt wear were divided by Zur [25] on two groups: these which act in a "point" manner (i.e. at particular locations on the conveyor such as: the feed, the cleaning devices, the drive, etc.) and those which act "linearly" (along the conveyor's route, e.g. rubbing against the rollers and the side stops, etc.). Assuming that the sum of "point" failures is proportional to the number of runs of the belt loop round the conveyor and the sum of "linear" failures is proportional to the distance covered by a specified cross-section of the belt, he proposed the following formula for belt durability measured in belt operating time t_t:

$$t_t = \frac{A_t L_t}{v \sum_p A_p + v L_t A_j} \text{ [s]} \tag{1}$$

where: L_t—the total length of the conveyor belt, m, A_t—amount of work resulting in the belt wear, J/m, ΣA_p—the total of "point" damage work, J/m, A_j—"linear" damage work, J/m^2, v—the velocity of the belt, m/s.

Formula (1) was transformed to a no dimensional form and verified statistically by Jurdziak [26]:

$$n_c = \frac{1}{\frac{\sum A_p}{A_t} + L_t \frac{A_j}{A_t}} \tag{2}$$

Thus belt durability, measured by number of cycles n_c, was expressed as a function of belt loop length and coefficients specifying the shares of "point" damage work and "linear" damage work in the wear of the belt loop for its one run round the conveyor. The relationships were verified and the two coefficients were calculated on the basis of operating data.

Recent results from the same mine as was tested in 1988 year (Fig. 2) has proven that even big increases of belt durability (roughly for about 60 %) have not changed the character of their influence on belt wear [2].

4.2 Influence of Conveyor Belt Load on Belt Durability

Based on earlier discussed assumptions and statistical data from one of underground copper mines it was established the effect of conveyor belt load upon belt durability measured in belt loop cycles and belt operating time [17] (Fig. 3).

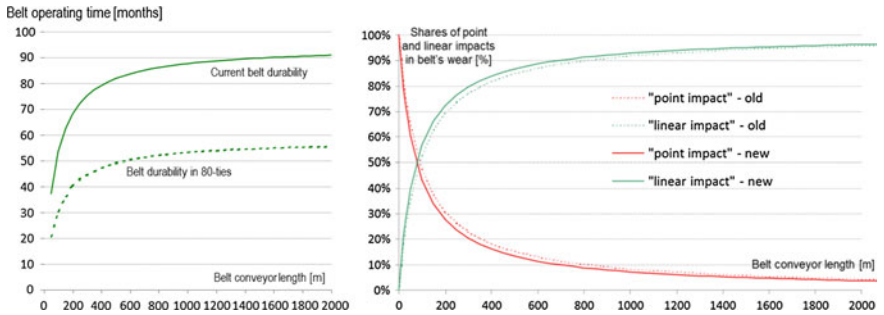

Fig. 2 Changes of belt durability for conveyors with different length (*left*) and variation of percentage contribution of "local" and "linear" damaging agents in conveyor belt wear process as a function of conveyor length (*right*) [2]

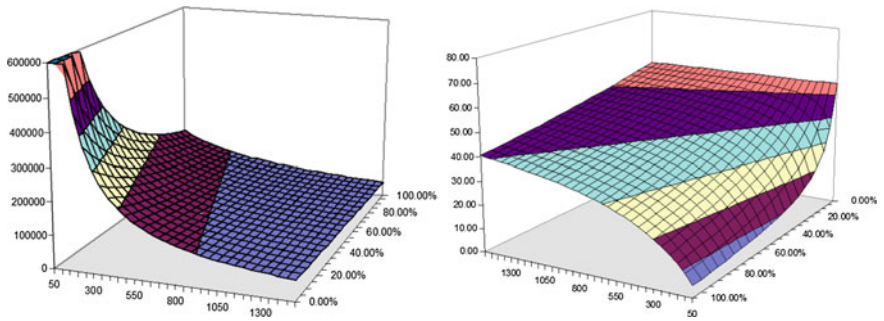

Fig. 3 Dependence of number of belt cycles (*left*) and months of belt operating time (*right*) on relative conveyor load (in % of theoretical load) and conveyor's length (in meters) for the reciprocal model [17]

5 The Increasing Need to Create an Own Diagnostic Device for Condition Monitoring of Conveyor Belts

The value of belts and costs of emergency stops together with scale of potential losses creates the need to build own device for conditional monitoring of conveyor belts [10]. First steps were undertaken in the beginning of twenty first century when the "Turów" lignite mine has purchased the first in Poland device called EyeQ. It was possible due to computer aided belt management in this mine was started in 1985 when the first system was built for this mine [5, 6]. Then the data base of belt failures with description was carried out in Excel taking into account the coded evaluation of belt condition [3]. Together with magnetic device that Turów mine

has implemented [12] belt management system called: *Computer Assisted Belt Card,* which moved databases from Excel to professional databases, was built. The EyeQ system however was an old solution requiring visual interpretation of changes in magnetic field registered about belt surface [13, 27]. The implementation of modernized equipment based on old EyeQ system's magnetic measurement head with completely new software and signal processing procedures [28] and interpretations [12, 29, 30] was a success.

6 An Intelligent System for the Automatic Examination and Continuous Diagnosis of the Condition of Conveyor Belts

A group of members of the Machinery Systems Division (MSD) in the Institute of Mining Engineering at Wroclaw University of Technology specializes in belt conveying systems analysing, calculating and design [31]. Within the division operates the certified Laboratory of Belt Transportation (LTT). Since few years, a group of several people have begun work on developing a comprehensive system for the automatic evaluation of condition of conveyor belts working in the mines. Group uses both magnetic devices developed by specialized companies servicing belts [31] and its own machine vision system developed for assessment of belts covers and edges during belt movement (up to 7 m/s) on the specially designed for this purpose the test conveyor [10]. There were also trials to apply other diagnostic methods [28].

Two years ago they got the research grant funded by the National Centre for Research and Development (NCBiR) for development of the system for automatic diagnosing of conveyor belts condition and aiding of rational belt management. On the basis of previously created diagnostic tool called ABCDE (Automatic Belt Condition Diagnostic Equipment) the five modules: vision—A, magnetic—B, preventive—C, forecasting—D, and determining safety factor—E are developed. They automatically interpret data about conveyor belts' condition to indicate the extent and timing of repairs, to prevent failures and to select the optimum moments for their replacements. The system uses results of ongoing research & development and planned research concerning modelling of belt wear using different algorithms. The reached stage of research allows starting providing scanning services to potential users (e.g. one of lignite mines in Poland which till now does not applied any belt diagnostics). The research is already pursued in real scale and new modules (C-E) being created are under intensive testing together with the whole system in working condition to calibrate it and optimize the economic effects.

7 Forecasts of Remaining Life of St Belts Based on Individual Trajectory of Belt's Core Condition

Application of two magnetic scanners: HRDS (modified EyeQ system developed in MSD at WTU) and the LRM scanner (developed by servicing firm Laboratory of Roman Martyna) were used to establish steel cord condition of belt loops in working environment. In the first case the belts in one of lignite mines were examined, and in the second case the belt loop in one of hard coal mines.

Number of failures per one meter of belts (belt's core wear density) was investigated. The regression curves for the rate of cord failures over time were selected. Given the demonstrated impact of the length of the conveyor onto the accumulated energy within one belt loop cycle around conveyor (Zur's belt wear model) the effect of these factors on the rate of belt failures increase a special 2 variables non-linear regression function was chosen (Fig. 4).

These are the first quantitative results of such research in Poland. The belief that over time the rate of appearance of defects increases was documented. This allows on forecasts of belt replacements time based on individual trajectory of belt's segment core wear development over time (Fig. 4).

All information about influence of conveyor length and load on belt durability can be utilized in preparation of multivariate model of changes of steel cord wear density based on statistical data and registered individual trajectory of wear density changes of particular belt segments (Fig. 5).

Number of data (measurements of belt core wear on conveyors having different lengths) is still too small to build reliable models but it is only a matter of time and next measurements using modernized EyeQ system or newly developed system based on Australian magnetic rod with better resolution [10, 29, 31] should allow on that. It is also possible that the new magnetic scanner will be developed for surface mines based on solution offered by LRM firm to hard coal mines.

8 Conclusions

Presented solution and approach is focused on gradual deterioration process connected with puncturing and wearing out of belts and their cores operating in hard conditions in different mines.

At the moment there is not enough data to build precise and reliable models but hitherto research and obtained results are very promising especially due to a deep experience of statistical analysis dealing with belt durability can be successfully used and implemented [3, 6, 9, 17, 21–23].

Obtained from condition monitoring results describing belt and its core state can be used not only to predict remaining belt life and determine optimal time for belt segment or its part replacement but also to show and determine areas of belt repairs helping in day by day management of belts.

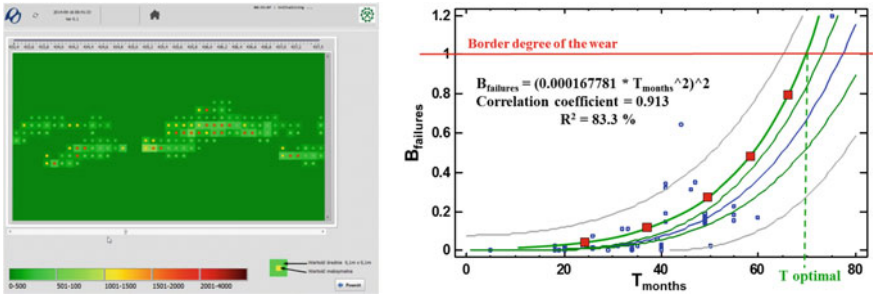

Fig. 4 2D visualization of steel cord failures (*left*) and individual belt segment failure density trace on the background of other statistical data for optimal belt replacement time selection

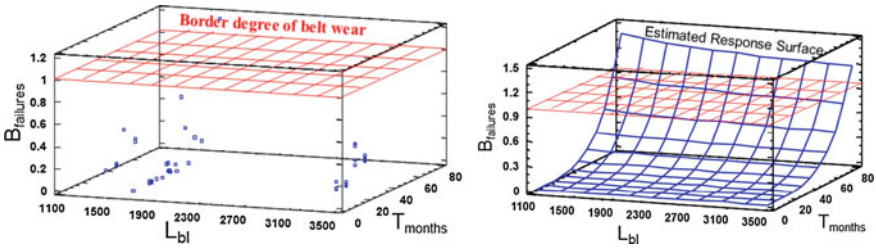

Fig. 5 Proposed method of the optimal belt replacement time forecast based on 2D model of the increase of belt cord's wear density ($B_{\text{failures}} = f(L_{\text{bl}}, T_{\text{months}})$) and the selected threshold degree of its wear

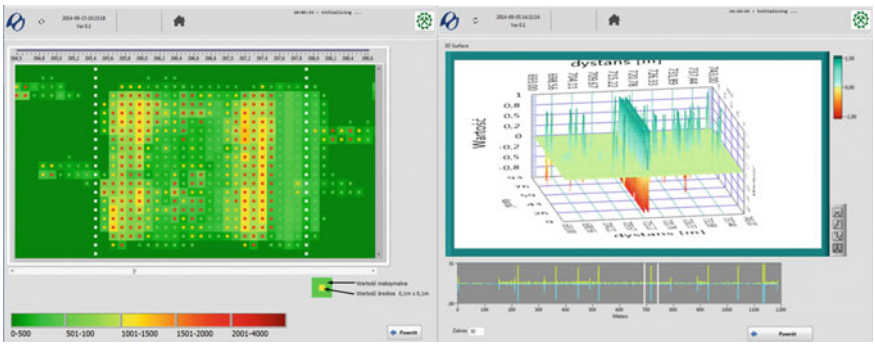

Fig. 6 2D and 3D visualisation of conveyor belt splice condition [30]

Further research will concentrate also on automation of belt splices condition monitoring and evaluation of their quality and current condition. At the moment belt splices are automatically identified and stored for visual inspection by operator who decides if it requires special action. Soon the automatic warning system will be

implemented to check if belt splice length changes and there is a threat of its dehiscence (Fig. 6).

Other more catastrophic failures (e.g. longitudinal rips) having sudden and random character are an object of separate research. Special devices preventing their occurrence and reducing their extent and costs are being developed and soon will be implemented and integrated with diagnostic device being developed.

Condition monitoring of steel cord belts using new described here device can additionally be used to prevent transverse belt rapture in weakened by cables cuts cross-sections of conveyor belts. This approach is described in separate paper [32].

Integrated approach used in belt monitoring approach and working out diagnostic device developed by Wroclaw team can be successfully implemented in non stationary operations of belt conveyors in Polish mines.

All information about current stage of project development can be found on the special web page devoted to the NCBiR programme [33].

Acknowledgments This project has been carried out as part of the Applied Research Programme, path A entitled: *An intelligent system for the automatic examination and continuous diagnosis of the condition of conveyor belts.*

References

1. Jurdziak L, Blazej R (2010) Estimation of costs of conveyor belts operation in a mine using different belt replacement strategies and methods of their failures detection (in Polish), Cuprum, no. 4, pp 5–18
2. Jurdziak L, Blazej R (2014) Estimation of belt replacement cost in underground mine, taking into account the consequences of belt failures and implementation of preventive devices (in Polish). In: Proceedings of the XIII underground school of exploitation, Cracow, 24–28 Feb, Instytut Gospodarki Surowcami Mineralnymi i Energią PAN, pp 1–11
3. Jurdziak L (1998) Application of linguistic variables to determination of belt wear degree—method of scheduling conveyor belts for replacement. In: Proceedings of the 5th international symposium of continuous surface mining (ISCSM). Wroclaw, 26–29 May, OficynaWydaw. PWroc., pp 181–188
4. Jurdziak L (2000) The conveyor belt wear index and its application in belts replacement policy. Mine planning and equipment selection 2000. In: Balkema AA (ed) Proceedings of the ninth international symposium on mine planning and equipment selection, Athens, 6–9 Nov, pp 589–594
5. Dalkowski BT, Jurdziak L, Kawalec W (1990) Personnel computer system for maintenance management of belt conveyor systems. In: Proceedings of the XXII international symposium on the application of computers and operations research in the mineral industry (APCOM'90), 17–21 Sept
6. Jurdziak L (1998) Belt management in mines—actual state and perspectives (in Polish). Górnictwo Odkrywkowe (Opencast Mining) 40(5/6):63–81
7. Kacprzak M, Kulinowski P, Wędrychowski D (2011) Computerized information system used for management of mining belt conveyors operation. Eksploatacja i Niezawodnosc (Maintenance and Reliability) 2:81–93
8. Stefaniak P, Zimroz R, Krol R, Gorniak-Zimroz J, Bartelmus W, Hardygora M (2012) Some remarks on using condition monitoring for spatially distributed mechanical system belt conveyor network in underground mine—a case study. Condition monitoring of machinery in

non-stationary operations. In: Fakhfakh T et al (ed) Proceedings of the 2nd international conference "Condition monitoring of machinery in non-stationary operations", CMMNO' 2012. Springer, Heidelberg, pp 497–507
9. Jurdziak L (2005) Analysis of steel cord belt failures intensity in the Turów lignite mine (in Polish). Gornictwo Odkrywkowe (Opencast Mining) 47(4/5):38–46
10. Blazej R, Jurdziak L, Zimroz R (2011) Need for developing in-house diagnostic equipment for automatic assessment of condition of conveyor belts in opencast mines (in Polish). Gornictwo i Geoinzynieria (Mining and Geoengineering). R. 35, no. 3/1, pp 63–71
11. Blazej R, Zimroz R, Jurdziak L, Hardygora M, Kawalec W (2014) Conveyor belt condition evaluation via non-destructive testing techniques. In: Drebenstedt C, Singhal R (eds) Mine planning and equipment selection: proceedings of the 22nd MPES conference, Dresden, Germany, vol. 2, 14–19 Oct 2013, Springer, Berlin, pp 1119–1126
12. Blazej R, Zimroz R, Nowak R, Grzyb K, Kurp L (2010) Extension of the functionality of the EyeQ system for the diagnosis of steel cord belts (in Polish). Transport Przemyslowy i MaszynyRobocze (Industrial Transport and Heavy Machinery), no. 3, pp 24–28
13. Harrison A (1996) 15 years of conveyor belt nondestructive evaluation, bulk solids handling 16/1
14. Blazej R, Jurdziak L (2011) Integrated diagnostic device for automatic assessment of conveyor belts condition. In: Proceedings of the 22nd World Mining Congress & Expo, 11–16 September, Istanbul-2011, vol 3. Sinasi Eskikaya, Ankara, pp 675–680
15. Bancroft B, Fromme Ch, Pilarski T (2003) Belt vision system for monitoring mechanical splices. In: Proceedings of Longwall USA international exhibition and conference 2003
16. Dworczynska M (2012) Modeling of volatility of load stream in systems of BWEs, belt conveyors and spreaders (in Polish, not published). Ph.D. thesis, Faculty of Geoengineering, Mining and Geology at Wroclaw University of Technology, Wroclaw
17. Jurdziak L, Hardygora M (2000) The effect of conveyor belt load upon belt durability. In: Balkema AA (ed) Proceedings of the 9th international symposium on mine planning and equipment selection, Athens, 6–9 Nov, pp 595–599
18. Kasztelewicz Z (2012) Multi bucket excavators and belt spreaders. Technology of operation (in Polish). Monography, AgencjaWydawniczo-Poligraficzna Art-Tekst, Kraków
19. Scheffzyk P, Jahn W (2004) Modern technology in belt conveyor drives (in Polish). Transport Przemysłowy (Industrial Transport) 3(17)
20. Jurdziak L (2006) Methodology of BWE efficiency analysis for power reduction of conveyor drives. In: Proceedings of the 8th international symposium of continuous surface mining ISCSM 2006. 24–27 Sept, Aachen, Mainz, pp 125–131 (2006)
21. Jurdziak L, Hardygora M (1995) Determination of the distribution function of conveyor belt operating time based on the belt model. In: Proceedings of the fourth international symposium on mine planing and equipment selection, Calgary, Canada, 31 Oct–3 Nov, Balkema
22. Jurdziak L (1990) Determination of optimum time for the replacement of conveyor belts meant for reconditioning. In: Proceedings of the XXII international symposium on the application of computers and operations research in the mineral industry (APCOM'90), 17–21 Sept
23. Jurdziak L (1999) Influence of belts durability changes on conveyors operating costs (in Polish). Wiadomości Górnicze (Mining News) 50(10):424–431
24. Jurdziak L (2000) Preventive replacement strategies of conveyor belts (in Polish). Scientific Works of Institute of Mining, Wroclaw University of Technology, no. 26, series no. 89, pp 123–143
25. Zur T (1983) Die Grundlageneiner Berechnungs-methode zur Bestimmung der Lebensdauer von Fördergurten, Neue Bergbautechnik 13 Jg., Heft 9, Sept
26. Jurdziak L (1988) The effect of conveyor length on belts durability in underground mines (in Polish). Fundamental problems of mine transport, Scientific Papers of the Mining Engineering Faculty, Wroclaw University of Technology, no. 50, Conferences no. 11, Wroclaw
27. Hardygora M, Bartelmus W, Zimroz R, Krol R, Blazej R (2012) Maintenance, diagnostics and safety of belt conveyors in the operations. Transp Logistics (Belgrade) 6:351–354

28. Blazej R, Zimroz R (2013) A procedure of damage detection in conveyor belts using infrared thermography. In: XII international technical systems degradation conference, TSD, Liptovsky Mikulas, 3–6 April. Warszawa: Polskie Naukowo-Techniczne Towarzystwo Eksploatacyjne, pp 66–69
29. Blazej R, Jurdziak L, Zimroz R (2013) Novel approaches for processing of multi-channels NDT signals for damage detection in conveyor belts with steel cords. Key Eng Mater 569 (570):978–985
30. Blazej R (2011) A comparison of experimental studies of the EyeQ and ABCD systems for damage detection in conveyor belts with steel cords. In: X international technical systems degradation conference, Liptovsky Mikulas, 27–30 April. Polskie Naukowo-Techniczne Towarzystwo Eksploatacyjne; Lublin: Wydawnictwo-Drukarnia Liber Duo, pp 64–66
31. Blazej R, Jurdziak L, Zimroz R, Hardygora M, Kawalec W (2013) Investigations of conveyor belts condition in the Institute of Mining Engineering at Wroclaw University of Technology. In: 23rd World Mining Congress, Montreal, Canada, 11–15 Aug, Canadian Institute of Mining, Metallurgy and Petroleum, pp 1–9
32. Blazej R, Jurdziak L, Kawalec W (2014) Operational safety of steel-cord conveyor belts under non-stationary loadings. In: The 4th international conference on condition monitoring of machinery in non-stationary operations CMMNO14, 15–16 Dec, Lyon, France
33. http://diagbelt.pwr.edu.pl/